

DEVELOPMENT OF A NEW DESIGN METHOD TO DEFINE THE ROTATION CAPACITY OF STEEL HOLLOW SECTIONS

A thesis

Submitted in fulfillment of the requirements for the degree

Of

Doctor in Applied Sciences

From Liège University

And

Doctor in Civil Engineering

From Saint-Joseph University

By

ELSY SALOUMI

28 July 2016

MEMBERS OF THE JURY

M. Benjamin Dewals (President of the jury)
University of Liège, Department Argenco
Chemin des Chevreuils, 1 B52
B – 4000 LIEGE – Belgium

M. Jean-Pierre Jaspart (Supervisor)
University of Liège, Department Argenco
Chemin des Chevreuils, 1 B52
B – 4000 LIEGE – Belgium

M. Fadi Geara (Supervisor)
Saint-Joseph University USJ, Engineering Faculty ESIB
Technologies and Sciences Campus, Mar Roukoz, Mkalles
Riad El Solh, Beyrouth, 11 07 2050 – Lebanon

M. Nicolas Boissonnade (Supervisor)
Laval University, Civil and Water Engineering Department
Adrien Pouliot Bldg., Office 2928G
1065, Avenue de la Médecine
Quebec, Canada G1V 0A6

M. Graham Couchmann
Steel Construction Institute
Imperial College London, Silwood Park Campus
Buckhurst Rd, Ascot SL5 7QN
United Kingdom

M. Markus Knobloch
Bochum University
Faculty of Civil and Environmental Engineering
Department of steel, light and Composite Construction
Building IC 5-59
Universitätsstraße 150,
44801 Bochum, Germany

M. Jean-Francois Demonceau
University of Liège, Department Argenco
Chemin des Chevreuils, 1 B52
B – 4000 LIEGE – Belgium

‘Success is not final, failure is not fatal: it is the courage to continue that counts’

‘Winston Churchill’

ACKNOWLEDGMENTS

The achievement of my PhD thesis: “Development of a new design method to define the rotation capacity of steel hollow sections” could not have been possible without the valuable contribution of a large number of people:

I would like to express my appreciation and thanks to my supervisor Prof. Nicolas Boissonnade, for his guidance and support during my PhD thesis and for increasing my knowledge throughout his expertise. I would also like to thank him for encouraging and motivating me.

I also express my gratitude for my PhD directors, Prof. Jean-Pierre Jaspart and Prof. Fadi Geara for their encouragements and advices that were necessary for my progress through my doctoral program.

I would also like to thank Dr Tak-Ming Chan for offering me the opportunity to do an exchange program at the Hong Kong Polytechnic University. I thank him for his valuable comments that have allowed me to question my results and to achieve better analysis. I would also like to thank him for making my stay there very enjoyable.

I am very grateful for my colleagues and friends for all the wonderful moment we spent together that distracted me from work, especially though the difficult moments of the PhD.

Finally I would like to thank my family and my husband for their infinite support every step of the way, and for bearing with me during the most difficult times.

Elsy Saloumi, July 2016

ABSTRACT

The present PhD thesis is dedicated to the characterisation of hollow section shapes' rotational capacity. More precisely, the effort was made towards suggesting new ways to resort to plastic analysis, by defining a new and accurate proposition to characterise the rotation capacity R_{cap} of sections, which could be associated with the rotation demand of a structure R_{dem} . Therefore, the purpose of this thesis is to establish a direct dependence of the rotation capacity R_{cap} with a newly defined cross-section slenderness λ_{cs} . Hence, current design standards disregard the rotation demand of the structure and allow plastic analysis based on a plate slenderness limit.

To achieve this purpose, an experimental campaign was performed consisting in 23 bending tests on square and rectangular hollow sections tested in bending, in addition to 8 stub columns. Then, a numerical model based on the finite element software FINELg was calibrated to well represent these experimental tests, as well as cold-formed bending tests from literature. Based on these results, a good agreement between experimental and numerical results was shown and the numerical software was therefore validated.

Accordingly, since the numerical software was proved to well represent the bending behaviour of hollow beams, around 8000 finite element simulations were performed while varying sections dimensions, material properties and loading configuration. These results reported that actual standards limitations were inappropriate, and stricter values were proposed. Moreover, based on the numerical computations, a continuous curve capable of describing the rotation capacity of sections as a function of the cross-section slenderness was proposed. The production route, loading application and yield strength were identified as key parameters having a major impact on the rotation capacity of sections. Consequently, different curves were proposed for each parameter; based on these curves, the rotation capacity of the section could be compared to the rotation demand of a structure in order to obtain a practical, safe, and reliable design calculation.

TABLE OF CONTENT

ACKNOWLEDGEMENTS	v
ABSTRACT.....	vii
NOTATIONS	xiii
1 INTRODUCTION.....	18
2 STATE OF THE ART	22
2.1 Plastic resistance	22
2.1.1 Brief review on the history of plastic behaviour of steel	22
2.1.2 Plastic moment calculation:	24
2.1.3 Elastic and inelastic behaviour of plates	25
2.1.4 Definition of rotation capacity	28
2.2 Plastic analysis.....	29
2.2.1 Behaviour of a simply supported beam:	29
2.2.1.1 Beam under uniform moment	30
2.2.1.2 Beams under moment gradient:	31
2.2.2 Rotation capacity quantification and sensibility	32
2.2.3 Basics of plastic design	34
2.2.4 Required rotation capacity	35
2.3 Plastic design	39
2.3.1 Treatment and background of main design codes.....	39
2.3.1.1 Slenderness limits	39
2.3.1.2 Material requirements	44
2.3.2 Currents shortcoming and aim of the thesis.....	45
2.4 Available experimental data	47

3	EXPERIMENTAL PROGRAM.....	51
3.1	General description, objective and test program.....	51
3.1.1	Cross-sectional dimensions.....	53
3.1.2	Tensile tests.....	56
3.1.3	Stub column tests.....	59
3.2	Bending tests.....	62
3.2.1	3-point bending tests.....	62
3.2.2	4-point bending tests.....	68
3.2.3	Propped-cantilever centrally loaded.....	74
3.2.4	Propped-cantilever off-centrally loaded.....	82
3.3	Conclusions.....	85
4	DEVELOPMENT AND VALIDATION OF FINITE ELEMENT MODELS.....	87
4.1	General scope	87
4.2	Assessment toward documented test data	87
4.2.1	Validation against tests performed at the University of Applied Sciences of Western Switzerland – Fribourg.....	87
4.2.1.1	Mesh density.....	90
4.2.1.2	Support conditions.....	94
4.2.1.3	Introduction of loading.....	96
4.2.1.4	Sensitivity to geometrical Imperfections.....	97
4.2.1.5	3-point and 4-point bending tests.....	101
4.2.1.6	Propped cantilever arrangements.....	107
4.2.2	Experimental tests performed at the University of Sydney.....	115
4.2.2.1	Numerical model characteristics.....	116
4.2.2.2	Validation of F.E. models.....	118
4.3	Conclusions.....	122
5	NUMERICAL INVESTIGATIONS.....	124

5.1 Modelling considerations.....	124
5.1.1 Material model for hot-formed and cold-formed tubes	124
5.1.2 Boundary conditions	128
5.2 Comprehensive analysis	129
5.2.1 Beam subject to a constant moment.....	129
5.2.2 Mesh density studies	133
5.2.3 Length variation sensitivity when constant moment is applied	137
5.2.4 Effect of residual stresses.....	145
5.2.5 Imperfection variation.....	150
5.2.6 Influence of yield stress to ultimate stress ratio.....	159
5.3 Parametric analysis.....	163
5.3.1 Parameters considered	163
5.3.2 Results.....	165
5.3.2.1 Hot-formed sections – Constant bending moment.....	165
5.3.2.2 Cold-formed sections – Constant bending moment.....	171
5.3.2.3 Hot-formed sections in 3-pt bending configuration.....	177
5.3.2.4 Cold-formed sections in 3-point bending configuration	187
5.4 Conclusions.....	190
6 PROPOSED DESIGN FORMULATIONS	192
6.1 Hot-formed sections, constant bending moment.....	193
6.2 Cold-formed sections, constant bending moment.....	200
6.3 Hot-formed sections, moment gradient.....	209
6.4 Cold-formed sections, moment gradient.....	212
6.5 Summary of recommendations.....	218
6.5.1 Hot-formed sections.....	218
6.5.2 Cold-formed sections	219

6.6 Worked example	220
6.6.1 Example 1	220
6.6.2 Example 2	221
6.7 Concluding remarks	222
7 CONCLUSIONS AND FUTURE STEPS.....	223
8 REFERENCES.....	227
9 LIST OF FIGURES	234
10 LIST OF TABLES.....	247
11 APPENDICES	249
11.1 APPENDIX 1.....	249
11.2 APPENDIX 2.....	255
11.3 APPENDIX 3.....	260

NOTATIONS

Abbreviations:

AISC	American Institute of Steel Construction
AS	Australian standard
CF	Cold-formed
CSM	Continuous Strength Method
EC3	Eurocode 3
EN	European Standard
FE	Finite Element
GMNIA	Geometrically, materially nonlinear analysis with imperfections
HF	Hot-formed
LBA	Linear buckling analysis
LVDT	Linear Variable Displacement Transducer
OIC	Overall Interaction Concept
PR_C	Propped cantilever centrally loaded
PR_O	Propped cantilever off-centrally loaded
RHS	Rectangular Hollow Section
SHS	Square Hollow Section
3pt	Three point bending configuration
4pt	Four point bending configuration

Latin letters:

A	Section's area
A_0	Original cross-sectional area
b	Section width

b_{mes}	Experimental average measured width of a section
D_M	Beam deflection at mid span
D_L	Beam average deflection at the loading points
E	Young's modulus of elasticity
E_t	Tangent modulus of steel
E_{LVDT}	Young's modulus from LVDTs
E_{SG}	Young's modulus from strain gauges
f	Stress
f_u	Material ultimate stress
$f_{u,corner}$	Material ultimate stress in the corner region of the section
f_y	Material yield stress
$f_{y,corner}$	Material yield stress in the corner region of the section
F	Applied force
$F_{ult,exp}$	Applied force at ultimate load for experimental tests
$F_{ult,FE}$	Applied force at ultimate load for numerical simulations
h	Section depth
h_{mes}	Experimental average measured depth of a section
I_y	Moment of inertia about the strong axis
k, k_σ	Plate buckling coefficient
L	Length
M_{crit}	Critical bending moment of a cross-section
M_{Ed}	Design value of the applied bending moment
M_{el}	Elastic cross-section resistance for pure bending moment
M_{pl}	Plastic cross-section resistance for pure bending moment
M_y	Bending moment about the strong axis (y-y)

M_{ult}	Bending moment at ultimate load
$M_{ult,span}$	Bending moment at ultimate load at span
$M_{ult,fixed\ end}$	Bending moment at ultimate load at the fixed-end
M_{max}	Maximum reached moment
N	Axial force
N_x	In plane stress according to x direction
$N_{pl,fy}$	Plastic cross-section resistance for pure axial force calculated from actual measured material yield stress
$N_{pl,fy=355}$	Plastic load for pure axial force calculated from nominal material yield stress that is equal to 355 N/mm ²
P_{ult}	Ultimate value of the applied load
$P_{ult,exp}$	Ultimate value of the applied load for experimental tests
$P_{ult,FE}$	Ultimate value of the applied load for numerical simulations
P_{pl}	Theoretical plastic collapse load of the system
P_y	Elastic load of the system
r	Corner radius at the neutral axis
r_e	External curvature radius
r_i	Internal curvature radius
R_{cap}	Rotation capacity of a section
R_{dem}	Rotation demand of a structure
R_{RESIST}	Resistance load multiplier
R_{STAB}	Critical load multiplier
$R_{STAB,CS}$	Critical load multiplier of a cross section
$R_{STAB,MB}$	Critical load multiplier of a member
t	Thickness
t_{mes}	Experimental average measured thickness of a section

t_f	thickness of the flange of an I section
t_w	thickness of the web of an I section
V_{Ed}	design shear force
$V_{pl,Rd}$	plastic design shear resistance
w	Deflection of local panel
W_{pl}	Plastic section modulus
W_{el}	Elastic section modulus
Greek letters:	
δ_c	Corrected stub column end-shortening
δ_{LVDt}	End-shortening recorded by LVDTs
ε	Yield factor equal to $\sqrt{\frac{235}{f_y}}$
ε_f	Elongation at failure
ε_y	Material yield strain
ε_{y2}	Material strain at end of the yield plateau
ε_u	Material strain at ultimate stress
ε_{50}	Elongation on a 50.8 mm gauge length
ϕ	Safety factor from AISC standard
γ_M	Safety factor from EC3 standard
θ	Beam's end rotation
θ_y	Yield rotation
θ_{pl}	Plastic rotation
θ_{pl2}	Beam's rotation after the ultimate load has been attained and when the plastic moment is reached again
θ_u	Beam's end rotation at ultimate load

$\theta_{u,a}$	Rotation at side a of the tested specimen at ultimate load
$\theta_{u,b}$	Rotation at side b of the tested specimen at ultimate load
λ_{rel}	Generalised overall relative slenderness
λ_{cs}	Cross-section slenderness
λ_p	Plate slenderness
κ	Curvature
κ_y	Yield curvature
κ_{ST}	Curvature at the beginning of strain hardening
κ_{LVDT}	Measured curvature from LVDTs measurements
κ_{gauges}	Measured curvature from strain gauges recording
σ	Stress
$\sigma_{0.2}$	0.2% proof stress
σ_{cr}	Critical stress
σ_{ult}	Ultimate stress
σ_y	Yield stress
ν	Poisson's ratio
v	Deflection
v_u	Deflection at ultimate load
$v_{u,a}$	Deflection under the loading point a of the tested specimen
$v_{u,b}$	Deflection under the loading point b of the tested specimen
χ	Buckling reduction factor
χ_{CS}	Cross-section reduction factor
χ_{CS+MB}	Member reduction factor

1 INTRODUCTION

Steel hollow sections are being more and more used in structural applications. This is due to both their aesthetic and static properties. Hence, hollow structural sections require less paint than open profile and also less maintenance cost since, for example, the water cannot accumulate on the flanges... Moreover, hollow sections possess a high torsional stiffness compared to that of wide flange beams and thus require less lateral-torsional restraints.

Nowadays, in order to take advantage of the full capacity of a structure, plastic design is starting to be more and more exploited mainly in the U.K. and North America. Structures loaded in bending, and where deflections are not significant, are the structures that benefit the most from plastic design.

Plastic analysis requires that a beam is able to attain its plastic moment M_{pl} and maintain it through a range of deformations, in order for the moment to be redistributed. This will allow a collapse mechanism to form without exhibiting local buckling in the cross sections.

This thesis is related to the rotational capacity of rectangular and square hollow sections. The main aim of this research work is to investigate new ways of defining the possibility to resort to a plastic analysis in practical design, and to improve current procedures and recommendations, in order to obtain a more consistent and mechanical approach.

Nowadays, major design standards allow designers to resort to a so-called “plastic analysis and design” on the sole (direct or indirect) determination of the rotation capacity of a section while disregarding the rotation demand of the structure. Furthermore, most codes suggest individual b / t ratios of the individual plates comprised within the section to give the cross-section overall response, regardless of many parameters such as moment distribution (gradient), level of shear, ultimate-to-yield stress, height-to-length ration, ductility reserves.... In addition, the section’s constituent plates are being considered under ideal support conditions, i.e. webs and flanges are assumed as pinned-pinned.

Current developments take place in the context of the development of the Overall Interaction Concept (O.I.C.) [1]. One of the main features of the O.I.C. is the generalised overall relative slenderness λ_{rel} (Equation 1.1), that allows to account for the behaviour of the whole cross-section, therefore taking into account its constituents’ plates interaction.

$$\lambda_{rel} = \sqrt{\frac{R_{RESIST}}{R_{STAB}}} \quad 1.1$$

R_{RESIST} represent the factor by which the initial loading has to be multiplied to reach the pure resistance limit, and R_{STAB} is the factor used to reach the buckling load of the ideal member (stability limit).

The O.I.C. is a new design approach that aims at a straightforward design check of the stability and resistance of steel members. Based on the use of a generalized relative slenderness λ_{rel} and so-called interaction buckling curves, it can be applied in a similar manner to cross-section and to member verifications. The relative slenderness value λ_{rel} would lead to the determination of a χ value called “reduction factor” that represents the penalty due to instability effects on the pure resistant behaviour. The O.I.C. steps and procedure is represented in Figure 1.1.

The O.I.C., among other things, is meant to remove the preliminary “Cross-section classification” design step, i.e. the classification of the cross-section into plastic (so-called “class 1” in European standards Eurocode 3), compact (class 2), semi-compact (class 3) or slender (class 4). This is achieved within the O.I.C. through the generalised overall relative slenderness λ_{rel} , and through associated cross-section interaction curves that lead to a smooth and continuous definition of the cross-sectional capacity. Consequently, the classification step becomes obsolete and disappears in the O.I.C. approach, avoiding many practical difficulties, inaccuracies and inconsistencies.

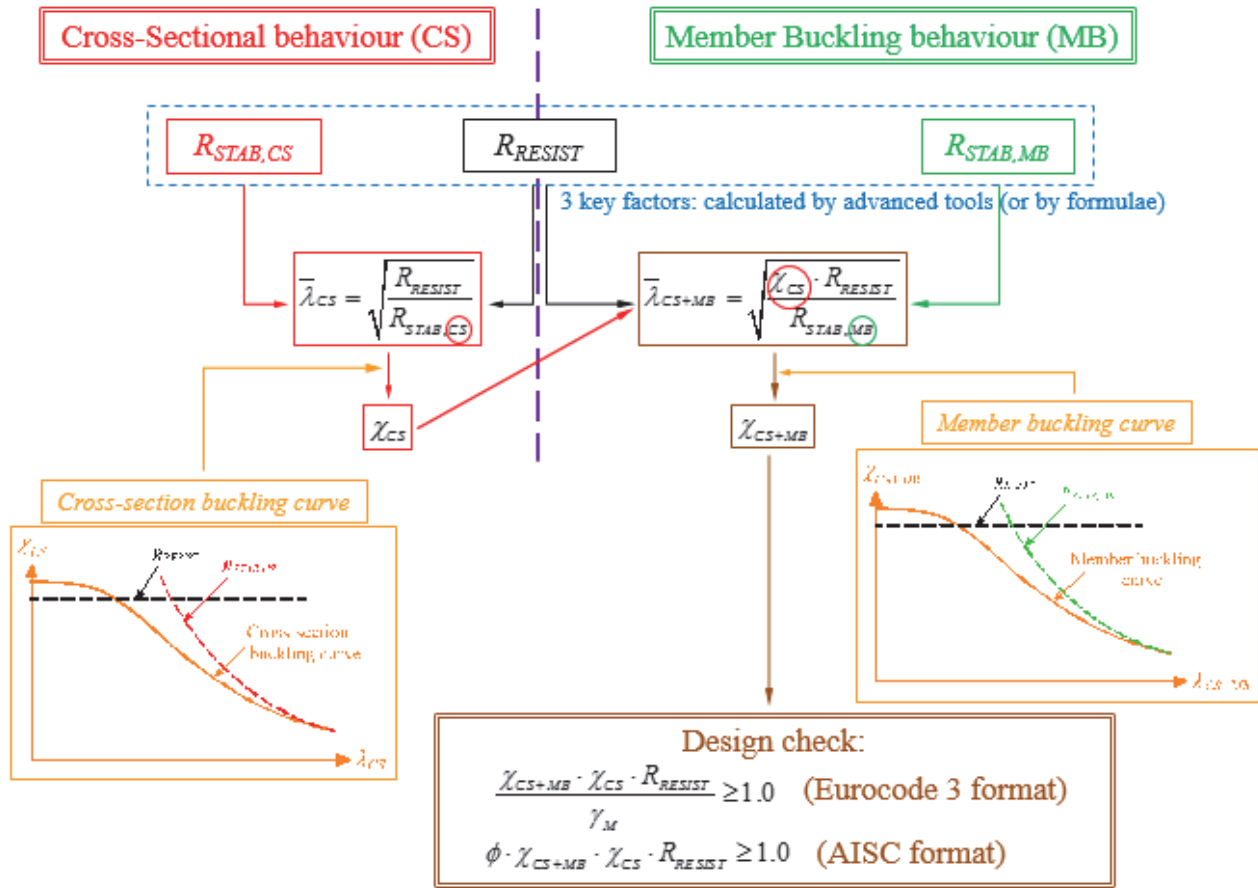


Figure 1.1 – OIC steps; χ_{CS} represents the cross-section reduction factor; χ_{CS+MB} represents the member reduction factor; γ_M and ϕ represent safety factors

With the disappearance of the classification system, the criterion allowing the designer to perform a plastic analysis (formerly allowed for class 1 sections) disappears as well. Therefore, the need to “re-introduce” such a criterion is clear, and is dealt with in this thesis.

In current work, the generalised overall relative slenderness λ_{rel} will be referred to as the cross-section slenderness λ_{CS} , since only the cross section behaviour of hollow sections is studied in simple bending. λ_{CS} therefore constitutes a measure of the cross-section sensitivity to local buckling.

The basic idea developed in the present thesis consists in an extended use of λ_{CS} factor to define two families of sections:

- sections allowing for plastic analysis and design (“class 1” sections, possessing sufficient rotational capacity for a plastic failure mechanism to develop);

- other sections for which the extent of local buckling precludes the attainment of sufficient ductile deformation for the development of a plastic mechanism, so that plastic analysis is to be avoided.

In other words, this thesis addresses the possibility to define limit values of λ_{CS} as a function of key parameters in order to replace the R_{dem} vs. R_{cap} criterion (see Figure 1.2), where R_{dem} is the rotation demand and R_{cap} is the rotation capacity.

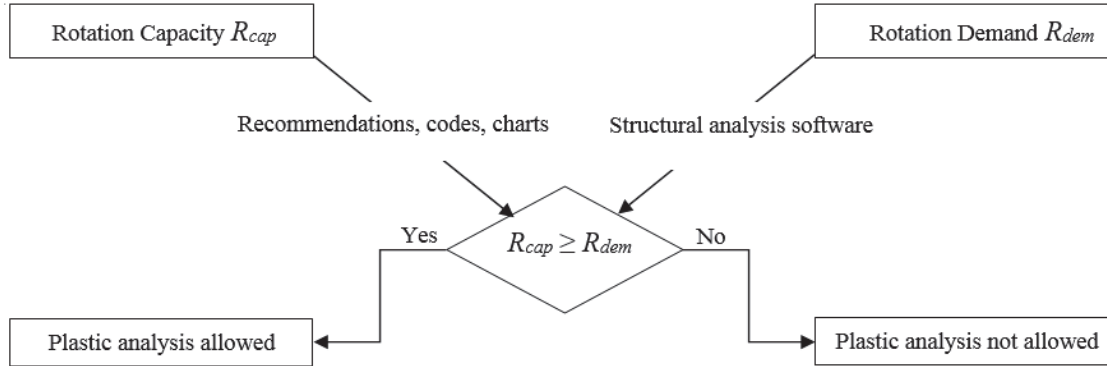


Figure 1.2 – Criterion to allow for plastic analysis

In this respect, the state of the art of present research will be presented along with current codes shortcoming to justify the aim of this thesis. Then, an experimental campaign to characterise the rotation capacity of beams will be detailed, and the numerical software will be calibrated against these tests, in order to use it extensively in a numerical campaign. The numerical campaign will aim at characterizing the cross-section rotational capacity for which many parameters play a significant role such as section slenderness, shear, yield strength, L/h ratio... After defining trends and lead parameters, the rotation capacity will be linked to the cross section slenderness λ_{CS} . In that way, sections that are capable to maintain their plastic moment to the minimum rotation requirements will be selected, i.e. depending on the rotation demand of a structure.

2 STATE OF THE ART

2.1 Plastic resistance

2.1.1 Brief review on the history of plastic behaviour of steel

In the nineteenth century, the design concept of steel structures was only based on the theory of elasticity. The basis of elastic design is attributed to Hooke's law (1635-1703), which states that stress is proportional to strain.

First tests were performed in order to affirm the elastic behaviour of steel beams, and the first yielding was considered as the limit load. According to Lay's notes [2], the theory of elasticity was confirmed due to two factors. The first factor being that the non-linear (inelastic) behaviour of the beam (after it reached its yield moment) was regarded as the beam failure. Hence, the point when first yielding occurred was considered as the limit load. On this subject, Lyse and Godfrey (1934) [3] wrote: *"Since the usefulness of beams is determined by the maximum load it can contain without excessive deflection, the determination of its yield point becomes the most important factor in testing.... The ultimate load has little significance beyond the fact that it is a measure of the toughness of the beam after it has lost its usefulness.... The yield point strength of the beam was used as the criterion for its load-carrying capacity"*. The second factor that led to confirm the elastic theory was that since open section were preliminary tested, the specimen was insufficiently braced against lateral torsional buckling which resulted in premature yielding (before the beam reached the plastic moment).

In order to demonstrate the applicability of plastic analysis to structural design problems, intensive research, both theoretical and experimental, was performed worldwide. The experimental work conducted was mainly on prototype structures mostly constituted by standard wide flange and I sections made from structural steel.

Ewing (1899) [4] was the first to mention the plastic theory and suggested a plastic distribution of the stress along the section. His suggestion remained a theory since no recorded tests were performed to confirm it. He stated that if the bending moment was increased beyond the elastic moment M_{el} , then: *"the outer layers of the beam are taking permanent set [yielding] while the inner layers are still following Hooke's Law... and any*

small addition to the stress produces a relatively very large amount of strain". Ewing [4] also determined the full plastic moment of a rectangular cross-section to be equal to $bh^2 / 4 f_y$, where b represents the width of the section, h the height and f_y the yield stress.

Probably, Meyer (1908) [5] conducted the first experiments to evidence the plastic behaviour of beams. Meyer tested simply supported beams of rectangular cross section with single point loads and noticed that once the plastic moment M_{pl} is reached, the deflection increases rapidly.

Kazinczy (1914) [6] may have been the first to suggest that due to the section plastification, a plastic hinge is developed. He tested H-shaped beams loaded uniformly and fixed on both ends by encasing them in concrete. He concluded that the system ultimate load is not reached until three plastic hinges are formed. He proposed to analyse static indeterminate structures with the use of a 'plastic solution'.

Kist (1920) [7] proposed the elastic-perfectly plastic law material (which is still used nowadays for hot formed steel) in order to calculate the ultimate load. In 1926, moment redistribution and the ultimate load theory was developed theoretically by Grüning (1926) [8].

The most known of the early researchers on plastic behaviour of beams was Maier-Leibnitz (1928, 1929) [9], [10]. He performed tests on simple, continuous and fixed-end beams and observed a considerable ductile behaviour. He then underwent some theoretical investigations based on the ideal plastic material law.

In 1930, Fritsche [11] was the first to derive equations for the plastic bending moment M_{pl} of rectangular and H-shaped cross-sections in the case of pure bending. He also concluded that for hot formed sections, no strain hardening is to be expected at low levels of strains and that 99% of the plastic moment M_{pl} is reached at a strain of 4-5%. Moreover, based on test by Meyer (1908) [5], Maier-Leibnitz (1928) [9] and Schaim (1930) [12], Fritsche concluded that the yield stress of mild steel represents the most critical parameter for the calculation of the ultimate load.

In 1931 and 1932, Girkmann [13] suggested a plastic design method for indeterminate frameworks that were based on his own tests, and wrote: *'Apart from the savings in weight that can be achieved, the use of this method makes it possible to reduce the maximum*

moments, to even out the differences in the thicknesses of the cross-sections required and hence to simplify the construction details and reduce their costs'.

Being inspired by the ultimate load test performed by Maier-Leibnitz, Baker and Roderick (1938, 1940) [14], [15] extended plastic analysis to complete structures, and tested small scales portal frames. They found that portal frames had a big reserve in strength compared to the point where the first yield is developed, and that large deflections only occur after a mechanism is formed. Their research resulted in the incorporation of the design of steel structures according to the ultimate load method in the British standard 449 in 1948.

Research into plastic design continued in Cambridge after World War 2. The first book on plastic theory of structural steel work was then published in 1956 by Baker & al [16]. This book summarised 10 years of research in the Cambridge University, the fundamental theorem of the ultimate load theory and provided a large list of references. By 1960, the plastic design method was widely accepted by the engineering community although some critics still remained.

In the 1970s, and even while some critics remained, the plastic theory was solid enough, and was promoted in the European recommendations for the plastic design of structural steel structures, mainly by Massonnet (1976) [17].

In the United States and at Lehigh University, a wide scope of investigation on plastic design of structures constructed from I-sections was performed in 1940-1960. The research program included tests on beams, large scale multi-story braced and unbraced frames, and developed design aids for use in plastic design. Results are mainly summarised by Driscoll et al. (1965) [18] and Galambos (1968) [19]. The Lehigh research forms the basis of the plastic design rules found in many steel design specifications in America and in Australia.

2.1.2 Plastic moment calculation:

When a beam is tested in bending, its deformation induce beam rotation denoted θ , curvature κ and strains ε . All these values that quantify the beam deformation are proportional and can be linked altogether. These deformations result in internal forces within the beam such as bending moments.

The plastic moment denoted M_{pl} is defined as the moment at which the entire cross section has reached its yield stress. As seen in Figure 2.1 for the case of a symmetrical cross-section

tested in bending, when strain hardening is reached, the plastic moment is exceeded. For hot-formed sections, strain hardening is initiated at high rotations values (also high strains and high curvatures); it is at this moment that the stress can exceed the yield stress. In the case of cold-formed RHS, strain hardening is reached directly after yielding; since there is no plastic plateau, the stress increases beyond the plastic moment M_{pl} at low strains.

In this thesis, for determining the plastic moment, steel is idealised as an elastic-perfectly plastic material for both hot-formed and cold-formed material law.

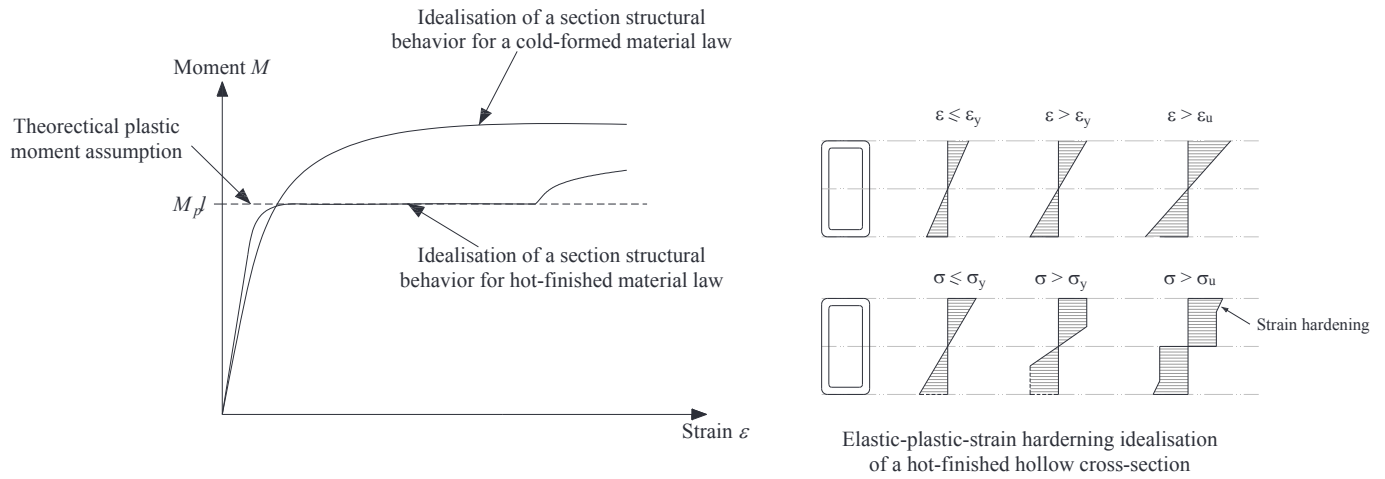


Figure 2.1 – Idealised moment-strain behaviour of a hollow cross-section

2.1.3 Elastic and inelastic behaviour of plates

To determine the ultimate capacity of a section, two primary concerns should be investigated: the first one deals with the strength of the section, i.e. the section plastic resistance defined in § 2.1.2; the second one deals with the ability of the section to support a specified load without undergoing instabilities. A brief review on the elastic and inelastic behaviour of plates is described hereafter.

To determine the elastic local buckling of thin rectangular plate, we can consider a long plate of width b and thickness t , with in plane stress N_x , as shown in Figure 2.2. The plate can buckle out-of-plane, with out-of-plane deflections w as represented in Figure 2.2.

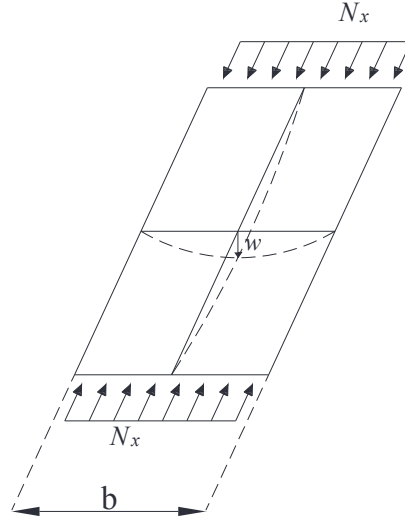


Figure 2.2 – Local buckling of a rectangular plate

The differential equation for elastic local buckling of the plate is given by Bryan (1891) [20], where E is the modulus of elasticity, ν is poisson's ratio:

$$\frac{Et^3}{12(1-\nu^2)} \left(\frac{\partial^4 w}{\partial x^4} + 2 \frac{\partial^4 w}{\partial x^2 \partial y^2} + \frac{\partial^4 w}{\partial y^4} \right) = -N_x \frac{\partial^2 w}{\partial x^2} \quad 2.1$$

The solution for the elastic local buckling stress σ_{cr} is given by:

$$\sigma_{cr} = \frac{k\pi^2 E}{12(1-\nu^2)(b/t)^2} = \frac{H^2}{(b/t)^2} \quad 2.2$$

Where k is the plate buckling coefficient which depends on the nature of the stress distribution across the plate and on the support conditions of the plate. Figure 2.3 shows the k values for simply supported plates subject to compression or bending. These two loading cases represent the cases of flanges and webs of rectangular and square hollow sections (RHS and SHS).

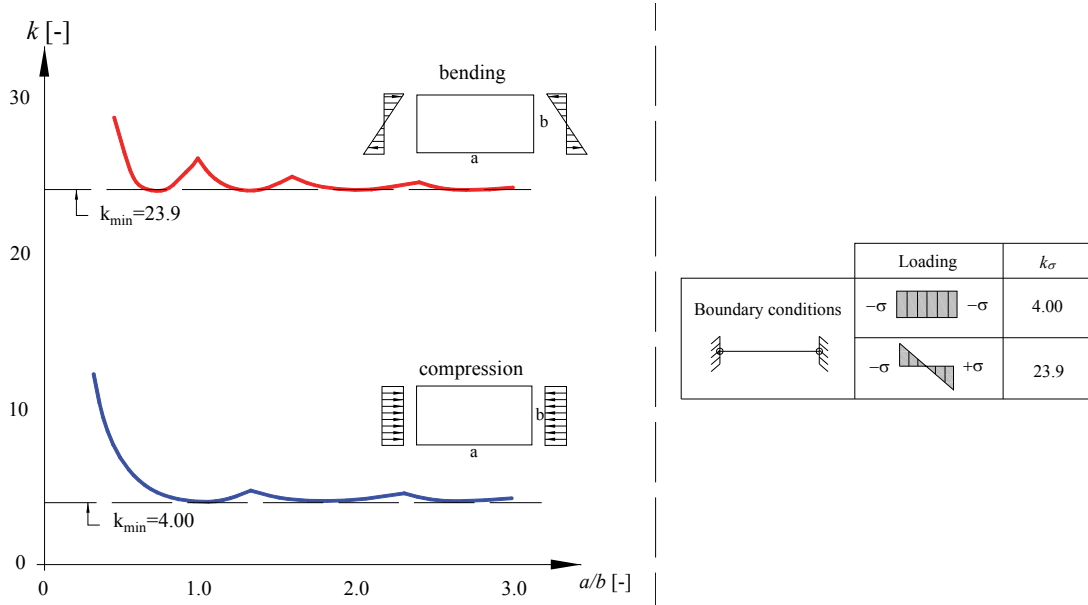


Figure 2.3 – Plate buckling coefficient

During the yielding process the material is heterogeneous since yielding takes place in so-called slip bands; the strain jumps from the yield strain to that at the beginning of strain hardening. Because of the yielding process, the material cannot be expected to remain isotropic. Therefore, general expressions for the buckling strength are derived assuming the material to have become orthogonally anisotropic [21]. When all the material has been strained to the strain hardening range, the material again becomes homogeneous. The differential equation that describes the inelastic local buckling load for thin rectangular plate subject to compression in the x direction may be written as given in Equation 2.3:

$$\left(\tau \frac{\partial^4 w}{\partial x^4} + 2\sqrt{\tau} \frac{\partial^4 w}{\partial x^2 \partial y^2} + \frac{\partial^4 w}{\partial y^4} \right) + \frac{N_x t}{D} \frac{\partial^2 w}{\partial x^2} = 0 \quad 2.3$$

Where $\tau = E_t / E$ (E_t is the tangent modulus of steel), and $D = \frac{Et^3}{12(1-\nu^2)}$

There are many other sources of information on elastic and inelastic local buckling of plates. Bleich (1952) [22], Haaijer (1956) [21], Galambos (1968) [19], Johnston (1976) [23], Ostapenko (1983) [24], and Timoshenko & Gere (1969) [25] provide significant summaries of plate local buckling.

2.1.4 Definition of rotation capacity

The capacity of a section has been exposed before; here, ways to define their reserve in ductility are investigated. This is made through the definition of the rotation capacity R_{cap} of a section, which is a mean to quantify the reserve in ductility of a section.

In the practice of plastic design of structures, ductility is defined as the capacity of a structure to undergo deformations after reaching its initial yield without any significant reduction in its ultimate strength. Hence, a steel beam cannot sustain infinite curvature, so, at a certain curvature, failure occurs. The most common mode of failure is local instability (buckling) of the plate elements in the section. The rotation capacity R_{cap} is defined as in Equation 2.4, where θ represents the beam end sections' rotation and its limit values θ_{pl} , θ_u and θ_{pl2} are defined in Figure 2.4 below. θ_{pl2} is the limiting rotation at which the moment drops below M_{pl} .

$$R_{cap} = \frac{\theta_{pl2} - \theta_{pl}}{\theta_{pl}} = \frac{\theta_{pl2}}{\theta_{pl}} - 1 \quad 2.4$$

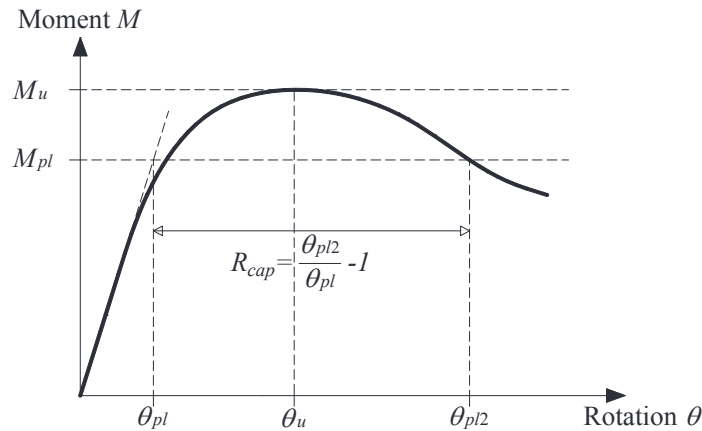


Figure 2.4 – Generalized moment-rotation curve and definition of the rotation capacity

Moreover, some beams may fail before reaching the yield moment or the plastic moment. The rotation capacity R_{cap} is only calculated once the plastic moment is reached. It is a measure of how much the plastic hinge can rotate before failure occurs. Figure 2.5 exhibits typical normalised moment-rotation curves for different sections. These sections are classified into groups depending on their behaviour under bending according to EC3 cross-section classification system. From Figure 2.5 we can see that a section is classified as

“class 2” if it can reach its plastic moment, but fail to attain a rotation capacity of 3; whereas a section is classified as “class 1” if it can reach a rotation capacity that is larger than 3.

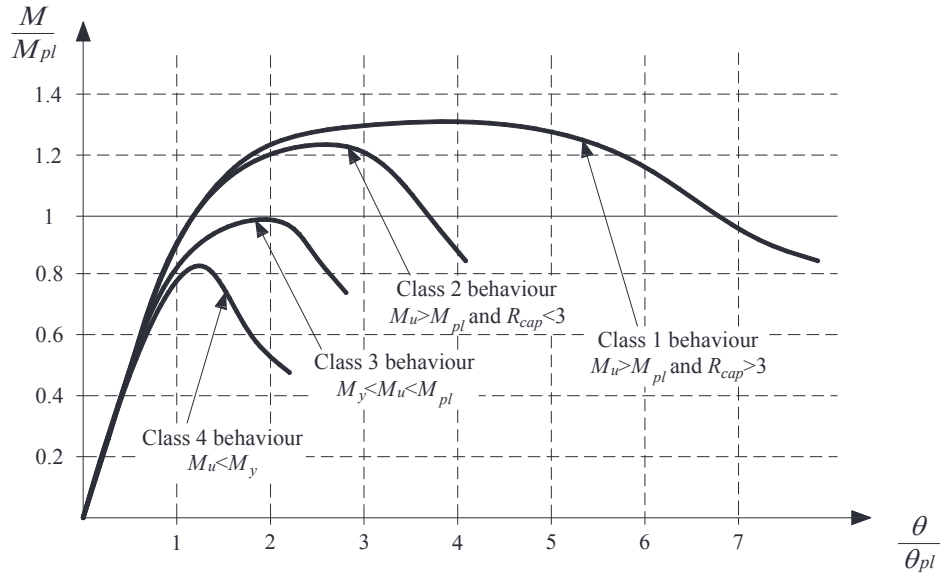


Figure 2.5 – Moment-rotation curve for different sections with the EC3 classification

2.2 Plastic analysis

In the previous section, we detailed the history of the plastic behaviour of steel and the cross-section capacity in term of resistance and instability for the case of bending. In the following section, the behaviour of simply supported beams will be detailed to explore how a beam with known cross-section properties will behave under a specified load and distribution. Then the basics of plastic design will be detailed along with the plastic rotation requirements for practical indeterminate structures.

2.2.1 Behaviour of a simply supported beam:

In this section, we present a brief review of the behaviour of beams loaded under major bending axis. Both cases of beams loaded under a moment gradient and the ones loaded under a uniform moment are presented. The plastification process is important for steel in plastic design, as it ensures that the plastic moments at yielded sections can be maintained for the cross section to sustain loading beyond its elastic limit. This section was mainly influenced by the paper of Kerfoot [26].

2.2.1.1 Beam under uniform moment

When a beam is loaded under uniform moment, a plastified region forms. Due to the discontinuous stress-strain relationship of steel, yielding takes place in small slip bands by a sudden jump of strain. Therefore yield lines occur at intervals along the region of uniform moment as shown in Figure 2.6 and additional deformation result in additional yield lines. The occurrence of yielding at discrete points results in discontinuities in the curvature. Some portions of the region of uniform moment are at curvature corresponding to the first yield κ_y and others are at the curvature corresponding to complete yield κ_{ST} (strain hardening).

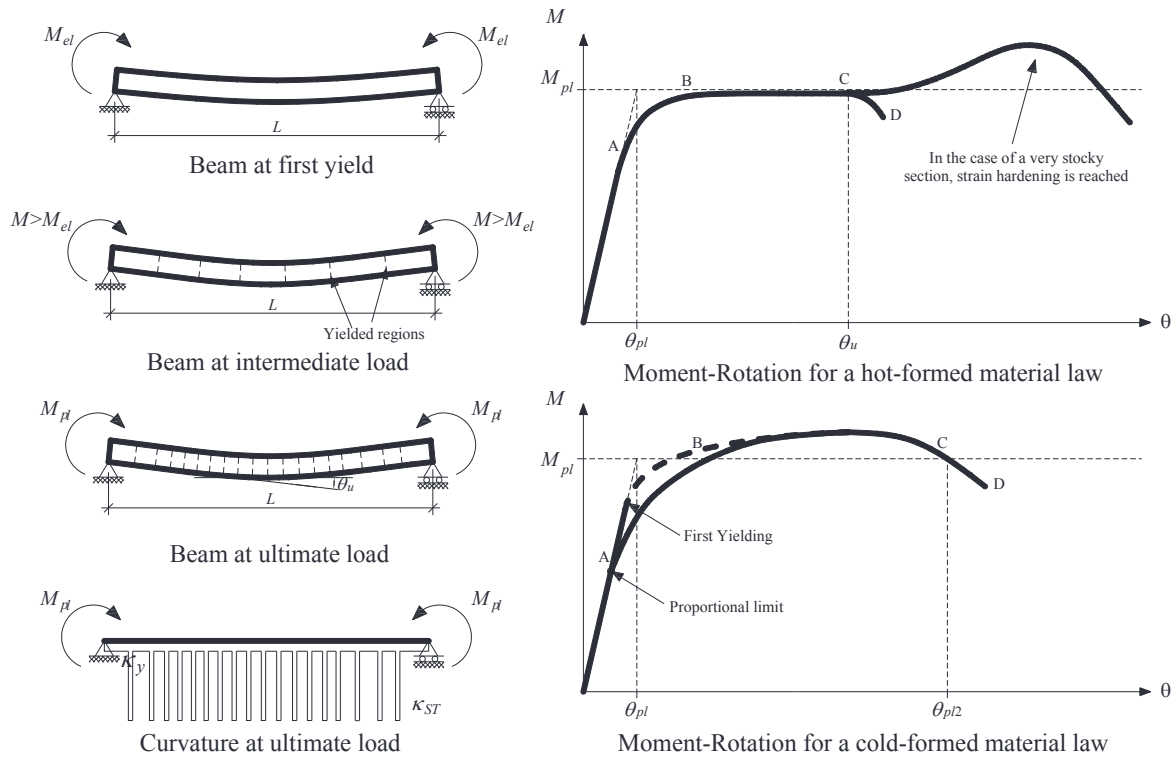


Figure 2.6 – Beam under uniform moment

Figure 2.6 shows the case of a beam under uniform moment. The applied load is plotted as a function of the rotation occurring on the beam end and consists in four parts:

- The elastic range (segment OA) in which the beam behaviour is linear
- The contained plastic flow region (segment AB) in which the curve becomes non-linear because of the effect of residual stresses, and of partial yielding. For cold formed cases, residual stresses are more important and affect the beam behaviour. For this case, the curve departs from the predicted curve at the proportional limit, which is

indicative of initial yielding of some fibres, and reveals a significant influence of residual stresses at the beginning of the plastic range.

- The segment BC in which large rotation occurs with little increase in load. For the case of the hot-formed material law, a plastic plateau is witnessed where the beam is yielded. In this range, the theoretical plastic moment is not fully reached due to some unyielded zones; for very stocky sections strain hardening occurs, and values beyond M_{pl} are reached. For cold formed sections, and since the material law exhibits a rounded response, the moment-rotation curve exhibits this same tendency and moments beyond M_{pl} are reached.
- The unloading region (segment DC) where the reduction in load is accompanied by large buckling of the individual plate elements of the section.
- For beams under uniform moment, the moment remains constant at M_{pl} until the average strain in the compressive flange reaches the strain hardening strain ε_{ST} value along the entire region of the uniform moment. Only then can the steel strain harden and the moment can exceed M_{pl} [27].

The rotation capacity of this beam is the difference in rotation between point A and C. It is the portion of the curve in which the plastic moment M_{pl} is exceeded.

Since hot-formed sections only achieve the plastic moment at high strains, due to their very large yield plateau, Stranghöner [28], Lay & Galambos [29], Sedlacek [30] and Chan & Gardner [31] based the rotation capacity on achieving 95% of the plastic moment.

2.2.1.2 Beams under moment gradient:

The behaviour of the beam under moment gradient differs significantly from that of a uniform moment distribution. In the moment gradient case, due to the stress-strain relationship of the material, a discontinuity of the curvature function is witnessed at the boundaries of the yielded zone (Figure 2.7). The strain, and thus the curvature, are at excess of the strain hardening value over the entire yielded region.

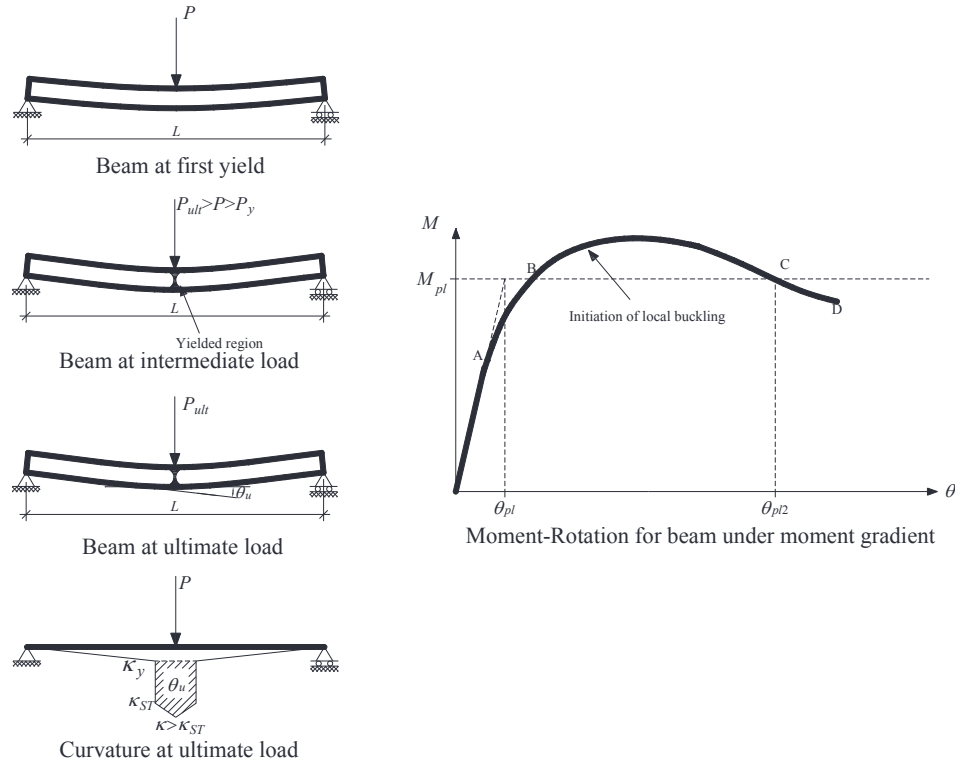


Figure 2.7 – Beam under moment gradient

The Moment rotation curve represents the influence of residual stresses, the shape factor, and strain hardening. Hence yielding start to occur at point A because of the presence of residual stresses which cause a slight reduction in stiffness. Then, the rotation start to increase rapidly once the plastic moment is reached and local buckling is observed. However, local buckling does not induce strength degradation, but the moment continues to increase. Under a moment gradient, yielding of the beam is confined to the region of maximum moment and cannot spread along the length of the beam unless the moment increases. Therefore, as soon as the plastic moment M_{pl} is reached, the steel strain hardens and the load can be increased and yielding can spread along the length. The onset of local buckling is only initiated when the compression flange has yielded over a length sufficient to form a buckled shape, and will continue to increase until the yielded length is equal to a full local buckling wavelength.

2.2.2 Rotation capacity quantification and sensibility

The behaviour of beams under bending have been detailed before, and the beam response was seen to vary depending on the load introduction, in terms of ultimate capacity and of ductility

(i.e. rotation capacity); therefore, ways to quantify and assess the sensibility of the rotation capacity to different parameters is investigated.

To date, many Researchers developed equations to quantify the plastic rotation capacity of steel members. To cite a few, Lay and Galambos (1967) [32], Kemp (1984) [33], Kato (1989) [34], , Ziemian & al (1992) [35]... proposed analytical expression for determining the plastic rotation capacity of I and H sections.

Moreover, efforts were also made to experimentally define key parameters that affect the rotation capacity.

In 1969, Luckey & Adams [36] identified from experimental tests that a section possess reserve in strength even after the local buckling load has been reached.

Kuhlmann (1989) [37] indicated three governing parameters for the rotation capacity: the flange slenderness, the web stiffness and the steepness of the moment gradient. She observed that the flange slenderness was the most important parameter. Kuhlmann also stated that higher rotation capacities were achieved for steep moment gradient. This observation was also reported theoretically by Lay & Galambos (1967) [32] and experimentally by Stranghoner & al (1994) [38].

Moreover, Kuhlmann [37], Ricles & al [39] and Wang & al [40] indicated that the yield to ultimate strength ratio of the material (also named strain hardening modulus) improves the postbuckling behaviour.

Wilkinson (1999) [41] assessed the plastic behaviour of cold formed rectangular hollow sections and found that class 1 slenderness limit for RHS were unconservative and proposed a new limit that incorporates flange-web interaction. He also found that the magnitude of the imperfection had an unexpectedly significant impact on the rotation capacity especially for stockier sections.

Boeraeve & Lognard (1993) [42] also stated that the initial geometrical imperfections of a beam influence the moment rotation curve and the plastic hinge formation mainly in its decreasing part (after the maximum bending moment has been reached).

More recently, the trend to define the rotation capacity of sections has been mainly investigated through numerical (finite element) methods. Current developments that consist

in determining the inelastic deformation capacity of a section are mainly developed as a preliminary step aimed to calculate the moment capacity of a section.

Shiffraw and Schafer (2007) [43] presented a relationship between the ultimate strain ε_u to the yield strains ε_y ratio and the cross-section slenderness for the case of pure bending. This method was used for the calculation of the inelastic moment capacity of cold-formed members, considering the influence of local buckling.

Moreover, strain based approaches have also been extensively developed for stainless steel and extended to carbon steel at Imperial college and resulted in the continuous strain method CSM [44]. The CSM features two key components: a base curve that defines the level of strain that a cross-section can carry and a material model that, combined with the proposed strain curve, is used to determine the cross-section resistance.

2.2.3 Basics of plastic design

Following the characterisation of the rotation capacity of sections, the rotation demand of indeterminate structures should be investigated in order to define recommendations to permit the use of a plastic analysis. Sections that are capable to maintain their plastic moment to the minimum rotation requirements would be eligible for plastic design. In this section, methods to define the plastic demand of structures are briefly detailed.

For a statically indeterminate structure, failure does not necessarily occur when the plastic moment is reached at a certain position. However, at this location, a plastic hinge is formed that maintain this plastic moment and undergo rotation so that loading is transferred to other parts of the structure. The structure fails when a collapse mechanism forms, that is when there is a sufficient number of plastic hinges.

The general methods to find the plastic limit load of a structure are based on two fundamental theorems: i) the lower bound, or Static theorem, where the load factor is computed based on an arbitrarily assumed bending moment diagram, due to external applied loading, and on the fact that the plastic moment M_{pl} is nowhere exceeded; ii) The upper bound, or Kinematic theorem, where the load factor is computed on the basis of an arbitrarily assumed mechanism.

The most commonly used analytical method for plastic analysis of indeterminate structures consists in the virtual work method. This method consists in equating the external work

(produced by loading) to the internal work (produced by the plastic moment at the plastic hinge), during a virtual movement of the collapse mechanism.

In order to perform a plastic analysis of a structure, many assumptions are made in the virtual work procedure:

- It is assumed that no instabilities can occur in term of plate buckling or global buckling of the beams or structure.
- The elastic deformations of the beam are disregarded.
- The hinge is considered of zero width, thus, the curvature is assumed infinite at the plastic hinge location.
- Strain hardening is disregarded. This lead to the assumption that the plastic moment is never exceeded (the reserve in strength from strain hardening is ignored), and that plastic hinges rotate with zero flexural stiffness. This approximation is however safe sided and generally induces small errors as stated by Neal (1977) [45].
- The plastic moment value of a section is not influenced by normal force or by high level of stress concentration induced by point loads.
- Second order effects due to the formation of hinges are disregarded.
- Initial geometrical imperfection are ignored.

Following these analytical and manual methods, early development of plasticity problems in a general finite element approach started in the late sixties. Nowadays, mathematical programming methods have become an important area of research in engineering plasticity. However, computer programs for plastic analysis of framed structures have been written as specialist programs and are consequently not available commercially. Therefore, very few are being used for daily routine design [46].

2.2.4 Required rotation capacity

In this section, the rotation demand of structures is investigated. Plastic rotation starts when a section reaches its plastic moment. Then, plastic hinges must be able to rotate a certain amount in order to redistribute the bending moment, and eventually form a plastic collapse mechanism in a particular structural situation. This rotation for which the plastic moment is maintained is called the rotation capacity requirement (or rotation demand). The required hinge rotation depends on the nature of the loading, the properties of the section, the structure

geometry and so on. Analytical studies have been performed throughout the years to determine maximum plastic rotation requirements for practical structures.

Kerfoot (1965) [26] analysed wide flange beams with three span and two point loadings per span. He found that only in extreme cases a rotation capacity greater than $M_{pl}L/EI$, where L is the span length, would be required to form a plastic collapse mechanism. Kerfoot replaced the term $M_{pl}L/EI$ with the term $2\varepsilon_y SL/d$ in order to show that the rotation capacity required to form a mechanism, is directly proportional to the yield strain and to the length-to-depth ratio (where d is the height of the section, S is the shape factor defined as $S = M_{pl}/M_{el}$ and ε_y is the yield strain). Hence, Kerfoot showed that a beam with high strength steel would require more rotation in order to form a plastic mechanism.

Driscoll (1958) [47] considered three span beams with distributed loads and extended the analysis to frames. He stated that higher rotations were required for multi-span frames than for single-span frames. This is expected in highly redundant structures, since a more extensive redistribution of moment is required in order for many hinges to form.

Moreover, for a highly redundant structure, the load-deflection curve converges towards the maximum load with large deflections. It happens that large rotations are sometimes required from some of the hinges to only create small increases in the capacity of the structure. Driscoll (1958) [47] analysed a double frame structure with dead loads and wind loads as represented in Figure 2.8. Wilkinson [41] summarised his results and stated that: *“at the ultimate load and formation of the plastic collapse mechanism, the first hinge had to rotate $1.52 M_{pl}L/EI$. At 98% of the ultimate load, the first hinge had rotated $0.54 M_{pl}L/EI$. In design situations, achieving slightly under the calculated maximum load is acceptable, and therefore the practical rotation capacity requirements can be less than the very large theoretical values of rotation calculated in some highly redundant frames.”*

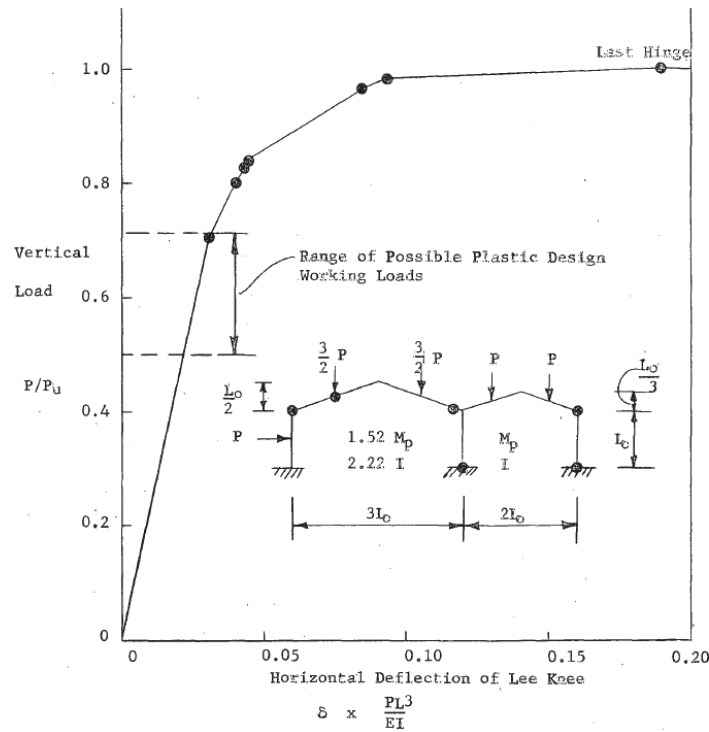


Figure 2.8 – Theoretical load-deflection curve for two-span pitched frame [47]

Since the required rotation capacity differ according to the loading and geometry of a structure and since the calculation of this value for complex structures can sometimes be complicated, time consuming and unreliable, as stated by Galambos (1968) [27] and Yura et al. (1978) [48], a limit value that covers most common practical situations was established.

The Eurocode 3 Editorial Group [49] summaries the maximum rotation requirements for different systems after varying a set of parameters (see Figure 2.9). They found that a value of $R_{dem} = 3$ was suitable, and was therefore chosen to derive the b/t ratios for I-sections. Yura, Galambos and Ravindra [48] also stated that the AISC specification based on $R_{dem} = 3$.

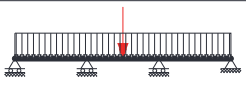
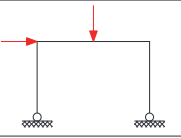
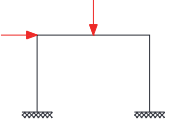
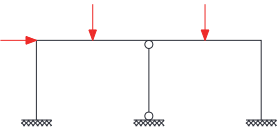
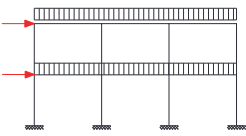
Structure	Rotation requirement
	3.0
	1.3
	2.5
	3.0
	2.5

Figure 2.9 – Rotation requirement for structures as summarised in [49]

Korol and Hudoba (1972) [50] considered hollow sections and stated that in order to cover most civil engineering structures for plastic design, a value of $R_{dem} = 4$ was recommended as the minimum necessary to ensure that a mechanism could form. Based on this recommendation, Hasan and Hancock [51] and Zhao and Hancock [52] used the limitation of $R_{dem} = 4$ to determine suitable plastic slenderness for the Australian Standard AS 4100.

Kuhlmann [37] analysed continuous beams on four supports loaded by a point load at mid-span, and suggested that a value of $R_{dem} = 2$ was sufficient for continuous beams. Neal [45] also gave the same recommendation for continuous beams.

Stranghöner, Sedlacek and Boeraeve [38] investigated the behaviour of hollow sections and highlighted that different rotation requirements are reached in this case, since the shape factor of hollow sections is different than I-sections. They found that $R_{dem} = 3$ was adequate for continuous beams.

As a general comment, it can be noted here that in seismic regions, greater rotation capacity needs to be provided for plastic analysis; however, this area is not the subject of this thesis.

As a summary, analysis was performed on the rotation capacity requirements for the most common structures and rotation of the order of 3 ~ 4 was found suitable and used in most standards for the derivation of plate slenderness limits.

It has also been outlined that the calculation of the required rotation capacity is difficult and time consuming. This process can also be sometimes unreliable (but generally always safe-sided), because some parameters that affect the results are neglected, and are listed below:

- Strain hardening is ignored. However, if included, smaller rotations capacities are required.
- In some extreme cases, the theoretical ideal hinge capacities are considerable due to zones of high moment gradient or to some extreme structures conception (single-story frames with very steep gables) where the ideal assumptions are invalid;
- Moreover, for extreme situations, it was shown that the rotation requirements are greatly diminished for a load just a few percent below the system peak load.
- Plastic analysis has been traditionally used under proportionally increasing loading. However, there are cases under which the traditional methods of plastic analysis cannot be applied (effect of foundation settlement, increasing temperature caused by fire...) [46].

Hence, the assumption made in current standards that defines the level of required rotation capacity is made for simplicity and rapidity of the design. This assumption ($R_{dem} = 3$ or 4) is based on traditional and simple structures where the number of plastic hinges is small before collapse occurs. Nevertheless, for highly redundant steel structures, it is more realistic to check the actual plastic rotation demand of the structure, because of the high number of plastic hinges that would occur and lead to large plastic rotations. The rotation demand should then be compared to rotation capacity of the section: $R_{dem} \leq R_{cap}$

2.3 Plastic design

2.3.1 Treatment and background of main design codes

2.3.1.1 Slenderness limits

Rules concerning local buckling are required for the design of structural steel members. Therefore, in any specification, the combination of cross-sectional dimensions and yield

strength are taken into account, in order to determine limits at which local buckling can be expected to occur for a designer. In other words, to prevent premature local buckling, slenderness limits for the plate elements in members have been established, and sections are considered as being constituted of individual flat plate elements. The elastic buckling stress given in Equation 2.2 can be rearranged in terms of the geometrical slenderness limit b/t :

$$\frac{b}{t} \leq \frac{H}{\sqrt{f_y}} \quad \text{or} \quad \frac{b}{t} \sqrt{f_y} \leq H \quad 2.5$$

The plate relative slenderness λ_p is defined as follows:

$$\lambda_p = \sqrt{\frac{f_y}{\sigma_{cr}}} = \sqrt{\frac{f_y}{k \cdot \frac{\pi^2 E}{12(1-\nu^2)} \cdot \left(\frac{t}{b}\right)^2}} \quad 2.6$$

Slenderness limit from different standard will be compared to point out the diversity among several specifications. The comparison will only be focused on rectangular sections subject to bending. The examined standards are listed below, and Table 2.1 summarises the terminology in these standards to avoid any confusion.

- (i) Eurocode 3 [53], (EC3), 1993, Common Unified code of practice for steel structures;
- (ii) AISC [54], (AISC), 2005, Specification for structural steel buildings;
- (iii) BS 5950 Part 1 [55], (BS 5950), 2000, Structural use of steelwork in building;
- (iv) DIN 18800 Teil 1 [56], (DIN 18 800), 1990, Steel structures, Design and construction;
- (v) AS 4100 [57], (AS 4100), 1998, SAA Steel structures Code.

Table 2.1 – Denomination of cross-section classes in each specification

Specification	Types of classes			
Eurocode 3	Class 1	Class 2	Class 3	Class 4
AISC	Compact	Non-compact		Slender
DIN 18800	P-P	E-P		E-E
BS 5950	Plastic	Compact	Semi-compact	Slender
AS 4100	Compact	Non-Compact		Slender

Since plastic design is the object of study in the present thesis, only the background of the limit between class 1 and 2 will be detailed hereafter. It is therefore reminded here, that this limit was based on the fact that a cross-section is able to maintain the yield stress for a

substantial amount of deformation to prevent premature local buckling, and hence allow moment redistribution and the formation of a plastic hinge.

Development of the plastic limit for plates in compression supported on both edges:

Haaiker & Thurlimann (1958) [58] first examined theoretically the problem of inelastic plate buckling under uniform compression, with the object of deriving plate buckling equation which is applicable to the strain-hardening range. The plastic limit for compressed hot-formed elements supported on two edges was determined for 36 ksi (248 MPa) steel while assuming an inelastic rotation capacity $R = 3$:

$$\frac{b-t}{t} \leq 32.3 \quad 2.7$$

Korol and Hudoba (1972) [50] investigated experimentally the behaviour of SHS, RHS and CHS in both hot-formed and cold-formed steel, with a total of 31 tests on single span and three span beams. Due to the lack of strain hardening and the high level of stress concentration induced by the load application method, most sections did not exceed the plastic moment calculated from measured properties. The proposed limit for RHS and SHS flanges was given for a rotation capacity of 4 and using the nominal yield stress guaranteed by the manufacturer:

$$\frac{b-2r_e}{t} \sqrt{\frac{f_y}{250}} \leq 25 \quad 2.8$$

The experimental work of Hasan and Hancock (1989) [51] and Zhao and Hancock (1991) [52], who performed bending tests of Grade C350 and C450 on cold-formed SHS and RHS under uniform moment, was combined; and the flange slenderness limit for plastic design assuming an inelastic rotation capacity $R = 4$, was given as:

$$\frac{b-2t}{t} \sqrt{\frac{f_y}{250}} \leq 30 \quad 2.9$$

Following the research work detailed before, slenderness limit have been defined in design standards. Table 2.2 gives the flange slenderness definition and plastic limits for square and rectangular hollow sections under major axis bending (flange is in compression) for Eurocode 3, AISC, DIN 18800, BS 5950 and AS 4100. It is to be noted here that only the

British standard BS 5950 takes into consideration the production route of the section, whether it is hot-rolled or cold-formed, and gives different slenderness limitations accordingly.

Table 2.2 – Plastic flange slenderness limits of RHS in bending

Specification	Fabrication process	Flange slenderness definition	Slenderness limits for plastic border
Eurocode 3	HF-CF	$\frac{b-2r_e}{t} \sqrt{\frac{f_y}{235}}$	33
AISC *	HF-CF	$\frac{b-2r_e}{t} \sqrt{\frac{f_y}{E}}$	1.12
DIN 18800	HF-CF	$\frac{b-2r_e}{t} \sqrt{\frac{f_y}{240}}$	32
BS 5950	HF	$\frac{b-3t}{t} \sqrt{\frac{f_y}{275}}$	$28 \text{ but } < 80 - \frac{b-3t}{t} \sqrt{\frac{275}{f_y}}$
	CF	$\frac{b-5t}{t} \sqrt{\frac{f_y}{275}}$	$26 \text{ but } < 72 - \frac{b-5t}{t} \sqrt{\frac{275}{f_y}}$
AS 4100	HF-CF	$\frac{b-2t}{t} \sqrt{\frac{f_y}{250}}$	30

*AISC considers $E = 29000 \text{ Ksi} (=200000 \text{ MPa})$

Development of the plastic limit for plates in bending supported on both edges:

Generally, in current design standards the same slenderness limits applies to the webs of RHS and I-sections. Most research on web slenderness limits consisted of tests of simple plates or I-sections. One can cite the main research performed: Lyse and Godfrey (1934) [3], Haaijer (1957) [59], and Haaijer and Thurlimann (1957) [60], Kerensky, Flint and Brown (1956) [61], Holtz and Kulak (1973, 1975) [62] [63], Perlynn and Kulak (1974) [64], Nash and Kulak (1976) [65], Horne (1979) [66], Dawe and Kulak (1986) [67], Della-Croce (1970) [68], Costley (1970) [69], Galambos (1976) [70], Edinger and Haaijer (1984) [71].

All of the previous research listed above indicates that the web slenderness limits are based on tests of I-sections. The slenderness limits in current design standards (see Table 2.3) are applicable to both RHS and I-sections, although the nature of the web restraint of an RHS is different to that of an I-section web: i) the centre of the flange of an I-section restrains the web, whereas the ends of the flange restrain the webs of an RHS, ii) the area of the two webs of an RHS consists of about 50 to 75 % of the total area of the section whereas for an I-

section the web is typically 35 - 45% of the total area, so the influence of the web is greater in RHS and SHS than in I-sections.

Also it can be noted that since the first manufactured RHS were either square or rectangular with low aspect ratios, thus, in bending, flange buckling would prevail before web buckling and therefore not much attention was given to this problem. Nowadays, since RHS have been produced with higher aspect ratios, a more global approach, that takes into account the flange web interaction and propose new limit to allow for plastic analysis, should be introduced. Hence, it is usually conservative to assume that the webs of RHS sections are simply along their edges, since the flanges normally provide some torsional restraints.

Table 2.3 present the web slenderness definition and plastic slenderness limits for SHS and RHS under bending for Eurocode 3, AISC, DIN 18800, BS 5950 and AS 4100.

Table 2.3 – Plastic web slenderness limits of RHS in bending

Specification	Fabrication process	web slenderness definition	Slenderness limits for plastic border
Eurocode 3	HF-CF	$\frac{h-2r_e}{t} \sqrt{\frac{f_y}{235}}$	72
AISC	HF-CF	$\frac{h-2r_e}{t} \sqrt{\frac{f_y}{E}}$	3.76
DIN 18800	HF-CF	$\frac{h-2r_e}{t} \sqrt{\frac{f_y}{240}}$	64
BS 5950	HF	$\frac{h-3t}{t} \sqrt{\frac{f_y}{275}}$	64
	CF	$\frac{h-5t}{t} \sqrt{\frac{f_y}{275}}$	56
AS 4100	HF-CF	$\frac{h-2t}{t} \sqrt{\frac{f_y}{250}}$	82



Different hypothesis and experiments lie behind the derivation of the limits for each standard which explain the different limitation in the codes. A more complete summary of limits in several steel design specifications and their background can be found in Bild & Kulak [72] and Wilkinson [41].

Since diverse definitions lie behind the flange and web slenderness limitations of the different standards, all values has been converted to the EC3 definition in order to be able to compare

the proposed limits. Table 2.4 shows the slenderness limit of the different standards according to the EC3 definition.

From Table 2.4, it can be shown that current standards display some disparities in their flange and web slenderness recommendations. It can also be pointed out that the AISC possesses the highest web slenderness limit in comparison with the other standards, while the AS 4100 has the lowest flange slenderness requirement. Based on these results that highlight the inconsistencies in the derivation of actual limits, new investigations should be performed to define more accurate propositions to allow the use of plastic design.

Table 2.4 – Class 1-2 slenderness limit according to EC3 definition

class 1-2 border according to EC3 definition $\Rightarrow \lambda_p = ?$					
Conditions	Eurocode 3	AISC	DIN 18800	BS 5950	AS 4100
	$33\varepsilon \Rightarrow$ $\lambda_p = 0.58$	$32.5\varepsilon \Rightarrow$ $\lambda_p = 0.57$	$30.8\varepsilon \Rightarrow$ $\lambda_p = 0.54$	HF: $30.3\varepsilon \Rightarrow$ $\lambda_p = 0.53$	$24.0\varepsilon \Rightarrow$ $\lambda_p = 0.42$
				CF: $28.1\varepsilon \Rightarrow$ $\lambda_p = 0.49$	
	$72\varepsilon \Rightarrow$ $\lambda_p = 0.52$	$109.6\varepsilon \Rightarrow$ $\lambda_p = 0.79$	$61.7\varepsilon \Rightarrow$ $\lambda_p = 0.44$	HF: $69.2\varepsilon \Rightarrow$ $\lambda_p = 0.50$	$65.6\varepsilon \Rightarrow$ $\lambda_p = 0.47$
				CF: $60.6\varepsilon \Rightarrow$ $\lambda_p = 0.44$	

2.3.1.2 Material requirements

In addition to the section slenderness specifications, current design standards have material ductility requirements in order for plastic analysis to be permitted. This is due to the fact that large strains are required so that moment is redistributed and a mechanism is formed. The material requirement of AISC, AS 4100 and Eurocode 3 design specifications are presented herein. These recommendations have been made following several investigations on the ductility requirement of the material for plastic design and their effect on the moment redistribution which are summarised by Wilkinson [41].

For the Eurocode 3, the ductility requirement is expressed in terms of limit for the f_u / f_y ratio (f_u being the ultimate tensile strength and f_y the yield strength), the elongation at failure

denoted ε_f on a gauge length of $5.65\sqrt{A_0}$ (A_0 is the original cross-sectional area), and the ultimate strain ε_u , where ε_u corresponds to the ultimate strength f_u

The limiting criteria for the three abovementioned values are the following:

$$\begin{aligned} f_u / f_y &\geq 1.2 \\ \varepsilon_f &\geq 15\% \\ \varepsilon_u / \varepsilon_y &\geq 20 \end{aligned}$$

Concerning the Australian standard, clause 4.5.2 of AS 4100 states the ductility conditions to be met for plastic design. These conditions can be summarised by the following requirements:

$$\begin{aligned} f_y &\leq 450 \text{ N} / \text{mm}^2 \\ f_u / f_y &\geq 1.2 \\ \varepsilon_f &\geq 15\% \end{aligned}$$

Moreover, AS 4100 restrict the use of plastic analysis to hot-formed steel and doubly symmetric I section. It also requires that the length of the yield plateau should be greater than $6\varepsilon_y$ and that the steel should exhibit strain hardening.

AISC only requires that the steel yield strength should be less than 65 Ksi to be eligible for plastic design ($f_y < 448 \text{ N/mm}^2$) (clause A5.1). In addition, and concerning the case of cold-formed section, clause A3.1.1a of AISC states that the requirements of ASTM A500 (“Standard” 1993) must also be met. ASTM A500 specifies that $\varepsilon_{50} \geq 21\%$ for Grade C steels (and slightly higher values for other steel grades), where ε_{50} is the elongation on a 50.8 mm gauge length.

2.3.2 Currents shortcoming and aim of the thesis

Current design standards have been shown to display many inconsistencies. A summary of the main shortcomings is detailed below:

Abovementioned design standards specify independent slenderness limits for flanges and webs, although many researchers have recommended slenderness limit that account for flange-web interaction.

To name a few, Kato (1989) [34] proposed an interaction formulae between web and flange slenderness to limit classes for I and H sections. For class 1 it was based on a rotation of 4 and the equation is given below:

$$\frac{\left(\frac{b}{t_f}\right)}{\left(\frac{181}{f_y}\right)} + \frac{\left(\frac{h}{t_w}\right)}{\left(\frac{1170}{\sqrt{f_y}}\right)} = 1 \text{ for ductility class 1 } (R_{dem} = 4) \quad 2.10$$

More researchers used experimental tests on I-sections to propose slenderness limit values that accounted for the flange-web interaction. Kemp (1985) [73], Kuhlmann (1989) [37], Daali & Korol (1995) [74]...

Stewart and Sivakumaran (1997) [75] used the finite strip method and proposed Class 1, 2 and 3 limits for I-section beams that accounted for flange-web interaction.

Wilkinson (1999) [41] studied cold-formed RHS and proposed a simple bi-linear interaction curve for the Class 1 limits to represent the flange-web interaction.

Seif and Schafer (2009, 2010) [76],[77] suggested equations for the plate buckling coefficient k as a function of the member geometry and loading conditions, that would represent the web-flange interaction.

Nevertheless, even though the connection between webs and flanges is clearly seen to provide some torsional restraint, and while many researchers have made propositions to account for this interaction, these recommendations are not yet incorporated in current design standards.

Moreover, current standards define web slenderness limits for class 1-2 border that are based on the behaviour of I-section, and has been applied to rectangular and square hollow section. This was previously stated not to be accurate since the restraint of webs of I and H sections is different from SHS and RHS.

Furthermore, different plate slenderness limitations are reached from web and flange slenderness values and highlight the inconsistencies in the derivation of the bounds of each standard.

In addition, the link between the rotation demand and the rotation capacity is disregarded, and the prescribed rotation demand on which all current limitations are based is defined from

simple and common structures. For very complex constructions, this value could be inappropriate and would jeopardize the safety of the structure.

Finally, current limitations have also been seen to be unconservative. Some sections, prescribed as class 1 in current design standards, experienced insufficient plastic rotations ([41], [40], [78]).

All these reasons justify the need to develop effective and accurate formulations to predict the rotation capacity of square and rectangular hollow sections for both hot-formed and cold-formed steel. Moreover, the rotation capacity should be linked to the rotation demand of a structure by verifying if the section is able to provide sufficient ductility. This procedure would could be more economical than current specifications for simple structures but definitely more accurate especially for very complex constructions.

Hence, and with the use of finite element software, the rotation capacity of hollow sections will be characterised and analytical formulations will be proposed to represent accurately the inelastic behaviour of hollow structural sections.

2.4 Available experimental data

Experimental data was collected for simply supported beams from many sources for hollow sections. A total number of 109 bending test were taken from Zhao & Hancock [79], Wilkinson & Hancock [80], Gardner & al [81], Wilkinson [41], Hasan & Hancoick [51], Rondal & al [82], Saloumi & al [83], Wang & al [40]. From present work (also reported in [83]), only the experimental data for RHS 150×100×8 was reported, since it was the only one that was not influenced by the loading introduction, and reached its plastic moment. The experimental database comprises different section geometries, material properties, tests setups (3-point and 4-point bending configuration), element lengths, loading introductions... Results are represented in Figure 2.10 and Figure 2.11; the normalised ultimate moment that a section can resist and its rotation capacity are shown as a function of the plate slenderness. Concerning the rotation capacity, the label “not reached” correspond to experimental tests where the moment rotation curve did not reach the plastic moment in its unloading path, i.e. after attaining its maximum load capacity (Figure 2.4). Collected data along with their corresponding references can be found in Appendix 1.

Table 2.5 – Collected bending test data for hollow sections

Source	Shape	Fabrication process	Number of tests	Test setup
Zhao & Hancock, 1991	RHS_SHS	CF	10	4-point
Wilkinson & Hancock, 1998	RHS_SHS	CF	44	4-point
Gardner, Saari, & Wang, 2010	RHS_SHS	CF-HF	6	3-point
Wilkinson, 1999	RHS	HF	2	4-point
Hasan & Hancock, 1989	RHS	CF	19	4-point
Stranghoner & al, 1995	SHS	CF	4	4-point
Saloumi et al, 2015	RHS	HF	2	3-point & 4-point
Wang et al, 2016	RHS_SHS	HF	22	3-point & 4-point

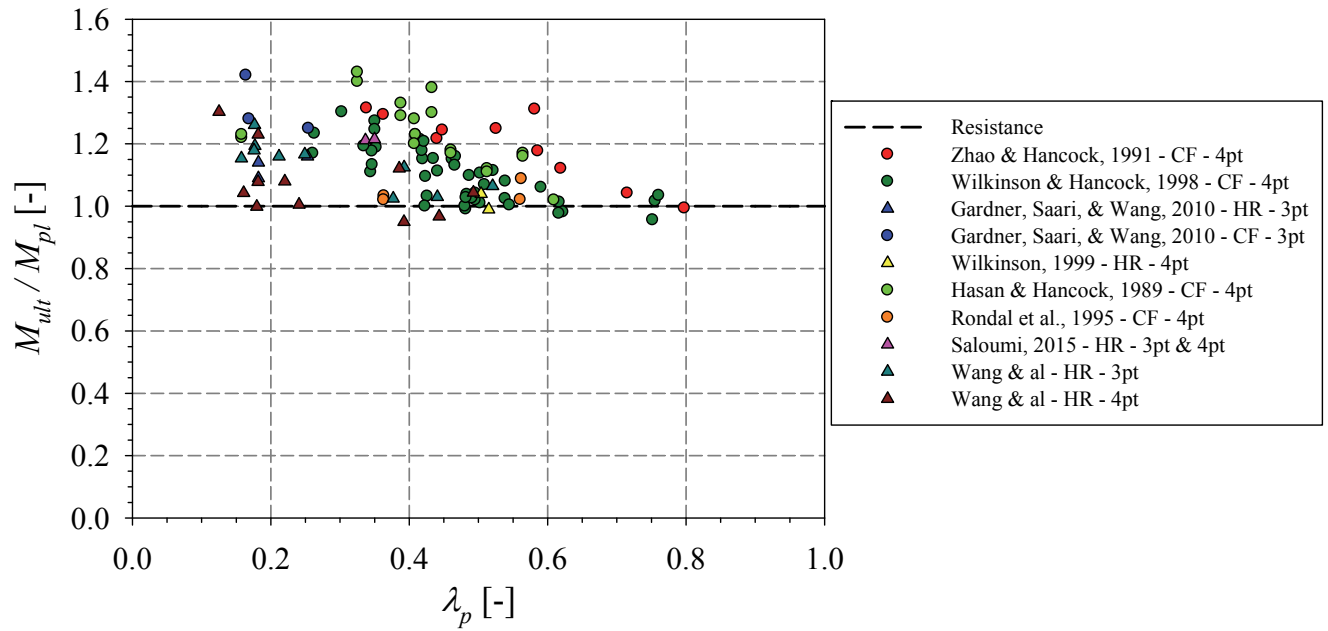


Figure 2.10 – Normalised ultimate as function of the plate slenderness from experimental data of hollow section

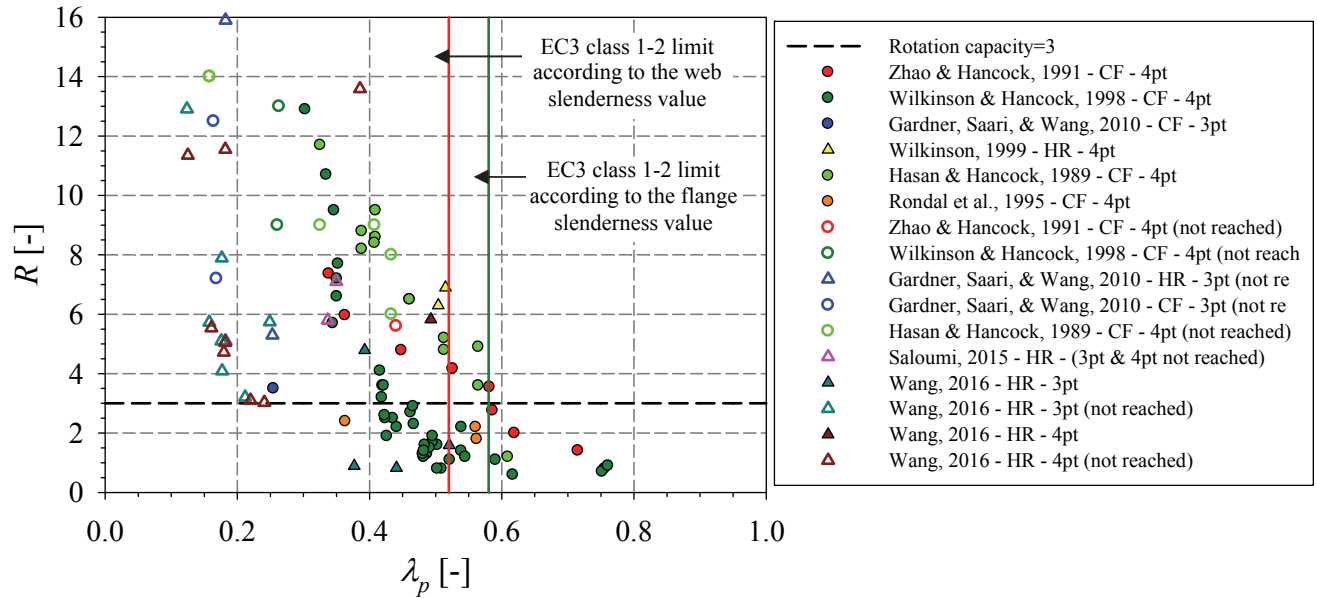


Figure 2.11 – Rotation capacity as function of the plate slenderness from experimental data of hollow section

Figure 2.11 displays a big scatter for the rotation capacity of hollow member; hence, for a same slenderness value, sections can display a difference in rotation capacity of the order of 10. Moreover, these experimental results highlight the need to investigate more the class 1-2 border since the current standards limitations are seen not to be appropriate. Thus, many sections although classified as class 1, fail to deliver the rotation capacity of 3. In addition, it can be clearly seen that the flange and web limitation result in different plate slenderness value. This highlights the lack of a consistent background to the derivation of the actual limits.

Moreover, some experimental data for open I and H section has been gathered from literature and are reported in Figure 2.12 and Figure 2.13. These figures enhance the fact that the current code recommendations should be revised and that the rotation capacity of experimental data present a big scatter with no clear tendencies. Experimental data has been collected from Sawyer [84], Lukey and Adams [85], Holtz and Kulak [62] [63], Perlynn and Kulak [64], Kuhlmann and Roik [86] [87] [88], Adams, Lay and Galambos [89] Dermott [90].

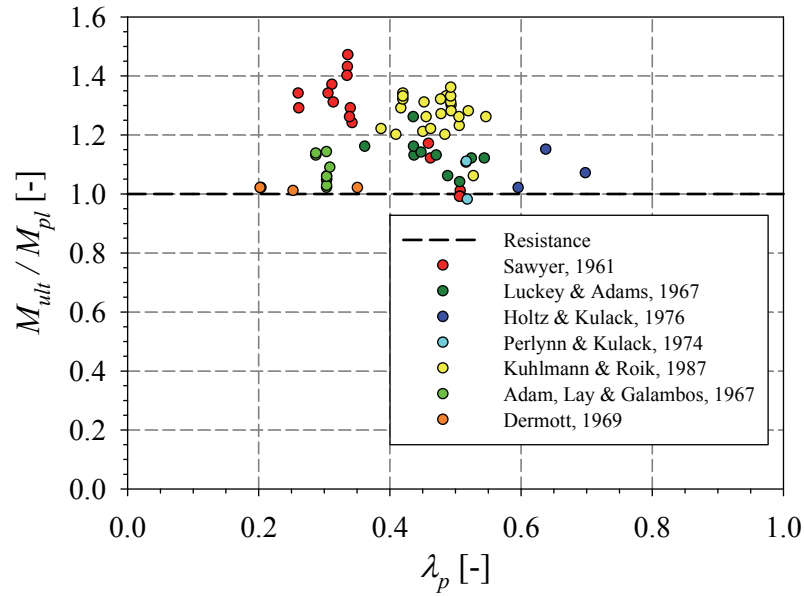


Figure 2.12 – Normalised ultimate as function of the plate slenderness from experimental data of open section

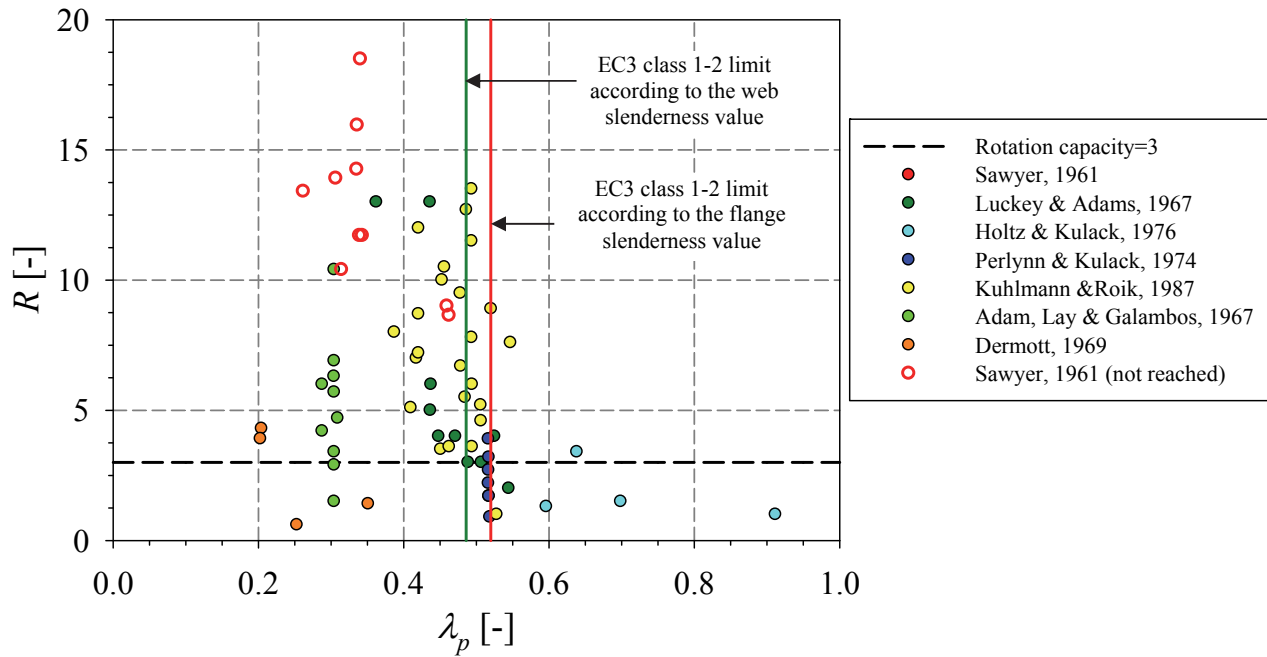


Figure 2.13 – Rotation capacity as function of the plate slenderness from experimental data of open section

3 EXPERIMENTAL PROGRAM

3.1 General description, objective and test program

The test program undertaken at the University of Applied Science of Western Switzerland – Fribourg consisted in bending tests on hollow structural shapes (either rectangular RHS or square hollow sections SHS). The main goal of the experimental campaign was i) to calibrate and validate the numerical model based on experimental results, ii) to provide experimental references on the inelastic behaviour of such members (ultimate load carrying capacity, available rotation...), iii) to improve the way the rotation capacity of tubular members are actually characterized and vi) to investigate new ways of defining the possibility to resort to a plastic analysis in design practice.

This chapter summarises experimental activities aimed towards the rotation capacity of tubular profiles; a series of 23 bending tests are detailed. Tested beams had a nominal steel grade of S355. Seven different cross-sections were considered. Six of them were hot-formed, and classified as class 1 sections according to the Eurocode. Their dimensions were chosen in order to have different relative slenderness values ranging from 0.2 to 0.56, in order to represent the plastic range. One section was cold-formed and corresponded to the class 3. Four different test setup configurations were considered: 3-point and 4-point bending static systems, with a span length of 2.6 *m*, to characterise the rotation capacity of these sections (see Figure 3.12, Figure 3.13, Figure 3.14 and Figure 3.19). Propped cantilever configurations with mid-span and outer loaded point loads, with a span length of 4.8 *m* were also performed to define the rotation demand of these sections for such configurations (see Figure 3.27 and Figure 3.35).

Six meter long profiles were received at the laboratory of Structural Engineering, from which 400 *mm* samples were kept for tensile tests. For the simple supported configuration (3-point and 4-point bending), the remaining 5.6 *m* was cut into two 2.8 *m* pieces, while for the propped cantilever configuration (centrally and off-centrally loaded) it was cut into a 4.9 *m* beam; the remaining segment, of length equal to three times the height of the cross section, was kept for stub column testing (Figure 3.1). Specimens' lengths were chosen long enough to assure that the failure mode would occur predominately by bending with little influence of

shear. The dimensions of each specimen were measured prior to testing. No measurements of the initial geometrical imperfections were undertaken because the accuracy of the available method at the laboratory (that consists of different set of LVDT) was not sufficient. Therefore, for the case of hollow sections, initial geometrical imperfections have little effect on the ultimate load, but considerable impact on the rotation capacity [41], [91], [92]. Hence, in the following validation model, different sets of geometric imperfections would be introduced in order to match the numerical results to the experimental ones. The test program is summarised in Table 3.1.

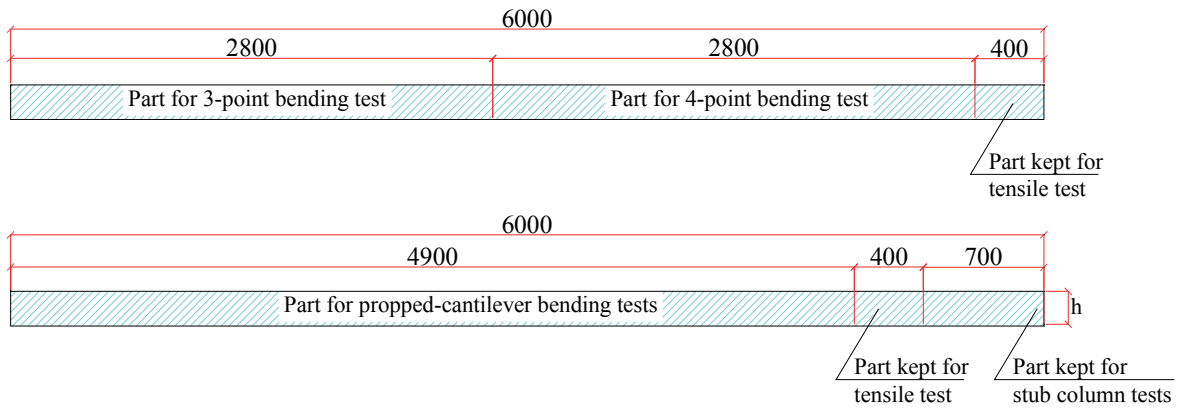


Figure 3.1 – Segmentation of received beams (dimensions in *mm*)

In the following, detailed measurements of the tested specimens' cross-sectional dimensions, tensile tests, and stub column tests will be presented. Then, bending tests will be detailed. For each configuration, the testing arrangement will be described and results will be summarised. Moreover, some typical specimens' response will be shown and analysed in detail. Finally, main conclusions will be presented.

Table 3.1 – Test program for cross-sectional tests

Test #	Name of specimen	Fabrication process	Nominal steel grade	Length [mm]	Span length [mm]	Test configuration
1	RHS_150×100×8_SS_3P	Hot-formed	S355	2800	2600	Simply supported; 3-point bending
2	RHS_180×80×4.5_SS_3P	Hot-formed	S355	2800	2600	Simply supported; 3-point bending
3	RHS_150×100×5_SS_3P	Hot-formed	S355	2800	2600	Simply supported; 3-point bending
4	RHS_220×120×6.3_SS_3P	Hot-formed	S355	2800	2600	Simply supported; 3-point bending
5	RHS_220×120×6.3_SS_3P*	Hot-formed	S355	2800	2600	Simply supported; 3-point bending
6	SHS_180×6.3_SS_3P	Hot-formed	S355	2800	2600	Simply supported; 3-point bending
7	SHS_180×8_SS_3P	Hot-formed	S355	2800	2600	Simply supported; 3-point bending
8	SHS_200×6.3_SS_3P	Cold-formed	S355	2800	2600	Simply supported; 3-point bending
9	RHS_150×100×8_SS_4P	Hot-formed	S355	2800	2600	Simply supported; 4-point bending
10	RHS_180×80×4.5_SS_4P	Hot-formed	S355	2800	2600	Simply supported; 4-point bending
11	RHS_150×100×5_SS_4P	Hot-formed	S355	2800	2600	Simply supported; 4-point bending
12	RHS_220×120×6.3_SS_4P	Hot-formed	S355	2800	2600	Simply supported; 4-point bending
13	SHS_180×6.3_SS_4P	Hot-formed	S355	2800	2600	Simply supported; 4-point bending
14	SHS_180×8_SS_4P	Hot-formed	S355	2800	2600	Simply supported; 4-point bending
15	SHS_200×6.3_SS_4P	Cold-formed	S355	2800	2600	Simply supported; 4-point bending
18	RHS_180×80×4.5_PR_C	Hot-formed	S355	4900	4800	Propped cantilever; centrally loaded
19	RHS_150×100×5_PR_C	Hot-formed	S355	4900	4800	Propped cantilever; centrally loaded
20	RHS_220×120×6.3_PR_C	Hot-formed	S355	4900	4800	Propped cantilever; centrally loaded
21	SHS_180×6.3_PR_C	Hot-formed	S355	4900	4800	Propped cantilever; centrally loaded
22	SHS_180×8_PR_C	Hot-formed	S355	4900	4800	Propped cantilever; centrally loaded
23	RHS_180×80×4.5_PR_O	Hot-formed	S355	4900	4800	Propped cantilever; off-centrally loaded
24	RHS_220×120×6.3_PR_O	Hot-formed	S355	4900	4800	Propped cantilever; off-centrally loaded
25	SHS_180×6.3_PR_O	Hot-formed	S355	4900	4800	Propped cantilever; off-centrally loaded
26	RHS_150×100×8_Stub(PR_C)	Hot-formed	S355	450	450	Stub column
27	RHS_180×80×4.5_Stub(PR_C)	Hot-formed	S355	540	540	Stub column
28	RHS_180×80×4.5_Stub(PR_O)	Hot-formed	S355	540	540	Stub column
29	RHS_150×100×5_Stub(PR_C)	Hot-formed	S355	450	450	Stub column
30	SHS_220×120×6.3_Stub(PR_C)	Hot-formed	S355	660	660	Stub column
31	SHS_220×120×6.3_Stub(PR_O)	Hot-formed	S355	660	660	Stub column
32	SHS_180×6.3_Stub(PR_C)	Hot-formed	S355	540	540	Stub column

* The rectangular cross-section 220x120x6.3 has two test specimens for the simply supported; 3-point bending

3.1.1 Cross-sectional dimensions

The cross-section dimensions represented in Figure 3.2, such as the depth (h), the width (b) and the thickness (t), were measured using calipers and micrometers at both ends of the specimens. Average measured values for all tested specimens are reported in Table 3.2 below. Detailed measurements can be found in appendix 3, along a comparison with

tolerances according to EN 10210-2 [93] for hot formed sections, and EN 10219-2 [94] for cold formed sections. An example is given in Figure 3.3 in which subscripts represent repeated measurements. The medium corners radius (r) was assumed equal to $1.5 t$ according to the prescription in EN 10210-2 and EN 10219-2.

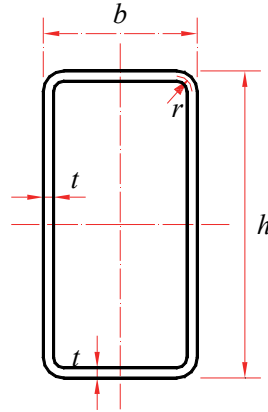
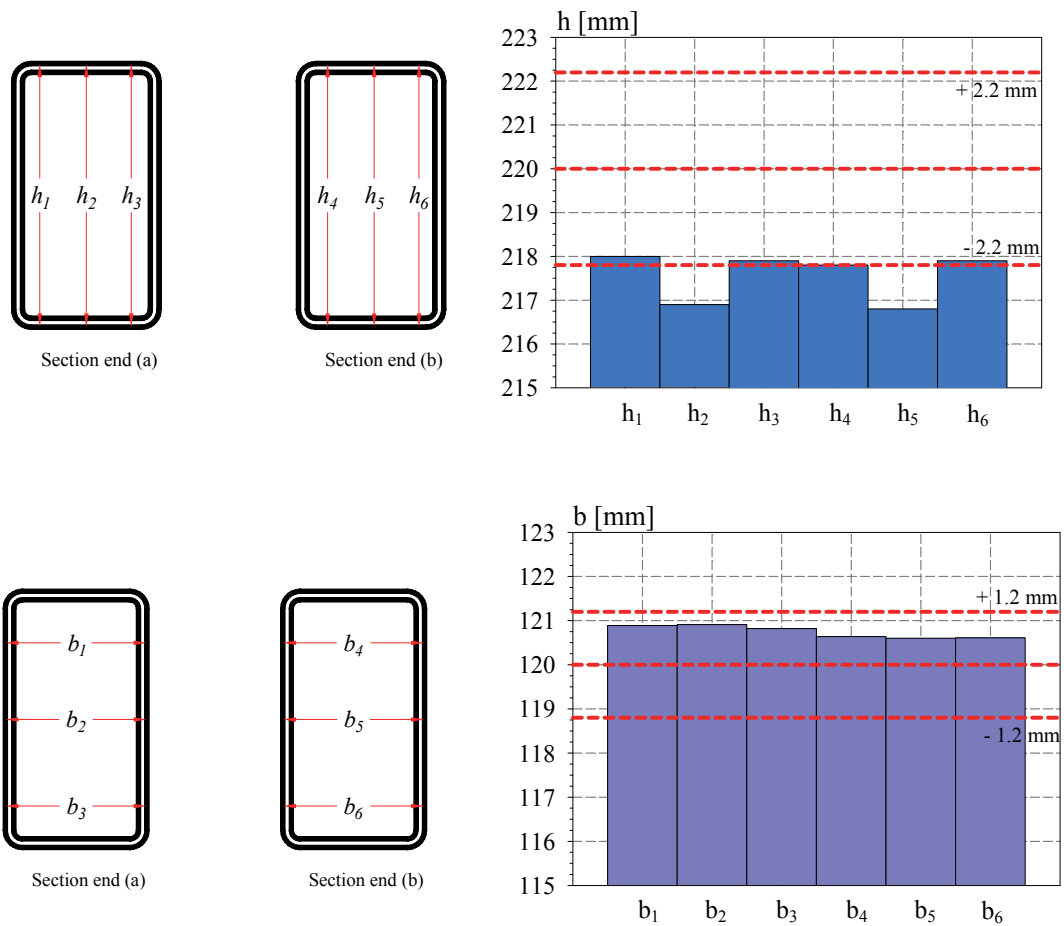


Figure 3.2 – Cross-section dimensions



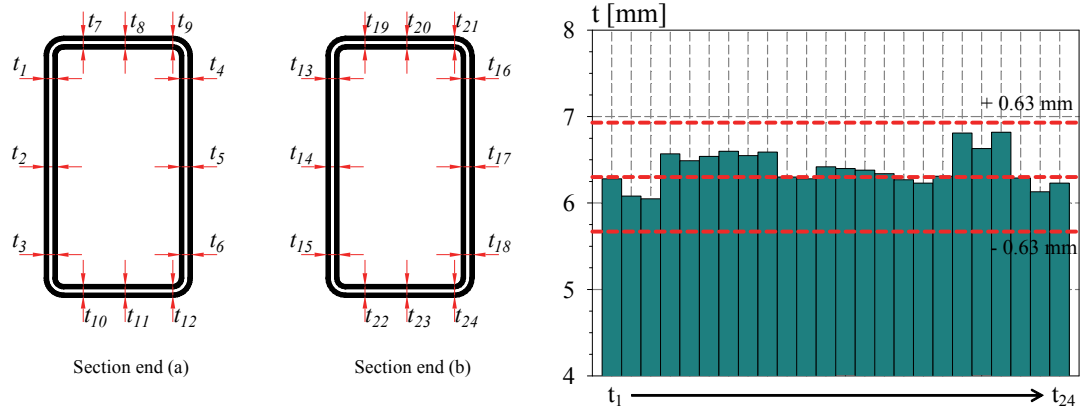


Figure 3.3 – Example of detailed cross-section measurement for RHS_220x120x6.3_SS_3P along with the Eurocode tolerances

Table 3.2 – Average measured dimensions

Name of specimen	h_{mes} [mm]	b_{mes} [mm]	t_{mes} [mm]	r [mm]
RHS_150×100×8_SS_3P	149.60	99.94	8.35	12.52
RHS_180×80×4.5_SS_3P	179.35	78.52	4.80	7.20
RHS_150×100×5_SS_3P	148.97	99.17	5.26	7.90
RHS_220×120×6.3_SS_3P*	219.25	120.60	6.39	9.58
RHS_220×120×6.3_SS_3P	217.55	120.75	6.40	9.60
SHS_180×6.3_SS_3P	179.42	179.76	6.58	9.87
SHS_180×8_SS_3P	179.46	179.42	7.89	11.83
SHS_200×6_SS_3P	200.53	200.87	5.83	8.74
RHS_150×100×8_SS_4P	149.48	99.86	8.16	12.24
RHS_180×80×4.5_SS_4P	179.59	79.71	4.81	7.21
RHS_150×100×5_SS_4P	149.13	99.48	5.13	7.69
RHS_220×120×6.3_SS_4P	219.40	120.86	6.42	9.64
SHS_180×6.3_SS_4P	179.43	179.93	6.68	10.02
SHS_180×8_SS_4P	179.20	179.58	7.91	11.86
SHS_200×6_SS_4P	200.84	200.42	5.80	8.70
RHS_180×80×4.5_PR_C	179.19	79.06	4.76	7.13
RHS_150×100×5_PR_C	148.78	99.49	5.20	7.81
RHS_220×120×6.3_PR_C	219.10	120.45	6.51	9.76
SHS_180×6.3_PR_C	179.44	179.70	6.72	10.09
SHS_180×8_PR_C	179.37	179.23	7.94	11.91
RHS_180×80×4.5_PR_O	178.96	79.45	4.63	6.95
RHS_220×120×6.3_PR_O	219.03	120.66	6.51	9.76
SHS_180×6.3_PR_O	180.02	179.08	6.53	9.80

* The rectangular cross-section 220x120x6.3 has two test specimens for the simply supported; 3-point bending

3.1.2 Tensile tests

The stress-strain behaviour of specimens was determined through 68 tensile tests. Tensile coupon samples were extracted from the flat faces of the profiles as indicated in Figure 3.5 (concerning the cold-formed section, the coupon location was shifted in faces containing a weld). The coupons were 270 mm in length (see Figure 3.5) and tested in a 100 kN testing machine with hydraulic grips for the load application, and under a constant strain rate of 2.5 mm/min. A 25 mm clip gauge was attached at the middle of the coupon segment to record axial elongation (see Figure 3.4). Some of the tested coupons are shown in Figure 3.6.

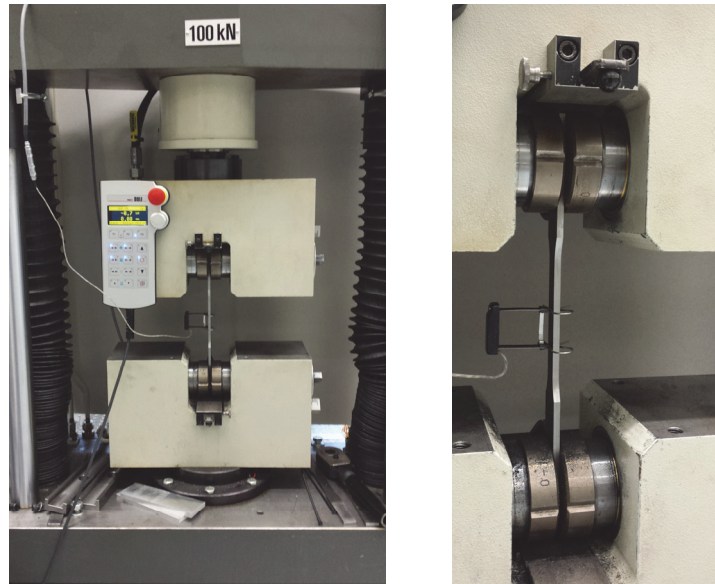


Figure 3.4 – Tensile coupon testing

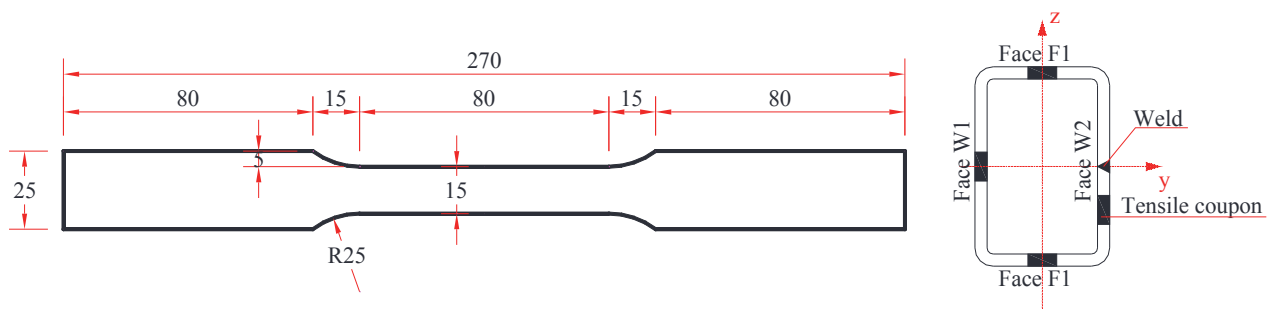


Figure 3.5 – Tensile coupon dimensions and locations of the tensile coupons



Figure 3.6 – Example of some tested coupons

Figure 3.7 exhibits typical stress-strain responses for some of the tested coupons. Hot-formed structural steels' results typically exhibit uniform material properties within the entire cross-section owing to their fabrication process. The stress strain curve for these profiles displays a sharply defined yield point and a yield plateau followed by strain hardening; the recorded yield stress f_y was taken as the average of the yield plateau. The young's modulus E was taken as the gradient between 20% and 80% of f_y using a linear regression analysis. Concerning the cold-formed section, the material shows a more rounded response. These steel members usually exhibit non-uniform material properties within the cross-section, and display strength enhancement in the corner region. The Young's modulus E was taken as the slope gradient from the point where the ratio of the successive secant moduli is less than 80% to 30% of f_y as recommended by Afshan & al [95]; the 0.2% proof stress was then determined.

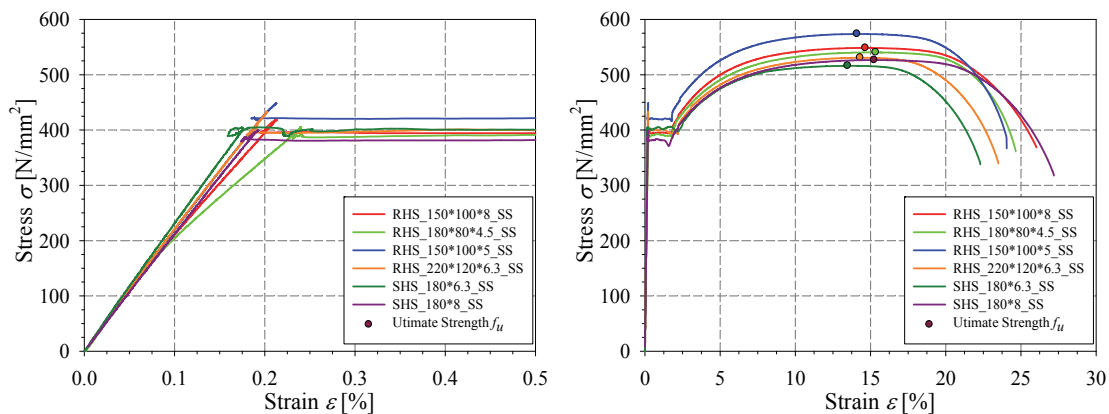


Figure 3.7 – Stress strain curve for RHS_150×100×8_SS coupon

Average values from the four coupons of all sections are reported in Table 3.3, and corresponding parameters are displayed in Figure 3.8. These values were used in the finite element calculations. Detailed measured data of each coupon test can be found in appendix 3.

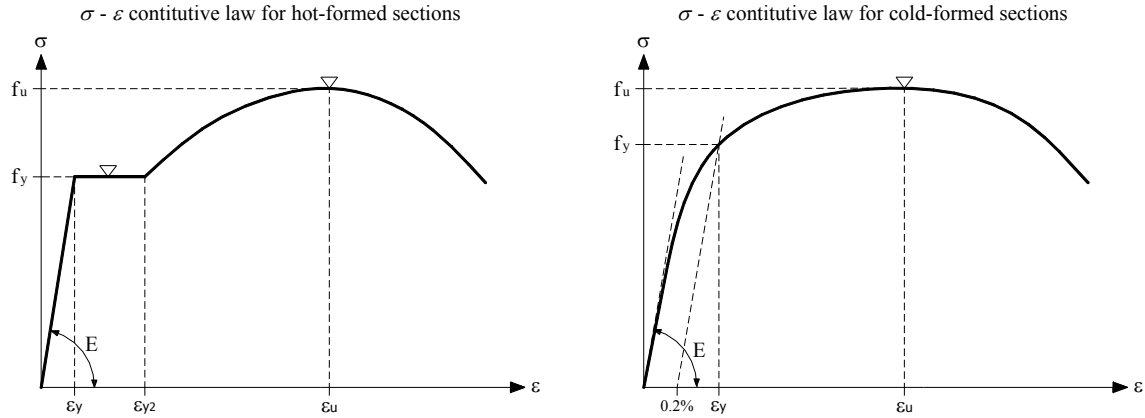


Figure 3.8 – Stress-strain constitutive law parameters

Table 3.3 – Average material properties of tested profiles

	f_y	f_u	E	ϵ_y	ϵ_{y2}	ϵ_u
	[N/mm ²]	[N/mm ²]	[N/mm ²]	[%]	[%]	[%]
RHS_HF_150×100×8_SS	391.2	554.0	205737	0.19	1.49	12.93
RHS_HF_180×80×4.5_SS	389.2	539.4	198504	0.20	1.76	16.98
RHS_HF_150×100×5_SS	419.8	573.0	211215	0.20	1.73	14.89
RHS_HF_220×120×6.3_SS*	394.2	534.4	208932	0.19	1.85	16.98
RHS_HF_220×120×6.3_SS	396.5	535.9	211087	0.19	1.88	15.28
SHS_HF_180×6.3_SS	393.2	523.8	206903	0.19	2.19	14.88
SHS_HF_180×8_SS	384.0	531.5	208013	0.18	1.69	17.47
SHS_CF_200×6_SS	481.5	569.6	210239	0.25	-	19.00
RHS_HF_150×100×8_PR_C	385.2	527.3	207854	0.19	1.78	19.66
RHS_HF_180×80×4.5_PR_C	403.9	547.3	213062	0.19	1.93	16.68
RHS_HF_150×100×5_PR_C	396.5	552.7	203267	0.20	1.72	12.61
RHS_HF_220×120×6.3_PR_C	393.0	531.8	202440	0.19	1.83	17.16
SHS_HF_180×6.3_PR_C	390.9	532.2	206819	0.19	1.79	17.62
SHS_HF_180×8_PR_C	384.8	529.5	213367	0.18	1.70	15.90
RHS_HF_180×80×4.5_PR_O	386.6	537.1	205414	0.19	1.85	18.47
RHS_HF_220×120×6.3_PR_O	393.6	533.2	210347	0.19	1.84	18.58
SHS_HF_180×6.3_PR_O	385.9	529.0	207744	0.19	1.77	17.08

* The rectangular cross-section 220x120x6.3 has two test specimens for the simply supported; 3-point bending

3.1.3 Stub column tests

A series consisting in seven stub column tests was performed in order to determine the load carrying capacities under pure compression. The stub columns lengths were chosen as being three times the height of the cross-section to avoid global flexural buckling. Each member length, cross-sectional dimension and weight were measured prior to testing, and were used for the calculation of the exact section's area, assuming a density of 7850 kg/m^3 . The ends of each specimen were carefully manufactured, namely regarding flatness (use of a flat marble stone) and parallel faces in order to ensure uniform distribution of load through the specimen. Two strain gauges have been attached at mid-height of the specimens and on adjacent plates, because if local buckling would occur on the gauge locations, these gauges would be able to capture the compressive and tensile responses of the stub column constituent plates. The testing machine was a 5000 kN hydraulic rig controlled by loading. Two $250 \times 250 \times 150$ of high strength steel ($f_y = 2200 \text{ N/mm}^2$) have been placed on each side of the stub column in order to protect the testing machine surface. Four LVDTs were positioned on the stub's ends to record the average end-shortening behaviour (Figure 3.9). The strains gauges indicated if the compression was kept concentrically-applied and provided the load displacement behaviour of the specimen in the elastic range, therefore the (indirect) corresponding Young's modulus. The failure shapes of all stub columns are shown in Figure 3.10.

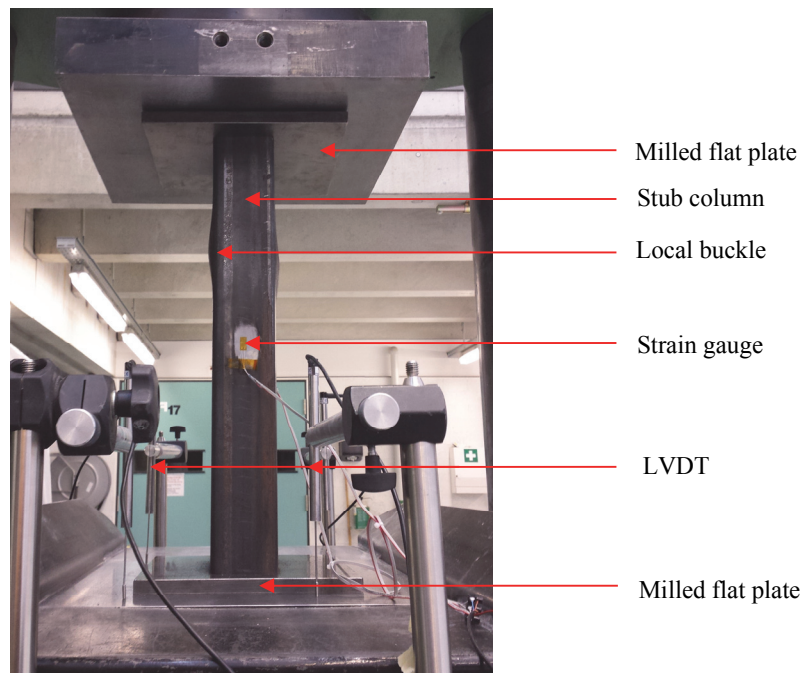


Figure 3.9 – General test set-up of stub columns



Figure 3.10 – Failure shapes of tested stub columns

In order to analyse tests results, cross-sections were first classified according to Eurocode 3 [53], for pure bending and compression cases. For sake of simplicity, nominal geometrical dimensions were used, and estimated yield strengths based on the tensile tests performed were adopted for each cross-section type; the selected values and corresponding results are shown in Table 3.4. Plate relative slenderness λ_p values are also reported in Table 3.4 and correspond to the maximum relative slenderness value λ_p of the cross-section constituent plates. Plate relative slenderness λ_p is given by:

$$\lambda_p = \sqrt{\frac{f_y}{\pi^2 E}} = \sqrt{\frac{f_y}{\sigma_{crit,p}}} \quad 3.1$$

where k is the buckling coefficient, ν is the poisson ratio and taken as $\nu = 0.3$, and ε is the yield factor: $\varepsilon = \sqrt{(235 / f_y)}$. In bending, all sections are classified as class 1, with relative slenderness values ranging for 0.2 to 0.56 for the hot formed sections; whereas the cold formed section SHS_200x6 is class 3. In compression, cross-sections are classified from class 1 to class 4.

Table 3.4 – Cross-section classification

Name of specimen	h	b	t	r	f_y	$(h-t-2r)/t \times \varepsilon$	$(b-t-2r)/t \times \varepsilon$	$\lambda_{p_compression}$	$\lambda_{p_bending}$	Class in compression	Class in bending
	[mm]	[mm]	[mm]	[mm]	[N/mm ²]	[-]	[-]	[-]	[-]		
RHS_150×100×8	150	100	8.0	12.00	400	19.2	11.1	0.34	0.20	1	1
RHS_180×80×4.5	180	80	4.5	6.75	400	47.0	18.0	0.83	0.34	4	1
RHS_150×100×5	150	100	5.0	7.50	420	34.8	21.4	0.61	0.38	2	1
RHS_220×120×6.3	220	120	6.3	9.45	400	40.3	19.6	0.71	0.35	3	1
SHS_180×6.3	180	180	6.3	9.45	400	32.1	32.1	0.56	0.56	1	1
SHS_180×8	180	180	8.0	12.00	400	24.1	24.1	0.42	0.42	1	1
SHS_200×6	200	200	6.0	9.00	400	38.3	38.3	0.67	0.67	3	3

Table 3.5 summarise the obtained results for all stub columns. For the RHS_180×80×4.5_PR_O, SHS_180×6.3_PR_C, RHS_220×120×6.3_PR_C sections, local buckling was seen to develop unevenly on one side owing to a slightly imperfect flatness on the end sections, which resulted in an unexpected moment introduction on the specimen. These experimental defaults as well as other experimental uncertainties may explain why some class 1 or 2 tests have reached ultimate loads slightly below the plastic load.

Table 3.5 – Measured properties and ultimate loads of stub columns

Name of specimen	Length	Weight	Area	f_y	$N_{pl,fy}$	$N_{pl,fy=355}$	$F_{ult,exp}$	$F_{ult,exp} / N_{pl,fy}$
	[mm]	[Kg]	[mm ²]	[N/mm ²]	[kN]	[kN]	[kN]	[-]
RHS_150×100×8_Stub_(PR_C)	450.5	12.85	3633.6	385.2	1440.6	1289.9	1807.2	1.25
RHS_180×80×4.5_Stub_(PR_C)	541.0	9.50	2237.0	403.9	861.6	794.1	822.6	0.95
RHS_180×80×4.5_Stub_(PR_O)*	540.5	9.40	2215.5	386.6	856.5	786.5	805.6	0.94
RHS_150×100×5_Stub_(PR_C)	541.0	8.35	2358.5	396.5	952.6	837.3	943.4	0.99
SHS_220×120×6.3_Stub_(PR_C)*	663.0	21.25	4083.0	393.0	1604.5	1449.5	1577.5	0.98
SHS_220×120×6.3_Stub_(PR_O)	662.0	21.35	4108.4	393.6	1616.9	1449.5	1613.7	1.00
SHS_180×6.3_Stub_(PR_C)*	540.0	19.05	4494.0	390.9	1756.7	1595.4	1749.8	1.00

*Buckling occurred on one side due to accidental moment introduction

Because the recorded deformation from the displacement transducers and the strain gauges are different, a correction that combines both sets of measurements was required. Hence, the strain gauges provided the correct Young's modulus slope since they were directly in contact with the column faces, while the displacement transducers provided good post-yield information, however including the elastic deformation of the end plates, thus leading to an incorrect initial Young's modulus value. A correcting method described by the Centre for Advanced Structural Engineering ([96], [97] & [98]) was used. The method consists in a correction factor k that represents the undesired displacement.

$$k = \frac{L}{2} \left(\frac{1}{E_{LVDT}} + \frac{1}{E_{SG}} \right) \quad 3.2$$

$$\delta_c = \delta_{LVDT} - 2kf \quad 3.3$$

In Equation 3.2 and 3.3, E_{LVDT} represents the initial Young's modulus calculated from the LVDT readings, E_{SG} represents the initial Young's modulus calculated from the strain gauges, and f represents the applied stress N/A . The corrected end shortening δ_c is then the difference between the LVDT displacements and the set-up displacement. Figure 3.11 provides typical results for RHS_220x120x6.3_PR_C. Figure 3.11a exhibits the normalized axial load $N/N_{pl,fy}$ ($N_{pl,fy}$ is the product of the cross-section area A and the tensile coupon yield stress f_y) as a function of the stubs end shortening δ before and after correction. Figure 3.11b represents the normalized axial load $N/N_{pl,fy}$ and measured strain $\varepsilon/\varepsilon_y$, ε_y being the strain at yield. Local buckling consists of alternate inward and outward buckles of the stub column constituent plates. Hence, we can explain why one of the strain curves reversed direction in Figure 3.11, based on the strain gauges location on either the tensile or compressive face of the buckled shape. Full details of the stub columns results are given in appendix 3.

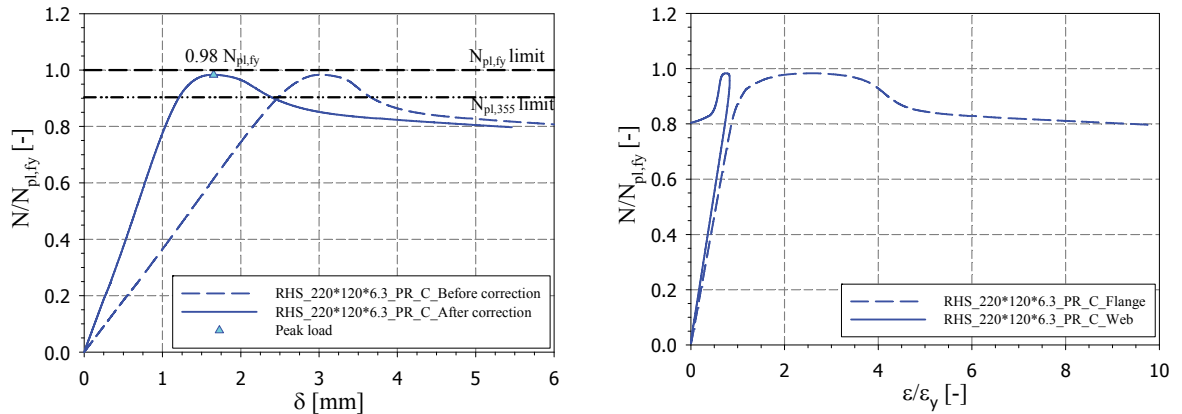


Figure 3.11 – a) Normalized load displacement curves – b) Strain gauges measurements

3.2 Bending tests

3.2.1 3-point bending tests

Eight beams were tested under a typical 3-point bending configuration (Figure 3.12). The experimental setup consisted in a simply-supported beam arrangement with 30 mm diameter rollers at the supports. Loading was applied by means of two hydraulic jacks used to generate

a concentrated force using two threaded bars connected to a loading beam. Loading was introduced to the specimen with half-round loading point and through a 40 *mm* thick and 50 *mm* wide plate, to avoid high levels of stress concentration. Detailed test setup is shown in Figure 3.12 and Figure 3.13.

Various transducers were used to monitor the beam's response:

- Load cells were located under each support and under the jacks to record the support reaction and the loading force respectively;
- Inclinometers were fixed at both ends of the beam to measure the beam end rotations;
- Linear variable displacement transducers (LVDTs) were positioned at different locations along the beam to record the beam deflection;
- Strain gauges were fixed on the tension flange to measure both its deformation and its curvature.

Loading was carried out under displacement control and all readings were taken using an electronic data acquisition system at a 2 *Hz* pace. Figure 3.15 displays the deformed shape of specimen RHS_150×100×5_SS_3P.

All six beams were tested up to and beyond failure. In most cases, local buckling occurred before beams reached their plastic moment, except for the case of the specimen RHS_150×100×8 for which strain hardening was reached, and the test had to be aborted before unloading, due to high deformations and experimental limitations.

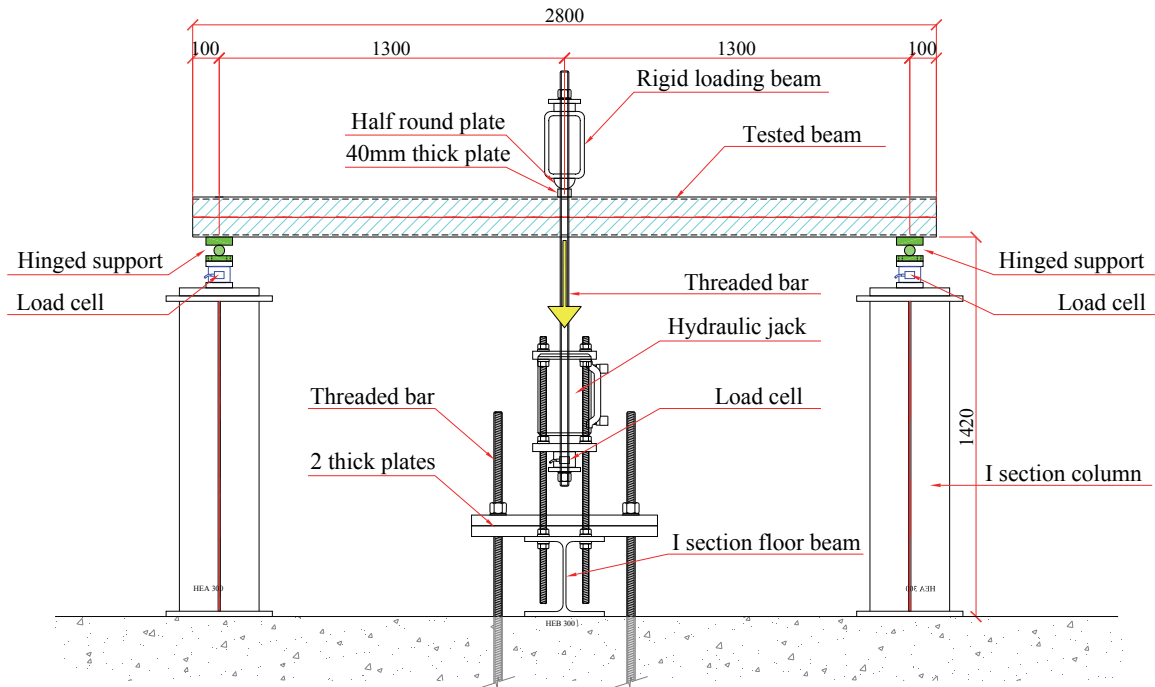


Figure 3.12 – Test setup of the 3-point bending beam, longitudinal view (dimensions in *mm*)

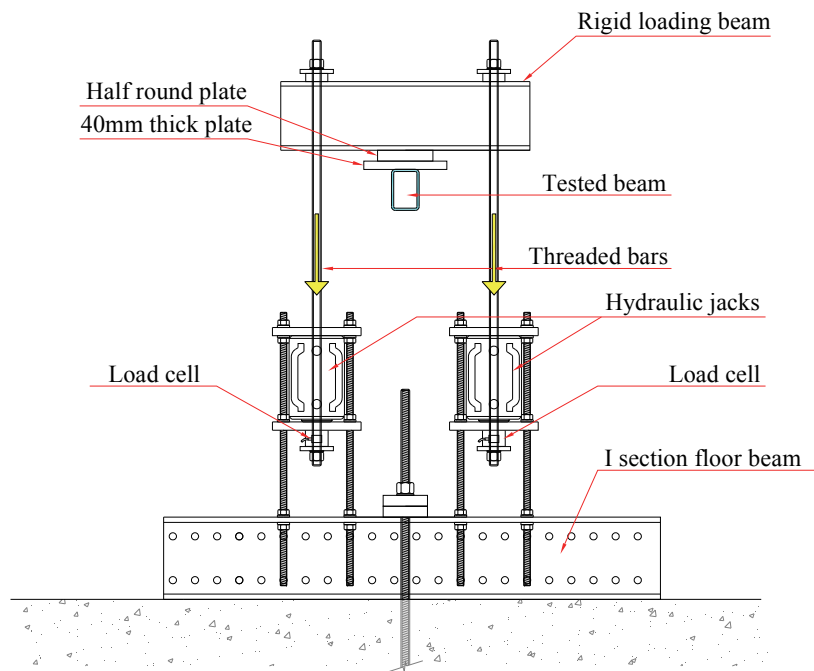


Figure 3.13 – Test setup of the 3-point bending beam, transversal view (dimensions in *mm*)

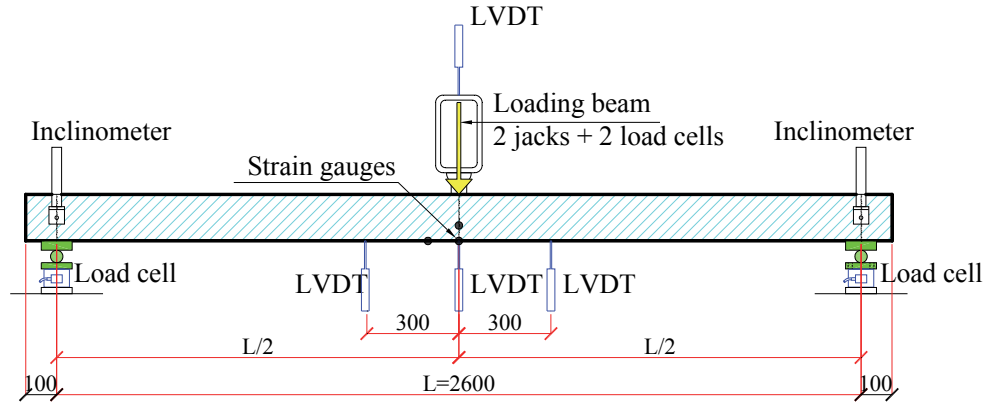


Figure 3.14 – Position of the variable transducers on the 3-point bending beam (dimensions in *mm*)

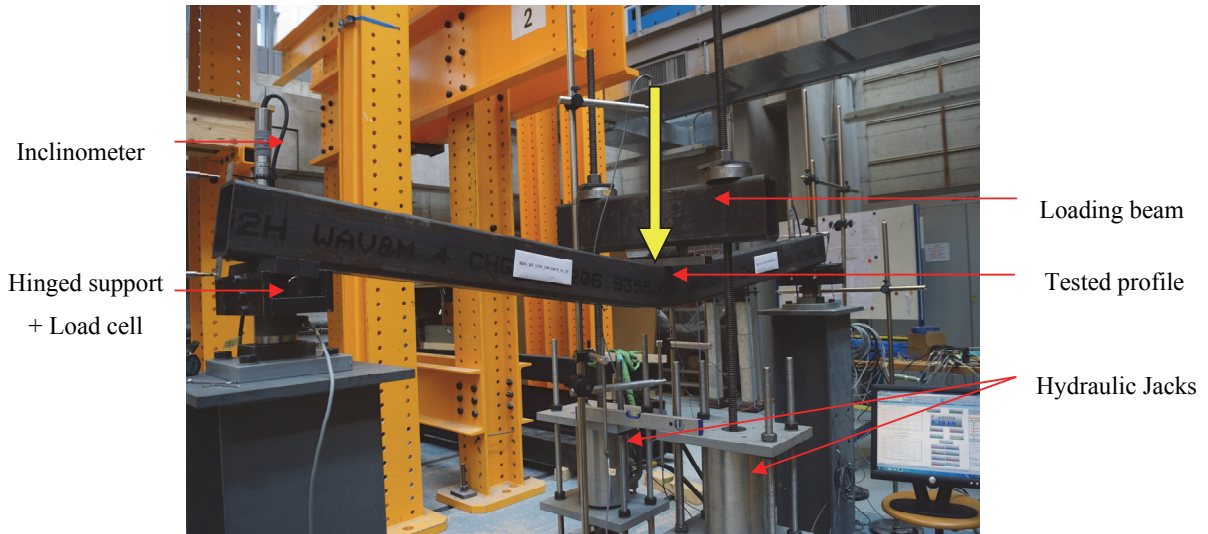


Figure 3.15 – Deformed shape a RHS_150×100×5_SS_3P

The maximum shear rate $V_{Ed} / V_{pl,Rd}$ for the 3-point bending configuration was equal to 32%, so no influence of shear on the obtained result is expected; Figure 3.16 shows that the plastic hinge that developed was of limited length due to the moment gradient. Moreover, the onset of local buckling was much localized due to the loading introduction that induced high levels of stress concentrations. Therefore, even with the loading applied through a 40 *mm* thick plate, loading was not uniformly distributed on the area of the plate but was mostly transferred through the plate extremities in contact with the corners edges and distanced by 5 *cm*. This can explain why beams failed prematurely and did not reach the plastic moment M_{pl} while being all class 1 in bending. The RHS_150×100×8_SS_3P, that possess a very stocky section ($\lambda_{rel,p,bending} = 0.2$), was not influenced by the load introduction and reached a

139 mm deflection at peak load. The behaviour of hollow sections is very sensitive to the bearing stresses imposed during loading, and is seen to be a function of the b / t ratio of the compression flange. EC3 part 1-3 [99] provide design rules to calculate the web crippling strength for cold formed sections (also known as the local transverse resistance of web) which can occur at support or point of structural members where concentrated load is applied. Nevertheless it was shown by Li & Young (2015) [100], who considered cold formed hollow sections, that the web crippling design strength predicted by current standard (EC3, AISI, AS) are either unconservative or very conservative, and are therefore not capable of predicting the design strength for cold formed hollow sections undergoing web crippling.

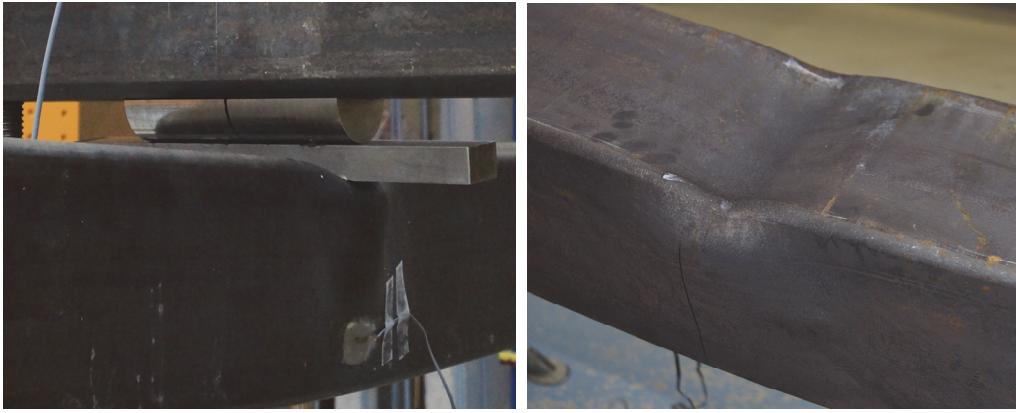


Figure 3.16 – Onset of local buckling

Figure 3.18a displays examples of moment-rotation curves in which M_{pl} is the plastic moment calculated with measured cross-sections properties (both geometry and material), and θ_y is the yield rotation at the beam ends – θ_y is calculated when the middle cross-section first reaches the elastic moment.

$$\theta_y = \frac{PL^2}{16EI} \quad 3.4$$

The moment M is calculated from the recording of the load cell under the left support multiplied by the half span distance $L / 2$, whereas the load P is calculated as the sum of the two load cells placed under the jacks. Figure 3.18b represents the total load vs. deflection for these specimens, where P_{pl} is the theoretical plastic collapse load of the system and v is the deflection of the beam at mid-span.

$$P_{pl} = \frac{4M_{pl}}{L} \quad 3.5$$

According to the plotted curves in Figure 3.18b, it appears clear that all beams failed prior to reaching their plastic capacity, however by a small amount except for the SHS 200x6 that reached $0.74 P_{pl}$. This was expected since this section was classified as class 3 according to EC3.

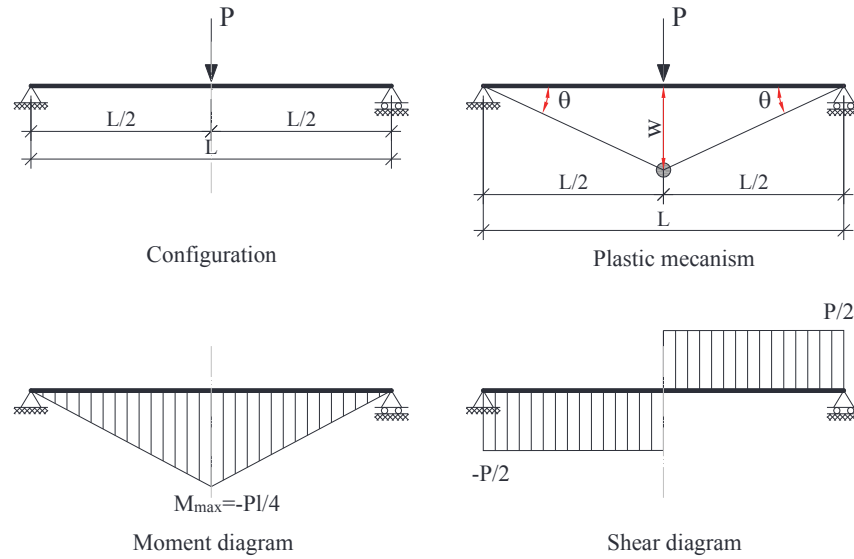


Figure 3.17 – 3-Point bending analysis

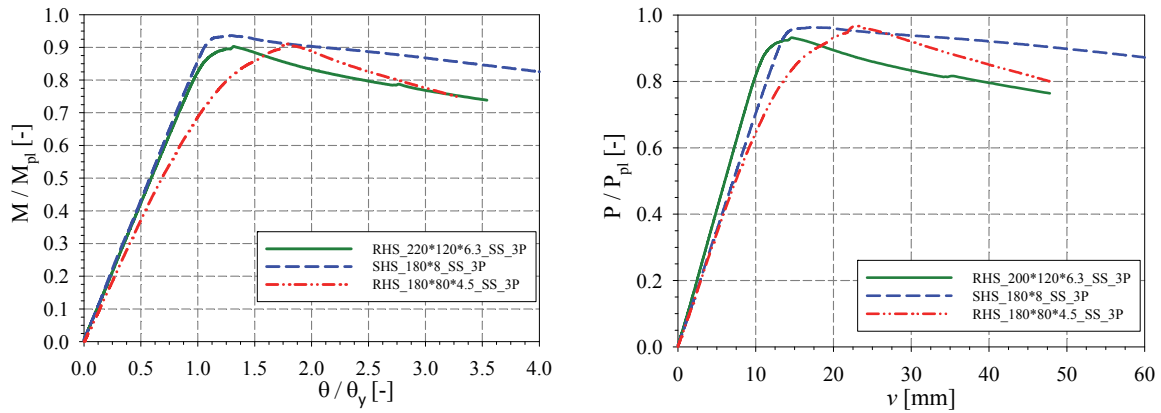


Figure 3.18 – a) Normalized moment - rotation curves – b) Normalized load - deflection curves

Table 3.6 summarises experimental values of the non-dimensional ultimate moments M_{ult} / M_{pl} , ultimate load P_{ult} / P_{pl} and their corresponding rotation θ_u and deflection v_u for all tested beams under the 3-point bending configuration, and report the values of M_{pl} , P_{pl} , θ_y that were used for normalization. It can be seen that the non-dimensional ratios M_{ult} / M_{pl} and P_{ult} / P_{pl} of a same specimen diverge by as much of 7% although they should be identical (3%

in average over the 15 simply supported tested specimens); this is due to experimental uncertainties related to the load cell recordings. Hence, the load cells used in the experimental setup have a precision that is equal to 5% the applied load.

Table 3.6 – Results at collapse for the 3-point bending tests

Name of specimen	$M_{pl,fy}$	$P_{pl,fy}$	θ_y	M_{ult}	M_{ult} / M_{pl}	P_{ult}	P_{ult} / P_{pl}	θ_u / θ_y	v_u	$\lambda_{rel_p_bending}$
	[kN.m]	[kN]	[°]	[-]	[-]	[-]	[-]	[-]	[mm]	[-]
RHS_150×100×8_SS_3P	69.8	107.4	0.95	84.6	1.21	134.8	1.26	7.53	138.9	0.20
RHS_180×80×4.5_SS_3P	50.5	77.6	0.81	46.3	0.92	75.3	0.97	1.59	22.9	0.34
RHS_150×100×5_SS_3P	50.5	77.6	0.99	46.6	0.92	76.7	0.99	1.94	33.4	0.38
RHS_220×120×6.3_SS_3P*	113.8	175.1	0.64	98.7	0.87	156.4	0.89	1.28	13.8	0.35
RHS_220×120×6.3_SS_3P	113.4	174.4	0.64	101.6	0.90	161.3	0.92	1.34	14.6	0.35
SHS_180×6.3_SS_3P	112.3	172.8	0.79	105.6	0.94	166.6	0.96	1.31	17.6	0.56
SHS_180×8_SS_3P	128.4	197.5	0.77	121.1	0.94	191.8	0.97	1.32	17.3	0.42
SHS_200×6_SS_3P	155.7	239.6	0.85	111.6	0.72	177.78	0.74	1.24	16.85	0.67

* The rectangular cross-section 220x120x6.3 has two test specimens for the simply supported; 3-point bending

3.2.2 4-point bending tests

Six beams were tested under 4-point loading configurations; Figure 3.19 shows SHS_180×6_SS_4P specimen at failure. The 4-point bending test setup differs from the 3-point bending arrangement by the addition of a spreader beam over the tested specimen in order to apply equivalent loads on both loading points located at quarter length of the hinged supports. The shear ratio $V_{Ed} / V_{pl,Rd}$ for the 4-point bending configuration is similar to the 3-point bending one except for the central segment of the specimen which is free from shear forces; shear should not significantly affect the behaviour – no influence of shear on the obtained result is expected (maximum shear rate $V_{Ed} / V_{pl,Rd} = 32\%$). LVDTs and strain gauges have been placed under the loading points and at mid span to record the beam response accurately as shown in Figure 3.20. Load cells were placed under both supports and hydraulic jacks; inclinometers were positioned at the beams' ends.

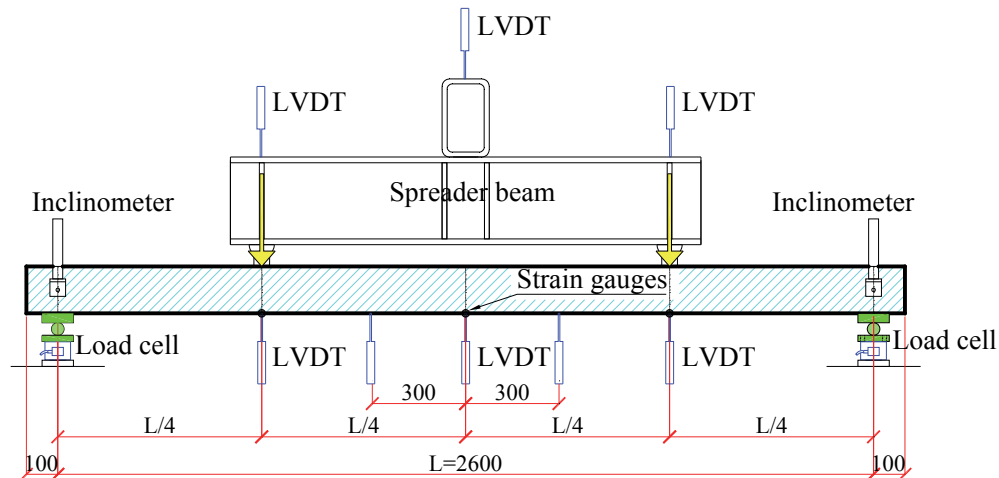


Figure 3.19 – Test setup of the 4-point bending beam

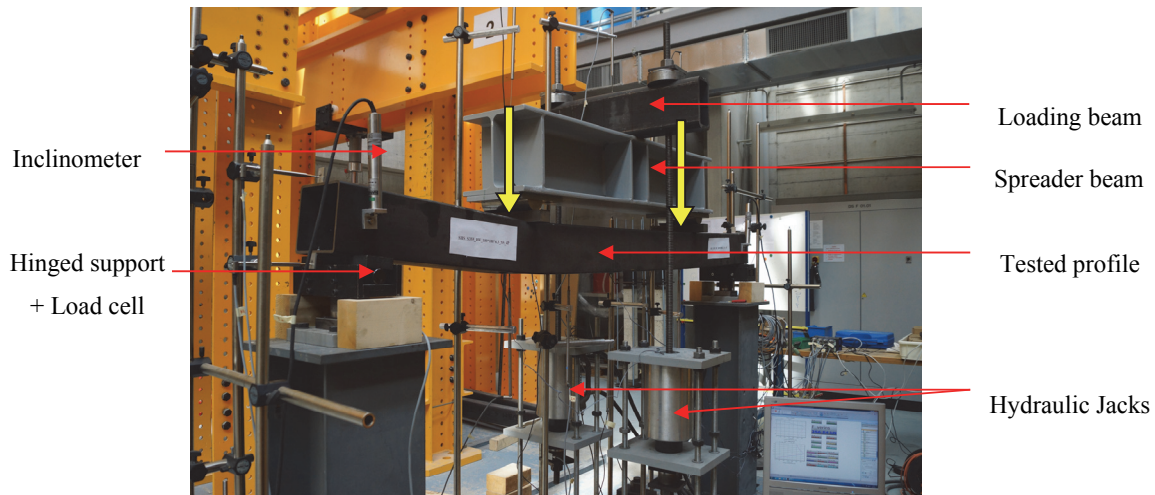


Figure 3.20 – Deformed shape of a 4-point bending beam

During testing, the beams' deflection remained symmetric until the peak load was reached, where local buckling failure mode started developing at either the right (side b) of left (side a) loading point while maintaining a constant moment. The failure mode became more pronounced in the post buckling unloading phase leading to an increased unsymmetrical deflection shape as shown in Figure 3.21b for RHS_180×80×4.5; this observation was previously observed and reported by Liew, 2014 [101]. The onset of local buckling was localized under the load application (either on the left or right loading point) due to a high level of stress concentration. Figure 3.22a shows how the load introduction may have influenced the beam's response, potentially explaining the lower results since local buckling is only pronounced and localized in the vicinity of the 50 mm thick plate.

Figure 3.21a presents moment as a function of the beam end rotations; the divergence between the two curves at the loading points highlights the occurrence of local buckling.

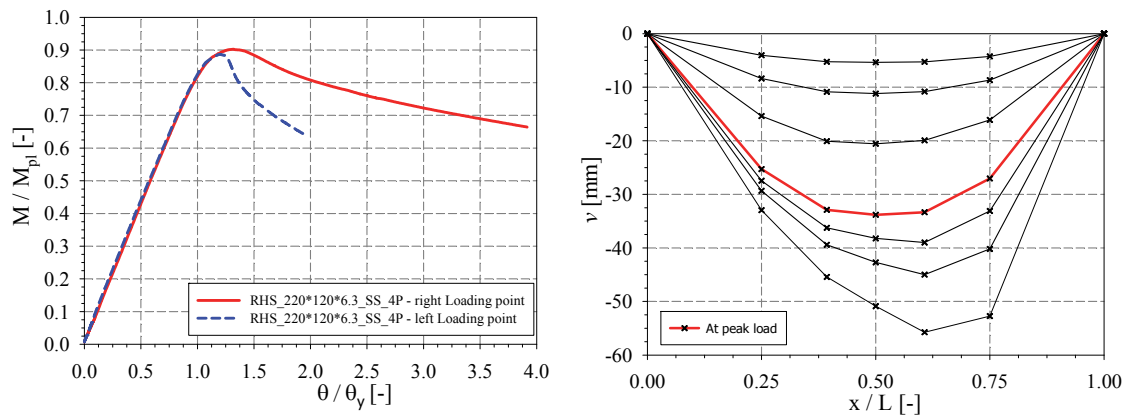


Figure 3.21 – a) Moment-rotation curve of RHS_220×120×6.3 – b) Relative deflected shape of RHS_180×80×4.5

Bending moments did not fully reach the plastic moment at the peak load in all tests except for the RHS_150×100×8 specimen who exhibited strain hardening effects but where loading was here stopped before reaching the peak load due to excessive vertical deformations; the beam deflected elastically and without the occurrence of local buckling until reaching a vertical displacement of 150 mm (that corresponds to the maximum hydraulic jack capacity) without attaining the system peak load (Figure 3.22b).



Figure 3.22 – a) Onset of local buckling for RHS_180x80x4.5 – b) Deflected shape of RHS_150×100×8

Table 3.7 summarises the experimental results for all the tested specimens. The rotation $\theta_{u,a}$ and $\theta_{u,b}$ are the rotation from the inclinometer of side a and b respectively and $v_{u,a}$ and $v_{u,b}$ are

the deflection under the loading point a or b. Yield rotation θ_y is calculated from the middle segment first reaching the elastic moment.

$$\theta_y = \frac{3PL^2}{32EI} \quad 3.6$$

While plastic collapse load P_{pl} (Equation 3.7) is computed for the beam attaining its plastic capacity.

$$P_{pl} = \frac{4M_{pl}}{L} \quad 3.7$$

It can also be noted that similarly to the 3-point bending case, the non-dimensional ultimate values M_{ult} / M_{pl} and P_{ult} / P_{pl} , even though should be equal, diverge by approximately 5% due to the load cells precision.

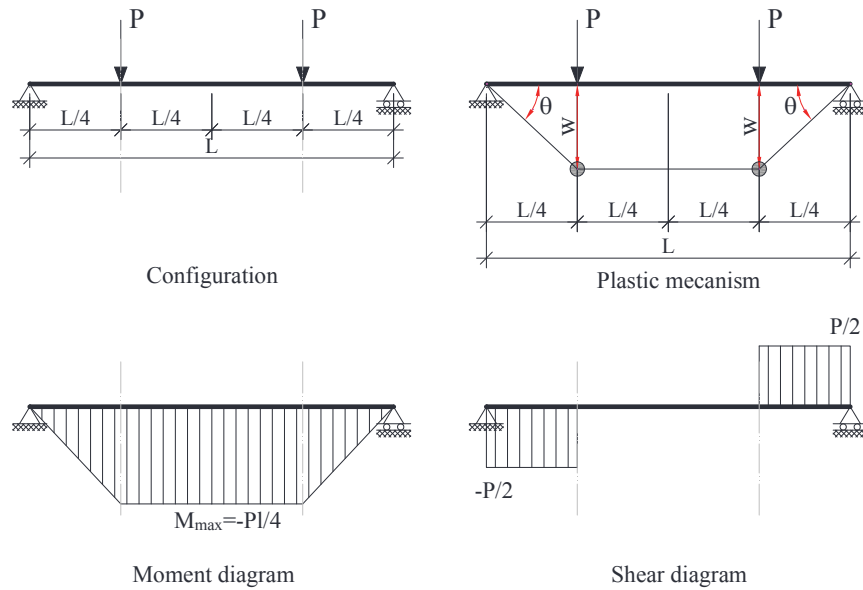


Figure 3.23 – 4-Point bending analysis

Table 3.7 – Collapse results for the 4-point bending tests

Name of specimen	$M_{pl,fy}$	$P_{pl,fy}$	θ_y	M_{ult}	M_{ult} / M_{pl}	P_{ult}	P_{ult} / P_{pl}	$\theta_{u,a} / \theta_y$	$\theta_{u,b} / \theta_y$	$v_{u,a}$	$v_{u,b}$
	[kN.m]	[kN]	[°]	[-]	[-]	[-]	[-]	[-]	[-]	[mm]	[mm]
RHS_150×100×8_SS_3P**	68.4	105.3	1.42	83.2	1.22	131.3	1.25	9.41	8.88	149.2	142.0
RHS_180×80×4.5_SS_3P	51.0	78.5	1.22	47.3	0.93	75.0	0.95	1.93	2.04	25.3	27.0
RHS_150×100×5_SS_3P	49.5	76.1	1.49	47.9	0.97	77.0	1.01	2.94	2.64	47.3	43.0
RHS_220×120×6.3_SS_3P	115.3	177.4	0.96	103.3	0.90	163.4	0.92	1.23	1.34	12.9	14.1
SHS_180×6.3_SS_3P	113.8	175.1	1.18	103.7	0.91	164.8	0.94	1.35	1.26	16.7	17.0
SHS_180×8_SS_3P	128.6	197.8	1.15	125.3	0.97	181.9	0.92	1.63	1.50	20.6	19.6
SHS_200×6_SS_3P	155.0	238.4	1.28	104.0	0.67	151.0	0.63	1.34	1.46	17.4	19.9

** Specimen didn't reach failure, but test was stopped due to excessive vertical deformations

The average curvature could be calculated from the LVDT displacements. Therefore, since the moment is constant between the load points, this results by the fact that this segment forms an arc of circle. The curvature can be thus determined according to the following equation given by [102], and [41].

$$\kappa_{LVDT} = \frac{1}{r} = \frac{8(D_M - D_L)}{4(D_M - D_L)^2 + L^2} \quad 3.8$$

With D_M being the deflection at mid span and D_L is the average of the deflection at the loading points. If this curvature is calculated over a shorter length that includes the buckled region, the post buckling curvatures would be notably higher and would result in a higher value of the rotation capacity. Moreover, the curvature has been calculated from the three gauges measurements placed on the tension flange by dividing the strain by half the height of the specimen section.

$$\kappa_{gauges} = \frac{\varepsilon}{h/2} \quad 3.9$$

This method displays some shortcomings, since once local buckling occurs, the curvature becomes concentrated at the location of the buckle while elastic unloading occur at the remaining part of the segment; additionally and since the strain gauges are only placed on the tension flange, deformations due to local buckling in the compression flange is therefore not recorded, which leads to a delayed unloading. These observations are displayed in Figure 3.24 that shows that curvatures as measured according to the different ways described previously, are practically identical in the elastic part but diverge in the post-buckling phase.

These values are normalized by the yield curvature κ_y and calculated from measured dimensions and material properties.

$$\kappa_y = \frac{M_{el}}{EI} \quad 3.10$$

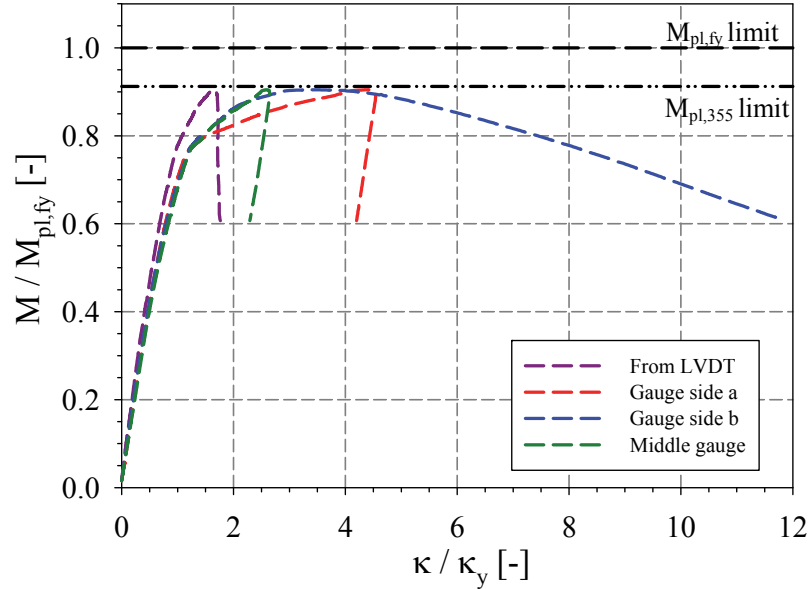


Figure 3.24 – Normalized moment curvature for RHS_180×80×4.5_SS_4P

Both for the 3-point bending and 4-point bending configurations, the system theoretical plastic collapse load is identical; the main differences between both configurations are the steepness of the moment gradient and the influence of shear. In the 4-point bending specimens, plastic hinges are theoretically expected to develop somewhere in the middle segment, i.e. between the loading points (constant bending moment). Experimentally, local buckling occurs at the loading points due to a high level of stress concentration, and either on the left or right side owing to uneven and askew arrangements. Figure 3.25 shows a comparison between the moment rotation curve of the 3-point bending and the 4-point bending configuration for the RHS_220×120×6.3 and the RHS_150×100×5; Table 3.8 summarises all results.

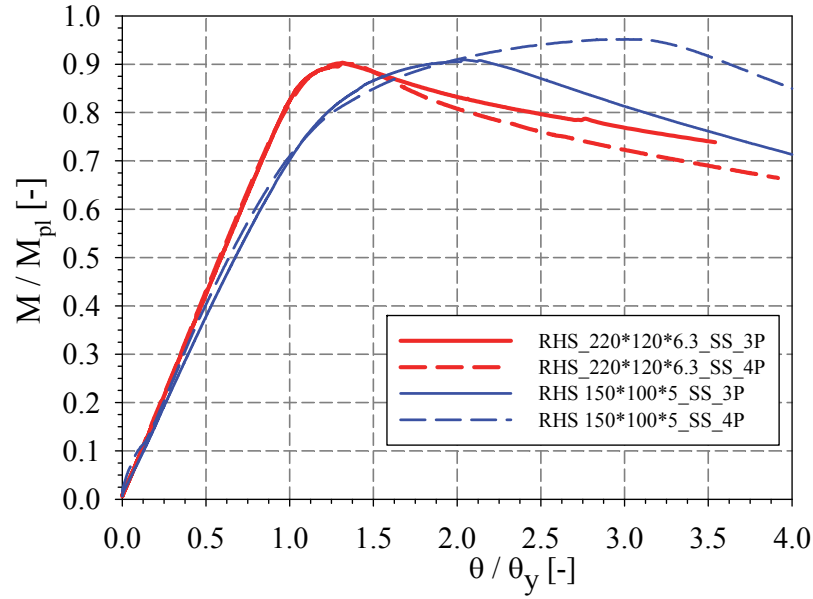


Figure 3.25 – Comparison between 3-point and 4-point configurations of RHS 220×120×6.3 and RHS 150×100×5

Table 3.8 – Comparison of ultimate bending moments between 3-point and 4-point bending configurations

Name of specimen	$M_{ult} / M_{pl} [-]$		Divergence [%]
	SS 3P	SS 4P	
RHS_150×100×8	1.21	1.22	-0.33
RHS_180×80×4.5	0.92	0.93	-0.99
RHS_150×100×5	0.92	0.97	-4.79
RHS_220×120×6.3*	0.87	-	-
RHS_220×120×6.3	0.90	0.90	0.10
SHS_180×6.3	0.94	0.91	3.16
SHS_180×8	0.94	0.97	-3.30
SHS_200×6	0.72	0.67	6.39

3.2.3 Propped-cantilever centrally loaded

Five propped-cantilever specimens of 4.8 m span length were tested with the loading being applied at mid-span. Specimens have been fixed to a braced support by welding a 30 mm thick plate to the beam's end and then bolting it with 8 10.9 M24 bolts (Figure 3.28b). The plate was chosen to be thick enough in order to be considered as perfectly rigid, and full penetration welds were realized.

In an attempt to monitor the specimens' strains and curvature at the hinges location without the interference of local buckling on readings, strain gauges were fixed on the tension flange; one was placed on the fixed-end 50 mm away from the plate due to the presence of the weld

and another one was placed at mid-span. The inclinometer was attached to the hinged end to measure the beam end rotation and a load cell was placed under the hinged support to measure the support reaction. Loading was introduced in the same way as for the simply supported beams and two load cells were placed under the jacks to record the applied force. LVDTs were placed at mid-span and at quarter span length to measure the beams deflection. The test setup is shown in Figure 3.27 below.

Plastic moment was always first reached at the fixed support with the development of a plastic hinge; additional bending moment was then redistributed to the middle span until plastic moment and system peak load were reached.

θ_y (Equation 3.11) was calculated when the system first reaches the elastic bending moment M_{el} . The system collapse load P_{pl} is calculated based on virtual work analysis and collapse mechanism with the assumption of having rigid-perfectly plastic hinges of zero length (Equation 3.12). Moments at mid-span and at fixed-end were determined through elastic methods.

$$\theta_y = \frac{PL^2}{32EI} \quad 3.11$$

$$F \cdot \frac{L}{2} \cdot \theta = M_{pl} \cdot \theta + M_{pl} \cdot 2\theta \quad \text{giving} \quad P_{pl} = \frac{6M_{pl}}{L} \quad 3.12$$

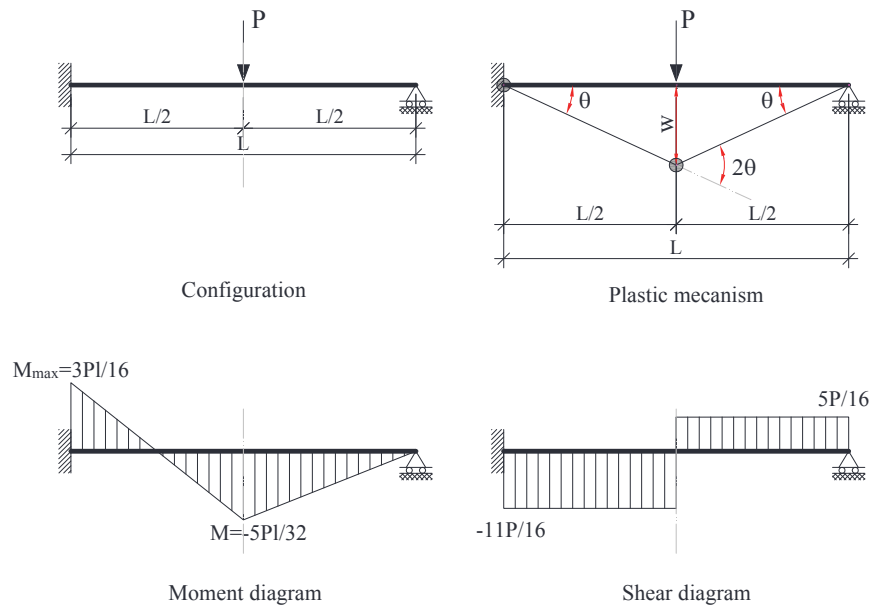


Figure 3.26 – Propped-cantilever centrally loaded analysis

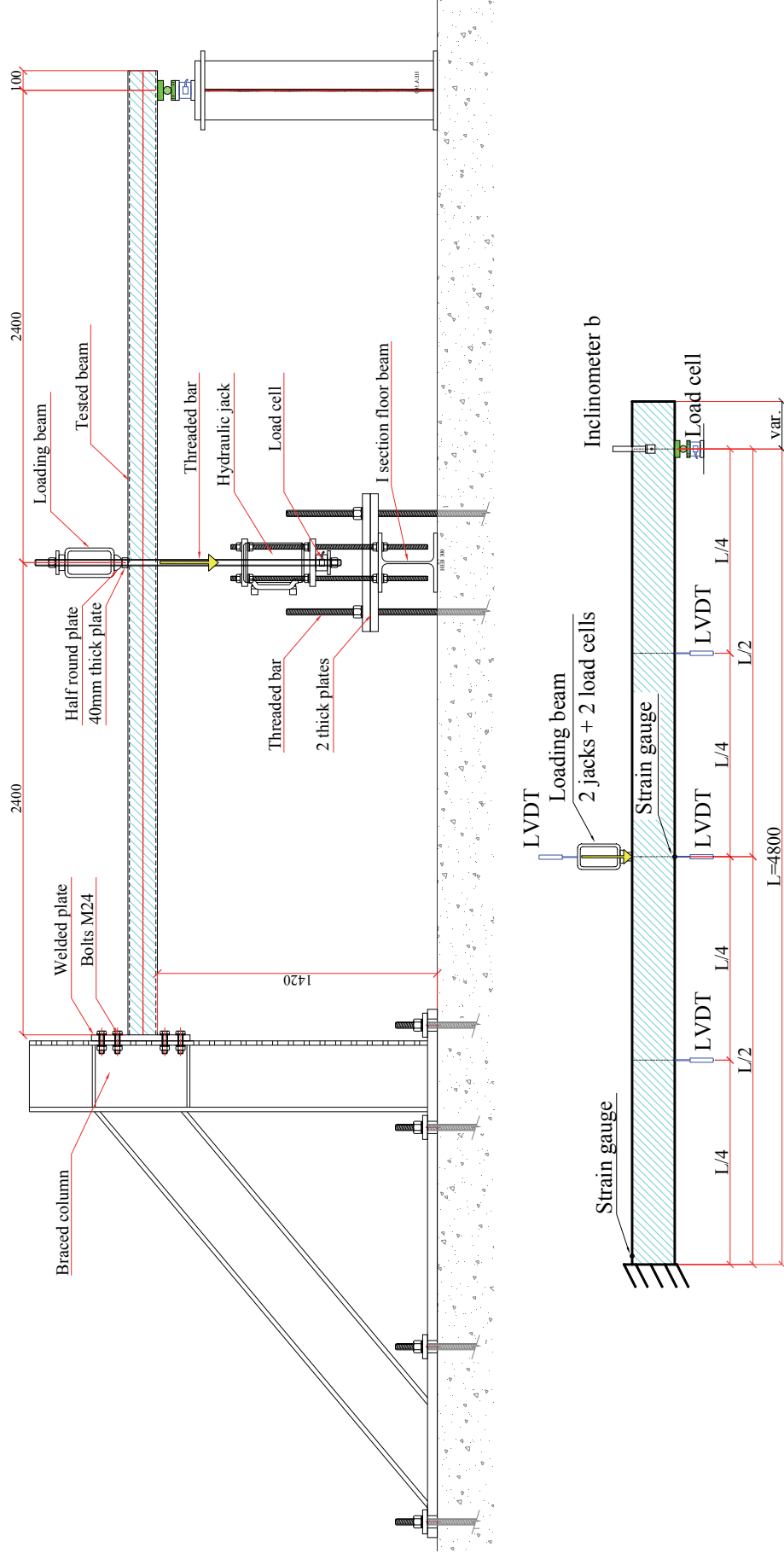


Figure 3.27 – Test setup of the propped cantilever centrally loaded



Figure 3.28 – a) Deformed shape of a propped cantilever centrally loaded – b) Connection detail on braced support

Moment-rotation curves have been plotted using the rotation given by the inclinometer at the hinged end, and moments at the mid-span and at the fixed-end are determined through elastic methods. Examples of results are shown for SHS_180×6.3 in Figure 3.29a. As expected, it is shown that, as the test progresses, fixed end moments are higher than at mid-span. System peak load is reached with premature local buckling at mid-span (i.e. before reaching the plastic moment in span), while the fixed-end end fully reaches the plastic moment due to welding restraint and to the absence of localised stresses. Table 3.9 summarises normalized span moments and fixed-end moment along with the system peak load for all the five tested specimens. The small area of load introduction induced concentrated load application that resulted in localized buckling. At the fixed end, a greater moment is reached (of about 30% M_{pl}). Even if an increase of moment is expected at the fixed-end due to the welding restraints and the moment gradient, a value of 30% M_{pl} is too high; this value is due to the load cell sensitivity, and mainly to the error generated if not uniformed loading is applied on its surface (see Figure 3.30). Therefore, after the peak load is reached, the beam deflection increase rapidly, and due to the load cell position in the test setup, tilted forces (and slightly off-set) are applied on the load cell, thus inducing error. Moreover, in Figure 3.29a, it can be observed that the system peak load occurred when the middle span reached its peak moment, or beyond for the cases of stockier sections where the system had reserve in resistance even though the span segment was unloading (Figure 3.31). Figure 3.29b displays the normalized moment-curvature with the yield curvature given in Equation 3.13. In the elastic phase, a linear region with the same elastic flexural stiffness EI_y for both the fixed-end and mid-span cross-sections

is shown, followed by a gradual reduction in stiffness for the fixed-end and a sudden loss of stiffness at mid-span.

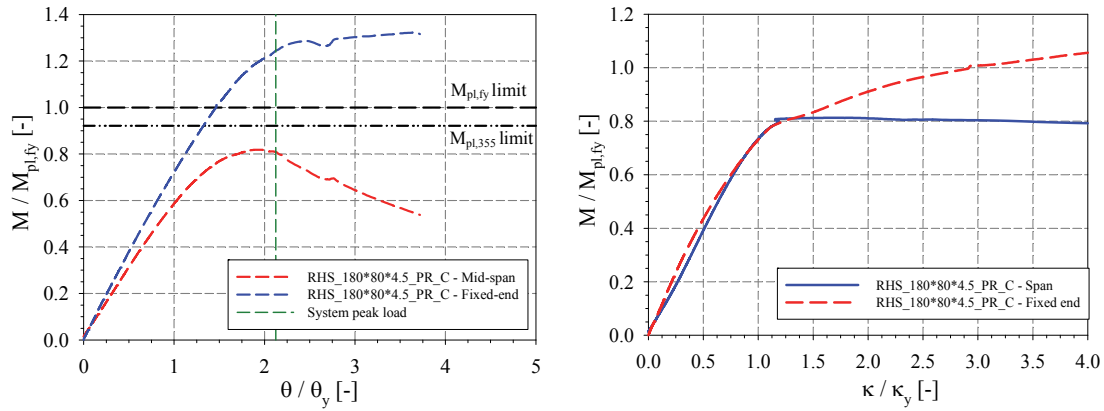


Figure 3.29 – a) Normalized moment - rotation of RHS_180×80×4.5 – b) Moment - curvature of RHS_180×80×4.5

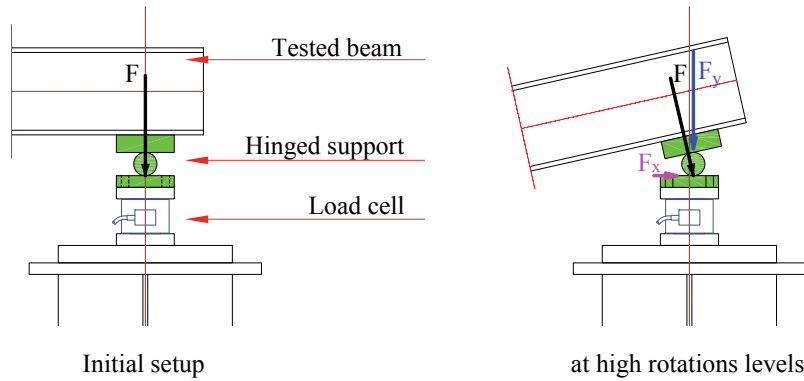
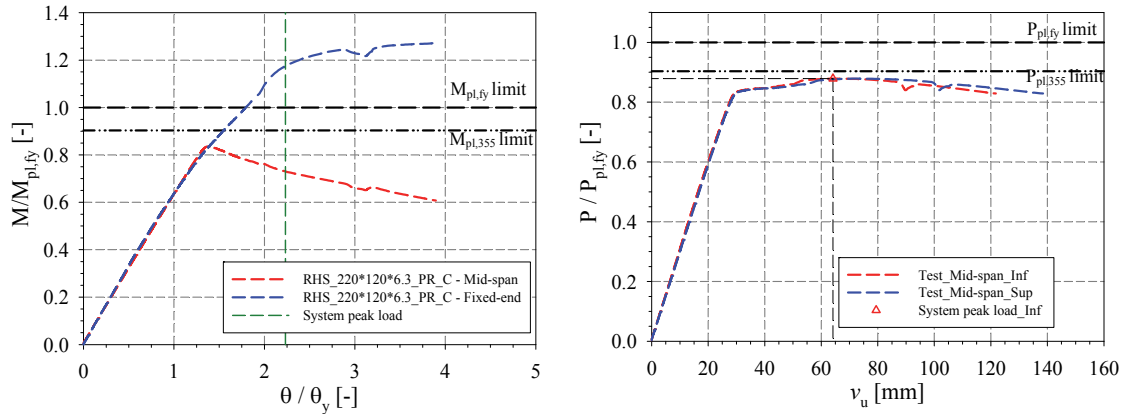


Figure 3.30 – Load cell arrangement in the test setup

For some of the test results (RHS_220×120×6.3_PR_C, SHS_180×6.3_PR_C and SHS_180×8_PR_C), beams' response was in contradiction with the theoretical expected ones in terms of moment redistributions. Hence, bending moment at the fixed end was not greater than the one in span (see Figure 3.31a). This is primarily due to the braced support. Due to experimental limitations, bolts had to be distanced horizontally by 160 mm, thus for all sections of width larger than 80 mm bolts were positioned on either side of the section (see Figure 3.32), and even though the plate was chosen thick enough to ensure a perfectly rigid connection, it resulted in a semi-rigid one (see Figure 3.32c for the case of SHS_180×8 in which the welded plate deformed after peak load was reached). This semi-rigid connection would therefore attract less moment and the span higher ones. Moreover, in the elastic part, bending moment at mid-span and the one at the fixed-end differ by 15% of the applied load P .

(see Figure 3.26). Hence, since the load cells precision is of the order of 5% the applied load P , their precision would have a great impact on the test data and would also justify the ambiguity that could occur in the elastic part.



* “inf” represents the deflection of the lower flange of the tested specimen and “sup” represents the deflection of the upper flange

Figure 3.31 – a) Normalized moment - rotation of RHS_220×120×6.3 – b) Normalized total load – span displacement of RHS_220×120×6.3

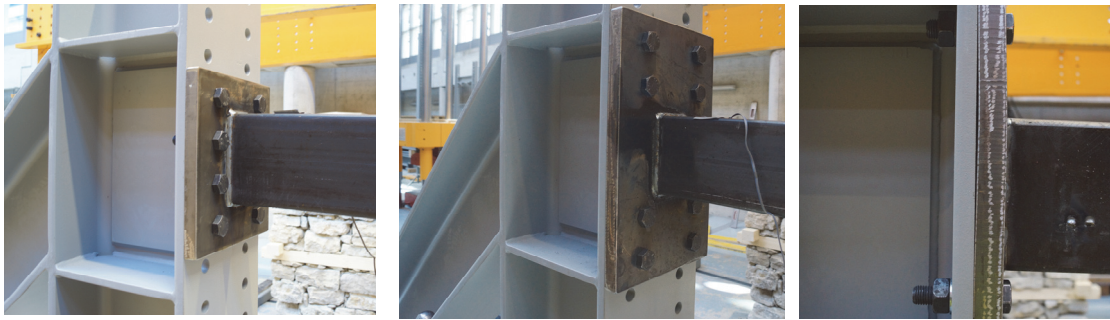


Figure 3.32 – a) braced connection for RHS_180×80×4.5 – b) RHS_150×100×5 – c) plate deformation for the case of RHS_220×120×6.3

Moreover, for comparison purposes, the moment-rotation curves have also been plotted using the moment value back-calculated from strain-gauges measurements (see appendix 2). This allows to plot moment-rotation curves from another set of data, and to confirm whether the obtained moment redistribution is caused from the braced support not being fully rigid, or from the inaccuracy of load cells measurements (it is also to be noted that some strain gauges were defective so no conclusion could be drawn to all specimens; refer to appendix 3). Moments from strain gauges have been calculated through reconstructing the stress diagram based on the measured material law and then integrating it. Calculations were based on the Bernoulli assumption. The strain on the compression flange was taken equal to that of the

tension flange (where the strain gauge was positioned) and the strain diagram was assumed linear in between. After the strain diagram was determined, the stress diagram as based on the measured material law was calculated. Then, the major axis bending moment M was determined by integrating the stress diagram around the major plastic axis of the section. Two methods have been used and compared: the first, analytical, was adopted with a simplified section that neglects the presence of corners and then the moment has then been normalized with the plastic moment from the simplified section for comparison purposes. The other method, numerical, consisted in discretizing the cross-section and then integrating the according stress of each element around the plastic neutral axis; the moment has then been normalized with the plastic moment.

Both methods gave the same results, and are described in detail in appendix 3. In Figure 3.33, for the case of RHS_180×80×4.5 specimen, we can see that in the elastic part, the moment from the strain gauges recording are in concordance with the moment calculated from the load cells measurement and to the theoretical curves (detailed calculation can be found in appendix 3). Moments calculated from the strain gauges can be more easily compared to the theoretical ones since their values are computed while assuming that the strain at the tensile flange is equivalent to the one at the compression flange; therefore, no reduction due to local buckling is taken into consideration, and the plastic moment is reached. Nonetheless, even if local buckling is not explicitly reported, its effect influences the strain gauges recordings and is displayed by the rapid loss in stiffness displayed in the moment-rotation curves. Moreover, the rounded response recorded by the gauges is due to the progressive propagation of yielding along the height and the length of the specimen and to the effect of residual stresses.

It can be noted in the moment-rotation graph (Figure 3.33), from the experimental curves computed from the gauges recording, that after the fixed-end first reaches the plastic moment, the moment is redistributed to the mid-span, and the curve at mid-span displays a premature sudden loss in stiffness due to the early initiation of local buckling. It is also shown that the system peak load is attained when both the span and fixed end reach the plastic moment.

In Figure 3.34, the theoretical load-displacement curve exhibits higher stiffness than the experimental one. This is due to the yielding process that spread in the transverse and longitudinal direction, and to second order effects. Moreover, it is due to the loading introduction that induced high level of stress concentrations and resulted in early local buckling, and hence a softer beam response.

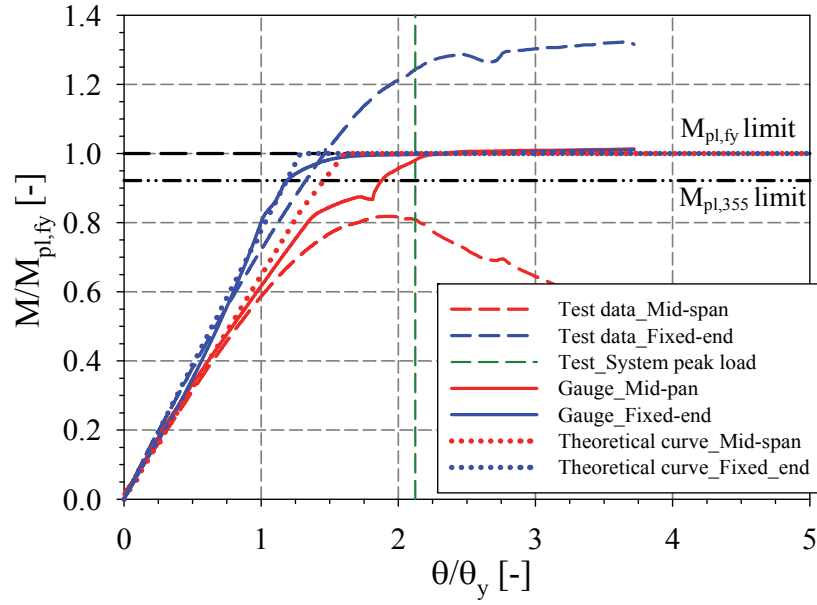


Figure 3.33 – Normalized moment - rotation of RHS_180×80×4.5 – comparison between moment from test load cells, strain gauges and theoretical calculations

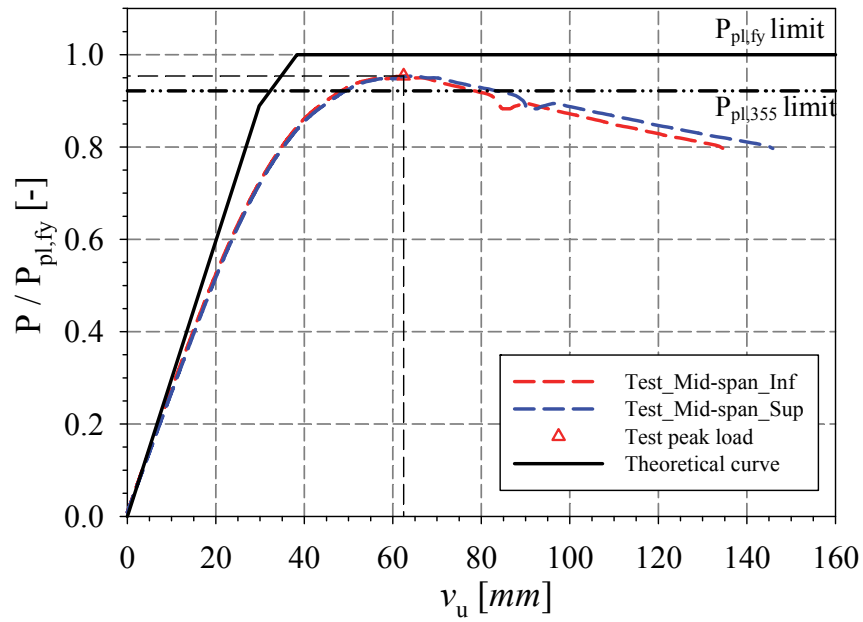


Figure 3.34 – Normalized load - displacement of RHS_180×80×4.5 – comparison between test results and theoretical calculations

Table 3.9 – Collapse results for the centrally loaded propped cantilever

Name of specimen	$M_{pl,fy}$	$P_{pl,fy}$	θ_y	P_{ult}	P_{ult} / P_{pl}	$M_{ult,span}$	$M_{ult,span} / M_{pl}$	$M_{ult,fix-end}$	$M_{ult,fix-end} / M_{pl}$	θ_u / θ_y	v_u
	[kN.m]	[kN]	[°]	[kN]	[-]	[kN.m]	[-]	[kN.m]	[-]	[-]	[mm]
RHS_180×80×4.5_SS_3P	49.6	62.0	0.95	59.2	0.95	40.4	0.81	66.1	1.33	2.12	62.4
RHS_150×100×5_SS_3P	48.1	60.1	1.17	61.4	1.02	46.0	0.96	58.1	1.21	2.82	106.9
RHS_220×120×6.3_SS_3P	115.1	143.9	0.81	126.4	0.88	97.9	0.85	144.1	1.25	2.23	64.2
SHS_180×6.3_SS_3P	113.8	142.3	0.96	123.9	0.87	97.8	0.86	134.9	1.18	1.36	36.0
SHS_180×8_SS_3P	129.1	161.4	0.92	152.2	0.94	112.96	0.87	169.7	1.31	3.16	99.6

3.2.4 Propped-cantilever off-centrally loaded

Three additional propped-cantilever specimens of 4.8 m span length were tested with loading applied at one third length from the hinged support. This arrangement was performed so that – unlike the propped-cantilever centrally loaded – the plastic hinge would first form in the span and then, due to moment redistribution, failure would occur by the fixed-end reaching the plastic collapse load. The test setup is shown in Figure 3.35 and Figure 3.36. Arrangements for the fixed end, hinged end and loading introduction were performed similarly to the centrally loaded cantilevers.

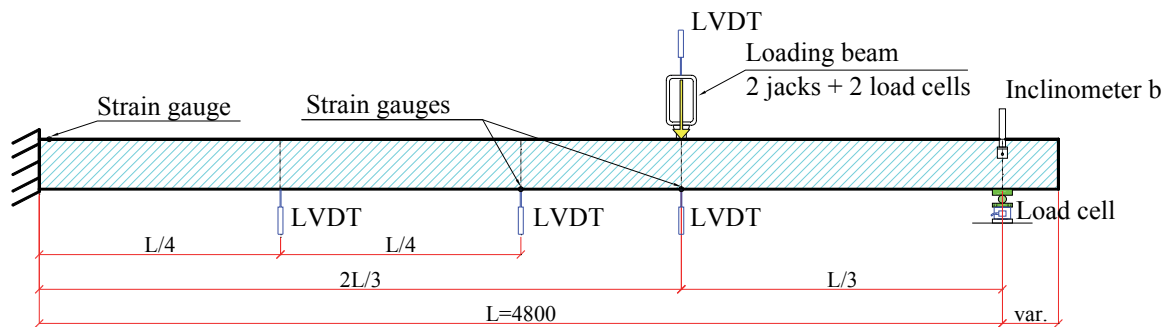


Figure 3.35 – Test setup of the propped cantilever off-centrally loaded



Figure 3.36 – Deflected shape of a propped cantilever off-centrally loaded

As shown in Figure 3.38a moment-rotation plot, span first reaches the plastic moment. Failure is then attained in the fixed-end reaching its plastic bending resistance. Before the system peak load is reached, span moment is higher than the fixed-end moment, after which the span moment decreases and the fixed-end moment increases to reach the plastic moment. Yield rotation and system collapse load P_{pl} are given in Equations 3.14 and 3.15.

$$\theta_y = \frac{PL^2}{27EI} \quad 3.14$$

$$F \cdot \frac{L}{3} \cdot \theta = M_{pl} \cdot \frac{\theta}{2} + M_{pl} \cdot \frac{3\theta}{2} \quad \text{giving} \quad P_{pl} = \frac{6M_{pl}}{L} \quad 3.15$$

Similarly, for the propped cantilever off-centrally loaded, a semi-rigid connection would also result in greater span moment and reduced fixed-end moment which would only emphasize the theoretically expected results. Nevertheless for the case of the RHS 180×80×4.5 where the braced connection is perfectly rigid, moment redistribution were in contradiction with the theoretical expected ones (i.e. fixed end moment were higher than of the span). This can be explained by the load cells precision and the fact that moments at the point load and at the fixed-end are close, thus an ambiguity may arises in the elastic regions of these curves. In addition, when plotting the back-calculated moments from the strain gauges readings, it can be seen that the fixed-end moment should be lower than that recorded by the load cells; however it should be noted that strain gauges at fixed end were defective for some specimens and therefore cannot be fully trustworthy.

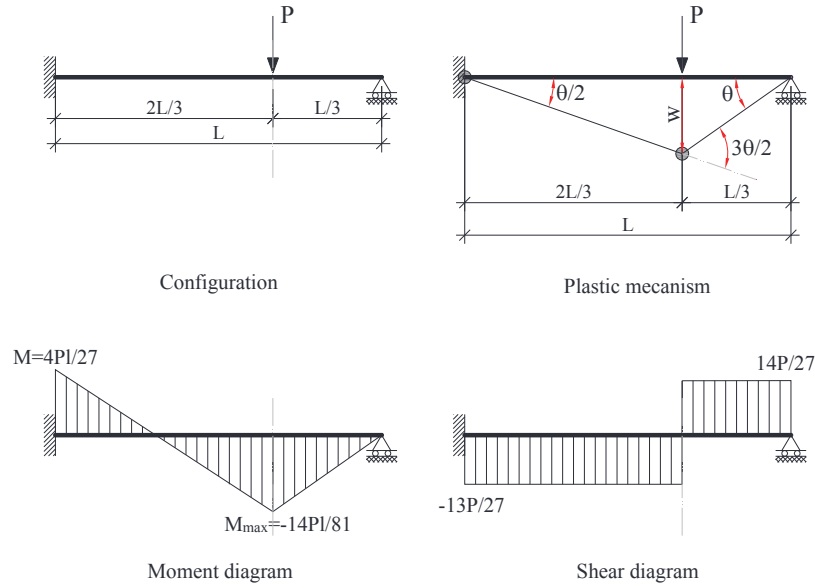


Figure 3.37 – Propped cantilever centrally loaded diagrams

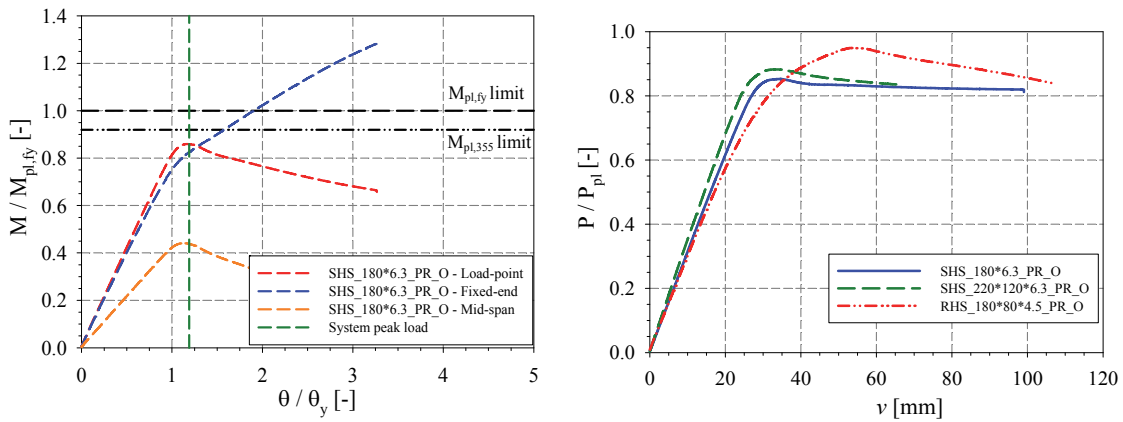


Figure 3.38 – a) Normalized moment - rotation of RHS_180×80×4.5 – b) Normalized total load – span displacement

In Figure 3.39, the moment-rotation curves calculated from the gauges shows clearly that local buckling is first reached at the point load position and this without reaching the plastic moment M_{pl} (as seen in Figure 3.39 by the curve calculated from load cells). Thus, no plastic hinge could be developed at the point load due to high level of stress concentrations. Hence, due to premature local instability, bending moment cannot be properly redistributed to the fixed-end which explains the high reduction in stiffness of the fixed-end moment curve and the reason why the attainment of the plastic moment is much delayed after the attainment of the system peak load.

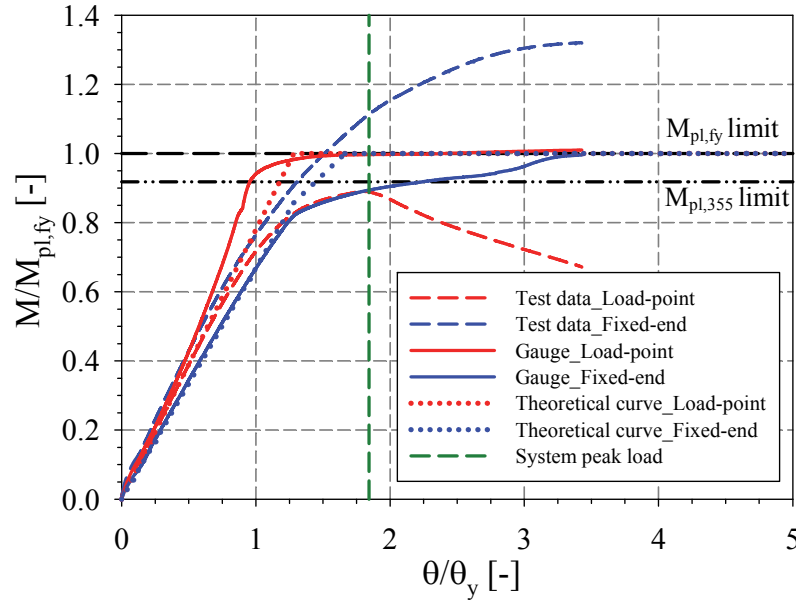


Figure 3.39 – a) Normalized moment - rotation of RHS_180×80×4.5 – comparison between moment from test load cells, strain gauges and theoretical calculations

System peak load occurred at variable vertical displacement levels ranging between 20 *mm* and 60 *mm*; the normalized total load is plotted as a function of the deflection for the three propped cantilever off-centrally loaded in Figure 3.38b. The deflection v is measured at the loading point. Table 3.10 summarises normalized span moments and fixed-end moments along with the system peak loads and corresponding end rotations θ_u for the 3 tested specimens.

Table 3.10 – Collapse results for the off-centrally loaded propped cantilever

Name of specimen	$M_{pl,fy}$	$P_{pl,fy}$	θ_y	P_{ult}	P_{ult} / P_{pl}	$M_{ult,span}$	$M_{ult,span} / M_{pl}$	$M_{ult,fixed-end}$	$M_{ult,fixed-end} / M_{pl}$	θ_u / θ_y	v_u
	[<i>kN.m</i>]	[<i>kN</i>]	[°]	[<i>kN</i>]	[-]	[<i>kN.m</i>]	[-]	[<i>kN.m</i>]	[-]	[-]	[<i>mm</i>]
RHS_180×80×4.5_SS_3P	48.7	60.9	1.24	57.5	0.95	43.3	0.89	64.3	1.32	1.84	53.2
RHS_220×120×6.3_SS_3P	115.4	144.2	1.01	127.8	0.89	103.8	0.90	122.8	1.06	1.48	33.7
SHS_180×6.3_SS_3P	109.46	136.83	1.22	116.6	0.85	94.07	0.86	140.41	1.28	1.25	34.5

3.3 Conclusions

Experimental works investigating the available rotation capacity of HSS have been presented. The test program included 4 different configurations, 6 cross-sections dimensions of S355 steel grade profiles from the hot-formed production process. Tensile tests were performed for

all sections. Moreover, seven stub column specimens were tested to measure the level of available ductility of the sections.

The simple supported test configurations resulted in five out of six sections to experience insufficient plastic rotation capacity due to high level of stress concentration imposed during loading, although sections were classified as class 1 according to Eurocode 3. It was shown that the bearing surface area was the key factor here and that further investigation are necessary to couple the width-to-thickness ratio of the compression flange with the bearing stress intensity imposed on that flange, in order to fully understand and characterize the observed experimental behaviour.

For the propped cantilever configurations, the fixed sections showed an increase in strength due to welding restraints while the span section did not reach its full plastic moment capacity due to high level of stress application. Early local buckling at the span prevented the attainment of the plastic moment and the formation of plastic hinge, thus prohibiting the formation of a mechanism and the characterisation of the rotation demand.

4 DEVELOPMENT AND VALIDATION OF FINITE ELEMENT MODELS

4.1 General scope

This chapter details the numerical model developed, and its validation against the 23 bending tests performed at the University of Applied Science of Western Switzerland – Fribourg, and against 32 cold-formed tests performed by Wilkinson at the University of Sydney – Australia. The finite element simulations were carried out with the finite element software FINELg. Special attention was given to the boundary conditions, load introduction, geometrical imperfections and measured material law and dimensions. Numerical results are then compared to their experimental counterpart, in order to validate the numerical model. Hence, after its validation, the numerical model will be extensively used in a consecutive numerical parametric study (reported in the next chapter) to generate a series of bending test data, in order to investigate the sensibility of the rotation capacity to different parameters.

4.2 Assessment toward documented test data

4.2.1 Validation against tests performed at the University of Applied Sciences of Western Switzerland – Fribourg

Numerical computations were performed with the use of the non-linear F.E. software FINELg, continuously developed at the University of Liège and Greisch Engineering Office since 1970 [103]. Cross-sections were modelled with the use of quadrangular 4-nodes plate-shell finite elements, and resorting to L.B.A. (Local Buckling Analysis) and G.M.N.I.A. (Geometrically and Materially Nonlinear Analysis with Imperfections) analyses. Detailed results for all specimens can be found in appendix 3.

The numerical models have been developed to represent the specimens' properties, as well as the test setup characteristics as closely as possible. Measured geometric dimensions described in Chapter 3 were implemented, and the section was modelled using 4 shell elements per corner, to suitably represent the geometric static characteristics of the tested specimen. Averaged measured stress-strain data was also included; for hot-formed sections, a multi-

linear material law was adopted as shown in Figure 4.1. For cold-formed sections, a simple Ramberg-Osgood material law was used for the flat regions (Equation 4.1) with $n = 22$.

$$\varepsilon = \frac{\sigma}{E} + 0.002 \left(\frac{\sigma}{\sigma_{0.2}} \right)^n \quad 4.1$$

This parameter was seen to provide curves in good concordance with the measured ones; moreover, due to the cold-forming process, sections usually exhibit strength enhancement in the corner regions, hence a multi-linear law was considered as described in Figure 4.2, with the corresponding yield and tensile stress given in Equation 4.2 and 4.3. These values have been adopted based on experimental measurements along with literature review and are summarised in [104]¹.

$$f_{y_corner} = 1.15 f_{y_flat} \quad 4.2$$

$$f_{u_corner} = 1.15 f_{u_flat} \quad 4.3$$

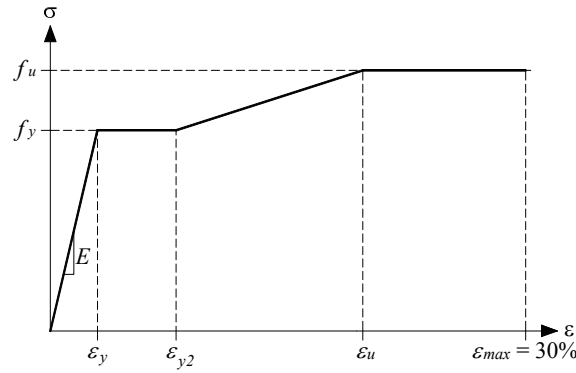


Figure 4.1 – a) Adopted material law for hot-formed sections

¹ It is to be noted that having such different material laws led to difficult convergences, especially in the post peak range.

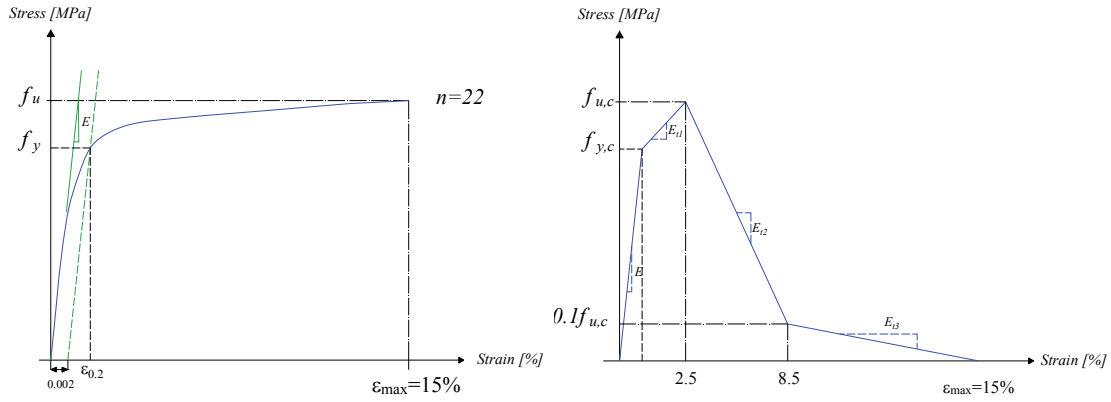


Figure 4.2 – a) Adopted simple Ramberg-Osgood material law for flat regions – b) Adopted multi-linear material law for corner regions [104]

For hot-formed sections, auto-equilibrated membrane residual stresses pattern were implemented with a reference yield stress $f_y = 235 \text{ N/mm}^2$ along with constant residual stresses patterns, shown graphically in Figure 4.3. Flexural residual stresses were adopted for cold-formed sections with a linear distribution. Flexural stresses were taken equal to $1.2 f_y$ ($f_y = 235 \text{ N/mm}^2$), in the flat regions and equal to f_y in the corner region. These values have been prescribed by Nseir (2015) [104] based on literature review and on some own measurements. It is to be noted that for cold-formed sections, residual stresses are somewhat implicitly incorporated in the stress-strain curve, due to the tensile coupon straightening during testing [105]. Nevertheless, they have been implemented in the numerical model to well represent the mechanical behaviour of the beams and to provide safe-sided numerical resistance predictions.

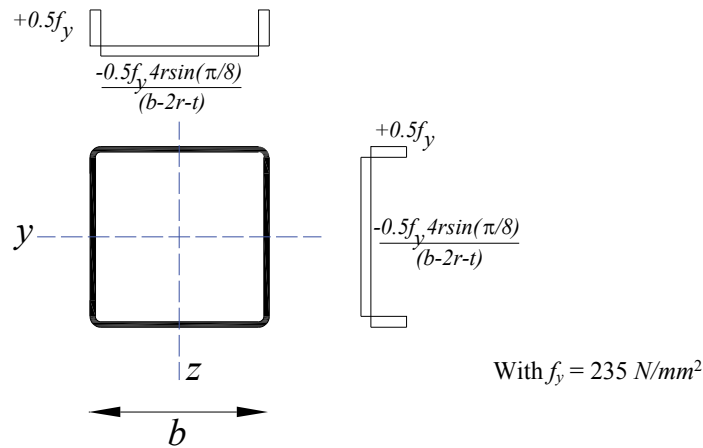


Figure 4.3 – Auto-equilibrated residual stress pattern for Hot-formed tubular profiles - SHS and RHS

4.2.1.1 Mesh density

In F.E. models, the distribution of the fine mesh is crucial in order to obtain trustworthy results. In the context of this study, a dense mesh was used in the yielding zones, where local buckling would develop, to obtain accurate results and well represent the beam behaviour (see Figure 4.5). Moreover, a slightly coarser mesh density was used in the zones adjacent to the ones where local buckling would spread, to minimise the computational time. Numerical models have been developed so that the hollow beam consists of 10 zones, allowing a variation of the meshing density in the longitudinal direction. In this way density can be increased in key areas.

For each of the tested specimen, three different mesh types have been adopted with the aim of checking the mesh densities that would provide accurate results (Figure 4.4). The adopted meshes were denoted Mesh 1, Mesh 2 and Mesh 3 with mesh densities spanning from coarse (for the case of Mesh 1) to very dense (Mesh 3). While Linear Buckling Analysis (L.B.A.) is the most sensitive to meshing variations, G.M.N.I.A. calculations were selected for validation purposes.

It can be observed in Figure 4.6 that different meshes resulted in relatively similar stiffness in the elastic part, but in differences concerning the peak load value and the post peak path. This is attributed to the elements' size which is not small enough to represent accurately the development of plastic mechanisms and local buckling. In Figure 4.6, we can clearly see that Mesh 2 and 3 give similar responses and a quite satisfactory behaviour.

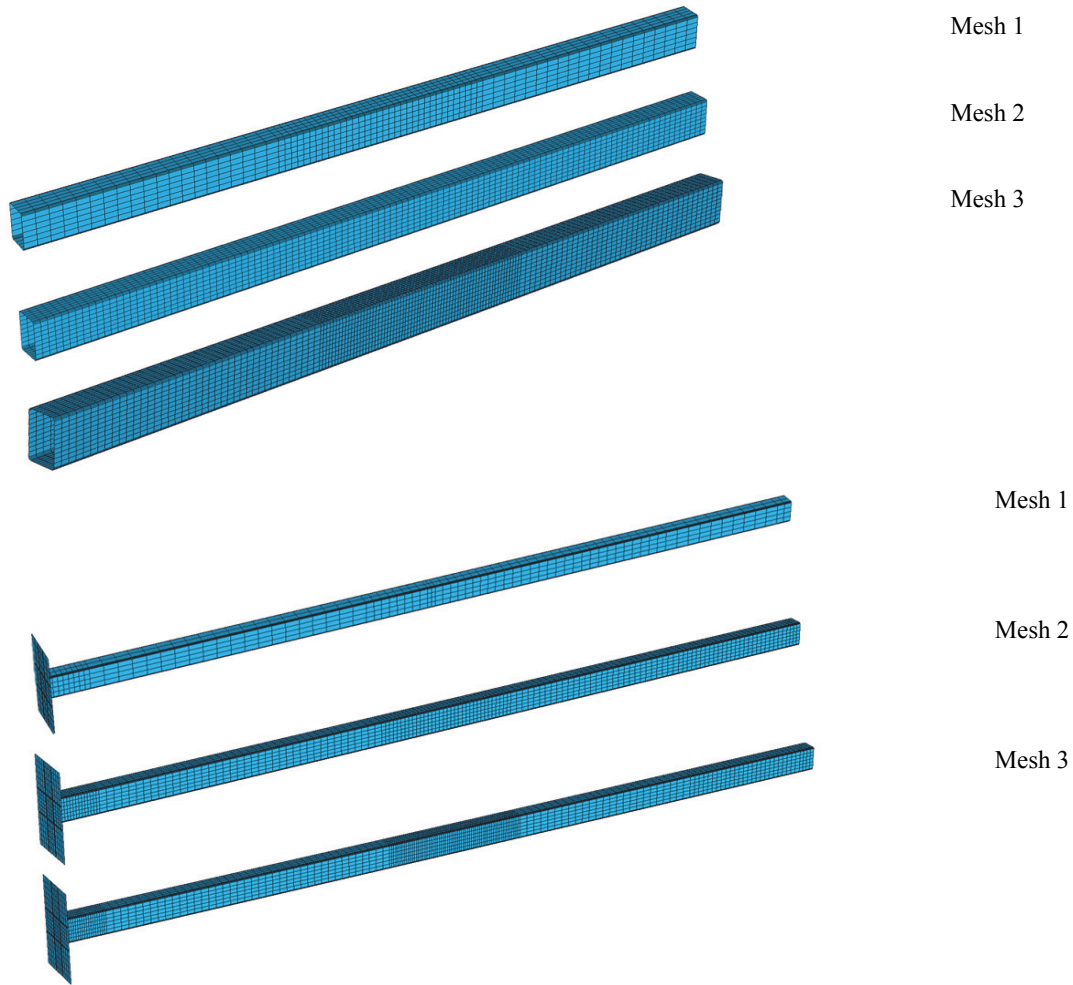


Figure 4.4 – Different adopted mesh densities

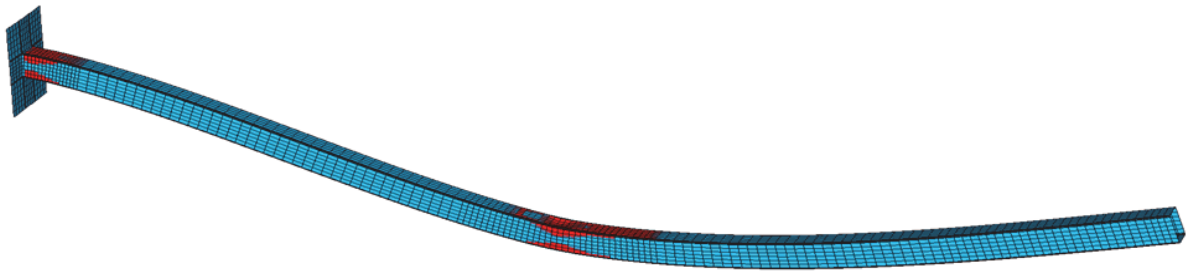


Figure 4.5 – Yield extent at final step

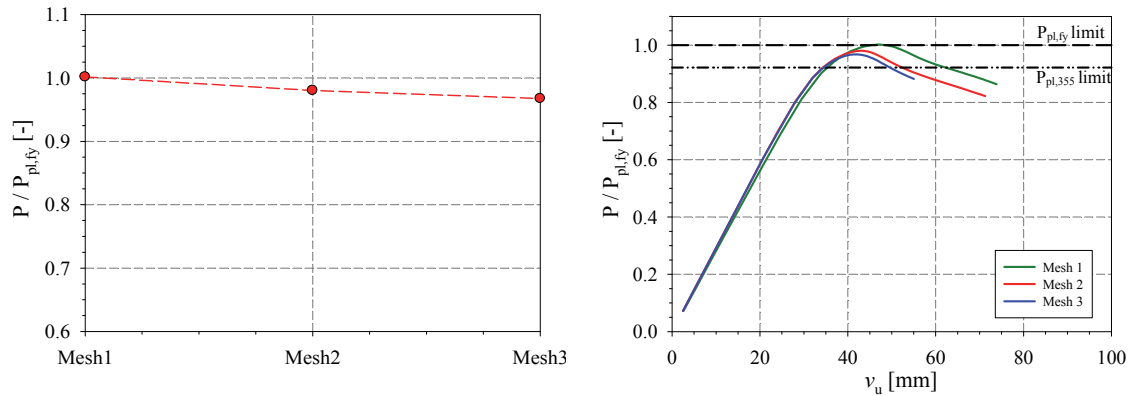


Figure 4.6 – G.M.N.I.A. results, maximum load and load-deflection curves for RHS_180×80×4.5_PR_C

Figure 4.7 to Figure 4.10 report results for all tests in terms of normalised ultimate moment for the simply supported arrangement, and normalised ultimate load for the propped cantilever configurations. From these figures, it can be observed that small differences occur between the three different meshes in the simply supported cases. For the propped cantilever configuration, more differences are observed between Mesh 1 – that is very coarse – and both Mesh 2 and Mesh 3. For the latter case (propped cantilever), bigger differences were expected since two plastic hinge form. Hence, a fine mesh capable of accurately representing the development of the yield lines in two locations – and thus the plastic mechanism – is required. For the cases of Mesh 2 and Mesh 3, small differences are displayed for all tests. These meshes were seen to provide accurate representations in terms of peak load and yield development. Hence, since results showed a quite satisfactory behaviour for the mesh 2 definition, it was therefore adopted for the remaining validation of tests, as it provides satisfactory accuracy and minimal computational time.

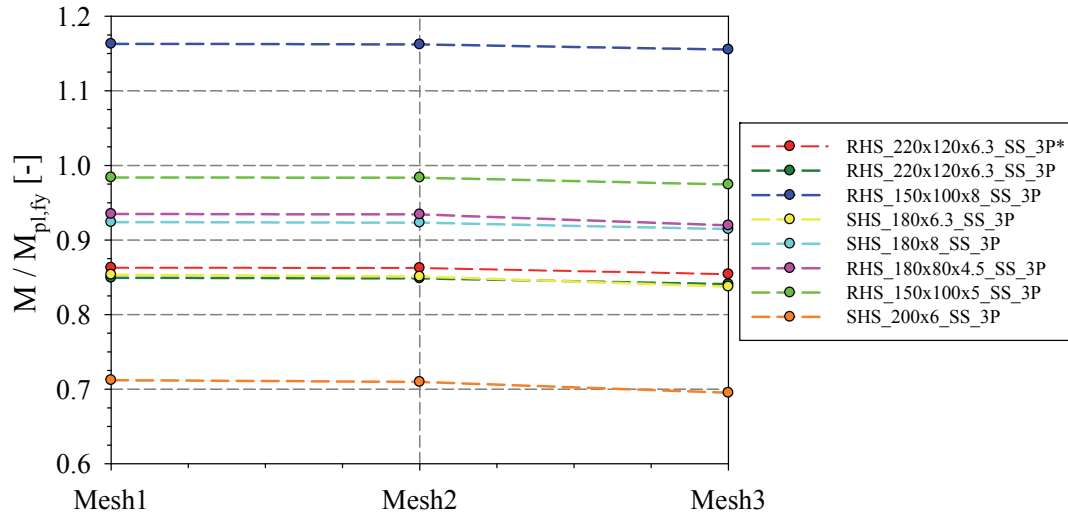


Figure 4.7 – G.M.N.I.A. results, normalised maximum moment of the 3-pt bending tests for different meshes

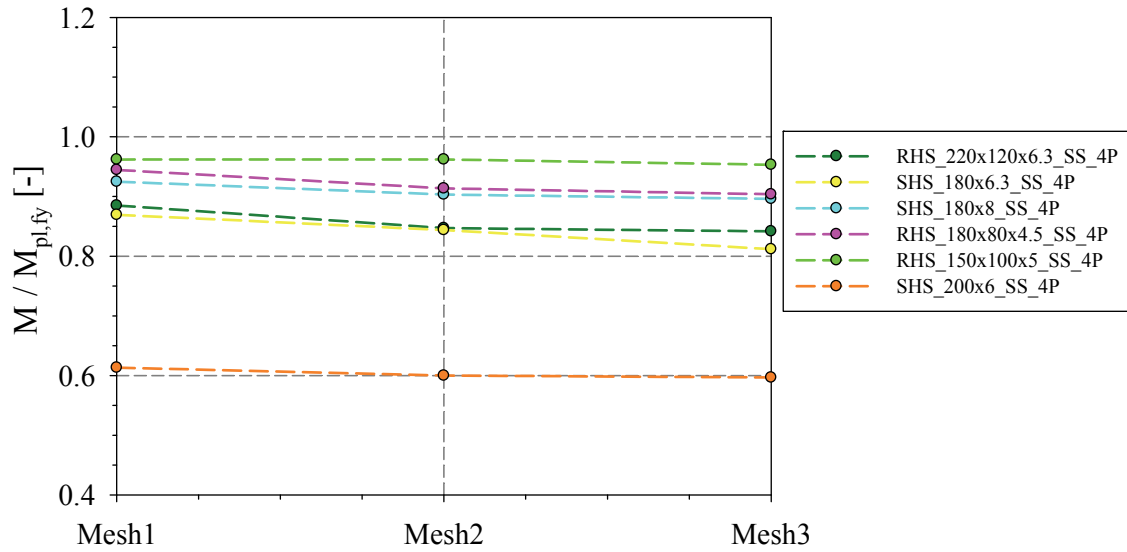


Figure 4.8 – G.M.N.I.A. results, normalised maximum moment of the 4-pt bending tests for different meshes

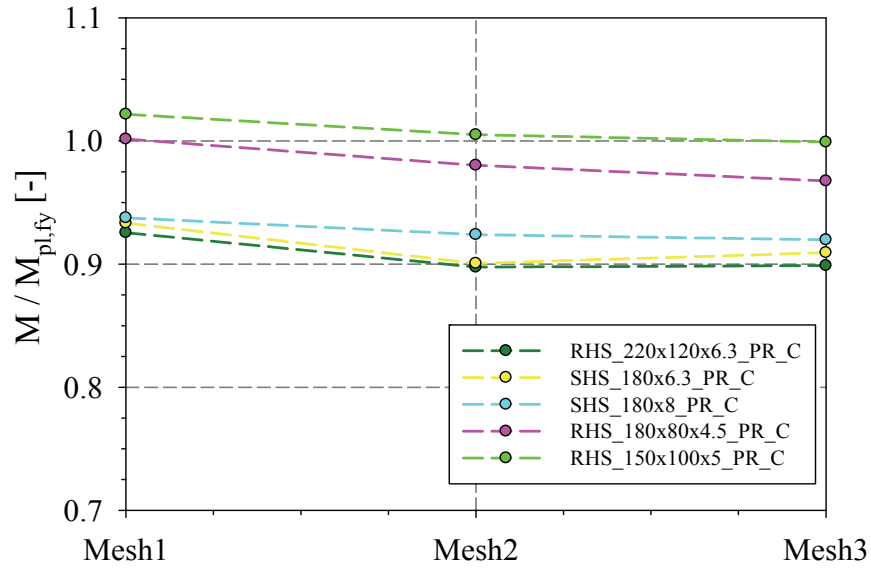


Figure 4.9 – G.M.N.I.A. results, normalised maximum load of the PR_C tests for different meshes

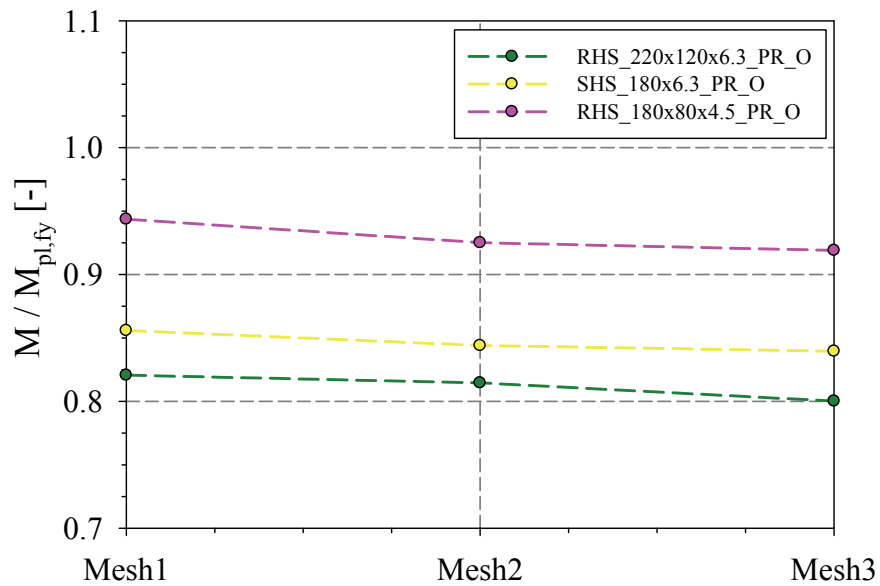


Figure 4.10 – G.M.N.I.A. results, normalised maximum load of the PR_O tests for different meshes

4.2.1.2 Support conditions

Special attention was given to the modelling of the support conditions to represent the test configuration as closely as possible. Hence, for the simply supported configurations and to represent the actual hinged connection, only the bottom flange nodes were supported at a

distance of 10 *cm* away from the section end as in the actual test. Moreover, a bearing plate of 20 *mm* thickness was added under the hinged support and was given an elastic material law in order to prevent its yielding. Concerning the propped cantilever, the end plate was modelled as well since it was shown to affect the response of the specimens. The same material law as for the main beam was adopted. Also, an increase in thickness was considered for the first 1 *cm* of the beam to model the weld with $f_y = 500 \text{ N/mm}^2$ and $f_u = 600 \text{ N/mm}^2$. Since the end-plate of the specimen was fixed by mean of 8 bolts, thus, when the beam is bended, the lower part of the end-plate is in compression and applying a compressive pressure against the column of the braced support, while the upper part of the end-plate is in tension, with the bolts retaining it to the braced support. In that respect, the compression part of the end-plate was completely fixed, and 4 supports were placed on the bolts positions in the tension part (Figure 4.12).

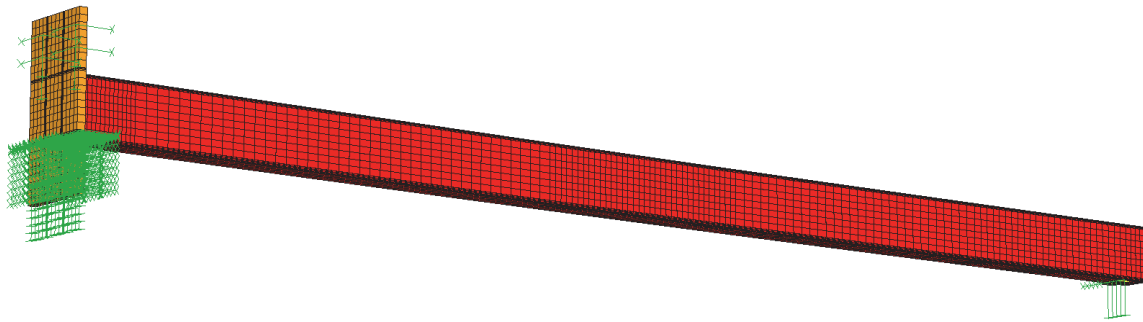


Figure 4.11 – Modelling of propped cantilever beam

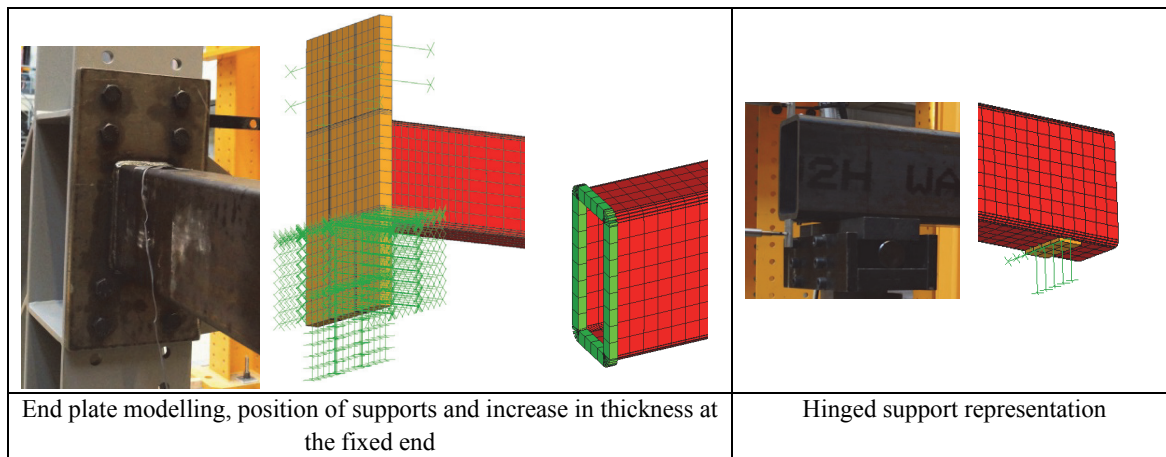


Figure 4.12 – Details of supports modelling

4.2.1.3 Introduction of loading

As for the modelling of the load introduction, the experimental conditions were taken into account as closely as possible, however through different possibilities. Loading was first introduced through 4 concentrated forces applied on the upper flange edges, and positioned at the 4 corners of the plate in contact with the tested beam, as it was observed to be in the actual test. Hence, due to the bending of the beam and the upper flange buckling, the 50 mm plate was in contact with the flange only at its extremities and not on the whole surface. Nevertheless, for sake of consistencies, three loading application were varied in order to see their effect on the beams response. Load 1 corresponds to the actual loading application and Figure 4.13 shows a picture of the tested beam where this phenomenon is highlighted; load 2 is applied uniformly on the junction between corner and flange on a distance of 50 mm, and load 3 is applied evenly on the flanges on two segments spaced of 50 mm (see Figure 4.13).

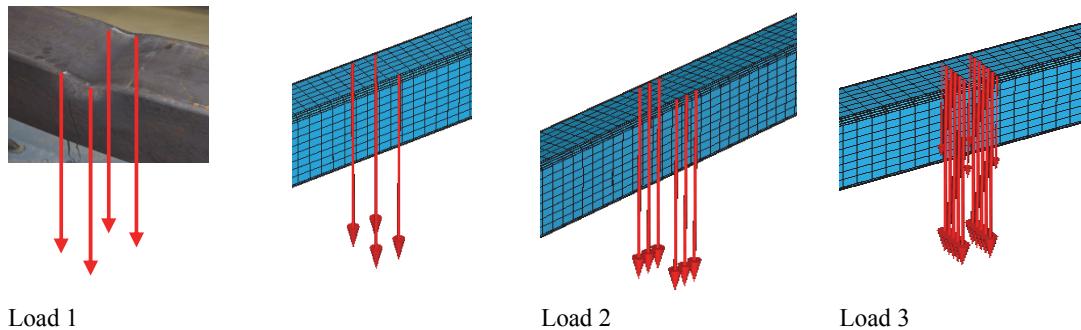


Figure 4.13 – Loading variation

Figure 4.14 clearly illustrates that the loading variation not only affects the ultimate capacity of the beam, but also its stiffness especially for the loading case 3. Therefore, load 1 was adopted since it seemed to well represent the loading conditions as well as the beams response in terms of moment-rotation behaviour (see section 4.2.2.1).

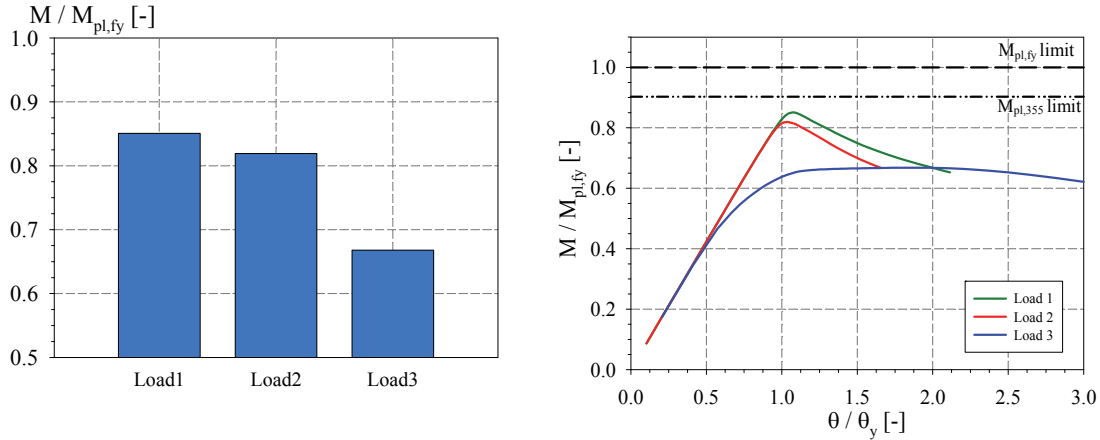


Figure 4.14 – Load introduction influence in term of maximum moment and moment-rotation curves for SHS_180x6.3_SS_3P

4.2.1.4 Sensitivity to geometrical Imperfections

Initial geometrical imperfection are shown to alter hollow section beams' response in the post peak (unloading) phase. Typically, when such beams are tested in bending, their rotation capacities may vary in a considerable extent, depending on the geometrical imperfections. In the experiments performed, initial geometrical imperfections were not measured prior to testing, because the measurement technique at our disposition was not sufficiently reliable to measure small amplitudes, and would therefore not help achieve a better understanding of the experimental results. Therefore, a set of different imperfection shape and amplitudes were varied numerically. Two types of geometrical imperfections were introduced. One is based on the deformation induced by the first eigenmode shape, for which the maximum amplitude is assigned. The second is introduced through an appropriate modification of node coordinates. Full independence between all global or local defaults is respected. Local geometrical imperfections are established for both webs and flanges with square half-wave shapes and with a chosen amplitude. The global default is introduced through a sinusoidal shape (similar to the member buckling shape), for both strong axis and weak axis; the maximum amplitude of each being an input parameter. Seven different geometrical imperfection pattern were selected and are represented in Figure 4.15 and Figure 4.16. Depending on the geometric imperfections introduced into the model, results were seen to be more or less close to the recorded experimental one in the unloading phase.

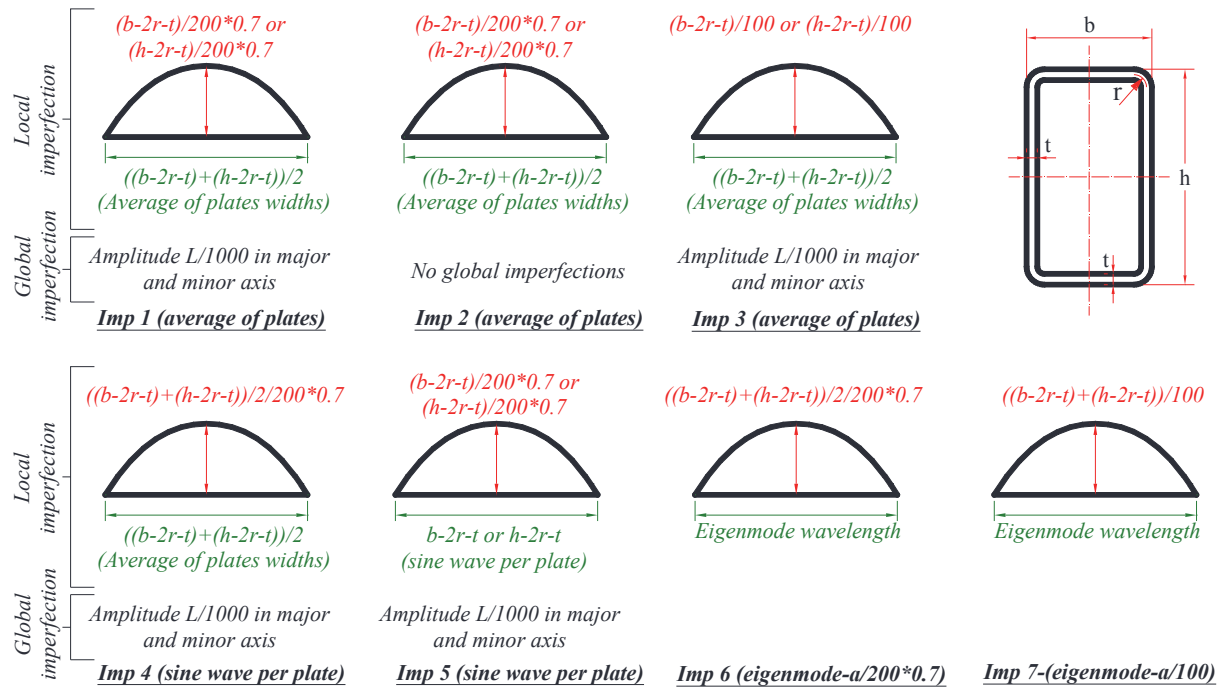


Figure 4.15 – Considered geometrical imperfections

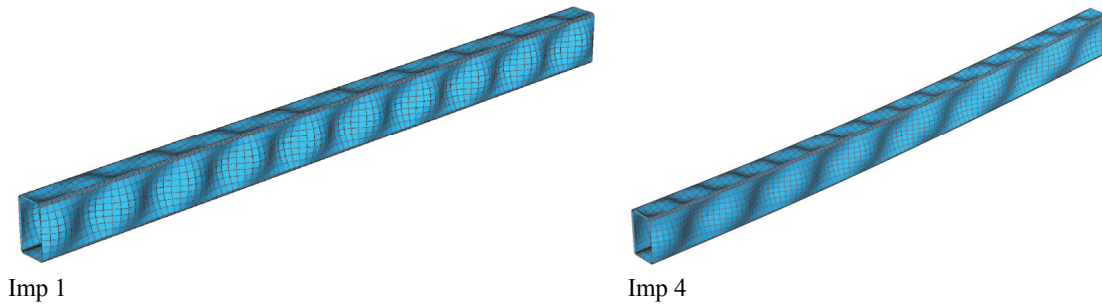


Figure 4.16 – Amplified geometrical imperfections

The geometrical imperfections did not affect the beam response in the elastic part, and no difference is depicted between curves. Moreover, an excellent correlation between the test results and the F.E. models prediction is observed, indicating that the modelling of the beams was adequate (in terms of support modelling, load introduction...) and represented well the system stiffness. Nevertheless, the imperfections shape and amplitude had a large influence on the post peak response, and therefore on the rotation capacity of the specimens. Because a limited set of imperfection was selected, the unloading phase observed in the F.E. simulations was not always nicely matching the experimental one, as Figure 4.17, Figure 4.18, and

Figure 4.19 show. In these figures, “Displacement inf” refers to the beam deflection recorded at the bottom flange.

Global geometrical imperfections had no influence on the beams tested in bending, since no difference between “Imp 1” and “Imp 2” moment rotation curves can be noticed. Global geometrical imperfections were nevertheless added to the local imperfections since they are present in a real specimen.

As a general trend, imperfections had an influence on the beam ultimate capacity as well as on its rotation capacity, as seen in Figure 4.17. It is also to be noted that even though the imperfection shape had an impact on the beam response, it is mainly their amplitude that lead to scatters in rotation capacities. An increase or decrease in strength when the imperfection is amplified is due to whether the initial geometrical buckle direction at the loading point is downward or upward. Furthermore, even for the cases based on the first eigenmode and since loading was introduced on the 4 corners, some configurations resulted in an upward buckle, explaining why the specimen could attain higher resistances when the amplitude was increased (Figure 4.18 and Figure 4.19). In some cases, for example for the case of RHS_150×100×5_SS_4P, some imperfection patterns had a major influence on the rotation capacity (Figure 4.18), but not on the ultimate strength. For other specimens, it is the ultimate capacity of the beam that was affected but not the post peak unloading phase. Would a numerous number of imperfections shape and amplitudes varied for the same tested specimen, an imperfection pattern shall lead to a similar behaviour as the experimental test and load-displacements curves would be matched in the post peak phase (as it was the case of the RHS_150×100×5_SS_4P reported in Figure 4.18).

In this sub-study, we limited our sensibility analysis to 7 cases. In this sensibility analysis, type 1 imperfection pattern was seen to lead to conservative results in term of rotation capacity. Further sensitivity studies toward a deeper understanding shall however be welcome and considered as additional developments. In the following section, when the numerical model is validated against the experimental tests, test results were compared to the numerical model that incorporate type 1 imperfection shape, even if other imperfections types led to closer results.

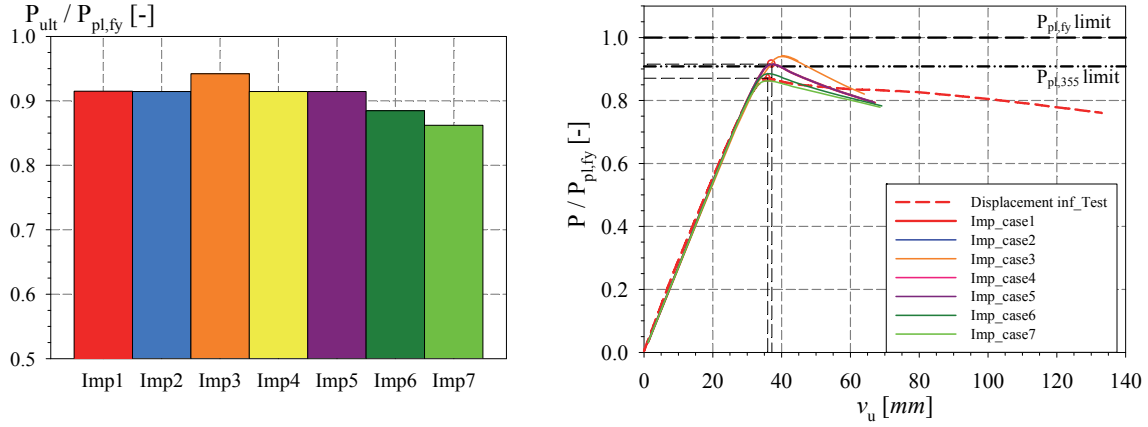


Figure 4.17 – Imperfections sensitivity for SHS_180×6.3_PR_C, a) comparison of the normalised ultimate load, b) load-displacement curves for the different imperfection patterns

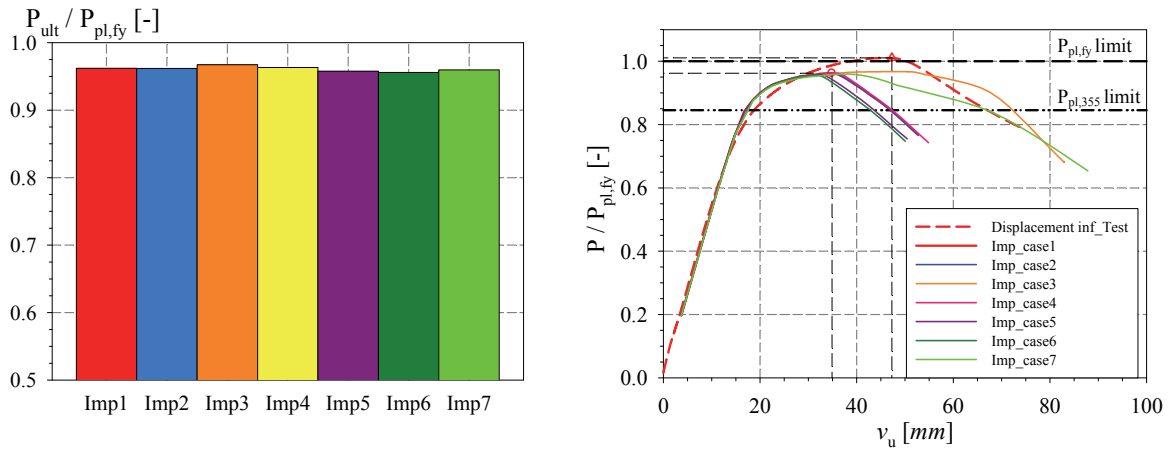


Figure 4.18 – Imperfections sensitivity for RHS_150×100×5_SS_4P, a) comparison of the normalised ultimate load, b) load-displacement curves for the different imperfection patterns

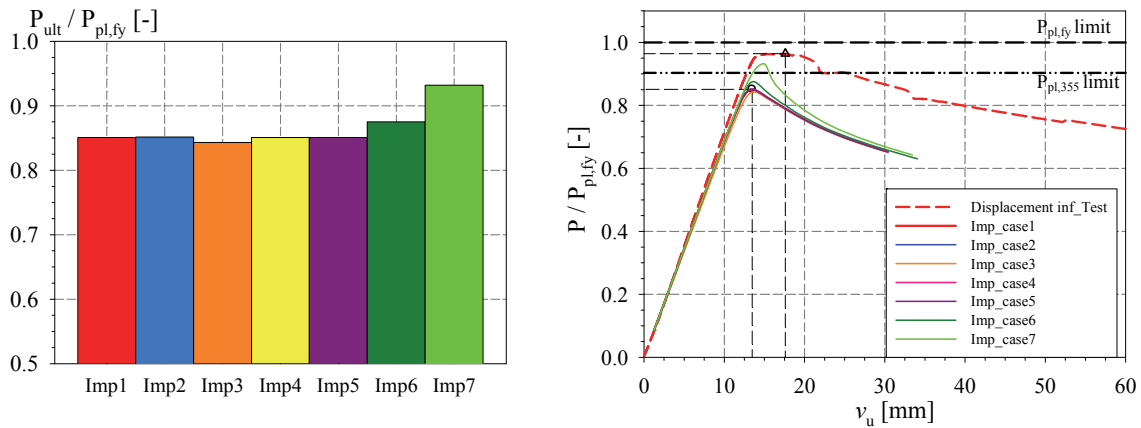


Figure 4.19 – Imperfections sensitivity for SHS_180×6.3_SS_3P, a) comparison of the normalised ultimate load, b) load-displacement curves for the different imperfection patterns

4.2.1.5 3-point and 4-point bending tests

In the present section, experimental results are compared to the numerically predicted ones, based on actual cross-sectional dimensions, material properties, initial imperfection type 1², and loading introduction type 1³ – except for the case of the SHS 200x6 _SS_4P specimen because no 50 *mm* thick plate was placed under the loading point. Loading was then modelled using “type 2” load application pattern, and was applied uniformly on the corners end over a distance of 4 *cm*.

Concerning the three point bending configuration, numerical simulations represented the real behaviour quite accurately, especially regarding the rigidity of the beams’ response. Hence Figure 4.20 depict how the numerical results match the experimental ones in the elastic part. Moreover, the numerical model predicts the moment capacity accurately. Hence, numerical results also outline that, similarly to experimental observations, and owing to the load introduction, cross-sections were not able to achieve their plastic limit and premature local buckling developed. The behaviour of hollow section in bending is thus represented accurately. A small divergence can usually be observed in the post peak phase and this is to be attributed to geometrical imperfection shape, as detailed previously. In Figure 4.20, “Displacement inf” refers to the vertical displacement of the tested beam at mid-span and at the bottom flange, while “Displacement sup” refers to the recording at the top flange. The difference between these two recording is attributed to the development of local buckling in the upper flange, which result in higher deformations at this point.

² Average sinewave of web and flange and a / 200 amplitude by plate, with a reduction of 30%

³ Four concentrated loads applied at the upper flange edges

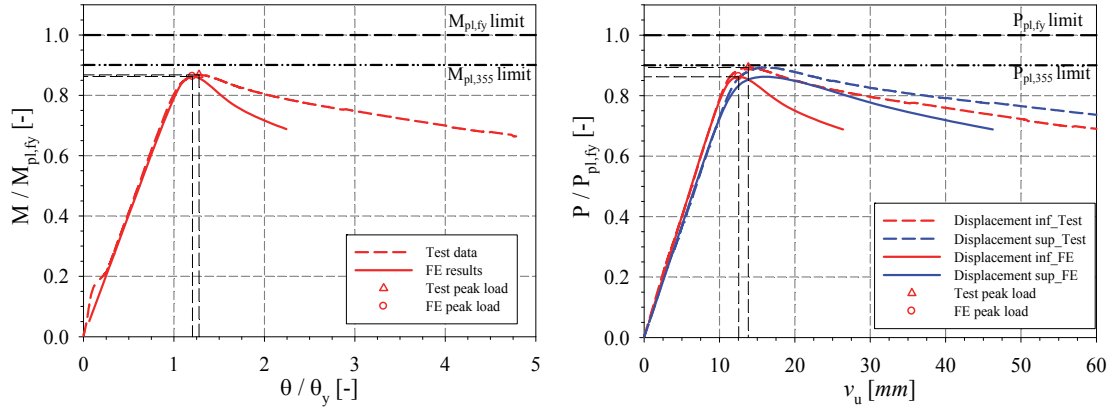


Figure 4.20 – RHS_220×120x6.3_SS_3P validation

Table 4.1 summarises numerical results for all specimens, and Table 4.2 displays a comparison between F.E. and tests results in terms of peak moment and equivalent peak rotation. On average, the deviation of numerical and experimental results in term of peak moment was less than 2%. In some cases the difference was larger (up to a maximum of 11%) which may be connected to laboratory effects that are difficult to quantify (load cells, load eccentricities, friction in the hinges...). These results demonstrate the ability of the numerical model to well predict the capacity of sections. In terms of rotation at failure, the average deviation of numerical vs. experimental results was smaller than 20% with a deviation of 9%. These values represent a good estimate of the rotation, since the large variability of the rotation capacity was previously identified and mainly attributed to the initial geometrical imperfections. We can also note that the numerical model always lead to a safe underestimate for all the specimens in terms of the ultimate rotation.

Table 4.1 – 3-pt bending numerical results

Test specimen	$M_{ult,FINELg}$	$M_{ult,FINELg} / M_{pl}$	$P_{ult,FINELg}$	$P_{ult,FINELg} / P_{pl}$	$\theta_{u,FINELg} / \theta_y$	v_u
	[kN.m]	[-]	[kN]	[-]	[-]	[mm]
RHS_150×100×8_SS_3P	81.1	1.16	124.8	1.16	6.15	113.9
RHS_180×80×4.5_SS_3P	47.1	0.93	72.5	0.93	1.37	18.1
RHS_150×100×5_SS_3P	49.6	0.98	76.4	0.98	1.46	23.9
RHS_220×120×6.3_SS_3P*	98.1	0.86	151.0	0.86	1.21	12.6
RHS_220×120×6.3_SS_3P	96.2	0.85	148.0	0.85	1.18	12.4
SHS_180×6.3_SS_3P	95.5	0.85	147.0	0.85	1.08	13.5
SHS_180×8_SS_3P	118.5	0.92	182.3	0.92	1.22	14.9
SHS_200×6_SS_3P	110.5	0.71	170.0	0.71	0.91	11.9

Table 4.2 – Numerical vs. experimental results for 3-pt bending tests

Test specimen	$P_{ult,exp}$	$P_{ult,exp} / P_{ult,FINElg}$	$M_{ult,exp}$	$M_{ult,exp} / M_{ult,FINElg}$	$\theta_{u,exp} / \theta_y$	$\theta_{u,exp} / \theta_{u,FINElg}$
	[-]	[-]	[-]	[-]	[-]	[-]
RHS_150×100×8_SS_3P	134.8	1.08	84.6	1.04	7.53	1.22
RHS_180×80×4.5_SS_3P	75.3	1.04	46.3	0.98	1.59	1.16
RHS_150×100×5_SS_3P	76.7	1.00	46.6	0.94	1.94	1.33
RHS_220×120×6.3_SS_3P*	156.4	1.04	98.7	1.01	1.28	1.06
RHS_220×120×6.3_SS_3P	161.3	1.09	101.6	1.06	1.34	1.13
SHS_180×6.3_SS_3P	166.6	1.13	105.6	1.11	1.31	1.21
SHS_180×8_SS_3P	191.8	1.05	121.1	1.02	1.32	1.08
SHS_200×6_SS_3P	177.8	1.05	111.6	1.01	1.24	1.37
max		1.13		1.11		1.37
min		1.00		0.94		1.06
mean		1.06		1.02		1.20
C.O.V.		0.04		0.05		0.09

Similarly, for the four point loading configuration, a good concordance between numerical and experimental results was found. Figure 4.21 displays a representative example for the SHS_180x8_SS_4P. It can also be observed that the stiffness of the beam response is well represented in the elastic part. In the unloading phase, results slightly diverge between numerical and experimental results but similar trends are observed. Figure 4.21 demonstrate the ability of the 4-pt bending model to well predict the experimental behaviour of such beams. Hence, a very good representation of the experimental curves is achieved.

In Figure 4.21, in terms of the ultimate moment reached (figure on the left), a difference of 8% is reported between the numerical and the experimental results. However in term of ultimate peak load (figure on the right), only a 2% is observed. The normalised peak load and peak moment achieved in the numerical model are identical, as expected due to simple engineering, and are reported in Table 4.3. However, this is not achieved experimentally and is attributed to the load cell precision as stated in Chapter 3.

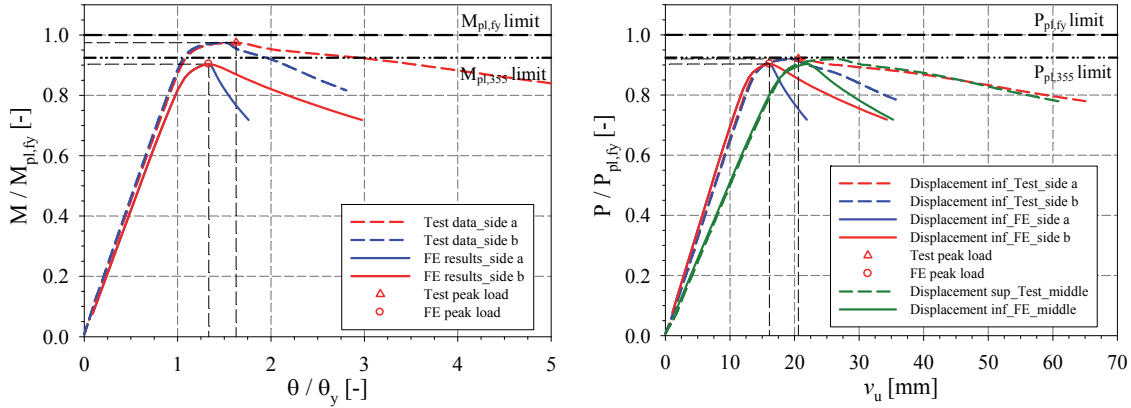


Figure 4.21 – SHS_180×8_SS_4P validation

Table 4.3 and Table 4.4 summarise results for all the tested specimens and show a good agreement between the numerical and experimental results. $\theta_{u,a}$ and $\theta_{u,b}$ represent the beam end rotation when the ultimate load P_{ult} is reached. $v_{u,a}$ and $v_{u,b}$ are the beam deflection recorded at the point load a or b when the ultimate load is attained. In terms of ultimate moment capacity, numerical and experimental results display a difference of 6% on average. A maximum of 12% and a minimum of 1% are reported, with the numerical model always leading to safe sided values. These results demonstrate the ability of the numerical model to represent the experimental behaviour quite accurately. Differences between numerical and experimental results in terms of ultimate rotation are on average equal to 16% with a standard deviation of 22%. These difference, although a bit high, are not at all alarming since they are attributed to the geometrical imperfection introduced in the model. This difference can be considerably diminished when varying the initial imperfection shape and amplitude (see § 4.2.1.4).

Table 4.3 – 4-pt bending numerical results

Test specimen	$M_{ult,FINELg}$	$M_{ult,FINELg} / M_{pl}$	$P_{ult,FINELg}$	$P_{ult,FINELg} / P_{pl}$	$\theta_{u,a} / \theta_y$	$\theta_{u,b} / \theta_y$	$v_{u,a}$	$v_{u,b}$
	[kN.m]	[-]	[kN]	[-]	[-]	[-]	[mm]	[mm]
RHS_150×100×8_SS_4P	76.2	1.11	117.3	1.11	13.13	12.85	207.81	203.52
RHS_180×80×4.5_SS_4P	46.6	0.91	71.7	0.91	1.60	1.60	20.57	20.59
RHS_150×100×5_SS_4P	47.6	0.96	73.2	0.96	2.18	2.18	34.92	34.93
RHS_220×120×6.3_SS_4P	97.7	0.85	150.3	0.85	1.28	1.29	12.95	12.97
SHS_180×6.3_SS_4P	96.0	0.84	147.7	0.84	1.08	1.06	15.24	14.80
SHS_180×8_SS_4P	116.1	0.90	178.6	0.90	1.33	1.34	16.11	16.16
SHS_200×6_SS_4P	93.0	0.60	143.0	0.60	0.97	0.9	12.2	11.1

Table 4.4 – Numerical vs. experimental results for 4-pt bending tests

Test specimen	$P_{ult,exp}$	$P_{ult,exp} / P_{ult,FINELg}$	$M_{ult,exp}$	$M_{ult,exp} / M_{ult,FINELg}$	$\theta_{u,a,exp} / \theta_y$	$\theta_{u,b,exp} / \theta_y$	$\theta_{u,a,exp} / \theta_{u,b,FINELg}$	$\theta_{u,b,exp} / \theta_{u,b,FINELg}$
	[-]	[-]	[-]	[-]	[-]	[-]	[-]	[-]
RHS_150×100×8_SS_4P	131.3	1.12	83.2	1.09	9.41	8.88	0.72	0.69
RHS_180×80×4.5_SS_4P	75.0	1.05	47.3	1.02	1.93	2.04	1.20	1.27
RHS_150×100×5_SS_4P	77.0	1.05	47.9	1.01	2.94	2.64	1.35	1.21
RHS_220×120×6.3_SS_4P	163.4	1.09	103.3	1.06	1.23	1.34	0.96	1.04
SHS_180×6.3_SS_4P	164.8	1.12	103.7	1.08	1.35	1.26	1.24	1.19
SHS_180×8_SS_4P	181.9	1.02	125.3	1.08	1.63	1.50	1.22	1.12
SHS_200×6_SS_4P	151.0	1.06	104.00	1.12	1.34	1.46	1.39	1.65
max		1.12		1.12			1.39	1.65
min		1.02		1.01			0.72	0.69
mean		1.07		1.06			1.15	1.17
C.O.V.		0.04		0.04			0.21	0.24

A graphical view that compares peak moments for 3 point and 4 point bending configurations is presented in Figure 4.22 and Figure 4.23. It can be seen that all numerical simulations provide ultimate moments values in excellent accordance with the test results. All numerical predictions give values close to the ideal line $M_{ult,exp} / M_{ult,FE} = 1$, while generally being safe-sided. This indicates that the numerical models have been well calibrated.

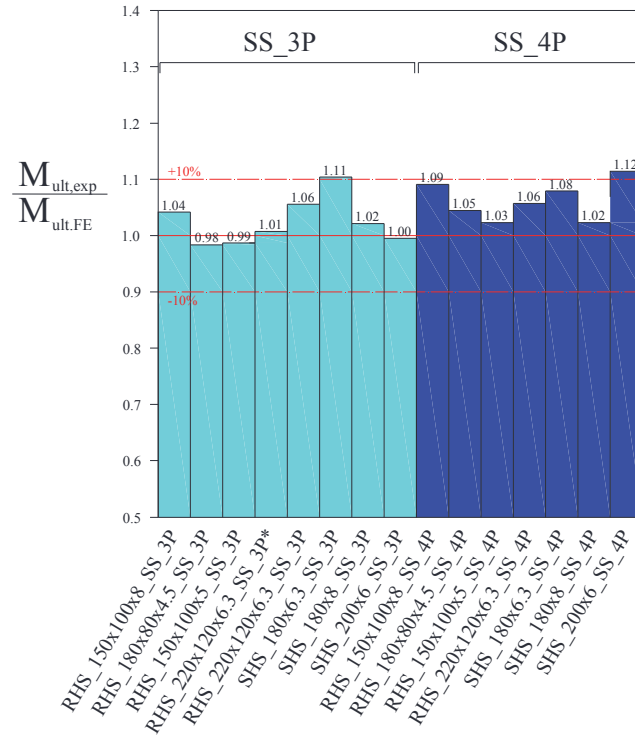
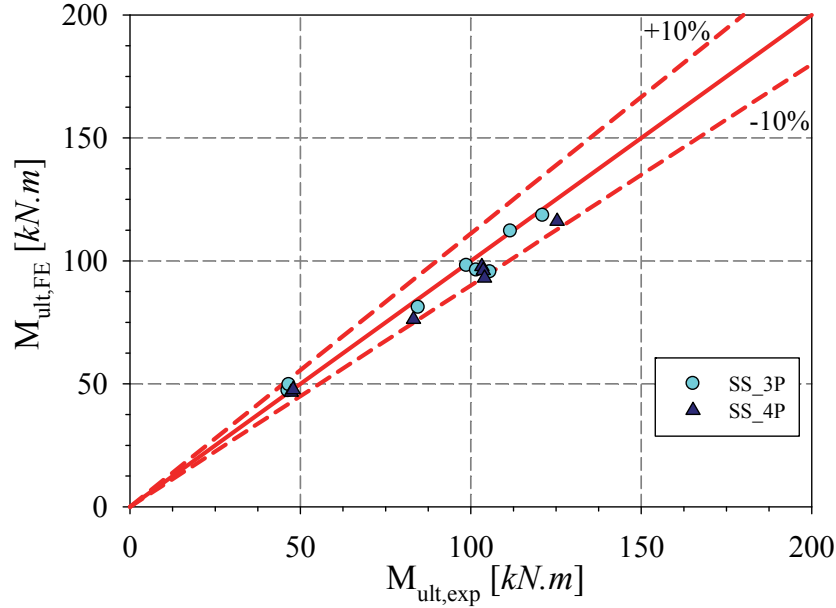


Figure 4.22 – Summary comparison of ultimate moments for the simply-supported configuration

Figure 4.23 – $M_{ult,exp}$ vs. $M_{ult,FE}$ for simply-supported configurations

4.2.1.6 Propped cantilever arrangements

For the propped cantilever configurations, end plates were modelled for sake of a fair comparison with the experimental results. Beams were also modelled using an ideally-fixed end by fixing all nodes of the end section as shown in Figure 4.25. This was intended at highlighting such effect on the system rigidity.

Figure 4.24 presents the bolts position on the end-plate for all sections. Their positioning was made following experimental limitations that consist in bolts being distanced horizontally by 160 mm and vertically by 80 mm. Bolts configuration was assigned considering minimum gages required. Only for the case of SHS_180×80×4.5, bolts could be placed near the section webs; this lead to a rigid connection for this case. Whereas for the other specimens, the connection was somehow semi-rigid, although the end plate was 30mm thick (the thickness of the end-plate was assigned in an attempt to ensure a perfectly rigid connection as stated in § 3.2.3).

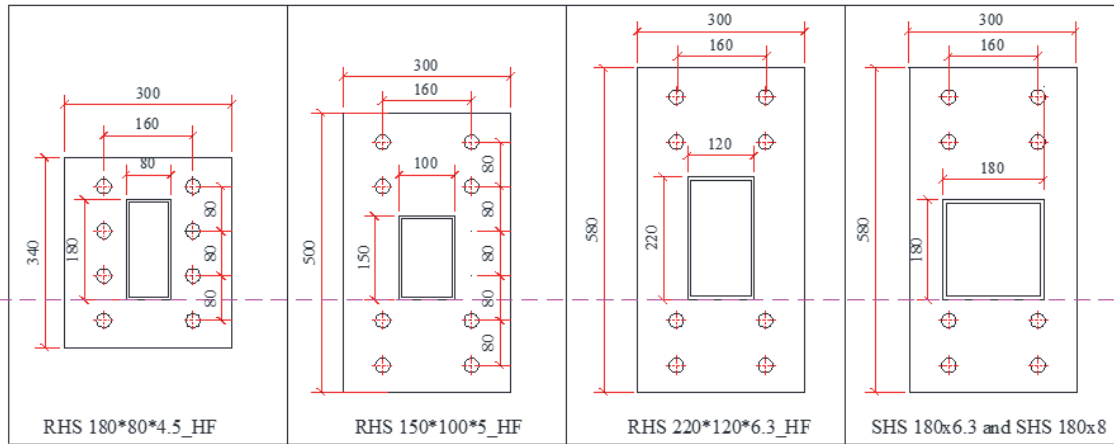


Figure 4.24 – Bolts distribution on the end-plate of the propped cantilever tests

For the SHS_180×80×4.5_PR_C case, as the fixed end was perfectly rigid through a good distribution of bolts, Figure 4.26 shows that results with the end plate modelled and the one with an ideally-fixed end are identical. Nonetheless for the case of SHS_180×6.3_PR_C (Figure 4.27), it can be seen that when the end plate is modelled, numerical results matches experimental ones in the elastic part, while if a perfect “ideal” fixed end is modelled, an increase in stiffness is observed.

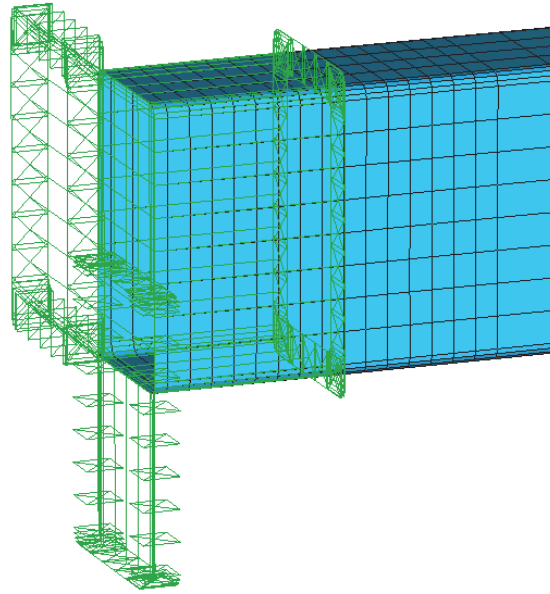


Figure 4.25 – Modelling of the ideally-fixed end for propped cantilever configurations

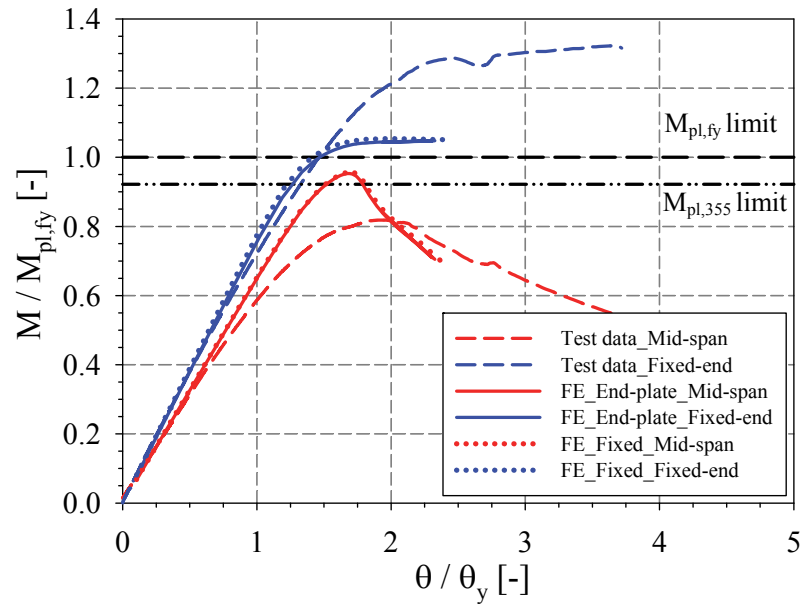


Figure 4.26 – SHS_180×80×4.5_PR_C; ideally-fixed end vs. end plate

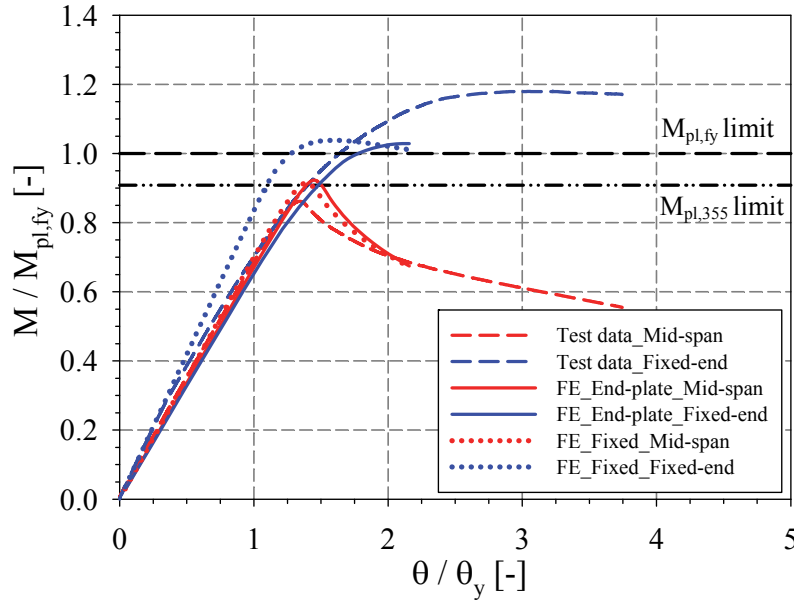


Figure 4.27 – SHS_180×6.3_PR_C; ideally-fixed end vs. end plate

Figure 4.28 shows an excellent accordance between numerical and experimental results for SHS_180×6.3_PR_C. For this case, we can see that the numerical curves are very similar to the experimental ones and that similar tendencies are observed in the load-displacement and in the moment-rotation representations. It is reminded here that the terminology “Inf” refers to the deflection recorded at the bottom flange while “Sup” refers to the deflection measured at the top flange. By comparing numerical and experimental curves for SHS_180×80×4.5_PR_C in Figure 4.29, it can be seen that the system peak load is well predicted, as well as the rigidity of the system. However, deflections at failure may sometimes differ; this divergence may be attributed to the imperfection shape and amplitude. When comparing moment-rotation curves, a bigger divergence is noticed between numerical and test results in terms of peak moment. Experimentally, it can be seen that the moment at the fixed end reached values 20% higher than the one obtained numerically. This difference could be explained by the fact that welding may have caused an increase in strength in a bigger portion of the beam than the one modelled. It is also attributed to the precision of the load cells that may have been affected after the peak load is reached. Hence, after the peak, the beam deflection becomes more pronounced and load was not strictly vertically and uniformly applied.

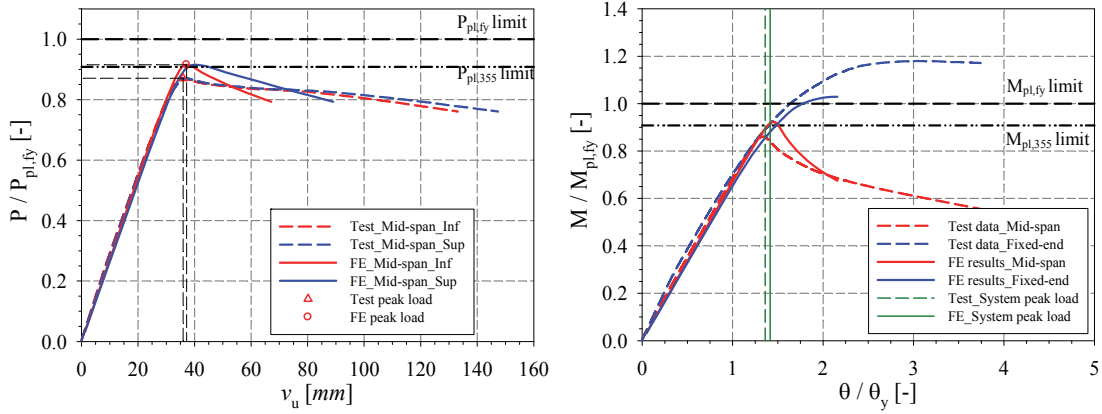


Figure 4.28 – SHS_180×6.3_PR_C validation

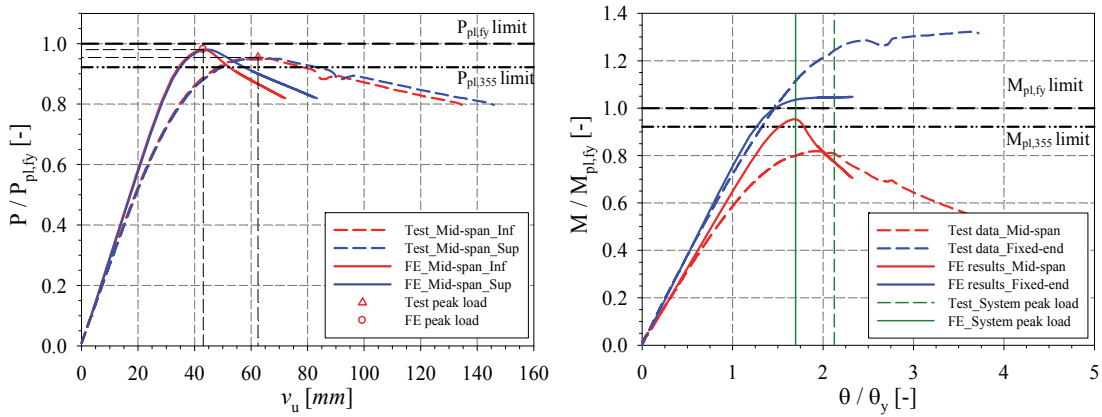


Figure 4.29 – Results for SHS_180×80×4.5_PR_C

Results of all propped cantilever centrally loaded specimens are summarised in Table 4.5 and Table 4.6 below. When comparing the ultimate load reached experimentally and the one achieved numerically, a very good correspondence is observed. On average, results diverged by 1% and a maximum deviation of only 5% is reached. A slightly higher divergence was noticed in term of rotations, as expected. These results demonstrate the capability of the numerical model to well predict the experimental behaviour of propped cantilever centrally loaded.

Table 4.5 – PR_C numerical results

Test specimen	P_{ult}	$P_{ult,FINElg} / P_{pl}$	$M_{ult,span}$	$M_{ult,span} / M_{pl}$	$M_{ult,fix-end}$	$M_{ult,fix-end} / M_{pl}$	θ_u / θ_y	v_u
	[kN]	[-]	[kN.m]	[-]	[kN.m]	[-]	[-]	[mm]
RHS_180×80×4.5_PR_C	60.82	0.98	52.00	1.05	47.30	0.95	1.70	43.08
RHS_150×100×5_PR_C	60.40	1.01	51.65	1.07	47.39	0.99	1.76	56.17
RHS_220×120×6.3_PR_C	129.18	0.90	120.15	1.04	101.53	0.88	1.51	32.77
SHS_180×6.3_PR_C	130.18	0.92	117.10	1.03	105.05	0.92	1.47	37.18
SHS_180×8_PR_C	149.12	0.92	136.50	1.06	120.63	0.93	1.62	41.09

Table 4.6 – Numerical vs. experimental results for PR_C tests

Test specimen	$P_{ult,exp}$	$P_{ult,exp} / P_{ult,FINElg}$	$\theta_{u,exp} / \theta_y$	$\theta_{u,exp} / \theta_{u,FINElg}$
	[-]	[-]	[-]	[-]
RHS_180×80×4.5_PR_C	59.2	0.97	2.12	1.25
RHS_150×100×5_PR_C	61.4	1.02	2.82	1.60
RHS_220×120×6.3_PR_C	126.4	0.98	2.23	1.48
SHS_180×6.3_PR_C	123.9	0.95	1.36	0.93
SHS_180×8_PR_C	152.20	1.02	3.16	1.95
max		1.02		1.95
min		0.95		0.93
mean		0.99		1.44
C.O.V.		0.03		0.27

For the propped cantilever off-centrally loaded, conclusions similar to the centrally loaded propped cantilever can be drawn. For the RHS_180×80×4.5_PR_O case (see Figure 4.30), identical responses and trends are observed for the model with end plate and the one with an “ideally” fixed end. However, an increase in stiffness at the fixed-end is observed for all propped cantilever centrally loaded. Figure 4.31 also reveals that experimental results are more accurately predicted by the model with an ideally-fixed end rather than by the one with an end plate. It is to be mentioned that the difference between models regarding the stiffness in the elastic part is only of the order of 5%; hence, this deviation is of the order of precision of the load cells. Moreover, the inaccuracy in the load cells is increased by the non-uniform load application due to the beam end rotation.

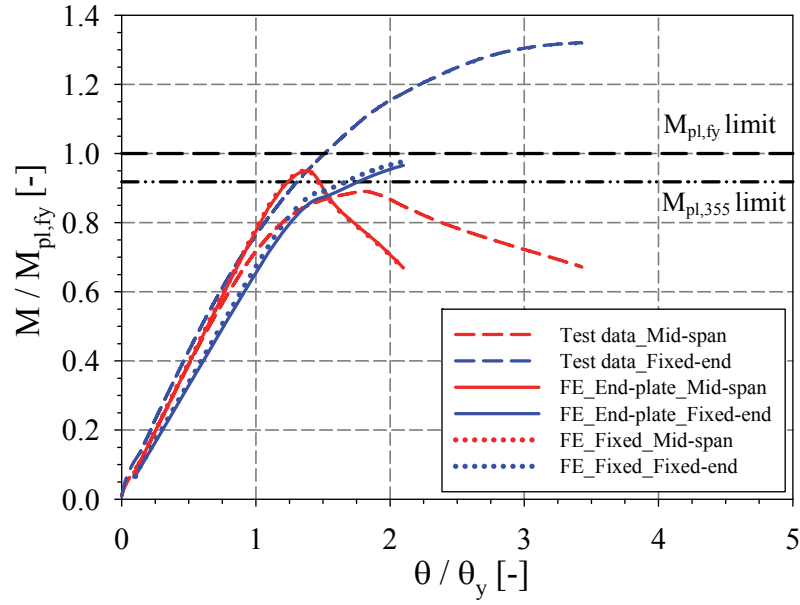


Figure 4.30 – RHS_180×80×4.5_PR_O; ideally-fixed end vs. end plate

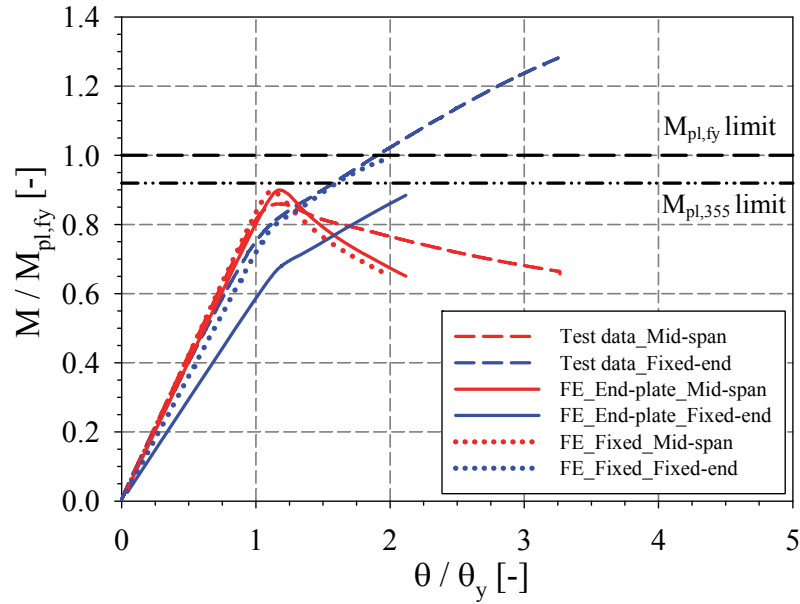


Figure 4.31 – SHS_180×6.3_PR_O; ideally-fixed end vs. end plate

Figure 4.32 displays validation curves for the SHS_180×6.3_PR_O test in terms of load deflection as well as in moment rotation curves. A perfect agreement is observed when comparing the stiffness of the beam response as well as the ultimate peak load, peak moment and the deflection at the peak load. Only 1% difference is achieved between the experimental recorded peak load and the one from numerical simulation, and a 5% divergence is reported

between the rotations at peak load. These results highlight the capacity of the numerical model to well simulate the bending behaviour of specimens. A faster unloading is noticeable in the numerical results, and could be attributed to geometrical imperfection and to the load introduction. Regarding the moment rotations curves (Figure 4.32 right graph), bigger discrepancies can be observed for the fixed end stiffness and the peak moment, the fixed end seemingly reaching a capacity 30% higher than the plastic limit.

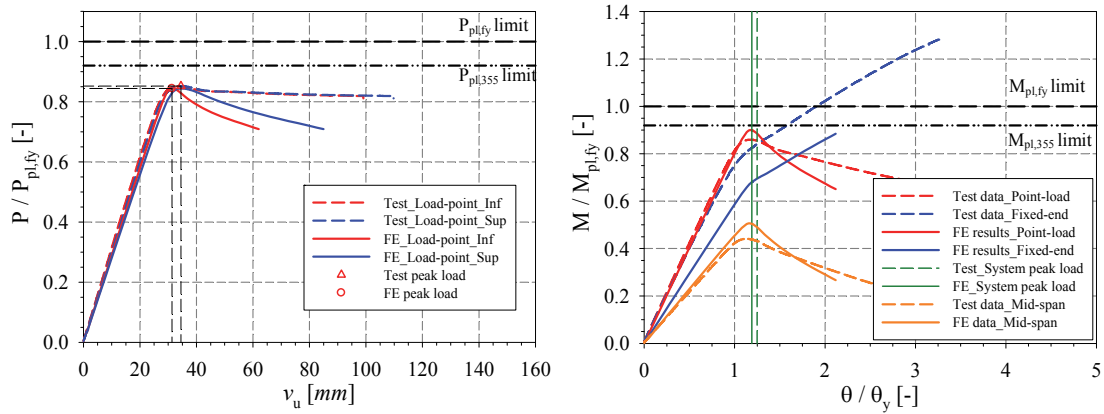


Figure 4.32 – Results for SHS_180×6.3_PR_O

Table 4.7 and Table 4.8 summarise numerical results achieved and a comparison with test values. A maximum deviation of 3% is reported between the numerical and the test ultimate loads, with an average value of 1% and a 1% standard deviation. These values indicate the good prediction of the peak load by the numerical model and its accuracy. In terms of ultimate rotation, an average of 17% deviation between numerical and experimental results is achieved. These results show that the numerical model is able to accurately represent the real behaviour of such members.

Table 4.7 – PR_O numerical results

Test specimen	P_{ult}	$P_{ult,FINElg} / P_{pl}$	$M_{ult,span}$	$M_{ult,span} / M_{pl}$	$M_{ult,fixed-end}$	$M_{ult,fixed-end} / M_{pl}$	θ_u / θ_y	v_u
	[kN]	[-]	[kN.m]	[-]	[kN.m]	[-]	[-]	[mm]
RHS_180×80×4.5_PR_O	56.31	0.93	47.02	0.97	46.24	0.95	1.40	37.61
RHS_220×120×6.3_PR_O	123.97	0.86	104.29	0.90	104.12	0.90	1.31	28.75
SHS_180×6.3_PR_O	115.38	0.84	97.29	0.89	98.48	0.90	1.19	31.39

Table 4.8 – Numerical vs. experimental results for PR_O tests

Test specimen	$P_{ult,exp}$	$P_{ult,exp} / P_{ult,FINElg}$	$\theta_{u,exp} / \theta_y$	$\theta_{u,exp} / \theta_{u,FINElg}$
	[-]	[-]	[-]	[-]
RHS_180×80×4.5_PR_O	57.5	1.02	1.84	1.32
RHS_220×120×6.3_PR_O	127.8	1.03	1.48	1.13
SHS_180×6.3_PR_O	116.6	1.01	1.25	1.05
max		1.03		1.32
min		1.01		1.05
mean		1.02		1.17
C.O.V.		0.01		0.12

A graphical comparison of the ultimate loads predicted by the F.E. simulations and of the experimental ones is shown in Figure 4.33, in which the red dashed lines indicate a deviation of +/- 10%. Results indicate that numerical simulations represented well the real behaviour of specimens. All values fluctuate very closely around $P_{ult,exp} / P_{ult,FE} = 1$, indicating an excellent agreement between test and numerical result. The ability of the numerical model to accurately predict the failure load is obvious. Larger discrepancies are noticed in the post-peak behaviour between numerical and experimental results, and can be attributed to previously mentioned numerical modelling considerations.

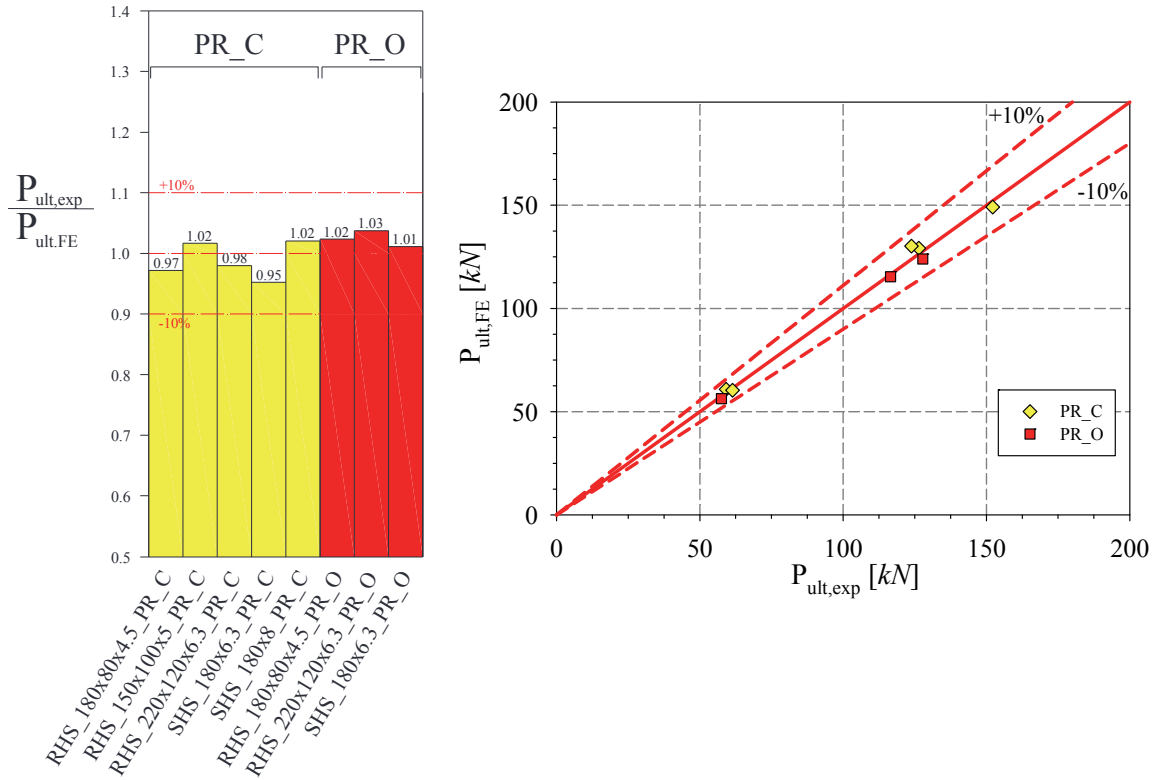


Figure 4.33 – Numerical vs. experimental results for the propped cantilever configurations

4.2.2 Experimental tests performed at the University of Sydney

In 1999, Tim Wilkinson [41] conducted experimental investigations on a variety of cold-formed RHS with two different steel grades: C350 and C450. These additional tests have been used to provide experimental reference data for the validation of the F.E. modelling of cold-formed tubes.

Wilkinson adopted the four-point bending arrangement and loading was applied through 3 different methods: the “parallel plate”, the “perpendicular plate”, and the “pin loading” method. Only the parallel plate approach has been considered and modelled in the present study, covering 32 out of 45 tests. The “parallel plate” loading method consists in welding plates parallel to the webs of the RHS beam. A schematic drawing of the test rig and the loading method is shown in Figure 4.34 below.

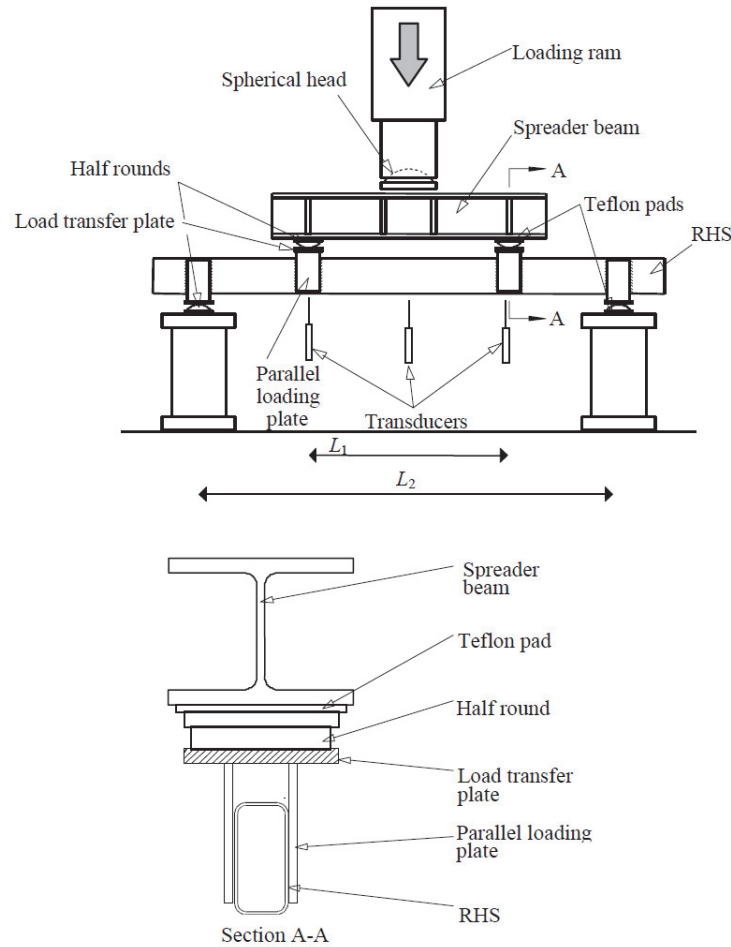


Figure 4.34 – Wilkinson test setup and the “parallel plate” loading method [41].

4.2.2.1 Numerical model characteristics

In FINELg, the loading plates were modelled at loading positions and in the support zones; elastic material behaviour was considered for these plates. Loading was applied through these plates at the mid-section location and on all nodes of both webs, as shown in Figure 4.35. As for support conditions, pinned conditions were attributed to end supports using linear constraints.

Measured geometric dimensions were implemented, and the hollow section was modelled using 2 shell elements per corner. Simple Ramberg-Osgood material law was used for the flat regions of the RHS (see Equation 4.1) with $n = 22$. Wilkinson reported that the yield stress in flanges was on average 10% higher than that of the webs and 20% higher in the corner regions due to the cold forming process (see Figure 4.36). Accordingly, 1.1 times the measured f_y was considered in the flange regions and a multi-linear law was used for corner

regions as described in Figure 4.2 (the corresponding yield and tensile stresses are equal to $1.2f_y$ and $1.2f_u$, respectively). Flexural residual stresses were also implemented as described in section 4.2.1. Geometrical imperfection type 1 was introduced (see Figure 4.15) and a dense mesh was adopted in order to obtain reliable results.

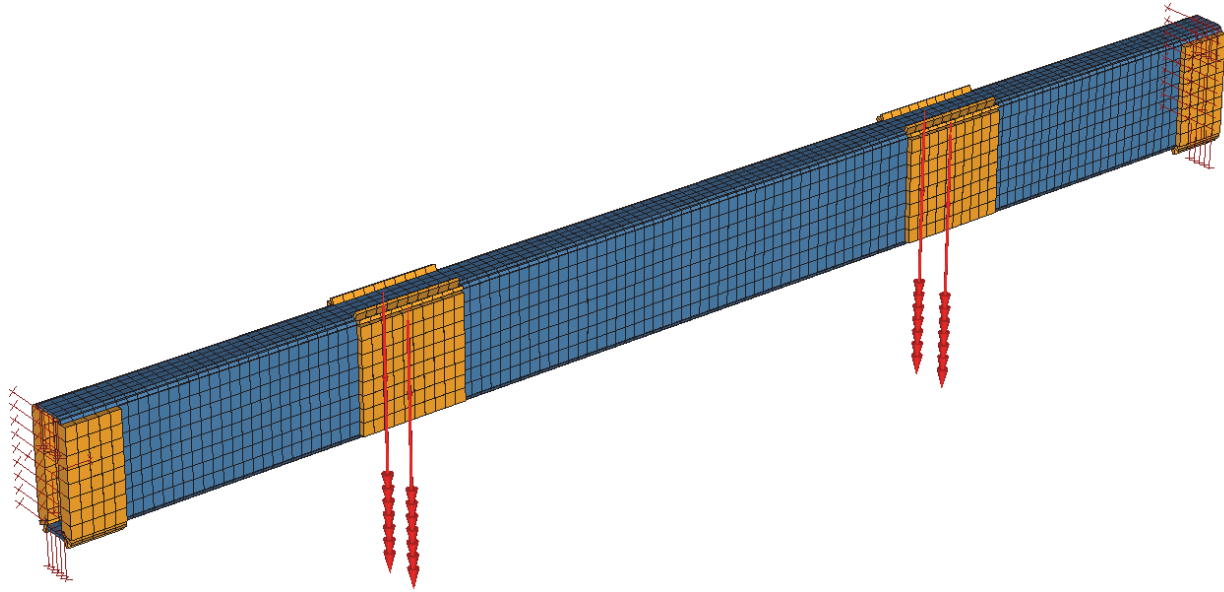


Figure 4.35 – FINELg model of Wilkinson 4-pt bending test setup using the “parallel plate” loading method.

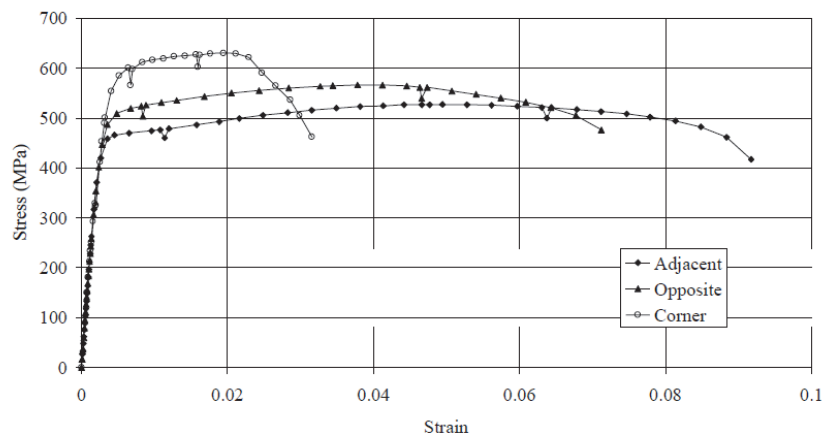


Figure 4.36 – Typical measured stress-strain curves [41].

Wilkinson’s tests have been also first used to asses a simplified model. This model consists in a short beam of length equal to the three times the average of the clear width of both webs and flanges; loading is introduced through equal bending moments applied at both ends, so as to get a constant bending moment distribution. This was performed in order to validate this “simplified model”. Then, it could be used to simulate cases where a constant moment is

applied, without resorting to the modelling of a full 4-pt bending arrangement. Hence, this model possesses many advantages. First, the effect of shear is completely avoided contrary to the 4-pt bending configuration. Secondly, this model allows for a better handling of the initial geometric imperfections so that results can be more easily analysed and the effect of each parameter sorted.

All considered parameters (material and geometric properties) were introduced as defined previously for the full model; only the test configuration was altered.

4.2.2.2 Validation of F.E. models

Numerical simulations with measured material and geometric properties were first performed. The experimental data of the 32 bending tests performed at the University of Sydney are reported in Table 4.9. Table 4.9 indicates the position of the point loads in the test arrangement, and gives a summary of the average measured materials and dimensions properties of sections. Moreover, it gives results in terms of the ultimate moment capacity and the rotation capacity achieved by each specimen tested. All these values have been used as reference to calibrate the numerical model.

It is to be mentioned that the rotation capacity R adopted here for the validation of the 4-pt bending test is based on the mid-segment curvature and is given by Equation 4.4. The curvature κ was calculated from the displacement values as previously seen in Equation 3.8.

$$R = \frac{\kappa}{\kappa_p} - 1 \quad 4.4$$

Nonetheless, concerning the simplified model, the rotation capacity was calculated from the beam end rotation (as stated in Equation 2.4).

Figure 4.37 displays the results obtained for the case of BS08B specimen. It can be seen that in this case, the numerical curve matches the experimental one in the elastic part and in the plastic range for both the full model and the simplified one. In terms of rotation capacity, the experimental values presented a 6% deviation from both numerical model values; the case of the simplified model displayed an over prediction while the full model an under prediction. In this particular case of BS08B specimen, the full model is seen capable of representing numerically the abrupt unloading after the peak moment is reached, whereas the simplified model presents a smoother post buckling response. This can be expected since for the first case the model is represented exactly as experimentally whereas in the simplified model,

different loading introduction were performed to achieve the case of a constant moment. Nonetheless, since the main aim of the simplified model analysis was to predict the rotation capacity, it was seen to deliver trustworthy results.

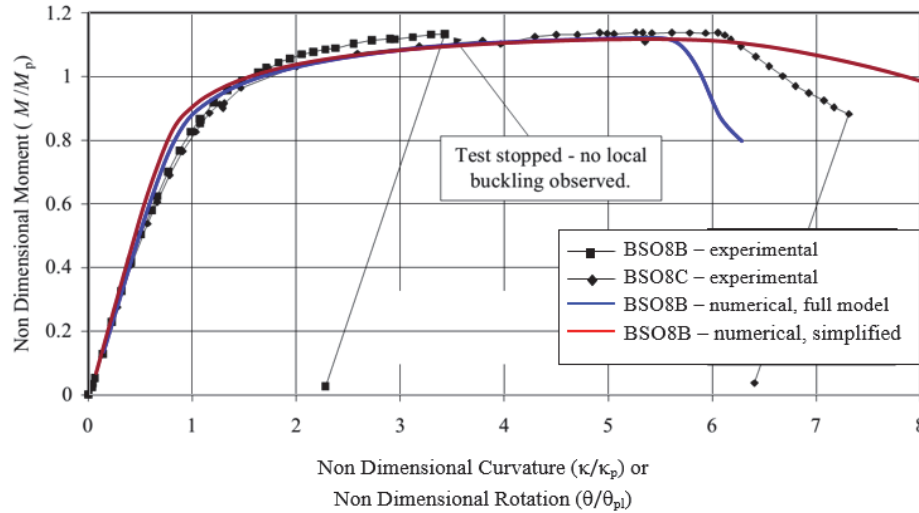


Figure 4.37 – BS08B validation [41].

All numerical results are summarised in Table 4.10 and are compared to the experimental values. In terms of ultimate section capacity, numerical results reached an average deviation with tests values of 3% for the full model and 4% for the simplified one with a deviation of 6%; both models achieved a maximum over prediction of 15% and an under prediction of 6%. These results indicate a very good agreement between both sources of numerical results. For what concerns the rotation capacity, a bigger disparity is reported. In average, the simplified model gave an under-prediction of 5% when compared to tests results whereas the full model gave, on average, an over-prediction of 10%. Nonetheless, better standard deviation was achieved for the case of the simplified model, with a value of 35% compared to 40% in the case of the full model. These large deviation values are mainly attributed to the sensibility of the rotation capacity to the initial geometrical imperfection. Moreover, the simplified model reached a maximum value of 54%, compared to 91% for the full model, and an under-prediction of 52%, compared to 72% for the full model. On the basis of these results, we can assert that the simplified model is more consistent in predicting the rotation capacity of hollow sections, and that both models give satisfactory estimates, taking into account the sensitivity of the rotation capacity to geometrical imperfections.

Table 4.9 – Results of Wilkinson’s bending tests.

Specimen	L_1	L_2	h	b	t	f_y	f_u	$M_{pl,y}$	M_{ult}	$M_{ult} / M_{pl,y}$	R_{test}
	[mm]	[mm]	[mm]	[mm]	[mm]	[N/mm ²]	[N/mm ²]	[kN.m]	[kN.m]	[-]	[-]
BSO1B	800	1700	151	50.25	4.92	441	495	35.51	43.8	1.23	>13.0
BSO1C	800	1700	150.9	50.41	4.9	441	495	35.14	41.1	1.17	>9.0
BSO2B	800	1700	150.4	50.27	3.92	457	527	30.32	38.6	1.27	6.6
BSO2C	800	1700	150.4	50.4	3.87	457	527	29.86	35.5	1.19	7.7
BF02	800	1700	150.2	50.16	3.89	423	480	28.06	33.02	1.18	9.5
BSO3A	800	1700	150.5	50.22	2.97	444	513	22.76	26.2	1.15	2.7
BSO3B	800	1700	150.8	50.01	2.95	444	513	22.68	26.3	1.16	2.3
BSO3C	800	1700	150.8	50.34	2.96	444	513	22.81	25.8	1.13	2.9
BSO4B	800	1700	150.4	50.15	2.6	446	523	20.3	20.8	1.02	1.4
BSO4C	800	1700	150.4	50.41	2.57	446	523	20.13	20.2	1.00	1.2
BSO5A	800	1700	150.7	50.64	2.25	444	518	17.73	17.4	0.98	0
BSO5B	800	1700	150.5	50.57	2.28	444	518	17.96	18.2	1.01	0.6
BSO5C	800	1700	150.4	50.7	2.26	444	518	17.71	17.3	0.98	0
BSO6B	800	1700	100.5	50.7	2.06	449	499	8.7	9.3	1.07	0.8
BSO6C	800	1700	100.5	50.55	2.07	449	499	8.71	8.8	1.01	0.8
BSO7B	500	1300	75.48	50.1	1.94	411	484	4.8	5	1.04	1.7
BSO7C	500	1300	75.63	50.31	1.95	411	484	4.86	4.96	1.02	1.9
BSO8B	500	1300	75.31	25.28	1.98	457	514	3.82	4.24	1.11	5.7
BSO8C	500	1300	75.33	25.23	1.95	457	514	3.75	4.25	1.13	*
BSO9B	500	1300	75.24	25.12	1.54	439	511	2.84	3.16	1.11	2.2
BSO9C	500	1300	74.9	25.2	1.54	439	511	2.82	3.25	1.15	2.5
BS10B	500	1300	75.27	25.12	1.55	422	456	2.81	2.9	1.03	1.9
BS10C	500	1300	75.19	25.25	1.56	422	456	2.82	2.82	1.00	2.6
BS11B	800	1700	150.5	50.13	3	370	429	19.11	23.2	1.21	4.1
BS11C	800	1700	150.5	50.19	2.96	370	429	18.84	21.7	1.15	3.6
BS12B	800	1700	100.9	50.43	2.06	400	450	7.77	7.7	0.99	1.2
BS12C	800	1700	100.8	50.52	2.05	400	450	7.75	7.75	1.00	1.3
BS13B	800	1700	125.6	75.84	2.92	397	449	18.42	18.9	1.03	1.5
BS13C	800	1700	125.4	75.74	2.93	397	449	18.4	19.1	1.04	1.6
BS19A	800	1700	100.4	100.3	2.88	445	502	17.86	18.16	1.02	0.8
BJ07	800	1700	150.3	50.21	3.9	349	437	22.8	29.7	1.30	12.9
BF01	800	1700	150.4	50.57	3.85	410	464	26.63	31.78	1.19	10.7

Table 4.10 – Numerical vs. experimental results for Wilkinson’s bending tests.

Specimen	FINELg results for full test modelling				FINELg results for modelling of segment with length = $3h$ under constant moment			
	$M_{ult,FINELg} / M_{pl,y}$	R_{FINELg}	$M_{ult,exp} / M_{ult,FINELg}$	R_{exp} / R_{FINELg}	$M_{ult,FINELg} / M_{pl,y}$	R_{FINELg}	$M_{ult,exp} / M_{ult,FINELg}$	R_{exp} / R_{FINELg}
	[-]	[-]	[-]	[-]	[-]	[-]	[-]	[-]
BSO1B	1.16	8.26	1.07	1.57	1.15	10.19	1.07	1.28
BSO1C	1.16	8.60	1.01	1.05	1.15	9.85	1.01	0.91
BSO2B	1.11	4.94	1.15	1.34	1.11	6.63	1.15	0.99
BSO2C	1.11	4.92	1.07	1.56	1.11	5.32	1.07	1.45
BF02	1.11	5.74	1.06	1.66	1.11	6.18	1.06	1.54
BSO3A	1.04	2.58	1.10	1.04	1.05	2.96	1.10	0.91
BSO3B	1.04	2.20	1.11	1.05	1.04	2.83	1.11	0.81
BSO3C	1.04	2.21	1.09	1.31	1.05	2.81	1.08	1.03
BSO4B	1.00	-	1.03	-	1.00	1.41	1.02	0.99
BSO4C	0.99	-	1.01	-	1.00	1.29	1.00	0.93
BSO5A	0.95	-	1.04	-	0.95	-	1.03	-
BSO5B	0.96	-	1.06	-	0.96	-	1.06	-
BSO5C	0.95	-	1.03	-	0.96	-	1.02	-
BSO6B	1.05	1.76	1.02	0.45	1.04	1.67	1.03	0.48
BSO6C	1.05	2.08	0.96	0.38	1.04	1.67	0.97	0.48
BSO7B	1.08	2.40	0.96	0.71	1.07	2.26	0.98	0.75
BSO7C	1.08	2.40	0.95	0.79	1.07	2.19	0.96	0.87
BSO8B	1.12	4.86	0.99	1.17	1.11	6.79	1.00	0.84
BSO8C	1.12	5.07	1.01	-	1.11	6.50	1.02	-
BSO9B	1.06	2.28	1.05	0.97	1.06	3.56	1.05	0.62
BSO9C	1.07	2.35	1.08	1.06	1.06	3.61	1.08	0.69
BS10B	1.06	2.32	0.97	0.82	1.06	3.84	0.97	0.49
BS10C	1.07	2.53	0.94	1.03	1.06	3.87	0.94	0.67
BS11B	1.06	3.66	1.14	1.12	1.06	4.38	1.14	0.94
BS11C	1.06	3.06	1.09	1.17	1.06	3.71	1.09	0.97
BS12B	1.05	2.15	0.94	0.56	1.05	2.12	0.94	0.57
BS12C	1.05	2.41	0.95	0.54	1.05	2.05	0.95	0.64
BS13B	1.07	2.65	0.96	0.57	1.06	2.09	0.97	0.72
BS13C	1.07	2.63	0.97	0.61	1.06	2.16	0.98	0.74
BS19A	0.96	-	1.06	-	0.95	-	1.07	-
BJ07	1.13	7.60	1.15	1.70	1.14	8.53	1.14	1.51
BF01	1.11	5.62	1.07	1.91	1.11	7.26	1.07	1.47
max			1.15	1.91			1.15	1.54
min			0.94	0.38			0.94	0.48
mean			1.03	1.05			1.04	0.90
C.O.V.			0.061	0.401			0.058	0.349

Figure 4.38 gives a graphical comparison between experimental and numerical results for all tests ultimate moment from the full model in terms of ultimate load. All results are close to the limit of 1, which indicate when experimental and numerical results coincide. On average the deviation of numerical simulations and tests results was less than 3%. For very few specimens, the deviation exceeds the 10% limit, and can be attributed to laboratories uncertainties. Hence, based on these comparisons and on the one reported in Table 4.10, we can state that the numerical models reproduce the real behaviour quite accurately, for both the full model and the simplified one, and can thus be accepted scientifically.

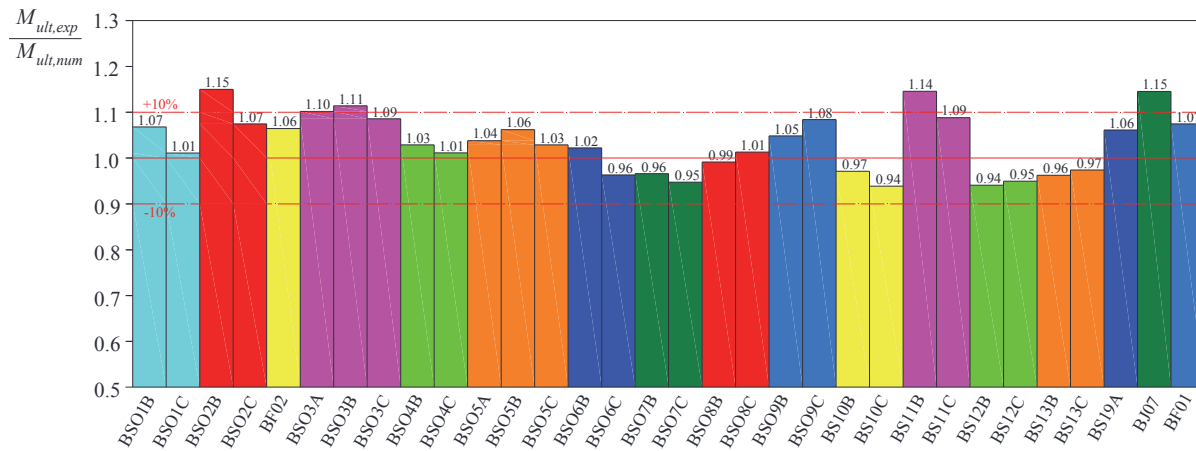


Figure 4.38 – Experimental ultimate vs. F.E. (full) model results – Wilkinson’s test data

4.3 Conclusions

Modelling of the bending tests performed at the University of Applied Sciences of Western Switzerland – Fribourg was done using the finite element software FINELg and a good agreement was found. Accurate replication of the initial stiffness, the ultimate moment capacity and the general form of the moment-rotation curves were achieved. Experimental and numerical values were seen to match closely. Nonetheless, some differences were observed and were associated with the numerical model, the experimental imprecisions of the geometrical and material measured properties and to the recording devices precisions.

All the load-displacement curves coincided with their numerically predicted counterparts in the elastic range, but sometimes not well in the unloading phase. These results showed that analyses using type 1 geometrical imperfection didn’t always meet test results after the peak

was reached, and several calibrations regarding imperfections shape and scaling had to be approved for each section type.

For the simply supported configurations, a good agreement was found in terms of peak load and equivalent rotation at peak; however, for the propped cantilever configurations, more divergences related to the rotation at peak were noticed for some sections; this was associated not only to local imperfections but also to the introduction of loading, along with the modelling of the fixed-end rigidity, the presence of welds and their effect on the system ductility.

Besides, 32 additional cold-formed bending tests performed by Tim Wilkinson at the University of Sydney were also considered. A good correspondence between the numerical and test results was found, and the numerical tools were shown to predict well the behaviour of the tested beam until failure. Divergence up to only 15% was recorded concerning the ultimate moment reached, for an average of 1.03 M_{pl} and a C.O.V. of 6.1%.

Hence, the ability of the numerical model to replicate adequately the behaviour of beams in bending is evidenced. Based on these comparisons, the F.E. models are assumed to represent the real behaviour quite accurately, and numerical results can be substituted safely and reliably to experimental ones in consecutive studies. The models will have to be slightly modified within the forthcoming parametric study, so as to account for more “standard” conditions (supports, material...). In the following chapter, detailed extensive numerical studies are described, where the main objectives are the identification of the key parameters towards the rotation capacity of steel hollow sections.

5 NUMERICAL INVESTIGATIONS

Numerical models being validated against test results, extensive numerical investigation were carried out in order to have a large data set from which conclusions and recommendations regarding the rotation capacity of square and rectangular cross section can be drawn.

In a first step, numerical assumptions are described, then, comprehensive analysis are performed with respect to the test modelling, material properties, imperfections and residual stresses in order to highlight their effect on the rotation capacity of hollow sections. The main aim of the analysis is to understand and characterize the development of inelastic local instability in hot-formed and cold-formed RHS beams. In a second step, an extensive parametric study, that cover a wide range of parameters from section dimensions, steel grade and testing configuration, was launched in the aim to determine trends for the rotation capacity. Finally, the results of the simulations are illustrated and analysed.

5.1 Modelling considerations

5.1.1 Material model for hot-formed and cold-formed tubes

For hot-formed carbon steel tubes, and in an attempt to model the true material behaviour over the entire strain range, full-range nominal stress-strain behaviour is modelled in a four linear material curve as shown in Figure 5.1, where key parameters are reported. This formulation has been based on a careful representation of a total number of 214 tensile coupon test data for hot-rolled carbon steel of yield stress varying from S235 to S690, as well as on a numerical validation against experimental data. This work and the proposed characterization of the stress strain curve was performed by Yun & Gardner [106] where the model can be presented using only three basic parameters: E , σ_y and σ_u . where E is Young's modulus, taken as 210000 N/mm² in EN-1993-1-1, ϵ_y is the yield strain at its corresponding yield stress σ_y , ϵ_u is the ultimate strain at the ultimate stress σ_u .

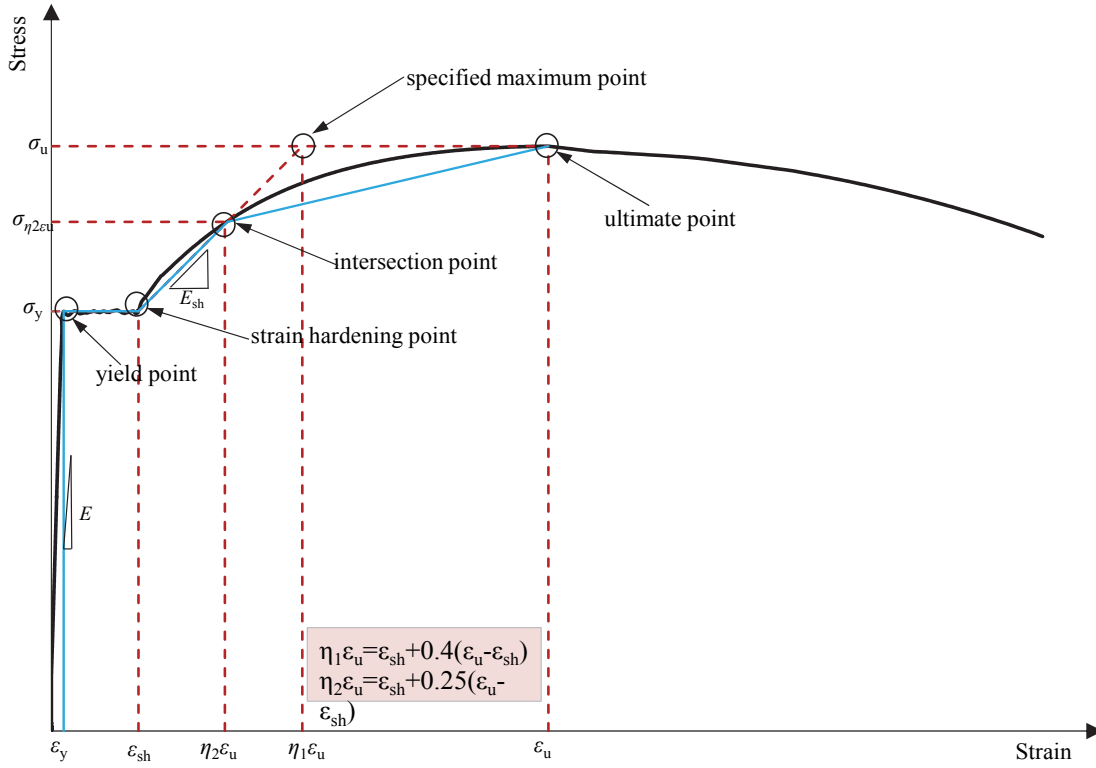


Figure 5.1 – Typical stress-strain curve of hot-rolled carbon steels and the proposed four-linear material model [106].

The empirical expressions for other parameters are summarised in the following equations:

$$\epsilon_u = 0.6 \left(1 - \frac{\sigma_y}{\sigma_u}\right) \quad 5.1$$

$$\epsilon_{sh} = \left(\frac{\sigma_y}{\sigma_u}\right)^6 \epsilon_u \quad 5.2$$

$$E_{sh} = \frac{\sigma_u - \sigma_y}{\eta_1 \epsilon_u - \epsilon_{sh}}, \text{ where } \eta_1 = \frac{\epsilon_{sh} + 0.4(\epsilon_u - \epsilon_{sh})}{\epsilon_u} \quad 5.3$$

$$\eta_2 = \frac{\epsilon_{sh} + 0.25(\epsilon_u - \epsilon_{sh})}{\epsilon_u} \quad 5.4$$

ϵ_{sh} is the strain at the onset of strain-hardening, E_{sh} is the strain hardening modulus, $\eta_1 \epsilon_u$ is the strain of the specified maximum point, which is used for the determination of E_{sh} as shown in Figure 5.2, $\eta_2 \epsilon_u$ represents the strain at the intersection point of the first stage strain hardening line and the stress-strain curve and $\sigma_{\eta_2 \epsilon_u}$ is its corresponding stress.

In the context of this thesis, three nominal steel grades were adopted: S235, S355 and S460 steel. The stress strain material laws for all these steel grades have been represented in Figure 5.2 and the key parameters have been summarised in Table 5.1. In Table 5.1, the strain, stress and tangent modulus have been reported for the different stages of each material law. The strain normalised by the yield strain $\varepsilon / \varepsilon_y$ has also been reported in order to compare dimensionless entities. It is pointed out for example, that S355 steel possesses the shorter dimensionless yield plateau. The maximum strain for the material law adopted in the F.E. analysis was set to a value of 30%.

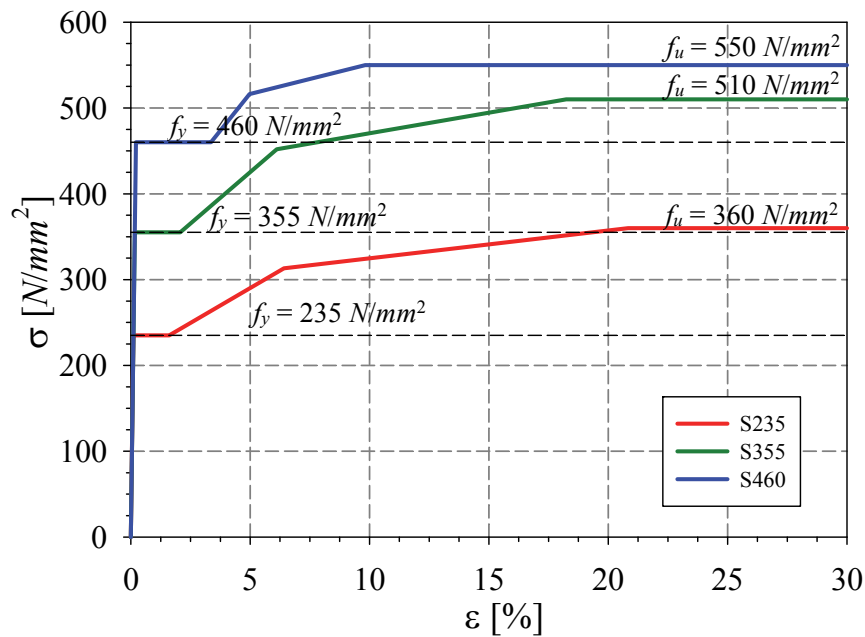


Figure 5.2 – Hot-formed material model considered for different yield strengths

Table 5.1 – Parameters for hot-formed material law for S235, S355 and S460

	S235, $f_u/f_y = 1.53$				S355, $f_u/f_y = 1.44$				S460, $f_u/f_y = 1.20$			
	ε	$\varepsilon / \varepsilon_y$	Stress σ	E_t	ε	$\varepsilon / \varepsilon_y$	Stress σ	E_t	ε	$\varepsilon / \varepsilon_y$	Stress σ	E_t
	[%]	[-]	[N/mm²]	[N/mm²]	[%]	[-]	[N/mm²]	[N/mm²]	[%]	[-]	[N/mm²]	[N/mm²]
Linear elastic	0.11	1.0	235	210000	0.17	1.0	355	210000	0.22	1.0	460	210000
Yield plateau	1.61	14.4	235	-	2.07	12.3	355	-	3.36	15.3	460	-
First stage strain hardening	6.42	57.3	313	1621	6.11	36.2	452	2389	4.97	22.7	516	3456
Second stage strain hardening	20.83	186.2	360	325	18.24	107.9	510	480	9.82	44.8	550	697

Concerning cold-formed carbon steel tubes, as stated in section 4.2.1, two different material laws were adopted. A simple Ramberg-Osgood was assumed for the flat region, and a

multilinear one with a strength enhancement for the corner region. Hence, due to the cold-forming process, the corner regions usually exhibit an increase in strength, and a decrease in ductility. The following simple Ramberg-Osgood material was included for the flat faces of cold-formed hollow sections in the FE parametric studies:

$$\varepsilon = \frac{\sigma}{E} + 0.002 \left(\frac{\sigma}{\sigma_{0.2}} \right)^{22} \quad 5.5$$

A multi-linear law was considered for the corner region of hollow sections. The yield stress and ultimate stress of the corner material have been enhanced by a factor of 1.15 than that of the yield and ultimate stresses values adopted for the flat faces. Figure 5.3 displays the adopted parameters for the material laws of cold formed sections.

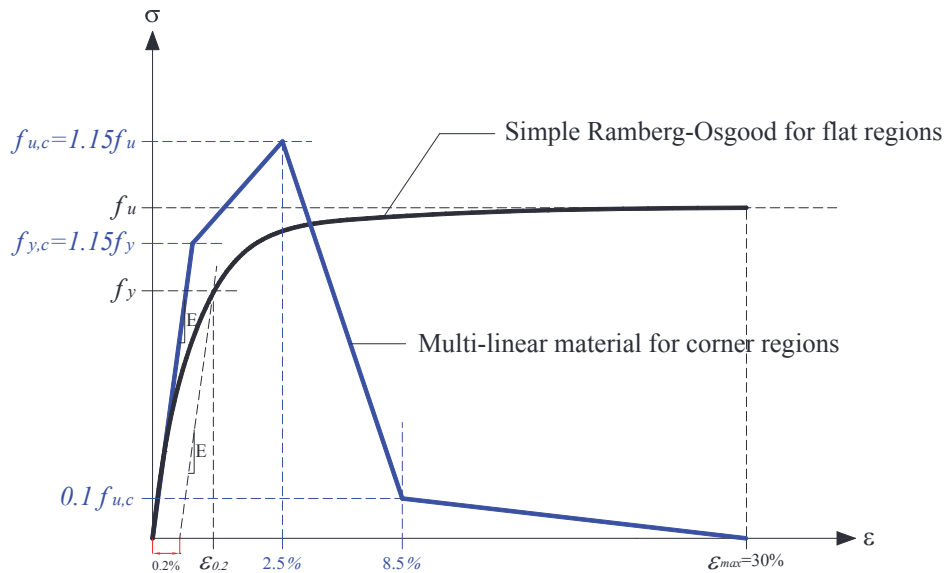


Figure 5.3 – Typical stress-strain curves for cold-formed carbon steels; simple Ramberg-Osgood law for flat regions and a multi-linear material model for corner regions.

The material laws for S235, S355 and S460 steels are represented in Figure 5.4. For the corner material law, after a strain value of 8.5% has been attained, corners becomes ineffective, but a marginal stress have been kept for convergences purposes. The maximum strain assigned for sections in the numerical analysis have been set to 30%. Table 5.2 summarises the parameters for the multi-linear material law assigned to the corners of cold formed hollow sections.

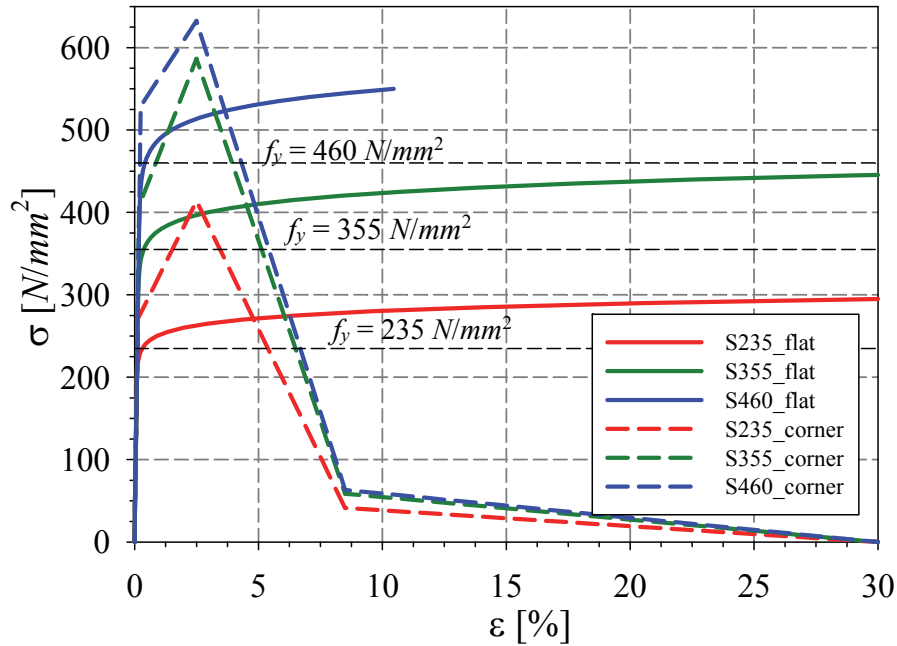


Figure 5.4 – Cold-formed material model considered in the flat and corner region for each nominal yield strength

Table 5.2 – Parameters of the corner region material for S235, S355 and S460 cold-formed sections

	Material for corner region for S235				Material for corner region for S355				Material for corner region for S460			
	ε	$\varepsilon / \varepsilon_y$	Stress σ	E_t	ε	$\varepsilon / \varepsilon_y$	Stress σ	E_t	ε	$\varepsilon / \varepsilon_y$	Stress σ	E_t
	[%]	[-]	[N/mm²]	[N/mm²]	[%]	[-]	[N/mm²]	[N/mm²]	[%]	[-]	[N/mm²]	[N/mm²]
Linear elastic	0.13	1.2	270	210000	0.19	1.2	408	210000	0.25	1.2	529	210000
Strain hardening	2.50	22.3	414	6062	2.50	14.8	587	7731	2.50	11.4	633	4604
first stage unloading	8.50	76.0	41	-6210	8.50	50.3	59	-8798	8.50	38.8	63	-9488
Second stage unloading	30.00	268.1	0	-193	30.00	177.5	0	-273	30.00	137.0	0	-294

Residual stresses were modelled as prescribed from previous chapter in section 4.2.1, i.e. membrane stresses were implemented for hot-formed sections while flexural stresses were introduced for the cold-formed ones.

5.1.2 Boundary conditions

After determining the material law models and residual stresses to be adopted for sections in the F.E. analysis, special attention was given to the modelling of the boundary conditions. Support conditions were accounted for using a linear constraints model for the axial (longitudinal) displacements of the beam edges at the supports. These linear constraints fulfil the simply supported fork conditions. It is assumed that hollow cross-sections' ends exhibit

three degrees of freedom: axial displacement as a whole, rotation around the major axis and rotation around minor axis. Warping is neglected since hollow section possesses high torsional stiffness. Thus, three independent nodes can completely determine the position of any other node. Using linear relationships between these three nodes at the extremities of the flanges, the axial displacements of all other nodes are constrained to respect linear relationships in the displacements of the three “free” nodes. In accordance, the different types of loading are applied at these nodes. Transverse supports have been placed along the flanges and web to prevent the end sections from local buckling. Moreover, additional fictitious nodes have been defined at the centroids of the end-cross-sections for the definition of the support conditions. External loading have been applied through four concentrated forces at the end of the flanges as reported in Figure 5.5.

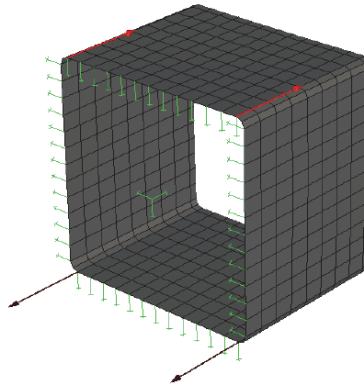


Figure 5.5 – Adopted boundary conditions and loading introduction.

5.2 Comprehensive analysis

5.2.1 Beam subject to a constant moment.

The basics assumptions to the modelling of beams in the F.E. software FINELg have been outlined in the previous paragraphs. Therefore, some comprehensive analysis will be performed to assess the behaviour of beams in bending. These analysis will be performed on a short length beam subjected to a constant moment. When a beam is bended, its deformation induce rotation, curvature and strain. In our case, the beam end's rotation is of interest and will be used to determine the rotation capacity of these beams. Nevertheless, in order to obtain a deeper understanding of the relation that exists between the rotation, curvature and strain, and to be able to link the present work to other studies, a relationship between these three

entities will be presented. Then the particular case of hot-formed beams will be detailed to assess their behaviour in bending and the influence of the plastic plateau on the beam response.

To be able to quantify the ductility of a section, some strain-based methods usually calculate a ratio between the ultimate strain ε_u and the yield strains ε_y , other use the curvature κ while in this thesis, the beam deformation is given as a function of its ends' rotation θ . If we assume that plane sections remain plane during bending, there is a proportional relationship between the strain, the rotation, and the curvature. In order to represent the relation between all these factors, their formulations are given hereafter. Figure 5.6 presents the deformed shape of a beam subjected to a constant bending moment.

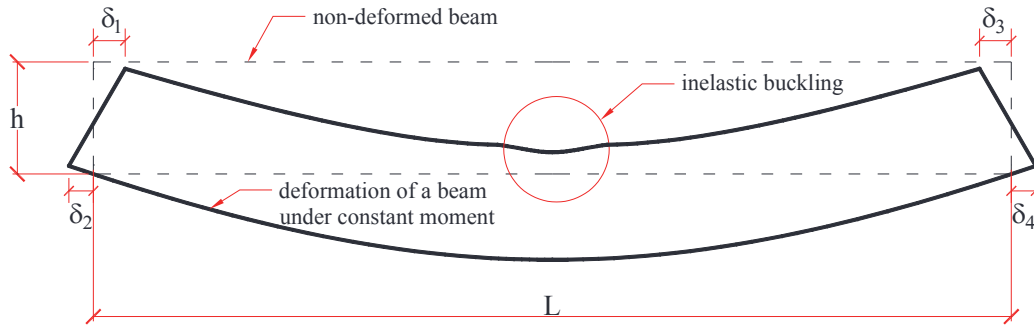


Figure 5.6 – Deformation of a beam under constant bending moment

The strain ε is calculated as the average strain over the entire length of the specimen so that the effect of local buckling is captured in a homogenous way. The strain ε is computed from the beam end displacement δ divided by the length. Its formulation is given by Equation 5.6. The end shortening δ is the average displacement of the flanges outer fibers $\delta_1, \delta_2, \dots$ (in compression and in tension).

$$\varepsilon = \frac{\delta}{L} \quad 5.6$$

In bending, the distribution of strain across the section is linear regardless of the stress state, and the curvature is proportional to the section outer fibres' strains. Equation 5.7 gives the formulation for the case of a symmetrical section in bending.

$$\kappa = \frac{\varepsilon}{h/2} \quad 5.7$$

The end rotation θ is calculated from the beam's average end shortening δ of the section ends divided by the height of the specimen.

$$\theta = \frac{\delta}{h} \quad 5.8$$

In this thesis, rotation and curvature have been normalized with their plastic counterparts θ_{pl} and κ_{pl} . In order to link these ratios to the elastic strain ε_y , the section shape ratio $S = M_{pl} / M_{el}$ was introduced together with the elastic modulus $W_{el} = \frac{I_y}{h/2}$. The plastic rotation for a beam under constant moment and the plastic curvatures are then given in Equation 5.9 and 5.10.

$$\theta_{pl} = \frac{M_{pl}L}{2EI} \rightarrow \theta_{pl} = \frac{S \cdot M_{el} \cdot L}{2EI} = \frac{S \cdot W_{el} \cdot E \cdot \varepsilon_y \cdot L}{2EI} = \frac{S \cdot \varepsilon_y \cdot L}{h} \quad 5.9$$

$$\kappa_{pl} = \frac{M_{pl}}{EI} \rightarrow \kappa_{pl} = \frac{S \cdot M_{el}}{EI} = \frac{S \cdot W_{el} \cdot E \cdot \varepsilon_y}{EI} = \frac{S \cdot 2\varepsilon_y}{h} \quad 5.10$$

Equation 5.11 and 5.12 gives the equivalence of the strain ratio $\varepsilon / \varepsilon_y$ to the curvature ratio κ / κ_{pl} and the rotation θ / θ_{pl} . These factors are equal when divided by the shape factor S .

$$\frac{\theta}{\theta_{pl}} = \frac{\delta/h}{\frac{S \cdot \varepsilon_y \cdot L}{h}} = \frac{\delta}{S \cdot \varepsilon_y \cdot L} = \frac{1}{S} \cdot \frac{\varepsilon}{\varepsilon_y} \quad 5.11$$

$$\frac{\kappa}{\kappa_{pl}} = \frac{\frac{\varepsilon}{h/2}}{\frac{S \cdot 2\varepsilon_y}{h}} = \frac{1}{S} \cdot \frac{\varepsilon}{\varepsilon_y} \quad 5.12$$

A relationship between the normalised strain, rotation and curvature for beams in bending have been presented. These entities were seen to be equal after introducing the shape factor S . The relationship is given in Equation (0.12) below:

$$\frac{\theta}{\theta_{pl}} = \frac{\kappa}{\kappa_{pl}} = \frac{1}{S} \cdot \frac{\varepsilon}{\varepsilon_y} \quad 5.13$$

Now, it is of interest to study the special case of hot-formed beams in bending. This particular case is detailed here since the hot-formed material law possess a large yield plateau, so the plastic moment M_{pl} cannot be reached before the occurrence of strain-hardening. This behaviour is important to detail, because the rotation capacity is only calculated after the

plastic moment is attained, so the need to set a new limit to calculate the rotation capacity R_{cap} is essential and should be proposed.

Hot-formed beams under constant moment exhibit a significant level of ductility before the plastic moment is reached due to the plastic plateau of the material law. Theoretically, for an elastic-plastic material law, full plasticity can only occur at infinite curvature. Hence, for the elastic - plastic - strain hardening material, the section yields completely at high values of curvature and it is only when strain hardening is initiated that the stress can exceed the yield stress.

Moreover, since the material yield plateau have a length varying from 12 to 15 ε_y , depending on the steel grade (see Table 5.1), and after detailing the relationship that exist between the strain and the rotation of a beam, we can assert that a section can undergo rotation capacities of the order of 12 before strain hardening is initiated. Examples of some cases are shown in Figure 5.7 and Figure 5.8; the section SHS 80x5 S355 (Figure 5.7) displays large ductility (normalised rotation of the order of 12) without reaching the plastic moment; while for section SHS 90x5 S355, strain hardening is only reached after a normalised rotation of about 10, and it is at this moment that the plastic moment is exceeded.

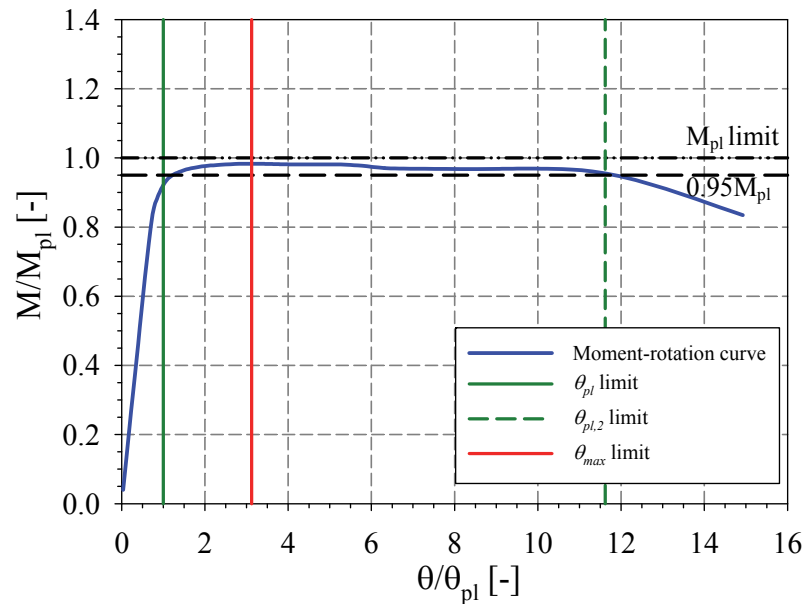


Figure 5.7 – Moment rotation curve for SHS 80x5 S355 under constant moment from FINELg calculations

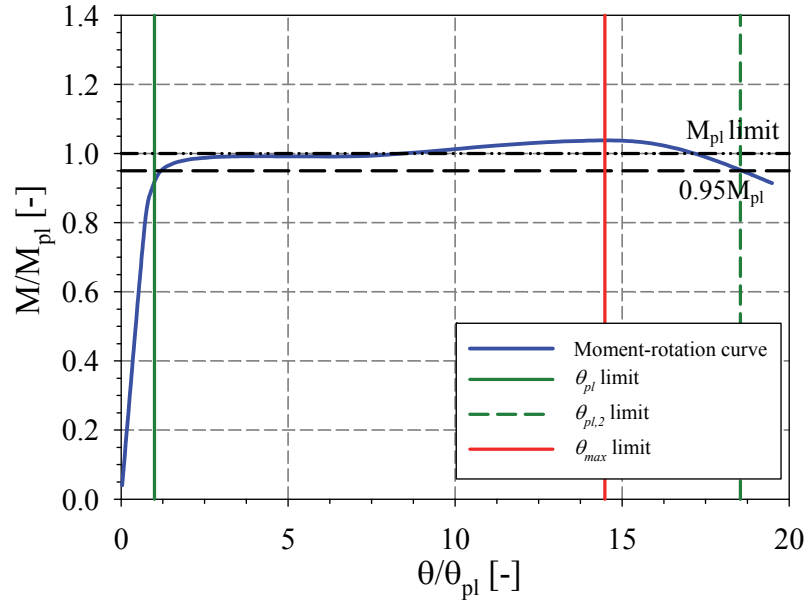


Figure 5.8 – Moment rotation curve for SHS 90x5 S355 under constant moment from FINELg calculations

In that respect, to account for the initial spread of plasticity when the bending moment generally lies just below M_{pl} , many researchers such as Chan & Gardner [31], Stranghoner [28], Sedlacek [30] and Lay & Galambos [29] calculated the rotation capacity based on achieving 95% of the plastic moment. This value was also adopted in this thesis for the case of hot-formed section tested under a uniform moment. Thus, in that case, $\theta_{pl,2}$ corresponds to the point where the curve reaches 95% of the plastic moment in the decreasing part, as shown in Figure 5.7 and Figure 5.8. For all other cases other than that of hot-formed sections subjected to a constant moment, $\theta_{pl,2}$ is calculated when the curve attains the plastic moment after buckling. The rotation capacity R_{cap} is given in Equation 5.14 below as reminder.

$$R_{cap} = \frac{\theta_{pl,2}}{\theta_{pl}} - 1 \quad 5.14$$

5.2.2 Mesh density studies

After determining the material model, residual stresses, boundary conditions and the calculation of the rotation capacity, an initial study that addresses the quality of several adopted meshes is presented here. Indeed, it is crucial to ensure that the density of the chosen meshes is sufficient to provide reliable results and a good representation of local buckling. Hence, a proper FE mesh that provides accurate results within minimum computational effort should be selected. GMNIA calculations were performed on hot-formed short members

subject to a constant bending moment (length = 3 times the average of flange and webs clear widths). Three different meshes were considered from coarse (Mesh 1) to very dense (Mesh 3); the investigated meshes dimensions are shown in Figure 5.9. 12 different cross-sections were selected with h / b ratios varying from 1 to 2.5 and having different slenderness defined through the b / t ratio.

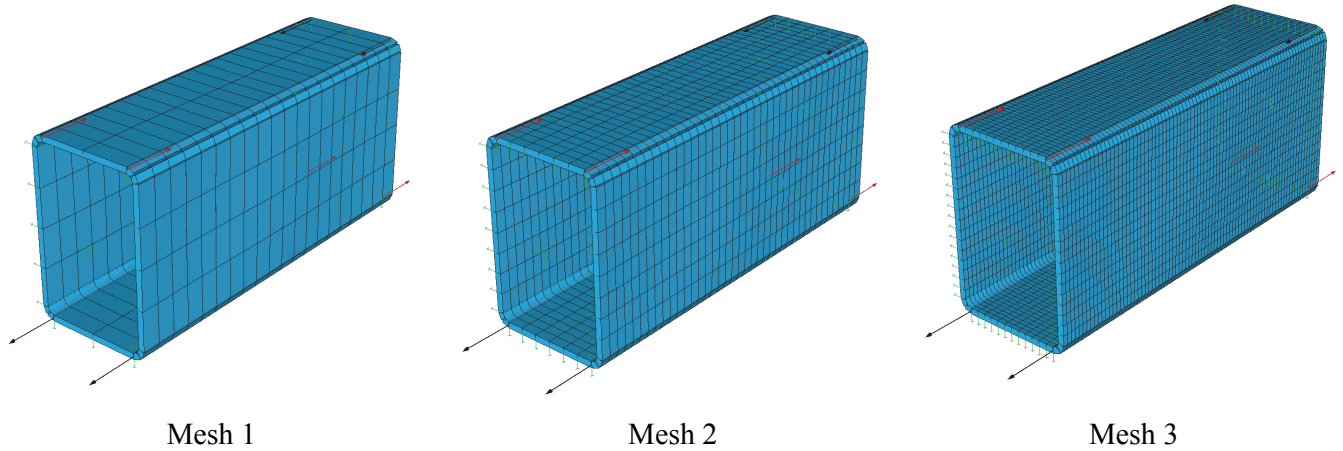


Figure 5.9 – Meshing types

In Figure 5.10 and Figure 5.11, comparisons between obtained results in terms of moment and rotation capacity are plotted for the different adopted meshes. Results show a minor difference in terms of ultimate capacity (Figure 5.10) while bigger discrepancies are observed in terms of rotation capacity (Figure 5.11).

Figure 5.12 to Figure 5.15 exhibit the moment-rotation curves for all sections considered. It can be clearly seen that Mesh 2 and Mesh 3 present an identical beam behaviour while mesh 1 displays a stiffer response. Both Mesh 2 and Mesh 3 display an identical behaviour in the post buckling range. It can also be reported that the moment rotation curve from Mesh 3 lies slightly above Mesh 2 curves in the postbuckling phase leading to slightly higher rotation capacities. Even though there is practically no difference between curves of Mesh 2 and Mesh 3 configurations in the postbuckling range, some differences in the rotation capacity of these configurations is reported in Figure 5.11. Hence, since hot-formed display a large yield plateau, a very small divergence between curves can lead to marginally bigger differences in terms of rotation capacity; with Mesh 2 reaching slightly lower values than that of Mesh 3 (Mesh 3 being the beam having the most dense mesh).

All these graphs ensures the reliability of Mesh 2 results which was therefore adopted for the following numerical studies since it can provide accurate results in terms of peak load and rotation capacity, thus, representing accurately the structural behaviour of cross-sections.

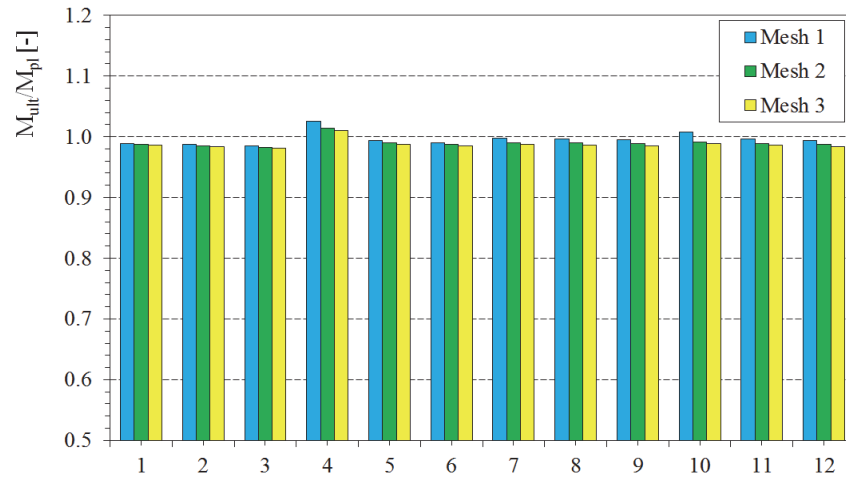


Figure 5.10 – Moment capacity of square and rectangular hollow section under constant moment for different meshes

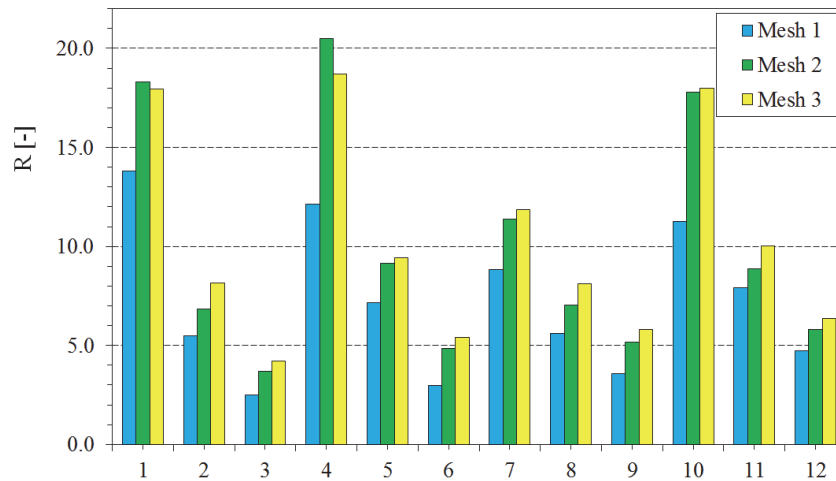


Figure 5.11 – Rotation capacity of square and rectangular hollow section under constant moment for different meshes

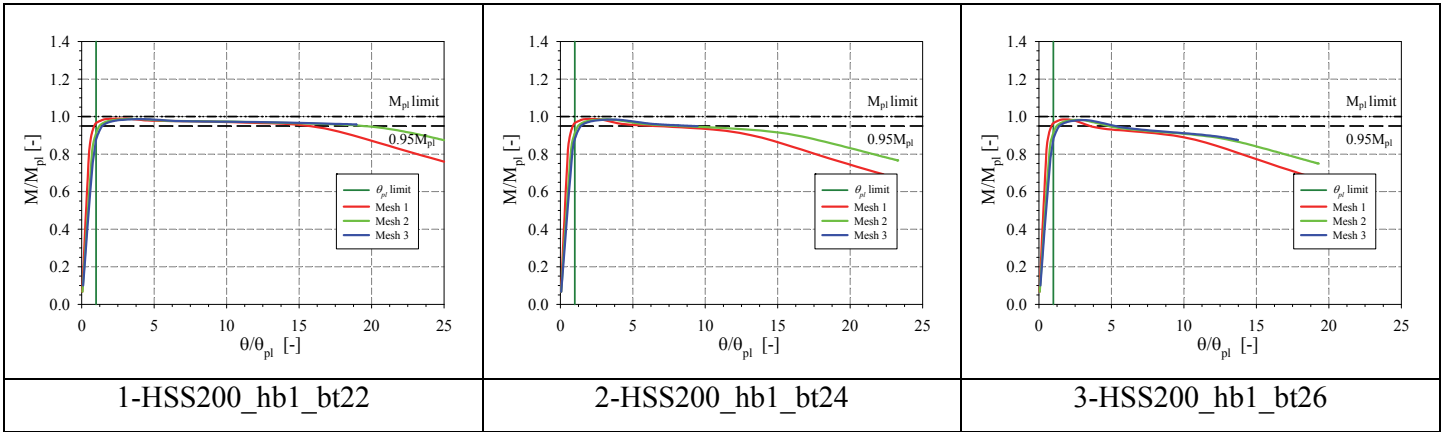


Figure 5.12 – Moment rotation curves of square hollow section under constant moment for different meshes;
HSS refers to Hollow Structural Shape

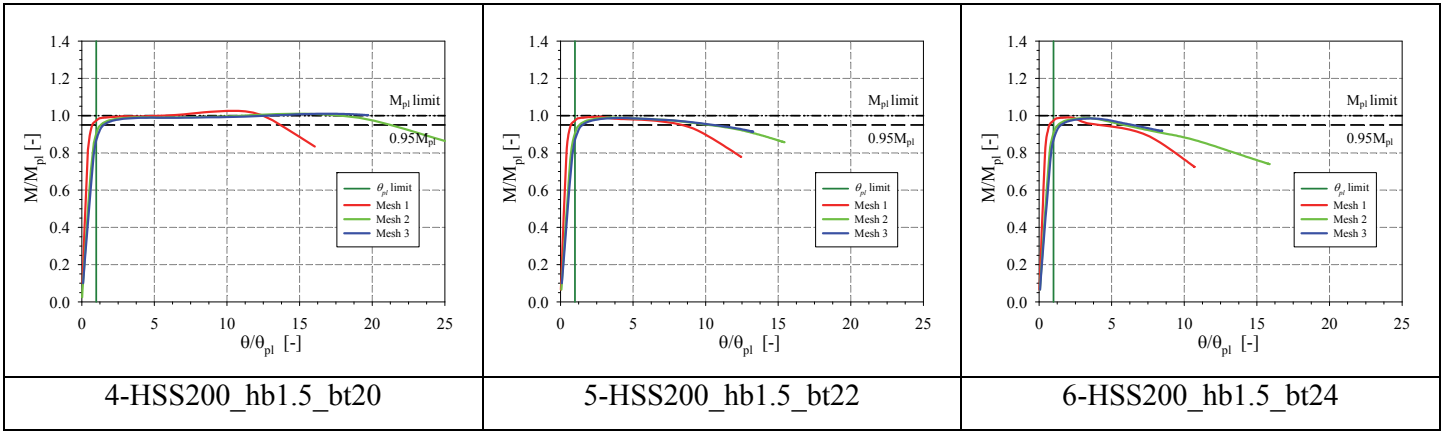


Figure 5.13 – Moment rotation curves of rectangular hollow section with $h/b=1.5$, under constant moment for different meshes; HSS refers to Hollow Structural Shape

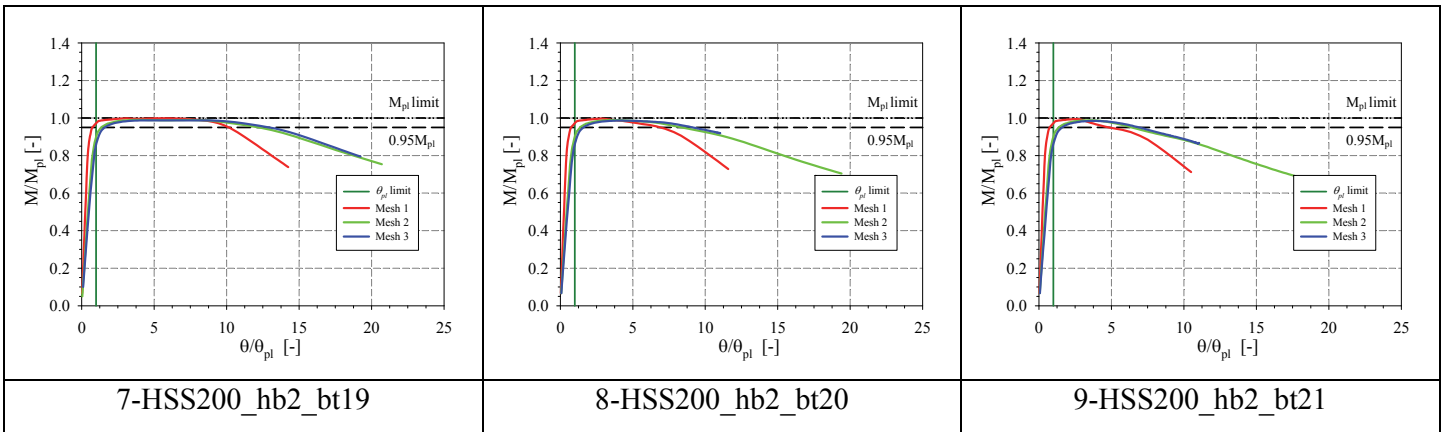


Figure 5.14 – Moment rotation curves of rectangular hollow section with $h/b=2$, under constant moment for different meshes; HSS refers to Hollow Structural Shape

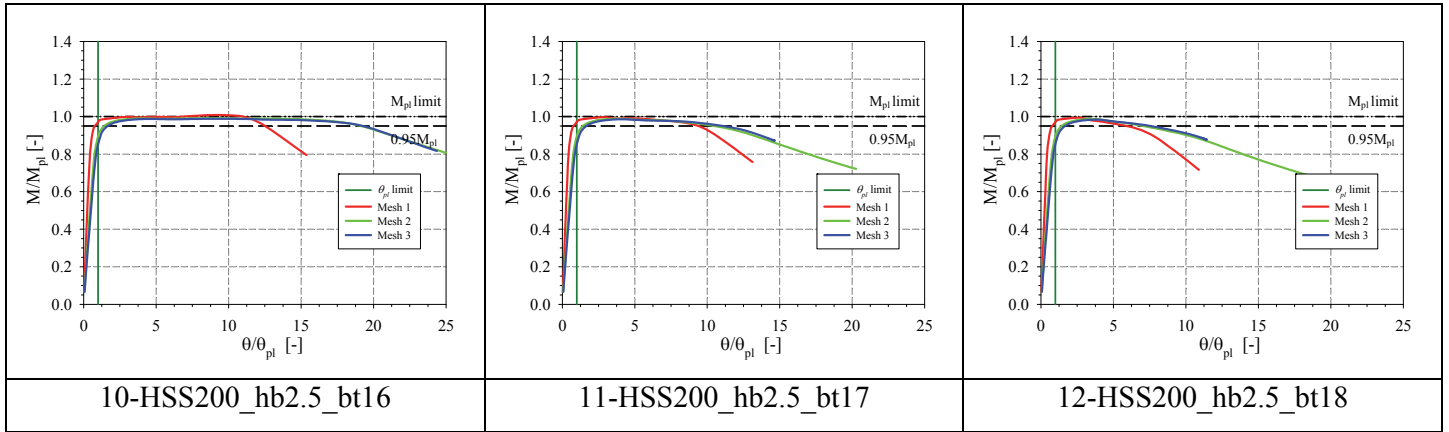


Figure 5.15 – Moment rotation curves of rectangular hollow section with $h/b=2.5$, under constant moment for different meshes; HSS refers to Hollow Structural Shape

5.2.3 Length variation sensitivity when constant moment is applied

The mesh to be adopted in the finite element simulations was selected; the analysis was performed on a short beam of length equal to three time the average of the clear width of both flanges and webs, subject to a constant moment. This section here is developed in order to justify the use of this simplify model that represent cases of constant moment, without resorting to the modelling of a full four point bending test.

Experimentally, a constant moment is obtained by means of a 4-pt bending configuration. Nevertheless, constant bending moment can be represented numerically by applying uniform end moments to a single beam of small length. This model will be referred to as the “simplified model”. This was also performed by many researchers; for instance, Shifferaw & Schafer [43] also modelled a segment of the constant moment region by applying uniform end rotations (moments) to a single beam. The length of the member was selected as a function of the elastic buckling halfwavelength. Their model was compared with test results of some 4-pt bending experiments and good overall agreement was found.

In this section, many simplified model configurations with different length are compared to 2 types of 4-point bending arrangement that act as reference, in order to adopt the model that would represent most accurately the inelastic local buckling of beams in constant bending.

Adopting a simplified model would not only represent accurately the behaviour of a beam subject to constant moment (as also seen in section 3.4) and reduce the computational time but it will also bring many other advantages. Most importantly, it will allow to suitably manipulate the initial geometrical imperfections, since they have been previously identified as

having substantial repercussions on the rotation capacity [41], [40] and [42]. Hence the simplified model will allow to disentangle the effect of each parameter on the rotation capacity in order to obtain clear tendencies.

Initial imperfections are introduced through square half-waves of length L_0 equal to the average clear width of each constituent plate of the cross section (refer to case of Imperfection 1 in Figure 4.15).

$$L_0 = \frac{1}{2} \cdot ((h - 2r - t) + (b - 2r - t)) \quad 5.15$$

We should note here that if the beam length is not taken as a function of the halfwave length L_0 and rather as a function of the cross-section height, this will lead to an unknown number of initial buckling waves depending on the cross-section geometry, and hence this will lead to different rotation capacity values.

Configurations 1 to 4 simplified models consist of different lengths. The minimal length was chosen to be equal to $3 L_0$ (and therefore obtain 3 initial buckling waves), based on the principle that the length is sufficiently small to prevent second order effects while long enough to avoid the influence of the boundary conditions [107]. Configurations 5 and 6 are 4-pt bending configurations with loading applied at third-length from the support. Loading is introduced uniformly trough all nodes of the webs (see Figure 5.19).

Configurations 1: Length = $3 L_0$. This is chosen in order to obtain 3 wavelength so that local buckling would always occur at mid-span.

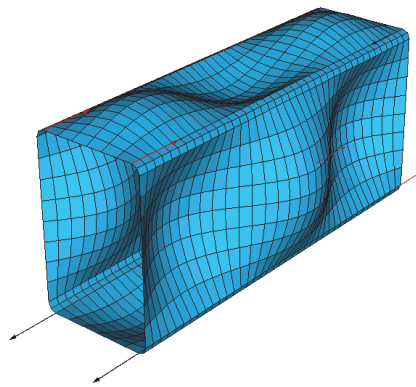


Figure 5.16 – Amplified imperfections for configuration 1

Configuration 2: $L = 5 L_0$. This arrangement is selected in order to have a longer beam length while maintaining an odd number of halfwave lengths and an upward first buckle on the flange so that local buckling would not occur near the boundaries.

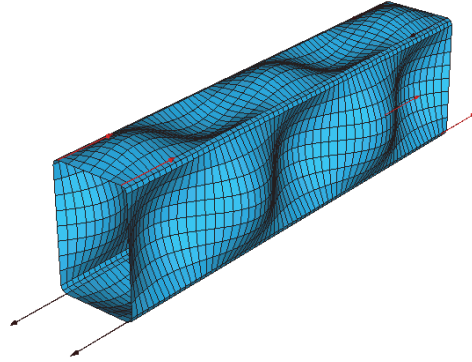


Figure 5.17 – Amplified imperfections for configuration 2

Configuration 3: $L = 3 h$. The length of the cross-section specimen is chosen equal to three times the height of the section. This configuration will lead to different initial geometric combinations – by having a different number of buckling waves – depending of the section geometry as seen in Figure 5.18. In Figure 5.18, a beam of length equal to 3 times the height with $h = 200 \text{ mm}$ and an aspect ratio $h / b = 1$, results in 4 initial geometrical buckles whereas for an aspect ratio $h / b = 2$, we obtain 5 buckles.

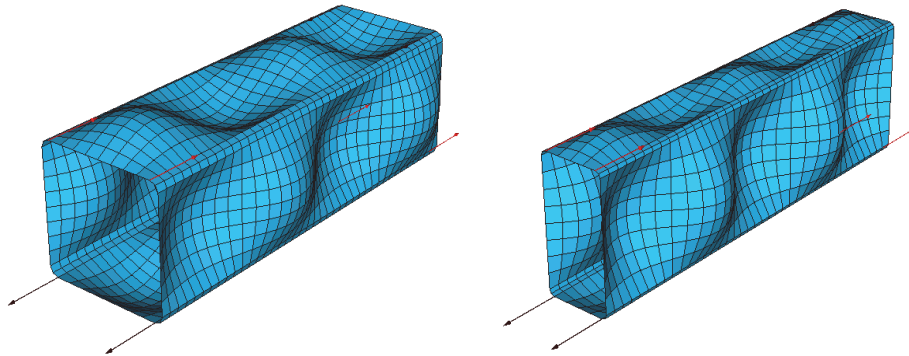


Figure 5.18 – Amplified imperfections for configuration 3; a) $h / b = 1$, b) $h / b = 2$

Configuration 4: $L = 5 h$. The length of the cross-section specimen is chosen equal to five times the height of the section.

Configuration 5: $L = 10 h$. this is a 4-pt bending configuration in which a part of length $3.33h$ is left with a constant moment.

Configuration 6: $L = 15 h$. this is a 4-pt bending configuration in which a part of length equal to $5h$ is left with a constant moment.

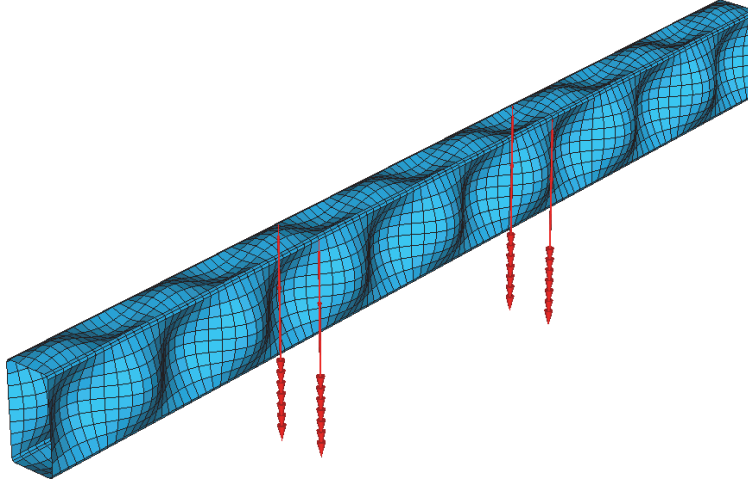


Figure 5.19 – Amplified imperfections for configuration 5 (4-pt bending)

Figure 5.20 compares the section normalised ultimate resistance M_{ult} / M_{pl} for the different modelling and Figure 5.21 displays the rotation capacity obtained. It is to be mentioned here that the rotation capacity for 4-pt bending configurations was based on the mid-segment curvature while for the simplified model it is based on the section end's rotations.

In Figure 5.20, in terms of ultimate moment, differences between models are very limited and negligible, with section 4 exhibiting the highest divergence of about 5%. This divergence is due to the initiation of strain hardening in some models.

For what concerns the rotation capacity, presented in Figure 5.21, a bigger disparity is reported. The first remark to note is that between the 4-pt bending configurations, we can observe a variation of 45% in the rotation capacity. Moreover, higher rotation capacity are reached randomly, sometimes by configuration 5, while other times by configuration 6. For example, section 2 and 11 reach higher rotation capacity values with configuration 5, while section 4 obtain higher values with configuration 6. These differences highlight the sensitivity of the rotation capacity and the need to adopt a model that would lead to consistent results.

Divergences between the simplified models are also non-negligible. However, it can be noticed that configuration 1 presents the closest results to the 4-pt bending configuration while configuration 4 displays the biggest discrepancies. Table 4.1 reports all the rotation capacity values for configuration 1 to 6 which are denoted R_1 to R_6 , respectively. Moreover,

R_{avg} consists in the average of the rotation capacity from configuration 5 and 6, and the deviation from R_{avg} is reported for all sections. It can be noted that configuration 1 displays the closest results to the 4-pt bending models with an average of 17% and the smaller standard deviation (11%) from the 4-pt bending results. Although these values are considerable, the divergence observed experimentally is much larger. Figure 2.11 shows the rotation capacity obtained experimentally for hollow sections and Figure 2.13 displays it for open section; In these figures large differences in the rotation capacity are observed between sections of same slenderness and the variation can be larger than 200%. Therefore, the differences are much larger experimentally than that observed numerically and is caused by the fact that experimentally, the geometrical and material properties of a beam are numerous and unpredictable.

Figure 5.22, Figure 5.23, Figure 5.24 and Figure 5.25 illustrate the moment-rotation curves obtained for all sections. The illustration show that configuration 1 presents the best accordance with the 4-pt bending arrangement and that it represents accurately the beam behaviour. Moreover it has been demonstrated in these numerical analysis, as well as experimentally, that the rotation capacity varies enormously for a slightly different parameter. Based on these observations, configuration 1 was considered to represent the bending behaviour of sections adequately and gave the closest rotation capacities results to the 4-pt bending configuration. In addition, this model possesses the best mechanical background, i.e. it allows to always have a fixed number of initial buckles and allows for inelastic local buckling to develop at mid-span; in that way, results are expected to be less scattered and consistent with each other. Therefore configuration 1 was adopted for the rest of the numerical studies.

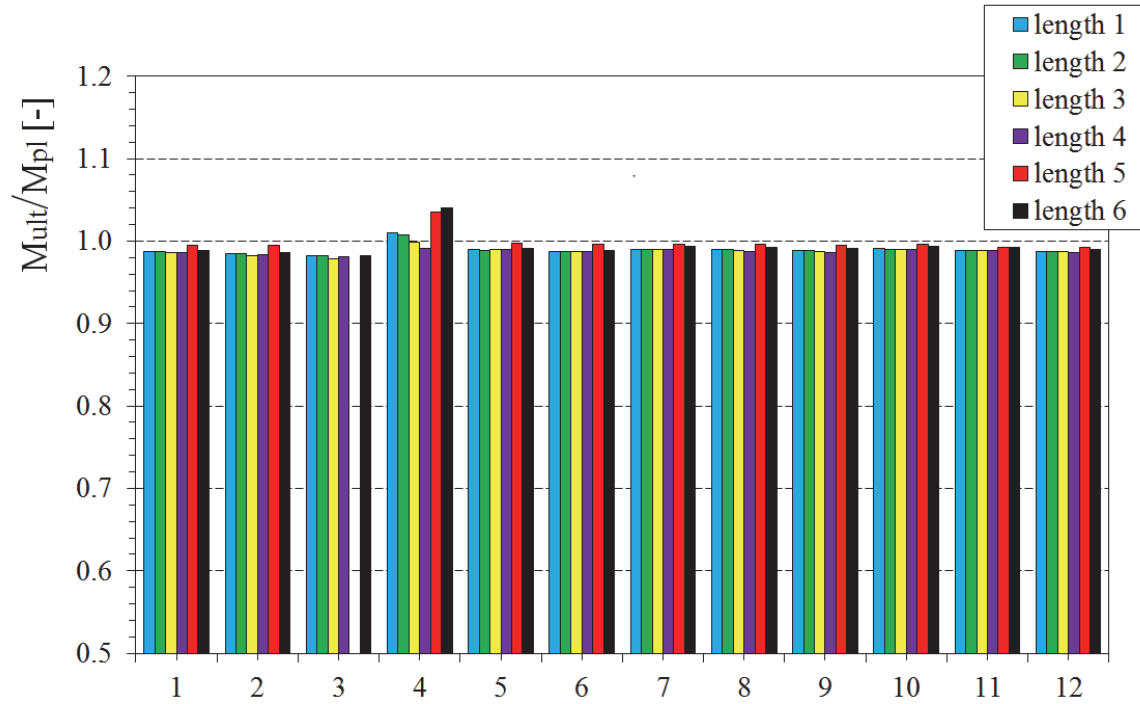


Figure 5.20 – Moment capacity for square and rectangular hollow section under constant moment with length variation

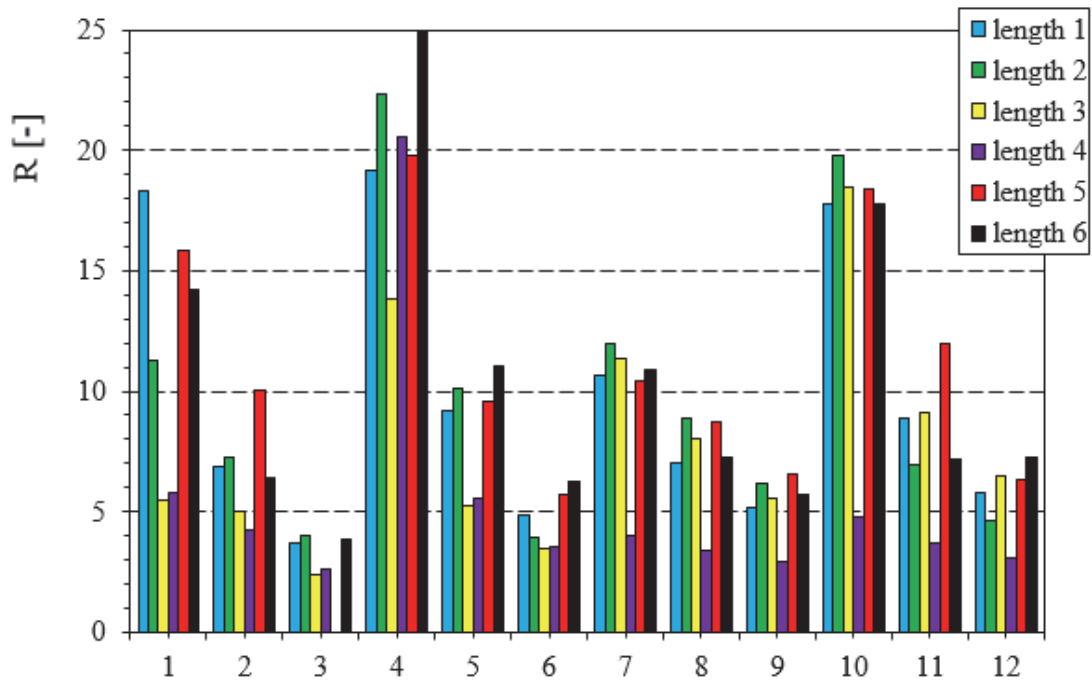


Figure 5.21 – Rotation capacity for square and rectangular hollow section under constant moment with length variation

Table 5.3 – Rotation capacity for different configurations and comparison

	R_1	R_2	R_3	R_4	R_5	R_6	R_{avg} $=(R_5+R_6)/2$	$(R_{avg}-R_1)/$ R_{avg}	$(R_{avg}-R_2)/$ R_{avg}	$(R_{avg}-R_3)/$ R_{avg}	$(R_{avg}-R_4)/$ R_{avg}
	[-]	[-]	[-]	[-]	[-]	[-]	[-]	[%]	[%]	[%]	[%]
section 1	18.3	11.3	5.5	5.8	16.8	15.3	16.0	-14.0	29.5	66.0	64.1
section 2	6.8	7.2	5.0	4.3	11.1	7.4	9.2	25.7	21.4	45.3	53.7
section 3	3.7	4.0	2.4	2.6	-	4.9	4.9	24.4	17.1	50.6	45.8
section 4	19.2	22.3	13.9	20.5	20.8	28.9	24.8	22.9	10.2	44.2	17.3
section 5	9.2	10.1	5.2	5.6	10.6	12.0	11.3	19.1	10.8	53.7	50.9
section 6	4.9	3.9	3.5	3.5	6.7	7.3	7.0	30.6	44.2	50.2	49.9
section 7	10.6	12.0	11.4	4.0	11.4	11.9	11.6	8.5	-3.1	2.3	65.6
section 8	7.0	8.9	8.0	3.4	9.7	8.2	9.0	21.5	1.2	10.5	61.9
section 9	5.2	6.2	5.6	3.0	7.6	6.7	7.1	27.4	13.5	21.8	58.6
section 10	17.8	19.7	18.5	4.8	19.4	18.8	19.1	6.6	-3.6	3.1	74.8
section 11	8.9	7.0	9.1	3.7	13.0	8.2	10.6	16.2	34.2	13.8	65.0
section 12	5.8	4.7	6.5	3.1	7.4	8.3	7.8	25.6	40.4	17.1	60.4
Average								17.9	18.0	31.6	55.7
Standard deviation								11.9	15.6	21.3	13.9

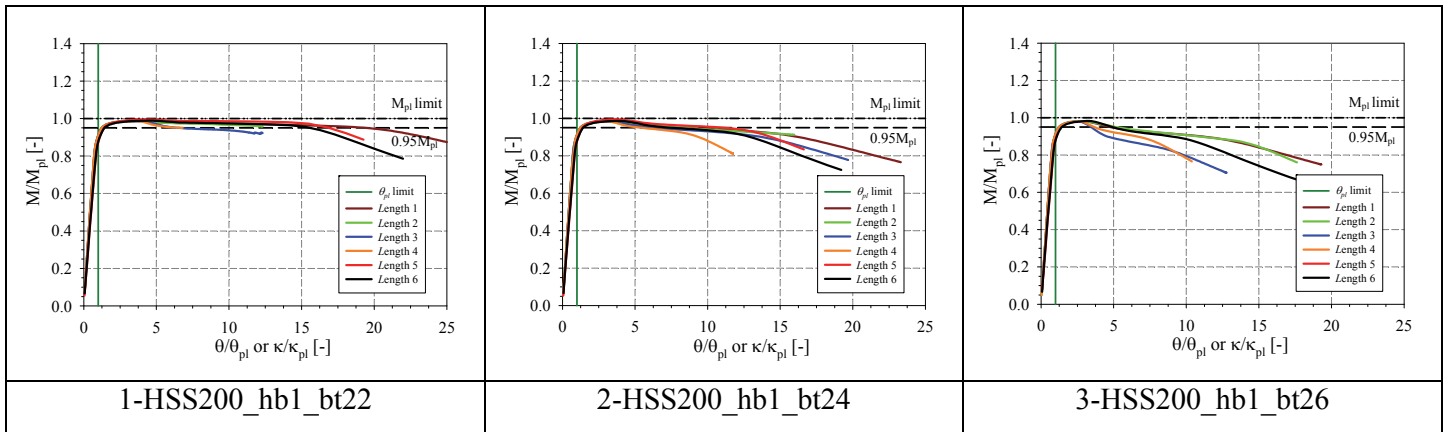


Figure 5.22 – Moment rotation curves for square hollow section under constant moment with length variation

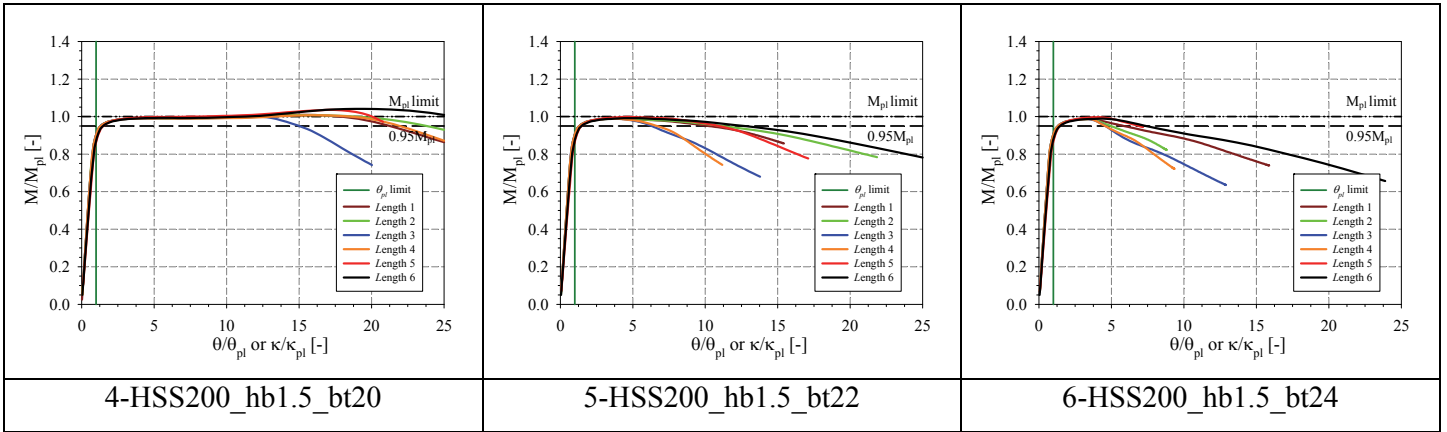


Figure 5.23 – Moment rotation curves for rectangular hollow section with $h/b=1.5$, under constant moment with length variation

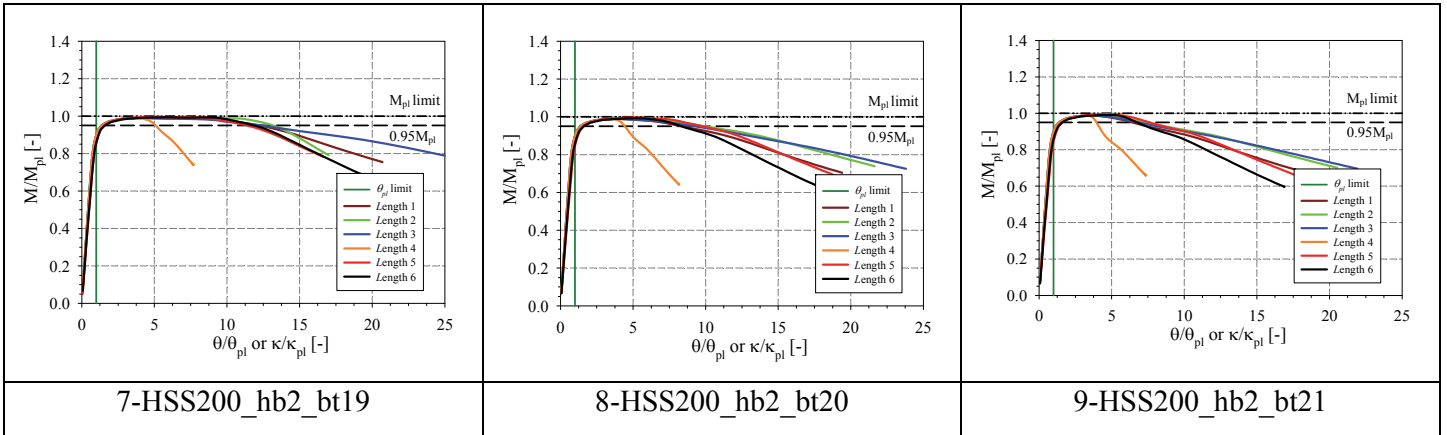


Figure 5.24 – Moment rotation curves for rectangular hollow section with $h/b=2$, under constant moment with length variation

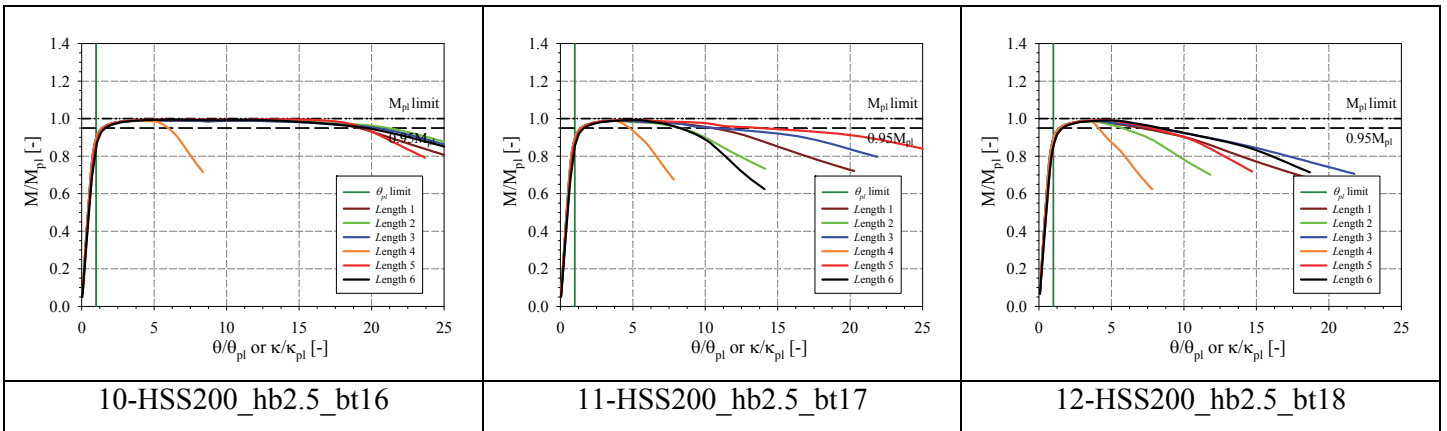


Figure 5.25 – Moment rotation curves for rectangular hollow section with $h/b=2.5$, under constant moment with length variation

5.2.4 Effect of residual stresses

In the present section, the effect of residual stresses on the inelastic bending behaviour of hollow beams is studied. Residual stresses are defined as self-equilibrated stresses present in materials under uniform temperature conditions without external loading. Their origin is related to the section production process.

For hot-formed sections, residual stresses result from differential cooling rates due to the variation in material thickness. The first region to cool is left with residual compression while the slower cooling parts are left in tension. Only longitudinal membrane residual stresses are taken into account for hot-formed sections in the numerical studies. As prescribed by Nseir, 2015 [104], residual compression was affected to corners whereas webs and flanges were left in residual tension. The adopted values are reported in section 4.2.1.

However, cold-formed sections exhibit flexural stresses due to the plastic deformation of flat strips into a square or rectangular hollow section, and membrane residual stresses are negligible. Figure 5.26 displays the amplification effect of flexural residual stresses. Flexural residual stresses were considered with a linear variation through the plate thickness as proposed by Key & Hancock [108] and Nseir [104]. Values implemented in the model are listed in section 4.2.1.

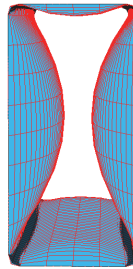


Figure 5.26 – Amplification of the effect of flexural residual stresses on a beam.

The influence of bending and membrane residual stresses on the rotation capacity of beams under constant bending moment was investigated numerically through GMNIA analyses. Their amplitudes have been previously described in Chapter 4.

10 sections with different cross-section slenderness varying from 0.3 to 0.5 were selected for each h/b ratio (1, 1.5, 2 and 2.5). The results of the study are presented in Figure 5.27 to Figure 5.34. The cross-section slenderness is given by Equation 5.16.

$$\lambda_{cs} = \sqrt{M_{pl}/M_{crit}} \quad 5.16$$

The elastic buckling critical moment M_{crit} was calculated with Linear Buckling Analysis (LBA) using FINELg.

The general influence of residual stresses in structural members is premature yielding which leads to a loss in stiffness. For hot-formed sections, a typical material response with and without membrane residual stresses is depicted in Figure 5.27. It is clearly seen that the membrane residual stresses generate a slight decrease in stiffness at the beginning of yielding and no effect is witnessed in the postbuckling phase. Figure 5.28 and Figure 5.29 exhibits the rotation capacity for all hot-rolled sections with and without residual stresses. They clearly demonstrate that membrane residual stresses induce no repercussion on the rotation capacity.

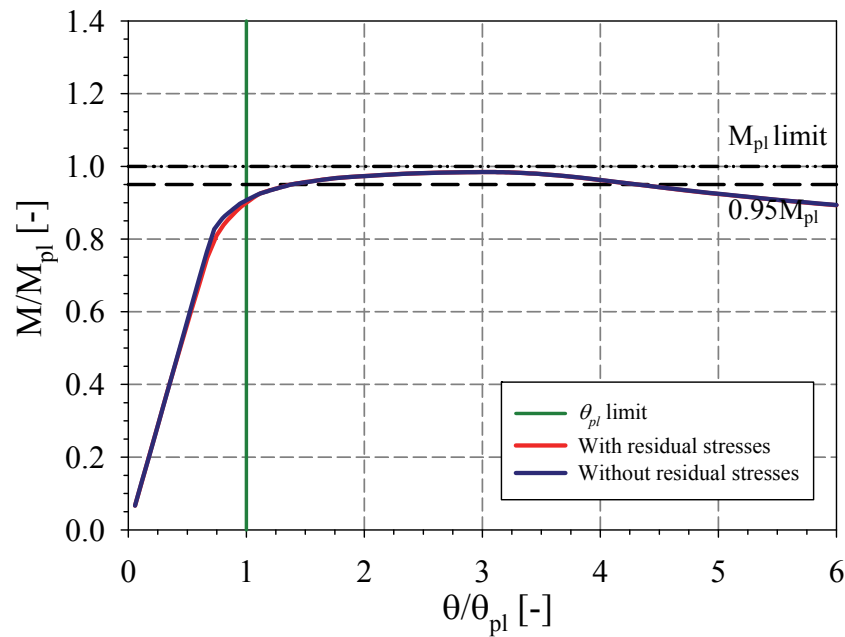


Figure 5.27 – Influence of residual stresses of hot-formed section in terms of moment rotation curves. Specific case of hollow structural sections, $h/b = 2$, $b/t = 23$ under constant moment

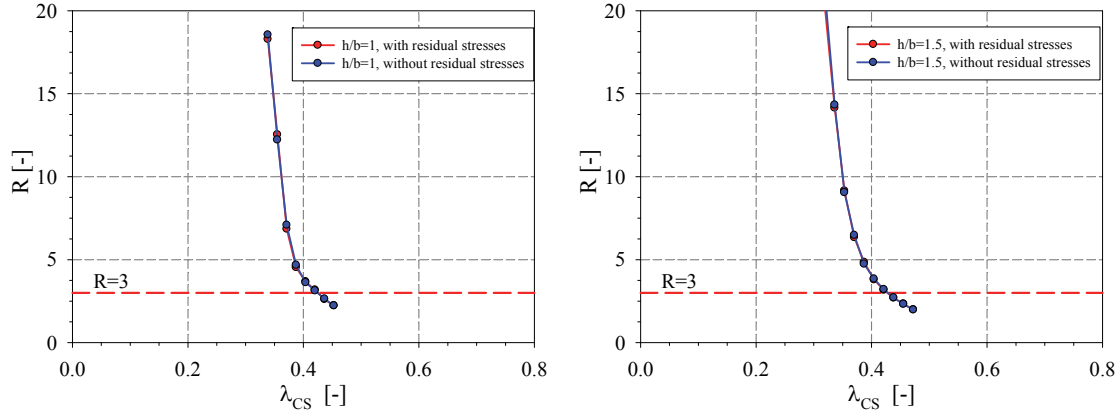


Figure 5.28 – Effect of residual stresses on the rotation capacity of hot-formed hollow structural sections under constant moment, a) $h/b = 1$, b) $h/b = 1.5$ – the rotation capacity limit of 3 represent the minimum required rotation in the EC3 for plastic analysis to be performed

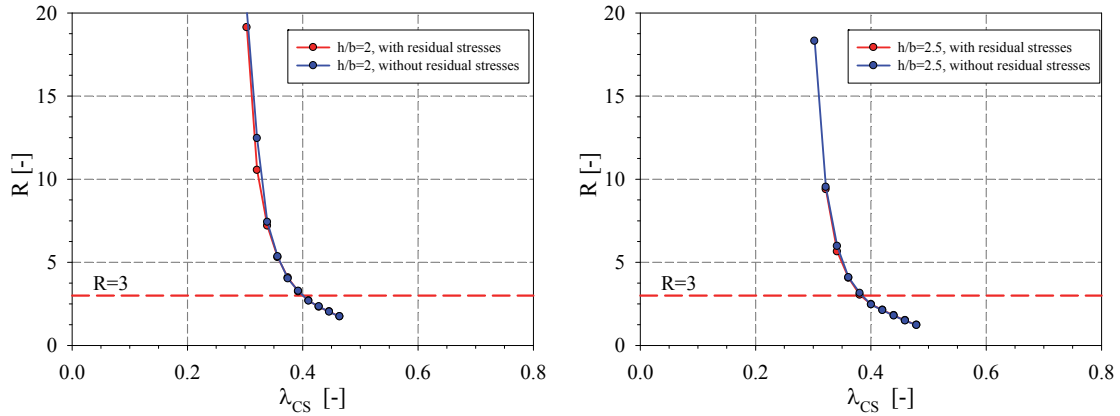


Figure 5.29 – Effect of residual stresses on the rotation capacity of hot-formed hollow structural sections under constant moment, a) $h/b = 2$, b) $h/b = 2.5$

As for the effect of flexural residual stresses, Figure 5.30 displays moment rotation curves for a typical section with and without bending residual stresses. It can be noted that although flexural residual stresses induce a reduction in stiffness at early stage, they are seen to have a slightly positive influence on the postbuckling behaviour.

Hence, according to Jandera & al ([109] and [110]), it was found that despite the fact that the secant modulus is being consistently reduced in the presence of residual stresses, a positive influence arises when failure strains coincide with a region of increased tangent modulus. For our cases, beams failure strain always coincided with increased tangent modulus regions, leading to slightly higher ultimate loads and rotation capacities. Figure 5.31, Figure 5.32,

Figure 5.33, and Figure 5.34 show the normalised ultimate load $\chi_{CS} = M_{ult}/M_{pl}$ (also called cross-section reduction factor) and rotation capacity for all considered cross-sections. From these figures, it can be concluded that flexural residual stresses have a slightly positive influence on the section behaviour. Nevertheless, Schafer & Pekoz [111] demonstrated that the inclusion of flexural residual stress has a significant qualitative effect on the behaviour of beams and that if residual stress are ignored, the yielding locations exhibit a lower level of complexity. They showed that early yielding on the face of the plates has a strong influence on stress distribution and on interpretations of the way the load is carried by the plate. They concluded that the primary importance of residual stresses is in how load is carried and not in the final magnitude since they have a small net effect. In conclusion, to well represent the mechanical behaviour of beams in bending, longitudinal membrane stresses were taken into account for hot-rolled sections whereas flexural stresses were implemented for cold-formed ones. Their amplitudes are described in Chapter 5.

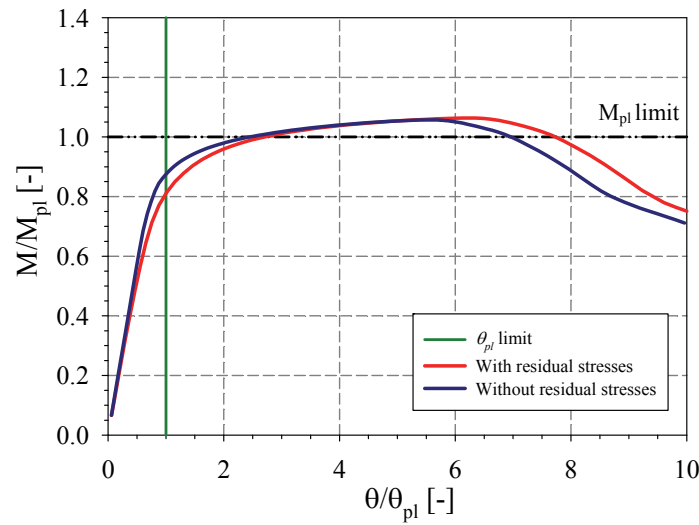


Figure 5.30 – Influence of residual stresses of cold-formed section in terms of moment rotation curves. Specific case of hollow structural sections, $h/b = 2$, $b/t = 23$ under constant moment

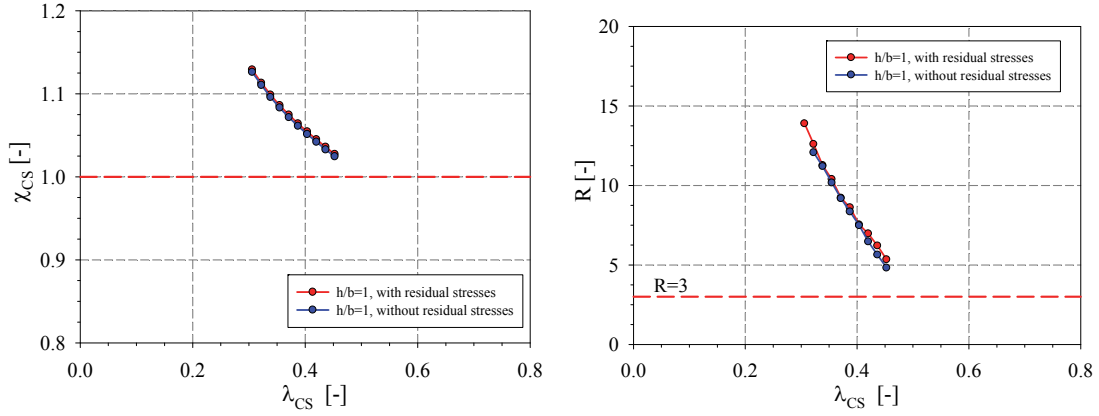


Figure 5.31 – Effect of residual stresses on the normalised ultimate capacity and rotation capacity of cold-formed hollow structural sections under constant moment for $h / b = 1$

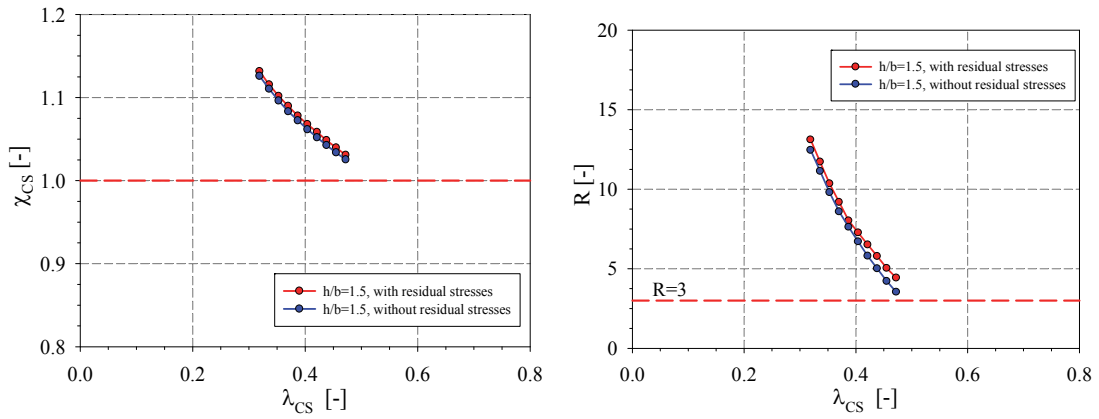


Figure 5.32 – Effect of residual stresses on the normalised ultimate capacity and rotation capacity of cold-formed hollow structural sections under constant moment for $h / b = 1.5$

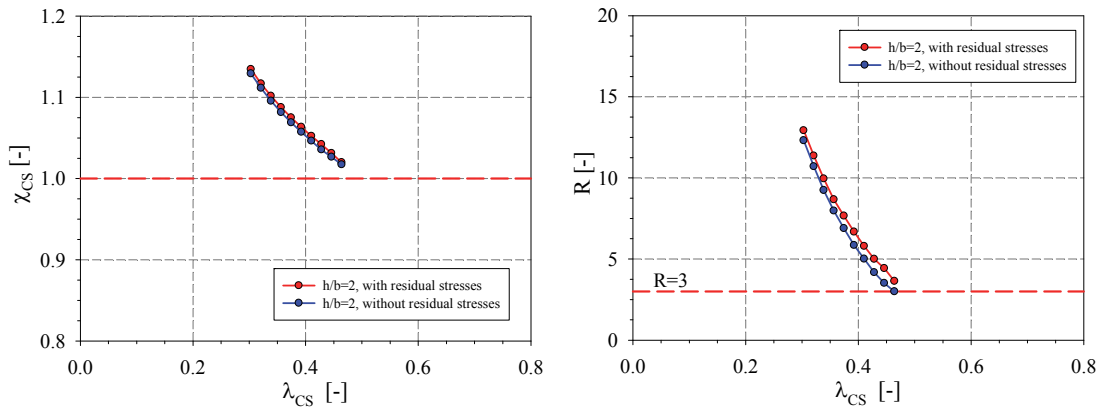


Figure 5.33 – Effect of residual stresses on the normalised ultimate capacity and rotation capacity of cold-formed hollow structural sections under constant moment for $h / b = 2$

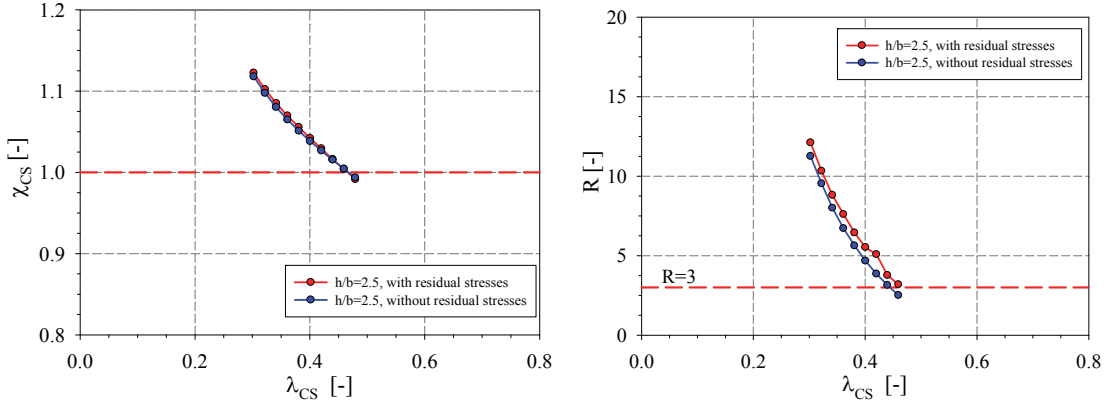


Figure 5.34 – Effect of residual stresses on the normalised ultimate capacity and rotation capacity of cold-formed hollow structural sections under constant moment for $h / b = 2.5$

5.2.5 Imperfection variation

For stocky sections, local geometrical imperfection shapes induce important effects on hollow profiles in terms of ultimate strength and post-buckling capacities. Hence, implementation of a proper geometric imperfection is crucial in order to obtain realistic results. Geometrical imperfections alter hollow beams response mainly in the post peak (unloading) phase, and therefore when such beams are tested in bending, their rotation capacities may differ depending on the geometrical imperfection introduced.

Six different shapes and amplitudes of initial local geometric imperfections on the cross-section capacity of the tested square and rectangular sections were selected and are represented in Figure 5.35 and Figure 5.36. The geometric imperfection is composed of an imperfection shape and an imperfection amplitude denoted ω_0 . No global initial imperfections were introduced as only cross section capacities are being examined.

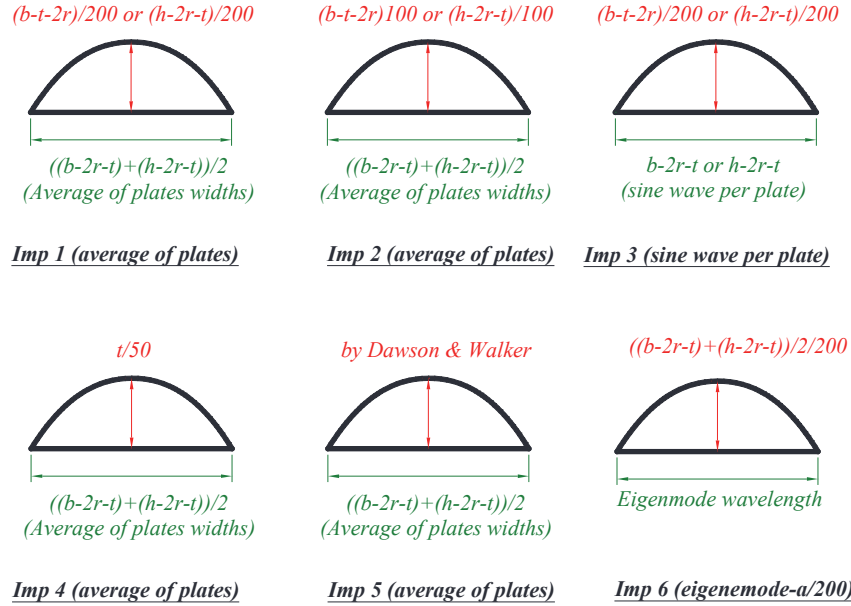
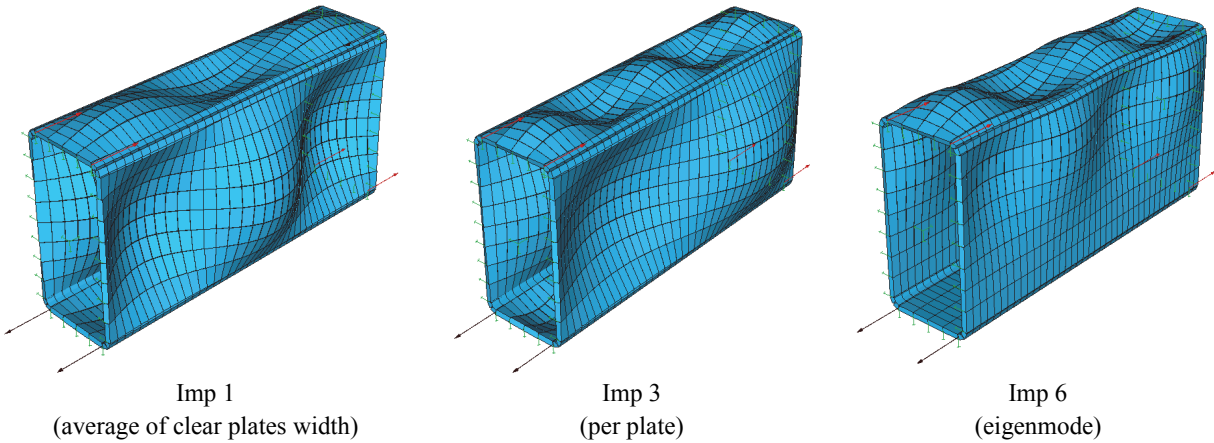


Figure 5.35 – Considered local geometrical imperfections


 Figure 5.36 – Amplified geometrical imperfections for RHS with $h/b=2$

In terms of imperfection shapes, two types were adopted. The first consists in an appropriate modification of node coordinates in square sine waves equations for each constituent plate. For this type of imperfection, two variables were considered: the first, as shown in Figure 5.36, consists in adopting a sine period equal to the average of the clear width of the webs and flanges. The second variable had different sinewaves for each plate with the amplitude corresponding to the clear width of the plate (Figure 5.36b). Type II consists in an

imperfection distribution based on the first eigenmode from linear buckling analysis (Figure 5.36c).

The adopted amplitudes are the following:

- Amplitude of $a/200$ as prescribed in EC3 [112] without a reduction of 30%, although the residual stress patterns were introduced in the calculations. Results are therefore considered as conservative. This model is a function of the plate width b , and is independent on the plate thicknesses which is more adapted for hot-formed section.
- Amplitude equal to $t / 50$ as stated by Wang & al [40]. Hence, for cold-formed steel, the imperfection amplitude is usually determined as a function of the plate thickness [113]. This method provides acceptable results in plates of small thicknesses but it can lead to unreasonably large imperfections in thicker plates.
- A value calculated from the predictive model of Dawson and given by Equation 5.18.

Dawson and Walker [114] prescribed 3 different models given by Equation 5.17, 5.18 and 5.19, where f_y is the material yield strength, σ_{cr} is the elastic critical buckling stress of the most slender constituent plate element in the section, and t is the plate thickness.

$$\omega_0 = \alpha t \quad 5.17$$

$$\omega_0 = \beta \left(f_y / \sigma_{cr} \right)^{0.5} t \quad 5.18$$

$$\omega_0 = \gamma \left(f_y / \sigma_{cr} \right) t \quad 5.19$$

Equation 5.17 gives a constant imperfection amplitude for all values of the plate width, and is only a function of the plate thickness, which gives unreasonable large imperfection values for stocky plates.

Equation 5.18 is a function of the plate width b and independent of the thickness t as the one prescribed by EC3. This model presented a better correlations between predicted values and experimental tests results according to Gardner & al [92] and was therefore recommended. Dawson and Walker [114] indirectly calculated $\beta = 0.2$ by fitting a resistance function to available test results. However, more reasonable values were proposed by Gardner & al [92] based on direct measurements. $\beta = 0.028$ for hot-rolled sections and $\beta = 0.034$ for cold-

formed sections were recommended. These values indicate slightly higher imperfections in the cold-formed sections.

Equation 5.19 gives an imperfection amplitude as a function of both the plate thickness and the plate width. This model gives the most reasonable imperfection amplitude function, especially for low b/t values where smaller imperfections are expected.

A more precise comparison between these imperfection amplitude functions is detailed and illustrated in Torabian & Schafer [91].

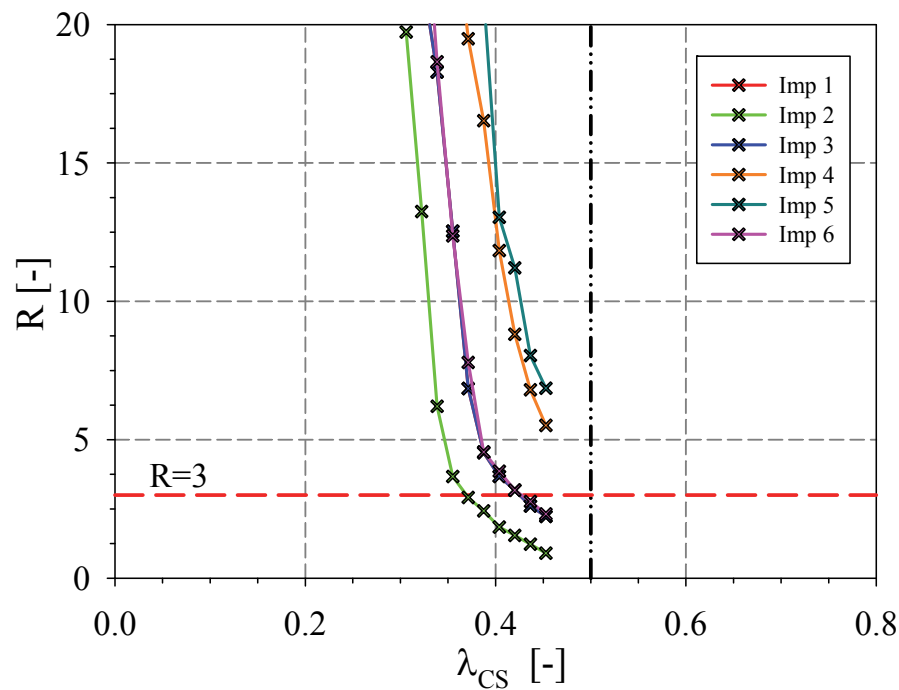


Figure 5.37 – Rotation capacity of hot-rolled square hollow section for different geometrical imperfection patterns

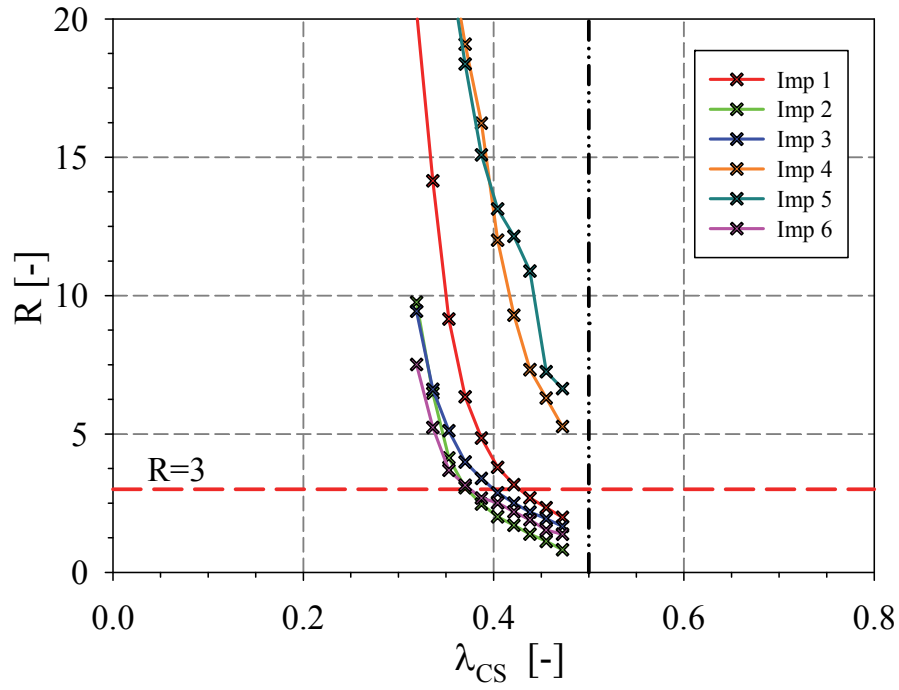


Figure 5.38 – Rotation capacity of hot-rolled rectangular hollow section with $h / b = 1.5$ for different geometrical imperfection patterns

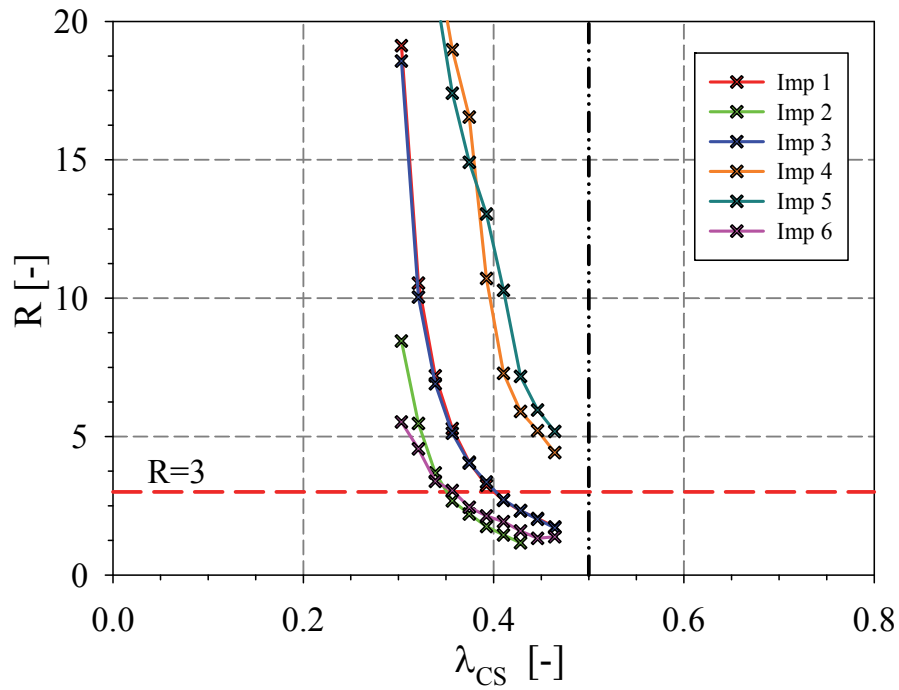


Figure 5.39 – Rotation capacity of hot-rolled rectangular hollow section with $h / b = 2$ for different geometrical imperfection patterns

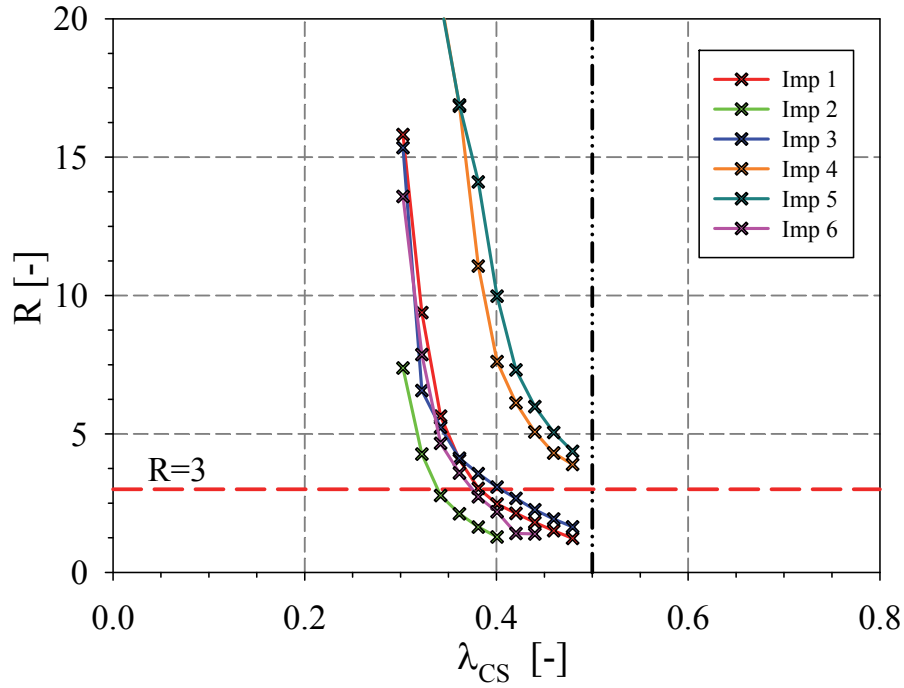


Figure 5.40 – Rotation capacity of hot-rolled rectangular hollow section with $h / b = 2.5$ for different geometrical imperfection patterns

Figure 5.37, Figure 5.38, Figure 5.39 and Figure 5.40 present the rotation capacities for hot-formed sections and for the different aspect ratios $h / b = 1, 1.5, 2$ and 2.5 respectively. Figure 5.41, Figure 5.42, Figure 5.43, and Figure 5.44 display the results corresponding to cold-formed cross-sections.

The following conclusions can be drawn from these figures:

- i) Geometrical imperfections induce a substantial effect on the rotation capacity of both hot-formed and cold-formed sections;
- ii) Rotation values about 10 times higher are reached for hot-formed sections between different imperfection models; this is primary due to the presence of the yield plateau that leads to the rotation capacity having a steep parabolic curve when represented as a function of the cross-section slenderness. Whereas for cold-formed sections, the difference in the rotation capacity between models with different imperfections is of the order of 2;
- iii) The sensitivity to the imperfection amplitude increased as the cross section slenderness decreased;

- iv) For a given imperfection shape and amplitude, clear tendencies are observed. This emphasises the need to take a unique imperfection pattern for all parametric studies in order to maintain consistent modelling, and thus obtain a small scatter. It also explains why experimentally, a large scatter is observed with an unclear disposition; a large variation is noticed due to the random properties of each beam whereas when consistent parameters are introduced numerically in the F.E. model, clear trends can be achieved;
- v) Imperfection 5 and 6 patterns give substantially higher rotation capacity values. These imperfections amplitudes are smaller than the $a / 200$ prescribed by EC3. These values have been obtained by calibration towards experimental tests. This shows that if tested beams are well manufactured, i.e. with a high level of planarity, high rotation capacities are achieved. Nevertheless, in order to remain safe sided, the $a / 200$ limit is more reasonable and is adequate with the allowed tolerances for hollow sections;
- vi) Both the amplitude and the imperfection shape have an impact on the rotation capacity, nonetheless it is clearly shown that it is the amplitude that alter the rotation capacity the most. In this respect, imperfection 1 and imperfection 6 are compared with Imperfection 1 shape obtained through an appropriate by-hand modification of node coordinates while Imperfection 6 shape is obtained by the first eigenmode shape. It can be seen that for the cases of square hollow section, close values of rotations capacity are reached despite the fact that these models display different imperfection shapes. However, for the aspect ratio of 1.5 and 2, lower rotation values are reached with Imperfection 6 (eigenmode wavelength); this is not only attributed to the imperfection shape, but also to the selected amplitude. Hence, in Imperfection 1, different amplitudes are given for webs and flanges according to the width of each plate respectively; however, in Imperfection 6, the adopted amplitude is given as an average of both webs and flanges width which leads to having a higher imperfection value attributed to the flange of the model with Imperfection 1. Since for aspect ratios smaller than 2, the flange buckles first, it can be explained why lower rotation values are reached with Imperfection 6. For the aspect ratio of 2.5, failure is due to web buckling, which is why results are for this case close to the ones of Imperfection 1;

- vii) Imperfection 2 (amplitude $a / 100$) leads to the lowest rotation capacity values. Although the motivation behind this study is to choose a safe-sided parameter, this value is not seen reasonable as was therefore disregarded;
- viii) For what concerns the resistance, minor differences between all the adopted initial imperfections was observed. A larger analysis relative to the effect of the initial imperfection on the cross-section resistance can be found in [104].

In conclusion, a big disparity is found between different initial imperfections configuration. In an attempt to remain on the safe side, initial geometrical Imperfection 1 was selected for the rest of the parametric study which consist in introducing square halfwavelength of length equal to average of plate widths; and an amplitude of $a / 200$ according to the corresponding plate. Although being quite widely used, the approach consisting in introducing imperfection patterns by means of the first buckling mode was seen to be less appropriate, and does not guarantee safer, conservative results [104]. Therefore, initial geometrical imperfections can be basically introduced through adequate modifications of node coordinates and Imperfection type 1 was selected for the remains of the studies.

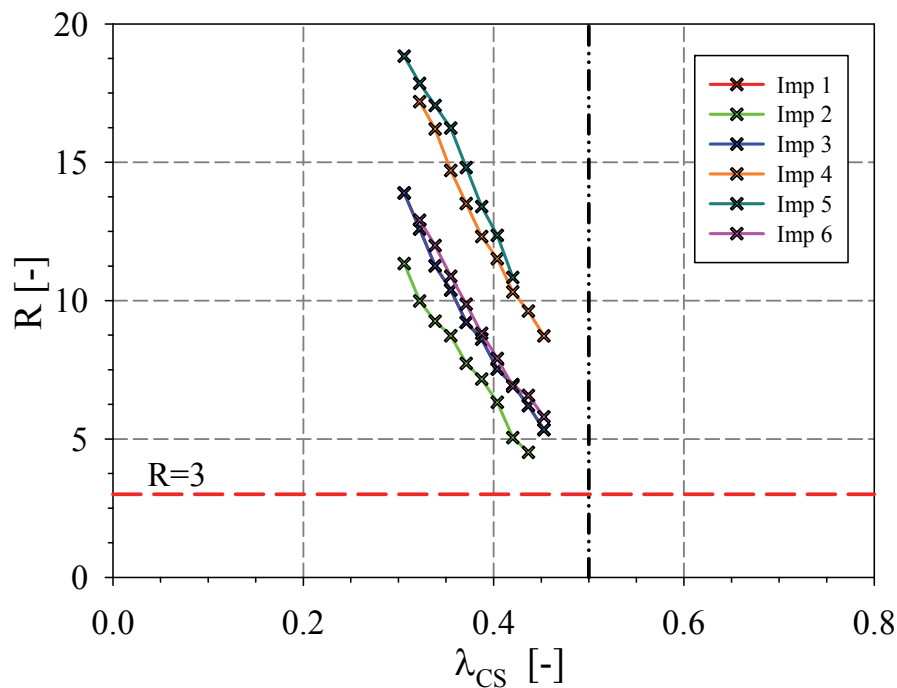


Figure 5.41 – Rotation capacity of cold-formed square hollow section for different geometrical imperfection patterns

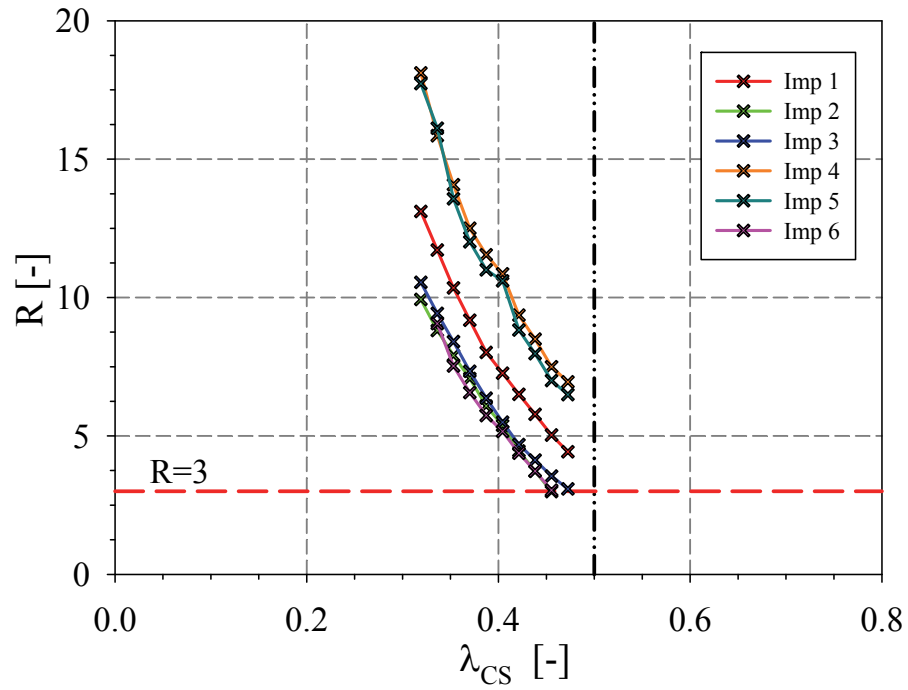


Figure 5.42 – Rotation capacity of cold-formed rectangular hollow section with $h/b=1.5$ for different geometrical imperfection patterns

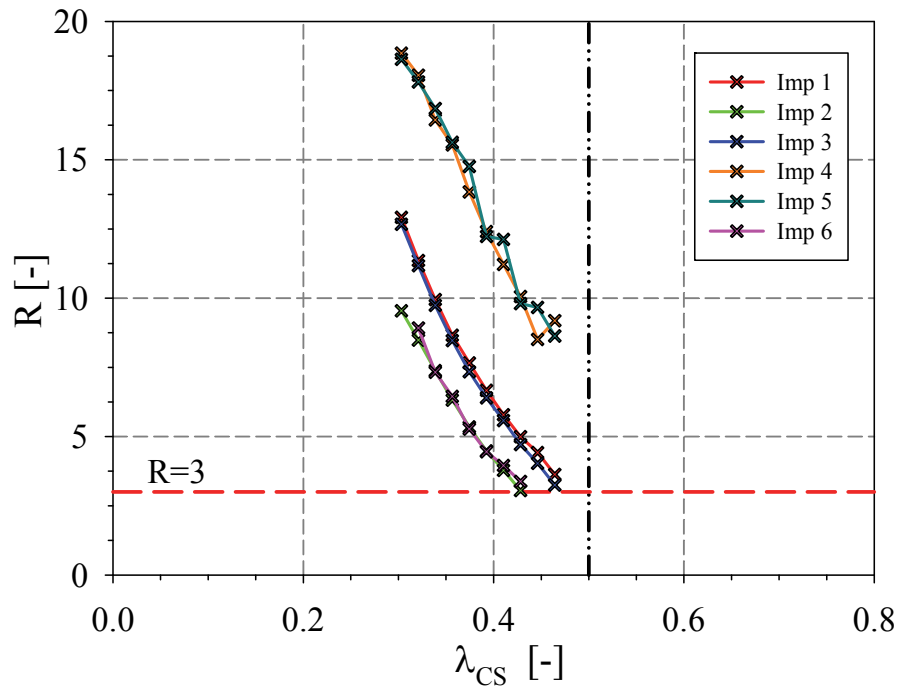


Figure 5.43 – Rotation capacity of cold-formed rectangular hollow section with $h/b=2$ for different geometrical imperfection patterns

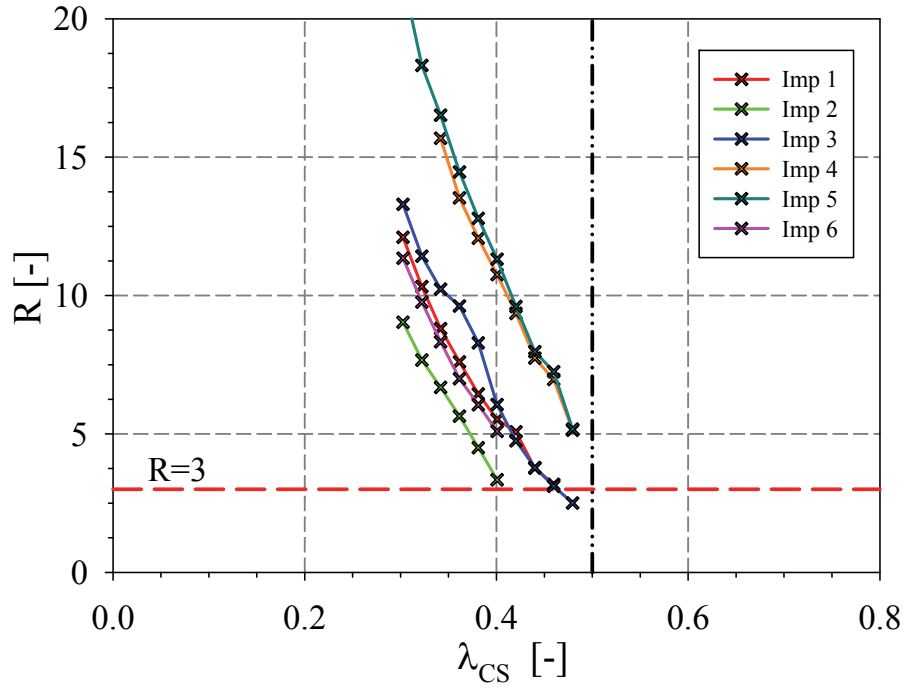


Figure 5.44 – Rotation capacity of cold-formed rectangular hollow section with $h/b=2.5$ for different geometrical imperfection patterns

5.2.6 Influence of yield stress to ultimate stress ratio

Since the material laws adopted for hot-formed and cold-formed sections are quite sophisticated and different, with various sets of parameters assigned depending on the steel grade, a small sub-study has been launched with a bilinear material law in order to isolate the effect of strain hardening on the rotation capacity. Thus, two materials law were selected, one with a strain hardening modulus equal to 2% the elastic modulus E , the other with a strain hardening modulus equal to 1% of E , as represented in Figure 5.45. Two different steel grades were chosen: S235 and S460 (see Figure 5.46).

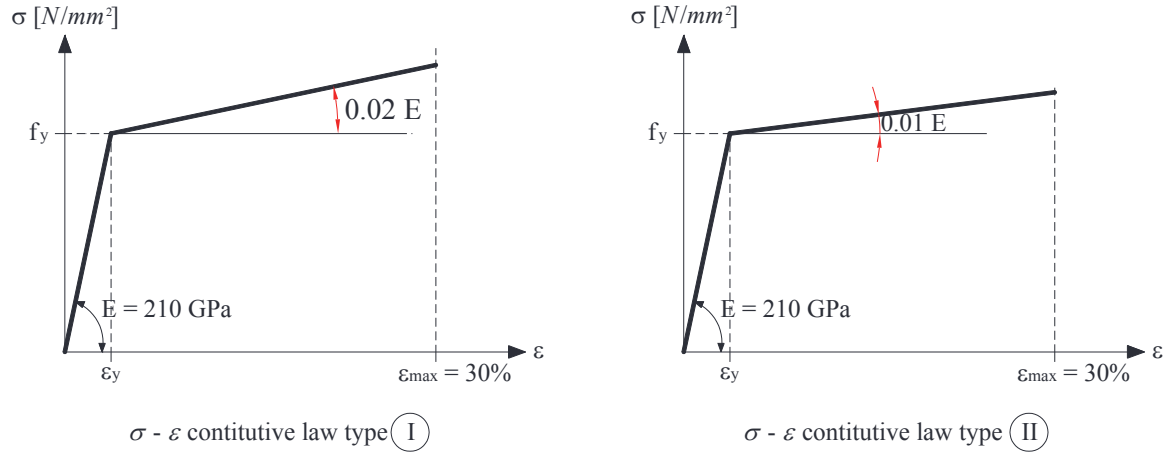


Figure 5.45 – Adopted material laws for the effect of strain hardening sub-study

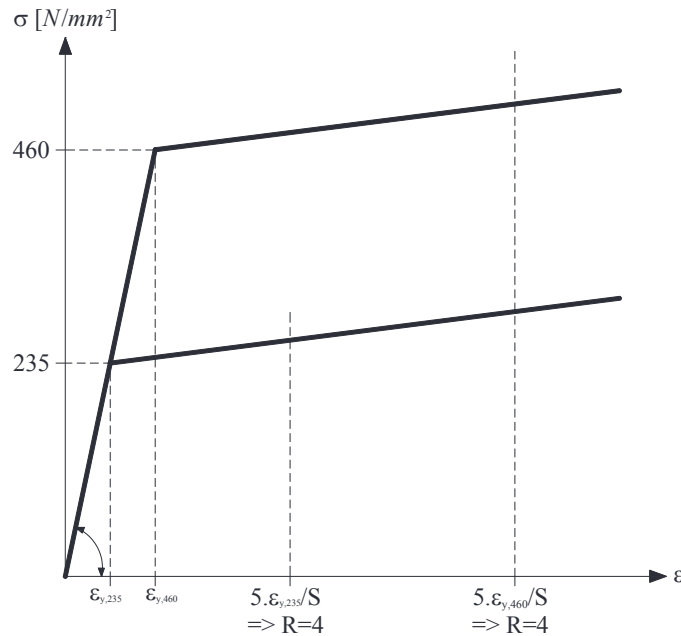


Figure 5.46 – Different steel grade for a material law

From Figure 5.47, Figure 5.48, Figure 5.49 and Figure 5.50, many conclusions can be drawn:

- i) Higher ultimate moment and rotation capacities were achieved by material law 1. This is expected since higher levels of strain hardening characterized by higher tangent stiffness in the inelastic range delay the onset of local buckling. In addition, after local buckling is initiated, a higher level of strain hardening also enables a greater contribution from the post-buckling membrane stresses leading to higher rotation capacities. Hence, we can conclude that strain hardening improves ultimate strength

and post buckling behaviour. Further studies on the effect of strain hardening can be found in Kuhlmann [37], Ricles & al [39] and Wang & al [40];

- ii) It is worth noting that for a given material law, a divergence in the rotation capacity curves is observed for different steel grades and only for low slenderness values. For higher values of yield strength, the rotation capacity decreases; this divergence is less noticeable for low values of strain hardening. For the material law 2, only a small divergence is perceived between S235 and S460;
- iii) In terms of normalized ultimate moment capacity, there is no distinction between the different steel grades for a same material law;
- iv) Divergences between curves of a same material law is seen to decrease when the aspect ratio h / b increases.

In conclusion, these curves highlight the effect of strain hardening on the structural response of beams in bending. They display clearly how strain hardening improves the ultimate capacity and postbuckling response of a beam. They also illustrate the fact that when the rotation capacity is represented as a function of the cross-section relative slenderness λ_{CS} , a difference is observed between different steel grades despite the fact that they have the exact dimensionless material law shape. This divergence is more pronounced for higher strain hardening modulus and for low aspect ratios.

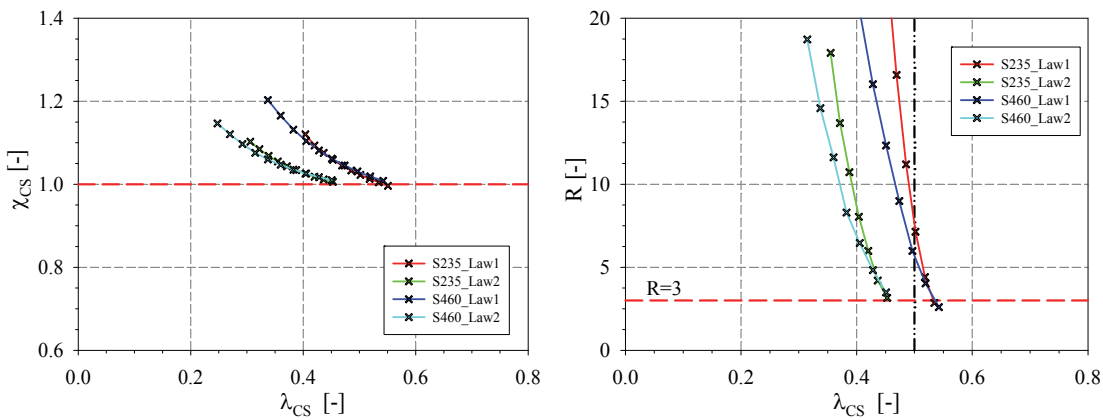
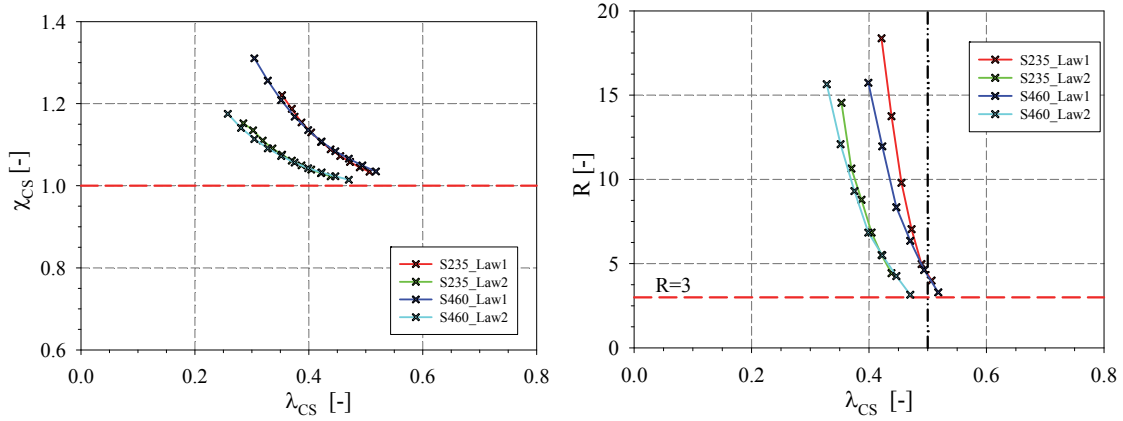
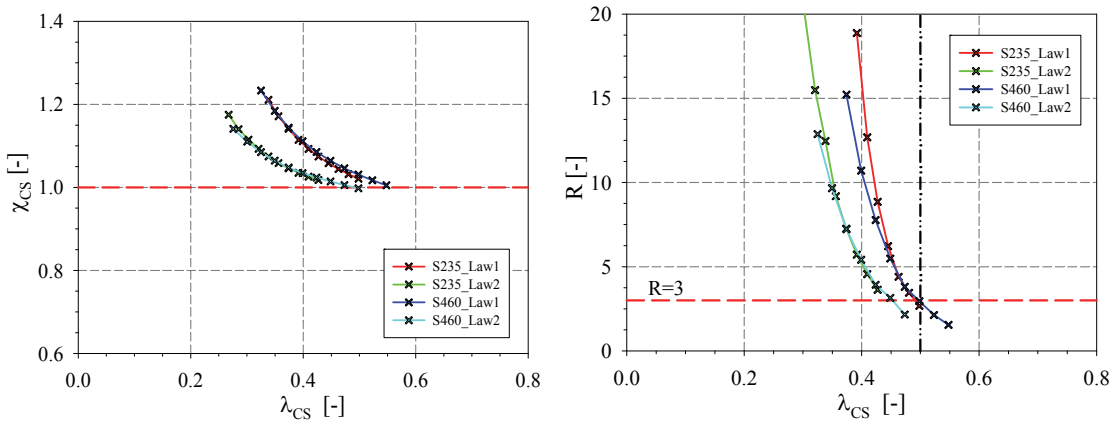
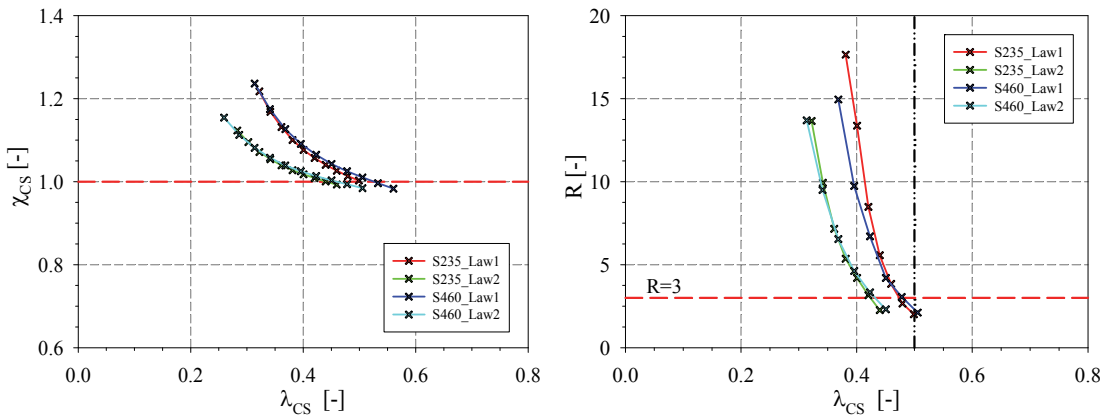


Figure 5.47 – Normalised load and rotation capacities as a function of λ_{CS} for different material law of $h / b = 1$


 Figure 5.48 – Normalised load and rotation capacities as a function of λ_{CS} for different material law of $h / b = 1.5$

 Figure 5.49 – Normalised load and rotation capacities as a function of λ_{CS} for different material law of $h / b = 2$

 Figure 5.50 – Normalised load and rotation capacities as a function of λ_{CS} for different material law of $h / b = 2.5$

5.3 Parametric analysis

5.3.1 Parameters considered

Extensive numerical parametric analysis have been carried out to characterise the rotation capacity of tubular sections. The rotation capacity was calculated for beams subjected to major axis bending moment, and different loading configurations were adopted with various section shapes, dimensions and steel grades.

Sections covered class 1 and 2 sections according to EN 1993-1. First, tubular geometries from the European catalogue satisfying the condition $\lambda_p < 0.6$ were selected. Secondly, an additional set of sections based on a height $h = 200 \text{ mm}$ was analysed. This was performed in order to visualize more distributed results based on the h / b and b / t ratios. Thus, 4 values of h / b ranging from square sections to highly rectangular ones have been considered: $h / b = 1, 1.5, 2, \text{ and } 2.5$. For each h / b proposed value, b / t values ranging from 10 to 20 with a step of 1 and from 20 to 34 with a step of 2 were considered.

Two different “testing” arrangement were considered: constant bending moment was applied for a beam length of 3 times the average of the webs and flanges clear widths (Figure 5.51) and 3-point bending configuration with load applied at mid-span (Figure 5.52). For the latter, the beam length were taken as 10, 15 and 20 times the height of the cross-section to study the effect of the steepness of the moment gradient. The lower value $L / h = 10$ was determined in order for shear not to influence the rotation capacity by fulfilling the condition of Equation 5.20.

$$V_{Ed} \leq 0.5 \cdot V_{pl,Rd} \quad 5.20$$

The shear ratio for a 3-pt bending configuration is $V_{Ed} = \frac{4M_{pl}}{L}$ at mid-span. At this position, the moment is also on its maximum hence there is a coupling between shear when the latter exceeds a value of $0.5 V_{pl,Rd}$. $V_{pl,Rd}$ is the plastic shear resistance of a section and is given in EC3-1.1:

$$V_{pl,Rd} = \frac{A_v \cdot (f_y / \sqrt{3})}{\delta_{M0}} \quad 5.21$$

A_v is calculated as $A_v = Ah / (b + h)$ as given in EC3 for rolled sections of constant thickness.

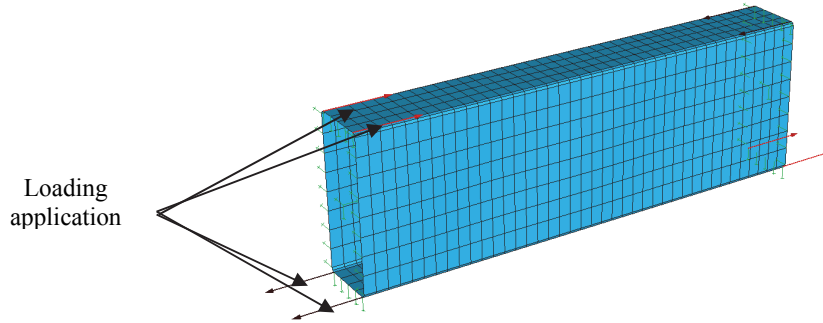


Figure 5.51 – Constant moment modelling

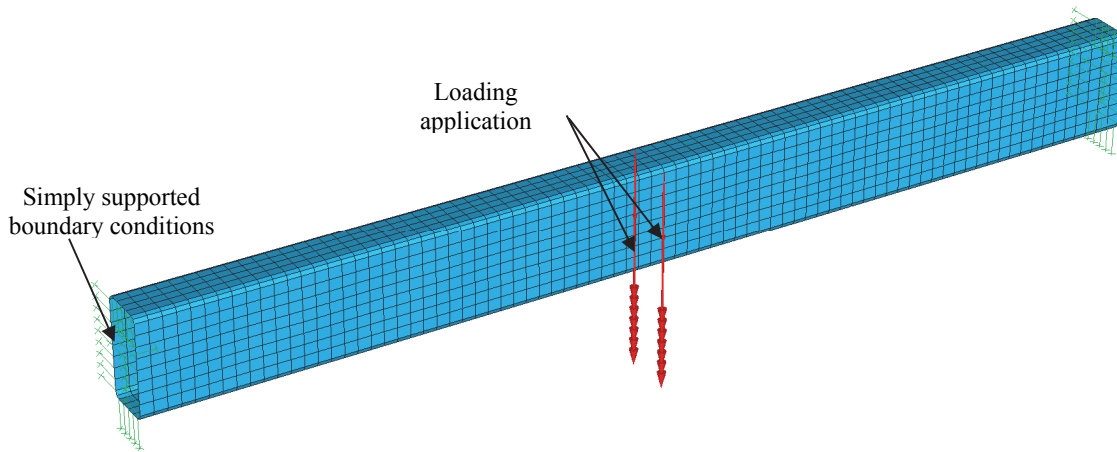


Figure 5.52 – 3-point bending modelling

For the case of the 3-pt bending, loading was applied uniformly through the webs as seen in Figure 5.52 in order to avoid web crippling. It has been observed experimentally that when loading is applied on the top flange, high levels of stress concentrations are induced, and lead to a premature elastic local buckling. Fork conditions using linear constraints were assigned for the support conditions. No global initial geometrical imperfections were taken into account since it has been previously demonstrated that they do not have an impact on the beams' response and local imperfection type 1 was implemented (see Figure 4.15). For the cross section slenderness value, the critical moment M_{crit}^4 was always calculated for the case

⁴ M_{crit} is the elastic buckling critical moment of a cross-section

of a short beam with a constant moment, with the use of FINELg software and through LBA analysis.

The formulation of the plastic rotation by which the beams end rotations have been normalized, is given for the two different setups by Equation 5.22 for beams under constant moment, and by Equation 5.23 for beams under a point load at mid-span.

$$\theta_{pl} = \frac{M_{pl}L}{2EI} \quad 5.22$$

$$\theta_{pl} = \frac{M_{pl}L}{4EI} \quad 5.23$$

5.3.2 Results

5.3.2.1 Hot-formed sections – Constant bending moment

Figure 5.53 plot results for hot-formed sections subjected to constant moment in terms of normalized ultimate moment capacity as a function of the cross section slenderness. The acronym CM refers to the case of constant moment. From this figure, it can be seen that strain hardening is reached for small slenderness values i.e. $\lambda_{CS} < 0.35$. Moreover, different capacities are reached for S235, S355 and S460, owing to different ultimate to yield ratios. In addition, we can point out that strain hardening is first reached for S355 and is due to the yield plateau length of the material. Hence as seen in Table 5.1, S355 possesses the shorter relative yield plateau when put as a function of the yield strain ε_y . For slenderness ranging from 0.35 to 0.6, no difference is observed between steel grades. Then, for $\lambda_{CS} > 0.6$, curves display a small deviation that is primarily due to the residual stresses effect as stated in detail by Nseir, 2015 [104], however these slenderness are not the object of this thesis.

Concerning the rotation capacity of hollow sections, Figure 5.54 and Figure 5.55 display results for hot-formed sections subjected to a constant moment. In Figure 5.54, the scale of the rotation capacity range from 0 to 50. In this figure different trends can be observed for very low slenderness values, i.e. $\lambda_{CS} < 0.35$, and are due to the different level of strain hardening achieved for different steel grades. Nonetheless, to limit the occurrence of excessive deformation in a structure, numerical results are plotted with the maximum value of $R=20$ in Figure 5.55. The material ductility requirement expressed in EN 1993-1-1 requires a minimum elongation at failure of 15%, however the adopted material law in the numerical

model was given a maximum strain of 30%, in order to be able to visualise the full moment-rotation curve for stocky sections. This allowed the occurrence of large deformations and large rotation capacities. Then, to remain in conformity with the material requirements given in EN 1993-1-1, results that achieved higher rotation capacities than $R=20$ were disregarded in the following studies.

In Figure 5.55, we can see that the difference between the rotation capacities reached for various steel grade is negligible. We can also note that for the range observed in Figure 5.55 ($0.35 < \lambda_{CS} < 0.6$), sections did not reach strain hardening, as seen in Figure 5.53, and beams failed before reaching the plastic moment M_{pl} . Hence, for these sections, the beam failure occurred within the yield plateau⁵. This explains the very steep increase in rotation capacity for slenderness value around 0.4. In this range, we can also highlight the fact that S355 steel exhibits slightly higher rotation capacity values. Hence, as explained in chapter 2, for hot-formed beams under constant moment, and due to the discontinuous stress-strain relationship, the mechanism of yielding is discontinuous and yielding occurs at discrete points by a sudden jump of strain that reached strain hardening. Nevertheless, the rotation capacity records the average strain reached by the beam in bending. Thus, even if strain hardening is not reached on average by the full beam, the small plateau length of S355 explains why higher rotation capacities are reached for this steel grade. In the more slender range, where failure is triggered by buckling at smaller strains, the influence of material grade on the normalised response is minimal and all results overlap with no distinction observed between steel grades.

⁵ For the case of hot-rolled sections subject to a constant moment, the rotation capacity was computed using the limit of $0.95M_{pl}$

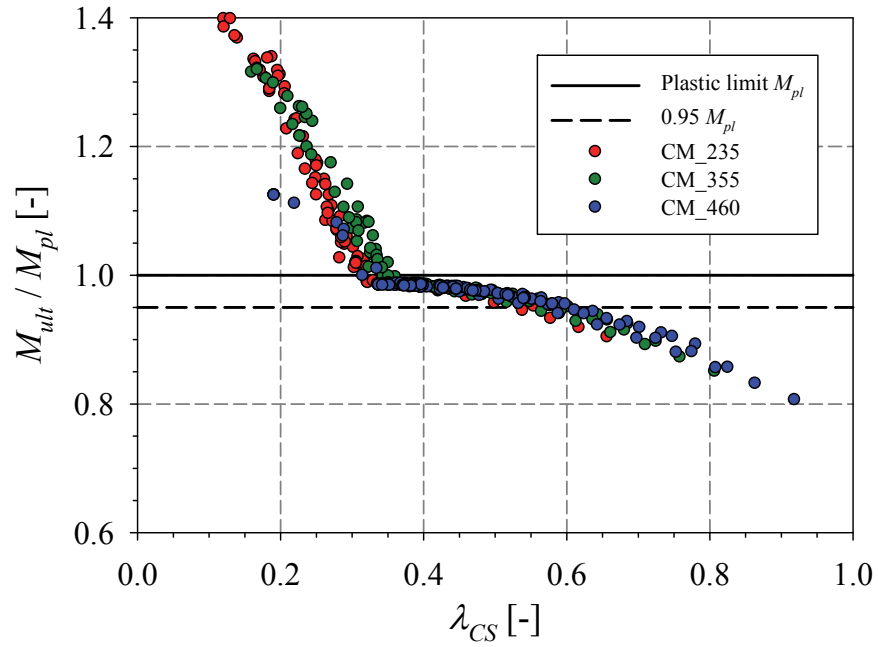


Figure 5.53 – Relative moment capacity of hot-formed sections subjected to constant moment

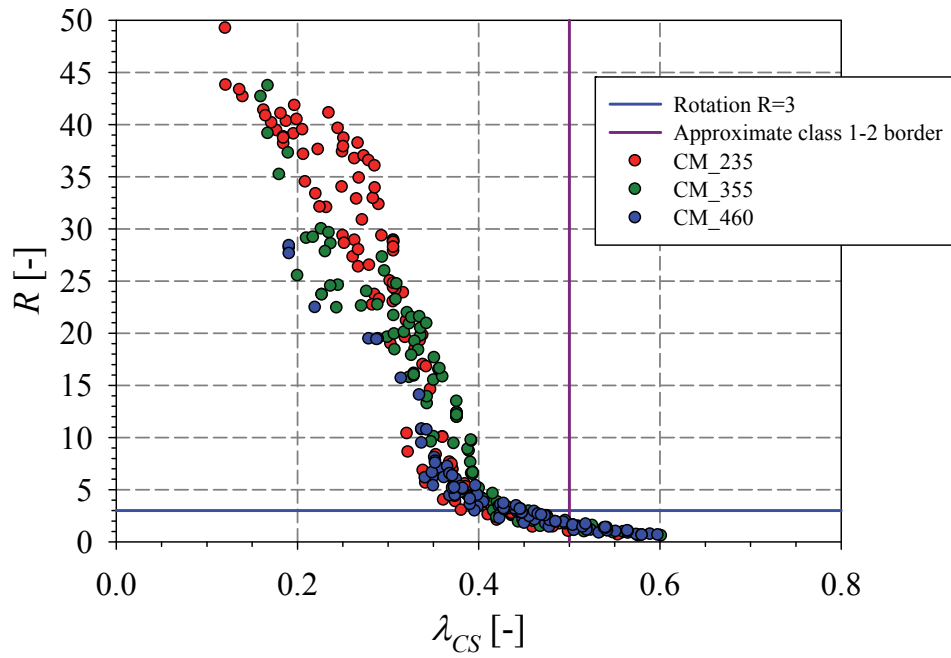


Figure 5.54 – Strain hardening effect on the rotation capacity of hot-formed sections subjected to constant moment – scale of the rotation capacity ranges from 0 to 50

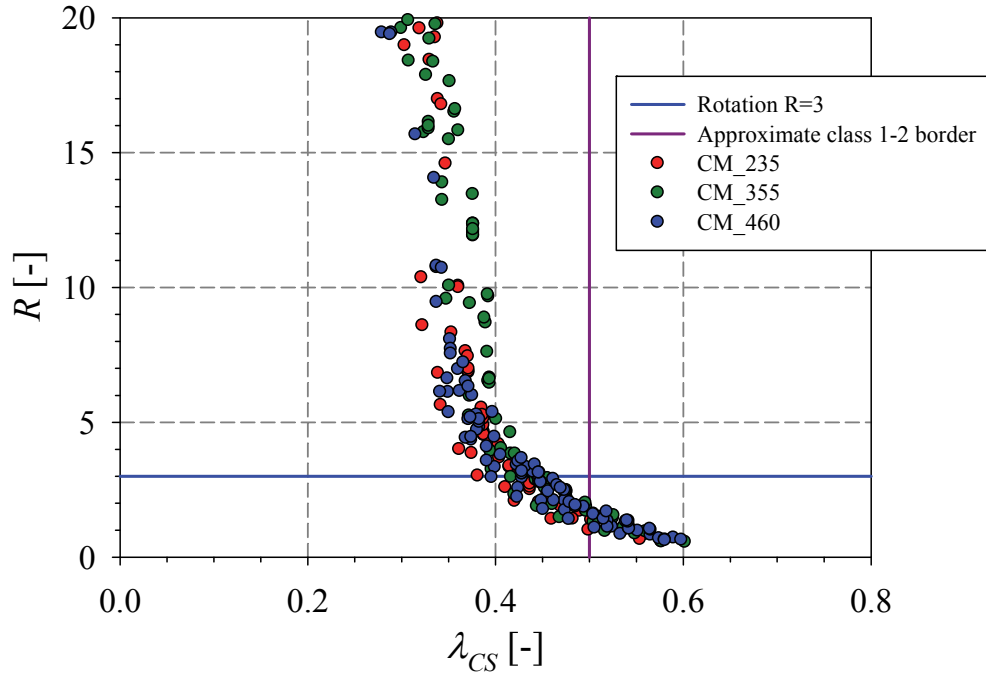


Figure 5.55 – Rotation capacity of hot-formed section subjected to constant moment – scale of the rotation capacity ranges from 0 to 20; sections with higher rotation capacities values were disregarded

In the following section, the impact of the cross-section aspect ratio h/b on the rotation capacity is discussed. In the majority of current standards, the interaction between the plate elements of the cross-section is disregarded. Nonetheless, different flexural performances are obtained for different aspect ratios. These differences are expected owing to the effects of plate element interaction on the local buckling performance.

The plate interactions can be quantified according to the plate slenderness definition λ_p as defined in Equation 2.6. Even though the inelastic buckling is of concern here, the plate slenderness, that is a function of the critical elastic buckling stress, is a good mean to rapidly quantify the plates' interaction. The plate slenderness takes into account the different type of stress distribution in the flanges and webs through the k_σ coefficient. It is also assumed that the corners of hollow sections are rigid and do not deform. Based on this equation, we can conclude that square hollow section should exhibit the highest capacities in bending since flanges are the first to reach the buckling load and the webs would therefore offer a good level of restraint. Moreover, from the plate slenderness definition, and if we neglect the corner radius, we can also calculate a limiting aspect ratio $h/b = 2.44$ at which the flange element in

compression and the webs in bending would have equal plate slenderness and therefore simultaneously elastically buckle. Nonetheless, while taking into consideration the corner radius (assumed as a function of the plate thickness: $r = 1.5 t$) and thus considering the flange and webs clear length, the limiting aspect ratio value ranges from $h/b = 1.9$ for stocky sections (for example $h = 200$ and $b/t = 10$) to values of $h/b = 2.3$ for more slender section (for example $h = 200$ and $b/t = 30$). This range represents the most unfavourable aspect ratio for box sections in bending where no benefits from the effects of plate element interaction on the local buckling response of the cross-section arises. For lower aspect ratios, the compression flange is the critical element in the cross-section while for high aspect ratios (approximately > 2), beams failure would be due to the web buckling.

The effect of the cross-section aspect ratio on the normalized bending moment capacity and rotation capacity of hollow structural sections is depicted in Figure 5.56 and Figure 5.57 for S235 steel. As expected, it can be clearly observed that the bending capacity decreases when the aspect ratio increases. Then, in the more slender range ($\lambda_{CS} > 0.45$), the effect of the aspect ratio on the cross-section rotation capacity is reduced.

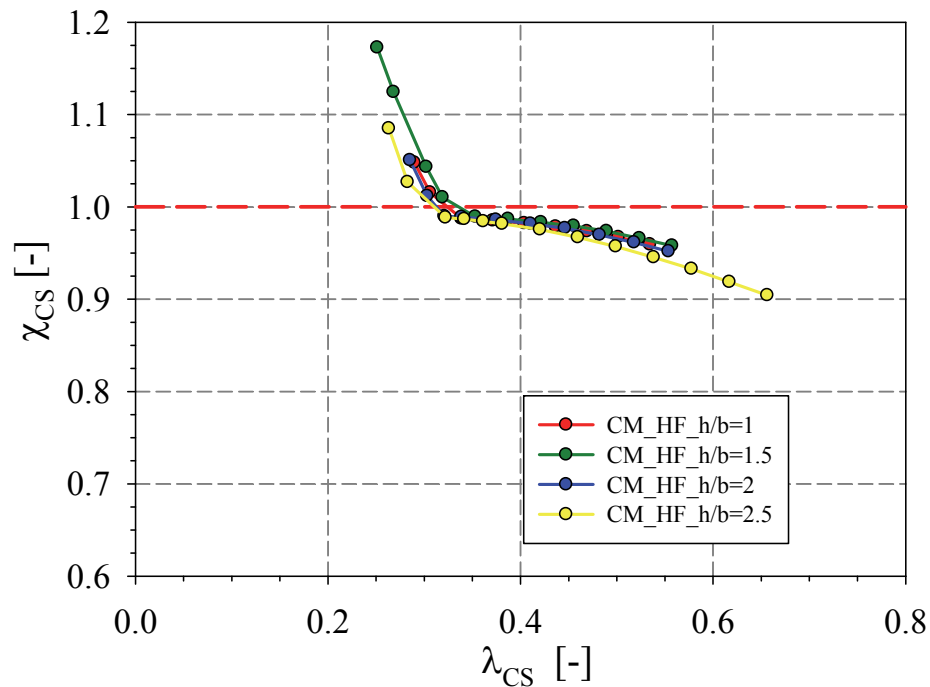


Figure 5.56 – Effect of aspect ratio on the moment capacity of hot-formed sections subject to constant moment for S235

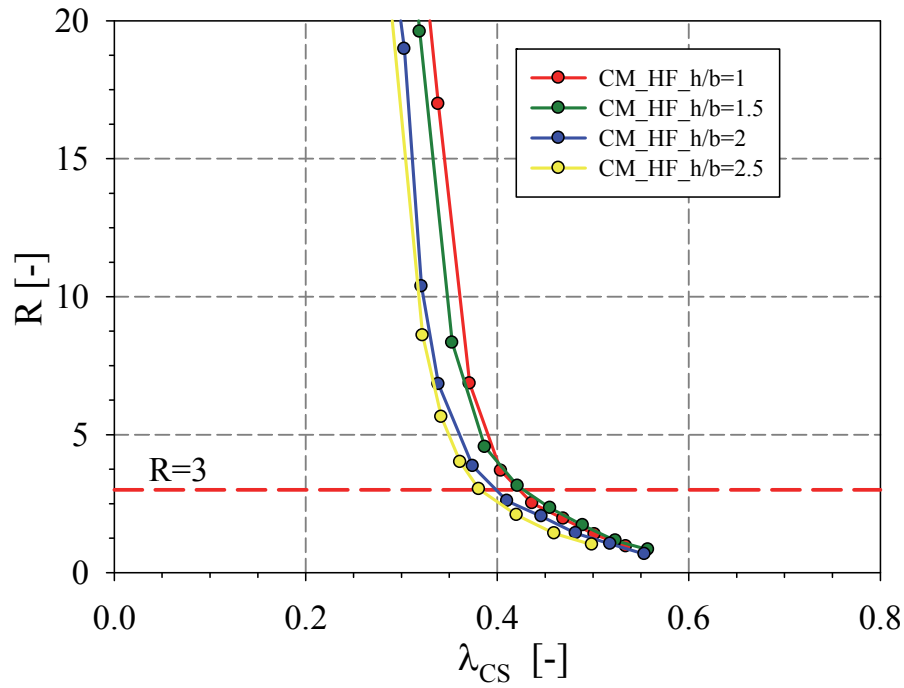


Figure 5.57 – Effect of aspect ratio on the rotation capacity of hot-formed sections subject to constant moment for S235

Figure 5.58 displays the available experimental data for hot-formed sections under a constant moment. Unfilled symbols represents the results for which the test had to be stopped before the moment rotation curve could reach the plastic capacity of the section in its decreasing part. The experimental results are in accordance with the numerical results but display a notable scatter which was previously justified by the high sensibility of the rotation capacity to initial geometric imperfection and also to the testing configuration.

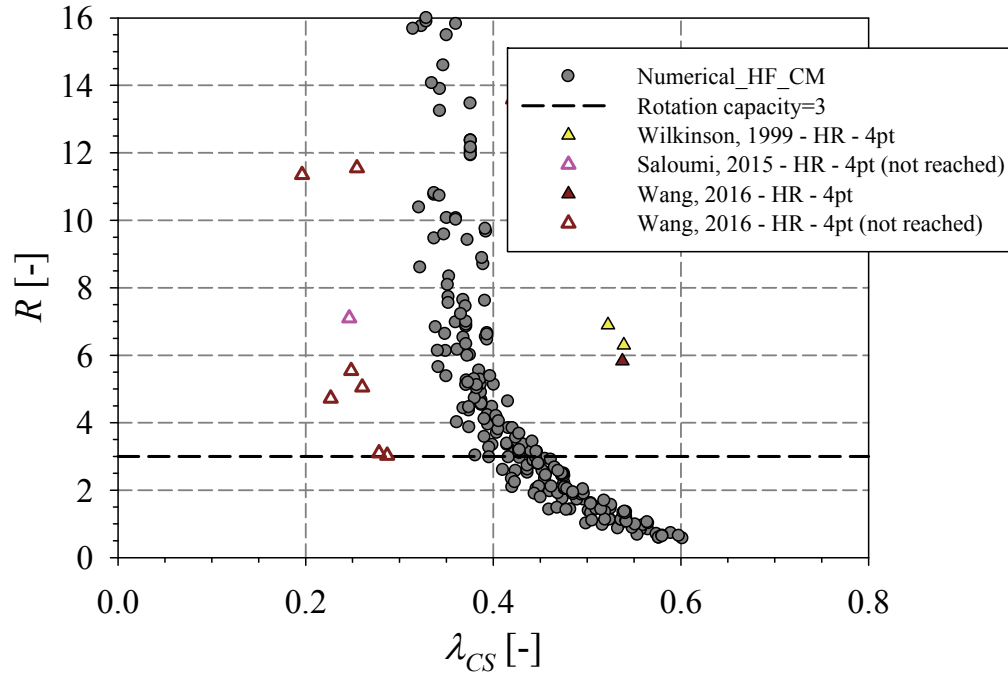


Figure 5.58 – Rotation capacity of experimental and numerical data for hot-formed section subject to constant moment

5.3.2.2 Cold-formed sections – Constant bending moment

Flexural capacities of cold-formed section under a constant moment and hot-formed one are first compared in Figure 5.59 and Figure 5.60.

In terms of ultimate capacity, cold-formed sections reaches higher values than hot-formed sections. This is due to the non-linear material law of cold-formed sections, where strain hardening is reached gradually from low strain. In addition, having a multi-linear material law for corners that possess a higher yield strength increases the section capacity.

When comparing the rotation capacity of cold-formed and hot-formed sections, one can clearly identify that for cross-section slenderness ranging from 0.35 to 0.6 higher rotation capacities are reached for cold-formed sections. This is due to strain hardening since it has previously been shown that strain hardening improves both the ultimate strength and post buckling behaviour of a section. For stockier sections, i.e. $\lambda_{CS} < 0.35$, lower rotation capacities are achieved by the cold-formed sections. Hence stocky sections can undergo higher stresses and therefore higher strains. Nonetheless, since the corner region material law is characterized by a low ductility and a maximum strain at 2.5%, once the section is stocky

enough to undergo large strain, corners become ineffective and lead to the failure of the entire cross-section.

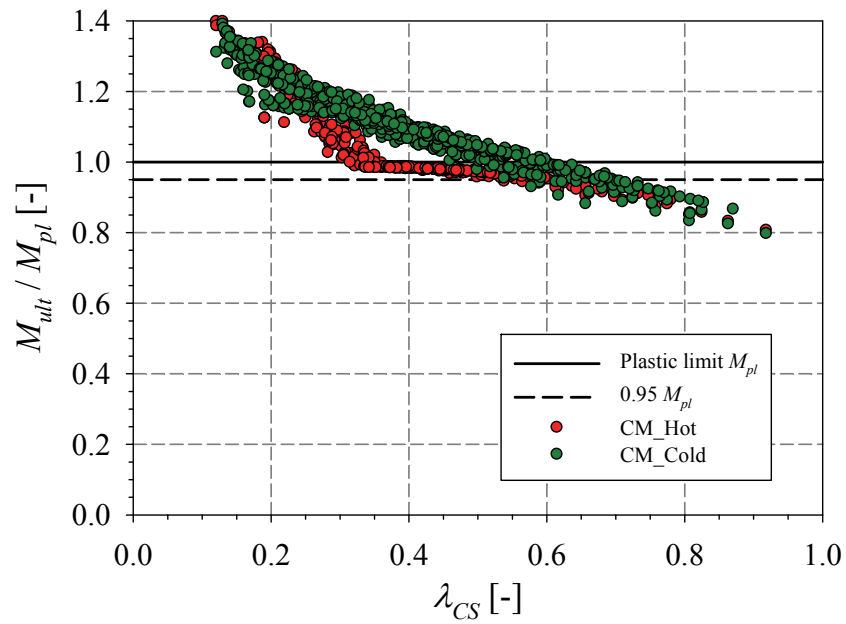


Figure 5.59 – Comparison between the moment capacity of cold-formed and hot-formed sections subjected to constant moment

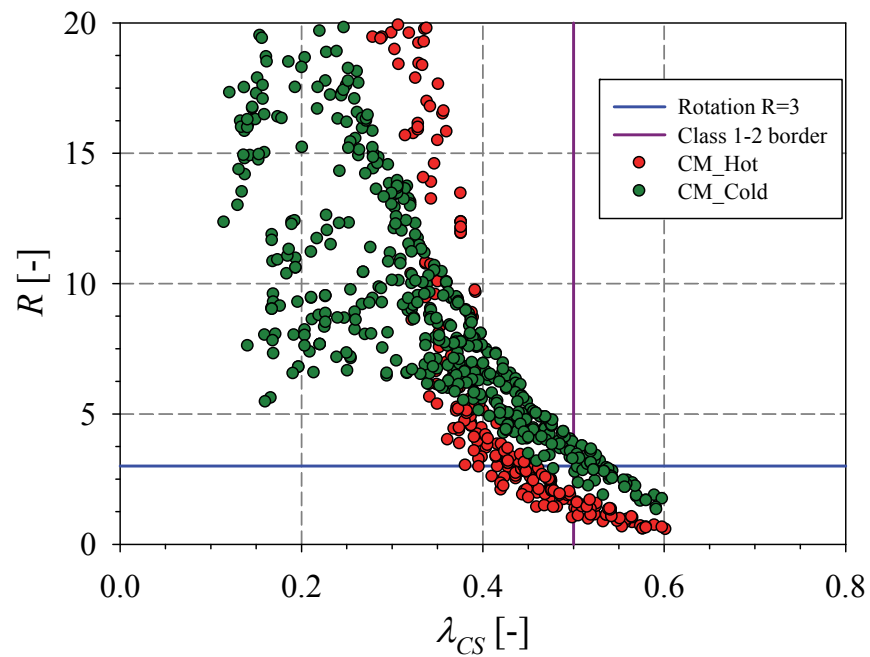


Figure 5.60 – Comparison between the rotation capacity of cold-formed and hot-formed sections subjected to constant moment

In Figure 5.61, Figure 5.62 and Figure 5.63, results for cold-formed sections are presented for different steel grades. Figure 5.61 shows that lower steel grades present higher rotation capacities due to the ultimate-to-yield stress ratio. Nonetheless, for $\lambda_{CS} > 0.55$, results are reversed because of the lower effect of residual stresses for higher steel grades and to the adopted nonlinear Ramberg-Osgood material law that is normalized with the plastic moment calculated from a perfectly plastic material law.

Figure 5.62 displays the rotation capacity for different steel grades. Different tendencies appear for different yield stresses since for cold-formed sections strain hardening is reached at acceptable deformation. Thus, clear and different trends can be observed for different steel grades due to the ultimate-to-yield ratio (the strain hardening modulus). It can also be attributed to the observation made in section 5.1.8, where lower rotation capacities were reached for higher yield strength, even for identical material law. In the more slender range, where failure is triggered by cross-section local buckling at low strains, practically no influence from the material grade on the normalised response is detected. Figure 5.63 represents the strain reached at the maximum capacity of the section. In this representation, results are much less scattered since the postbuckling is always more unstable and thus leads to bigger discrepancies.

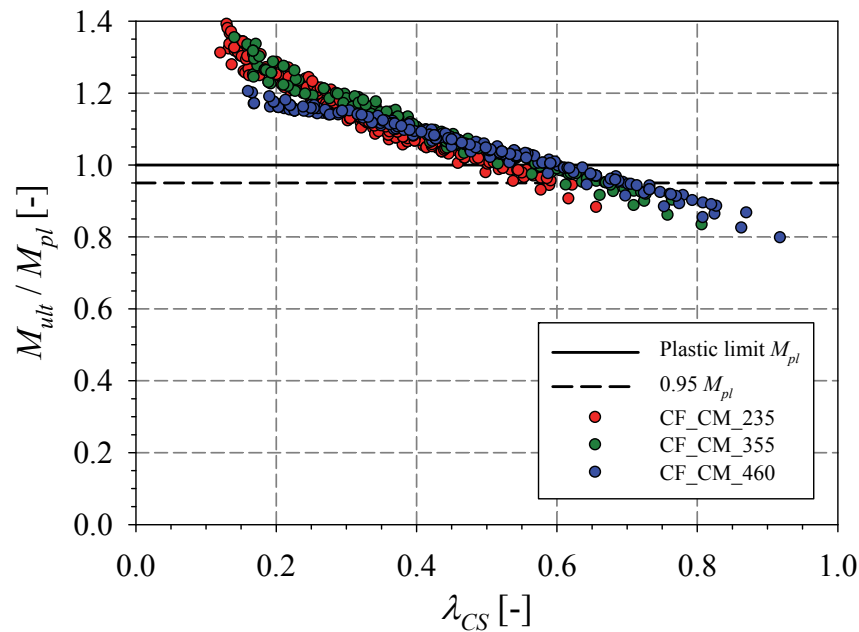


Figure 5.61 – Normalised moment capacity of cold-formed sections subjected to constant moment for various steel grades

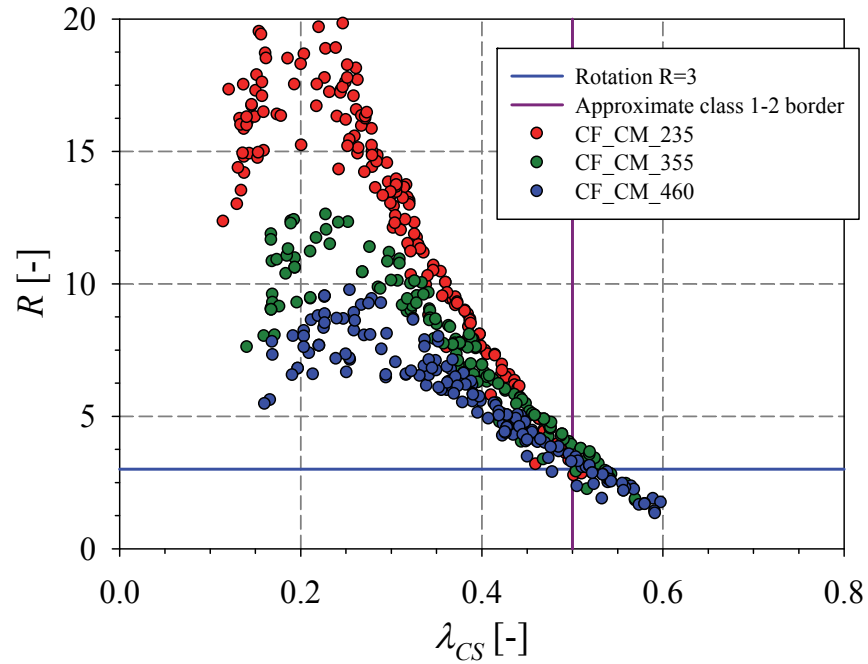


Figure 5.62 – Rotation capacity of cold-formed sections subjected to constant moment for various steel grades

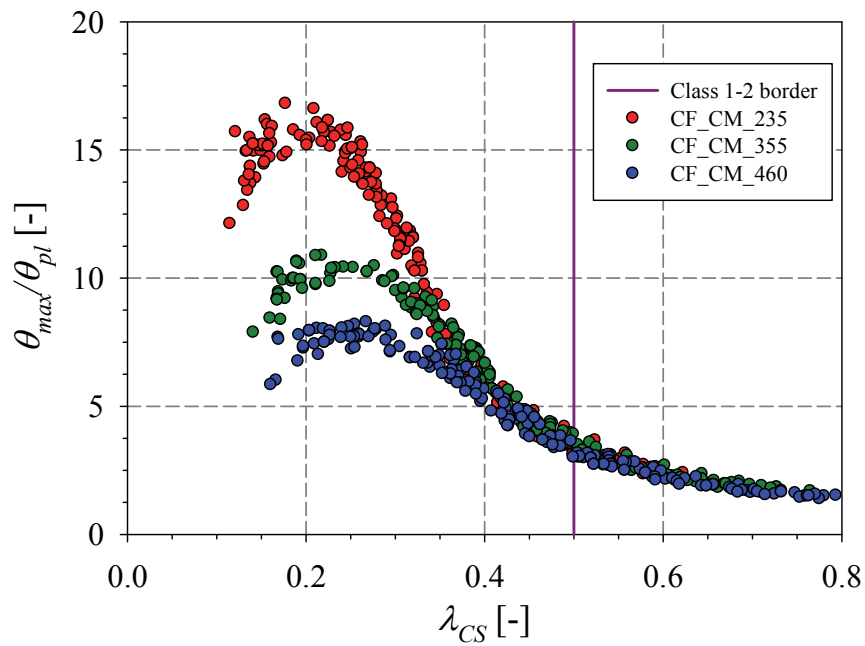


Figure 5.63 – Normalised ultimate strain of cold-formed sections subjected to constant moment

Another significant phenomenon is reported here and consist in a decrease of the rotation capacity for very stocky sections (around $\lambda_{CS} < 0.25$). This observation is due to the corners

material law and area. Hence, since the corner radius is a function of the section thickness, the stockier the section, the larger the corner radius. Thus the corner constitutes a bigger portion of the entire cross-section. Since corners of cold-formed sections exhibit very low ductility, and since for stocky sections the corner is bigger in proportion, sections display lower ductility and hence lower rotation capacities. Moreover, it is worth noting that for S235, the maximum of the lower bound data, lies around a value of $\lambda_{CS} = 0.2$, whereas for S460, this point is around $\lambda_{CS} = 0.3$. Hence, the maximum strain of the corner material law is set to 2.5% and, based on Table 5.2, this value, when normalized to the yield strain ε_y , consists in $\varepsilon_{u,corner} = 22.3\varepsilon_y$ for S235, $14.8\varepsilon_y$ for S355 and $11.4\varepsilon_y$ for S460; therefore, the higher the yield stress, the lower the ductility of the corner material law. In other words, if the section is stocky enough to resist strains higher than the maximum strain of the corner material law, a stockier section only then lead to a decrease in rotation capacity since more portions of it exhibits low ductility.

Figure 5.64 display moment-rotation curves for different cross-section slenderness of cold-formed section. From Figure 5.64, we can note that for section with a cross-section slenderness up to $\lambda_{CS} = 0.4$, curves matches in the increasing part, until buckling occurs and leads to different rotation capacities. For these sections, the flange yields first and yielding does not reach the corner region. Nonetheless, for higher slenderness, the moment-rotation curves becomes steeper from low strains. For these sections, where corners represent a large portion of the total section area, corners are deformable which leads to their yielding and result in an increase in the section capacity at low strain. Moreover, Figure 5.64 displays that cold-formed sections exhibit a sudden loss of stiffness after the peak is reached, which is due to the corner material law that is less ductile. It can be noted that the stockier the section, the steeper the unloading becomes.

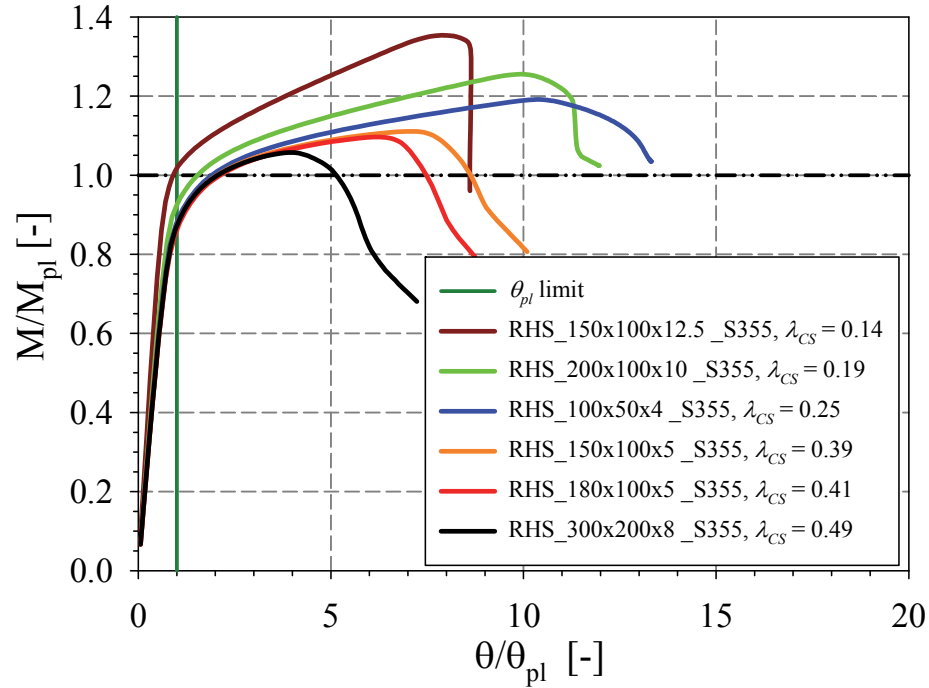


Figure 5.64 – Moment-rotation curves for different cross-section slenderness of cold-formed sections

Figure 5.65 plots results for different aspect ratios for the case of S235 steel grade. As observed in hot-formed sections, different tendencies are observed for different aspect ratio in terms of ultimate and rotation capacity with high aspect ratios exhibiting lower rotation capacities. Nonetheless, the divergence is not much pronounced.

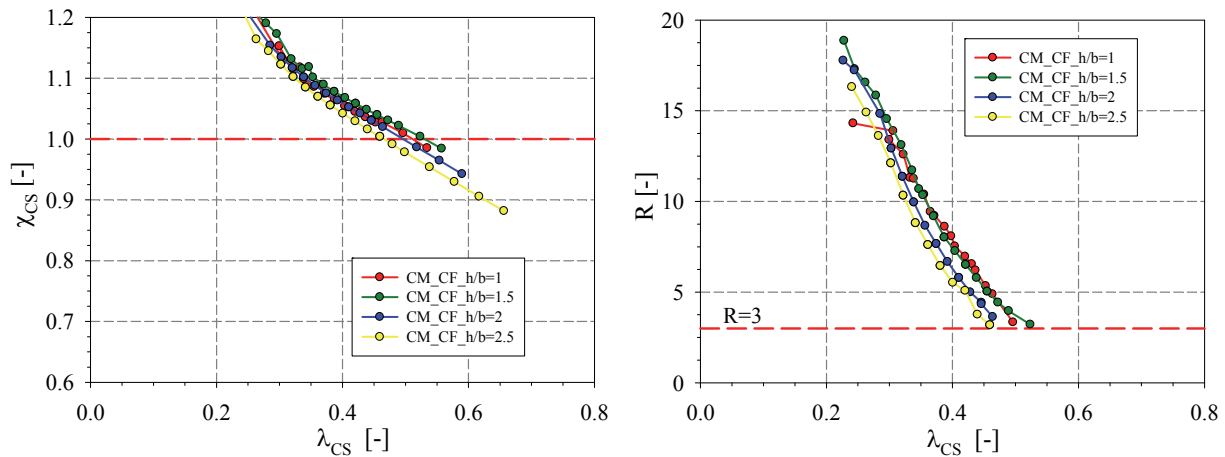


Figure 5.65 – Effect of aspect ratio on the flexural capacity cold-formed sections subject to constant moment for S235

Figure 5.66 presents numerical and experimental data for cold-formed sections under a constant moment. The experimental results match the numerical ones and display the same tendencies. Some results from Wilkinson & Hancock and Rondal & al lie below the numerical data. This was expected for the case of Wilkinson & Hancock since cross-sections tested possess an aspect ratio $h/b = 3$, that is not treated in this thesis. The remaining results achieve higher rotation capacities than the numerical computed data. Hence the parameters adopted in the numerical model are always consistent and safe sided, while experimentally a big variability is present, especially for what concerns initial geometric imperfection. Therefore a bigger scatter is always achieved experimentally.

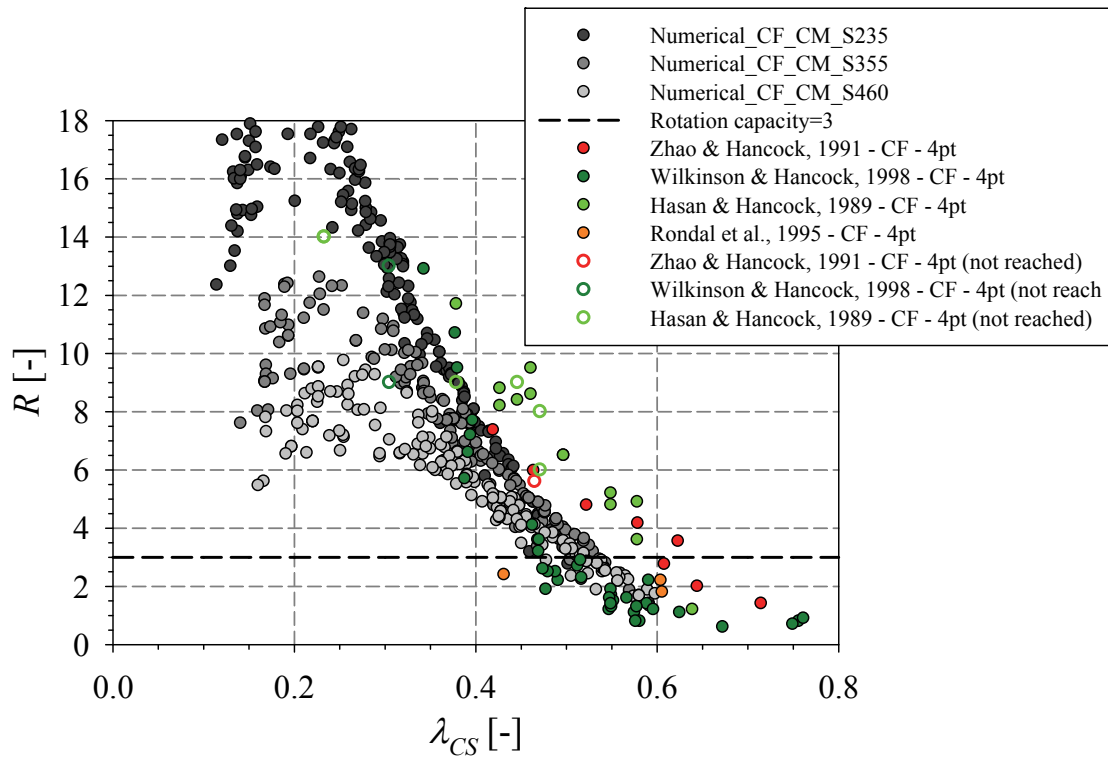


Figure 5.66 – Rotation capacity of experimental and numerical data for cold-formed section subjected to constant moment

5.3.2.3 Hot-formed sections in 3-pt bending configuration

For hot-formed sections in the 3-pt bending arrangement, special attention was given to the initial geometrical imperfection distribution. Since the number of initial geometrical buckles is always hand-defined as an integer, and because loading is applied at mid-span, 3 types of geometrical imperfections can be obtained at this point: imperfection shape A occurs for an even number of recurrence of the halfwavelength, and loading is thus applied on the

intersection of two buckling waves as seen in Figure 5.67. Moreover, if the number of half wavelength is odd, two possibilities can arise: imperfection shape B where loading is applied at the middle of an inward buckle at the upper flange or imperfection shape C where the flange buckle is outward. In order to identify the effect of each shape on the bending response of square and rectangular hollow structural shape (HSS), 2 sections were selected. Their length was chosen equal to 10 times their cross-section height and a S355 steel grade. Section 1 is a square section SHS200 with $b/t = 15$ and section 2 is slightly more slender with $b/t = 16$. These sections have been denoted as: Section 1: SHS200_bt15_Lh10_S355, Section 2: SHS200_bt16_Lh10_S355. Due to their geometrical dimensions, section 1 exhibits an even number of half wavelength L_0 as represented by Imperfection A while section 2 have an odd number. In order to visualise the effect of the imperfection, imperfection B was also assigned to section 1, and section 2 was studied under imperfection shape B and C (inward and outward flange buckle). As can be seen in Figure 5.68, practically no difference exist if the initial geometrical imperfection is of type A or B (on the intersection of two buckle or on an inward one). Hence both were adopted in the numerical study, in an attempt to obtain a square pattern of the initial buckles. For section 2, and when having an upward buckle on the flange, the beam reached up to two times more rotation capacity as compared to the inward buckle shape and was therefore not used in the present study. Hence, only type A and B imperfection shapes were adopted in the numerical study so as to obtain a safe sided and small scatter of results.

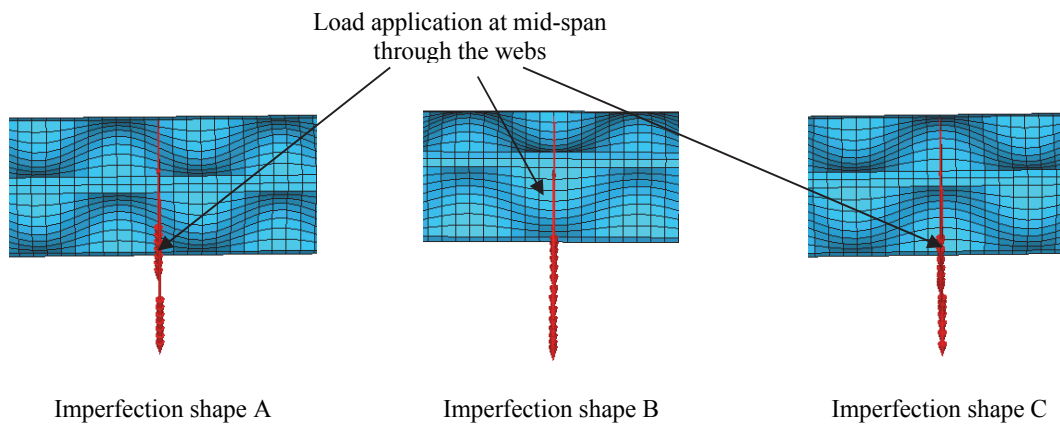


Figure 5.67 – Amplified initial imperfection possibilities for 3-pt bending configuration

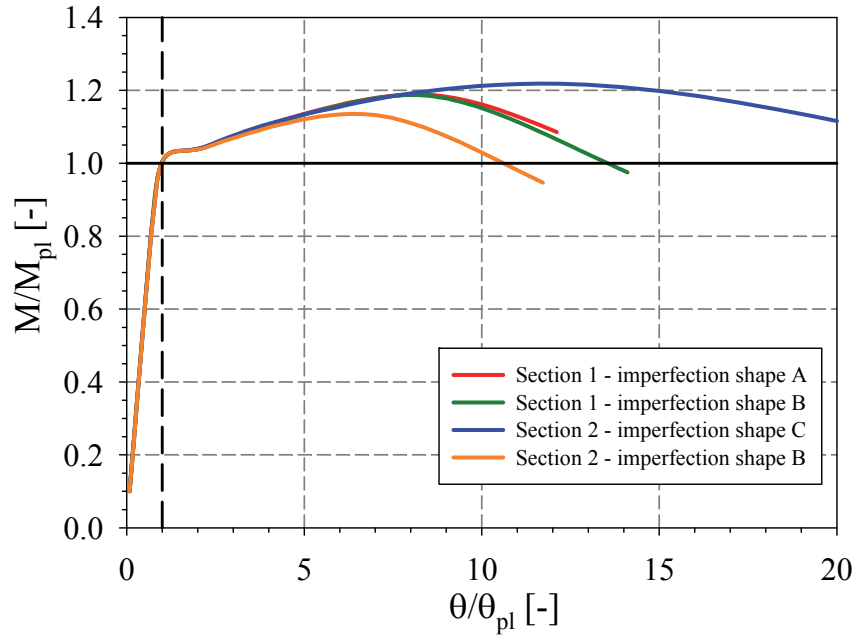


Figure 5.68 – Moment rotation response of two beams under different Initial imperfection possibilities

Figure 5.69 and Figure 5.70 compares the flexural behaviour of beams under a constant moment to the 3-point bending configuration in terms of moment and rotation capacities. In terms of ultimate moment capacity, the 3-point bending configuration reaches higher values than beams with constant moment. This was expected since in 3-pt bending, due to the moment gradient, as soon as the plastic moment M_{pl} is reached at the mid-section, the steel strain hardens and yielding spreads along the length until the yielded length is sufficient to form a buckled shape. Moreover, Figure 5.68 display how values higher than the plastic moment capacity are reached at small strains.

However, for what concerns the rotation capacity, lower values are observed for all tested sections (Figure 5.70). This was also predictable in the 3-pt bending case since a moment gradient leads to having a confined region of maximum moment. Hence, the segments adjacent to the plastic hinge are at lower stress levels and provide a certain level of restraint. Therefore, yielding and thus also local buckling cannot spread plainly along the length of the beam, contrary to the case of constant moment where local buckling can develop freely. For this reason, lower rotation capacities are reached when beams are tested under a point load. Similar conclusions were underlined by Lay, 1965 [115], Lay & Galambos, 1967 [32] and Wang & al, 2016 [40]

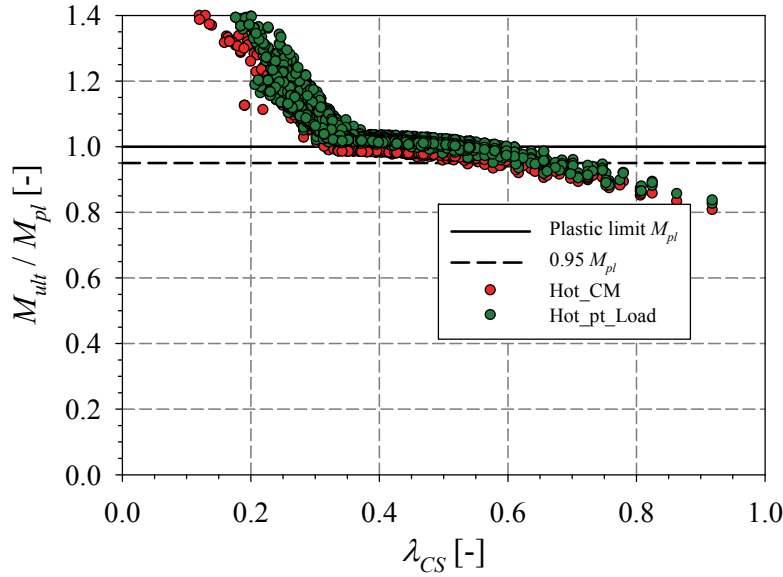


Figure 5.69 – Moment capacities of beams under a constant moment versus 3-point bending configuration

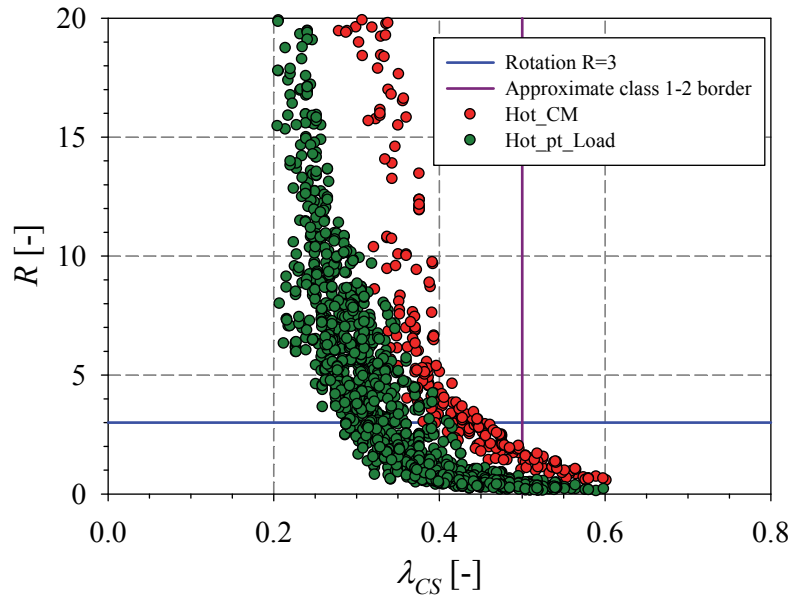


Figure 5.70 – Rotation capacities of beams under a constant moment versus 3-point bending configuration

Figure 5.71 and Figure 5.72 present all 3-pt bending results under different yield stresses. We can note that higher rotation capacities were achieved by the grade S235 and S355 beams compared with S460 beams. Therefore, in the 3-pt bending configuration, strain hardening is reached as soon as yielding starts to spread, hence, higher strain hardening tangent stiffness would lead to higher rotation capacities because a higher degree of strain hardening will delay the onset of local buckling and improve the post-buckling response. For S460, the ultimate-to-

yield stress ratio is much lower than that of S235 and S355 and this is also reflected by lower strain hardening modulus which leads to lower rotation capacities. Moreover since S460 have a f_u / f_y ratio of 1.2, this leads to sections reaching a maximum rotation capacity level of around 6.

In order to well visualize the effect of strain hardening, the specific case of square hollow section with a length equal 10 times the height of the cross section is presented in Figure 5.73 and Figure 5.74. It can be seen that S460 presents much lower rotation capacities than S235 and S355 grades. Moreover, for the cross section slenderness range varying around 0.35 to 0.45, beams of S355 grades reach higher rotation capacities. This is due to the fact that S355 material possesses a smaller yield plateau length and a higher first stage strain hardening modulus (see Table 5.1). Nevertheless, for stockier sections, which yield at higher strains, higher rotation capacities are reached for S235 since it possesses a higher f_u / f_y ratio (that is also reflected by a higher second stage strain hardening). In the more slender range, where failure is triggered by the cross-section local buckling at small strains, the rotation capacity is independent of the material steel grade.

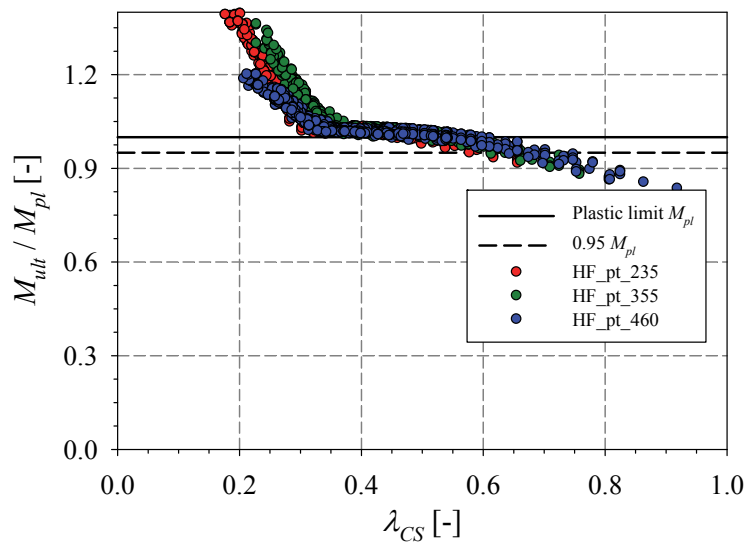


Figure 5.71 – Ultimate moment capacity for the 3-pt bending configuration for different yield stresses

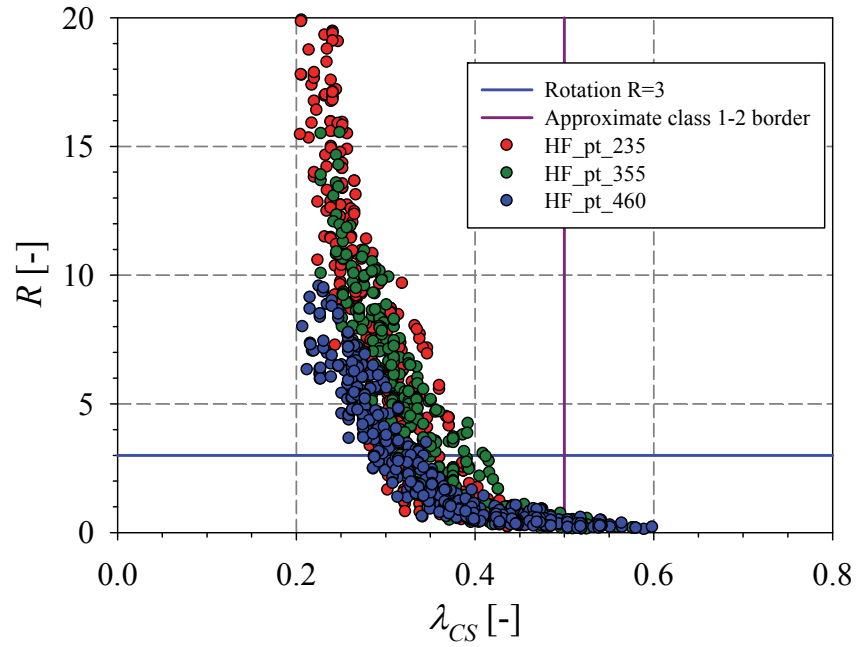
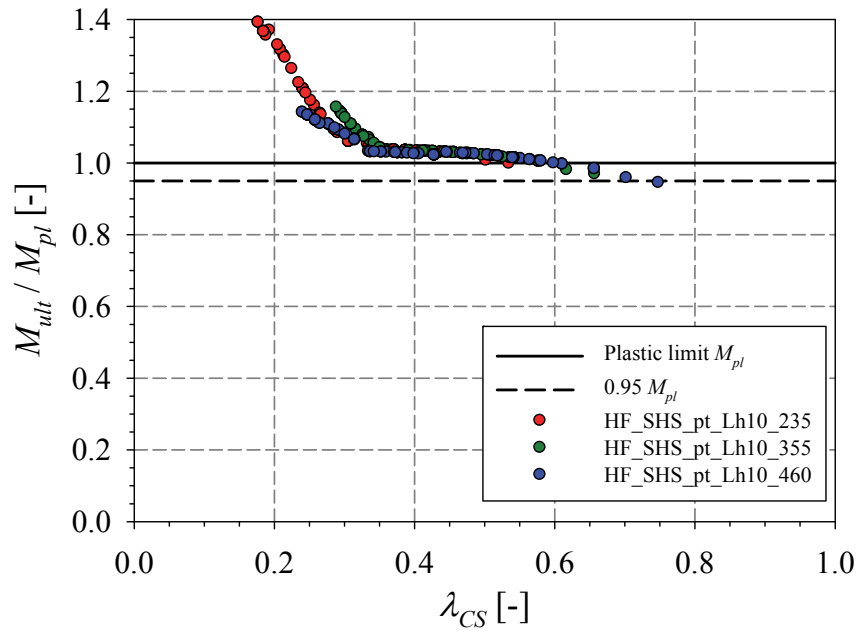


Figure 5.72 – Rotation capacity for the 3-pt bending configuration for different yield stresses


 Figure 5.73 – Ultimate moment capacity for square hollow sections, $L/h=10$, for different yield stresses

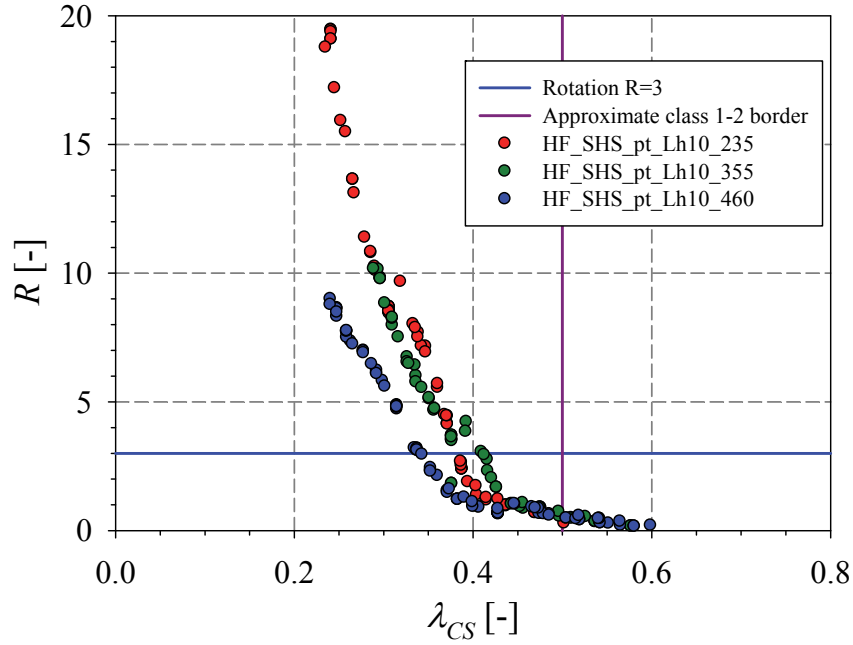


Figure 5.74 – Rotation capacity for square hollow sections, $L/h=10$, for different yield stresses

Figure 5.75 and Figure 5.76 represent the response of square hot-formed sections with 3-pt bending configuration and S235 yield stress for various L/h ratios. These graphs highlight the influence of the moment gradient on the flexural responses of beams and their dependence on the steepness of the moment gradient. The moment gradient steepness is characterized by the ratio of the span length L over the section height h .

The moment gradient is seen to have a minimal influence on the normalized moment capacity of beams as seen in Figure 5.75, but a more pronounced effect on the cross-section rotation capacity R (Figure 5.76) where higher rotations are reached for smaller L/h ratios. This is due to the fact that small L/h ratios lead to higher moment gradient which in turn enable a greater participation of strain hardening. Hence, since strain hardening enhances the flexural capacities of a section, and thus its rotation capacity, higher values are reached for low L/h ratios.

Moreover, in 3-pt bending configurations, local buckling occurs at mid-span. As the average stress in this region depends on the moment gradient, hence for a same maximum moment, a steeper gradient means a smaller average stress which will delay local buckling and provide a greater amount of deformation capacity.

Nonetheless, it is also worth noting that for a same section, the buckled region has about the same length, but that beams under a steep moment gradient would lead to a relatively smaller yielded region since a higher level of restraint from the adjacent segment is present. However, the rotation capacity R is calculated by dividing the beam end rotation θ by its plastic value θ_{pl} given in Equation 5.23. From the plastic rotation capacity equation, we can expose its dependency on the span length whereas the beams ends rotation θ is mainly a result of the deformation of the buckled region which has about the same length for a long or for a short span. These observations were reported theoretically by Lay & Galambos, 1967 [32] and experimentally by Kuhlmann, 1989 [37], that stated that yielding in a beam under a point load will be limited to a certain length that is independent from the span of the beam and the moment gradient. As a consequence, the deformation caused by local buckling has greater importance on the rotation capacity of a short span beam.

All these effects leads to the conclusion that specimens with a steep moment gradient buckle later and provide a greater amount of deformation capacity. These conclusions have also been observed both experimentally and theoretically by Ricles & al, 1998 [39], Lay & Galambos, 1993 [116], Kuhlmann, 1989 [37] and Wang & al, 2016 [40].

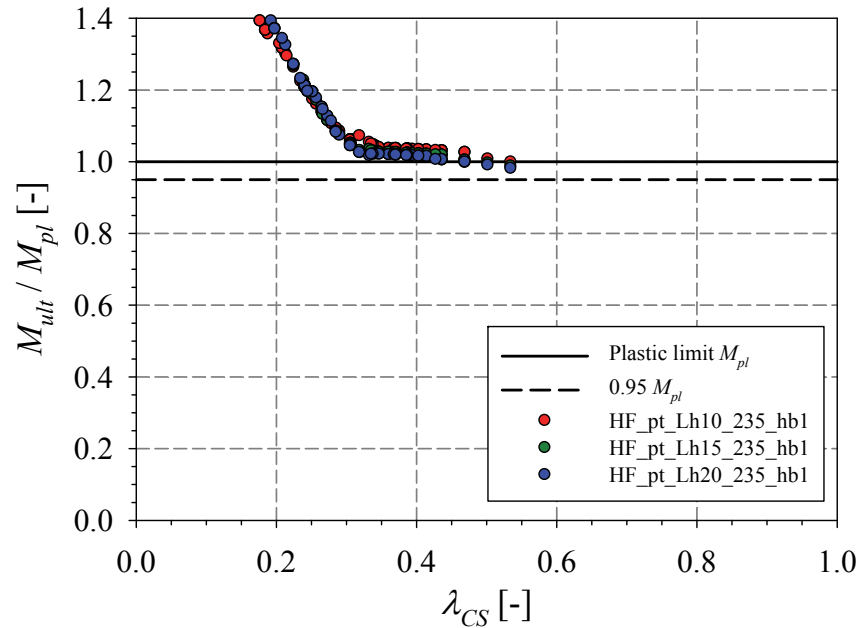


Figure 5.75 – Normalised ultimate moment capacity for Square, hot-formed section with 3-pt bending configuration and S235 yield stress for various L / h ratios.

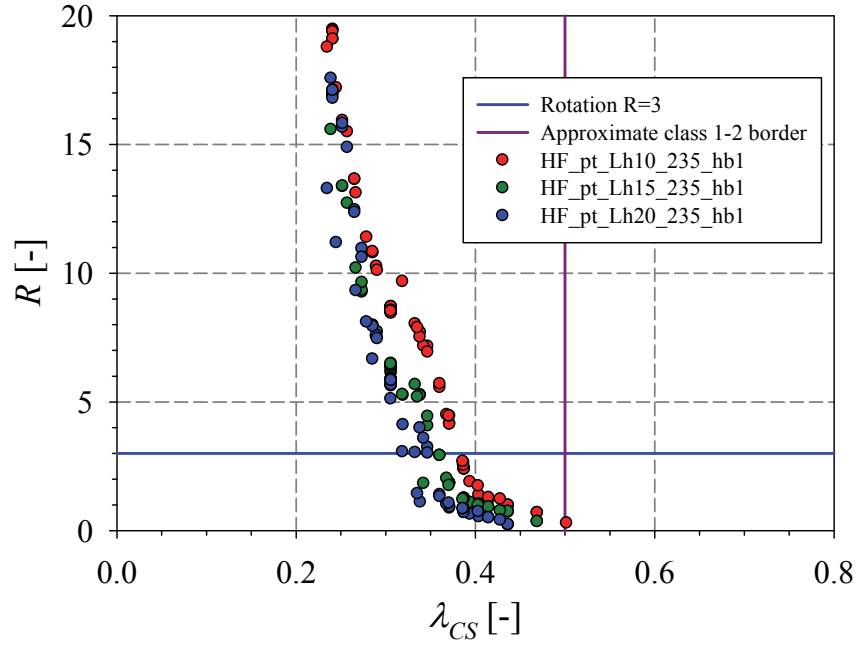


Figure 5.76 – Rotation capacity for Square, hot-formed section with 3-pt bending configuration and S235 yield stress for various L/h ratios.

Moreover, in the 3-point bending configuration of hot-formed sections, the aspect ratio is seen to influence the rotation capacity. An example in Figure 5.77 is given for S235, $L/h = 10$ under different h/b ratios. In Figure 5.78, the rotation capacity is plotted for all the considered hot-formed sections of S235 yield stress, and for different moment gradient. It can be evidenced here that the differentiation between curves is not very noticeable since, as seen previously, many parameter influence the cross section response (aspect ratio, yield strength...) which justify the big scatter in the rotation capacity.

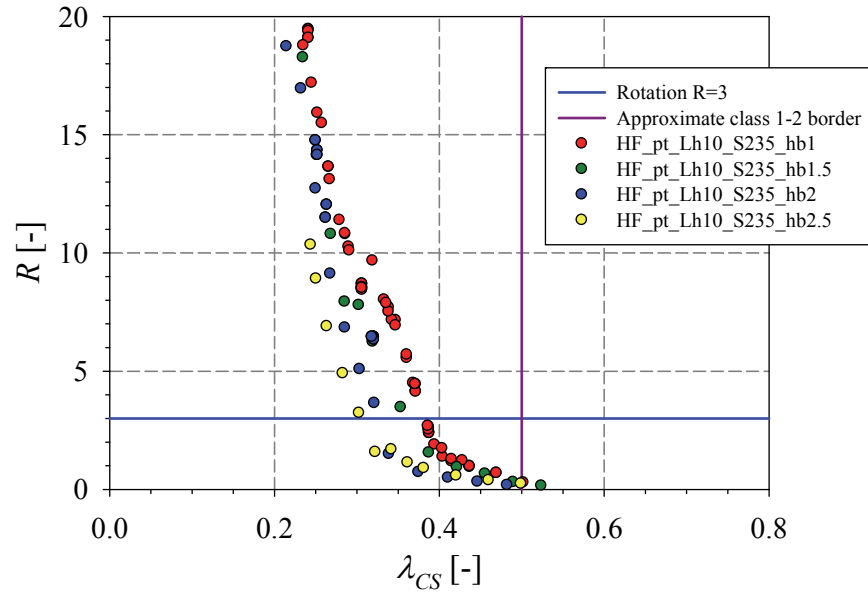


Figure 5.77 – Effect of the aspect ratio on the rotation capacity for 3-pt bending beams

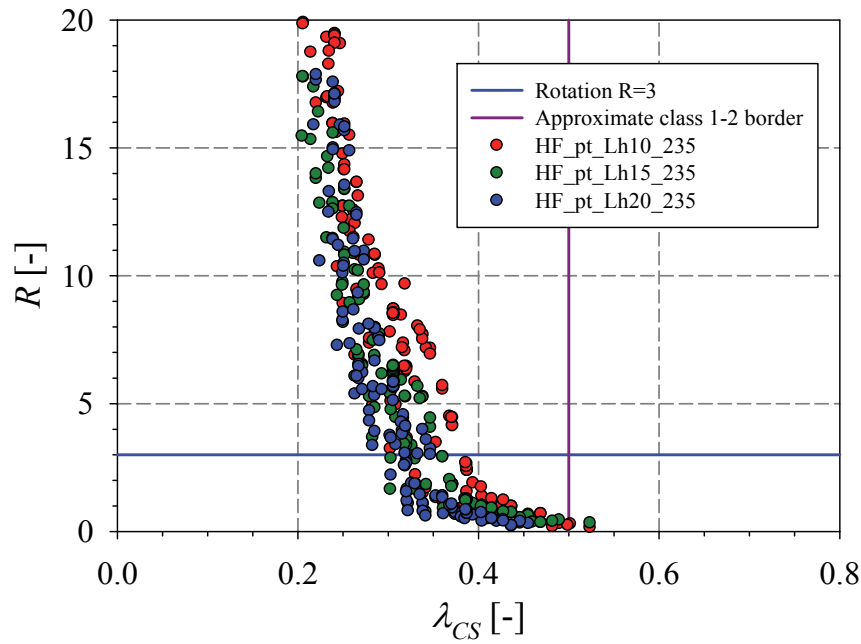


Figure 5.78 – Rotation capacity for hot-formed section with 3-pt bending configuration and S235 yield stress for various L/h ratios.

In Figure 5.79, experimental results from literature are plotted with the numerical ones. This figure highlight the fact that experimental and numerical results are in agreement and exhibit the same tendencies.

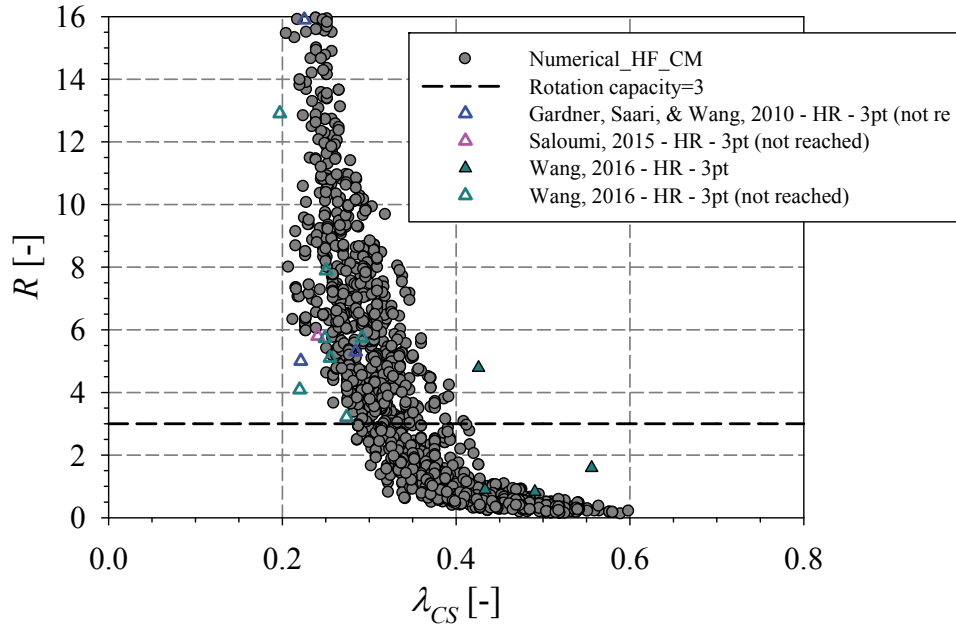


Figure 5.79 – Experimental and numerical data for hot-formed section in the 3-pt bending arrangement

5.3.2.4 Cold-formed sections in 3-point bending configuration

For cold-formed section in 3-pt bending arrangement, as we can observe in Figure 5.81, rotation capacities lower than the case of a constant moment are reached. Moreover different tendencies are observed for the different yield stresses. The drop in ductility that appear for stockier sections is due to the material law affected to corners, as explained for the case of a constant moment for cold-formed sections. Moreover, it is worth noting that the S460 grade reach rotation capacities lower than 3 for practically all the considered sections.

In Figure 5.82, different tendencies are displayed when different moment gradients are applied, with higher rotation capacities reached for low L / h ratios (steep moment gradients), similarly to the hot-formed cases.

Few experimental results are present in the literature for cold-formed sections tested in 3-pt bending. The available results have been reported in Figure 5.83 and are in accordance with the numerical results.

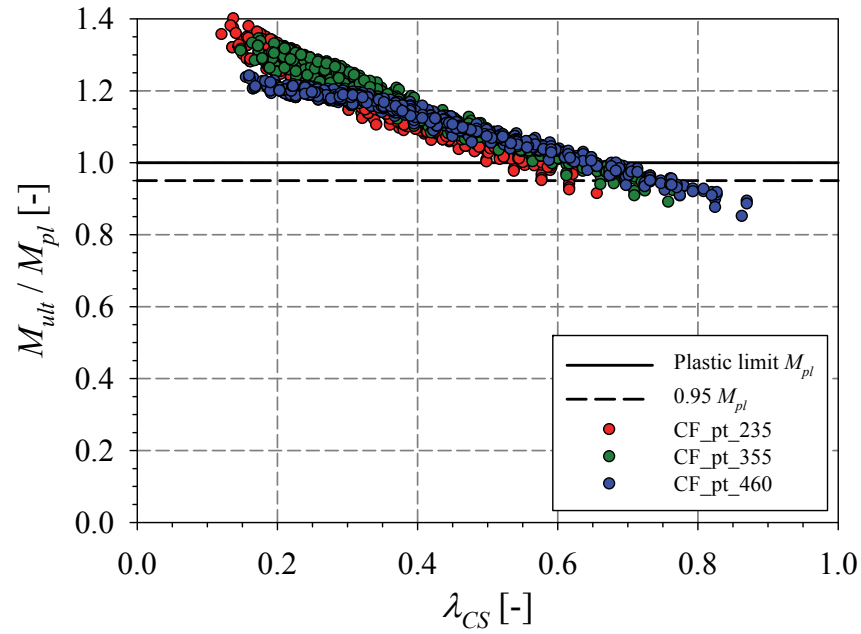


Figure 5.80 – Normalised moment capacity of cold-formed sections in the 3-pt bending configuration and for different yield stresses

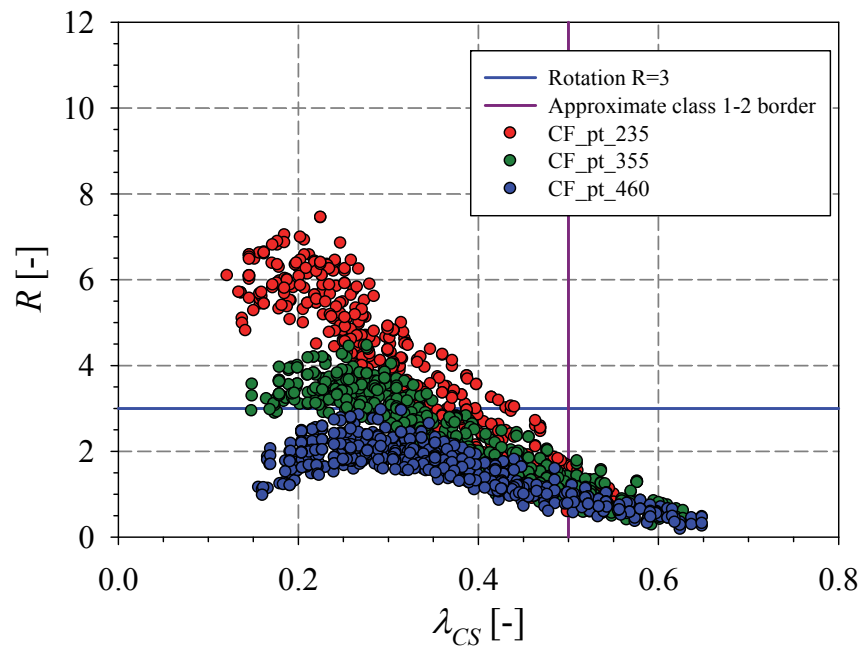


Figure 5.81 – Rotation capacity of cold-formed sections in the 3-pt bending configuration and for different yield stresses

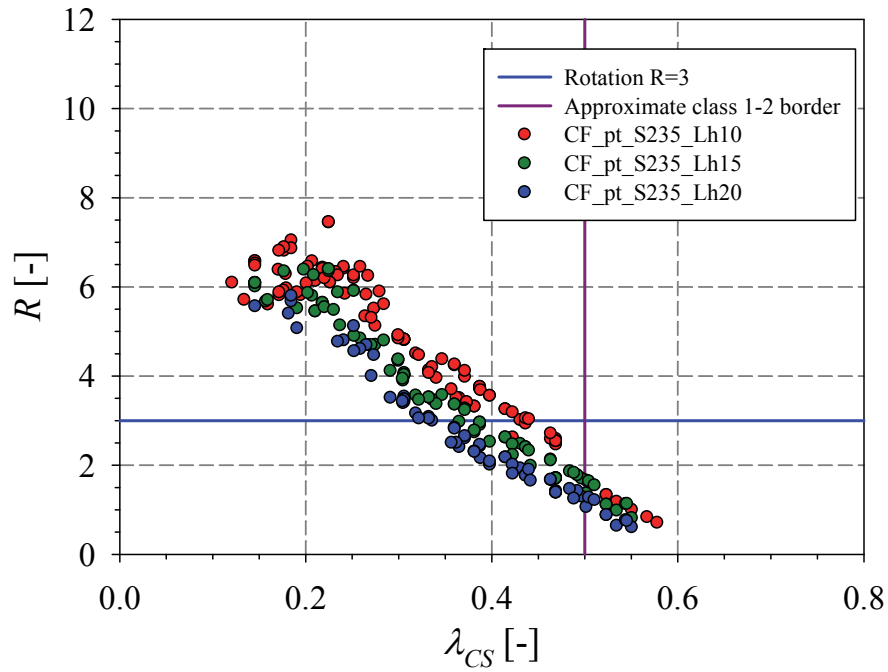


Figure 5.82 – Rotation capacity of S235 cold-formed sections in the 3-pt bending configuration for different moment gradient.

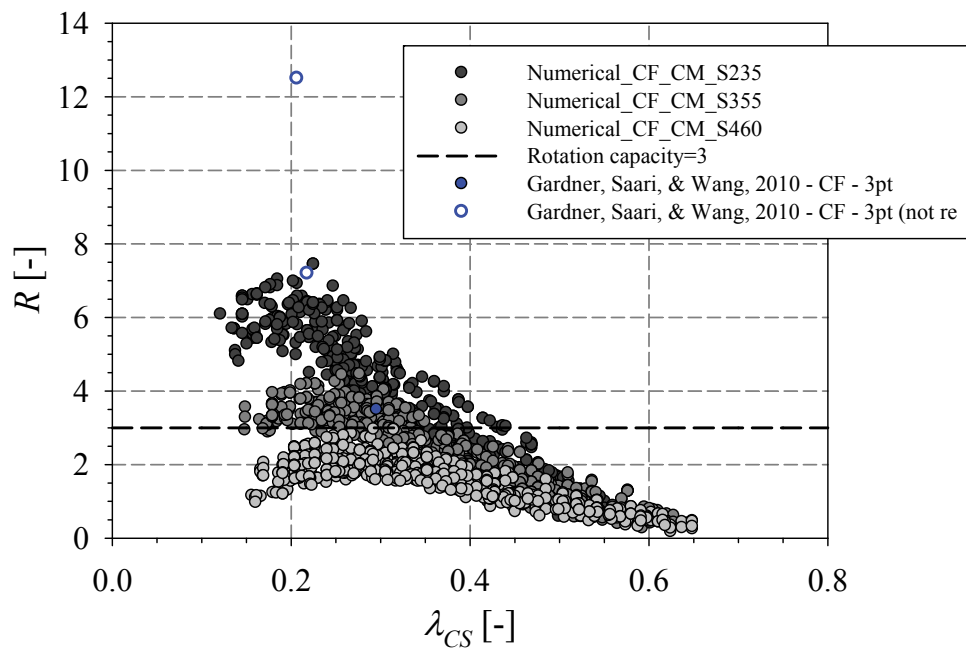


Figure 5.83 – Rotation capacity of experimental and numerical data for cold-formed section under 3-pt bending arrangement.

5.4 Conclusions

Based on the numerical investigation carried in this section, many parameters were identified as influencing the inelastic flexural behaviour of hollow structural sections. Conclusions can be summarised as follows:

- It was concluded that beams in a 4-pt bending configuration can be represented by a small beam of length equal to 3 times the average of the clear width of both flanges and webs with a constant moment applied at its ends.
- The effect of membrane residual stresses is negligible on the rotation capacity of hot-formed sections while flexural residual stresses had a small impact on the inelastic flexural behaviour of cold-formed section and lead to slightly higher values.
- The initial geometrical imperfections, both in amplitude and shape, lead to considerable differences in the rotation capacity and justified why experimental results are scattered. In order to remain on the safe side, an amplitude of $a / 200$ was adopted with square half-waves.
- The considered material law was seen to lead to different behaviour. Strain hardening was identified as delaying the onset of local buckling and improving the post-buckling behaviour. Hence, higher rotation capacities were achieved for higher strain hardening modulus. It was also identified that for a same material law, lower rotation capacities are reached for high steel grades.
- Different tendencies were reached for different aspect ratio h / b with square section leading to the higher values. This was due to the interaction between the plate elements of the cross-section. Hence, for a square section in bending, the web provides high restrains to the flange and thus delay the onset of inelastic local buckling. The higher the aspect ratio, the lower the restraint from the flange becomes.
- Cold-formed sections lead to higher rotation capacity than hot-formed section for a cross-section slenderness $0.35 < \lambda_{CS} < 0.6$, due to the material non-linearity of cold-formed sections (where strain hardening is reached as low strain). Nonetheless, for stocky sections $\lambda_{CS} < 0.35$, cold-formed sections displayed lower rotation capacity due to the brittle material law affected to the corner.

- Sections tested under a point load (cold-formed and hot-rolled) displayed lower rotations than those under a constant moment while achieving higher moment capacities. This is due the fact that buckling is restraint to a small region whereas in the constant moment case, buckling is free to develop.
- For steeper moment gradients, higher rotation capacities are reached. The steepness of the moment gradient was expressed by the L / h ratio. Hence, a high moment gradient would enable a greater participation of strain hardening which enhances the flexural capacities of a section.

6 PROPOSED DESIGN FORMULATIONS

An extensive parametric study that covered hot-rolled and cold-formed sections tested in bending has been performed. A large set of parameters from section dimensions, steel grade and testing configuration have been varied and different trends have been observed for the rotation capacity. Consequently, some recommendations and some design curves will be proposed regarding the rotation capacity of square and rectangular cross-sections.

Two methodologies to allow for plastic design are developed:

The first is similar to the one presently adopted in current design standards. A limiting value of the plate slenderness, which ensures that the cross-section can reach a rotation capacity equal to 3 (given by Eurocode3 and AISC), is proposed. The rotation demand value of 3 was seen as sufficient to approximately all common structures in order to develop a plastic mechanism and was adopted in the present work. Here, new and accurate limiting values are given based on the present numerical data. These recommendations, in term of the cross-section or plate slenderness, are only based on the numerical case of a constant bending moment, since this case provides the full rotation capacity of a cross-section without any restraint occurring from the presence of a moment gradient. On that account, it have been previously shown that when a beam is subject to a point load (which lead to a moment gradient) lower rotation capacity are reached. Nevertheless, since this methodology is a simplified procedure that consists in adopting a rotation demand of 3 for all structures, and is thus very penalizing on the rotation demand part, we were therefore less restrictive for what concerns the rotation capacity. It is to be kept in mind that the numerical results are generated with safe-sided parameters, and the proposed limitations will also be based on the numerical data lower bound. In conclusion, this methodology is a rapid procedure that is generally conservative since the majority of structures require a smaller amount of rotation demand than 3; nevertheless, for some few complex cases, as stated in the state of the art, it may also be unconservative.

A second and more precise procedure consisting in linking the rotation demand to the section rotation capacity is also developed. For this procedure, a continuous relationship between the cross-section slenderness and the cross-section rotation capacity is given. In a first step, the engineer calculates the required rotation that a structure should undergo in order for plastic

analysis to be performed. Then based on the cross-section slenderness and the type of loading applied on the structure, he can identify whether the section is able to deliver the required rotation. This continuous relationship is bounded by two limits, the first limit is based on a maximum rotation capacity of 15 so that no excessive deformation occurs, the second limit concerns the maximum cross-section slenderness after which sections will undergo elastic local buckling (elastic local buckling will prevent moment redistribution and the formation of a plastic mechanism). This limit was based on the fact that a section would reach a minimum of 95% of the plastic capacity for hot-formed and cold-formed sections.

6.1 Hot-formed sections, constant bending moment

For hot-formed sections, a continuous function of the general form given by Equation 6.1 was fitted to the test data. This function is similar in form to the Euler relation between normalized critical elastic buckling strain and plate slenderness. However, in order to derive a relationship between the rotation capacity and cross-section slenderness, the effects of inelastic buckling, imperfections, residual stresses and post-buckling response should be taken into account.

$$R = \frac{A}{\lambda^B} \quad 6.1$$

The values of A and B were determined following a regression fit of to the numerical data by representing results in a logarithmic scale as can be seen in Figure 6.1. It is clearly shown in Figure 6.1 that the numerical data are linearly aligned in a logarithmic scale which justify the logarithmic curve proposed in Equation 6.1. A linear regression curve (Equation 6.2) was best fitted using the least square approach. Then, the best-fitted curve was shifted in order to enclose all results and in that way give a lower bound to the numerical data (Equation 6.3). This will ensure that the proposed curve would always provide safe sided values of the rotation capacity. Then, the A and B coefficient were obtained from the linear regression coefficients a and b by means of Equations 6.4 and 6.5.

$$\ln(R) = a \cdot \ln(\lambda_{CS}) + b \quad 6.2$$

$$\ln(R) = 5.2 \cdot \ln(\lambda_{CS}) - 3.9 \quad 6.3$$

$$A = e^b \quad 6.4$$

$$B = -a \quad 6.5$$

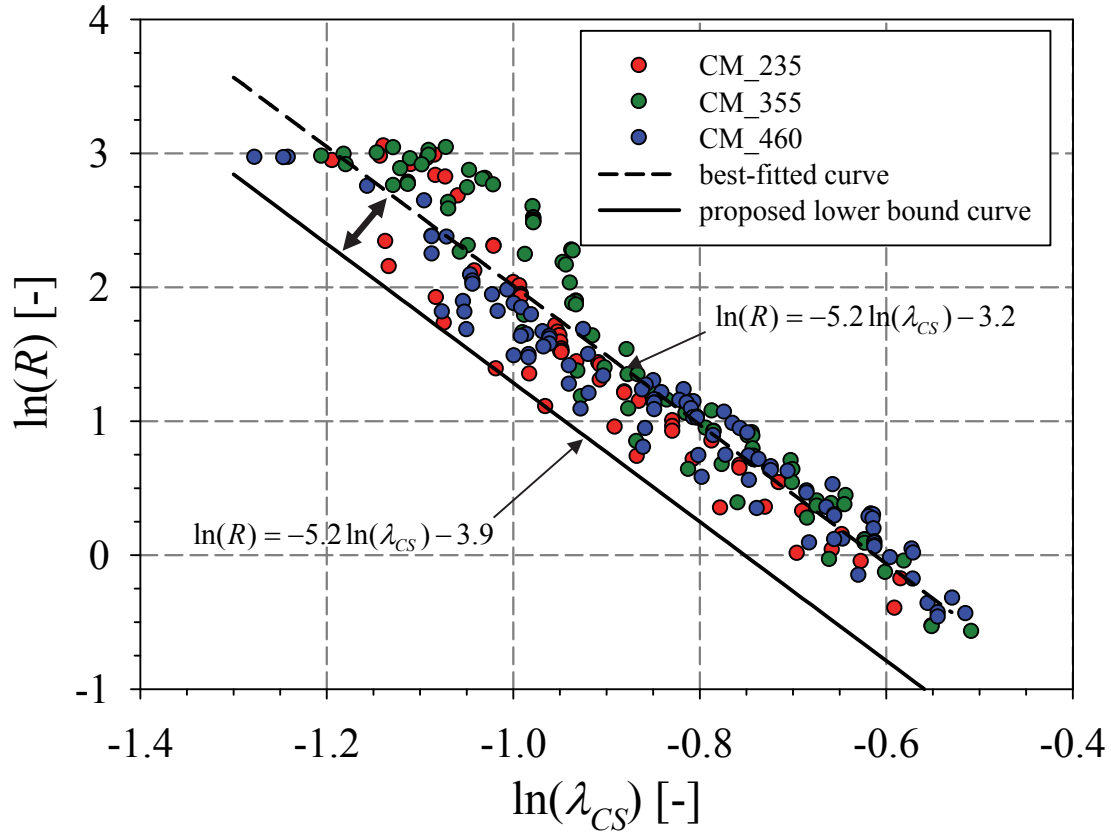


Figure 6.1 – Hot-formed numerical results represented in a logarithmic scale

The curve derived for hot-formed section is given by Equation 6.6. This regression curve gives a continuous relationship between cross-section slenderness and cross-section rotation capacity.

$$R = \frac{0.02}{\lambda_{CS}^{5.2}} \quad 6.6$$

Two limits have been set to this function: an upper limit consists of $R=15$ and a lower limit of $\lambda_{CS} = 0.53$, after which plastic analysis cannot be performed. The limiting value of λ_{CS} for which plastic analysis can be performed has been set to $\lambda_{CS} = 0.53$ on the basis of reaching 0.95 of M_{pl} as seen in Figure 6.3. From the proposed curve given in Equation 6.6, $\lambda_{CS} = 0.38$ can be obtained as the limits for section who can reach a rotation capacity of 3 from those who cannot.

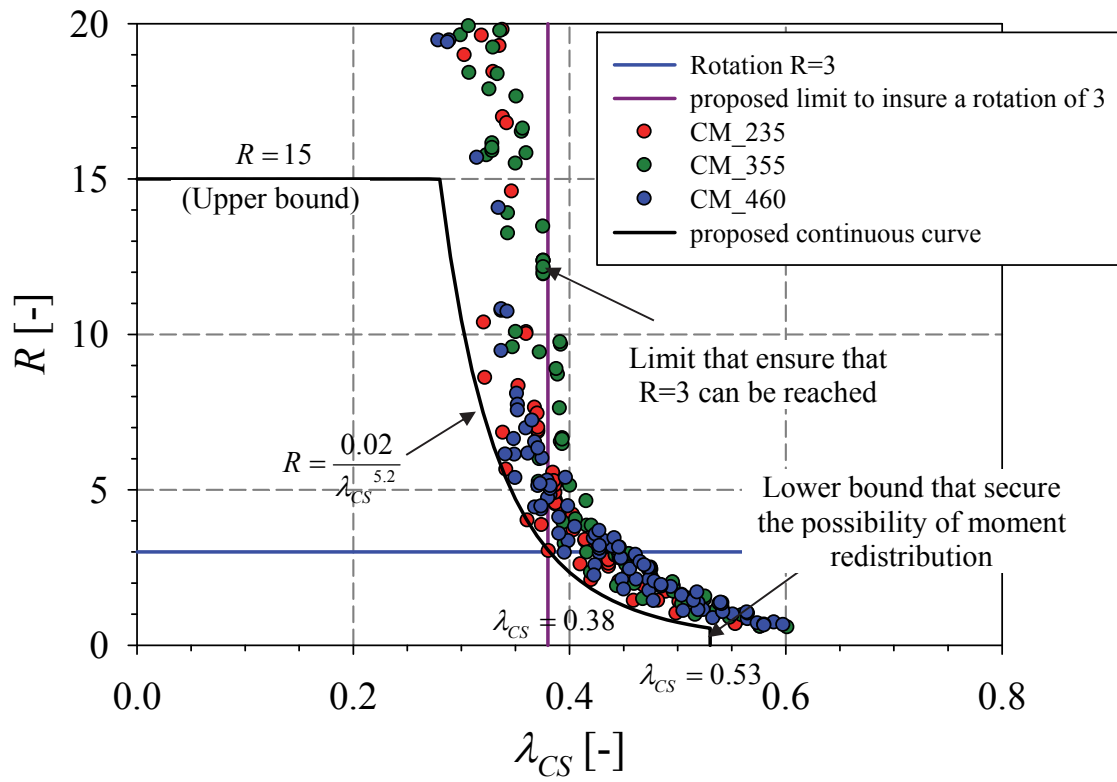


Figure 6.2 – Proposed curve for hot-formed sections under constant moment

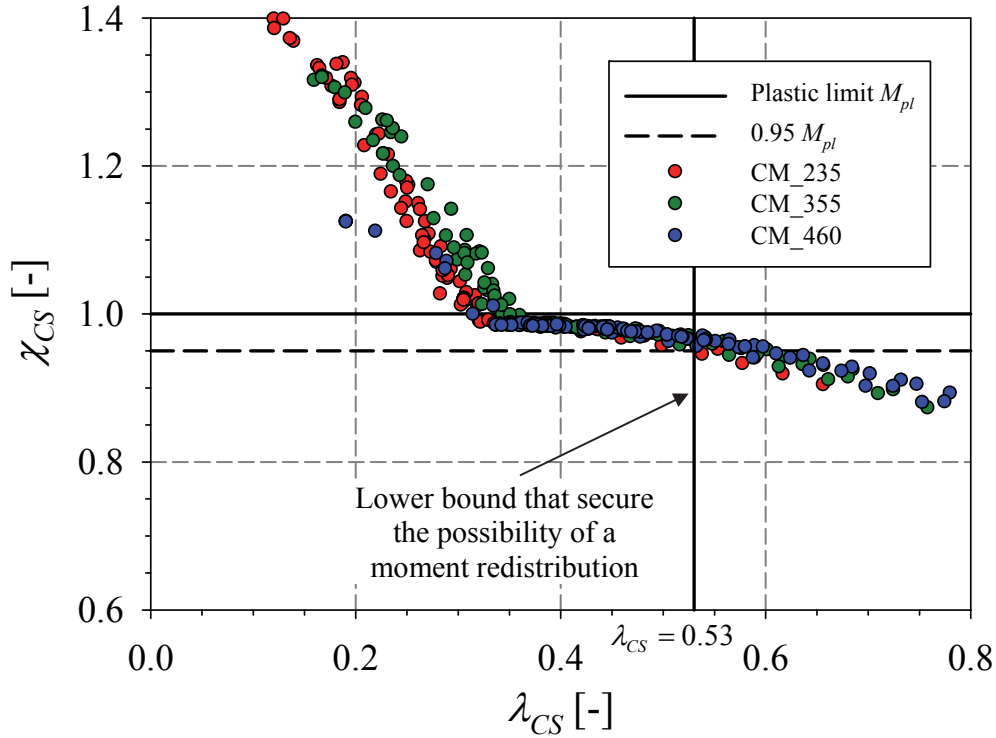


Figure 6.3 – Cross-section slenderness limiting value that ensures 95% of M_{pl} is reached.

In addition, the rotation capacity of hot-formed sections was also plotted as a function of the plate slenderness λ_p in order to compare it to the EC3 actual design procedure and to propose a new suitable value based on the cross-section dimensions, as currently prescribed by the Eurocode. Results are displayed in Figure 6.4 as a function of the plate slenderness as defined in EC3. We can note that when the rotation capacity is plotted as a function of the plate slenderness, a bigger scatter is displayed in comparison with the results plotted against the cross-section slenderness computed numerically, which was expected since the plate slenderness disregard the cross-section plates interactions. Moreover, in Figure 6.4, results were differentiated for sections where failure is governed by flange buckling from those governed by web buckling. For the numerical data represented in Figure 6.4, a limiting value of $\lambda_{CS} = 0.33$ was set which ensures that all sections can deliver a rotation capacity of 3. This

limit would lead to a new proposed flange slenderness limit $\frac{b-2r_e}{t} \sqrt{\frac{f_y}{235}} = 18$ as opposed to

the current EC3 value of 33 and a web slenderness limit $\frac{h-2r_e}{t} \sqrt{\frac{f_y}{235}} = 45$ in comparison to

72. From these values we can conclude that the EC3 prescription are considerably

unconservative and would compromise the safety of the structures. Results are graphically represented in Figure 6.5 and Figure 6.6.

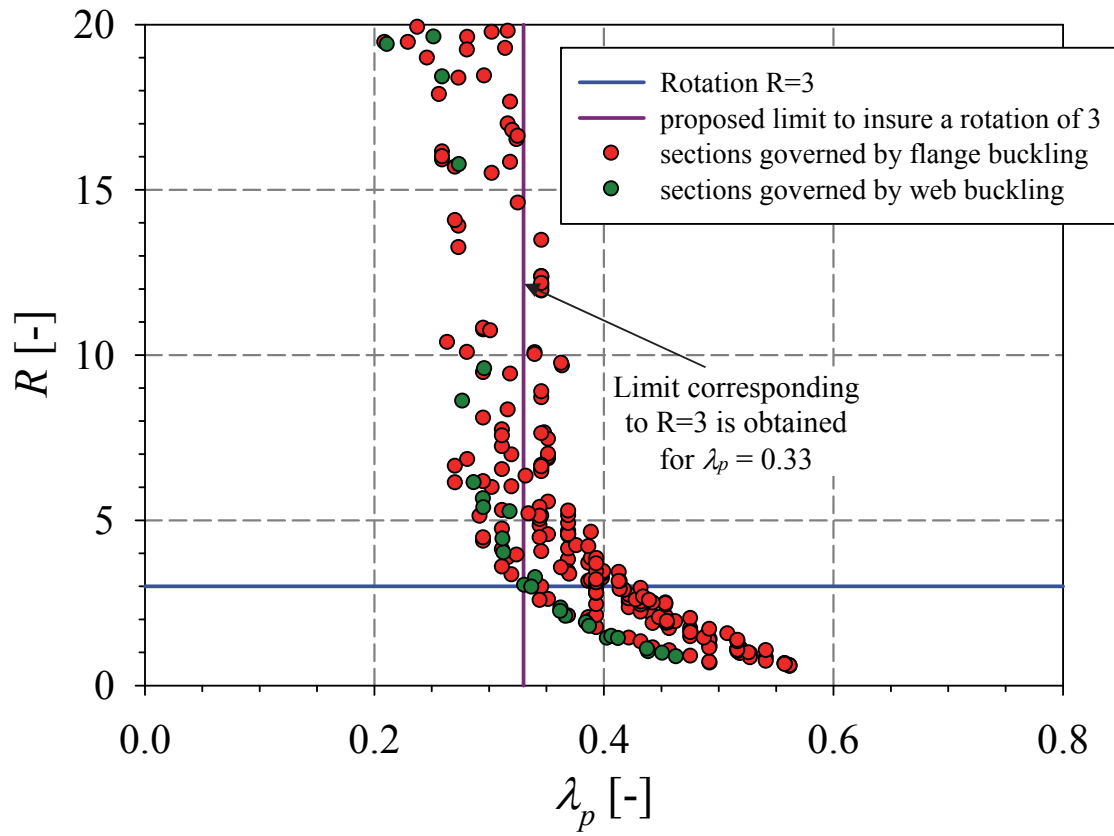


Figure 6.4 – Rotation capacity of hot-formed sections under constant moment as a function of plate slenderness.

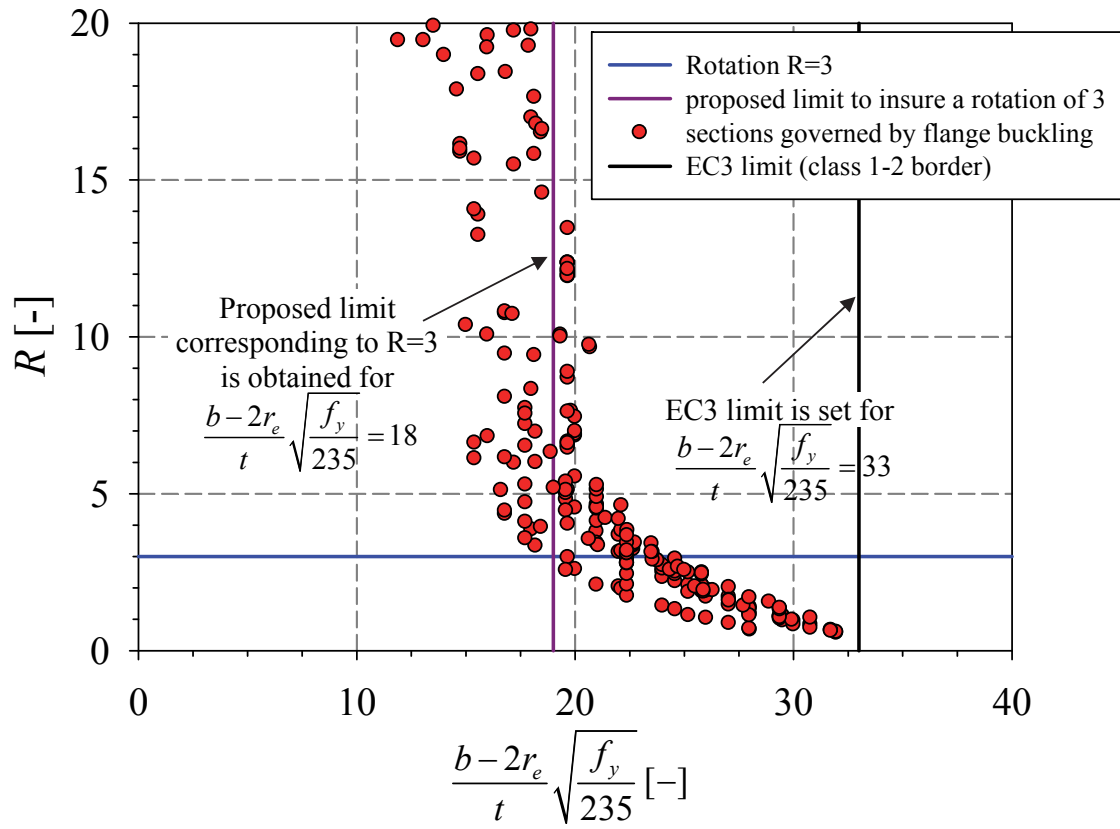


Figure 6.5 – Proposed flange slenderness limit for hot-formed sections.

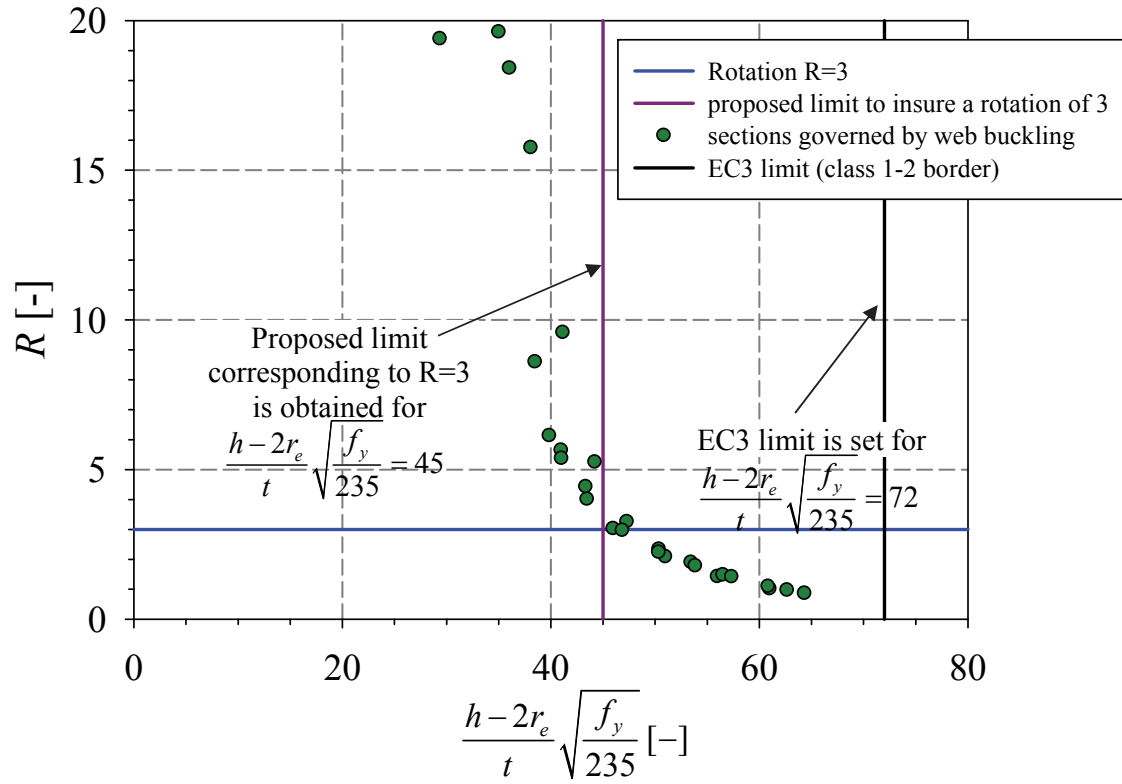


Figure 6.6 – Proposed web slenderness limit for hot-formed sections.

6.2 Cold-formed sections, constant bending moment

As seen previously for cold-formed sections, different tendencies are observed for each steel grade (S23, S355 and S460). In this respect, a curve was proposed for each grade. Moreover, numerical data of a same steel grade present two trends: an increase in rotation capacity for low slenderness followed by a decreasing part. The increasing part is due to the corner material that predominate in the stocky range, and the decreasing part, where the section is more slender, have a similar behaviour to the Euler relationship between critical elastic buckling strain and plate slenderness. Hence, in order to derive a curve that represents the mechanical behaviour of cold-formed sections, a curve was suggested for each fragment and then combined to describe cold-formed section behaviour in a continuous manner.

For the increasing part, the behaviour was also modelled by a logarithmic curve denoted C given by Equation 6.7. The initial C stand for the corner material that have a predominant effect in this portion.

$$R_C = A \cdot \lambda_{CS}^B \quad 6.7$$

The decreasing part was modelled in the same manner as previously for the case of hot-formed sections. The logarithmic curve is denoted F that stands for the material of the flat region and is given by Equation 6.8 as followed.

$$R_F = \frac{C}{\lambda_{CS}^D} \quad 6.8$$

The interaction between both curves can be obtained by linking the effect of both observed behaviour as given in Equation 6.9. This equation can be rearranged as in Equation 6.10 and was adopted in this study. It is worth noting that combining two mechanical behaviour consist the basis of the present process for determining a member capacity. They were introduced by merchant-Rankine and Ayrton-Perry. More details on the derivation of the member interaction curves can be found in Rondal ([117] and [118]).

$$\frac{1}{R} = \frac{1}{R_C} + \frac{1}{R_F} \quad 6.9$$

$$R = \frac{1}{\frac{1}{A\lambda_{CS}^B} + \frac{1}{\frac{C}{\lambda_{CS}^D}}} \quad 6.10$$

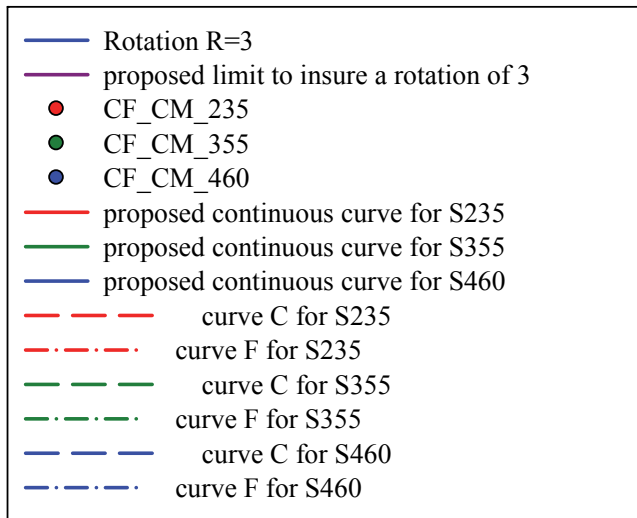
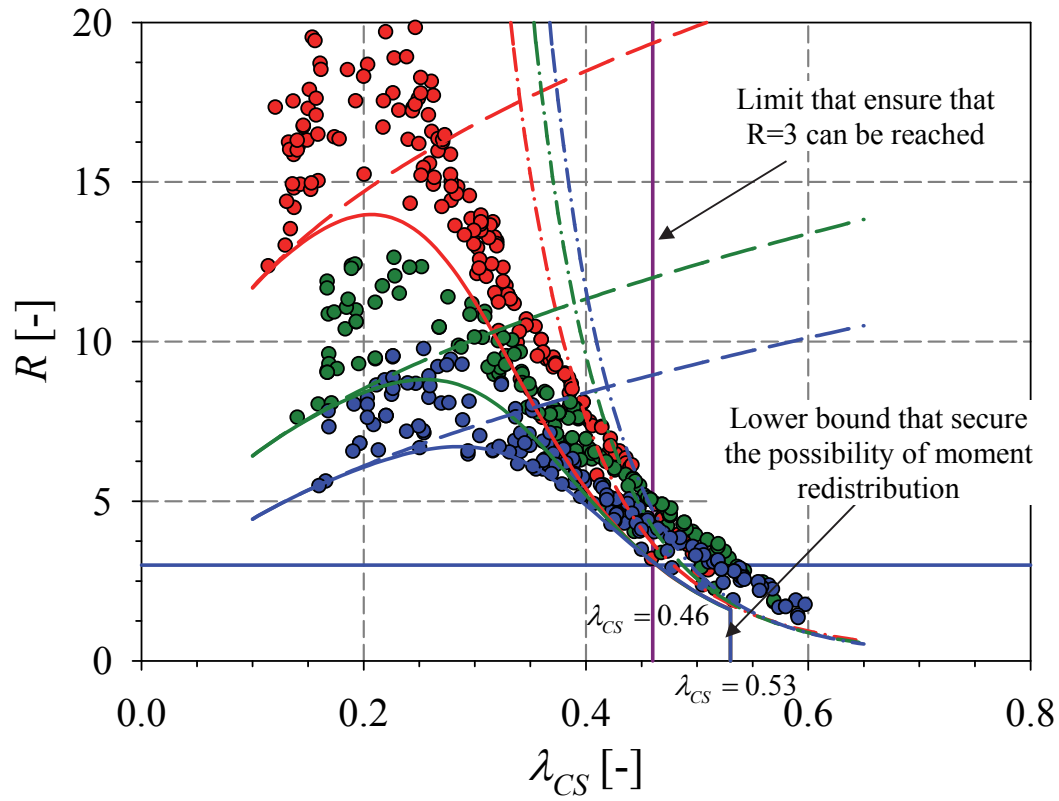


Figure 6.7 – Proposed curve for cold-formed sections under constant moment

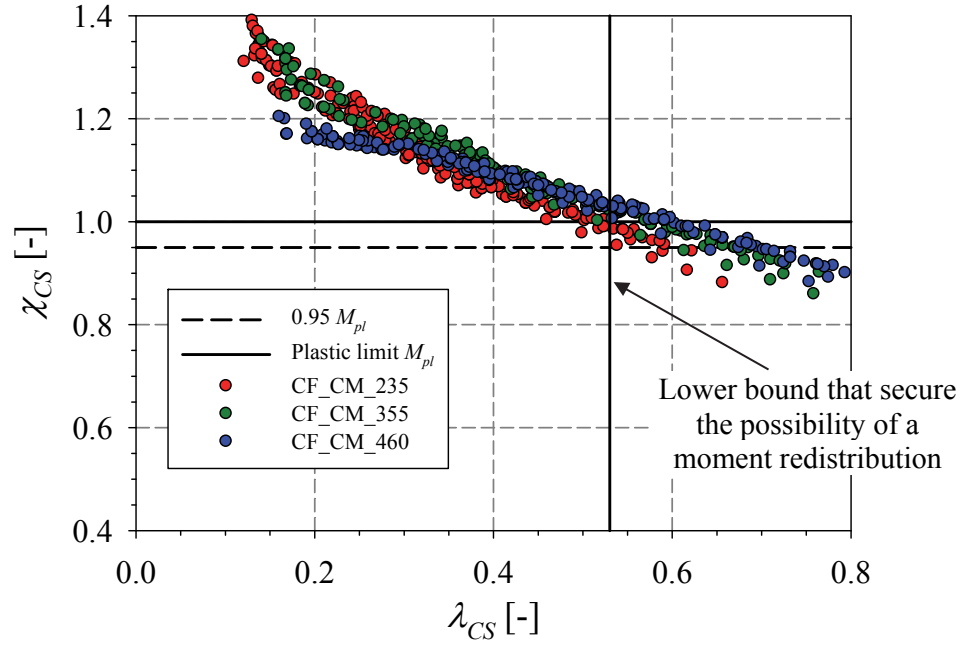


Figure 6.8 – Cross-section slenderness limiting value that would eventually permit plastic analysis.

For cold-formed sections, the limit after which plastic analysis cannot be considered was also set to $\lambda_{CS} = 0.53$ like for the hot-formed case since it has been seen to be adequate as seen in Figure 6.8.

Proposed curves for cold-formed sections are given in Equation 6.15, 6.16 and 6.17. Variables has been deducted in order for the proposed curve to stand as a lower bound for numerical results. A relationship between the cross-section rotation capacities of different steel grades was found. This relation was based on the yield strength and was expressed with the use of $235 / f_y$ ratio. Thus, parameters A, B, C and D are given for S235, S355 and S460 as a function of $235 / f_y$ ratio.

$$A = 25 \cdot \frac{235}{f_y} \quad 6.11$$

$$B = 0.33 \cdot \sqrt{\frac{f_y}{235}} \quad 6.12$$

$$C = 0.065 \cdot \frac{235}{f_y} \quad 6.13$$

$$D = 5.2 \cdot \left(\frac{f_y}{235} \right)^{0.3} \quad 6.14$$

For the S235 steel grade, the rotation capacity is given by:

$$R = \frac{1}{\frac{1}{25\lambda_{CS}^{0.33}} + \frac{\lambda_{CS}^{5.2}}{0.065}} \quad 6.15$$

For the S355 steel grade, the rotation capacity is given by:

$$R = \frac{1}{\frac{1}{16.5\lambda_{CS}^{0.41}} + \frac{\lambda_{CS}^{5.9}}{0.043}} \quad 6.16$$

For the S460 steel grade, the rotation capacity is given by:

$$R = \frac{1}{\frac{1}{12.8\lambda_{CS}^{0.46}} + \frac{\lambda_{CS}^{6.4}}{0.033}} \quad 6.17$$

Derived curves have also been presented separately for each steel grade in Figure 6.9, Figure 6.10 and Figure 6.11 for S235, S355 and S460 respectively. From these curves' equations, the rotation capacity reached can be determined. For S235, we can conclude that a maximum rotation capacity of 14 is achieved for a cross-section slenderness $\lambda_{CS} = 0.21$. For S355, a maximum rotation capacity of 8.8 is reached for $\lambda_{CS} = 0.26$ and for S460, a maximum rotation capacity of 6.7 is attained at $\lambda_{CS} = 0.29$. Hence these curves clearly denote the fact that less ductility is reached for high yield strength due to the material law (in the flat and corner regions) and the ultimate to yield ratio. Moreover they also represent the fact that the Peak rotation capacity is reached for lower slenderness when the steel grade increases which is due to the corner material law parameters as explained previously. For higher slenderness ($\lambda_{CS} > 0.4$), all curves converge altogether since failure occurs at low strain.

From the proposed curves of cold-formed sections (Equation 6.15, 6.16 and 6.17), a unique limit of $\lambda_{CS} = 0.46$ can be obtained that bounds section that can reach a rotation capacity of 3 from those who cannot.

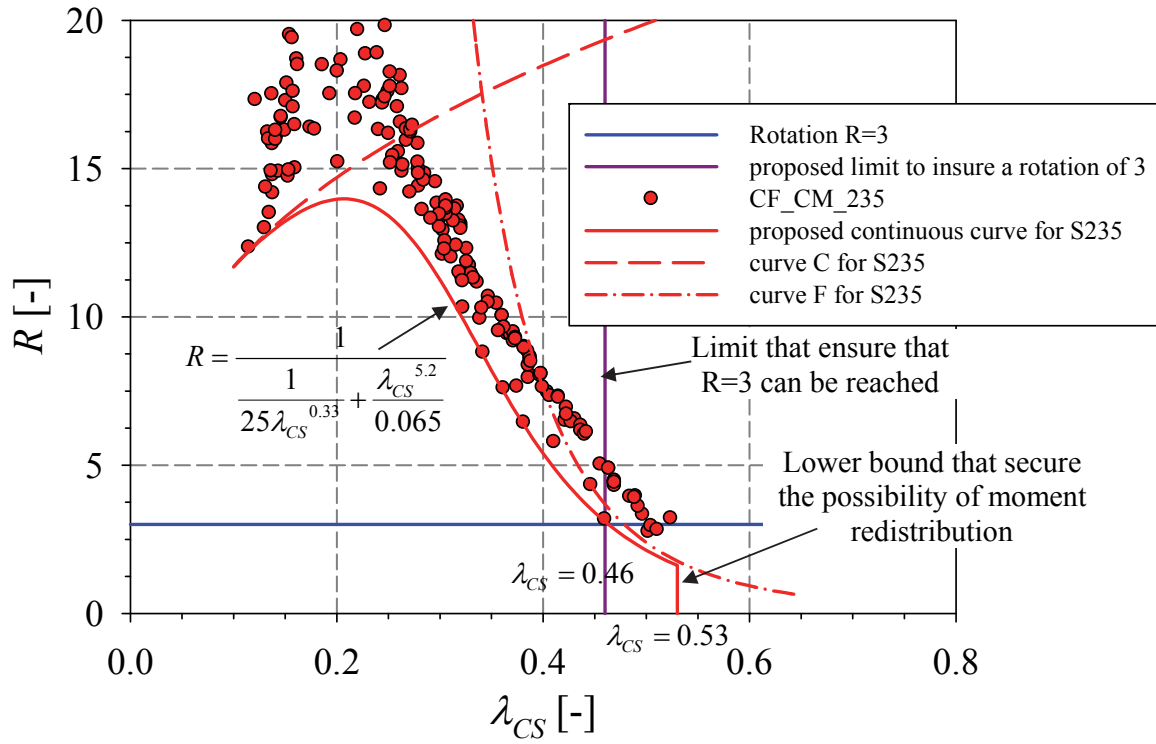


Figure 6.9 – Proposed curve for S235 cold-formed sections under constant moment

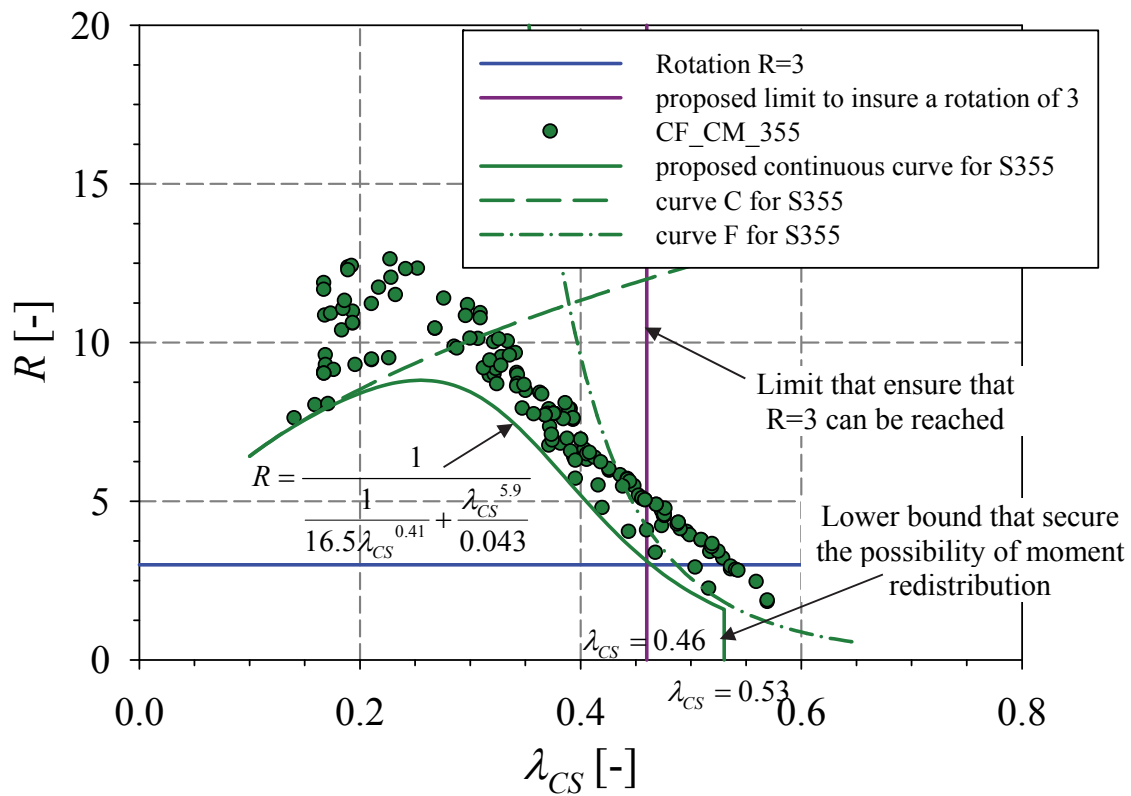


Figure 6.10 – Proposed curve for S355 cold-formed sections under constant moment

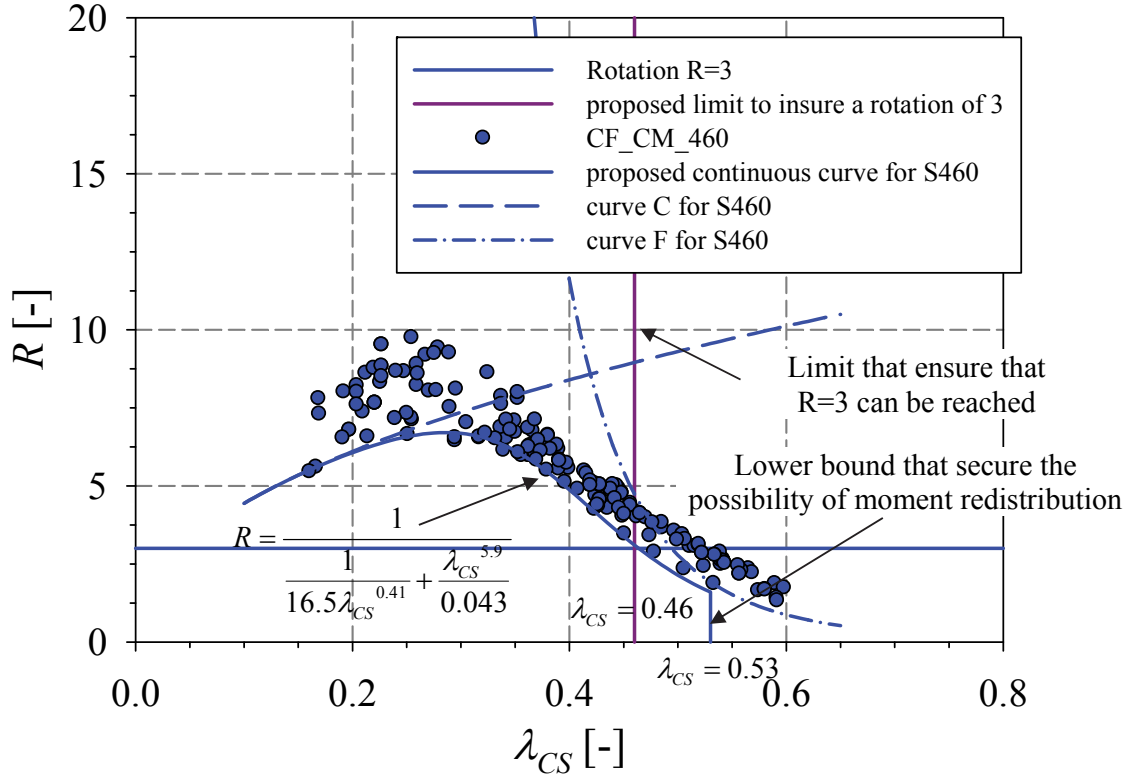
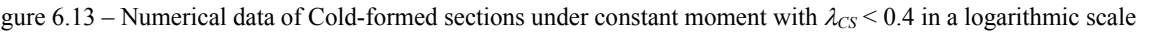
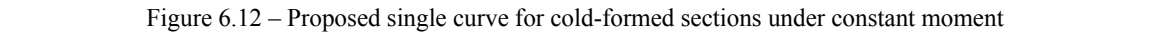


Figure 6.11 – Proposed curve for S460 cold-formed sections under constant moment

Moreover, in an attempt to simplify the mathematical formulation of the rotation capacity for different steel grades, a single curve was also proposed for all cold-formed sections – comparably to the hot-formed case – but bounded by different values for each grade. This curve was computed for all numerical data that have a cross-section slenderness greater than 0.4 since it has been observed that the behaviour of sections in this range is comparable. The numerical data considered are plotted in black dots in Figure 6.12; these considered data are represented in a logarithmic scale in Figure 6.13 to obtain the corresponding parameters that depict the flexural behaviour of cold-formed sections. The proposed curve is given by Equation 6.18.

$$R = \frac{0.26}{\lambda^{3.15}} \quad 6.18$$

From this equation, the limiting value of $\lambda_{CS} = 0.46$ is also deducted and ensures that a rotation capacity of 3 is reached. For S235, a rotation capacity of $R = 12.5$ is set as an upper bound. For S355, the value is established for $R = 7.5$ and $R = 5.5$ for S460.



Numerical results has also been represented as a function of the plate slenderness in order to define a criteria that is Eurocode like. Results are shown in Figure 6.14 in which sections that fail due to flange buckling has been identified from those who fail from web buckling. From this representation a value of $\lambda_p = 0.4$ can be identified as ensuring a rotation capacity of 3. Rotation capacity is also presented as a function of flange and web slenderness in Figure 6.15 and Figure 6.16. The limiting value of flange slenderness that certify a rotation capacity of 3 can be deduced as $\frac{b-2r_e}{t} \sqrt{\frac{f_y}{235}} = 23$ and the one for web slenderness is identified as $\frac{h-2r_e}{t} \sqrt{\frac{f_y}{235}} = 56$. These values also demonstrate that Eurocode3 (also AISC LRFD, AS 4100...) limitations are unconservative and that a number of sections, which are currently classified as Class 1 (or compact), demonstrate insufficient rotation capacity for plastic design. It is nonetheless mentioned here that the gap between the proposed limit and the one in the current standard is bigger for the case of hot-formed sections than that of cold-formed. This was expected since actual standard defines one limit for both cold and hot-formed sections whereas it has been previously shown that cold-formed sections exhibit higher rotation capacities.

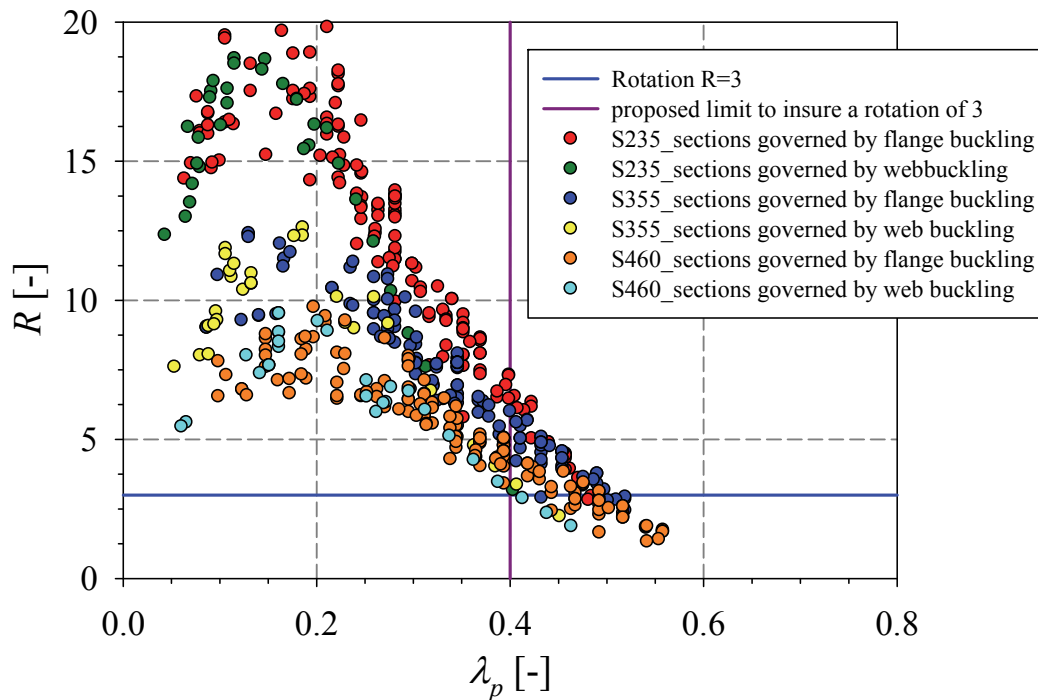


Figure 6.14 – Proposed plate slenderness limit for cold-formed sections

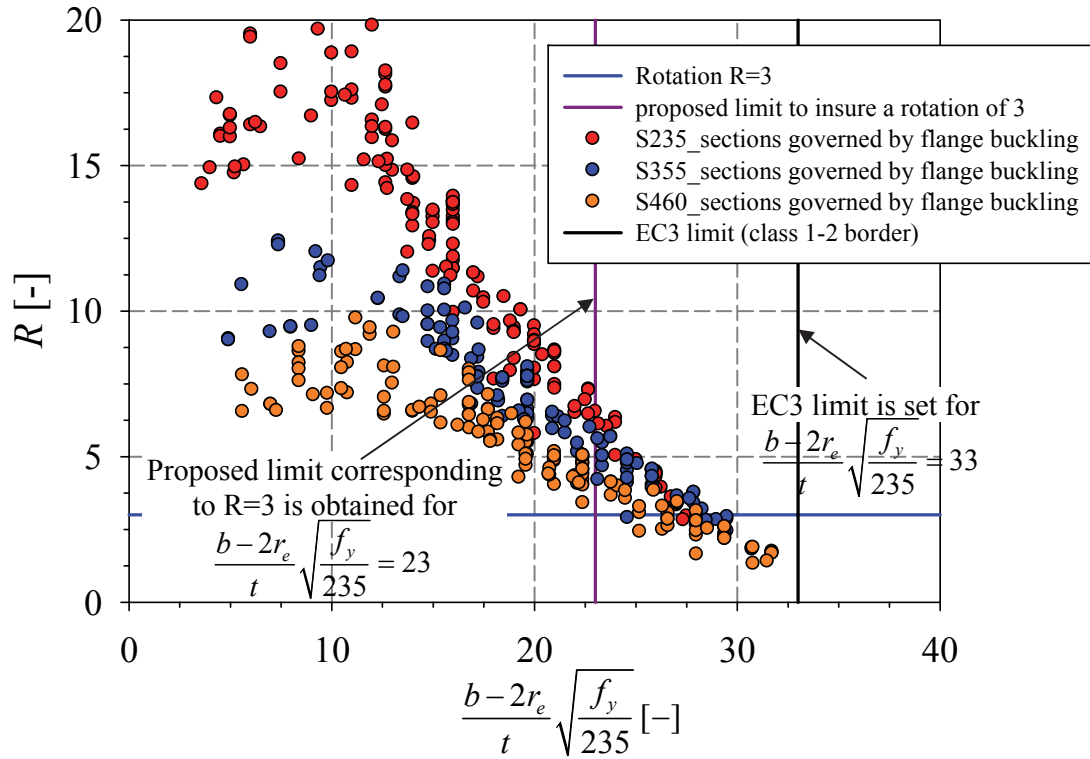


Figure 6.15 – Proposed flange slenderness limit for cold-formed sections

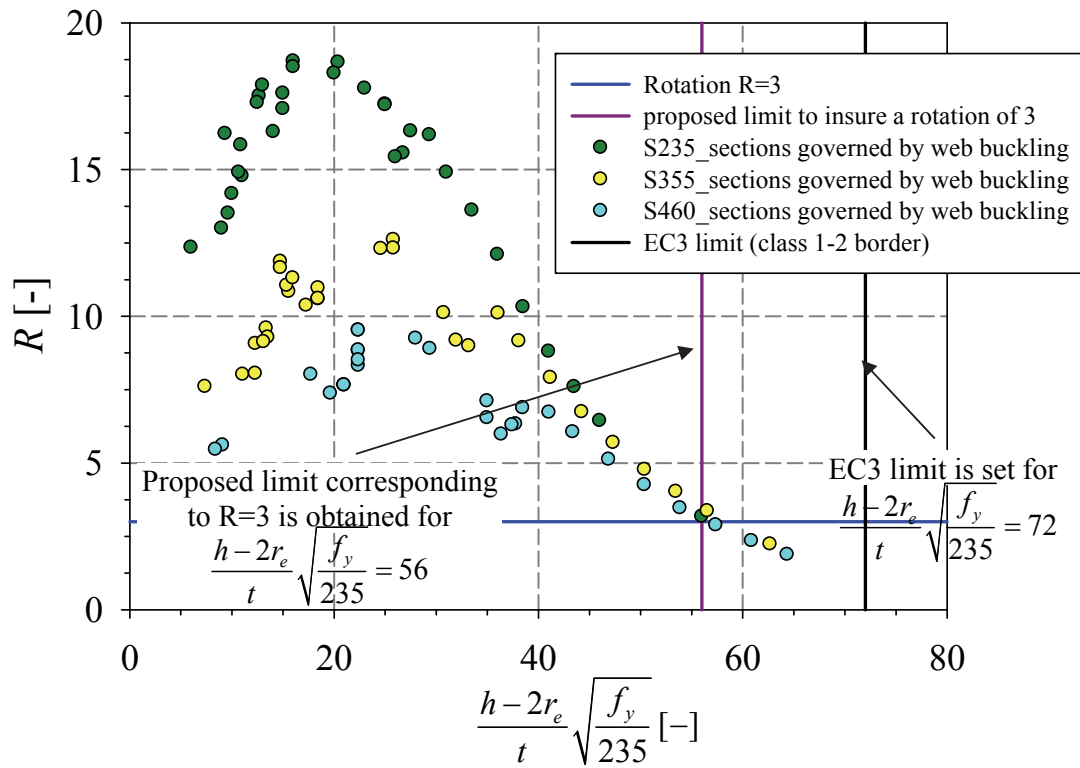


Figure 6.16 – Proposed web slenderness limit for cold-formed sections

6.3 Hot-formed sections, moment gradient

As seen previously for hot-formed sections, one tendency is observed for all yield stresses expect for the case of S460 where the rotation capacity is seen to be limited to a value around 6. Hence, all results has been plotted in a logarithmic scale except for those of grade S460 that reached rotations higher than 6. Results are plotted in Figure 6.17 and display a linear tendency. A curve depicting the behaviour of cross-sections has been best fitted and a lower bound was also suggested to the numerical data given by Equation 6.19 and as represented in Figure 6.17. The curve proposed for hot-rolled sections under a point load is given in Equation 6.20 and represented graphically in Figure 6.18. An upper value of $R=15$ was allocated to S235 and S355 whereas a rotation of 6 was seen suitable for S460 grade. Concerning the lower bound, the minimal value of cross-section slenderness $\lambda_{CS} = 0.53$ was also seen appropriate for hot-rolled sections under a moment gradient as shown in Figure 6.19. Nevertheless, it is worth noting that although beams under a point load exceed the plastic moment for $\lambda_{CS} = 0.53$, the rotation capacity delivered is trivial for such cross-section slenderness.

The rotation capacity has also been plotted as a function of the plate slenderness in Figure 6.20. It can be point out that for cases under a moment gradient, numerical results represent a slightly larger scatter compared to those represented with the cross-section slenderness.

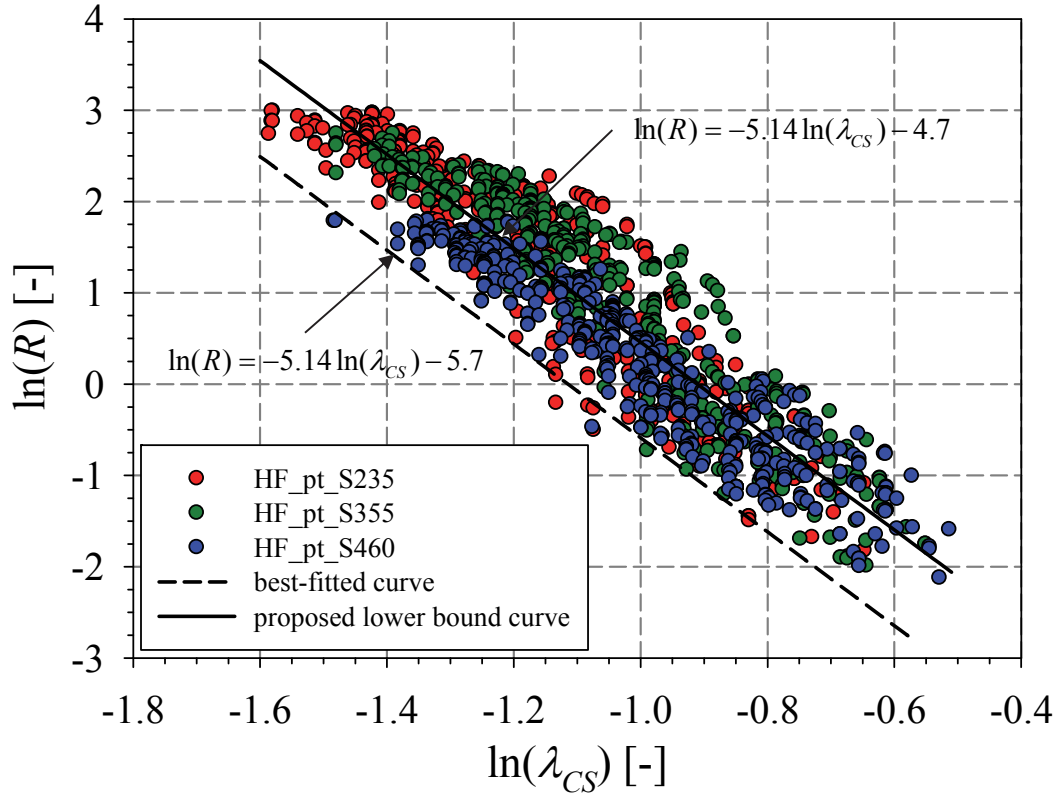


Figure 6.17 – Numerical results of hot-formed section under a point load represented in a logarithmic scale

$$\ln(R) = 5.14 \cdot \ln(\lambda_{CS}) - 5.7 \quad 6.19$$

$$R = \frac{0.0035}{\lambda_{CS}^{5.14}} \quad 6.20$$

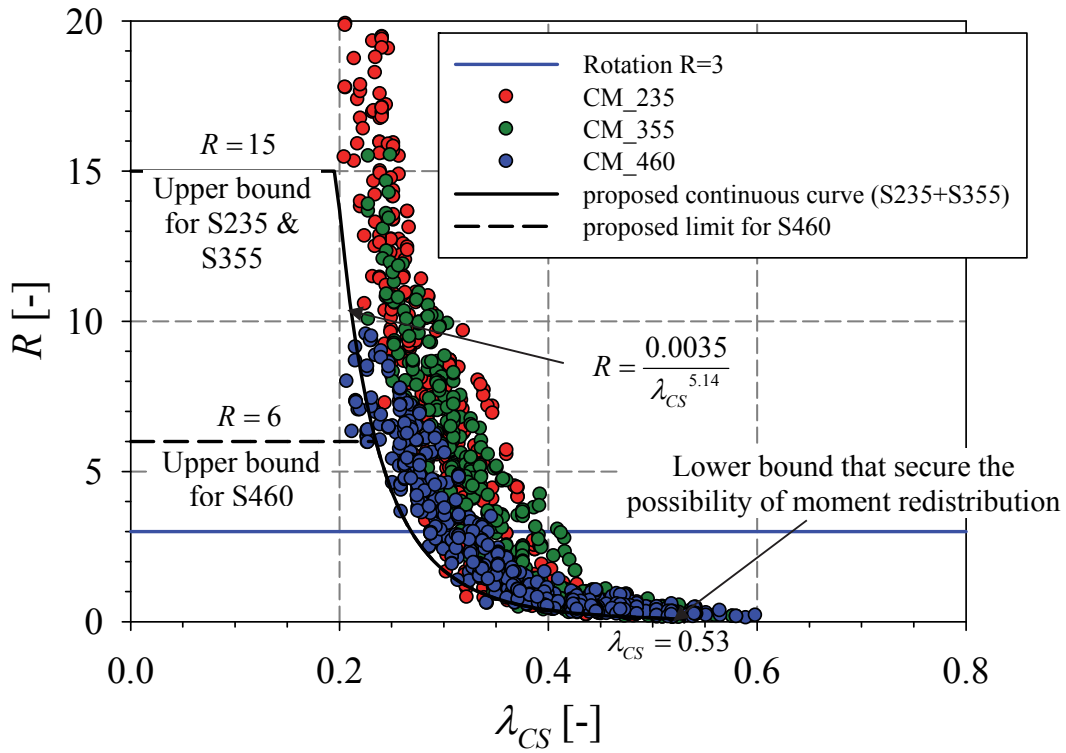


Figure 6.18 – Proposed curve for hot-formed sections under a point load

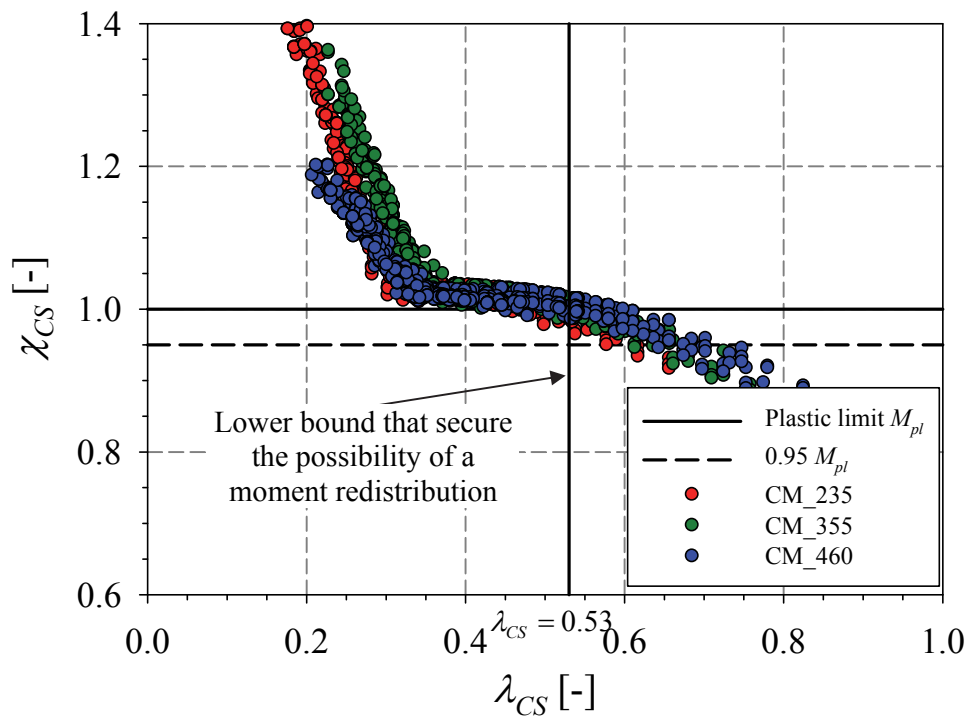


Figure 6.19 – Cross-section slenderness limiting value for plastic analysis.

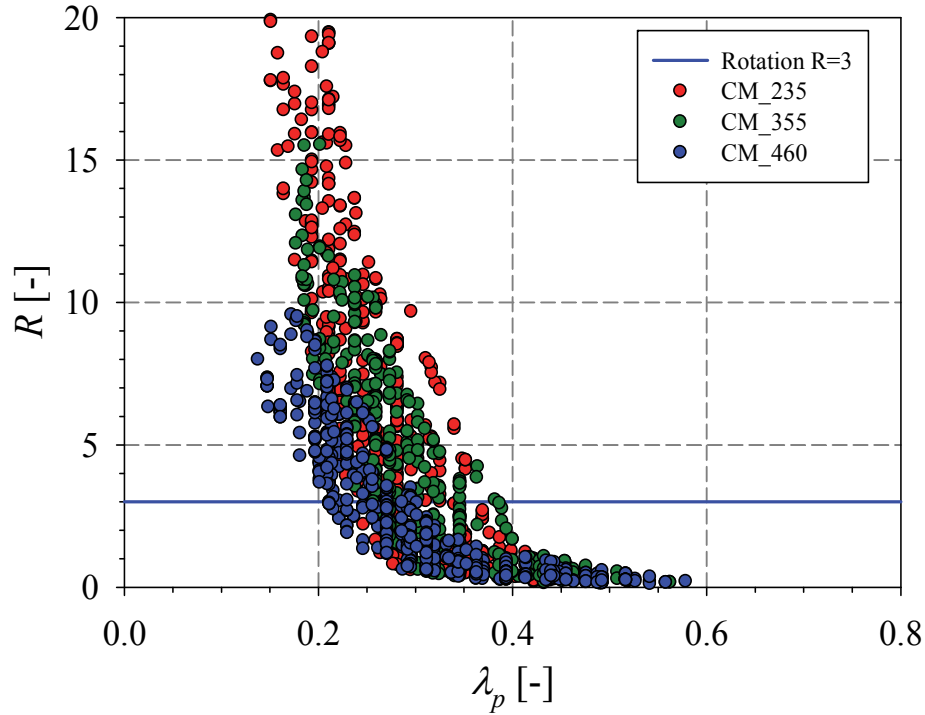


Figure 6.20 – Rotation capacity of hot-formed section under a moment gradient as a function of plate slenderness.

6.4 Cold-formed sections, moment gradient

For cold-formed sections under a moment gradient, same tendencies as for the case of cold-formed section subject to a constant moment are observed with the difference that lower rotations capacities are reached. Hence, in a first step curves have been proposed as an interaction between two main curves, and are represented in Figure 6.21. A transition between curves of different yield stresses has also been made with the use of the 235 / f_y ratio and was found suitable. The A, B, C, and D parameters has been expressed accordingly.

$$A = 16 \cdot \frac{235}{f_y} \quad 6.21$$

$$B = 0.6 \cdot \frac{f_y}{235} \quad 6.22$$

$$C = 0.035 \cdot \frac{235}{f_y} \quad 6.23$$

$$D = 4 \cdot \left(\frac{f_y}{235} \right)^{0.3} \quad 6.24$$

These values led to the expression of the curves for S235, S355 and S460 steels.

For the S235 steel grade, the rotation capacity is given by:

$$R = \frac{1}{\frac{1}{16\lambda_{CS}^{0.6}} + \frac{\lambda_{CS}^4}{0.035}} \quad 6.25$$

For the S235 steel grade, the rotation capacity is given by:

$$R = \frac{1}{\frac{1}{10.6\lambda_{CS}^{0.9}} + \frac{\lambda_{CS}^{4.5}}{0.023}} \quad 6.26$$

For the S235 steel grade, the rotation capacity is given by:

$$R = \frac{1}{\frac{1}{8.2\lambda_{CS}^{1.2}} + \frac{\lambda_{CS}^{4.9}}{0.018}} \quad 6.27$$

The proposed curves are represented in Figure 6.23, Figure 6.24 and Figure 6.25. From these figures we can notice that for S355 grade, the proposed curve provides slightly lower values than the numerical results rotations capacities and this for the range of $\lambda_{CS} < 0.3$. However, this curve was accepted and found suitable for ensuring a transition between curves of different steel grades and because this proposed curve for S355 provides safe-sided values. Moreover, the lower value of $\lambda_{CS} = 0.53$ was also perceived as adequate for limiting the use of plastic analysis, if sufficient rotation capacity is reached to form a mechanism. This conclusion was achieved based on the normalized ultimate moment capacities for cold-formed sections plotted in Figure 6.22.

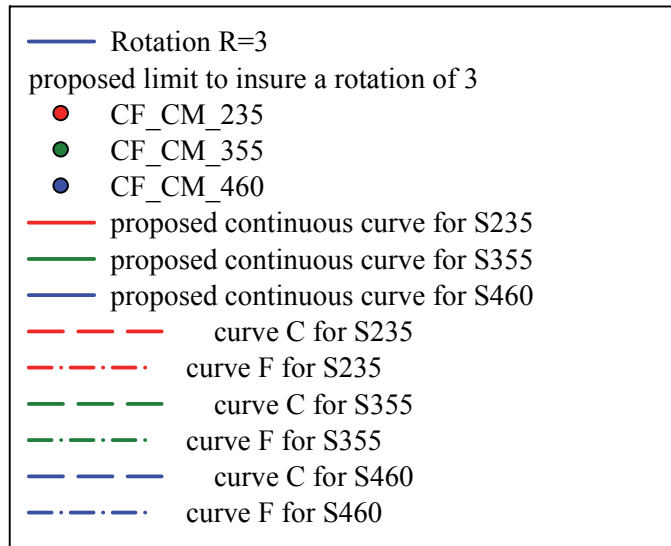
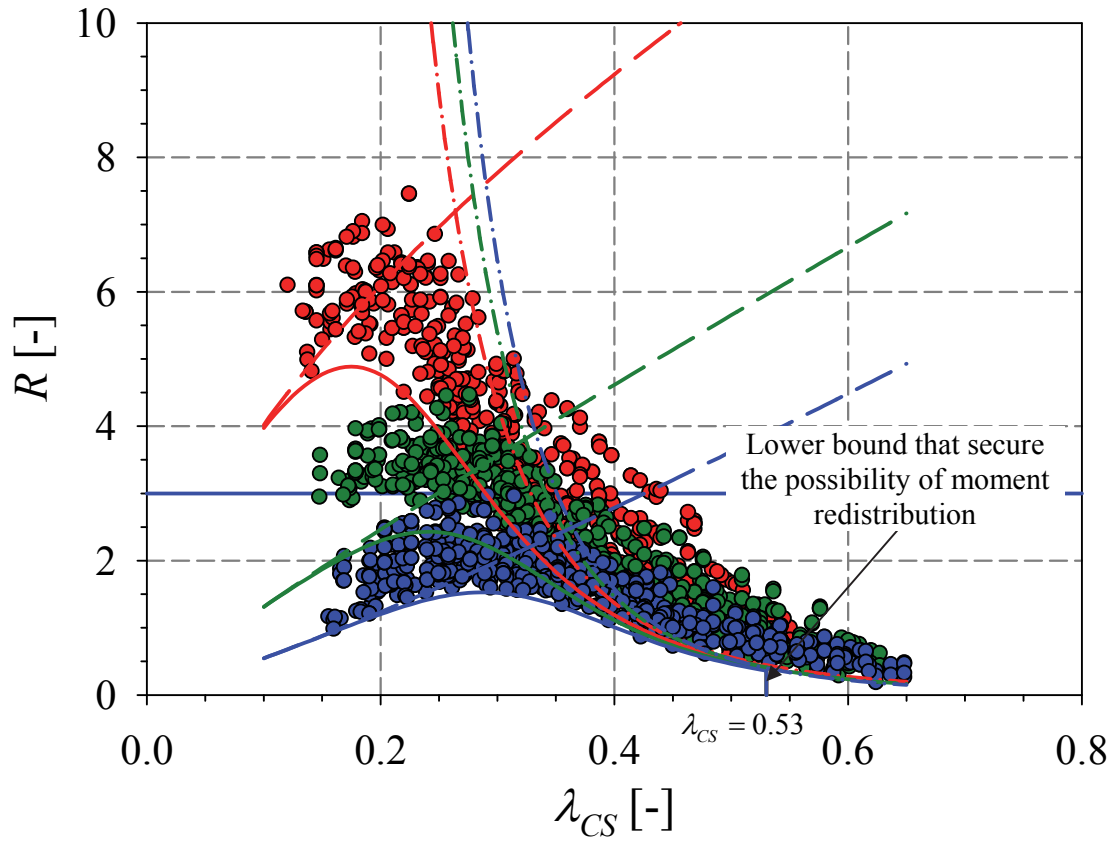


Figure 6.21 – Proposed curve for cold-formed sections under a point load

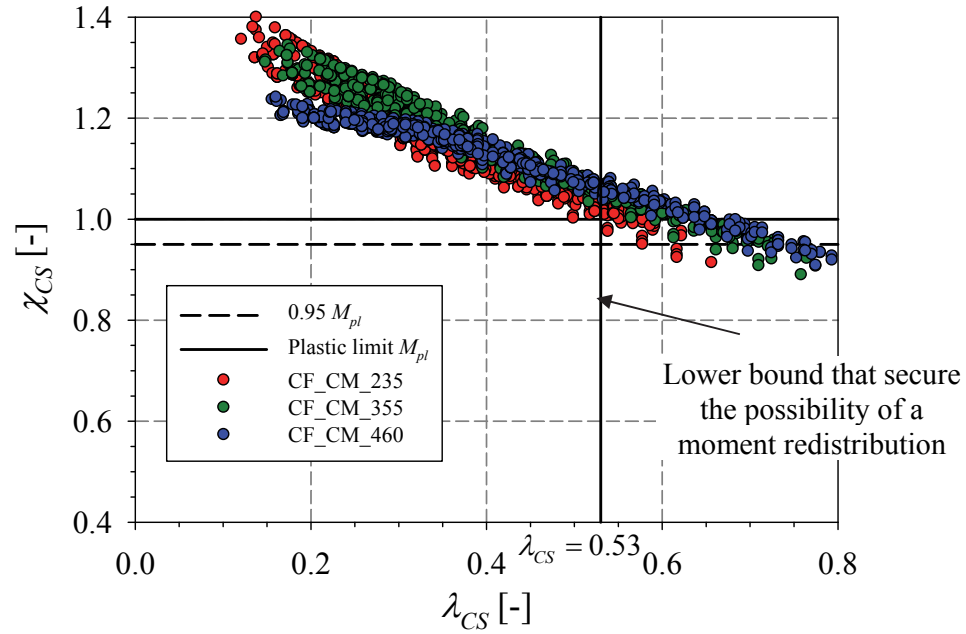


Figure 6.22 – Cross-section slenderness limiting value to allow for plastic analysis.

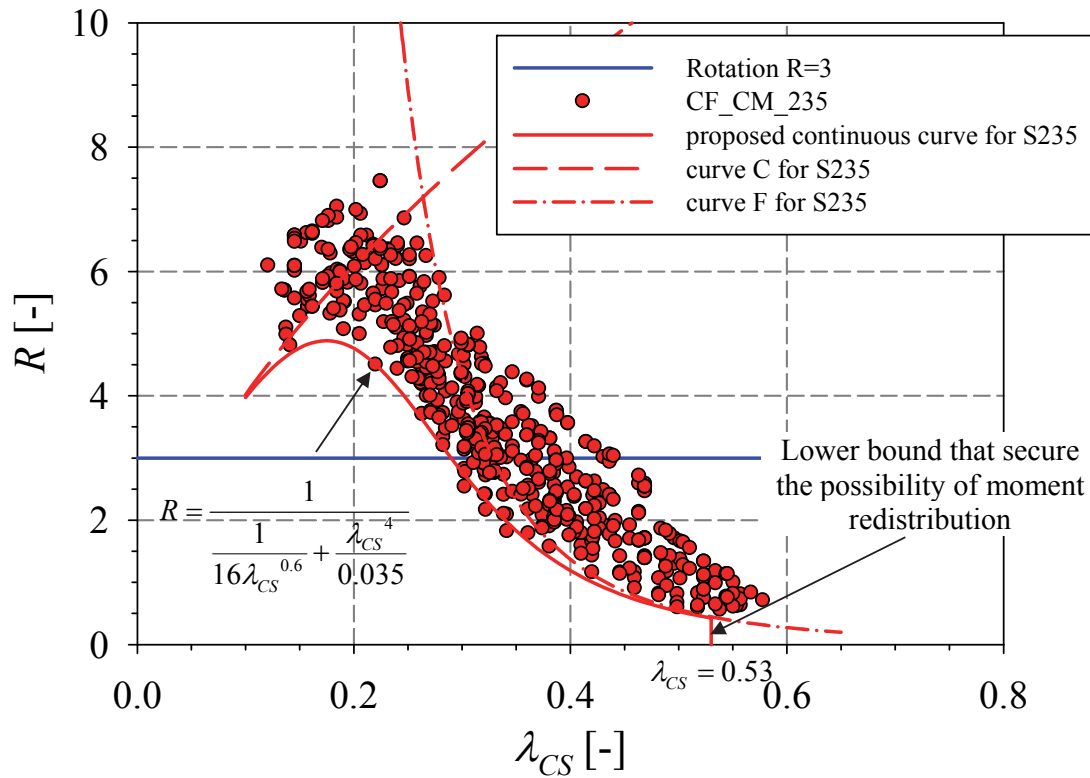


Figure 6.23 – Proposed curve for S235 cold-formed sections under a point load

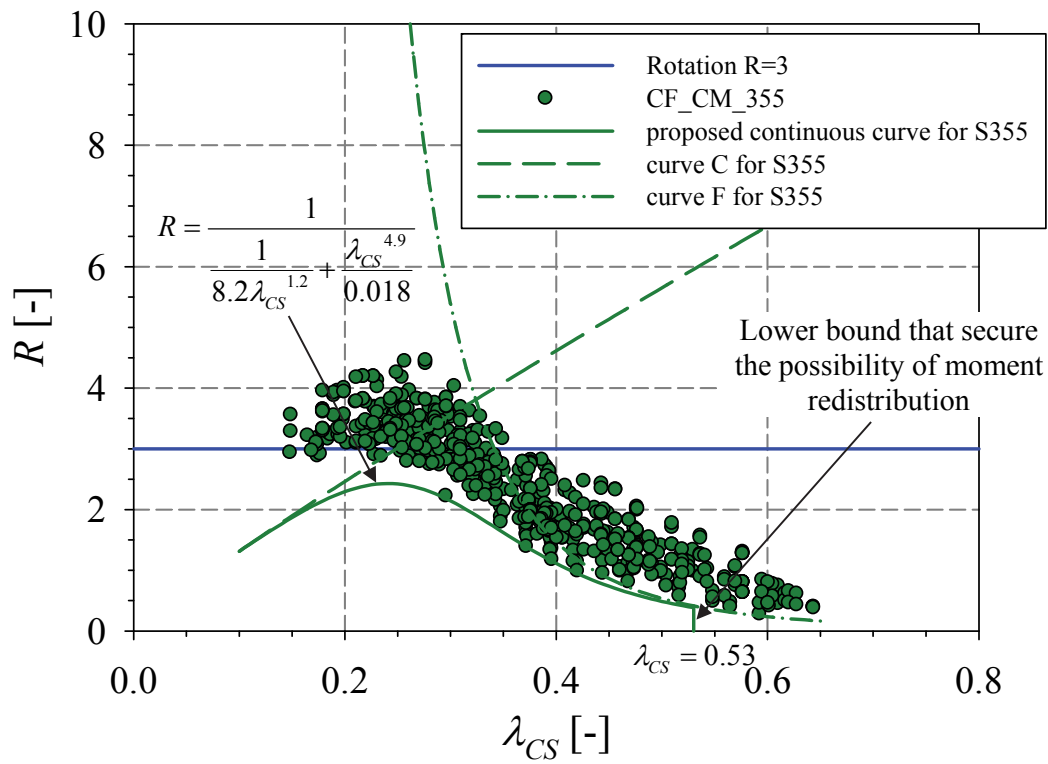


Figure 6.24 – Proposed curve for S355 cold-formed sections under a point load

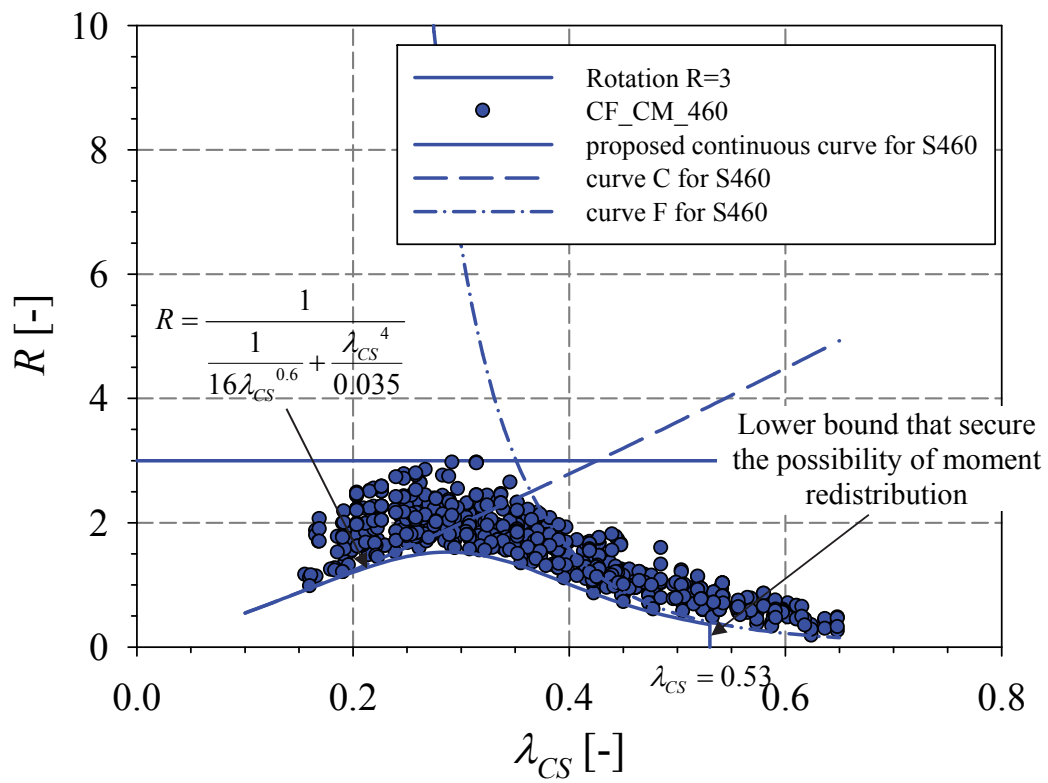


Figure 6.25 – Proposed curve for S460 cold-formed sections under a point load

Moreover, a single curve was also proposed for cold-formed section under a moment gradient and was derived from the numerical data of section having a cross-section slenderness $\lambda_{CS} > 0.4$. Considered data are graphically represented in Figure 6.26 and Figure 6.27 and the resulting curve is given by Equation 6.28. An upper bound of $R=4.5$ was attributed to S235 grade, while $R=2.5$ and $R=1$ was assigned for S355 and S460 respectively.

$$R = \frac{0.06}{\lambda_{CS}^3} \quad 6.28$$

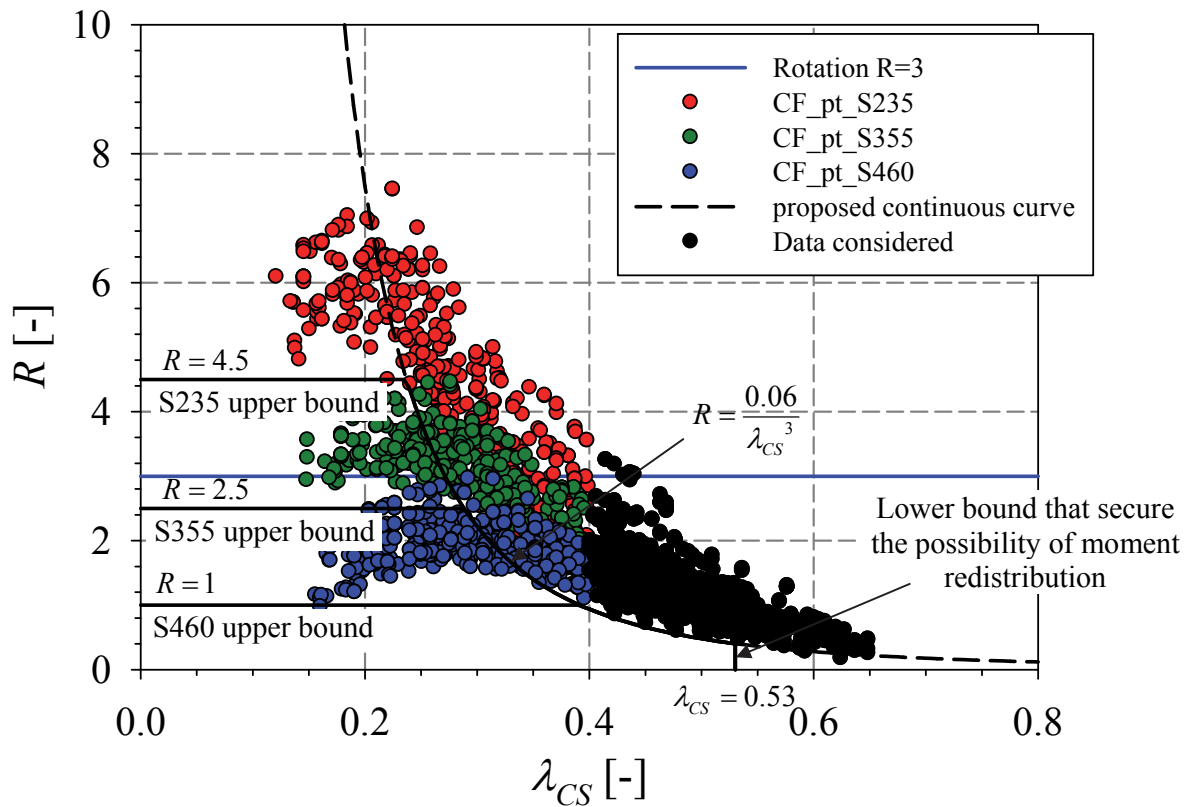


Figure 6.26 – Proposed single curve for cold-formed sections under a point load

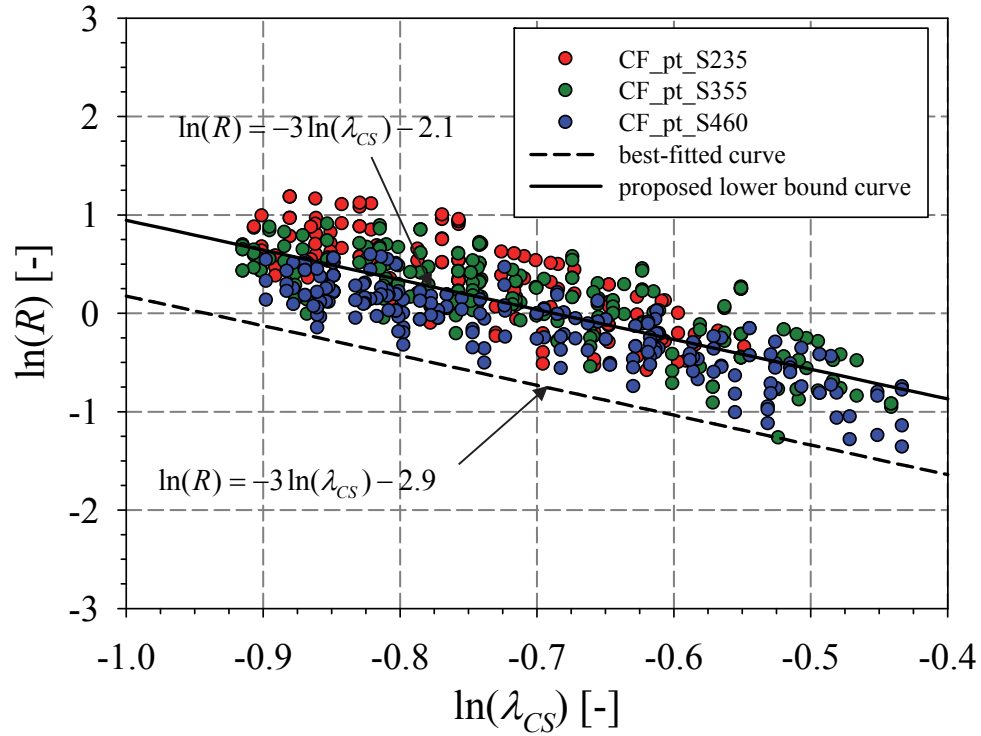


Figure 6.27 – Numerical data of Cold-formed sections under a point load with $\lambda_{CS} < 0.4$ in a logarithmic scale

6.5 Summary of recommendations

6.5.1 Hot-formed sections

Method 1				
Sections satisfying $\lambda_{CS} < 0.38$ or $\lambda_p < 0.33$ are eligible for plastic design				
Method 2: detailed method to be used after R_{dem} has been computed				
Loading	Steel grade	Proposed curve	Upper bound	Lower bound
Constant moment	$f_y \leq 460$	$R = \frac{0.02}{\lambda_{CS}^{5.2}}$	R=15	$\lambda_{CS} \leq 0.53 \rightarrow R=0.5$
Moment gradient	$f_y \leq 355$	$R = \frac{0.0035}{\lambda_{CS}^{5.14}}$	R=15	$\lambda_{CS} \leq 0.53 \rightarrow R=0.09$
	$355 < f_y \leq 460$		R=6	

6.5.2 Cold-formed sections

Method 1				
Sections satisfying $\lambda_{CS} < 0.46$ or $\lambda_p < 0.4$ are eligible for plastic design				
Method 2 : detailed method to be used after R_{dem} has been computed				
Loading	Steel grade	Proposed curve	Upper bound	Lower bound
Constant moment	S235	$R = \frac{1}{\frac{1}{25\lambda_{CS}^{0.33}} + \frac{\lambda_{CS}^{5.2}}{0.065}}$	$\lambda_{CS} = 0.1 \rightarrow R=11.7$	$\lambda_{CS} \leq 0.53 \rightarrow R=1.6$
	S355	$R = \frac{1}{\frac{1}{16.5\lambda_{CS}^{0.41}} + \frac{\lambda_{CS}^{5.9}}{0.043}}$	$\lambda_{CS} = 0.1 \rightarrow R=6.4$	$\lambda_{CS} \leq 0.53 \rightarrow R=1.6$
	S460	$R = \frac{1}{\frac{1}{12.8\lambda_{CS}^{0.46}} + \frac{\lambda_{CS}^{6.4}}{0.033}}$	$\lambda_{CS} = 0.1 \rightarrow R=4.4$	$\lambda_{CS} \leq 0.53 \rightarrow R=1.6$
Moment gradient	S235	$R = \frac{1}{\frac{1}{16\lambda_{CS}^{0.6}} + \frac{\lambda_{CS}^4}{0.035}}$	$\lambda_{CS} = 0.1 \rightarrow R=4.0$	$\lambda_{CS} \leq 0.53 \rightarrow R=0.4$
	S355	$R = \frac{1}{\frac{1}{10.6\lambda_{CS}^{0.9}} + \frac{\lambda_{CS}^{4.5}}{0.023}}$	$\lambda_{CS} = 0.1 \rightarrow R=1.3$	$\lambda_{CS} \leq 0.53 \rightarrow R=0.4$
	S460	$R = \frac{1}{\frac{1}{8.2\lambda_{CS}^{1.2}} + \frac{\lambda_{CS}^{4.9}}{0.018}}$	$\lambda_{CS} = 0.1 \rightarrow R=0.6$	$\lambda_{CS} \leq 0.53 \rightarrow R=0.4$
Method 3 : semi-detailed method to be used after R_{dem} has been computed				
Loading	Steel grade	Proposed curve	Upper bound	Lower bound
Constant moment	S235	$R = \frac{0.26}{\lambda^{3.15}}$	R=12.5	$\lambda_{CS} \leq 0.53 \rightarrow R=1.9$
	S355		R=7.5	
	S460		R=5.5	
Moment gradient	S235	$R = \frac{0.06}{\lambda_{CS}^3}$	R=4.5	$\lambda_{CS} \leq 0.53 \rightarrow R=0.4$
	S355		R=2.5	
	S460		R=1	

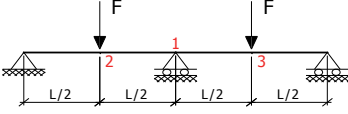
6.6 Worked example

6.6.1 Example 1

The particular case of a continuous beam of two identical span of length L charged with 2 point loads at mid-span is considered. The cross-section is considered hot-formed with $f_y = 235$ Mpa.

For this particular case, the first plastic hinge occur at the central support denoted 1 after which moment is redistributed to the mid-span where the second hinges occur simultaneously at point 2 and 3 and a mechanism is formed. The limiting load values and rotations are reported in Table 6.1. This leads to a rotation demand $R_{dem} = 0.25$ as detailed in Equation 6.29

Table 6.1 – Theoretical limit values

	$F_{pl,1} = 16 \cdot M_{pl} / (3L)$	$\theta_{pl1} = \frac{M_{pl}}{EI} \cdot \frac{L^2}{32}$
	$F_{pl,2} = F_{pl,3} = \frac{9}{8} \cdot F_{pl,1}$	$\theta_{pl2} = \theta_{pl1} + \frac{F_{pl,2} / 8}{EI} \cdot \frac{L^2}{16}$

$$R_{dem} = \frac{\theta_{pl2,3} - \theta_{pl1}}{\theta_{pl1}} = \frac{\theta_{pl2,3}}{\theta_{pl1}} - 1 = \frac{5FL^2 / 128EI_y}{FL^2 / 32EI_y} - 1 = 0.25 \quad 6.29$$

To determine the limiting cross section slenderness for which plastic analysis can be performed, both methods were used.

Method 1: for the case of hot-formed sections, sections providing $\lambda_{CS} \leq 0.38$ can be used while disregarding the rotation demand.

Method 2: After calculating the rotation demand that is equal to 0.25 for such a structure, the continuous curve proposed for hot-formed section under a point load, that is represented by the following equation: $R = \frac{0.0035}{\lambda_{CS}^{5.14}}$, is considered. From this formula we can deduct that

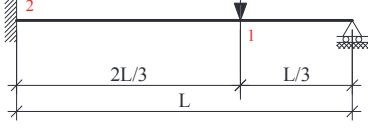
sections having $\lambda_{CS} \leq 0.44$ can be considered. This emphasize the fact that when the detailed approach is considered, design become more economical.

6.6.2 Example 2

A propped cantilever of span of length L loaded with a point load at $1/3$ the length from the pinned support is studied. Beams are considered to be cold-formed with S460 steel grade.

For this case, the first plastic hinge occur at the position of the position of the point load P , then moment is redistributed to the fixed support where the second hinge forms and leads to the structure failure. The limiting load values and rotations are reported in Table 6.2. This leads to a rotation demand $R_{dem} = 0.3$ as detailed in Equation 6.30.

Table 6.2 – Theoretical limit values

	$P_1 = \frac{81M_{pl}}{14L}$	$\theta_{pl1} = \frac{3M_p L}{14EI}$
	$P_{pl} = \frac{6M_{pl}}{L}$	$\theta_{pl2} = \frac{5M_{pl} L}{18EI}$

$$R_{dem} = \frac{\theta_{pl2}}{\theta_{pl1}} - 1 = \frac{5M_{pl}L/18EI_y}{3M_{pl}L/14EI_y} - 1 = 0.3 \quad 6.30$$

When considering the simplified method 1 for cold-formed sections, plastic analysis can be performed for sections satisfying $\lambda_{CS} < 0.46$, while disregarding the rotation demand.

Method 2: since for this structure the rotation demand $R_{dem} = 0.3$, the continuous curve proposed for cold-formed section under a point load for S460 is used and is given

by $R = \frac{1}{\frac{1}{8.2\lambda_{CS}^{1.2}} + \frac{\lambda_{CS}^{4.9}}{0.018}}$. The continuous curve possess a lower bound $\lambda_{CS} \leq 0.53$. This

limiting values leads to a rotation capacity $R=0.36$ which lead to the conclusion that cold-formed sections eligible for plastic design can deliver a minimal rotation capacity of 0.36. Hence, for our specific case of propped cantilever, sections satisfying $\lambda_{CS} \leq 0.53$ can be used for plastic design. From this value, it can also be highlighted that the detailed approach provides more economical recommendations.

6.7 Concluding remarks

With respect to the numerical results, new recommendations that allows the use of plastic design were proposed. The recommendations were given through two approaches.

The first approach is in line with the Eurocode and consists of giving a slenderness value that would ensure enough rotation capacity is available for a plastic mechanism to develop.

When determining the limiting values of cross sections slenderness that ensures a rotation capacity of 3, only the case where a constant moment is applied was taken into account. This resulted in a value of $\lambda_{CS} = 0.38$ or $\lambda_p = 0.33$ for hot-formed sections and $\lambda_{CS} = 0.46$ or $\lambda_p = 0.4$ for cold-formed sections. These recommendations highlight the fact that the current standards provisions are unconservative.

The second approach consists of linking the rotation demand to the rotation capacity of section and thus establishing continuous curves for the rotation capacity as a function of the cross-section slenderness.

Based on the extensive numerical parametric analysis, different behaviours were observed for cold-formed-sections and hot-formed sections and for beams under a constant moment as well as for beams subject to a moment gradient.

Since a large scatter is expected when representing the rotation capacity of sections, a lower bound curve was proposed. Moreover, the effect of the aspect ratio and the moment gradient was disregarded when proposing a suitable continuous curve for determining the rotation capacity. Moreover, for the case of hot-formed sections, the influence of the steel grade was negligible due to the presence of the yield plateau and was therefore disregarded; whereas for cold-formed section the effect of the yield stress was significant and thus taken into account.

Based on the conclusions underlined previously, new actual recommendations regarding the rotation capacity of square and rectangular cross section should be proposed since actual standard are unconservative. The most suitable procedure would be to link the rotation demand to the rotation capacity to obtain the most economical and reliable result.

7 CONCLUSIONS AND FUTURE STEPS

The present dissertation was devoted to the characterization of hollow section shapes' rotational capacity. The objective was to establish a relationship between the rotation capacity R_{cap} with the cross-section slenderness λ_{CS} .

After introducing the subject, development made toward the characterization of the rotation capacity and the rotation demand of a structure was reported in chapter 2 along with how current design standard allow the use of plastic design.

Experimental work was performed in order to investigate the rotation capacity of hollow structural sections and are detailed in Chapter 3; preliminary measurements relative to the material law and geometrical dimensions were described together with the beam response in respect to its ultimate capacity and deformation capacity. Sections were seen to experience insufficient plastic rotation capacity although classified as class 1. This highlighted the fact that current codes provisions should be revised. It was also attributed to high level of stress concentration due to the loading method imposed.

Then, the experimental tests have been accurately modelled with the use of the finite element software FINELg in Chapter 4. A good agreement was found between numerical and experimental results when comparing the ultimate capacity of a section and some divergence was observed at the beam deformation at failure. This was predictable since the rotation capacity is very sensible to initial geometrical imperfections. In all, the numerical model was found to well simulate the behaviour of beams in bending and it was then extensively used to launch a numerical campaign to study the rotation capacity of cold-formed and hot-formed section in addition to investigate their sensibility to various parameters.

Subsequently, an extensive numerical campaign was reported in Chapter 5 along with some comprehensive analysis. Numerical investigations highlighted the influence of the initial geometrical imperfections on the rotation capacity and explained the big scatter observed experimentally when reporting the rotation capacity of a section as a function of the plate slenderness. Moreover, it was identified that the material law influences the inelastic behaviour of the beam and that strain hardening improves its post-buckling behaviour. Cold-formed sections were seen to achieve higher rotations than hot-formed sections. For very stocky cold-formed sections, a decrease in the rotation capacity was observed due to the

brittle behaviour of the material law in the corner (attributed to the cold-forming process). In addition, sections tested under a point load displayed lower rotations than those under a constant moment since buckling is restraint to a small region.

Accordingly with the obtained results, new propositions were made to allow the use of plastic design in Chapter 6. The personal contributions made in this thesis are listed below and consist in:

- Collecting an experimental database of 109 results from literature. These data were compared to the numerical results and served as reference for deriving the adequate limits and curves needed to allow the use of a plastic analysis.
- Proposing stricter element slenderness values based on the EC3 definition to allow sections to be used in plastic design. A comparison between the Eurocode 3 recommendations and the new proposed limit was made
- Development of a continuous curve capable of describing the rotation capacity of sections as a function of the cross-section slenderness in order to compare it with the rotation demand.
- Different curves were proposed to cold-formed and hot-formed sections in contrast to current design standards that generally ignore the production route. The yield strength was also identified as a key parameters for the determination of the design curves.
- The loading arrangement imposed on the beam was reported to be a governing parameter on the rotation capacity of sections and was taken into consideration to allow the use of plastic design.
- It has been stated that the procedure that consist in imposing a ductility requirements for plastic design, which is based on the traditional practice, can lead to both very conservative recommendations for simple structures and unreliable results for complex constructions. Hence, the best procedure recommended is to check the plastic rotation capacity of a sections against the required plastic rotation of a structure.

Chapter 6 also gives a summary of the proposed design recommendations for practical design followed by worked examples to illustrate the design procedure and the benefit from the newly developed design proposals.

The investigations carried out in this thesis represent a first step towards the improvement of current design standards. Several areas where further research is required were identified and consist in the following:

- The rotation capacity of sections should be studied under more loading configurations like for instance distributed loading.
- The case of high strength steel should be examined to identify if enough ductility can be obtained to allow moment redistribution.
- Rectangular hollow sections with high aspect ratios should be inspected. In addition to failing by web buckling, these sections becomes sensible to lateral torsional buckling.
- The effect of shear should also be investigated since the rotation capacity may be affected when shear stresses exceed the web buckling strength.
- Web crippling due to high stress concentration should be considered and design recommendation should be given to include its effect or determine ways to avoid it.
- Combined actions of bending moment and axial force should also be investigated. This study is important for the case of framed structures. When normal forces are applied to a beam, the cross section may cripple due to axial force while the section is undergoing plastic bending.
- These area of research should be extended to the case of open sections. For this case, the effect of lateral torsional buckling should be considered and recommendations toward the complex relationship between the unbraced length and the cross-section slenderness to the rotation capacity should be specified. In other terms, rules that control lateral and local buckling until sufficient rotation capacity develops should be presented.
- The application of the current design method should include other materials (stainless steel...) and composite beams.
- The ability of the connections to act as plastic hinges in a structure should also be inspected.
- Ways to determine the rotation demand of a structure that include the second order effect should be examined in order for the plastic analysis method to be faster, more accurate, and more economical.

- Research should also be extended to include seismic cases, cyclic loading, fatigue and fire.

8 REFERENCES

- [1] N. Boissonnade, J. Nseir, and E. Saloumi, "The Overall Interaction Concept: an Alternative Approach to the Stability and Resistance of Steel Sections and Members." Proceedings of the Annual Stability Conference, Structural Stability Research Council, St. Louis, Missouri, 2013.
- [2] M. G. Lay, "Plastic Design of High Strength Steel: the Experimental Bases for Plastic Design - A Survey of the Literature." Fritz Engineering Laboratory Report No 297.3, Department of Civil Engineering, Lehigh University, Bethlehem, Pennsylvania, USA., 1963.
- [3] M. Lyse and H. J. Godfrey, "Investigation of Web Buckling in Steel Beams." Transactions, American Society of Civil Engineers, paper No 1907, 1934, pp. 675-695, 1934.
- [4] J. A. Ewing, "The Strength of Materials." Cambridge, 1899.
- [5] E. Meyer, "Die Berechnung der Durchbiegung von Staben deren Material dem Hook'schen Gesetze nicht folgt." Zeitschrift des Vereines Deutscher Ingenieure, 52(5), p.167, 1908.
- [6] G. Kazinczy, "Trials with fixed-end beams." Betonszemle, Issue 2, pp. 68-71, 83-87 & 101-104, 1914.
- [7] N. C. Kist, "Die Zahigkeit des Materials als Grundlage fur die Berechnung von Brucken, Hochbauten und ahnlichen konstruktionen aus Flubeisen." Der Eisenbau 11, No. 23, pp. 425-428, 1920.
- [8] M. Gruning, "Die Tragfahigkeit Statisch Unbestimmter Tragwerke Aus Stahl Bei Beliebiger Haufg Wiederholter Belastung." Berlin: Springer, 1926.
- [9] H. Maier-Leibnitz, "Beitrag Zur Frage Der Tatsachlichen Tragfahigkeit Einfacher Und Durchlaufender Balkentrager aus Baustahl." St 37 und Holz, Die Bautechnik 6, pp. 11-14 & 27-31, 1928.
- [10] H. Maier-Leibnitz, "Versuche mit eingespannten Balken von I-Form aus Baustahl St 37." Die Bautechnik 7, pp. 20 & 313-318, 1929.
- [11] J. Fritsche, "Die Tragfahigkeit von Balken aus Stahl mit Berucksichtigung des plastischen Verformungsvermogens." Der bauingenieur 11, pp. 851-855, 873-874 & 888-893, 1930.
- [12] J. H. Schaim, "Der durchlaufende Trager unter Berucksichtigung der Plastizitat." Stahlbau 3, pp. 13-15, 1930.
- [13] K. Girkmann, "Bemessung von Rahmentragwerken unter Zugrundelegung eines ideal plastischen Stahles." in: Sitzungsberichte der Akademie der Wissenschaften in Wien, math-naturw. Klasse Abt. IIa, 140, Band, H. 9u 10, Wien, 1931.
- [14] J. F. Baker and J. W. Roderick, "An experimental Investigation of the Strength of Seven Portal Frames." First interim Report, Research Committee of the Institute of Welding, Transactions of the Institute of Welding, Vol 1, No4, 1938.

-
- [15] J. F. Baker and J. W. Roderick, "Further tests on Beams and Portals." Second interim Report, Research Committee of the Institute of Welding, Transactions of the Institute of Welding, Vol 3, No2, 1940.
- [16] J. F. Baker, M. R. Horne, and J. Heyman, *The Steel Skeleton, Volume 2: Plastic Behaviour and Design*, Cambridge University Press, Cambridge, England. 1956.
- [17] C. Massonnet, "Die europaischen Empfehlungen (EKS) fur die plastische Bemessung von Stahltragwerken." *Acier-Stahl-Steel* 32, pp.146-156, 1976.
- [18] G. C. Driscoll, L. S. Beedle, T. V. Galambos, L. W. Lu, J. W. Fisher, A. Ostapenko, and J. H. Daniels, "Plastic design of multi-story frames-Lecture Notes." Lehigh University, Bethlehem, Pennsylvania, USA, 1965.
- [19] T. V. Galambos, "Structural Members and Frames." Prentice-Hall Series in Structural Analysis and Design (W. J. Hall, editor), Prentice-Hall, London, U.K., 1968.
- [20] B. G. Bryan, "On the Stability of a Plane Plate Under Thrusts in its Own Plane with Application on the Buckling of the Sides of a Ship Proceedings of the London Mathematical Society, 1891, p. 54." Proceedings of the London Mathematical Society, 1891, p. 54., 1891.
- [21] G. Haaijer, "Local buckling of wf shapes in the plastic range, Ph. D. Dissertation, Lehigh University,(1956)," 1956.
- [22] F. Bleich, "Buckling Strength of Metal Structures." Engineering Societies Monographs, McGraw-Hill, New York, USA., 1952.
- [23] B. (Ed. . Johnston, "Guide to Stability Design Criteria for Metal Structures." Structural Stability Research Council, 3rd edition, John Wiley., 1976.
- [24] A. Ostapenko, "Local Buckling." Structural Steel Design, Chapter 17, (L. Tall editor) Robert Kreiger Publishing, Malabar, Florida, USA., 1983.
- [25] S. Timoshenko and J. Gere, "Theory of Elastic Stability, 2nd edition." McGraw-Hill, New York, New York, USA, 1969.
- [26] R. P. Kerfoot, "Rotation capacity of beams, June 1965," 1965.
- [27] T. V. Galambos, "Deformation and energy absorption capacity of steel structures in the inelastic range," *Steel Research Constr.*, 1968.
- [28] N. Stranghoner, "Untersuchungen zum Rotationsverhalten von Trägern aus Hohlprofilen." PhD thesis, RWTH Aachen, Institute of Steel Construction, 1995.
- [29] M. G. Lay and T. V. Galambos, "Inelastic steel beams under uniform moment." Journal of the Structural Division, ASCE 1965;91(6):67-93., 1965.
- [30] G. Sedlacek, Ed., *Investigation of the rotation behaviour of hollow section beams: final report*. Luxembourg: Off. for Off. Publ. of the Europ. Communities, 1998.
- [31] T. M. Chan and L. Gardner, "Bending strength of hot-rolled elliptical hollow sections," *J. Constr. Steel Res.*, vol. 64, no. 9, pp. 971-986, Sep. 2008.
- [32] M. G. Lay and T. V. Galambos, "Inelastic beams under moment gradient." Journal of the Structural Division, ASCE, 1967.
- [33] A. R. Kemp, "Slenderness limits normal to the plane of bending for beam-columns in plastic.pdf." Journal of Constructional Steel Research 4, 135-150, 1984.
-

-
- [34] B. Kato, "Rotation capacity of H-section members as determined by local buckling." *Journal of Constructional Steel Research* 13, 95-109, 1989.
- [35] R. D. Ziemian, W. McGuire, and G. G. Deierlein, "Inelastic limit states design, Part I: Planar frame studies." *J. of St. Eng., ASCE*, 118(9), pp. 2532–2549., 1992.
- [36] A. F. Luckey and P. F. Adams, "Rotation capacity of beams under moment gradient." *J. Struct. Div., Proceedings of ASCE*, 95(ST6) 1173, 1969.
- [37] U. Kuhlmann, "Definition of flange slenderness limits on the basis of rotation capacity values," *J. Constr. Steel Res.*, vol. 14, no. 1, pp. 21–40, 1989.
- [38] N. Stranghoner, G. Sedlacek, and P. Boeraeve, "Rotation requirement and rotation capacity of rectangular, square and circular hollow section beams." *Tubular structures VI*, Grundy, Holgate & Wong (eds), 1994.
- [39] J. M. Ricles, S. Sause, and P. S. Green, "High-strength steel: implications of material and geometric characteristics on inelastic flexural behavior." *Eng. Struct.* 20 (4–6), 323–335., 1998.
- [40] J. Wang, S. Afshan, M. Gkantou, M. Theofanous, C. Baniotopoulos, and L. Gardner, "Flexural behaviour of hot-finished high strength steel square and rectangular hollow sections," *J. Constr. Steel Res.*, vol. 121, pp. 97–109, Jun. 2016.
- [41] T. Wilkinson, "The Plastic Behaviour of Cold-Formed Rectangular Hollow Sections." 1999.
- [42] P. Boeraeve and B. Lognard, "Elasto-plastic behaviour of steel frame works." *Journal of Constructional Steel Research* 27, 3-11, 1993.
- [43] Y. Shifferaw and B. W. Schafer, "Inelastic bending capacity in cold-formed steel members." *Annual SSRC Stability Conference*, 2007.
- [44] S. Afshan and L. Gardner, "The continuous strength method for structural stainless steel design." *Thin-Walled Structures* 68: 42-49, 2013.
- [45] B. G. Neal, *The plastic methods of structural analysis*. London; New York: Chapman and Hall ; Wiley, 1977.
- [46] B. Wong, *Plastic analysis and design of steel structures*, 1st ed. Amsterdam ; Boston: Butterworth-Heinemann, 2009.
- [47] G. C. Driscoll Jr, "Rotation capacity requirements for beams and frames of structural steel, Ph. D. Dissertation, Lehigh University,(1958)," 1958.
- [48] J. Yura, T. V. Galambos, and M. Ravindra, "The bending resistance of steel beams." *Journal of the structural division*, 1978.
- [49] Eurocode 3 Editorial Group, "The b/t Ratios Controlling the Applicability of Analysis Models in Eurocode 3." Document 5.02, Background Documentation to Chapter 5 of Eurocode 3, Aachen University, Germany., 1989.
- [50] R. M. Korol and J. Hudoba, "Plastic Behavior of Hollow structural sections.pdf." *Journal of the structural division, American Society of Civil Engineers*, Vol 98, No ST5, pp 1007-1023, 1972.
- [51] S. W. Hasan and G. J. Hancock, "Plastic Bending Tests of Cold-Formed Rectangular Hollow Sections." 1989.
-

-
- [52] X. L. Zhao and G. J. Hancock, "Tests to determine plate slenderness limits for cold-formed rectangular hollow sections of grade C450." *Journal of the Australian Steel Institute* 25(4):2-16, 1991.
- [53] EN 1993-1-1, "Eurocode 3: Design of steel structures, Part 1-1: General rules and rules for buildings." 2005.
- [54] AISC, "Specification for Structural Steel Buildings." American Institute of Steel Construction, Chicago, IL, 2005.
- [55] BS 5950-1:2000, "British Standard BS 5950-1 Structural use of steelwork in buildings, Part 1: Code of practice for design - Rolled and Welded Sections." Great Britain-2000.
- [56] DIN 18800, "DIN 18800_1 Stahlbauten Bemessung & Konstruktion 2." 1990.
- [57] AS 4100, "Australian Standard AS 4100 Steel Structures." 1998.
- [58] G. Haaijer and B. Thurlimann, "On inelastic buckling in steel, *Proc. ASCE*, 84 (EM2), p. 1581,(also *Trans. ASCE*, Vol. 125,(1960), Reprint No. 124 (60-2)," 1958.
- [59] G. Haaijer, "Plate Buckling in the Inelastic Range." *Journal of the Engineering Mechanics Division, Proceedings of the American Society of Civil Engineers*, Vol 83. No EM 2, April 1957, Proceedings Paper No 1212, 1957.
- [60] G. Haaijer and B. Thürlimann, "On inelastic buckling in steel." 1957.
- [61] O. A. Kerensky, A. R. Flint, and W. C. Brown, "The Basis for Design of Beams and Plate Girders in the Revised British Standard 153." *Proceedings of the Institute of Civil Engineers*, Part 3, Vol 5, August 1956, pp 396 - 461, Structural Paper No 48, 1956.
- [62] N. M. Holtz and G. L. Kulak, "Web Slenderness Limits for Compact Beams." *Structural Engineering Report No. 43*, Department of Civil Engineering, University of Alberta, Edmonton, Canada, 1973.
- [63] N. M. Holtz and G. L. Kulak, "Web Slenderness Limits for Non-Compact Beam." *Structural Engineering Report No.51*, Department of Alberta, Edmonton, Canada, 1975.
- [64] M. J. Perlynn and G. L. Kulak, "Web Slenderness Limits for Compact Beam Columns." *Structural Engineering Report No.50*, Department of Alberta, Edmonton, Canada, 1974.
- [65] D. S. Nash and G. L. Kulak, "Web Slenderness Limits for Non-Compact Beam-Columns." *Structural Engineering Report No 53*, Dept of Civil Engineering, University of Alberta, Canada., 1976.
- [66] M. R. Horne, "Plastic Theory of Structures, 2nd edition." nd Pergamon Press, Sydney, Australia, 1979.
- [67] J. L. Dawe and G. L. Kulak, "Local Buckling Behaviour of Beam-Columns." *Journal of Structural Engineering*, American Society of Civil Engineers, Vol 112, No 11, November 1986, pp 2447-2461., 1986.
- [68] A. Della-Croce, "The Strength of Continuously Welded Girders with Unstiffened Webs." *CESRL Thesis No 70-1*, University of Texas at Austin, USA, 1970.
- [69] H. E. Costley, "Lateral and Local Stability of Continuous Beams." *CESRL Thesis No 70-2*, University of Texas at Austin, USA, 1970.
- [70] T. V. Galambos, "Proposed Criteria for Load and Resistance Factor Design of Steel Building Structures." *Research Report No 45*, Civil Engineering Department,
-

-
- Washington University, St. Louis, Mo., USA. (Also published as American Iron and Steel Institute (AISI), Bulletin No 27, January 1978), 1976.
- [71] J. A. Edinger and G. Haaijer, "Plastic Design Requirements of the AISC Proposed LRFD Specification." Plastic and Other Limit States Methods for Design Evaluation, (V. B. Watwood, ed), Proceedings from Structures Congress 1984, San Francisco, California, pp 54 - 73, American Society of Civil Engineers, New York, New York, USA, 1984.
 - [72] S. Bild and G. L. Kulak, "Local Buckling Rules for Structural Steel Members." Journal of Constructional Steel Research 20: 1-52, 1991.
 - [73] A. R. Kemp, "I Interaction of Plastic Local and Lateral Buckling," *J. Struct. Eng.*, vol. 111, no. 10, pp. 2181–2196, 1985.
 - [74] M. L. Daali and R. M. Korol, "Prediction of local buckling and rotation capacity at maximum moment." Journal of Constructional Steel Research 32 (1995) 1-13, 1995.
 - [75] J. Stewart and K. S. Sivakumaran, "Analysis for Local Buckling Limits and Ductility of Steel Members." Proceedings, 1997 Annual Conference of the Canadian Society for Civil Engineering, Sherbrooke, Canada, May 1997, Vol 4, pp 59-68, 1997.
 - [76] M. Seif and B. W. Schafer, "Local buckling of structural steel shapes." Journal of Constructional Steel Research, 2010.
 - [77] M. Seif and B. W. Schafer, "Elastic buckling finite strip analysis of the AISC sections database and proposed local plate buckling coefficients." Structures ASCE, 2009.
 - [78] M. D'Aniello, E. M. Güneyisi, R. Landolfo, and K. Mermerdaş, "Analytical prediction of available rotation capacity of cold-formed rectangular and square hollow section beams," *Thin-Walled Struct.*, vol. 77, pp. 141–152, Apr. 2014.
 - [79] X. L. Zhao and G. J. Hancock, "RHS Tubular Sections Grade C450 Plate Slenderness Limits." 1991.
 - [80] T. Wilkinson and G. J. Hancock, "Tests to examine compact web slenderness of cold-formed RHS," *J. Struct. Eng.*, vol. 124, no. 10, pp. 1166–1174, 1998.
 - [81] L. Gardner, N. Saari, and F. Wang, "Comparative experimental study of hot-rolled and cold-formed rectangular hollow sections," *Thin-Walled Struct.*, vol. 48, no. 7, pp. 495–507, Jul. 2010.
 - [82] J. Rondal, P. Boeraeve, G. Sedlacek, N. Stranghoner, P. Langenberg, and A. D'Hernoncourt, "Rotation Capacity of Hollow Beam Sections." 1995.
 - [83] E. Saloumi, M. Hayeck, J. Nseir, and N. Boissonnade, "Experimental characterization of the rotational capacity of hollow structural shapes." Proceeding of the 15th International Symposium on Tubular Structures, 2015.
 - [84] H. A. Sawyer, "Post-Elastic Behavior of Wide-flange Steel Beams." ASCE Journal of structural Division, Vol. 87, No. ST 8, Paper 3016, pp 43-71, 1961.
 - [85] A. F. Lukey and P. F. Adams, "Rotation Capacity of Wide-Flange Beams under moment Gradient." ASCE Journal of the Structural Division, Vol 95. No. ST.6 Paper 6599, pp. 1173-1188, 1969.
 - [86] K. Roik and U. Kuhlmann, "Experimentelle Ermittlung der Rotationskapazität biegebeanspruchter I-Profil (Teil 2)." Der Stahlbau (56), Heft 12, 1987.
-

-
- [87] K. Roik and U. Kuhlmann, "Rechnerische Ermittlung der Rotationskapazität biegebeanspruchter I-Profile (Teil 1)." *Der Stahlbau* (56), Heft 11, 1987.
- [88] U. Kuhlmann, "Rotationskapazität von I-Profilen unter Berücksichtigung des plastischen Beulens." Dissertation Bochum, 1986.
- [89] P. F. Adams, M. G. Lay, and T. V. Galambos, "Experiments on High-Strength Steel Beams." Welding Research Council, Bulletin No. 110, 1965.
- [90] I. F. Mc.Dermott, "Local plastic buckling of A514 Steel Members." *ASCE Journal of the structural Division*, Vol. 95, No. St9, pp. 1897-1850, 1969.
- [91] S. Torabian and B. W. Schafer, "Role of local slenderness in the rotation capacity of structural steel members," *J. Constr. Steel Res.*, vol. 95, pp. 32–43, Apr. 2014.
- [92] L. Gardner, N. Saari, and F. Wang, "Comparative experimental study of hot-rolled and cold-formed rectangular hollow sections." *Thin-Walled Structures* 48: 495-507, 2010.
- [93] EN 10210-2, "Hot finished structural hollow sections of non-alloy and fine grain steels, Part 2: Tolerances, dimensions and sectional properties." 2006.
- [94] EN 10219-2, "Cold formed welded structural hollow sections of non-alloy and fine grain steels, Part 2: Tolerances, dimensions and sectional properties." 2006.
- [95] S. Afshan, B. Rossi, and L. Gardner, "Strength enhancements in cold-formed structural sections — Part I: Material testing," *J. Constr. Steel Res.*, vol. 83, pp. 177–188, Apr. 2013.
- [96] K. J. R. Rasmussen and Hancock, "Design of cold-formed stainless steel tubular members I: columns." *Journal of Structural Engineering*, American Society of Civil Engineers, Vol. 119, pp 2349-2367, 1993.
- [97] K. J. R. Rasmussen and Hancock, "Design of cold-formed stainless steel tubular members II: Beams." *Journal of Structural Engineering*, American Society of Civil Engineers, Vol. 119, pp 2368-2386, 1993.
- [98] K. J. R. Rasmussen, "Recent research on stainless steel tubular structures." *Journal of structural engineering*, Vol 54, No. 1, pp. 75-88, 2000.
- [99] EN 1993-1-3, "Eurocode 3: Design of steel structures - Part 1.3: General rules - Supplementary rules for cold-formed members and sheeting." 2006.
- [100] H. T. Li and B. Young, "Experimental investigation of cold-formed high strength steel tubular sections undergoing web crippling." 15th International Symposium on Tubular Structures 27-29 May 2015, 2015.
- [101] A. Liew, "Design of Structural Steel Elements with the Continuous Strength Method." 2014.
- [102] T. M. Chan and L. Gardner, "Bending strength of hot-rolled elliptical hollow sections," *J. Constr. Steel Res.*, vol. 64, no. 9, pp. 971–986, Sep. 2008.
- [103] Greish and Ulg, Finelg, "Non linear finite element analysis software." University of Liege- The engineering office Greisch, 1999.
- [104] J. Nseir, "Development of a new design method for the cross-section capacity of steel hollow sections," 2015.
-

-
- [105] O. Zhao, B. Rossi, L. Gardner, and B. Young, "Behaviour of structural stainless steel cross-sections under combined loading – Part II: Numerical modelling and design approach," *Eng. Struct.*, vol. 89, pp. 247–259, Apr. 2015.
- [106] X. Yun and L. Gardner, "Four-linear Full-Range Stress-strain Model for Hot-rolled Carbon Steels." submission expected in-2016.
- [107] R. Greiner, M. Kettler, A. Lechner, B. Freytag, J. Linder, J. P. Jaspart, N. Boissonnade, E. Bortolotti, K. Weynand, C. Ziller, and R. Oerder, "SEMI-COMP: RFSR-CT-2004-00044 Plastic Member Capacity of Semi-Compact Steel Sections - a more Economic Design." 2008.
- [108] P. W. Key and G. J. Hancock, "A theoretical investigation of the column behaviour of cold-formed square hollow sections." *Thin-walled structures* 16, 31-64, 1993.
- [109] M. Jandera, L. Gardner, and J. Machacek, "Residual stresses in cold-formed stainless steel hollow sections." *Journal of Constructional Steel Research* 64, 1255-1263, 2008.
- [110] M. Jandera and J. Machacek, "Residual stress pattern of Stainless steel." 2010.
- [111] B. W. Schafer and T. Pekoz, "Computational modeling of cold-formed steel characterizing geometric imperfections and residual stresses." *Journal of Constructional Steel Research*, 1998.
- [112] EN 1993-1-5, "Eurocode 3: Design of Steel Structures, Part 1-5: Plated structural elements." 2005.
- [113] V. M. Zeinoddini and B. W. Schafer, "Simulation of geometric imperfections in cold-formed steel members using spectral representation approach." *Thin-Walled Struct*;60:105–17., 2012.
- [114] R. G. Dawson and A. C. Walker, "Post-buckling of geometrically imperfect plates." *Journal of Structural division ASCE*;98(1): 75-94, 1972.
- [115] M. G. Lay, "Some studies of flange local buckling in wide-flange shapes, *Proc. ASCE*, Vol. 91, ST6, December 1965, Publication No. 288 (65-23)," 1965.
- [116] M. G. Lay and T. V. Galambos, "Inelastic beams under moment gradient." *J. Struct. Div. ASCE* 93 (1) (1967) 381–399., 1993.
- [117] R. Maquoi and J. Rondal, "Mise en equation des nouvelles courbes européennes de flambement," *Constr. Métallique N 1 Pp* 17-30, 1978.
- [118] J. Rondal, "Contribution à l'étude de la stabilité des profils creux à parois minces." Université de Liège, 1984.

9 LIST OF FIGURES

Figure 1.1 – OIC steps; χ_{CS} represents the cross-section reduction factor; χ_{CS+MB} represents the member reduction factor; γ_M and ϕ represent safety factors.....	20
Figure 1.2 – Criterion to allow for plastic analysis	21
Figure 2.1 – Idealised moment-strain behaviour of a hollow cross-section.....	25
Figure 2.2 – Local buckling of a rectangular plate	26
Figure 2.3 – Plate buckling coefficient	27
Figure 2.4 – Generalized moment-rotation curve and definition of the rotation capacity	28
Figure 2.5 – Moment-rotation curve for different sections with the EC3 classification.....	29
Figure 2.6 – Beam under uniform moment	30
Figure 2.7 – Beam under moment gradient.....	32
Figure 2.8 – Theoretical load-deflection curve for two-span pitched frame [47]	37
Figure 2.9 – Rotation requirement for structures as summarised in [49].....	38
Figure 2.10 – Normalised ultimate as function of the plate slenderness from experimental data of hollow section	48
Figure 2.11 – Rotation capacity as function of the plate slenderness from experimental data of hollow section	49
Figure 2.12 – Normalised ultimate as function of the plate slenderness from experimental data of open section	50
Figure 2.13 – Rotation capacity as function of the plate slenderness from experimental data of open section.....	50
Figure 3.1 – Segmentation of received beams (dimensions in <i>mm</i>).....	52
Figure 3.2 – Cross-section dimensions	54

Figure 3.3 – Example of detailed cross-section measurement for RHS_220x120x6.3_SS_3P along with the Eurocode tolerances	55
Figure 3.4 – Tensile coupon testing	56
Figure 3.5 – Tensile coupon dimensions and locations of the tensile coupons	56
Figure 3.6 – Example of some tested coupons.....	57
Figure 3.7 – Stress strain curve for RHS_150×100×8_SS coupon.....	57
Figure 3.8 – Stress-strain constitutive law parameters.....	58
Figure 3.9 – General test set-up of stub columns.....	59
Figure 3.10 – Failure shapes of tested stub columns.....	60
Figure 3.11 – a) Normalized load displacement curves – b) Strain gauges measurements	62
Figure 3.12 – Test setup of the 3-point bending beam, longitudinal view (dimensions in <i>mm</i>)	64
Figure 3.13 – Test setup of the 3-point bending beam, transversal view (dimensions in <i>mm</i>)	64
Figure 3.14 – Position of the variable transducers on the 3-point bending beam (dimensions in <i>mm</i>).....	65
Figure 3.15 – Deformed shape a RHS_150×100×5_SS_3P	65
Figure 3.16 – Onset of local buckling	66
Figure 3.17 – 3-Point bending analysis.....	67
Figure 3.18 – a) Normalized moment - rotation curves – b) Normalized load - deflection curves	67
Figure 3.19 – Test setup of the 4-point bending beam.....	69
Figure 3.20 – Deformed shape of a 4-point bending beam.....	69
Figure 3.21 – a) Moment-rotation curve of RHS_220×120×6.3 – b) Relative deflected shape of RHS_180×80×4.5	70

Figure 3.22 – a) Onset of local buckling for RHS_180x80x4.5 – b) Deflected shape of RHS_150x100x8.....	70
Figure 3.23 – 4-Point bending analysis.....	71
Figure 3.24 – Normalized moment curvature for RHS_180x80x4.5_SS_4P.....	73
Figure 3.25 – Comparison between 3-point and 4-point configurations of RHS 220x120x6.3 and RHS_150x100x5.....	74
Figure 3.26 – Propped-cantilever centrally loaded analysis	75
Figure 3.27 – Test setup of the propped cantilever centrally loaded	76
Figure 3.28 – a) Deformed shape of a propped cantilever centrally loaded – b) Connection detail on braced support	77
Figure 3.29 – a) Normalized moment - rotation of RHS_180x80x4.5 – b) Moment - curvature of RHS_180x80x4.5	78
Figure 3.30 – Load cell arrangement in the test setup	78
Figure 3.31 – a) Normalized moment - rotation of RHS_220x120x6.3 – b) Normalized total load – span displacement of RHS_220x120x6.3	79
Figure 3.32 – a) braced connection for RHS_180x80x4.5 – b) RHS_150x100x5 – c) plate deformation for the case of RHS_220x120x6.3	79
Figure 3.33 – Normalized moment - rotation of RHS_180x80x4.5 – comparison between moment from test load cells, strain gauges and theoretical calculations	81
Figure 3.34 – Normalized load - displacement of RHS_180x80x4.5 – comparison between test results and theoretical calculations	81
Figure 3.35 – Test setup of the propped cantilever off-centrally loaded	82
Figure 3.36 – Deflected shape of a propped cantilever off-centrally loaded	83
Figure 3.37 – Propped cantilever centrally loaded diagrams	84

Figure 3.38 – a) Normalized moment - rotation of RHS_180×80×4.5 – b) Normalized total load – span displacement.....	84
Figure 3.39 – a) Normalized moment - rotation of RHS_180×80×4.5 – comparison between moment from test load cells, strain gauges and theoretical calculations	85
Figure 4.1 – a) Adopted material law for hot-formed sections	88
Figure 4.2 – a) Adopted simple Ramberg-Osgood material law for flat regions – b) Adopted multi-linear material law for corner regions [104].....	89
Figure 4.3 – Auto-equilibrated residual stress pattern for Hot-formed tubular profiles - SHS and RHS	89
Figure 4.4 – Different adopted mesh densities.....	91
Figure 4.5 – Yield extent at final step	91
Figure 4.6 – G.M.N.I.A. results, maximum load and load-deflection curves for RHS_180×80×4.5_PR_C	92
Figure 4.7 – G.M.N.I.A. results, normalised maximum moment of the 3-pt bending tests for different meshes	93
Figure 4.8 – G.M.N.I.A. results, normalised maximum moment of the 4-pt bending tests for different meshes	93
Figure 4.9 – G.M.N.I.A. results, normalised maximum load of the PR_C tests for different meshes	94
Figure 4.10 – G.M.N.I.A. results, normalised maximum load of the PR_O tests for different meshes	94
Figure 4.11 – Modelling of propped cantilever beam.....	95
Figure 4.12 – Details of supports modelling	95
Figure 4.13 – Loading variation.....	96

Figure 4.14 – Load introduction influence in term of maximum moment and moment-rotation curves for SHS_180×6.3_SS_3P.....	97
Figure 4.15 – Considered geometrical imperfections	98
Figure 4.16 – Amplified geometrical imperfections	98
Figure 4.17 – Imperfections sensitivity for SHS_180×6.3_PR_C, a) comparison of the normalised ultimate load, b) load-displacement curves for the different imperfection patterns	100
Figure 4.18 – Imperfections sensitivity for RHS_150×100×5_SS_4P, a) comparison of the normalised ultimate load, b) load-displacement curves for the different imperfection patterns	100
Figure 4.19 – Imperfections sensitivity for SHS_180×6.3_SS_3P, a) comparison of the normalised ultimate load, b) load-displacement curves for the different imperfection patterns	100
Figure 4.20 – RHS_220×120×6.3_SS_3P validation.....	102
Figure 4.21 – SHS_180×8_SS_4P validation	104
Figure 4.22 – Summary comparison of ultimate moments for the simply-supported configuration	106
Figure 4.23 – $M_{ult,exp}$ vs. $M_{ult,FE}$ for simply-supported configurations	106
Figure 4.24 – Bolts distribution on the end-plate of the propped cantilever tests.....	107
Figure 4.25 – Modelling of the ideally-fixed end for propped cantilever configurations.....	108
Figure 4.26 – SHS_180×80×4.5_PR_C; ideally-fixed end vs. end plate.....	108
Figure 4.27 – SHS_180×6.3_PR_C; ideally-fixed end vs. end plate	109
Figure 4.28 – SHS_180×6.3_PR_C validation	110
Figure 4.29 – Results for SHS_180×80×4.5_PR_C.....	110
Figure 4.30 – RHS_180×80×4.5_PR_O; ideally-fixed end vs. end plate	112

Figure 4.31 – SHS_180×6.3_PR_O; ideally-fixed end vs. end plate.....	112
Figure 4.32 – Results for SHS_180×6.3_PR_O.....	113
Figure 4.33 – Numerical vs. experimental results for the propped cantilever configurations	115
Figure 4.34 – Wilkinson test setup and the “parallel plate” loading method [41].	116
Figure 4.35 – FINELg model of Wilkinson 4-pt bending test setup using the “parallel plate” loading method.....	117
Figure 4.36 – Typical measured stress-strain curves [41].....	117
Figure 4.37 – BS08B validation [41].	119
Figure 4.38 – Experimental ultimate vs. F.E. (full) model results – Wilkinson’s test data ...	122
Figure 5.1 – Typical stress-strain curve of hot-rolled carbon steels and the proposed four- linear material model [106].	125
Figure 5.2 – Hot-formed material model considered for different yield strengths	126
Figure 5.3 – Typical stress-strain curves for cold-formed carbon steels; simple Ramberg- Osgood law for flat regions and a multi-linear material model for corner regions.....	127
Figure 5.4 – Cold-formed material model considered in the flat and corner region for each nominal yield strength.....	128
Figure 5.5 – Adopted boundary conditions and loading introduction.....	129
Figure 5.6 – Deformation of a beam under constant bending moment.....	130
Figure 5.7 – Moment rotation curve for SHS 80x5 S355 under constant moment from FINELg calculations	132
Figure 5.8 – Moment rotation curve for SHS 90x5 S355 under constant moment from FINELg calculations	133
Figure 5.9 – Meshing types	134

Figure 5.10 – Moment capacity of square and rectangular hollow section under constant moment for different meshes.....	135
Figure 5.11 – Rotation capacity of square and rectangular hollow section under constant moment for different meshes.....	135
Figure 5.12 – Moment rotation curves of square hollow section under constant moment for different meshes; HSS refers to Hollow Structural Shape	136
Figure 5.13 – Moment rotation curves of rectangular hollow section with $h/b=1.5$, under constant moment for different meshes; HSS refers to Hollow Structural Shape	136
Figure 5.14 – Moment rotation curves of rectangular hollow section with $h/b=2$, under constant moment for different meshes; HSS refers to Hollow Structural Shape	136
Figure 5.15 – Moment rotation curves of rectangular hollow section with $h/b=2.5$, under constant moment for different meshes; HSS refers to Hollow Structural Shape	137
Figure 5.16 – Amplified imperfections for configuration 1	138
Figure 5.17 – Amplified imperfections for configuration 2	139
Figure 5.18 – Amplified imperfections for configuration 3; a) $h / b = 1$, b) $h / b = 2$	139
Figure 5.19 – Amplified imperfections for configuration 5 (4-pt bending).....	140
Figure 5.20 – Moment capacity for square and rectangular hollow section under constant moment with length variation	142
Figure 5.21 – Rotation capacity for square and rectangular hollow section under constant moment with length variation	142
Figure 5.22 – Moment rotation curves for square hollow section under constant moment with length variation.....	143
Figure 5.23 – Moment rotation curves for rectangular hollow section with $h/b=1.5$, under constant moment with length variation	144
Figure 5.24 – Moment rotation curves for rectangular hollow section with $h/b=2$, under constant moment with length variation	144

Figure 5.25 – Moment rotation curves for rectangular hollow section with $h/b=2.5$, under constant moment with length variation	144
Figure 5.26 – Amplification of the effect of flexural residual stresses on a beam.....	145
Figure 5.27 – Influence of residual stresses of hot-formed section in terms of moment rotation curves. Specific case of hollow structural sections, $h / b = 2$, $b / t = 23$ under constant moment	146
Figure 5.28 – Effect of residual stresses on the rotation capacity of hot-formed hollow structural sections under constant moment, a) $h / b = 1$, b) $h / b = 1.5$ – the rotation capacity limit of 3 represent the minimum required rotation in the EC3 for plastic analysis to be performed	147
Figure 5.29 – Effect of residual stresses on the rotation capacity of hot-formed hollow structural sections under constant moment, a) $h / b = 2$, b) $h / b = 2.5$	147
Figure 5.30 – Influence of residual stresses of cold-formed section in terms of moment rotation curves. Specific case of hollow structural sections, $h / b = 2$, $b / t = 23$ under constant moment.....	148
Figure 5.31 – Effect of residual stresses on the normalised ultimate capacity and rotation capacity of cold-formed hollow structural sections under constant moment for $h / b = 1$	149
Figure 5.32 – Effect of residual stresses on the normalised ultimate capacity and rotation capacity of cold-formed hollow structural sections under constant moment for $h / b = 1.5$..	149
Figure 5.33 – Effect of residual stresses on the normalised ultimate capacity and rotation capacity of cold-formed hollow structural sections under constant moment for $h / b = 2$	149
Figure 5.34 – Effect of residual stresses on the normalised ultimate capacity and rotation capacity of cold-formed hollow structural sections under constant moment for $h / b = 2.5$..	150
Figure 5.35 – Considered local geometrical imperfections.....	151
Figure 5.36 – Amplified geometrical imperfections for RHS with $h/b=2$	151
Figure 5.37 – Rotation capacity of hot-rolled square hollow section for different geometrical imperfection patterns.....	153

Figure 5.38 – Rotation capacity of hot-rolled rectangular hollow section with $h / b = 1.5$ for different geometrical imperfection patterns	154
Figure 5.39 – Rotation capacity of hot-rolled rectangular hollow section with $h / b = 2$ for different geometrical imperfection patterns	154
Figure 5.40 – Rotation capacity of hot-rolled rectangular hollow section with $h / b = 2.5$ for different geometrical imperfection patterns	155
Figure 5.41 – Rotation capacity of cold-formed square hollow section for different geometrical imperfection patterns	157
Figure 5.42 – Rotation capacity of cold-formed rectangular hollow section with $h/b=1.5$ for different geometrical imperfection patterns	158
Figure 5.43 – Rotation capacity of cold-formed rectangular hollow section with $h/b=2$ for different geometrical imperfection patterns	158
Figure 5.44 – Rotation capacity of cold-formed rectangular hollow section with $h/b=2.5$ for different geometrical imperfection patterns	159
Figure 5.45 – Adopted material laws for the effect of strain hardening sub-study	160
Figure 5.46 – Different steel grade for a material law	160
Figure 5.47 – Normalised load and rotation capacities as a function of λ_{CS} for different material law of $h / b = 1$	161
Figure 5.48 – Normalised load and rotation capacities as a function of λ_{CS} for different material law of $h / b = 1.5$	162
Figure 5.49 – Normalised load and rotation capacities as a function of λ_{CS} for different material law of $h / b = 2$	162
Figure 5.50 – Normalised load and rotation capacities as a function of λ_{CS} for different material law of $h / b = 2.5$	162
Figure 5.51 – Constant moment modelling	164
Figure 5.52 – 3-point bending modelling	164

Figure 5.53 – Relative moment capacity of hot-formed sections subjected to constant moment	167
Figure 5.54 – Strain hardening effect on the rotation capacity of hot-formed sections subjected to constant moment – scale of the rotation capacity ranges from 0 to 50	167
Figure 5.55 – Rotation capacity of hot-formed section subjected to constant moment – scale of the rotation capacity ranges from 0 to 20; sections with higher rotation capacities values were disregarded	168
Figure 5.56 – Effect of aspect ratio on the moment capacity of hot-formed sections subject to constant moment for S235.....	169
Figure 5.57 – Effect of aspect ratio on the rotation capacity of hot-formed sections subject to constant moment for S235.....	170
Figure 5.58 – Rotation capacity of experimental and numerical data for hot-formed section subject to constant moment.....	171
Figure 5.59 – Comparison between the moment capacity of cold-formed and hot-formed sections subjected to constant moment	172
Figure 5.60 – Comparison between the rotation capacity of cold-formed and hot-formed sections subjected to constant moment	172
Figure 5.61 – Normalised moment capacity of cold-formed sections subjected to constant moment for various steel grades.....	173
Figure 5.62 – Rotation capacity of cold-formed sections subjected to constant moment for various steel grades	174
Figure 5.63 – Normalised ultimate strain of cold-formed sections subjected to constant moment.....	174
Figure 5.64 – Moment-rotation curves for different cross-section slenderness of cold-formed sections	176
Figure 5.65 – Effect of aspect ratio on the flexural capacity cold-formed sections subject to constant moment for S235.....	176

Figure 5.66 – Rotation capacity of experimental and numerical data for cold-formed section subjected to constant moment	177
Figure 5.67 – Amplified initial imperfection possibilities for 3-pt bending configuration....	178
Figure 5.68 – Moment rotation response of two beams under different Initial imperfection possibilities.....	179
Figure 5.69 – Moment capacities of beams under a constant moment versus 3-point bending configuration	180
Figure 5.70 – Rotation capacities of beams under a constant moment versus 3-point bending configuration	180
Figure 5.71 – Ultimate moment capacity for the 3-pt bending configuration for different yield stresses.....	181
Figure 5.72 – Rotation capacity for the 3-pt bending configuration for different yield stresses	182
Figure 5.73 – Ultimate moment capacity for square hollow sections, $L/h=10$, for different yield stresses.....	182
Figure 5.74 – Rotation capacity for square hollow sections, $L/h=10$, for different yield stresses	183
Figure 5.75 – Normalised ultimate moment capacity for Square, hot-formed section with 3-pt bending configuration and S235 yield stress for various L / h ratios.	184
Figure 5.76 – Rotation capacity for Square, hot-formed section with 3-pt bending configuration and S235 yield stress for various L / h ratios.....	185
Figure 5.77 – Effect of the aspect ratio on the rotation capacity for 3-pt bending beams	186
Figure 5.78 – Rotation capacity for hot-formed section with 3-pt bending configuration and S235 yield stress for various L / h ratios.	186
Figure 5.79 – Experimental and numerical data for hot-formed section in the 3-pt bending arrangement.....	187

Figure 5.80 – Normalised moment capacity of cold-formed sections in the 3-pt bending configuration and for different yield stresses	188
Figure 5.81 – Rotation capacity of cold-formed sections in the 3-pt bending configuration and for different yield stresses	188
Figure 5.82 – Rotation capacity of S235 cold-formed sections in the 3-pt bending configuration for different moment gradient.....	189
Figure 5.83 – Rotation capacity of experimental and numerical data for cold-formed section under 3-pt bending arrangement.	189
Figure 6.1 – Hot-formed numerical results represented in a logarithmic scale	194
Figure 6.2 – Proposed curve for hot-formed sections under constant moment.....	195
Figure 6.3 – Cross-section slenderness limiting value that ensures 95% of M_{pl} is reached.	196
Figure 6.4 – Rotation capacity of hot-formed sections under constant moment as a function of plate slenderness.....	197
Figure 6.5 – Proposed flange slenderness limit for hot-formed sections.	198
Figure 6.6 – Proposed web slenderness limit for hot-formed sections.	199
Figure 6.7 – Proposed curve for cold-formed sections under constant moment.....	201
Figure 6.8 – Cross-section slenderness limiting value that would eventually permit plastic analysis.	202
Figure 6.9 – Proposed curve for S235 cold-formed sections under constant moment.....	204
Figure 6.11 – Proposed curve for S355 cold-formed sections under constant moment.....	204
Figure 6.12 – Proposed curve for S460 cold-formed sections under constant moment.....	205
Figure 6.13 – Proposed single curve for cold-formed sections under constant moment	206
Figure 6.14 – Numerical data of Cold-formed sections under constant moment with $\lambda_{CS} < 0.4$ in a logarithmic scale.....	206

Figure 6.15 – Proposed plate slenderness limit for cold-formed sections	207
Figure 6.16 – Proposed flange slenderness limit for cold-formed sections	208
Figure 6.17 – Proposed web slenderness limit for cold-formed sections.....	208
Figure 6.18 – Numerical results of hot-formed section under a point load represented in a logarithmic scale	210
Figure 6.19 – Proposed curve for hot-formed sections under a point load	211
Figure 6.20 – Cross-section slenderness limiting value for plastic analysis.....	211
Figure 6.21 – Rotation capacity of hot-formed section under a moment gradient as a function of plate slenderness.	212
Figure 6.22 – Proposed curve for cold-formed sections under a point load	214
Figure 6.23 – Cross-section slenderness limiting value to allow for plastic analysis.....	215
Figure 6.24 – Proposed curve for S235 cold-formed sections under a point load	215
Figure 6.25 – Proposed curve for S355 cold-formed sections under a point load	216
Figure 6.26 – Proposed curve for S460 cold-formed sections under a point load	216
Figure 6.27 – Proposed single curve for cold-formed sections under a point load.....	217
Figure 6.28 – Numerical data of Cold-formed sections under a point load with $\lambda_{cs} < 0.4$ in a logarithmic scale	218

10 LIST OF TABLES

Table 2.1 – Denomination of cross-section classes in each specification.....	40
Table 2.2 – Plastic flange slenderness limits of RHS in bending	42
Table 2.3 – Plastic web slenderness limits of RHS in bending.....	43
Table 2.4 – Class 1-2 slenderness limit according to EC3 definition	44
Table 2.5 – Collected bending test data for hollow sections.....	48
Table 3.1 – Test program for cross-sectional tests.....	53
Table 3.2 – Average measured dimensions.....	55
Table 3.3 – Average material properties of tested profiles	58
Table 3.4 – Cross-section classification.....	61
Table 3.5 – Measured properties and ultimate loads of stub columns	61
Table 3.6 – Results at collapse for the 3-point bending tests	68
Table 3.7 – Collapse results for the 4-point bending tests	72
Table 3.8 – Comparison of ultimate bending moments between 3-point and 4-point bending configurations.....	74
Table 3.9 – Collapse results for the centrally loaded propped cantilever	82
Table 3.10 – Collapse results for the off-centrally loaded propped cantilever	85
Table 4.1 – 3-pt bending numerical results	102
Table 4.2 – Numerical vs. experimental results for 3-pt bending tests	103
Table 4.3 – 4-pt bending numerical results	105
Table 4.4 – Numerical vs. experimental results for 4-pt bending tests	105
Table 4.5 – PR_C numerical results.....	111

Table 4.6 – Numerical vs. experimental results for PR_C tests.....	111
Table 4.7 – PR_O numerical results.....	113
Table 4.8 – Numerical vs. experimental results for PR_O tests	114
Table 4.9 – Results of Wilkinson’s bending tests.	120
Table 4.10 – Numerical vs. experimental results for Wilkinson’s bending tests.....	121
Table 5.1 – Parameters for hot-formed material law for S235, S355 and S460	126
Table 5.2 – Parameters of the corner region material for S235, S355 and S460 cold-formed sections	128
Table 5.3 – Rotation capacity for different configurations and comparison.....	143
Table 6.1 – Theoretical limit values.....	220
Table 6.2 – Theoretical limit values.....	221

11 APPENDICES

11.1 APPENDIX 1 – Experimental database for hollow sections

Zhao & Hancock 1991

Sample	Origin	fabrication process	Loading method	Test configuration	h [mm]	B [mm]	t [mm]	r [mm]	f_y [N/mm ²]	f_u [N/mm ²]	M_{ply} [kN.m]	M_{max} [kN.m]	$M_{max} / M_{ply} [-]$	R_{cap}	λ_{CS}	λ_p
SHS 100x100x3.8-CF	Zhao & Hancock 1991	Cold formed	Parallel	4-pt bending	100.27	100.17	3.797	7.60	459	513	24.33	30.39	1.249	4.17	0.58	0.53
SHS 100x100x3.3-CF		Cold formed	Parallel	4-pt bending	100.18	100.2	3.467	6.27	435	495	21.17	27.75	1.311	3.55	0.62	0.58
SHS 100x100x2.8-CF		Cold formed	Parallel	4-pt bending	100.17	100.17	2.77	4.12	466	520	18.37	18.26	0.994	-	0.81	0.80
SHS 75x75x3.3-CF		Cold formed	Parallel	4-pt bending	75.17	75.13	3.37	5.82	462	521	12.04	14.65	1.217	>5.6	0.47	0.44
SHS 75x75x2.8-CF		Cold formed	Parallel	4-pt bending	75.13	75.17	2.783	4.11	490	535	10.72	12.62	1.177	2.76	0.61	0.59
SHS 75x75x2.3-CF		Cold formed	Parallel	4-pt bending	75.17	75.08	2.297	3.35	469	520	8.58	8.94	1.042	1.41	0.71	0.72
SHS 65x65x2.3-CF		Cold formed	Parallel	4-pt bending	64.93	65.1	2.277	3.36	479	528	6.44	7.22	1.121	2	0.64	0.62
RHS 125x75x3.8-CF		Cold formed	Parallel	4-pt bending	125.02	75.12	3.76	7.62	448	491	26.97	34.90	1.294	5.97	0.46	0.36
RHS 125x75x3.3-CF		Cold formed	Parallel	4-pt bending	125.03	75.1	3.273	5.86	452	499	23.91	29.74	1.244	4.79	0.52	0.45
RHS 100x50x2.8-CF		Cold formed	Parallel	4-pt bending	100.02	50.18	2.823	4.09	451	519	11.88	15.62	1.315	7.37	0.42	0.34

Sample	Origin	fabrication process	Loading method	Test configuration	D [mm]	B [mm]	t [mm]	r [mm]	f_y [N/mm ²]	f_u [N/mm ²]	M_{ply} [kN.m]	M_{max} [kN.m]	$M_{max} / M_{ply} [-]$	R_{cap}	λ_{CS}	λ_p
SHS 100x100x3.8-CF	Zhao & Hancock 1991	Cold formed	Parallel	4-pt bending	100.27	100.17	3.797	7.60	459	513	24.33	30.39	1.249	4.17	0.58	0.53
SHS 100x100x3.3-CF		Cold formed	Parallel	4-pt bending	100.18	100.2	3.467	6.27	435	495	21.17	27.75	1.311	3.55	0.62	0.58
SHS 100x100x2.8-CF		Cold formed	Parallel	4-pt bending	100.17	100.17	2.77	4.12	466	520	18.37	18.26	0.994	-	0.81	0.80
SHS 75x75x3.3-CF		Cold formed	Parallel	4-pt bending	75.17	75.13	3.37	5.82	462	521	12.04	14.65	1.217	>5.6	0.47	0.44
SHS 75x75x2.8-CF		Cold formed	Parallel	4-pt bending	75.13	75.17	2.783	4.11	490	535	10.72	12.62	1.177	2.76	0.61	0.59
SHS 75x75x2.3-CF		Cold formed	Parallel	4-pt bending	75.17	75.08	2.297	3.35	469	520	8.58	8.94	1.042	1.41	0.71	0.72
SHS 65x65x2.3-CF		Cold formed	Parallel	4-pt bending	64.93	65.1	2.277	3.36	479	528	6.44	7.22	1.121	2	0.64	0.62
RHS 125x75x3.8-CF		Cold formed	Parallel	4-pt bending	125.02	75.12	3.76	7.62	448	491	26.97	34.90	1.294	5.97	0.46	0.36
RHS 125x75x3.3-CF		Cold formed	Parallel	4-pt bending	125.03	75.1	3.273	5.86	452	499	23.91	29.74	1.244	4.79	0.52	0.45
RHS 100x50x2.8-CF		Cold formed	Parallel	4-pt bending	100.02	50.18	2.823	4.09	451	519	11.88	15.62	1.315	7.37	0.42	0.34

Wilkinson & Hancock 1998

Sample	Origin	fabrication process	Loading method	Test configuration	h [mm]	b [mm]	t [mm]	r [mm]	f_v [N/mm ²]	f_u [N/mm ²]	M_{ply} [kN.m]	M_{max} [kN.m]	M_{max}/M_{ply}	R_{cap}	λ_{CS}	λ_p
150x50x5.0 C450	Wilkinson & Hancock 1998	Cold formed	Parallel	4-pt bending	151.04	50.25	4.92	7.44	441	495	35.51	43.8	1.23	0	0.30	0.26
150x50x5.0 C450		Cold formed	Parallel	4-pt bending	150.92	50.41	4.9	8.25	441	495	35.14	41.1	1.17	>9.0	0.30	0.26
150x50x4.0 C450		Cold formed	Parallel	4-pt bending	150.43	50.27	3.92	4.84	457	527	30.32	38.6	1.27	6.6	0.39	0.35
150x50x4.0 C450		Cold formed	Parallel	4-pt bending	150.44	50.4	3.87	5.37	457	527	29.86	35.5	1.19	7.7	0.40	0.35
150x50x4.0 C450		Cold formed	Pin	4-pt bending	150.42	50.11	3.89	5.36	457	527	29.93	37.3	1.25	7.2	0.39	0.35
150x50x4.0 C450		Cold formed	Parallel	4-pt bending	150.21	50.16	3.89	3.46	423	480	28.06	33.02	1.18	9.5	0.38	0.35
150x50x3.0 C450		Cold formed	Parallel	4-pt bending	150.47	50.22	2.97	4.42	444	513	22.76	26.2	1.15	2.7	0.51	0.46
150x50x3.0 C450		Cold formed	Parallel	4-pt bending	150.79	50.01	2.95	4.33	444	513	22.68	26.3	1.16	2.3	0.52	0.47
150x50x3.0 C450		Cold formed	Parallel	4-pt bending	150.8	50.34	2.96	4.22	444	513	22.81	25.8	1.13	2.9	0.52	0.47
150x50x2.5 C450		Cold formed	Parallel	4-pt bending	150.43	50.15	2.6	3.30	446	523	20.3	20.8	1.02	1.4	0.59	0.54
150x50x2.5 C450		Cold formed	Parallel	4-pt bending	150.39	50.41	2.57	3.32	446	523	20.13	20.2	1.00	1.2	0.60	0.54
150x50x2.5 C450		Cold formed	Perp.	4-pt bending	150.35	50.23	2.59	3.51	446	523	20.18	21.8	1.08	2.2	0.59	0.54
150x50x2.5 C450		Cold formed	Pin	4-pt bending	150.31	50.4	2.64	3.98	440	506	20.28	22.6	1.11	1.1	0.57	0.52

Sample	Origin	fabrication process	Loading method	Test configuration	h [mm]	b [mm]	t [mm]	r [mm]	f_y [N/mm ²]	f_u [N/mm ²]	M_{ply} [kN.m]	M_{max} [kN.m]	M_{max}/M_{ply} [-]	R_{cap}	λ_{CS}	λ_p
150x50x2.3 C450	Wilkinson & Hancock 1998	Cold formed	Parallel	4-pt bending	150.65	50.64	2.25	3.48	444	518	17.73	17.4	0.98	0	0.68	0.62
150x50x2.3 C450		Cold formed	Parallel	4-pt bending	150.51	50.57	2.28	3.06	444	518	17.96	18.2	1.01	0.6	0.67	0.62
150x50x2.3 C450		Cold formed	Parallel	4-pt bending	150.37	50.7	2.26	3.67	444	518	17.71	17.3	0.98	0	0.68	0.62
100x50x2.0 C450		Cold formed	Parallel	4-pt bending	100.45	50.7	2.06	2.77	449	499	8.7	9.3	1.07	0.8	0.58	0.51
100x50x2.0 C450		Cold formed	Parallel	4-pt bending	100.49	50.55	2.07	2.87	449	499	8.71	8.8	1.01	0.8	0.58	0.50
100x50x2.0 C450		Cold formed	Perp.	4-pt bending	100.46	50.24	2.04	3.68	449	499	8.47	9.3	1.10	1.3	0.58	0.49
100x50x2.0 C450		Cold formed	Pin	4-pt bending	100.45	50.22	2.04	2.38	423	479	7.91	8.75	1.11	1.6	0.57	0.50
75x50x2.0 C450		Cold formed	Parallel	4-pt bending	75.48	50.1	1.94	3.43	411	484	4.8	5	1.04	1.7	0.55	0.50
75x50x2.0 C450		Cold formed	Parallel	4-pt bending	75.63	50.31	1.95	3.43	411	484	4.86	4.96	1.02	1.9	0.55	0.50
75x25x2.0 C450		Cold formed	Parallel	4-pt bending	75.31	25.28	1.98	2.71	457	514	3.82	4.24	1.11	5.7	0.39	0.34
75x25x2.0 C450		Cold formed	Parallel	4-pt bending	75.33	25.23	1.95	3.03	457	514	3.75	4.25	1.13	*	0.39	0.35
75x25x1.6 C450		Cold formed	Parallel	4-pt bending	75.24	25.12	1.54	2.33	439	511	2.84	3.16	1.11	2.2	0.49	0.44
75x25x1.6 C450		Cold formed	Parallel	4-pt bending	74.9	25.2	1.54	2.63	439	511	2.82	3.25	1.15	2.5	0.49	0.44
75x25x1.6 C450		Cold formed	Perp.	4-pt bending	74.98	25.08	1.56	3.12	439	511	2.83	3.1	1.10	2.5	0.48	0.42
75x25x1.6 C350		Cold formed	Parallel	4-pt bending	75.27	25.12	1.55	2.63	422	456	2.81	2.9	1.03	1.9	0.48	0.43
75x25x1.6 C350		Cold formed	Parallel	4-pt bending	75.19	25.25	1.56	2.62	422	456	2.82	2.82	1.00	2.6	0.47	0.42
150x50x3.0 C350		Cold formed	Parallel	4-pt bending	150.46	50.13	3	4.70	370	429	19.11	23.2	1.21	4.1	0.46	0.42
150x50x3.0 C350		Cold formed	Parallel	4-pt bending	150.5	50.19	2.96	5.02	370	429	18.84	21.7	1.15	3.6	0.47	0.42
150x50x3.0 C350		Cold formed	Perp.	4-pt bending	150.45	50.51	3	5.30	382	430	19.69	23.2	1.18	3.2	0.47	0.42
150x50x3.0 C350		Cold formed	Pin	4-pt bending	150.38	50.51	3	4.80	382	430	19.79	23.9	1.21	3.6	0.47	0.42
100x50x2.0 C350		Cold formed	Parallel	4-pt bending	100.91	50.43	2.06	2.57	400	450	7.77	7.7	0.99	1.2	0.55	0.48
100x50x2.0 C350		Cold formed	Parallel	4-pt bending	100.83	50.52	2.05	2.78	400	450	7.75	7.75	1.00	1.3	0.55	0.48
125x75x3.0 C350		Cold formed	Parallel	4-pt bending	125.56	75.84	2.92	5.14	397	449	18.42	18.9	1.03	1.5	0.55	0.49
125x75x3.0 C350		Cold formed	Parallel	4-pt bending	125.4	75.74	2.93	5.44	397	449	18.4	19.1	1.04	1.6	0.55	0.48
125x75x3.0 C350		Cold formed	Perp.	4-pt bending	125.4	75.56	2.91	5.65	397	449	18.2	18.7	1.03	1.4	0.55	0.48
125x75x2.5 C350		Cold formed	Pin	4-pt bending	125.4	75.1	2.53	2.64	374	441	15.32	16.25	1.06	1.1	0.62	0.59
100x100x3.0 C450		Cold formed	Parallel	4-pt bending	100.43	100.27	2.88	3.76	445	502	17.86	18.16	1.02	0.8	0.76	0.76
100x100x3.0 C450		Cold formed	Pin	4-pt bending	100.53	100.33	2.91	3.55	445	502	18.09	17.3	0.96	0.7	0.75	0.75
100x100x3.0 C450		Cold formed	Perp.	4-pt bending	100.53	100.25	2.86	3.77	445	502	17.78	18.4	1.03	0.9	0.76	0.76
150x50x4.0 C350		Cold formed	Parallel	4-pt bending	150.32	50.21	3.9	5.95	349	437	22.8	29.7	1.30	12.9	0.34	0.30
150x50x4.0 C350		Cold formed	Parallel	4-pt bending	150.39	50.57	3.85	5.58	410	464	26.63	31.78	1.19	10.7	0.38	0.33

Gardner & al 2010

Sample	Origin	fabrication process	Loading method	Test configuration	h [mm]	b [mm]	t [mm]	r [mm]	f_y [N/mm ²]	f_u [N/mm ²]	M_{ply} [kN.m]	M_{max} [kN.m]	M_{max}/M_{ply} [-]	R_{cap}	λ_{CS}	λ_p
RHS 60x40x4-HR	Gardner & al 2010	Hot rolled	Loading at upper flange + insertion of wooden block	3-pt bending	60.09	40.24	3.90	3.86	468	554	6.27	7.14	1.14	>15.9	0.23	0.18
RHS 60x40x4-CF		Cold formed		3-pt bending	60.04	40.09	3.93	4.04	400	452	5.37	7.59	1.42	>12.5	0.21	0.16
SHS 40x40x4-HR		Hot rolled		3-pt bending	39.75	40.00	3.91	4.12	496	572	3.51	3.84	1.09	>5.1	0.22	0.18
SHS 40x40x4-CF		Cold formed		3-pt bending	40.31	40.42	3.70	4.95	410	430	2.83	3.61	1.28	>7.2	0.22	0.17
SHS 40x40x3-HR		Hot rolled		3-pt bending	39.87	40.20	3.05	3.60	504	581	2.97	3.44	1.16	>5.3	0.28	0.25
SHS 40x40x3-CF		Cold formed		3-pt bending	40.16	40.11	2.80	4.03	451	502	2.48	3.09	1.25	3.5	0.30	0.25

Wilkinson PhD – Appendix B

Sample	Origin	fabrication process	Loading method	Test configuration	h [mm]	b [mm]	t [mm]	r [mm]	f_y [N/mm ²]	f_u [N/mm ²]	M_{ply} [kN.m]	M_{max} [kN.m]	M_{max}/M_{ply} [-]	R_{cap}	λ_{CS}	λ_p
250x150x6.3 S275	Wilkinson PhD- appendix B	Hot formed	Parallel	4-pt bending	249.31	149.61	5.6	6.2	349	495	124.1	129.6	1.04	6.3	0.54	0.50
200x150x6.3S275		Hot formed		4-pt bending	200.69	150.3	5.78	4.11	362	486	97.25	96.5	0.99	6.9	0.52	0.51

Rondal & al 1995

Sample	Origin	fabrication process	Loading method	Test configuration	h [mm]	b [mm]	t [mm]	r [mm]	f_y [N/mm ²]	f_u [N/mm ²]	M_{ply} [kN.m]	M_{max} [kN.m]	M_{max}/M_{ply} [-]	R_{cap}	λ_{CS}	λ_p
SHS 100x5	Rondal & al 1995	cold formed	perpendicular	4-pt bending	100.13	100.18	4.88	12.88	493.86	-	30.95	31.98	1.03	-	0.43	0.36
SHS 100x5		cold formed		4-pt bending	100.17	100.19	4.87	13	494.00	-	30.85	31.48	1.02	2.40	0.43	0.36
SHS 100x4		cold formed		4-pt bending	99.89	99.95	3.82	7.75	535.26	-	27.48	28.06	1.02	2.20	0.60	0.56
SHS 100x4		cold formed		4-pt bending	99.89	99.94	3.81	7.75	535.26	-	27.40	29.81	1.09	1.80	0.61	0.56

Hasan & Hancock 1988

Sample	Origin	fabrication process	Loading method	Test configuration	h [mm]	b [mm]	t [mm]	r [mm]	f_y [N/mm ²]	f_u [N/mm ²]	M_{ply} [kN.m]	M_{max} [kN.m]	M_{max}/M_{ply}	R_{cap}	λ_{CS}	λ_p
152x152x4.9 C350	Hasan & Hancock 1988	Cold formed	parallel	4-pt bending	152.0	152.0	4.90	9.80	416	475.00	63.92	65.2	1.02	1.2	0.64	0.61
254x254x9.5 C350		Cold formed		4-pt bending	254.8	255.0	9.50	19.00	418	474.00	339.29	380	1.12	5.2	0.55	0.51
254x254x9.5 C350		Cold formed		4-pt bending	254.8	255.0	9.50	19.00	418	474.00	340.54	378	1.11	4.8	0.55	0.51
203x102x9.5 C350		Cold formed		4-pt bending	201.4	103.8	9.55	19.10	438	478.00	139.34	170	1.22	>14	0.23	0.16
203x102x9.5 C350		Cold formed		4-pt bending	201.4	103.8	9.55	19.10	438	478.00	139.02	171	1.23	>14	0.23	0.16
203x152x6.3 C350		Cold formed		4-pt bending	199.8	151.6	6.43	12.86	368	441.00	106.50	131	1.23	9.5	0.46	0.41
203x152x6.3 C350		Cold formed		4-pt bending	199.8	151.6	6.43	12.86	368	441.00	106.50	131	1.23	8.6	0.46	0.41
127x127x4.9 C350		Cold formed		4-pt bending	127.6	127.9	4.99	9.98	378	440.00	39.32	46.4	1.18	6.5	0.50	0.46
127x127x4.9 C350		Cold formed		4-pt bending	127.6	127.9	4.99	9.98	378	440.00	39.32	46	1.17	6.5	0.50	0.46
102x102x4.0 C350		Cold formed		4-pt bending	102.1	102.3	4.17	8.34	373	422.00	20.36	28.1	1.38	>6	0.47	0.43
102x102x4.0 C350		Cold formed		4-pt bending	102.1	102.3	4.17	8.34	373	422.00	20.23	26.3	1.3	>8	0.47	0.43
102x76x3.6 C350		Cold formed		4-pt bending	101.3	76.1	3.74	7.48	341	421.00	13.86	19.4	1.4	>9	0.38	0.33
102x76x3.6 C350		Cold formed		4-pt bending	101.3	76.1	3.74	7.48	341	421.00	13.92	19.9	1.43	11.7	0.38	0.33
89x89x3.6 C350		Cold formed		4-pt bending	88.6	88.9	3.74	7.48	358	410.00	13.44	17.2	1.28	>9	0.45	0.41
89x89x3.6 C350		Cold formed		4-pt bending	88.6	88.9	3.74	7.48	358	410.00	13.42	16.1	1.2	8.4	0.45	0.41
76x76x3.2 C350		Cold formed		4-pt bending	76.3	76.2	3.28	6.56	344	396.00	8.37	10.8	1.29	8.2	0.43	0.39
76x76x3.2 C350		Cold formed		4-pt bending	76.3	76.2	3.28	6.56	344	396.00	8.35	11.1	1.33	8.8	0.43	0.39
76x76x2.6 C350		Cold formed		4-pt bending	76.4	76.3	2.51	3.77	347	429.00	7.12	8.33	1.17	4.9	0.58	0.56
76x76x2.6 C350		Cold formed		4-pt bending	76.4	76.3	2.51	3.77	347	429.00	7.12	8.26	1.16	3.6	0.58	0.56

Saloumi & al 2015

Sample	Origin	fabrication process	Loading method	Test configuration	h [mm]	b [mm]	t [mm]	r [mm]	f_y [N/mm ²]	f_u [N/mm ²]	M_{ply} [kN.m]	M_{max} [kN.m]	M_{max}/M_{ply}	R_{cap}	λ_{CS}	λ_p
RHS 150x100x8	Saloumi & al 2015	HR	Loading at upper flange	3-point	149.0	99.2	5.26	7.90	391.2	554.0	69.79	84.56	1.21	>8	0.24	0.34
RHS 150x100x8		HR		4-point	149.1	99.5	5.13	7.69	391.2	554.0	68.43	83.19	1.22	>9	0.25	0.35

Wang & al 2016

Sample	Origin	fabrication process	Loading method	Test configuration	h [mm]	b [mm]	t [mm]	r [mm]	f_y [N/mm ²]	f_u [N/mm ²]	M_{ply} [kN.m]	M_{max} [kN.m]	M_{max}/M_{ply}	R_{cap}	λ_{CS}	λ_p
S460 50x50x5	Wang & al 2016	HR	Loading at upper flange	3-point	50.3	50.4	5.01	5.51	505.0	620.2	7.26	8.67	1.19	9	0.22	0.18
S460 50x50x4		HR		3-point	50.3	50.4	3.86	4.93	523.0	622.7	6.14	7.17	1.17	4	0.29	0.25
S460 100x100x5		HR		3-point	99.8	100.0	5.28	7.39	511.0	616.4	34.57	38.88	1.12	4.8	0.43	0.39
S460 90x90x3.6		HR		3-point	89.6	89.6	3.66	5.83	500.0	655.1	19.47	20.73	1.06	1.6	0.56	0.52
S460 100x50x6.3		HR		3-point	99.8	49.8	6.35	9.18	498.0	698.5	24.30	39.26	1.62	91	0.20	0.12
S460 100x50x4.5		HR		3-point	99.6	49.9	4.65	8.33	498.0	644.9	18.78	23.68	1.26	9	0.25	0.18
S690 50x50x5		HR		3-point	50.5	50.6	4.97	6.15	759.0	789.6	10.83	12.56	1.16	1	0.27	0.21
S690 100x100x5.6		HR		3-point	100.5	100.4	5.66	8.51	782.0	798.1	56.55	58.25	1.03	0.8	0.49	0.44
S690 90x90x5.6		HR		3-point	90.7	90.3	5.77	8.22	774.0	790.0	45.46	46.59	1.02	0.9	0.43	0.38
S690 100x50x6.3		HR		3-point	100.3	49.9	6.47	8.49	799.0	820.3	40.26	46.44	1.15	3	0.25	0.16
S690 100x50x5.6		HR		3-point	100.5	49.9	5.73	8.87	777.0	811.1	35.36	41.69	1.18	0	0.25	0.18
S460 50x50x5		HR		4-point	50.5	50.3	4.83	5.92	505.0	620.2	7.04	7.03	1.00	2	0.23	0.18
S460 50x50x4		HR		4-point	50.4	50.6	3.92	5.34	523.0	622.7	6.22	6.25	1.01	3	0.29	0.24
S460 100x100x5		HR		4-point	99.7	99.4	5.30	7.65	511.0	616.4	34.42	38.61	1.12	59	0.42	0.39
S460 90x90x3.6		HR		4-point	90.0	89.7	3.76	6.88	500.0	655.1	19.94	20.81	1.04	5.8	0.54	0.49
S460 100x50x6.3		HR		4-point	99.8	49.8	6.45	8.10	498.0	698.5	24.91	32.46	1.30	35	0.20	0.13
S460 100x50x4.5		HR		4-point	99.6	50.0	4.63	7.32	498.0	644.9	18.93	23.28	1.23	55	0.25	0.18
S690 50x50x5		HR		4-point	50.4	50.5	4.91	5.71	759.0	789.6	10.74	11.59	1.08	0	0.28	0.22
S690 100x100x5.6		HR		4-point	100.6	100.5	5.66	8.33	782.0	798.1	56.78	54.91	0.97	-	0.49	0.44
S690 90x90x5.6		HR		4-point	90.3	90.6	5.71	7.36	774.0	790.0	45.14	42.88	0.95	-	0.44	0.39
S690 100x50x6.3		HR		4-point	100.2	49.9	6.46	7.73	799.0	820.3	40.51	42.25	1.04	4	0.25	0.16
S690 100x50x5.6		HR		4-point	100.5	49.9	5.64	8.32	777.0	811.1	35.13	37.87	1.08	5	0.26	0.18

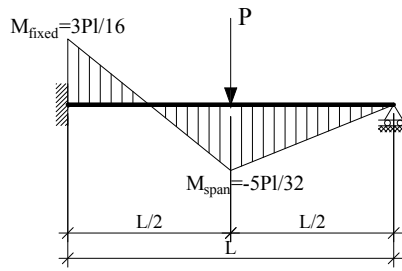
11.2 APPENDIX 2 – Theoretical values for the propped cantilever configurations

11.2.1 Propped-cantilever centrally loaded

From the cinematic method, the system peak load is computed.

$$P_{pl} = \frac{6M_{pl}}{L} \quad 11.1$$

1st step:



1st step

Figure 11.1 – Propped-cantilever centrally loaded - step 1

Maximum moment is reached at the fixed end giving $M_{fixed} = \frac{3PL}{16} = M_{pl}$;

The loading corresponding to $M_{fixed} = M_{pl}$ is then $P_1 = \frac{16M_{pl}}{3L}$ and the moment at mid-span

$$M_{span} = \frac{5M_{pl}}{6}$$

Rotation at the hinged end is given by $\theta = \frac{PL^2}{32EI}$; and for the load P_1 , $\theta_1 = \frac{M_p L}{6EI}$

The vertical displacement at mid-span is $f = \frac{7PL^3}{6EI}$; and for the load P_1 , $f_1 = \frac{7M_p L^2}{144EI}$

2nd step: the first hinge is reached at the fixed-end giving the following moment distribution represented in Figure 11.1.

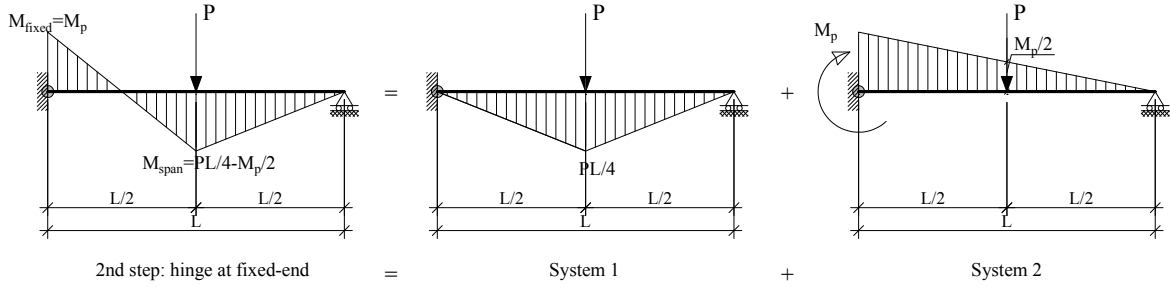


Figure 11.2 – Propped-cantilever centrally loaded - step 2: hinge at fixed-end

According to Figure 11.2, system maximum load P_{pl} is reached when the mid-span moment M_{span} equal the plastic moment M_{pl} :

$$\frac{PL}{4} - \frac{M_{pl}}{2} = M_{pl} \text{ giving } P_{pl} = \frac{6M_{pl}}{L}$$

The rotation at the hinged-end is computed as the sum of the rotation from systems 1 and 2.

$$\theta = \frac{PL^2}{16EI} - \frac{M_{pl}L}{6EI} \text{ giving for } P = P_{pl} \theta_2 = \frac{5M_{pl}L}{24EI}$$

As well for the vertical displacement at mid-span: $f = \frac{PL^3}{48EI} - \frac{M_{pl}L^2}{16EI}$ giving for $P = P_{pl}$

$$f_2 = \frac{M_{pl}L^2}{16EI}$$

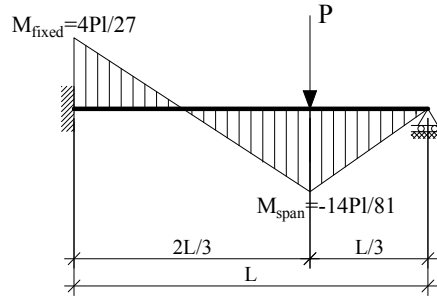
As a summary:

	1 st step	2 nd step
Load P	$P_1 = \frac{16M_{pl}}{3L}$	$P_{pl} = \frac{6M_{pl}}{L}$
Moment at fixed-end M_{fixed}	M_{pl}	M_{pl}
Moment at span M_{span}	$M_{span} = \frac{5M_{pl}}{6}$	M_{pl}
Rotation at hinged end θ	$\theta_1 = \frac{M_{pl}L}{6EI}$	$\theta_2 = \frac{5M_{pl}L}{24EI}$
Vertical displacement at mid-span f	$f_1 = \frac{7M_{pl}L^2}{144EI}$	$f_2 = \frac{M_{pl}L^2}{16EI}$

11.2.2 Propped-cantilever off-centrally loaded

$$P_{pl} = \frac{6M_{pl}}{L} \quad 11.2$$

1st step:



1st step

Figure 11.3 – Propped cantilever centrally loaded - step 1

Maximum moment is reached at the span (at the position of the point load)

$$M_{span} = \frac{14PL}{81} = M_{pl} ;$$

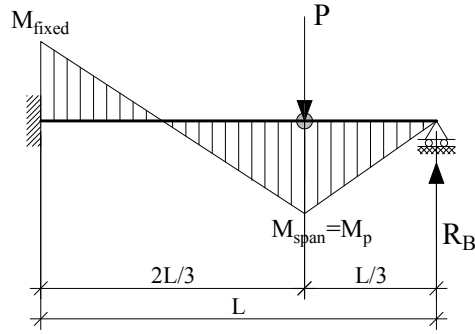
The loading corresponding to $M_{span} = M_{pl}$ is then $P_1 = \frac{81M_{pl}}{14L}$ and the moment at fixed-end

$$M_{fixed} = \frac{6M_{pl}}{7}$$

Rotation at the hinged end is given by $\theta = \frac{PL^2}{27EI}$; and for the load P_1 , $\theta_1 = \frac{3M_p L}{14EI}$

The vertical displacement at mid-span is $f = \frac{20PL^3}{3^7 EI}$; and for the load P_1 , $f_1 = \frac{10M_p L^2}{189EI}$

2nd step: the first hinge is reached at the load point position giving the following moment distribution represented in Figure 11.3.



2nd step: hinge at span

Figure 11.4 – Propped cantilever centrally loaded - step 2: hinge at span

According to Figure 11.4, and in order to compute the system maximum load P_{pl} , the support

reaction R_B at the hinged end is computed: $R_B \cdot \frac{L}{3} = M_{pl}$ thus $R_B = \frac{3M_{pl}}{L}$

Then the moment at the fixed-end is calculated and equalled to the plastic moment M_{pl}

$$M_{fixed} = P \cdot \frac{2L}{3} - R_B \cdot L = M_{pl} \text{ giving the system peak load } P_{pl} = \frac{6M_{pl}}{L}$$

The load increment ΔP is then calculated: $\Delta P = P_{pl} - P_1 = \frac{3M_{pl}}{14L}$

The beam deflection increment at the hinged-end is computed as for a cantilever of span $L/3$ shown in Figure 11.5.

$$\Delta f = \frac{P \left(\frac{2}{3}L \right)^2}{3EI} \text{ giving for } \Delta P: \Delta f = \frac{4M_{pl}L^2}{189EI} ; \text{ hence the total displacement}$$

$$f_2 = f_1 + \Delta f = \frac{14M_{pl}L^2}{189EI}$$

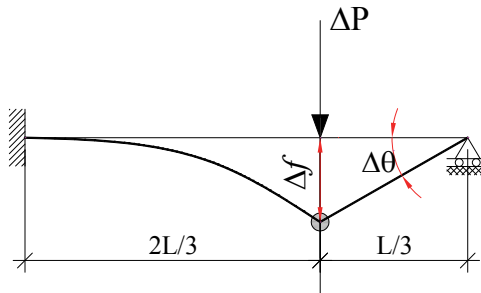


Figure 11.5 – Propped cantilever centrally loaded – considerations for the calculation of the additional deflection

The rotation is then computed: $\theta = \arctan\left(\frac{3\Delta f}{L}\right) + \theta_1$ giving

$$\theta_2 = \arctan\left(\frac{12M_{pl}L}{189EI}\right) + \frac{3M_{pl}L}{14EI}$$

As a summary:

	1 st step	2 nd step
Load P	$P_1 = \frac{81M_{pl}}{14L}$	$P_{pl} = \frac{6M_{pl}}{L}$
Moment at fixed-end M_{fixed}	$M_{fixed} = \frac{6M_{pl}}{7}$	M_{pl}
Moment at span M_{span}	M_{pl}	M_{pl}
Rotation at hinged end \square	$\theta_1 = \frac{3M_{pl}L}{14EI}$	$\theta_2 = \arctan\left(\frac{12M_{pl}L}{189EI}\right) + \frac{3M_{pl}L}{14EI}$
Vertical displacement at mid-span f	$f_1 = \frac{10M_{pl}L^2}{189EI}$	$f_2 = \frac{14M_{pl}L^2}{189EI}$

11.3 APPENDIX 3 – Detailed experimental results

11.3.1 Geometrical dimensions of tested specimens

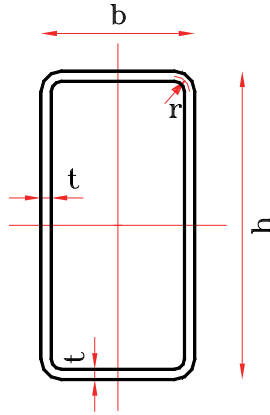


Figure 11.6 – Cross-section dimensions

Table 11.1 – Measured parameters

Test #	h ₁	h ₂	h ₃	b ₁	b ₂	b ₃	t ₁	t ₂	t ₃	t ₄	t ₅	t ₆	t ₇	t ₈	t ₉	t ₁₀	t ₁₁	t ₁₂
	[mm]	[mm]	[mm]	[mm]	[mm]	[mm]	[mm]	[mm]	[mm]	[mm]	[mm]	[mm]	[mm]	[mm]	[mm]	[mm]	[mm]	[mm]
1	149.50	149.26	150.37	99.91	99.94	100.13	8.32	8.20	8.42	8.38	8.26	8.27	8.20	8.41	8.75	8.41	8.21	8.36
	149.36	149.16	149.97	100.04	99.85	99.79	8.74	7.78	8.17	8.27	8.44	8.62	8.53	8.26	8.51	8.37	8.15	8.28
2	179.00	179.09	179.75	78.25	78.48	79.05	4.97	4.66	4.56	4.34	4.68	4.59	5.02	4.96	4.60	5.06	5.39	5.34
	179.80	179.09	179.38	78.54	78.22	78.58	4.44	4.66	4.77	4.83	4.63	4.17	4.57	4.64	4.76	5.03	5.33	5.16
3	149.20	148.63	148.93	99.14	99.32	99.21	5.64	5.42	4.77	5.08	5.15	5.15	5.55	5.27	5.57	5.38	5.23	5.44
	149.45	148.59	149.01	99.10	99.08	99.15	4.89	5.38	5.21	5.29	5.26	4.75	5.79	5.46	5.36	5.11	5.03	5.15
4	219.50	219.10	218.90	120.54	120.58	120.72	6.42	6.47	6.38	6.38	6.18	6.19	6.76	6.45	6.30	6.51	6.23	6.41
	219.70	218.80	219.50	120.62	120.48	120.63	6.15	6.29	6.46	6.19	6.49	6.45	6.23	6.18	6.13	6.65	6.78	6.59
5	218.00	216.90	217.90	120.89	120.91	120.82	6.28	6.08	6.05	6.57	6.49	6.54	6.60	6.55	6.59	6.30	6.28	6.42
	217.80	216.80	217.90	120.64	120.60	120.61	6.40	6.38	6.34	6.27	6.23	6.31	6.81	6.63	6.82	6.29	6.13	6.23
6	179.55	178.82	179.24	179.67	179.85	179.67	6.97	6.72	6.68	6.59	6.40	6.40	6.94	6.68	6.76	7.17	7.19	6.87
	179.55	179.51	179.82	179.75	179.35	180.26	6.99	6.43	6.37	6.27	6.02	5.84	6.59	6.48	6.33	6.64	6.15	6.41
7	179.65	178.83	179.38	179.35	179.20	179.39	7.97	7.80	7.59	7.98	7.86	7.71	8.22	8.21	8.20	7.47	7.38	7.54
	179.94	179.37	179.60	179.16	179.98	179.41	8.27	8.08	7.99	7.73	7.59	8.13	8.00	8.07	8.33	7.51	7.77	7.90
8	200.07	201.46	200.61	200.56	202.27	200.09	5.75	6.02	5.83	6.00	5.91	6.04	6.14	6.01	5.82	5.94	5.77	5.96
	200.64	200.56	199.81	200.76	201.47	200.06	5.78	5.74	5.72	5.66	5.73	5.72	5.72	5.71	5.76	5.81	5.66	5.68
9	150.13	148.96	149.42	99.83	99.94	100.01	7.54	7.48	8.15	8.30	8.00	7.60	8.02	7.86	8.14	8.22	7.82	8.67
	149.81	148.90	149.66	99.69	99.84	99.82	8.35	8.45	8.25	8.01	7.81	8.36	8.60	8.19	8.65	8.45	8.45	8.47
10	180.02	179.88	179.70	79.89	81.35	80.83	4.61	4.27	4.33	4.49	4.63	5.04	5.04	5.04	5.24	4.87	4.87	5.31
	179.80	178.72	179.40	78.57	78.54	79.06	4.77	4.49	4.90	4.57	4.39	4.38	5.04	5.00	5.14	5.05	4.96	4.97
11	149.14	148.04	148.78	99.61	99.43	99.31	5.55	5.50	5.31	5.48	5.37	4.78	5.32	5.23	5.35	5.39	5.00	5.14
	149.79	148.97	150.05	99.46	99.46	99.61	4.93	4.93	4.78	4.89	4.21	5.11	5.37	5.27	5.40	4.95	4.85	4.89

12	219.50	219.20	219.40	120.67	120.88	120.74	6.72	6.30	6.40	6.68	6.53	6.28	6.50	6.20	6.36	6.69	6.55	6.75
	219.50	219.40	219.40	120.79	121.16	120.92	6.56	6.46	6.41	6.25	6.12	6.14	6.54	6.49	6.59	6.05	6.10	6.52
13	179.76	178.77	179.62	180.34	179.48	180.92	6.69	6.42	6.42	6.81	6.56	6.55	6.45	6.46	6.54	7.06	7.06	7.09
	179.72	179.10	179.63	179.81	179.37	179.68	6.52	6.40	6.34	7.19	7.11	7.07	6.51	6.59	6.87	6.22	6.53	6.81
14	179.40	178.80	179.35	179.57	179.12	179.56	8.10	7.97	8.01	7.99	7.78	8.05	8.10	7.99	8.20	7.85	7.79	8.03
	179.53	178.74	179.38	179.57	179.57	180.10	7.66	7.34	7.46	8.11	8.17	8.29	8.13	7.86	7.71	7.95	7.69	7.55
15	200.14	202.13	201.64	200.28	201.62	200.35	5.96	5.84	5.84	5.76	5.70	5.79	5.88	5.96	6.02	5.94	5.87	5.90
	200.04	201.32	199.76	199.74	200.38	200.16	5.71	5.73	5.80	5.77	5.74	5.78	5.70	5.70	5.73	5.67	5.67	5.81
16	179.23	178.75	179.58	78.63	79.11	79.53	4.76	4.46	4.75	4.81	4.67	3.98	4.86	4.75	4.95	5.20	4.95	4.92
	179.25	178.72	179.61	79.05	79.51	78.55	4.74	4.48	4.76	4.79	4.69	4.21	4.83	4.77	4.90	5.02	4.93	4.94
17	149.49	148.04	148.79	99.89	99.19	99.37	4.94	5.20	5.04	5.28	5.48	4.92	5.63	5.43	5.48	4.92	4.90	5.23
	149.30	148.42	148.62	99.20	99.88	99.39	4.92	5.22	5.05	5.26	5.50	5.13	5.42	5.45	5.23	4.94	5.08	5.25
18	219.60	218.49	219.20	120.38	120.58	120.39	6.58	6.41	6.48	6.51	6.39	6.24	6.71	6.63	6.63	6.68	6.31	6.52
	219.63	218.50	219.18	120.39	120.57	120.41	6.56	6.38	6.50	6.46	6.41	6.46	6.53	6.64	6.61	6.70	6.29	6.55
19	179.38	179.87	179.39	180.12	179.12	179.86	7.04	6.76	7.05	6.48	6.73	7.02	6.66	6.65	7.08	6.35	6.45	6.42
	179.05	179.86	179.07	180.05	179.23	179.84	7.00	6.94	6.88	6.66	6.81	6.80	6.61	6.67	6.83	6.57	6.48	6.44
20	179.10	179.69	179.31	179.16	179.11	179.40	8.43	8.16	8.24	7.89	7.80	7.77	7.83	7.74	7.71	7.78	7.85	8.04
	179.12	179.65	179.35	179.21	179.19	179.33	8.10	8.22	8.19	7.91	7.88	7.79	7.79	7.85	7.77	7.83	7.83	8.08
21	179.26	178.61	178.99	79.18	79.84	79.28	4.14	4.30	4.60	4.87	4.55	4.33	4.89	4.96	4.81	4.68	4.56	4.73
	179.27	178.59	179.02	79.73	79.42	79.23	4.28	4.33	4.56	4.89	4.50	4.34	4.86	5.02	4.79	4.70	4.53	4.96
22	219.50	218.46	219.10	120.50	120.71	120.77	6.67	6.53	6.59	6.39	6.41	6.28	6.56	6.43	6.74	6.48	6.51	6.57
	219.54	218.55	219.05	120.51	120.69	120.80	6.61	6.56	6.53	6.34	6.43	6.34	6.54	6.40	6.76	6.45	6.49	6.59
23	180.00	179.89	180.14	178.88	179.41	178.91	6.75	6.72	6.48	6.45	6.28	6.26	6.83	6.74	6.49	6.57	6.50	6.35
	180.05	179.92	180.10	178.93	179.46	178.87	6.93	6.49	6.50	6.42	6.26	6.28	6.77	6.77	6.43	6.52	6.52	6.41

11.3.2 Tensile tests

Table 11.2 reports on the material properties from tensile tests: Young's modulus E , tensile yield strength f_y and ultimate yield strength f_u ... (For the determination of the average Young modulus E , Values higher than 220000 and lower than 190000 have been disregarded).

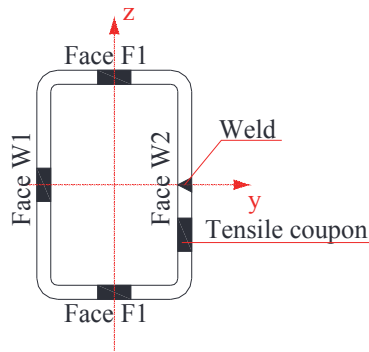


Figure 11.7 – Locations of the tensile coupons

Table 11.2 – Geometric dimensions and material properties of tested profiles

Section reference #	Coupon location	f_y	f_u	E	ε_y	ε_{y2}	ε_u
		[N/mm ²]	[N/mm ²]	[N/mm ²]	[%]	[%]	[%]
RHS_150*100*8_SS	flange 1	383.65	548.99	—	—	—	—
	web 1	394.77	567.13	197648.92	0.20	1.34	11.53
	flange 2	395.02	548.46	196012.99	0.20	1.80	14.66
	web 2	391.24	551.61	231637.92	0.17	1.47	13.98
RHS_180*80*4.5_SS	flange 1	385.37	525.93	194288.19	0.20	1.88	24.49
	web 1	393.08	555.44	—	—	1.44	15.43
	flange 2	390.19	540.39	166549.90	0.23	1.77	15.35
	web 2	388.14	535.74	202720.00	0.19	1.95	12.64
RHS_150*100*5_SS	flange 1	422.04	571.52	215135.82	0.20	1.74	21.88
	web 1	431.11	594.62	235298.12	0.18	1.50	9.44
	flange 2	419.58	573.77	215784.47	0.19	1.78	14.10
	web 2	406.57	551.95	198805.20	0.20	1.88	14.16
RHS_220*120*6.3_SS*	flange 1	389.51	536.33	206278.63	0.19	1.74	17.72
	web 1	401.74	537.67	206394.77	0.19	1.60	21.88
	flange 2	386.78	531.31	216536.39	0.18	1.78	14.07
	web 2	398.88	532.32	206519.83	0.19	2.27	14.26
RHS_220*120*6.3_SS	flange 1	392.83	537.52	202589.20	0.19	1.66	13.42
	web 1	394.21	536.33	208539.30	0.19	1.63	19.80
	flange 2	398.03	530.67	216060.80	0.18	2.15	14.32
	web 2	400.83	539.09	217159.55	0.18	2.06	13.60
SHS_180*6.3_SS	flange 1	392.72	531.42	210915.62	0.19	2.08	18.49
	web 1	385.21	531.52	212558.95	0.18	1.54	11.76
	flange 2	402.98	516.18	227400.14	0.18	2.11	13.48
	web 2	391.75	516.25	176739.05	0.22	3.04	15.78
SHS_180*8_SS	flange 1	395.83	546.29	208368.11	0.19	1.73	25.06
	web 1	378.08	527.03	204513.54	0.18	1.64	16.11
	flange 2	381.16	526.55	209586.10	0.18	1.68	15.24
	web 2	380.97	526.19	330469.60	0.12	1.70	13.47
SHS_200*6_SS_3P	flange 1	502.00	608.15	192957.19	0.26	not applicable	10.79
	web 1	460.00	562.80	154402.82	0.30	not applicable	11.63
	flange 2	480.00	550.92	214596.13	0.18	not applicable	26.79
	web 2	484.00	556.67	279001.00	0.17	not applicable	26.79
RHS_150*100*8_PR_C	flange 1	403.11	562.85	172131.31	0.23	1.68	9.48
	web 1	381.73	539.81	199588.00	0.19	1.68	13.11
	flange 2	399.79	552.28	183481.38	0.22	1.81	14.56
	web 2	401.18	555.99	206946.45	0.19	1.70	13.30
RHS_180*80*4.5_PR_C	flange 1	390.10	535.64	191034.35	0.20	2.00	21.15
	web 1	385.40	525.22	213568.56	0.18	1.73	25.14
	flange 2	374.45	519.99	177444.79	0.21	2.12	16.18
	web 2	390.75	528.37	213406.79	0.18	1.29	—
RHS_150*100*5_PR_C	flange 1	413.43	558.94	—	—	—	—
	web 1	393.43	544.35	225522.77	0.17	1.64	18.27
	flange 2	407.31	545.11	210685.60	0.19	2.32	15.29
	web 2	401.39	540.87	190517.03	0.21	2.13	14.90
RHS_220*120*6.3_PR_C	flange 1	396.90	538.90	212755.32	0.19	1.52	23.65
	web 1	387.56	533.91	192962.53	0.20	1.58	18.23
	flange 2	390.90	520.41	198995.53	0.20	2.16	12.80
	web 2	396.54	534.15	205047.30	0.19	2.07	13.98
SHS_180*6.3_PR_C	flange 1	386.34	532.02	200670.53	0.19	1.53	18.19
	web 1	390.68	533.34	203457.07	0.19	1.54	22.46
	flange 2	395.85	533.39	211953.33	0.19	2.07	14.65
	web 2	390.74	530.25	211195.84	0.19	2.04	15.18
SHS_180*8_PR_C	flange 1	390.89	545.42	215722.81	0.18	1.37	14.22

	web 1	381.28	527.27	212070.75	0.18	1.51	20.22
	flange 2	384.74	523.52	207162.21	0.19	1.94	14.37
	web 2	382.36	521.94	218513.61	0.17	1.97	14.78
RHS_180*80*4.5_PR_O	flange 1	396.38	555.14	208390.32	0.19	1.89	23.69
	web 1	373.69	529.95	—	—	1.53	22.76
	flange 2	388.90	540.87	182761.10	0.21	1.82	15.04
	web 2	387.41	522.32	202438.46	0.19	2.17	12.39
RHS_220*120*6.3_PR_O	flange 1	387.38	527.88	199415.47	0.19	1.75	21.03
	web 1	402.96	544.20	223101.85	0.18	1.54	24.08
	flange 2	385.28	523.84	207146.46	0.19	1.96	14.73
	web 2	398.67	536.82	211724.40	0.19	2.10	14.48
SHS_180*6.3_PR_O	flange 1	381.30	520.17	205047.56	0.19	1.60	17.42
	web 1	388.69	536.80	183180.57	0.21	1.55	20.94
	flange 2	388.11	531.63	213714.67	0.18	1.93	14.55
	web 2	385.63	527.22	207164.35	0.19	1.99	15.43

11.3.3 Back-calculated moment from strain measurements

Calculations were based on the Bernoulli assumption (i.e. that plane sections remain plane and normal to the deflected neutral axis) which lead to the conclusion that the deformation diagram remains linear. The strain on the compression flange was taken equal to that of the tension flange (where the strain gauge was positioned) and the strain diagram was assumed linear in between.

11.3.3.1 Analytical method

After the strain diagram is determined, the corresponding stress diagram was then calculated from the measured material law of the specimen as shown in Figure 11.8. Then, it was integrated around the major plastic axis of the section as detailed in the formulas below in order to determine the moment M .

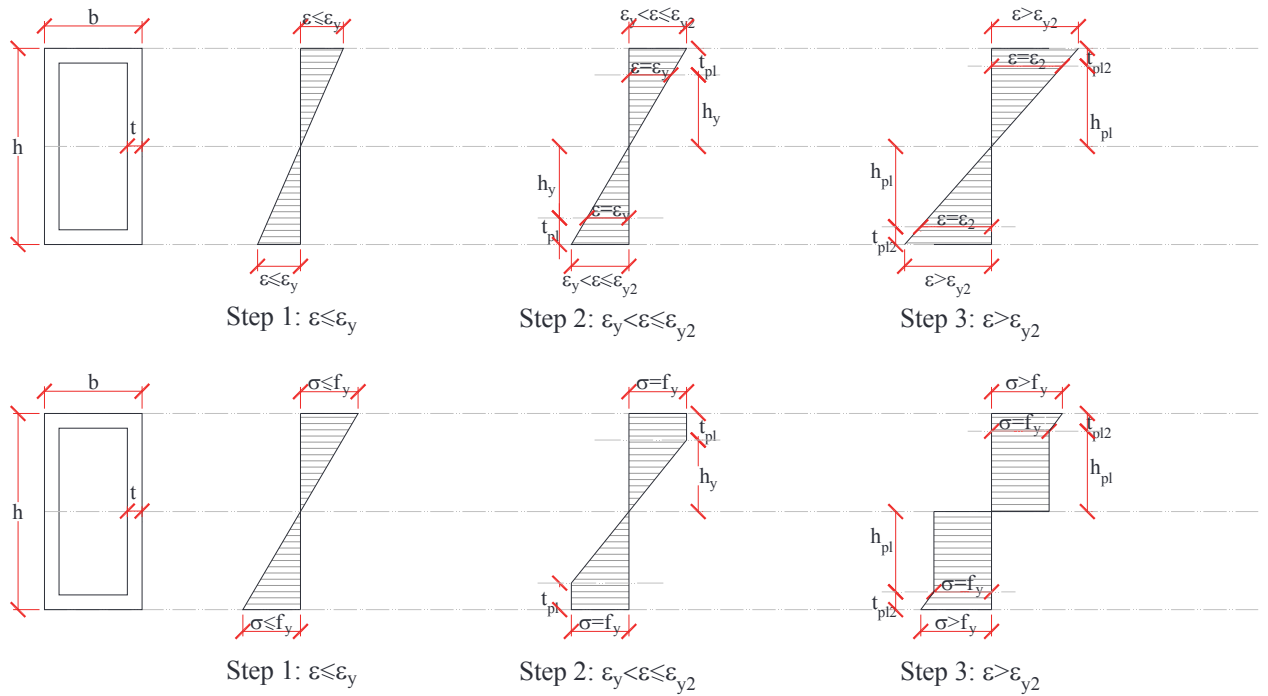


Figure 11.8 – Reconstruction of the stress diagram from the strain measurements

Basic assumptions:

$$I_y = 2 \cdot \left(\frac{b \cdot t^3}{12} + b \cdot t \times \left(\frac{h-t}{2} \right)^2 + (h-2t)^3 \cdot \frac{t}{12} \right)$$

$$M_{pl,y} = 2 \cdot \left(b \cdot t \left(\frac{h-t}{2} \right) + 2 \cdot \left(\left(\frac{h-2 \cdot t}{2} \right) \left(\frac{h-2 \cdot t}{4} \right) \cdot t \right) \right) \cdot f_y$$

$$h_y = \frac{\varepsilon_y \cdot h/2}{\varepsilon} \quad \text{and} \quad t_{pl} = h/2 - h_y$$

$$\text{Step 1: } \varepsilon \leq \varepsilon_y : W_{el} = \frac{I_y}{h/2} \text{ and } M_{res} = W_{el} \cdot (E \cdot \varepsilon)$$

$$\text{Step 2: } \varepsilon_y < \varepsilon \leq \varepsilon_{y2}$$

$$\text{If } t_{pl} \leq t$$

$$W_{el} = I_y - 2 \cdot \left(\frac{t_{pl}^3 \cdot b}{12} + t_{pl} \cdot b \cdot \left(\frac{h}{2} - \frac{t_{pl}}{2} \right)^2 \right) / h_y \quad \text{and} \quad W_{pl} = 2 \cdot \left(t_{pl} \cdot b \cdot \left(\frac{h}{2} - \frac{t_{pl}}{2} \right) \right)$$

$$\text{If } t_{pl} > t$$

$$W_{el} = 2 \cdot \frac{(2 \cdot h_y)^3 \cdot t}{12} / h_y$$

$$W_{pl} = 2 \cdot \left(t \cdot b \cdot \frac{h-t}{2} + \left(2 \cdot (h/2 - h_y - t) \cdot t \cdot \left(h_y + \frac{h/2 - h_y - t}{2} \right) \right) \right)$$

$$M_{res} = (W_{el} + W_{pl}) \cdot f_y$$

$$\text{Step 2: } \varepsilon > \varepsilon_{y2}$$

$$\text{If } t_{pl2} \leq t$$

$$W_{pl} = 2 \cdot \left(t \cdot b \cdot \frac{h-t}{2} + \left(2 \cdot (h/2 - t) \cdot t \cdot \left(\frac{h/2 - t}{2} \right) \right) \right)$$

$$W_{el2} = 2 \cdot \left(\frac{t_{pl2}^3 \cdot b}{12} + t_{pl} \cdot b \cdot \left(\frac{h}{2} - \frac{t_{pl2}}{2} \right)^2 \right) / \left(\frac{h}{2} \right)$$

$$\text{If } t_{pl2} > t$$

$$W_{pl} = 2 \cdot \left(t \cdot b \cdot \frac{h-t}{2} + \left(2 \cdot (h/2 - t) \cdot t \cdot \left(\frac{h/2 - t}{2} \right) \right) \right)$$

$$W_{el2} = 2 \cdot \left(\frac{t^3 \cdot b}{12} + t \cdot b \cdot \left(\frac{h}{2} - \frac{t}{2} \right)^2 + \frac{(h/2 - h_{pl} - t)^3 \cdot t}{12} + (h/2 - h_{pl} - t) \cdot t \cdot \left(h_y + \frac{(h/2 - h_{pl} - t)}{2} \right)^2 \right) \bigg/ \left(\frac{h}{2} \right)$$

$$M_{res} = W_{pl} \cdot f_y + W_{el2} \cdot E_2 \cdot (\varepsilon - \varepsilon_{y2})$$

Finally, the resistant moment is nomalised by the plastic moment calculated for the approximate section: $M_{res} / M_{pl,app}$

11.3.3.2 Numerical

The moment M was also computed using a specially developed Matlab tool which is capable to take into account the effect of the cross-section corners. The cross-section plates elements and corners are discretized into n elements as shown in Figure 11.9 for example.

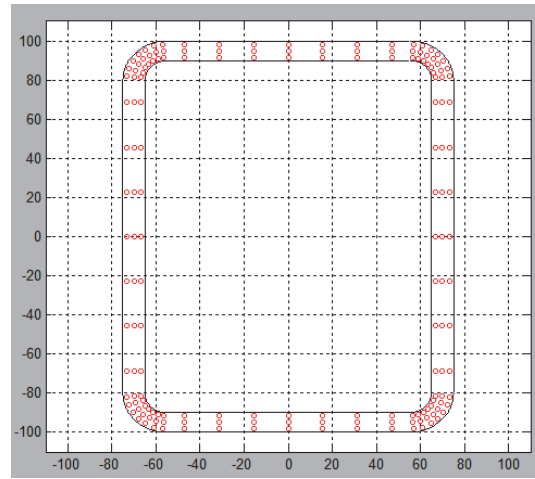
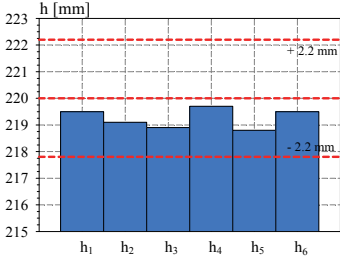
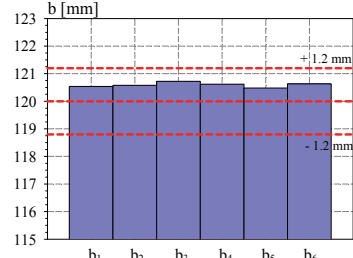
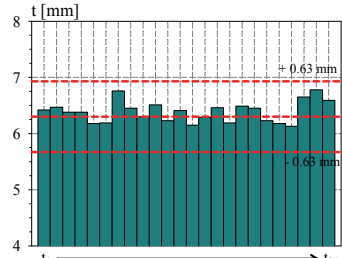



Figure 11.9 – Discretization of a RHS by Matlab tool

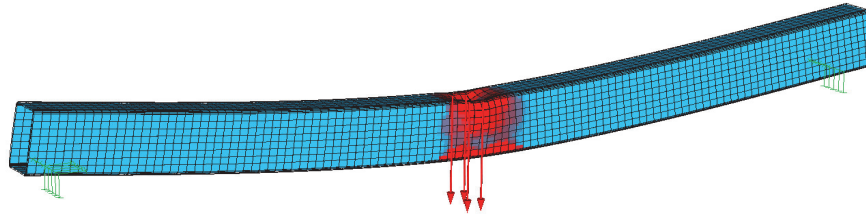
After the strain diagram is determined, the stress corresponding to each meshing element is then calculated from the measured material law of the specimen. Then, the stress of each element is integrated around the major plastic axis of the section in order to determine the major axis moment M .

11.3.4 Summary of 3-point bending results and numerical validation

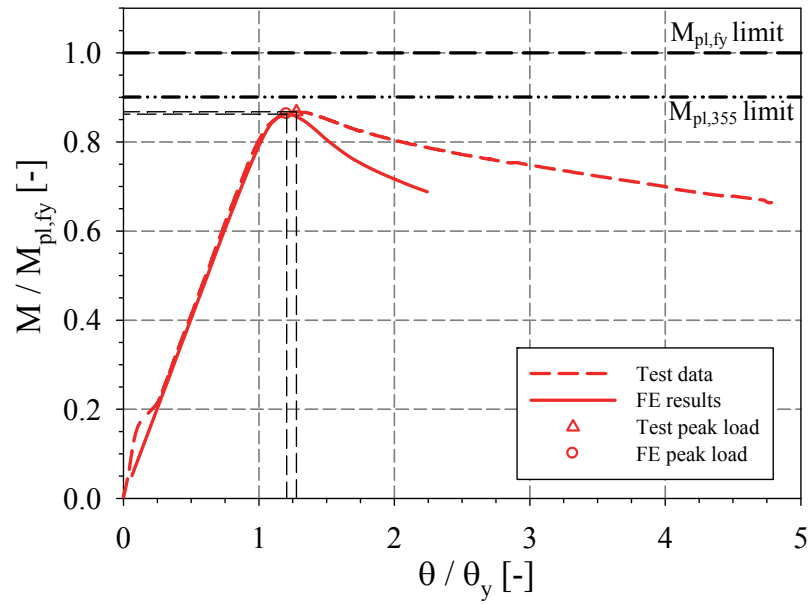
11.3.4.1 RHS_220×120×6.3_SS_3P*

Specimen name	Nominal Details	Average measured material properties
RHS_220×120×6.3_SS_3P*	Shape: Rectangular Hollow Section Nominal Steel grade: 355 N/mm ² Load case: 3-point bending $h=200\text{mm}$ $b=120\text{mm}$ $t=6.3\text{mm}$ Fabrication process: Hot-rolled	$f_y = 394.2 \text{ N/mm}^2$ $f_u = 534.4 \text{ N/mm}^2$ $E = 208932 \text{ N/mm}^2$ $\epsilon_y = 0.19 \%$ $\epsilon_{y2} = 1.85 \%$ $\epsilon_u = 16.98 \%$
 <p>Average $h = 219.25 \text{ mm}$</p>	 <p>Average $b = 120.60 \text{ mm}$</p>	 <p>Average $t = 6.39 \text{ mm}$</p>
RHS_220×120×6.3_SS_3P* at failure 		

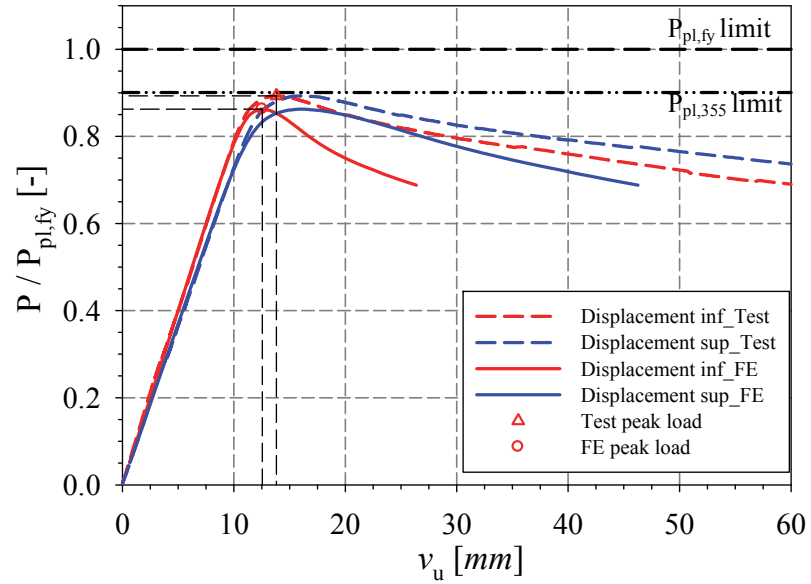
Yield pattern of RHS_220×120×6.3_SS_3P* at failure

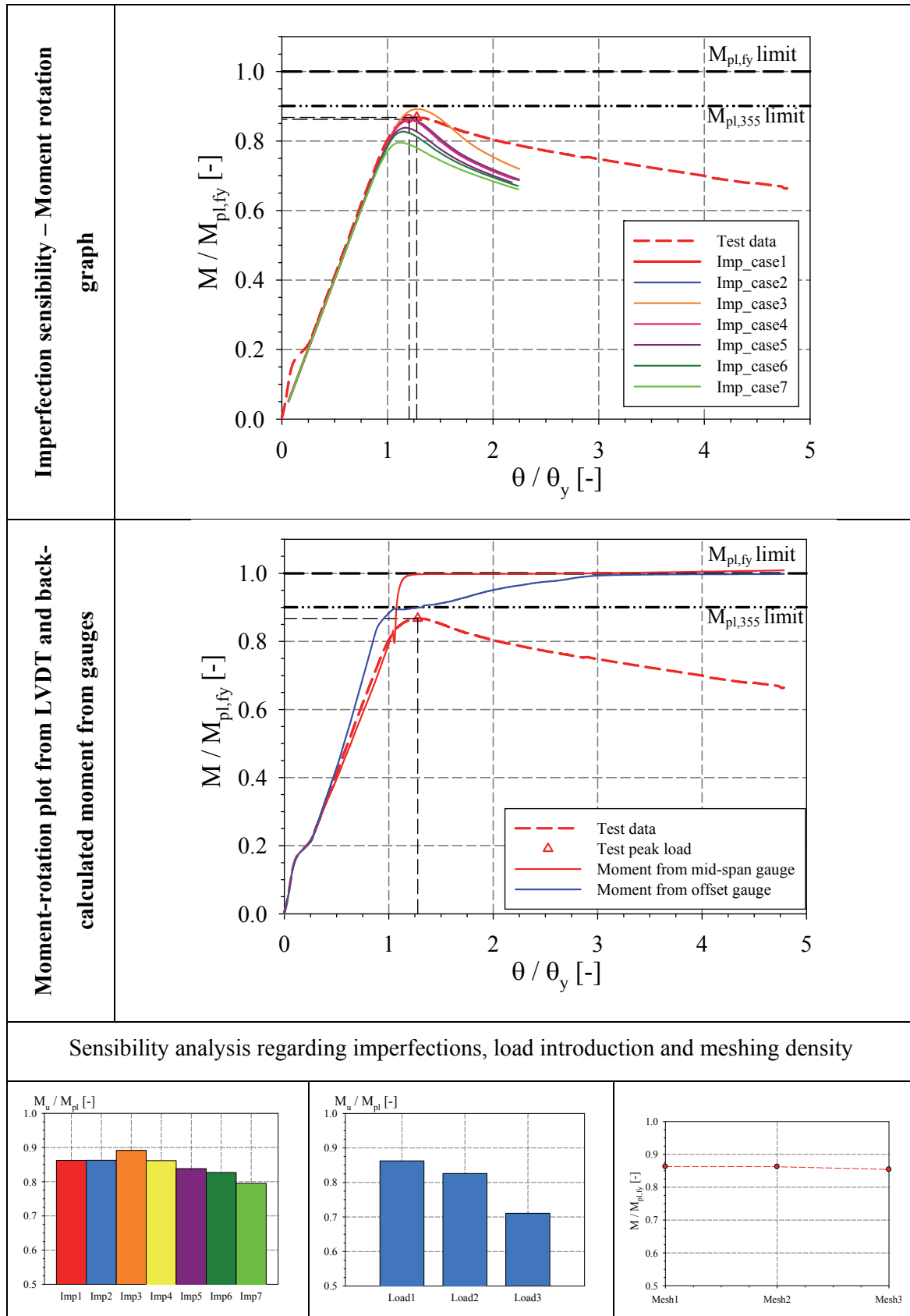


Moment-rotation

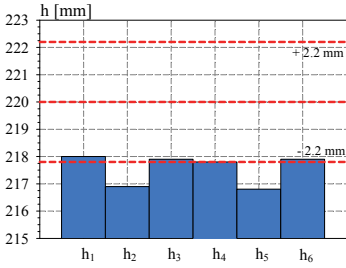
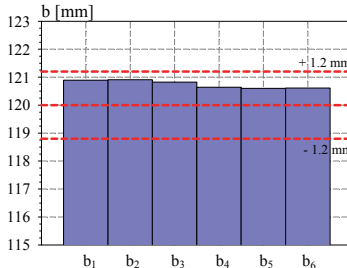
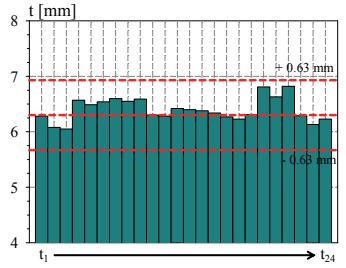
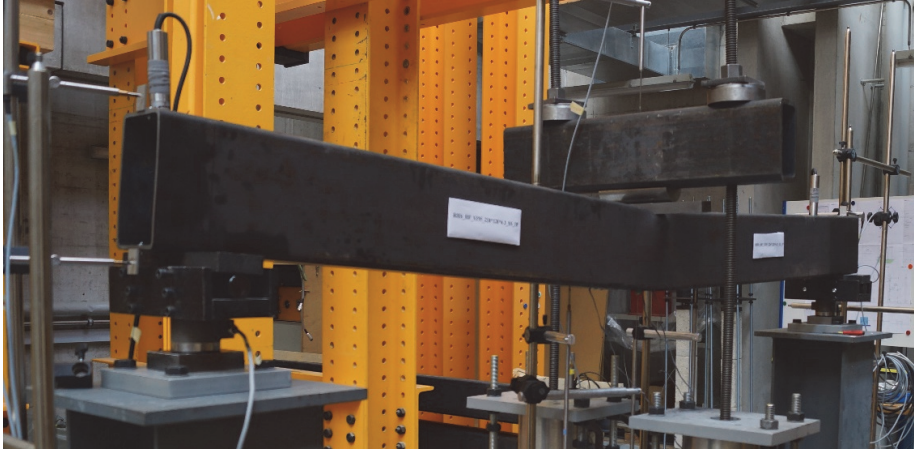
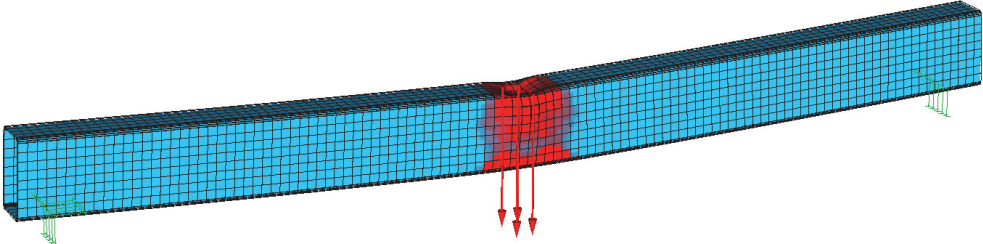


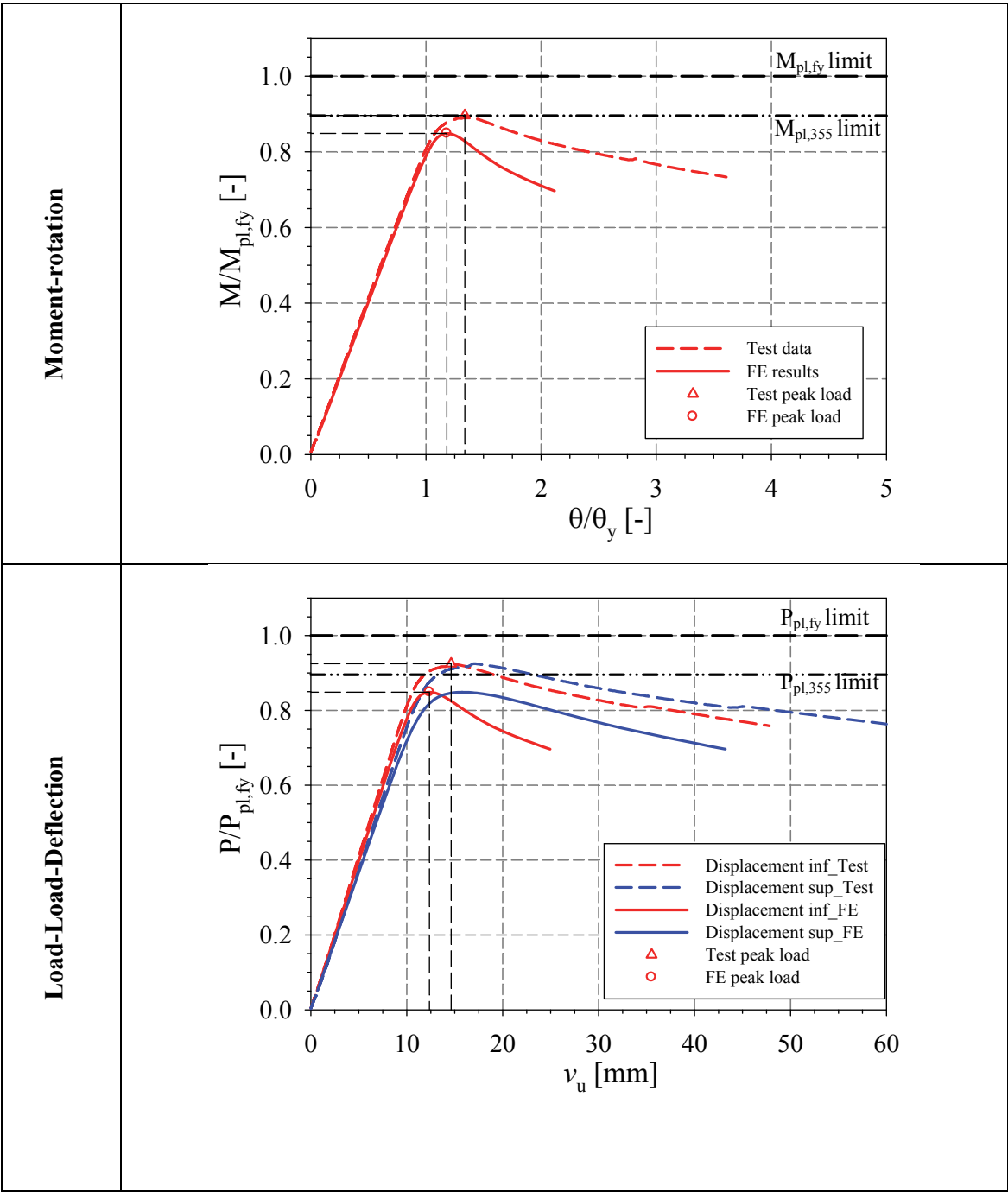
Load-Deflection

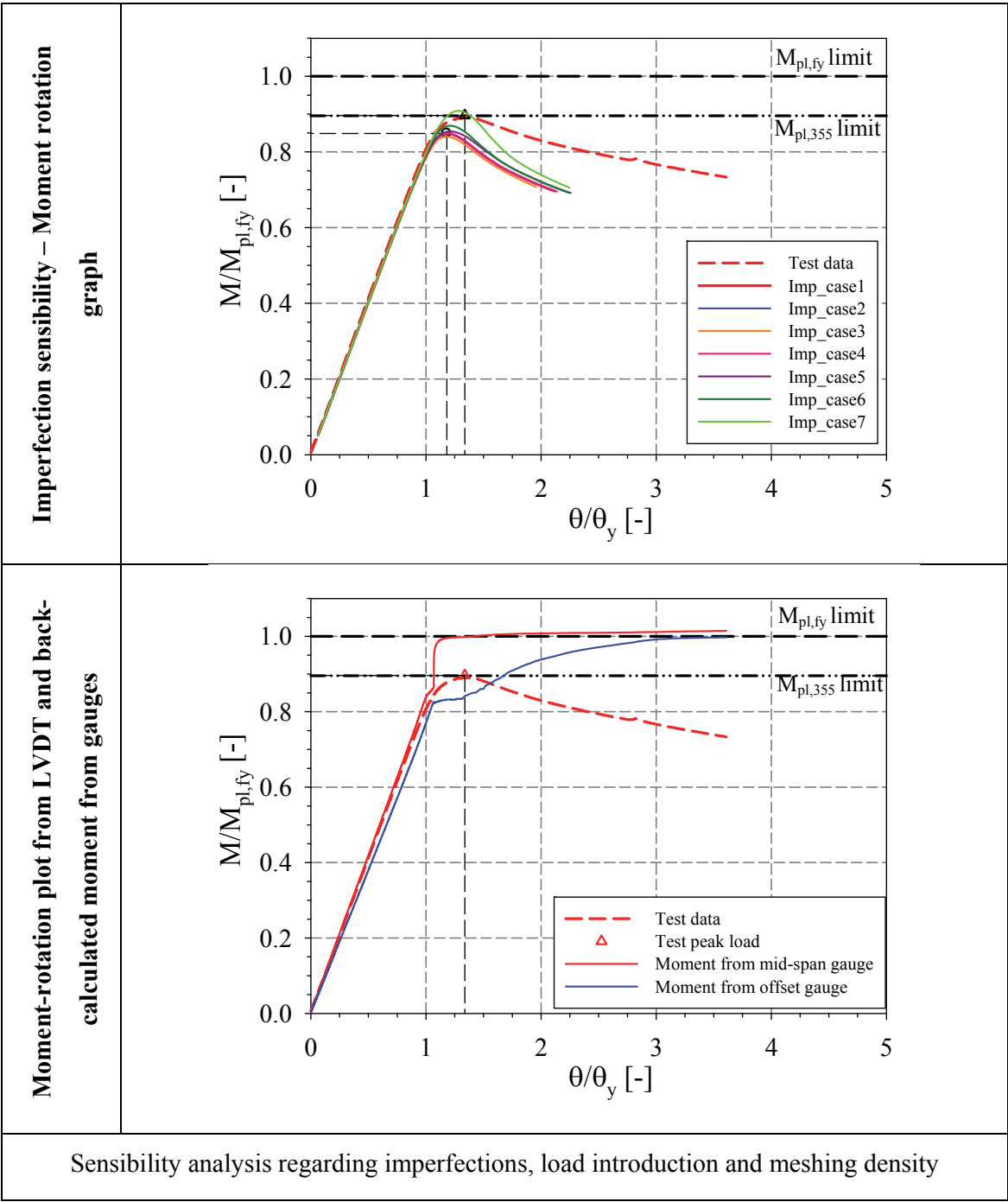


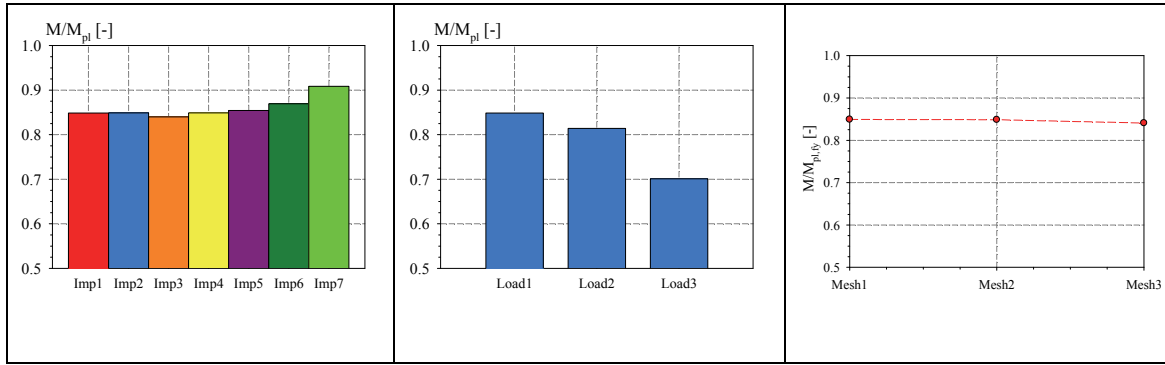


11.3.4.2 RHS_220×120×6.3_SS_3P

Specimen name	Nominal Details	Measured material properties (average)
RHS_220×120×6.3_SS_3P	Shape: Rectangular Hollow Section Nominal Steel grade: 355 N/mm ² Load case: 3-point bending $h=200$; $b=120$; $t=6.3$ Fabrication process: Hot-rolled	$f_y = 396.5 \text{ N/mm}^2$ $f_u = 535.9 \text{ N/mm}^2$ $E = 211087 \text{ N/mm}^2$ $\varepsilon_y = 0.19 \%$ $\varepsilon_{y2} = 1.88 \%$ $\varepsilon_u = 15.28 \%$
 <p>Average $h = 217.55 \text{ mm}$</p>	 <p>Average $b = 120.75 \text{ mm}$</p>	 <p>Average $t = 6.40 \text{ mm}$</p>
RHS_220×120×6.3_SS_3P at failure 		
Yield pattern of RHS_220×120×6.3_SS_3P at failure 		





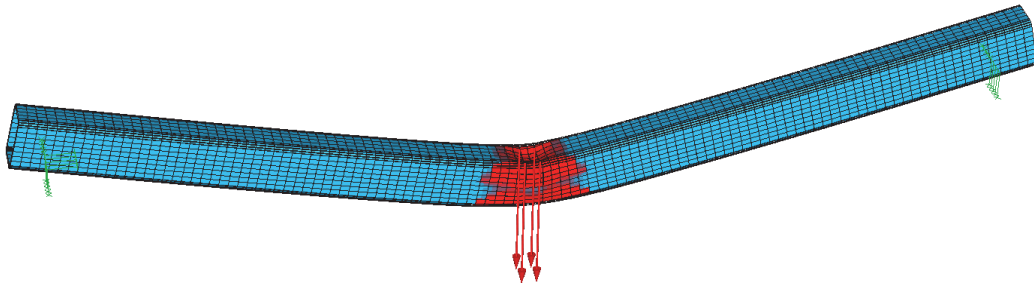
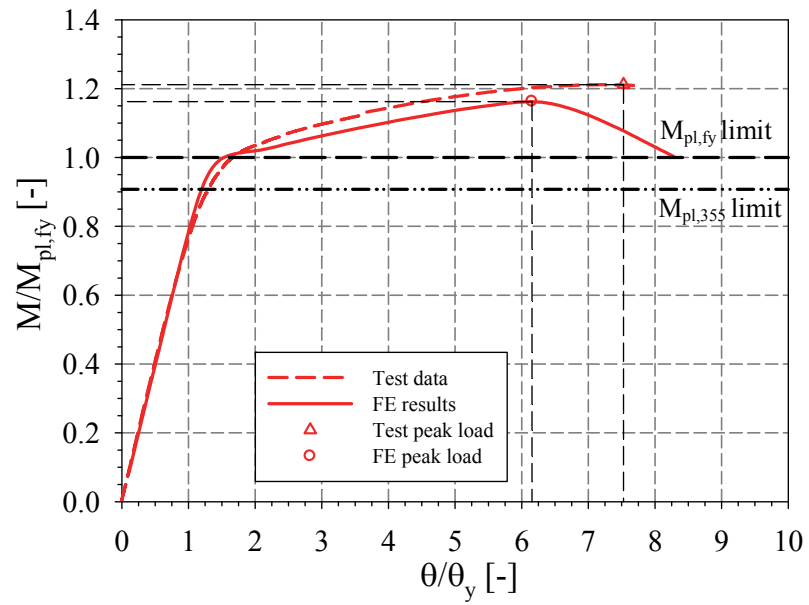


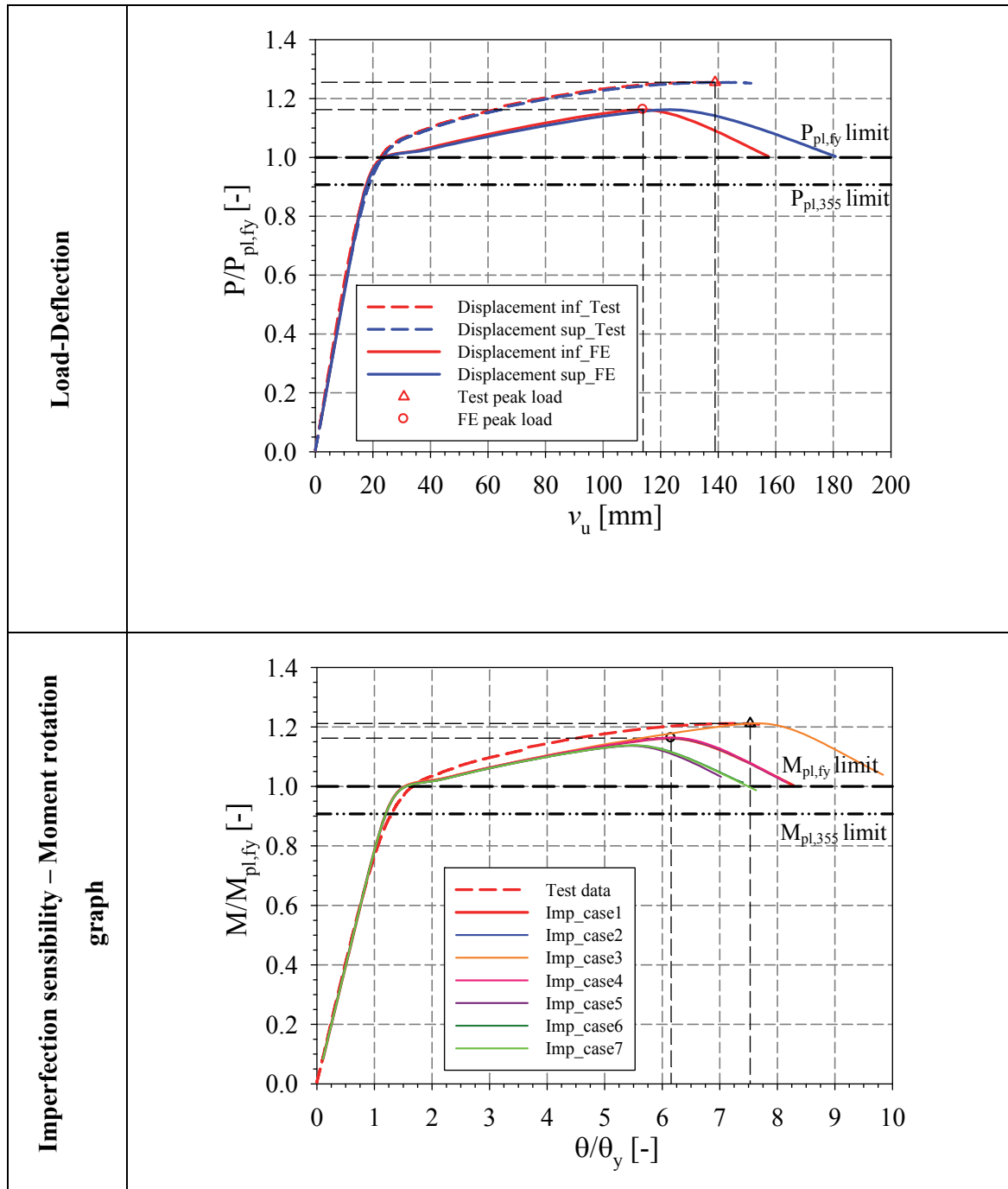
11.3.4.3 RHS_150×100×8_SS_3P

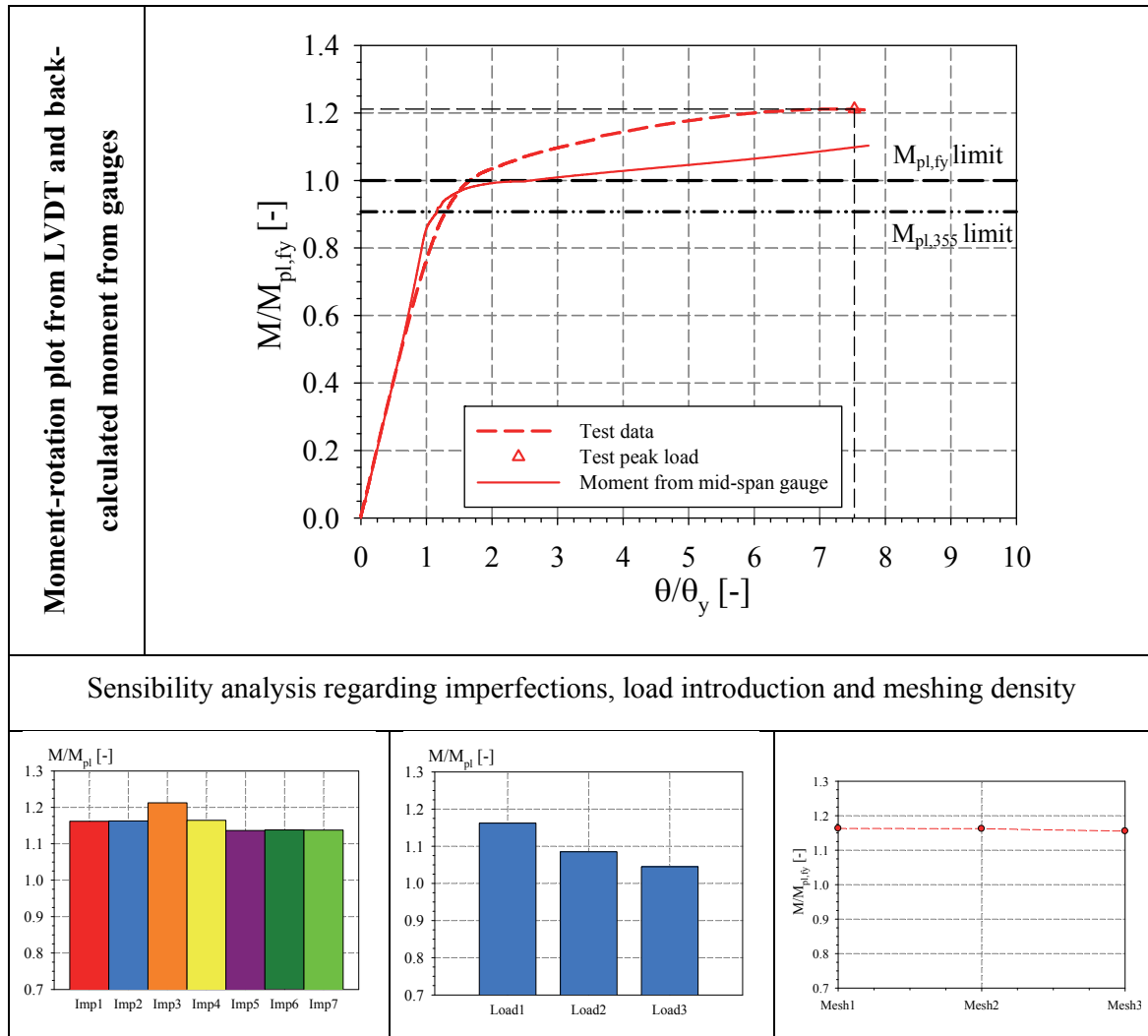
Specimen name	Nominal Details	Measured material properties (average)
RHS_150×100×8_SS_3P	Shape: Rectangular Hollow Section Nominal Steel grade: 355 N/mm^2 Load case: 3-point bending $h=150mm$ $b=100mm$ $t=8mm$ Fabrication process: Hot-rolled	$f_y = 391.2 N/mm^2$ $f_u = 554.0 N/mm^2$ $E = 205737 N/mm^2$ $\varepsilon_y = 0.19 \%$ $\varepsilon_{y2} = 1.49 \%$ $\varepsilon_u = 12.93 \%$
<p>Average $h = 149.60 mm$</p>	<p>Average $b = 99.94 mm$</p>	<p>Average $t = 8.35mm$</p>

RHS_150×100×8_SS_3P at failure



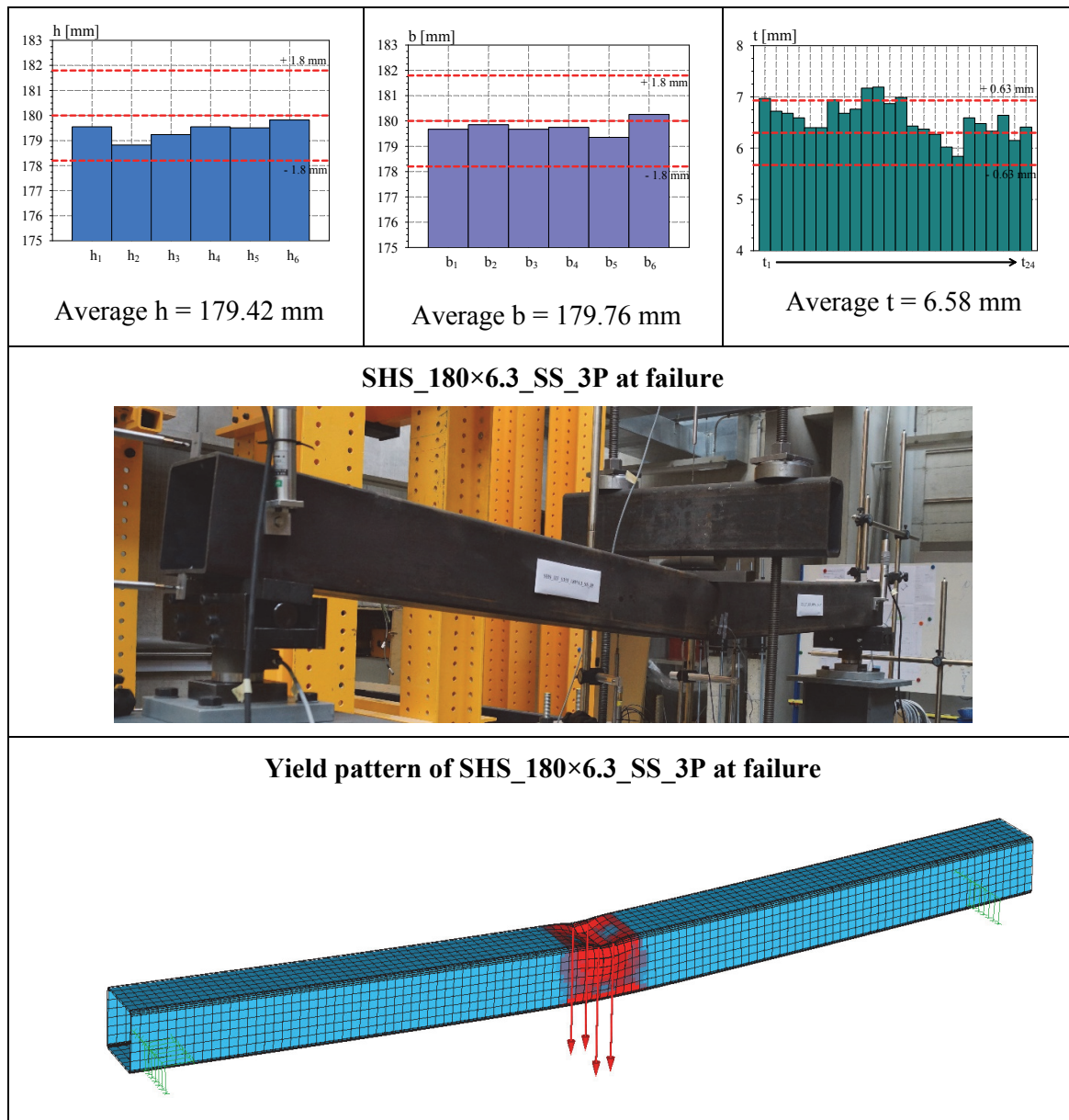
Yield pattern of RHS_150×100×8_SS_3P at failure**Moment-rotation**

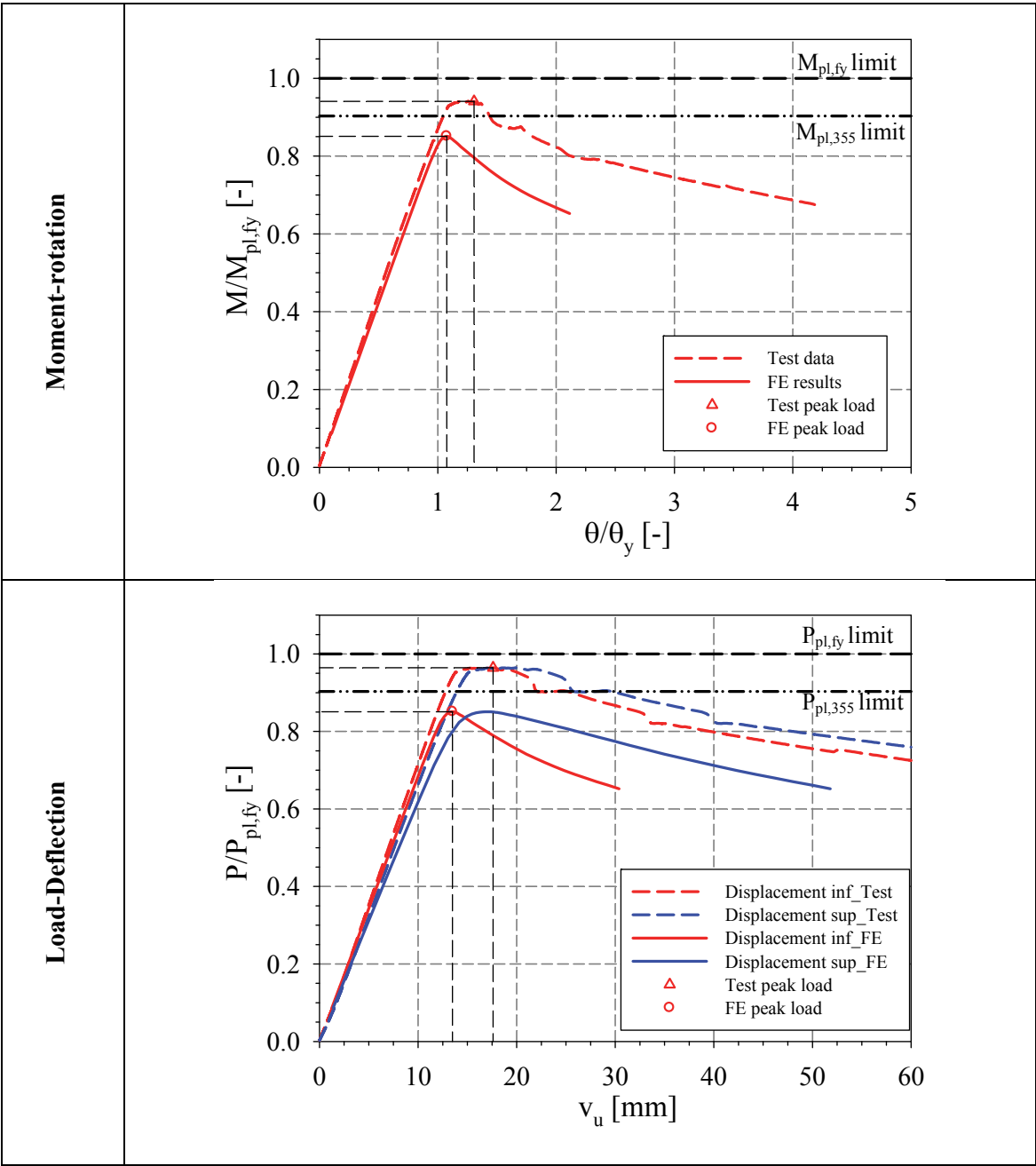


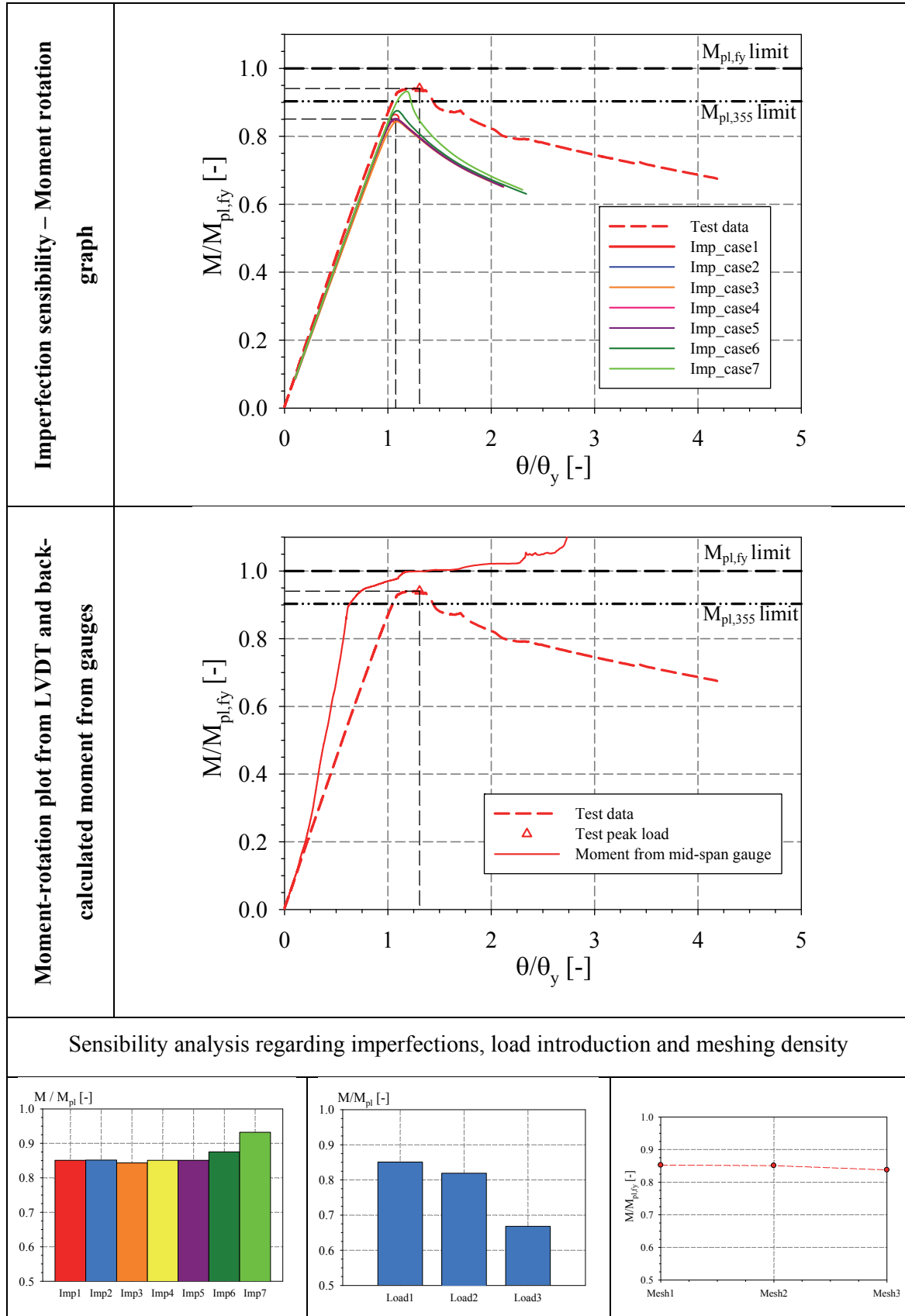


11.3.4.4 SHS_180×6.3_SS_3P

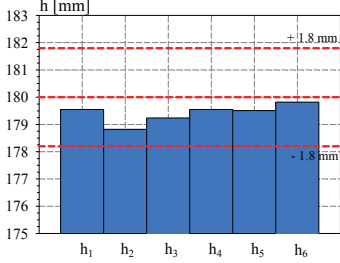
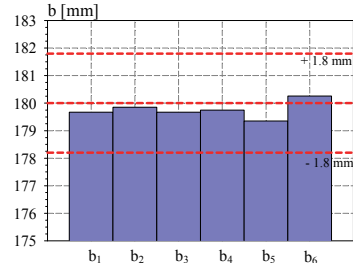
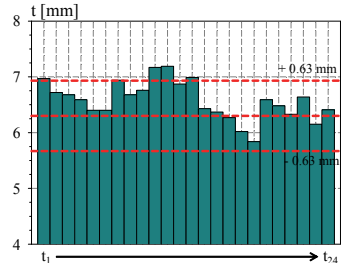
Specimen name	Nominal Details	Measured material properties (average)
SHS_180×6.3_SS_3P	Shape: Square Hollow Section Nominal Steel grade: 355 N/mm^2 Load case: 3-point bending $h=180mm$ $b=180mm$ $t=6.3mm$ Fabrication process: Hot-rolled	$f_y = 393.2 \text{ N/mm}^2$ $f_u = 523.8 \text{ N/mm}^2$ $E = 206903 \text{ N/mm}^2$ $\varepsilon_y = 0.19 \%$ $\varepsilon_{y2} = 2.19 \%$ $\varepsilon_u = 14.88 \%$







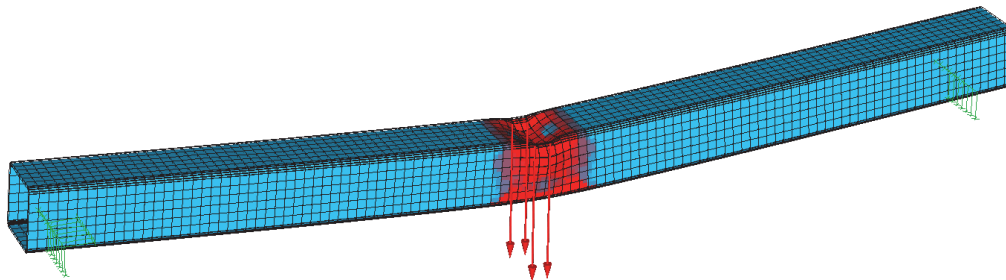
11.3.4.5 SHS_180×8_SS_3P

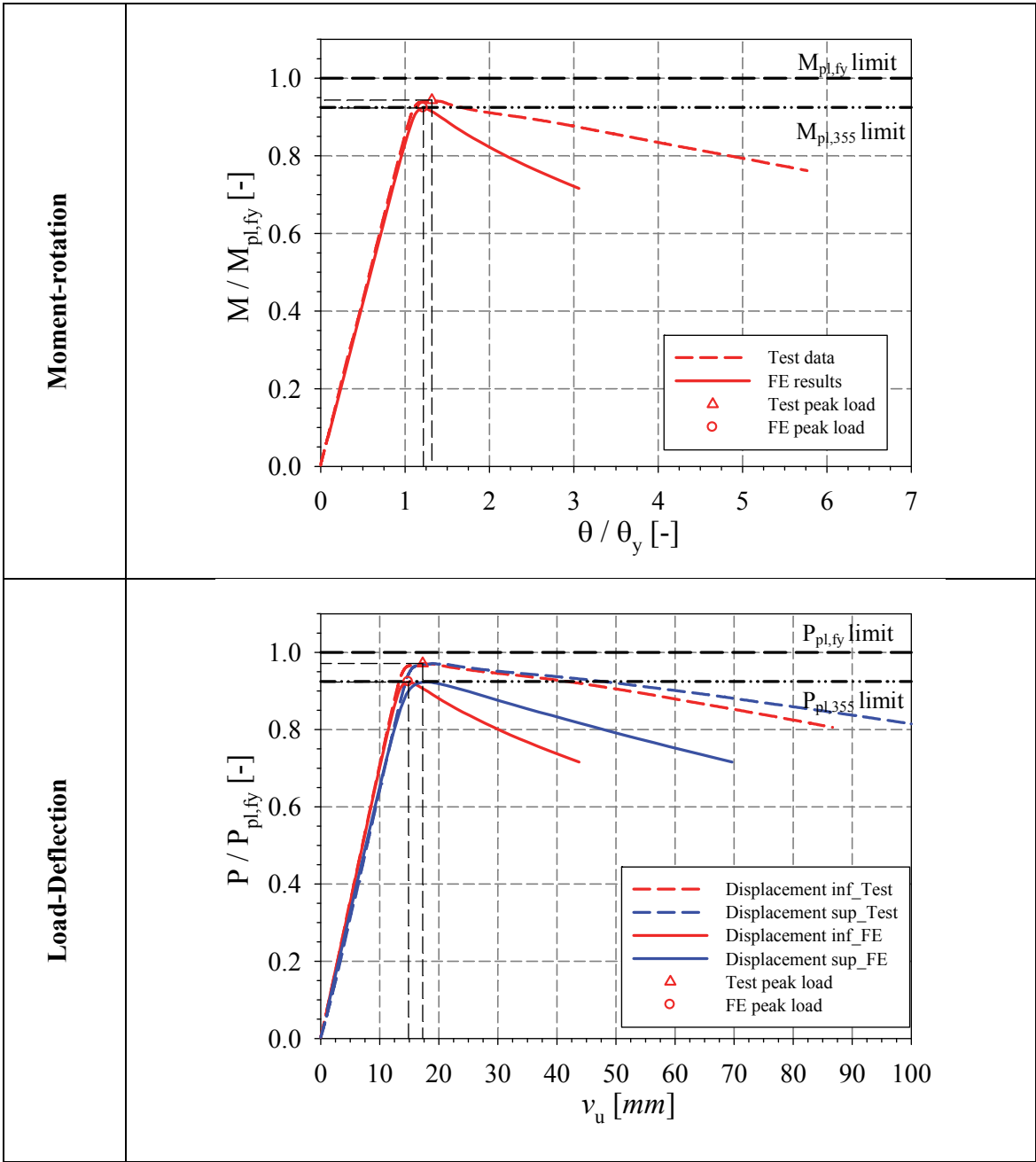
Specimen name	Nominal Details	Measured material properties (average)
SHS_180×8_SS_3P	Shape: Square Hollow Section Nominal Steel grade: 355 N/mm ² Load case: 3-point bending h=180mm b=180mm t=8mm Fabrication process: Hot-rolled	$f_y = 384.0 \text{ N/mm}^2$ $f_u = 531.5 \text{ N/mm}^2$ $E = 208013 \text{ N/mm}^2$ $\varepsilon_y = 0.18 \%$ $\varepsilon_{y2} = 1.69 \%$ $\varepsilon_u = 17.47 \%$
 <p>Average h = 179.46 mm</p>	 <p>Average b = 179.42 mm</p>	 <p>Average t = 7.89 mm</p>

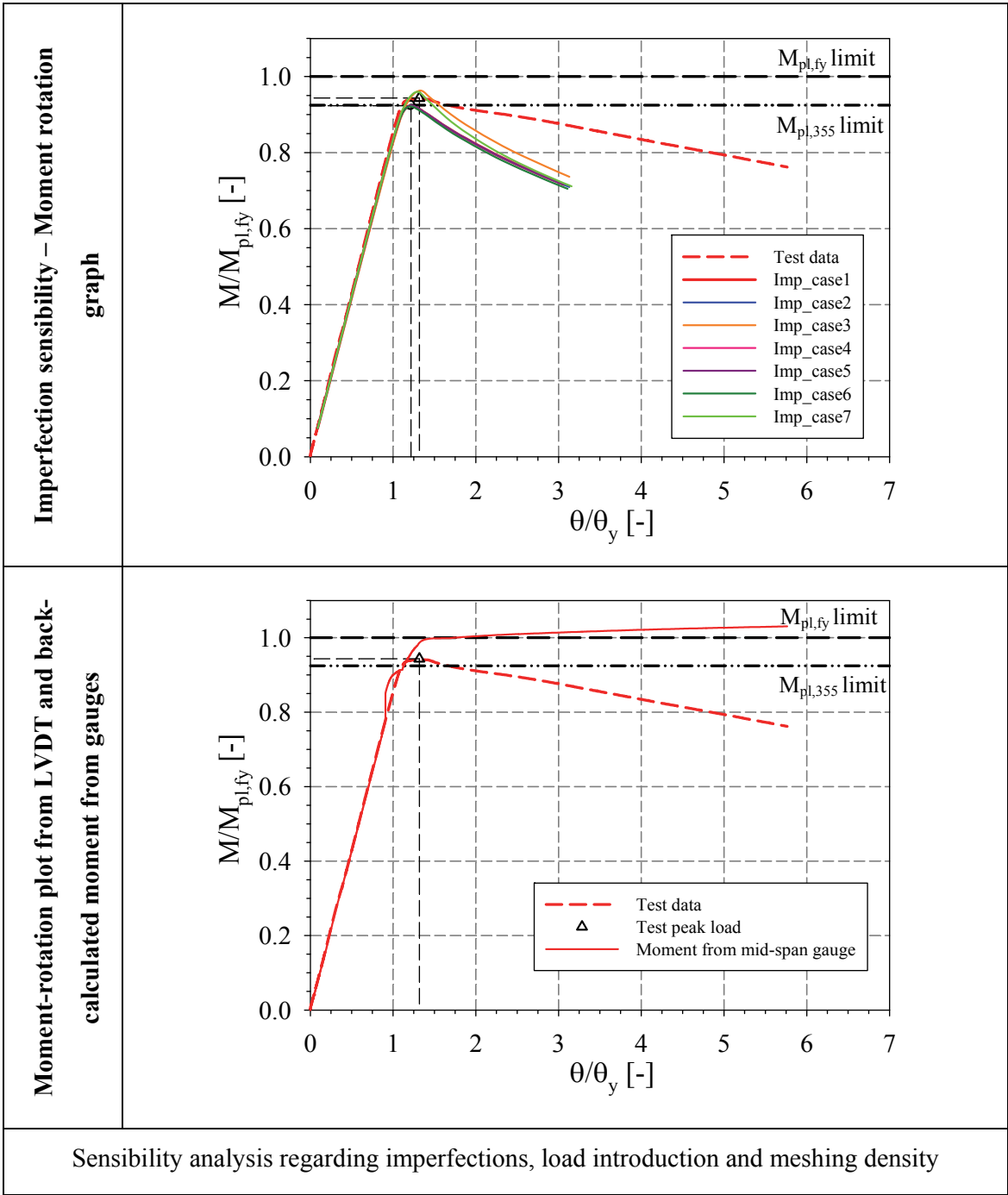
SHS_180×8_SS_3P at failure

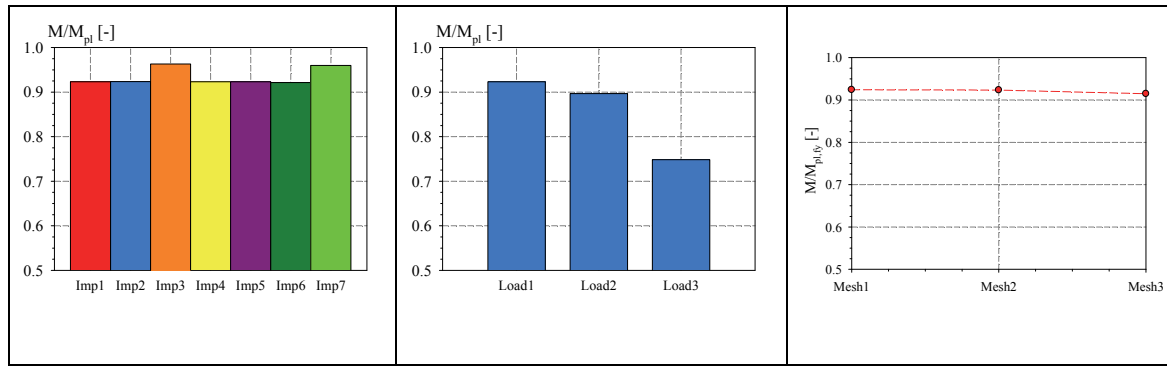


Yield pattern of SHS_180×8_SS_3P at failure







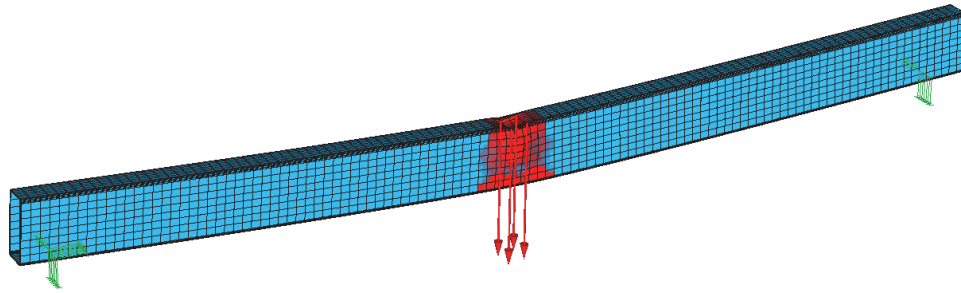
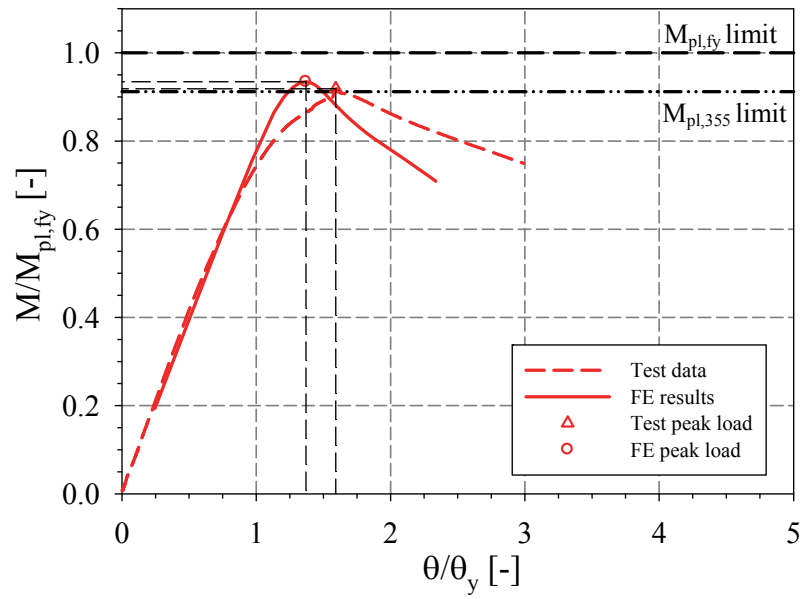


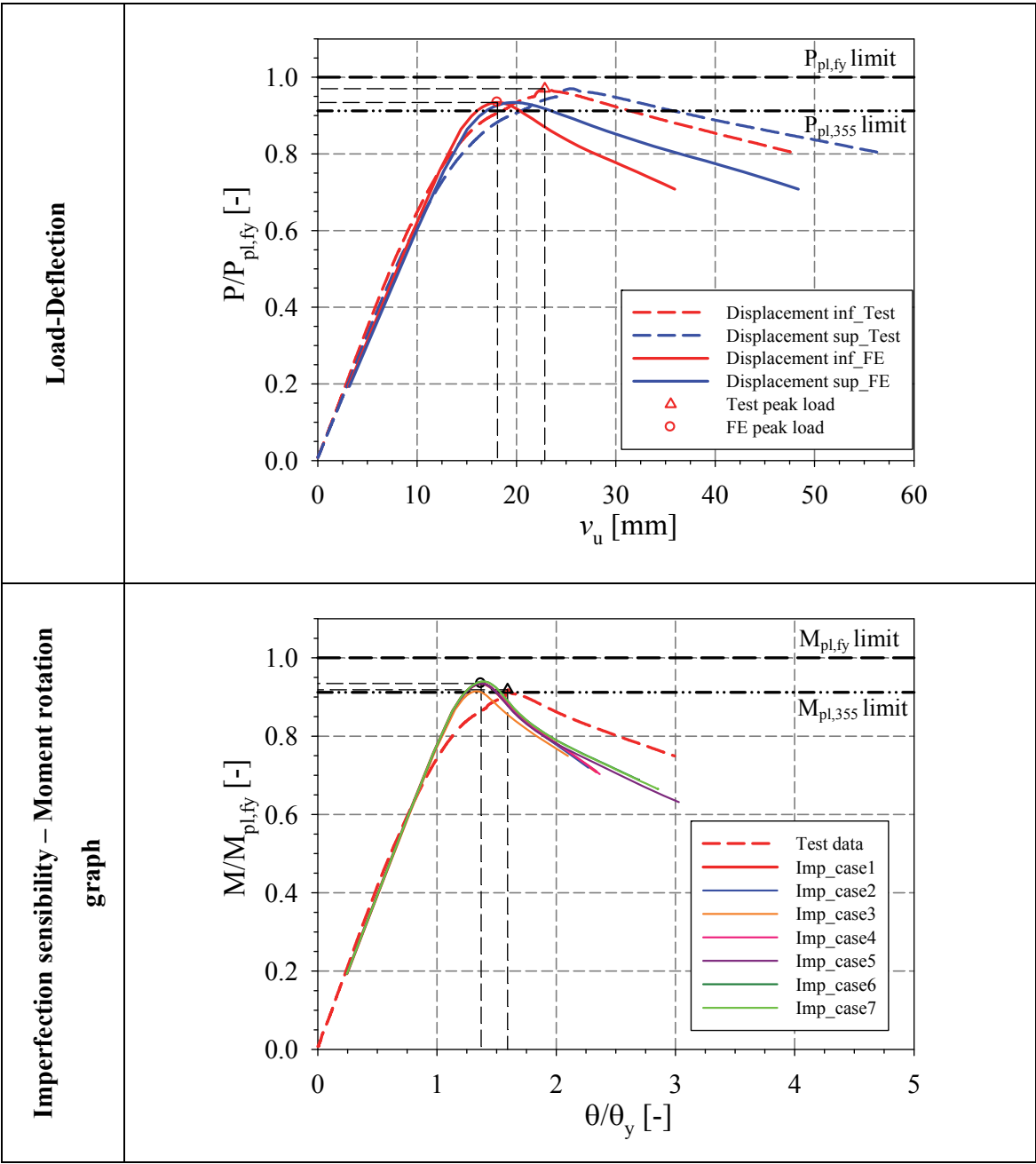
11.3.4.6 RHS_180×80×4.5_SS_3P

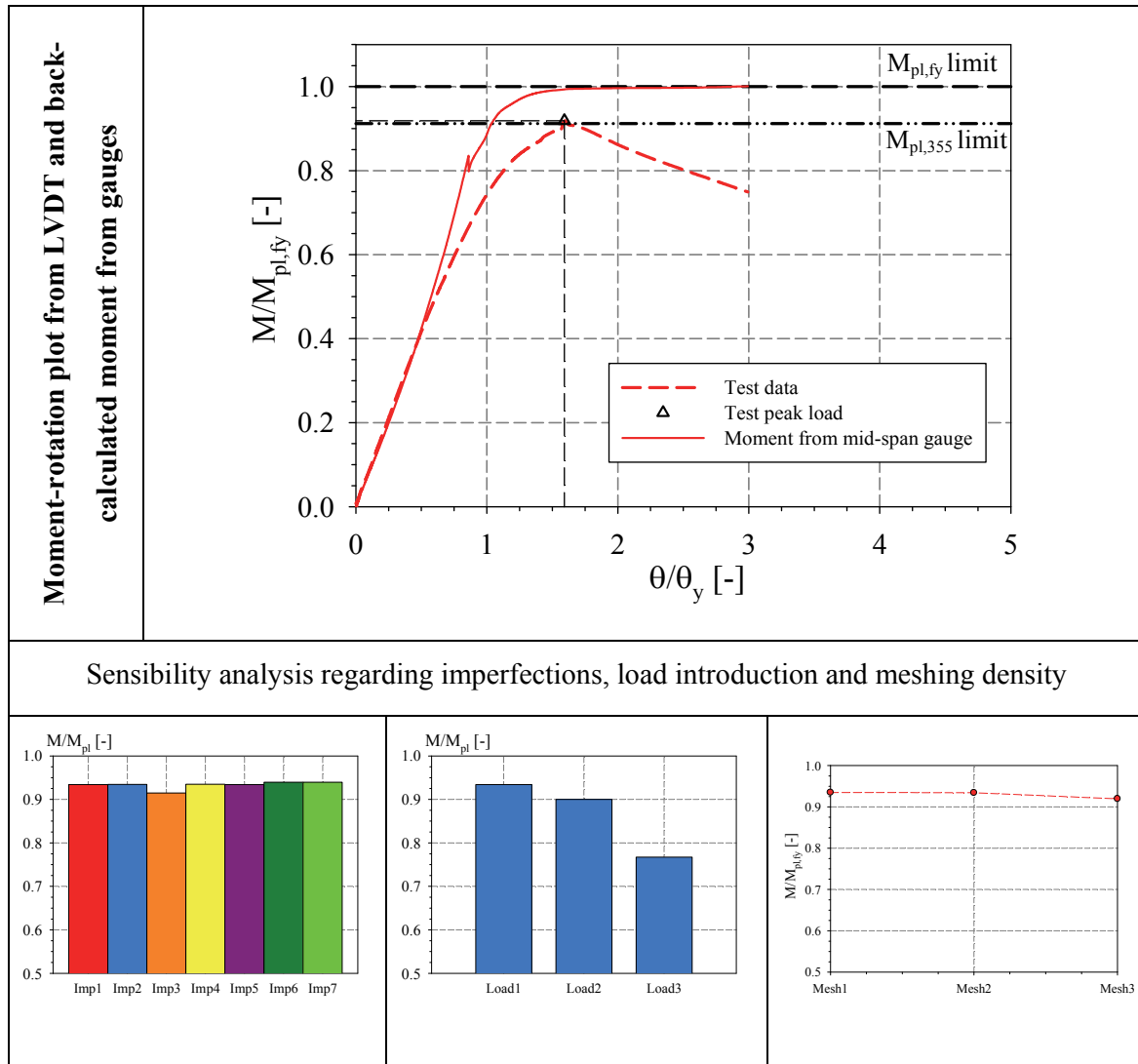
Specimen name	Nominal Details	Measured material properties (average)
RHS_180×80×4.5_SS_3P	Shape: Rectangular Hollow Section Nominal Steel grade: 355 N/mm^2 Load case: 3-point bending $h=180mm$ $b=80mm$ $t=4.5mm$ Fabrication process: Hot-rolled	$f_y = 389.2 N/mm^2$ $f_u = 539.4 N/mm^2$ $E = 198504 N/mm^2$ $\varepsilon_y = 0.20 \%$ $\varepsilon_{y2} = 1.76 \%$ $\varepsilon_u = 16.98 \%$
<p>Average $h = 179.35 mm$</p>	<p>Average $b = 78.52 mm$</p>	<p>Average $t = 4.80 mm$</p>

RHS_180×80×4.5_SS_3P at failure



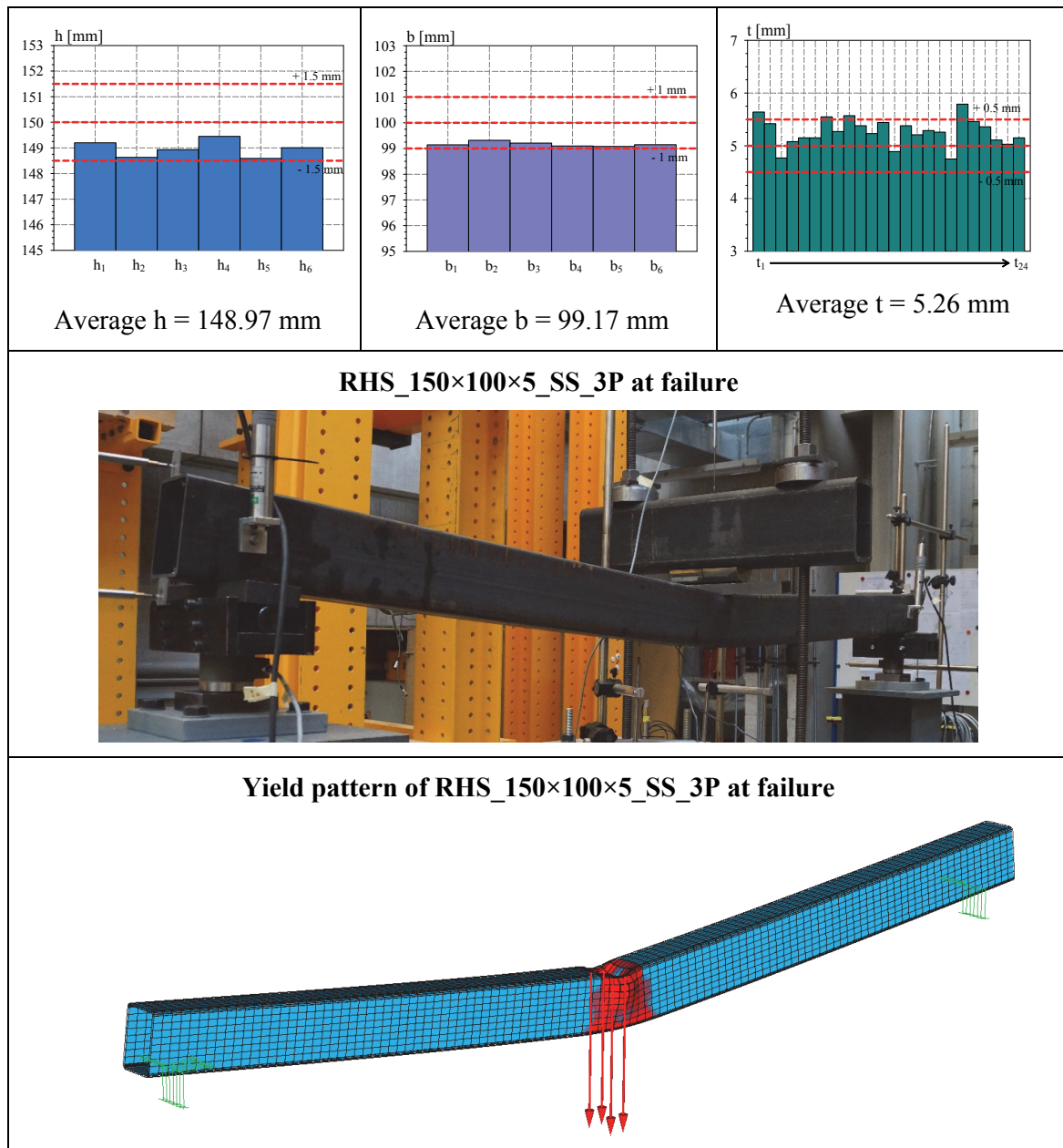
Yield pattern of RHS_180×80×4.5_SS_3P at failure**Moment-rotation**

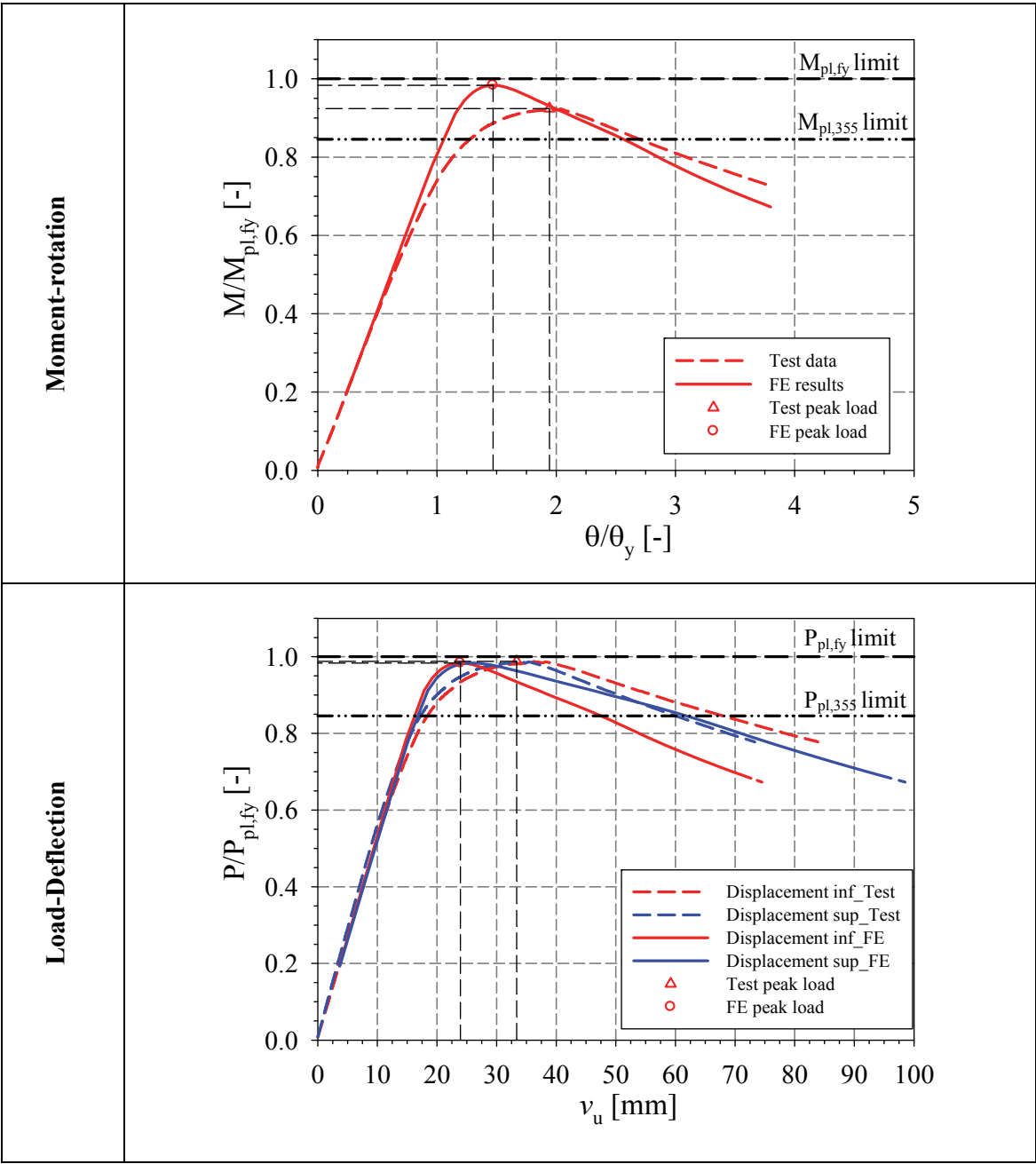


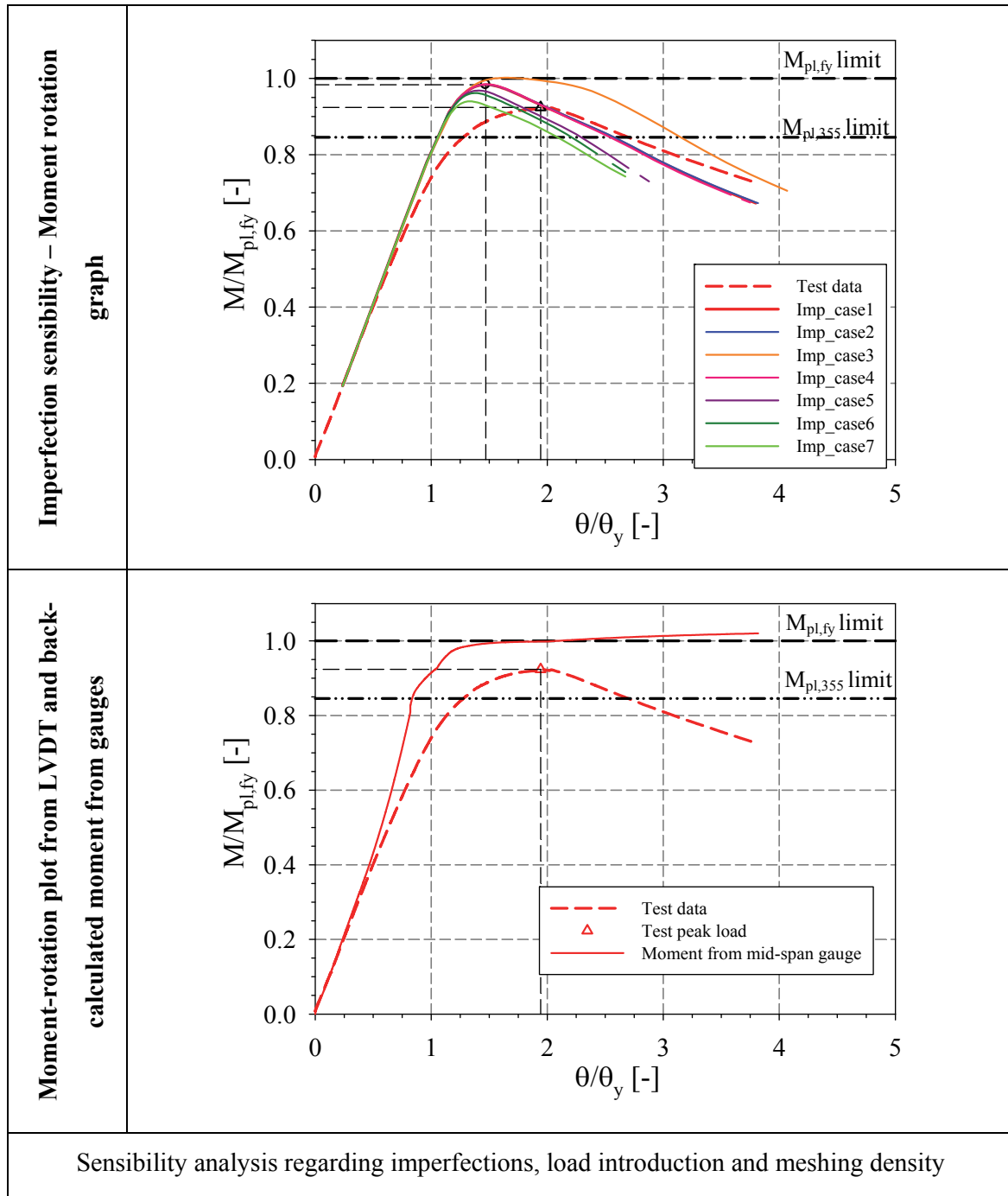


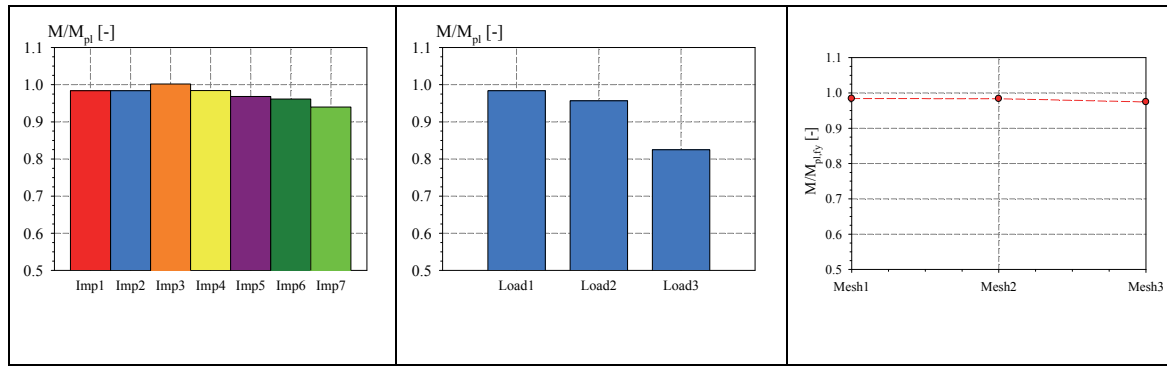
11.3.4.7 RHS_150×100×5_SS_3P

Specimen name	Nominal Details	Measured material properties (average)
RHS_150×100×5_SS_3P	Shape: Rectangular Hollow Section Nominal Steel grade: 355 N/mm^2 Load case: 3-point bending $h=150mm$ $b=100mm$ $t=5mm$ Fabrication process: Hot-rolled	$f_y = 419.8 \text{ N/mm}^2$ $f_u = 573.0 \text{ N/mm}^2$ $E = 211215 \text{ N/mm}^2$ $\varepsilon_y = 0.20 \%$ $\varepsilon_{y2} = 1.73 \%$ $\varepsilon_u = 14.89 \%$







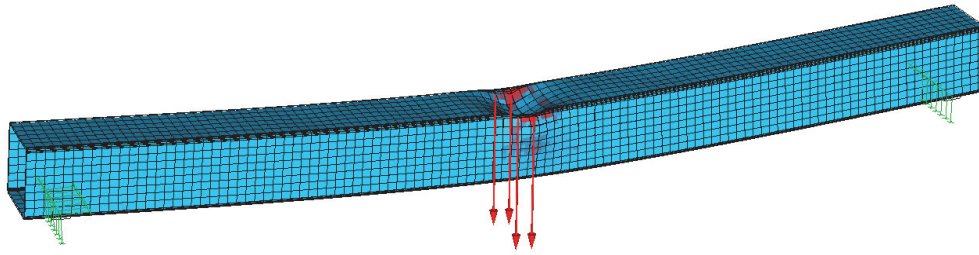
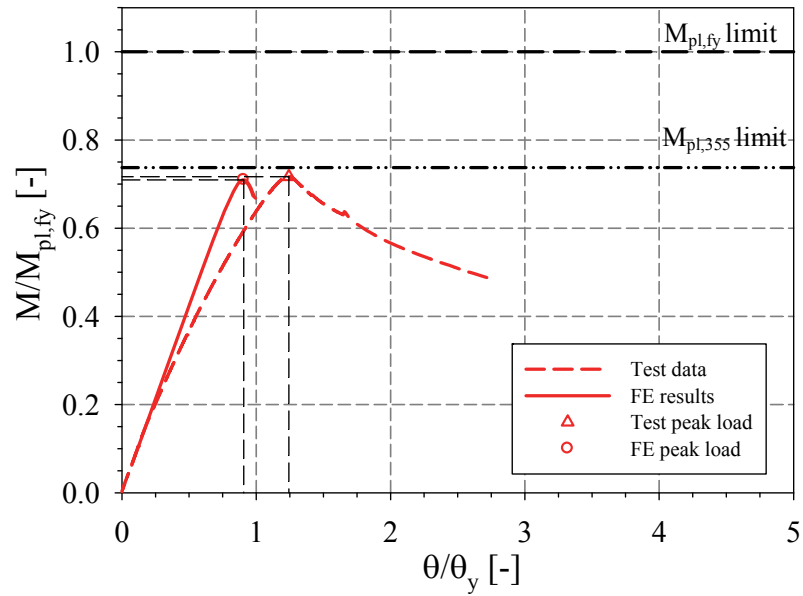


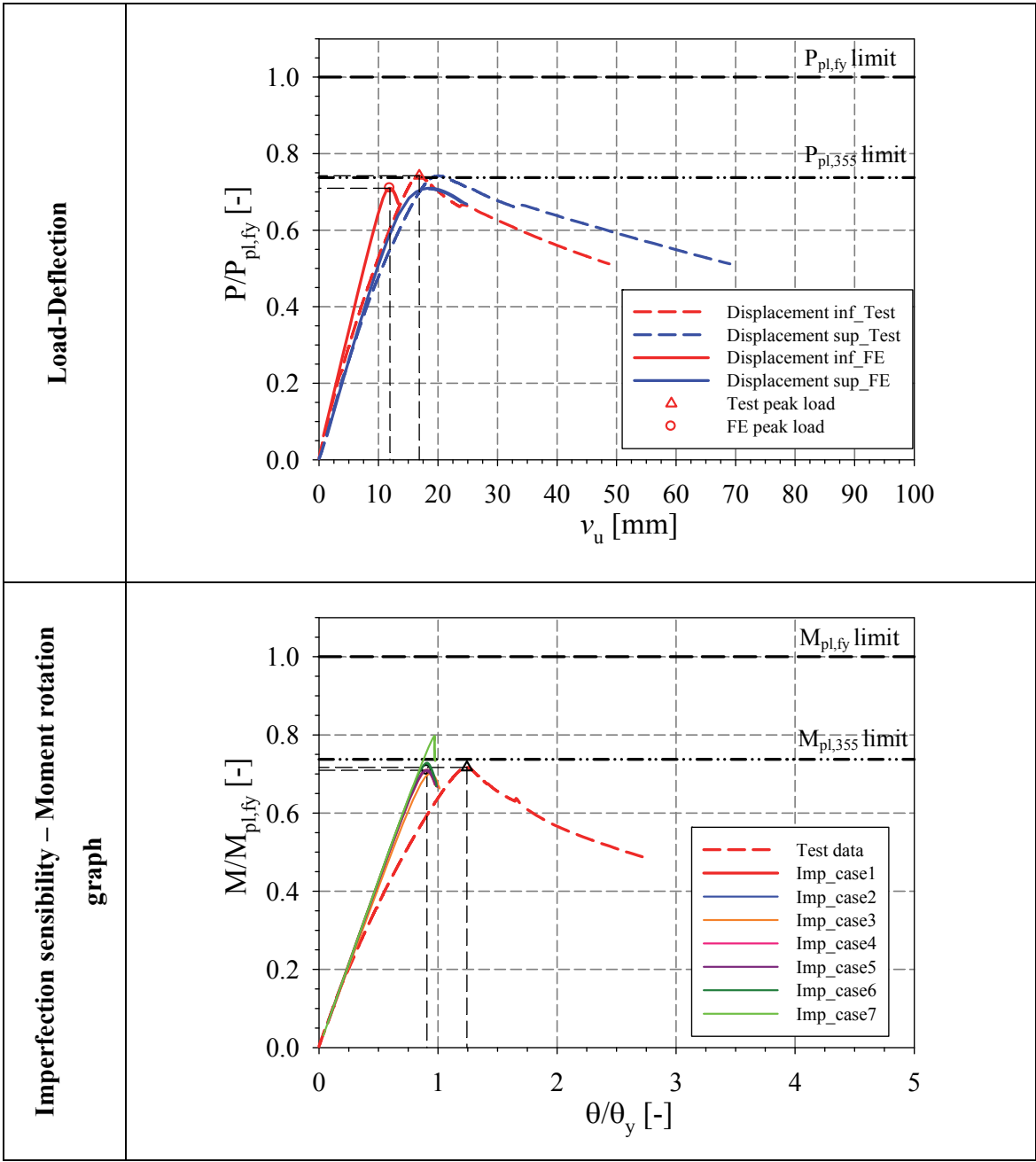
11.3.4.8 SHS_200x6_SS_3P

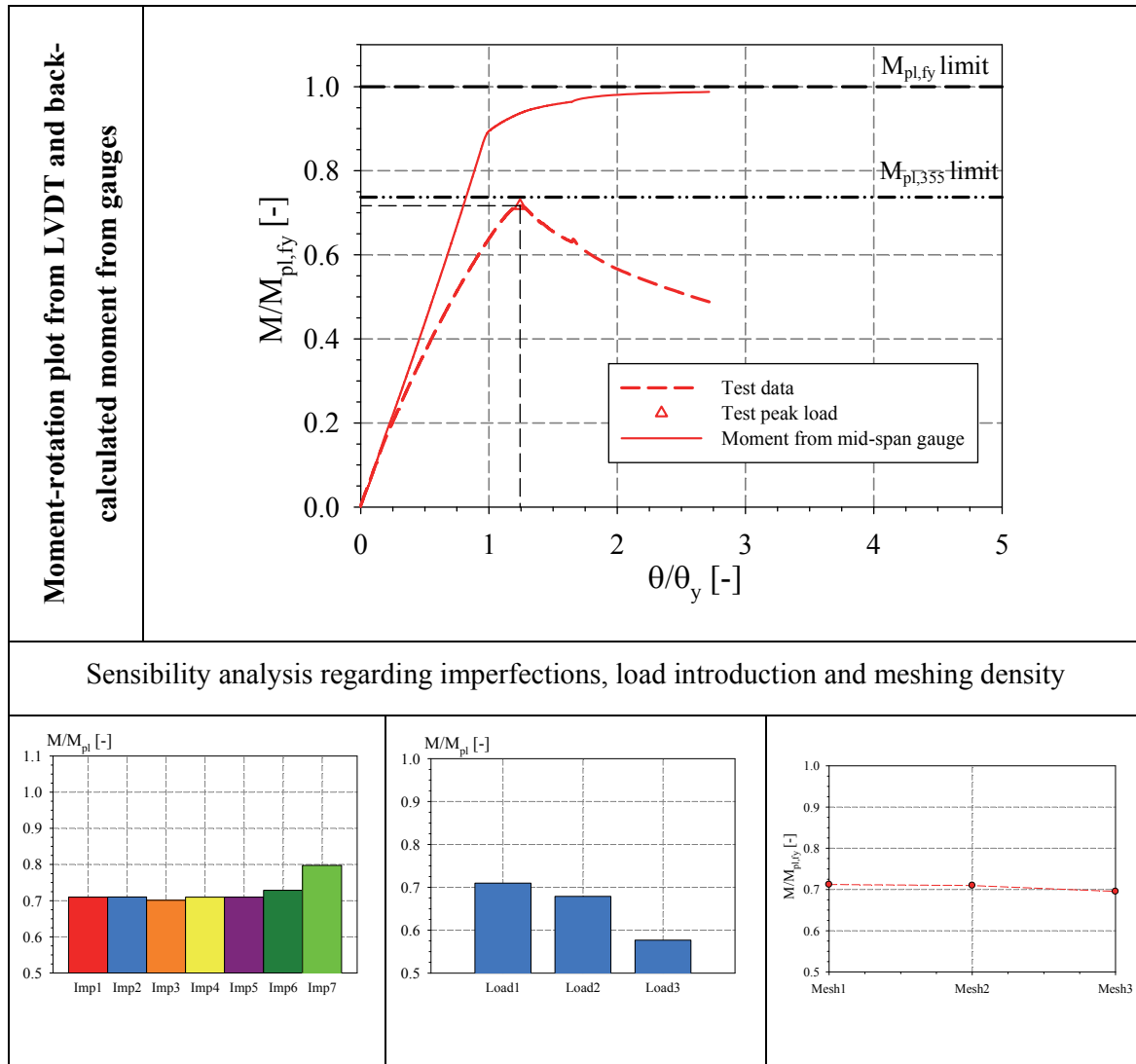
Specimen name	Nominal Details	Measured material properties (average)
SHS_200×6_SS_3P	Shape: Square Hollow Section Nominal Steel grade: 355 N/mm^2 Load case: 3-point bending $h=200mm$ $b=200mm$ $t=6mm$ Fabrication process: Cold formed	$f_y = 481.5 N/mm^2$ $f_u = 569.6 N/mm^2$ $E = 210239 N/mm^2$ $\varepsilon_y = 0.25 \%$ $\varepsilon_u = 19.00 \%$
<p>Average $h = 200.53 mm$</p>	<p>Average $b = 200.87 mm$</p>	<p>Average $t = 5.83 mm$</p>

SHS_200×6_SS_3P at failure



Yield pattern of SHS_200×6_SS_3P at failure**Moment-rotation**

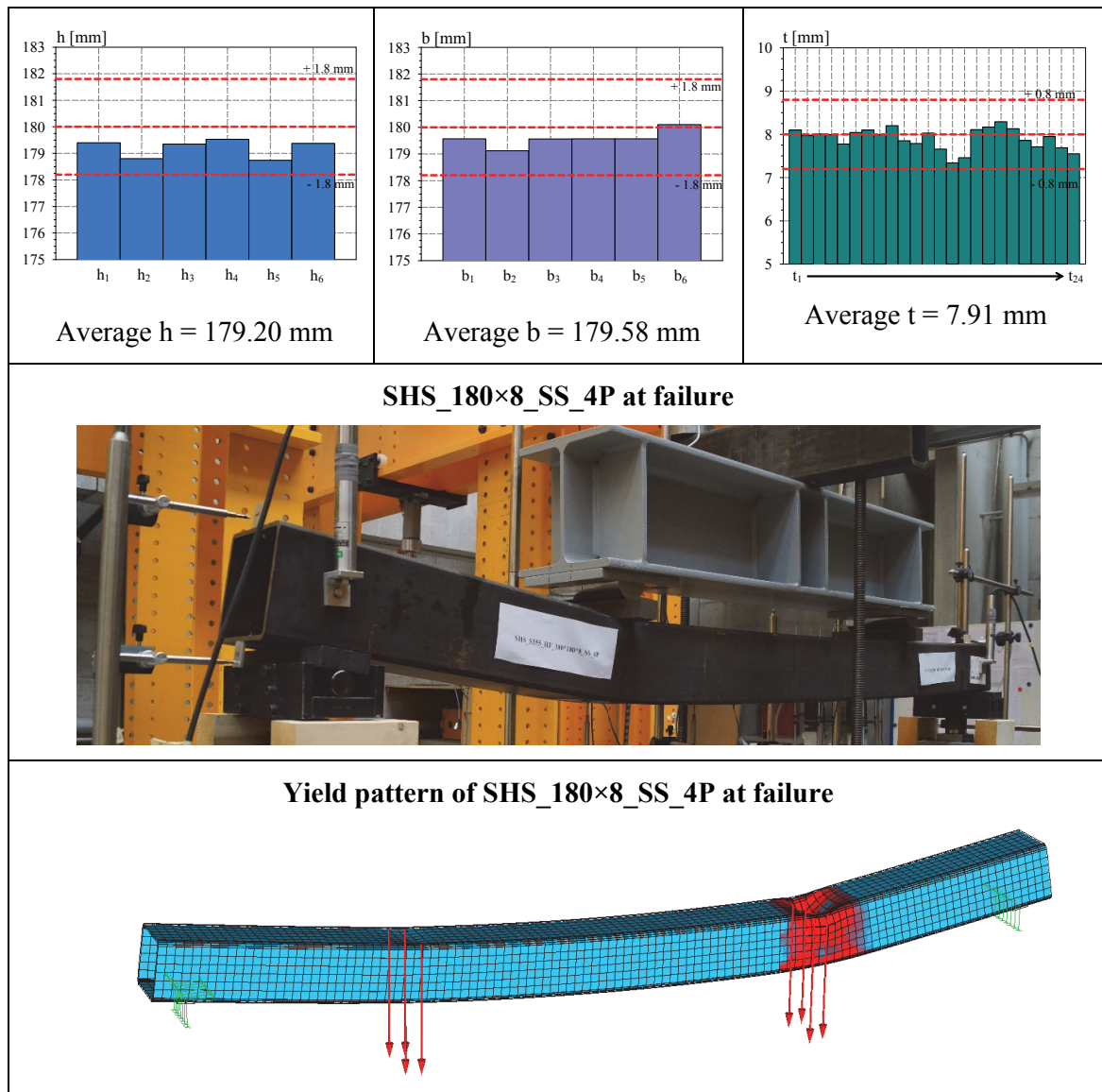


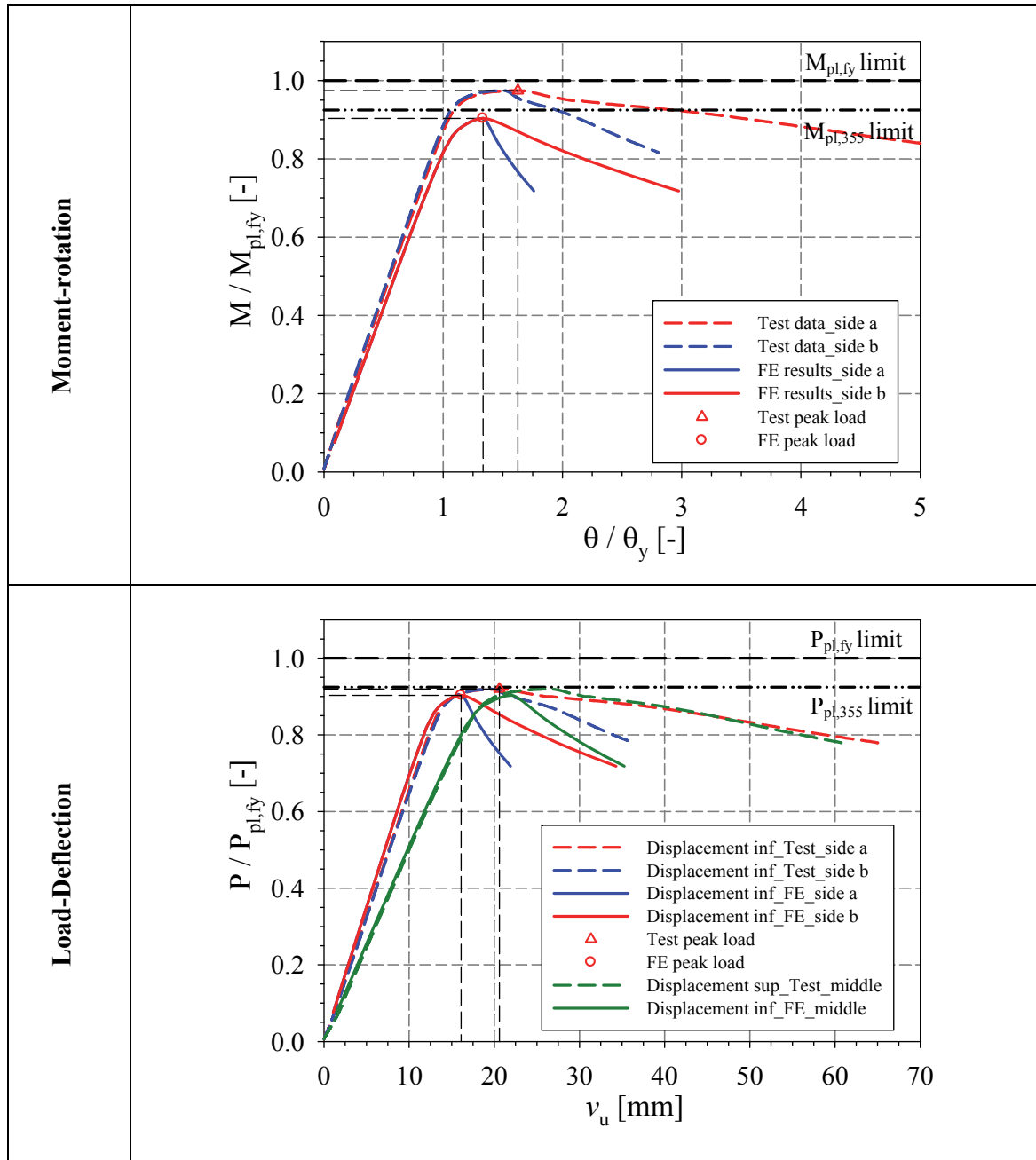


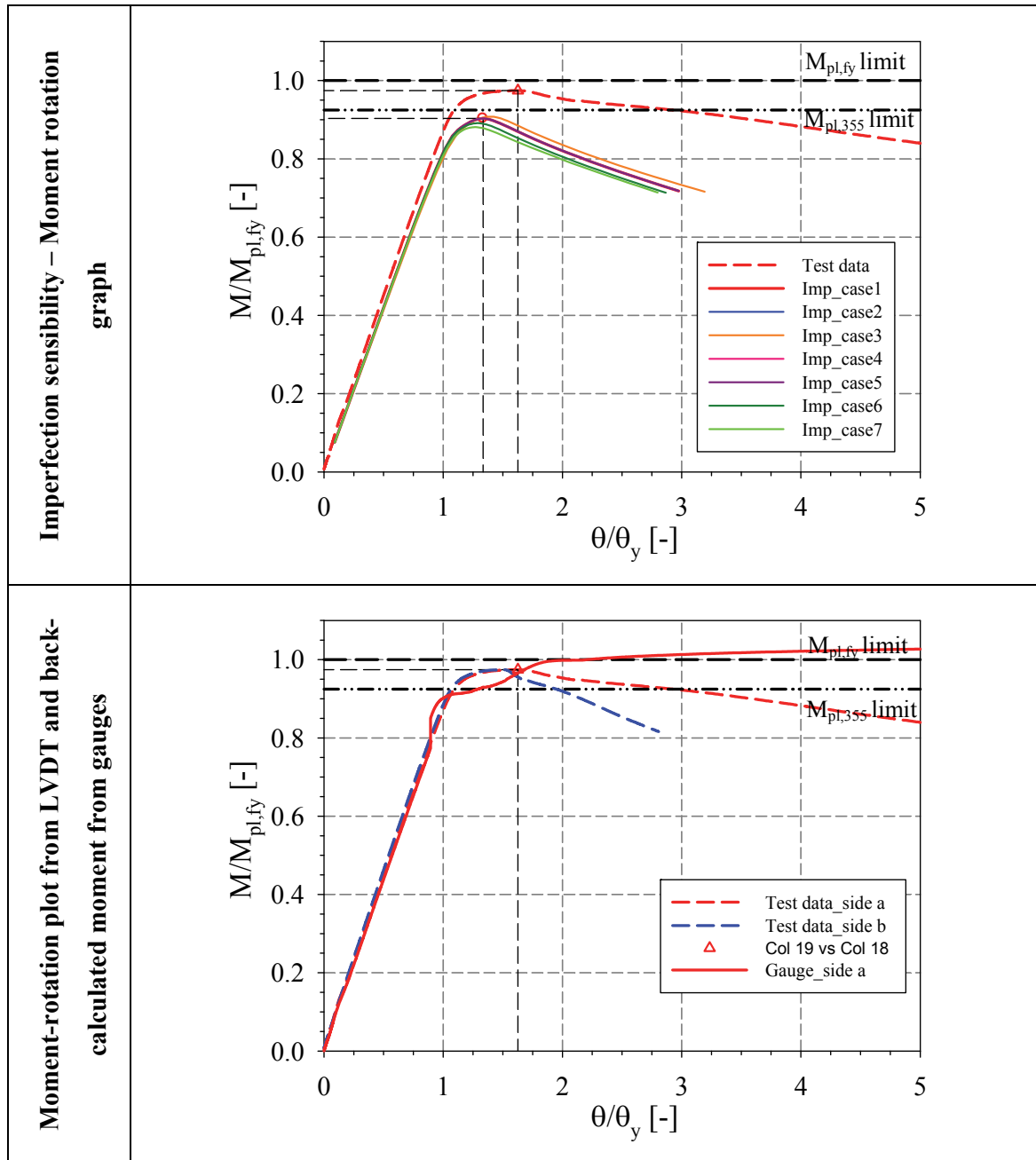
11.3.5 Summary of 4-point bending results and numerical validation

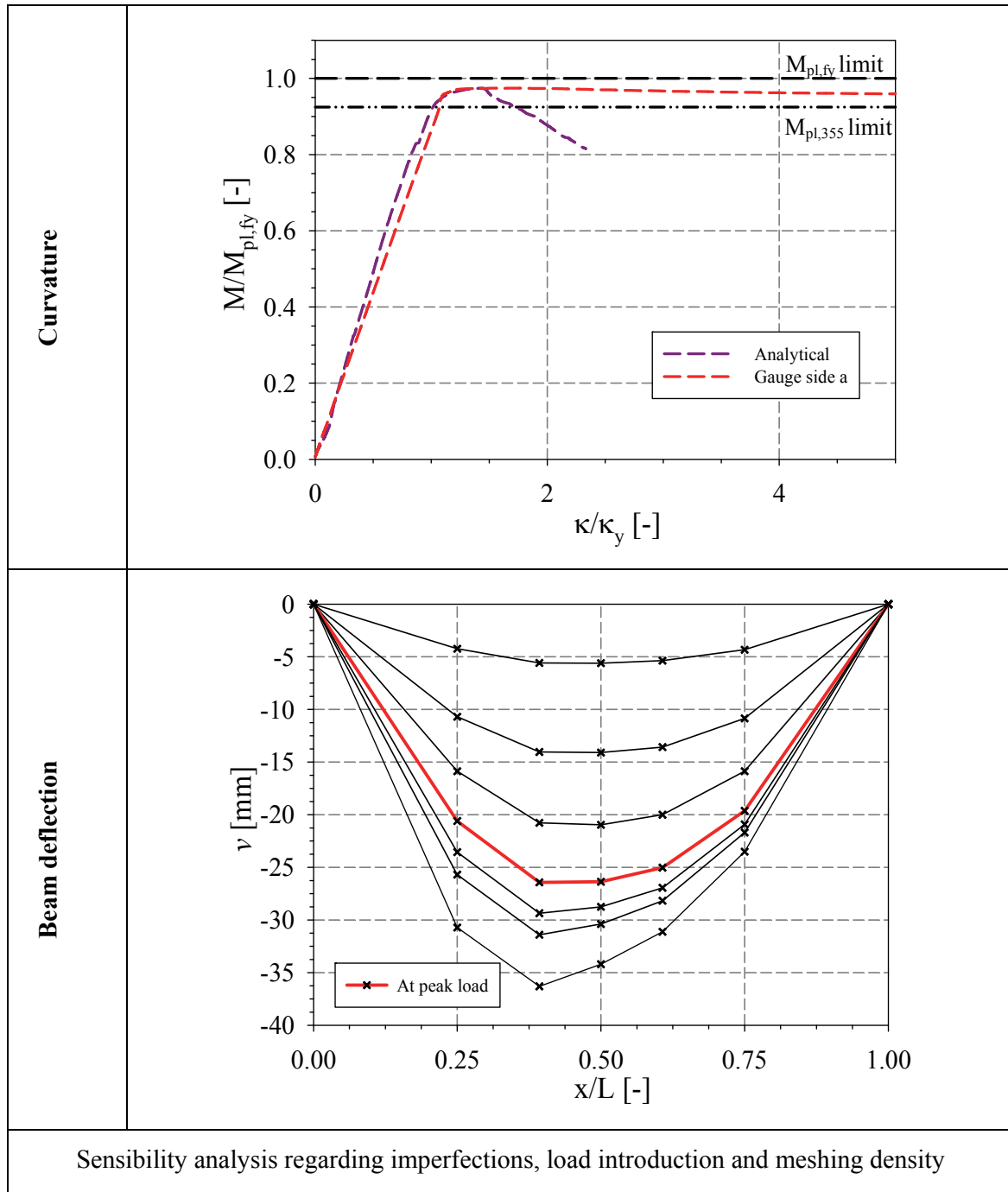
11.3.5.1 SHS_180x8_SS_4P

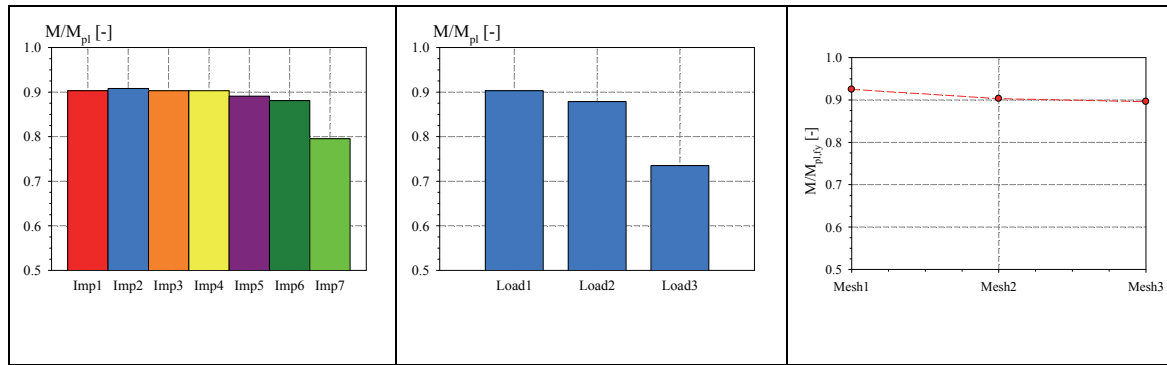
Specimen name	Nominal Details	Measured material properties (average)
SHS_180×8_SS_4P	Shape: Square Hollow Section Nominal Steel grade: 355 N/mm ² Load case: 4-point bending h=180mm b=180mm t=8mm Fabrication process: Hot-rolled	$f_y = 384.0 \text{ N/mm}^2$ $f_u = 531.5 \text{ N/mm}^2$ $E = 208013 \text{ N/mm}^2$ $\varepsilon_y = 0.18 \%$ $\varepsilon_{y2} = 1.69 \%$ $\varepsilon_u = 17.47 \%$







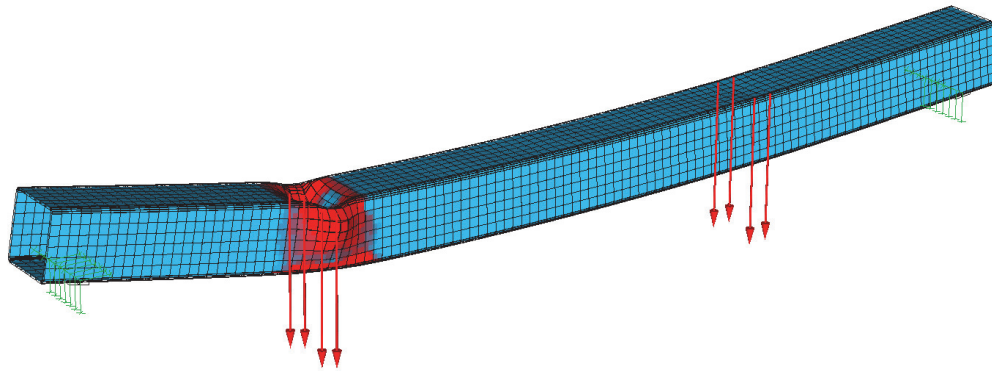




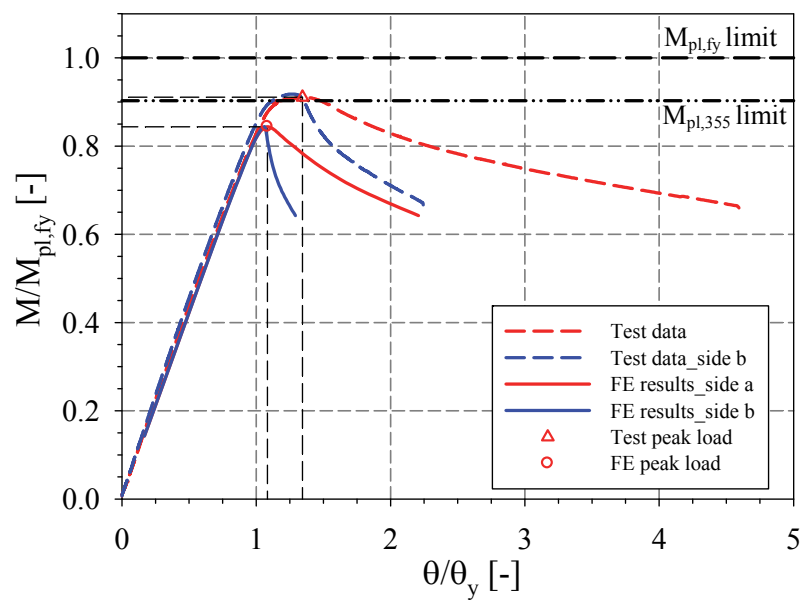
11.3.5.2 SHS_180x6.3_SS_4P

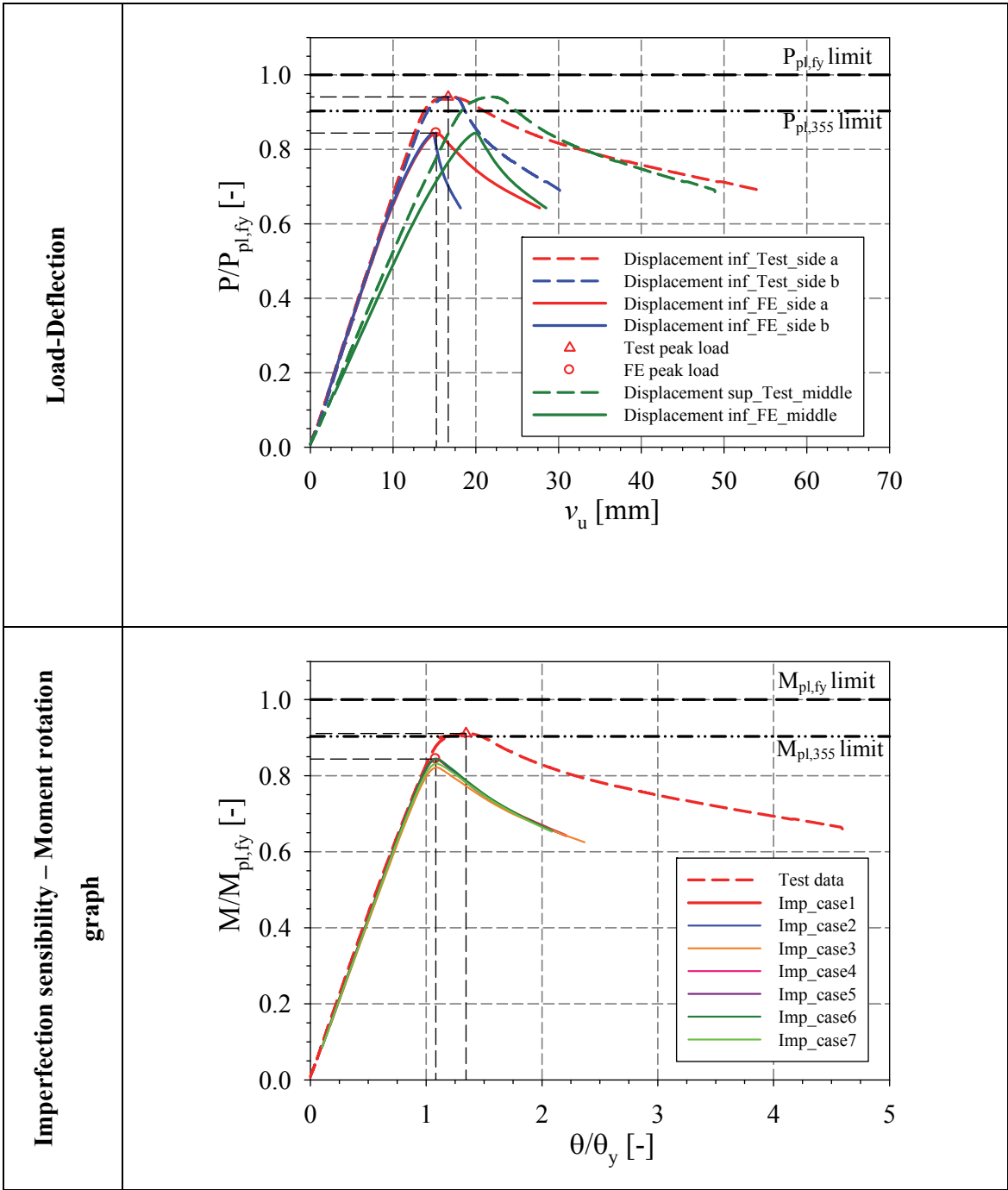
Specimen name	Nominal Details	Measured material properties (average)
SHS_180x6.3_SS_4P	Shape: Square Hollow Section Nominal Steel grade: 355 N/mm^2 Load case: 4-point bending $h=180mm$ $b=180mm$ $t=6.3mm$ Fabrication process: Hot-rolled	$f_y = 393.2 N/mm^2$ $f_u = 523.8 N/mm^2$ $E = 206903 N/mm^2$ $\varepsilon_y = 0.19 \%$ $\varepsilon_{y2} = 2.19 \%$ $\varepsilon_u = 14.88 \%$
<p>Average $h = 179.43 mm$</p>	<p>Average $b = 179.93 mm$</p>	<p>Average $t = 6.68 mm$</p>

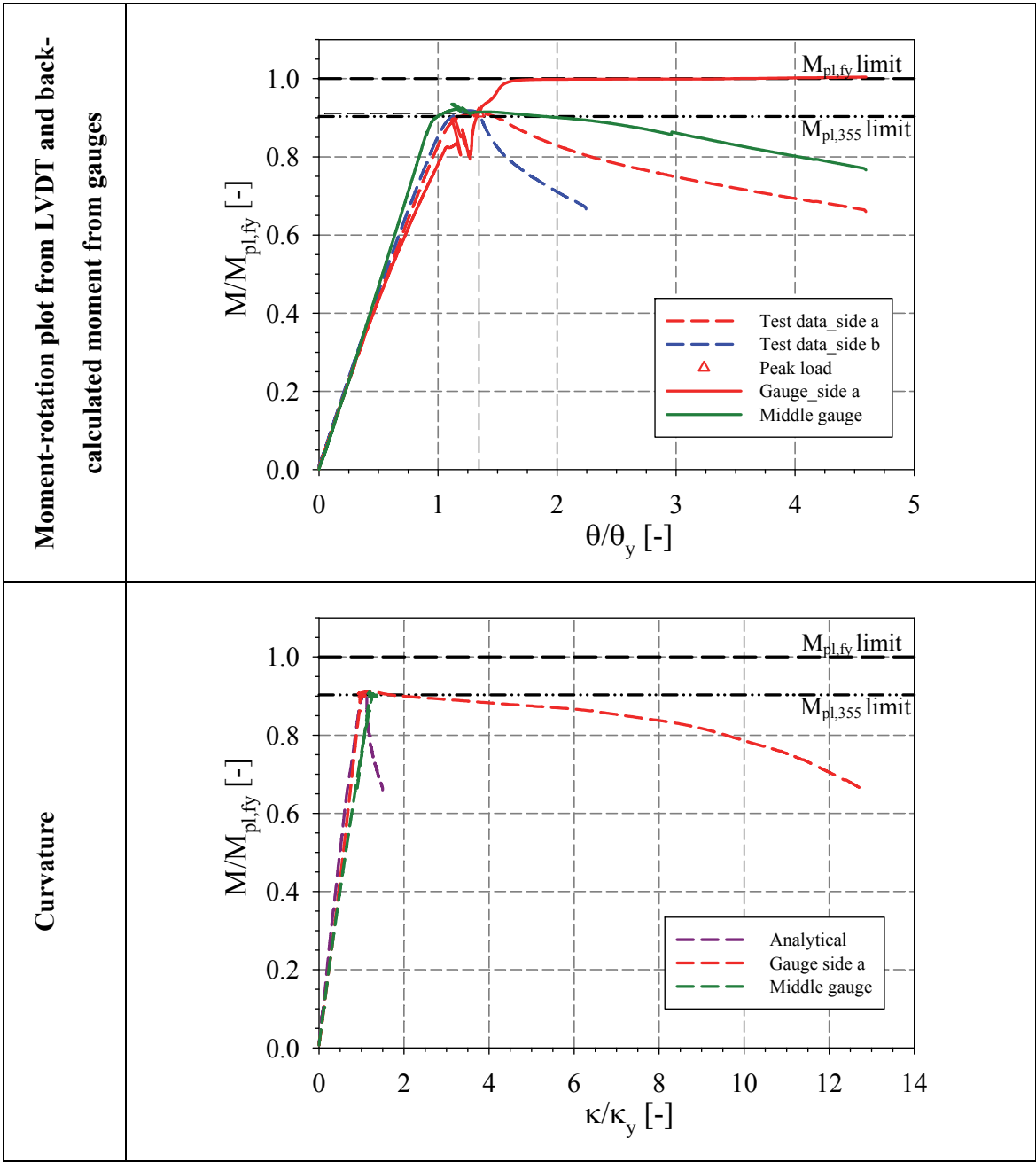
Yield pattern of SHS_180×6.3_SS_4P at failure

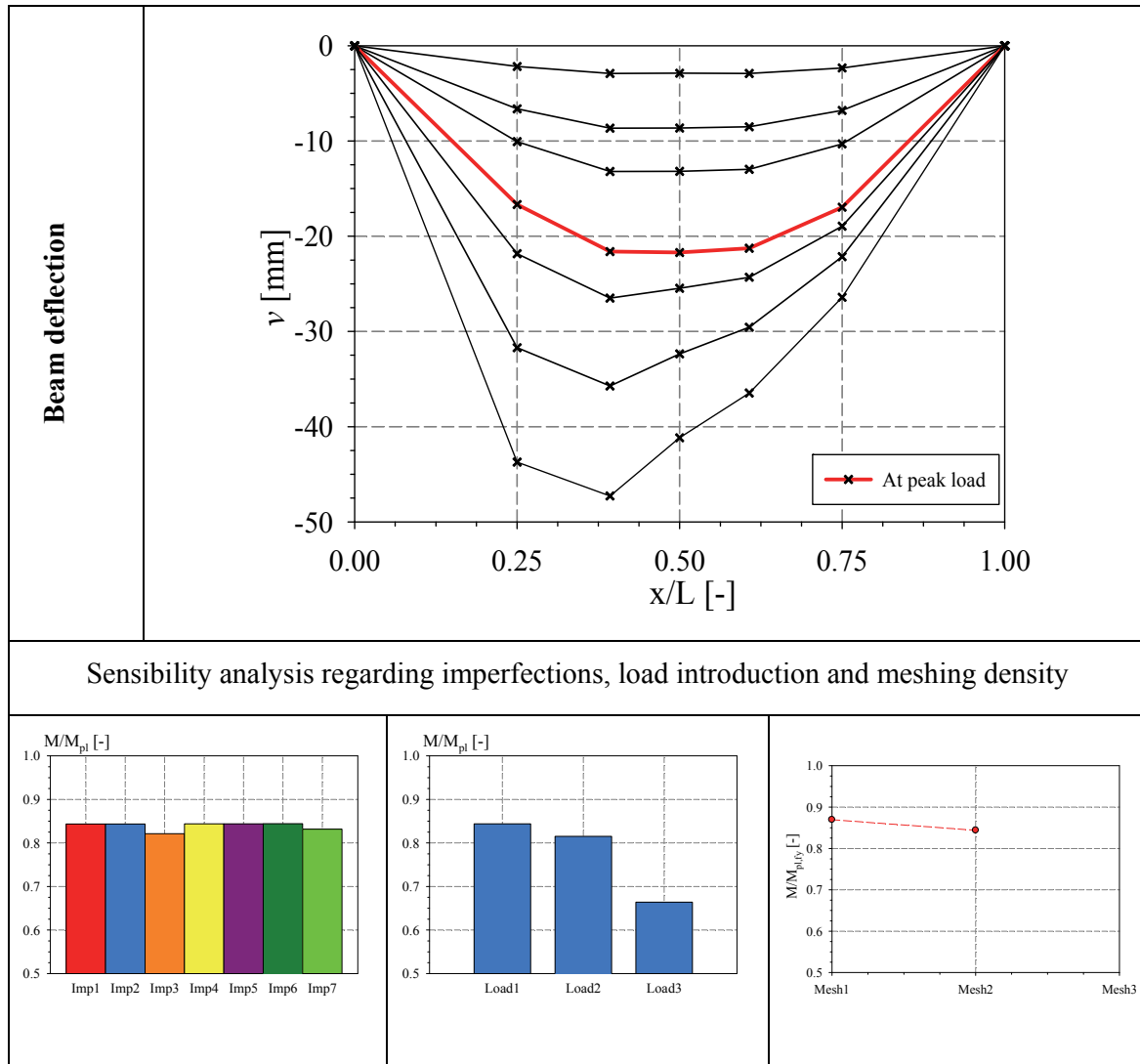


Moment-rotation



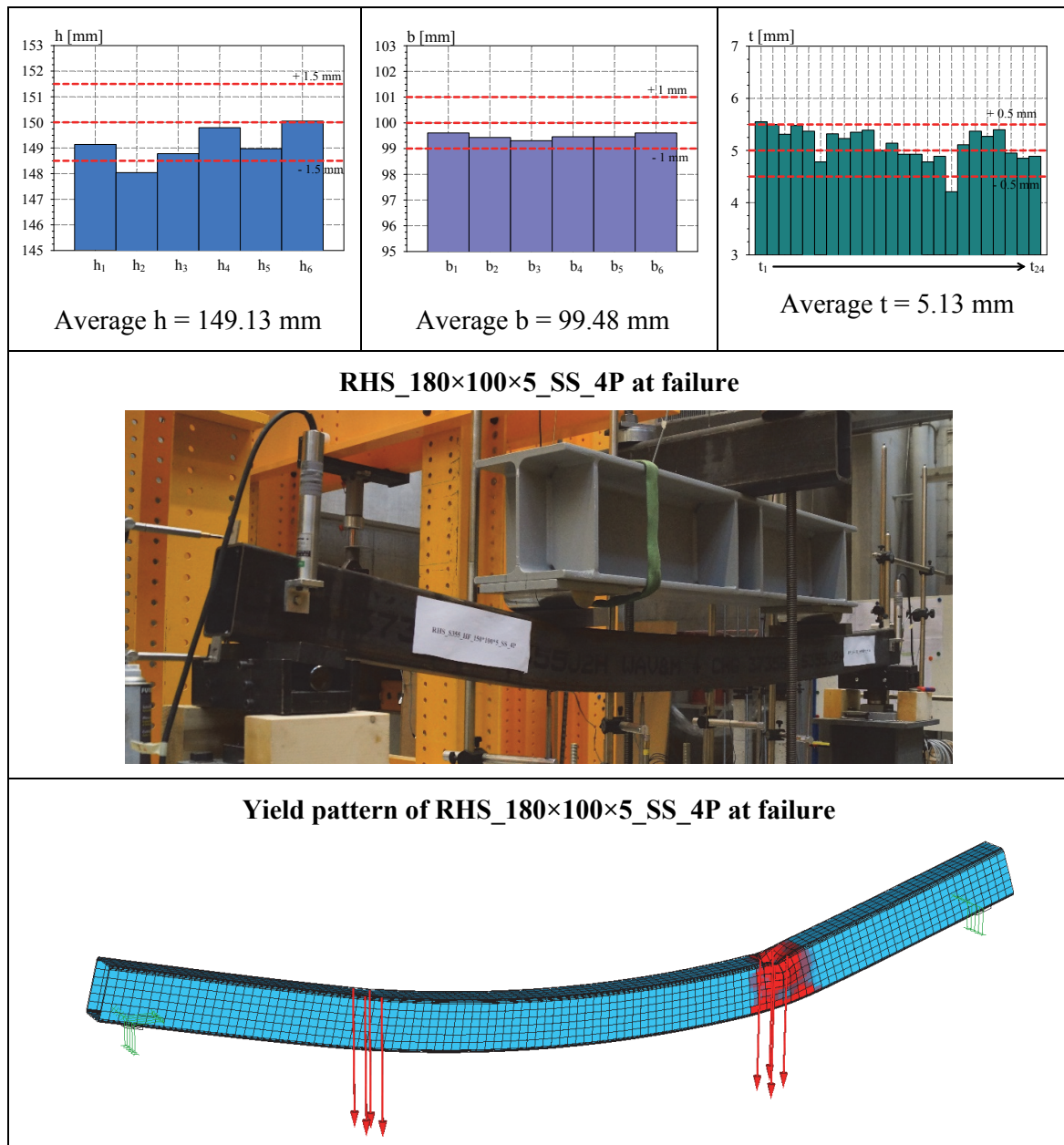


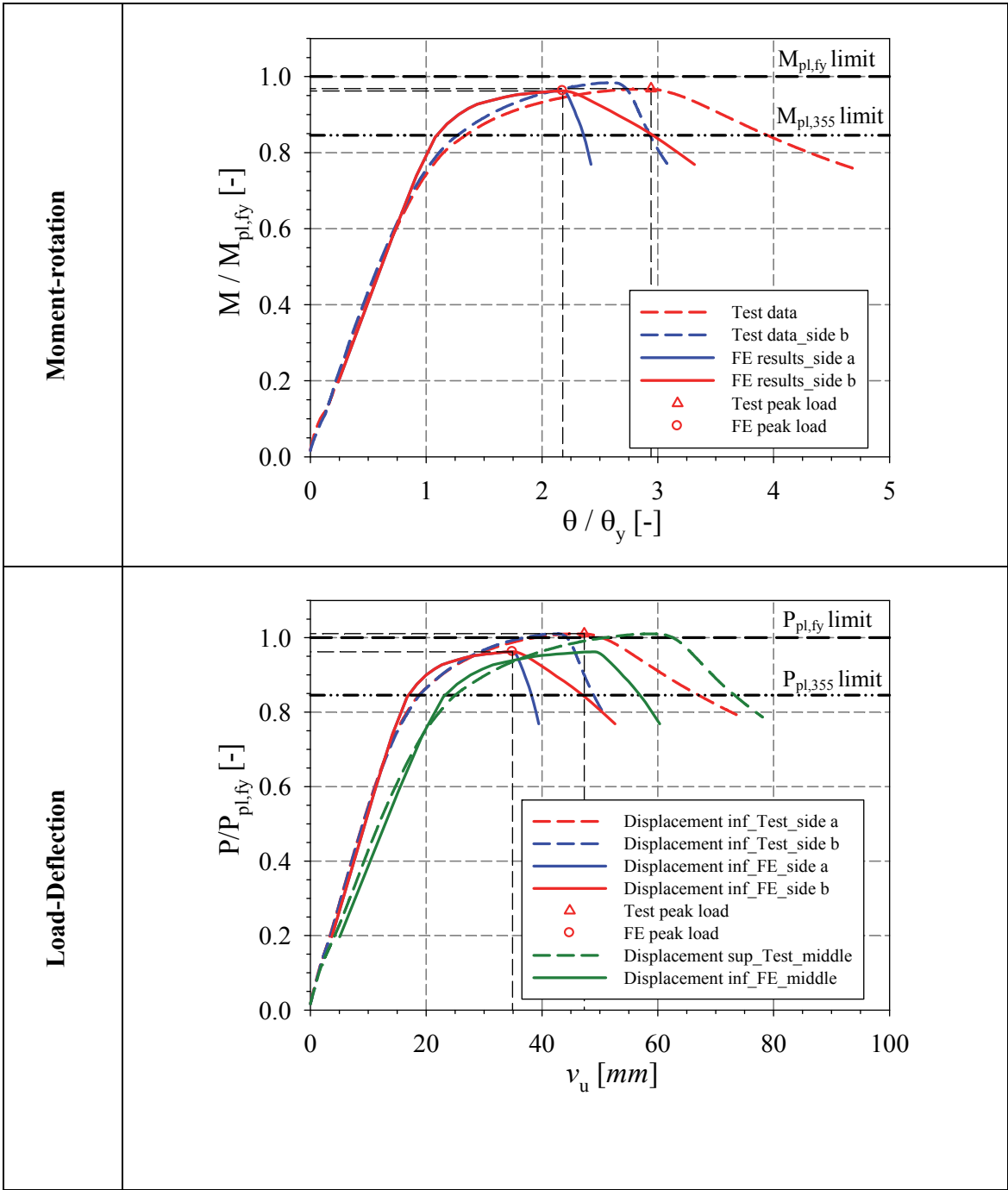


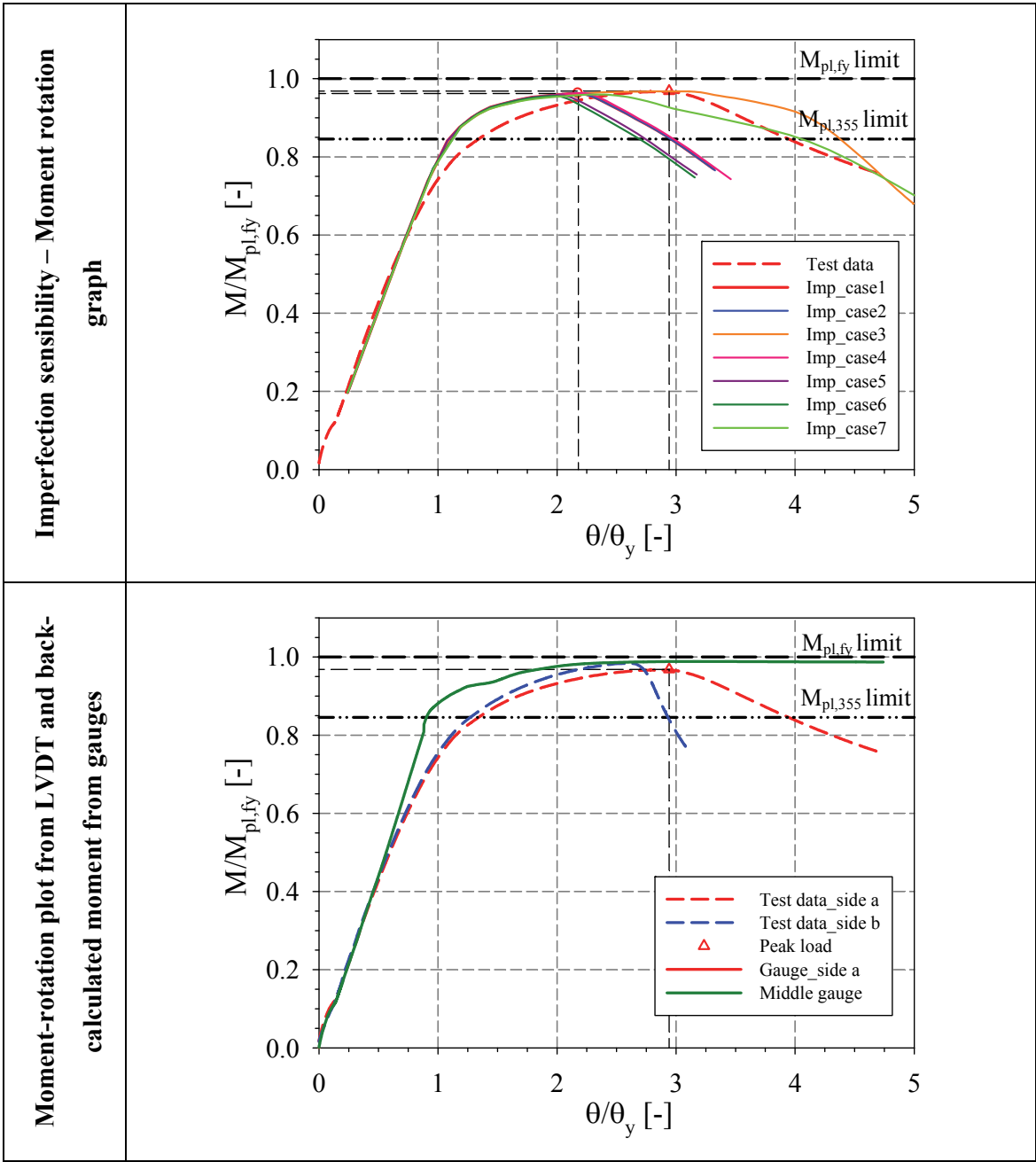


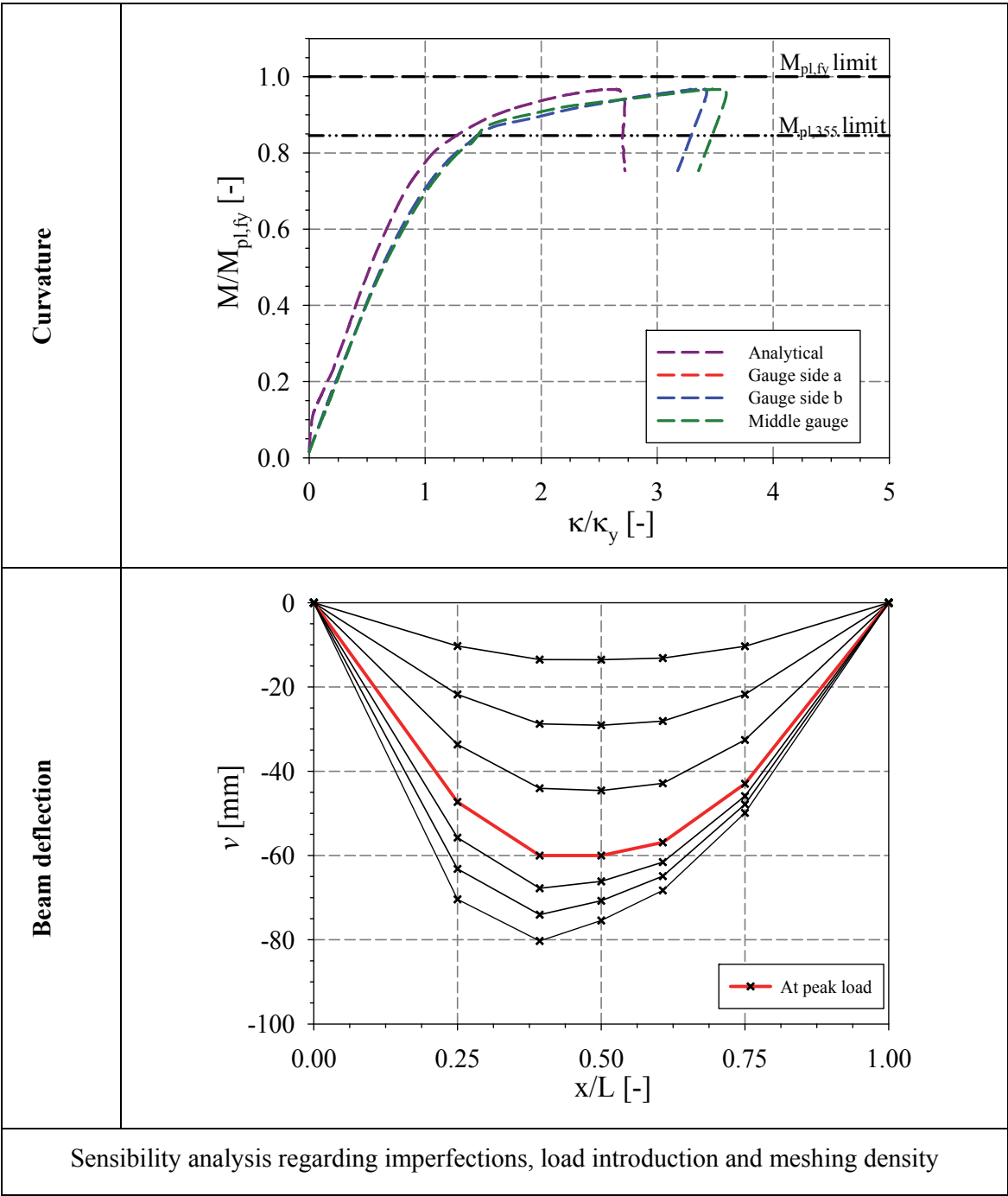
11.3.5.3 RHS_150×100×5_SS_4P

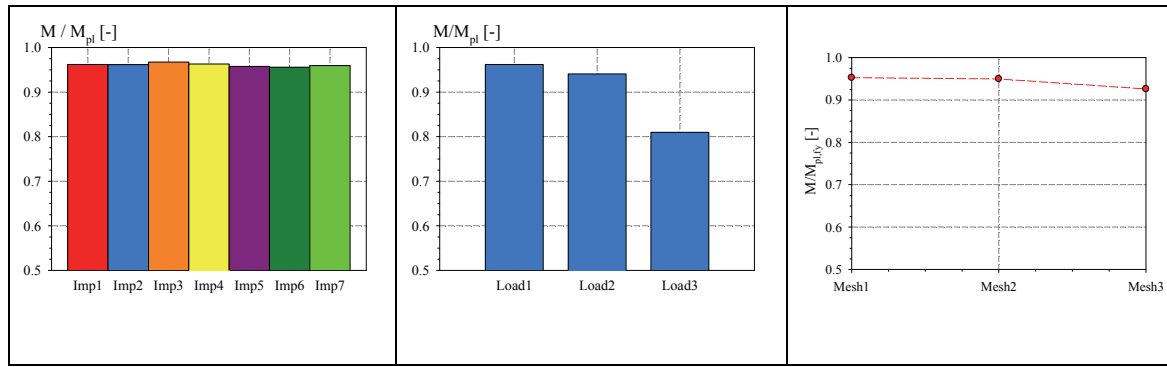
Specimen name	Nominal Details	Measured material properties (average)
RHS_150×100×5_SS_4P	Shape: Rectangular Hollow Section Nominal Steel grade: 355 N/mm^2 Load case: 4-point bending $h=150mm$ $b=100mm$ $t=5mm$ Fabrication process: Hot-rolled	$f_y = 419.8 N/mm^2$ $f_u = 573.0 N/mm^2$ $E = 211215 N/mm^2$ $\varepsilon_y = 0.20 \%$ $\varepsilon_{y2} = 1.73 \%$ $\varepsilon_u = 14.89 \%$







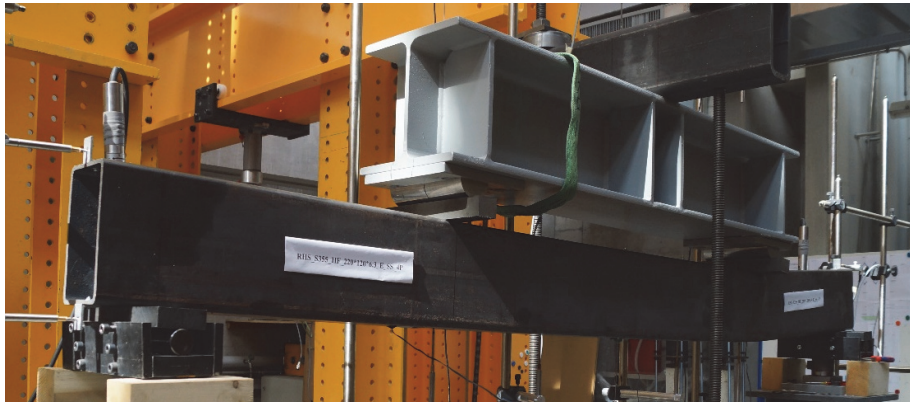


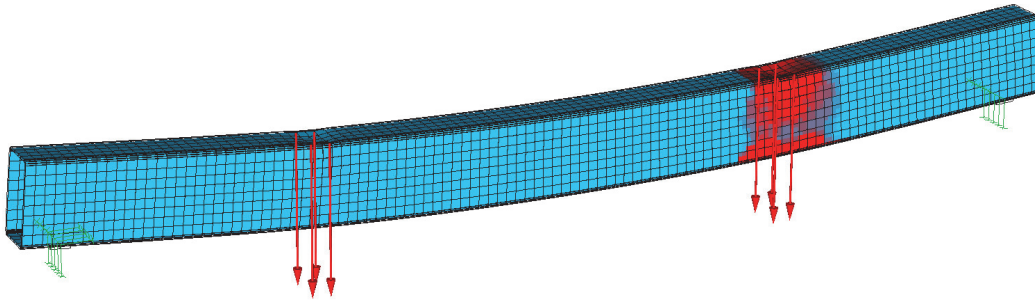
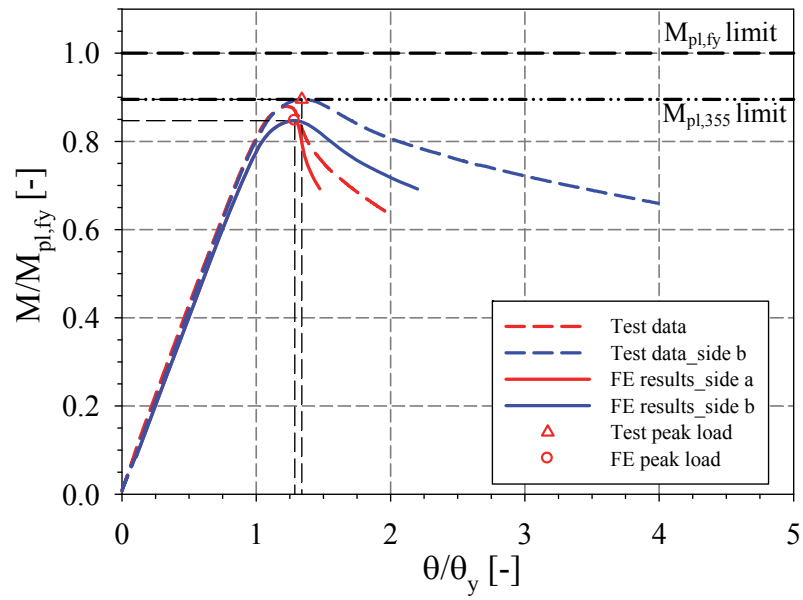


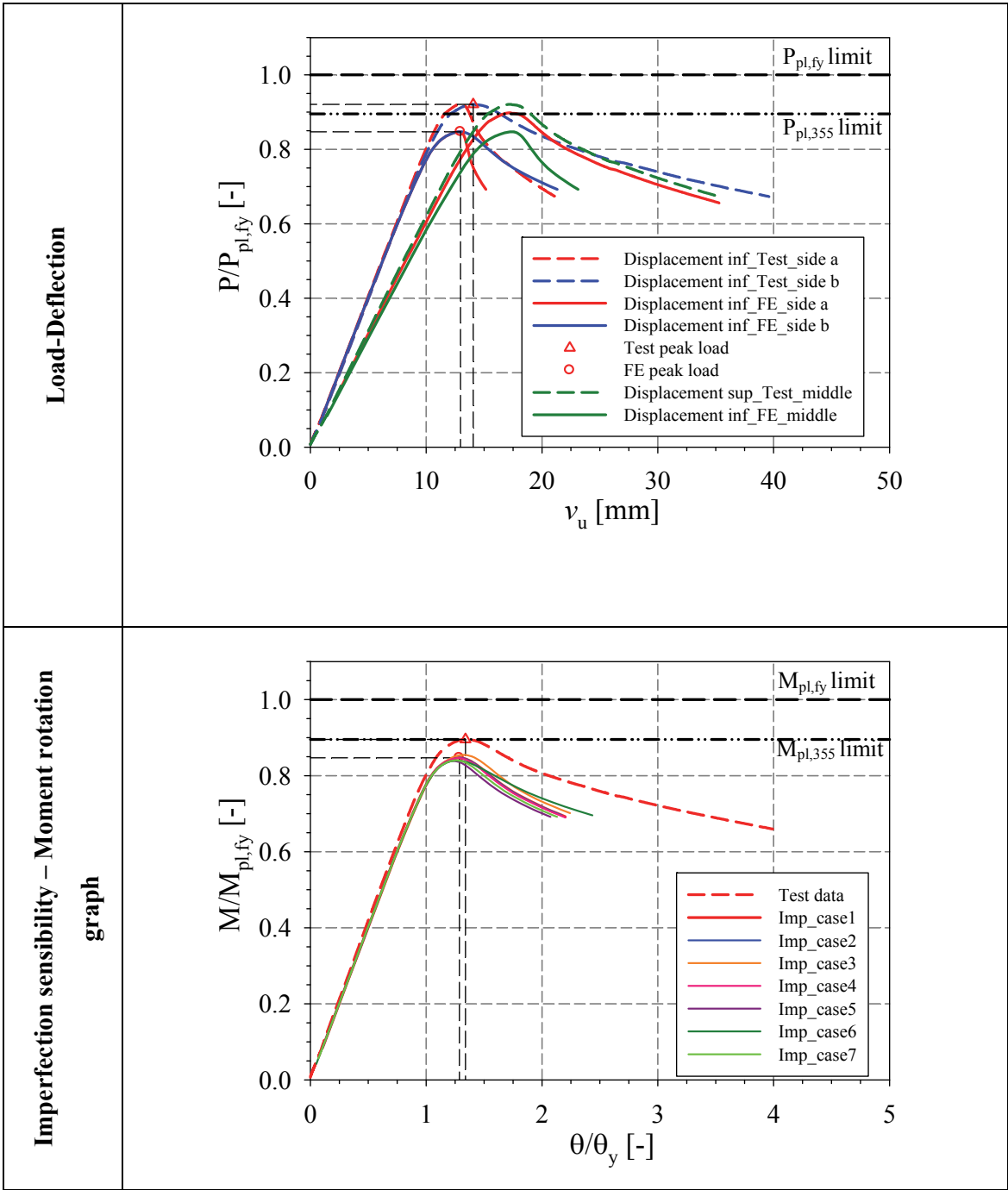
11.3.5.4 RHS_220×120×6.3_SS_4P

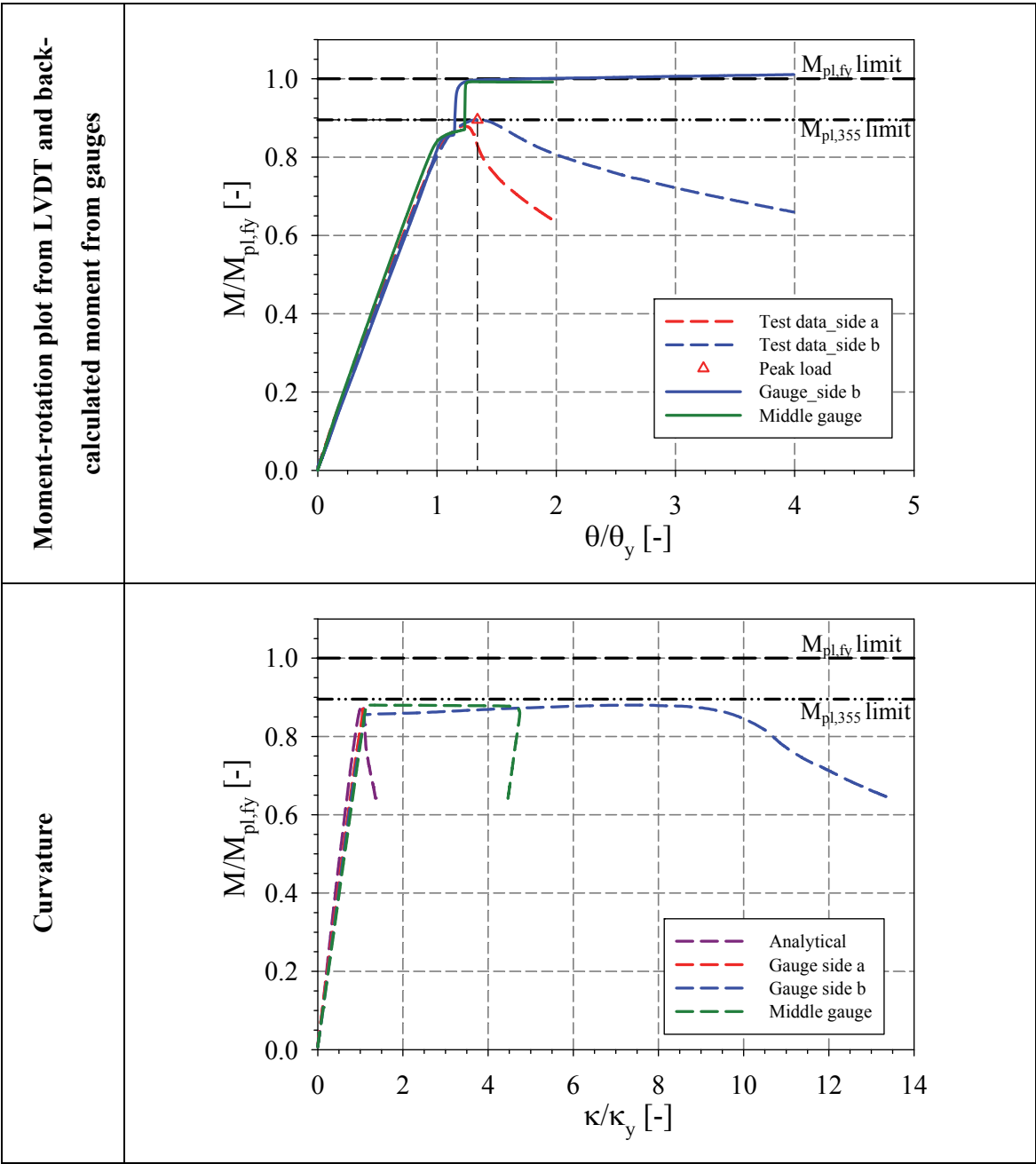
Specimen name	Nominal Details	Measured material properties (average)
RHS_220×120×6.3_SS_4P	Shape: Rectangular Hollow Section Nominal Steel grade: 355 N/mm^2 Load case: 4-point bending $h=200mm$ $b=120mm$ $t=6.3mm$ Fabrication process: Hot-rolled	$f_y = 396.5 N/mm^2$ $f_u = 535.9 N/mm^2$ $E = 211087 N/mm^2$ $\varepsilon_y = 0.19 \%$ $\varepsilon_{y2} = 1.88 \%$ $\varepsilon_u = 15.28 \%$
<p>Average $h = 219.40 mm$</p>	<p>Average $b = 120.86 mm$</p>	<p>Average $t = 6.42 mm$</p>

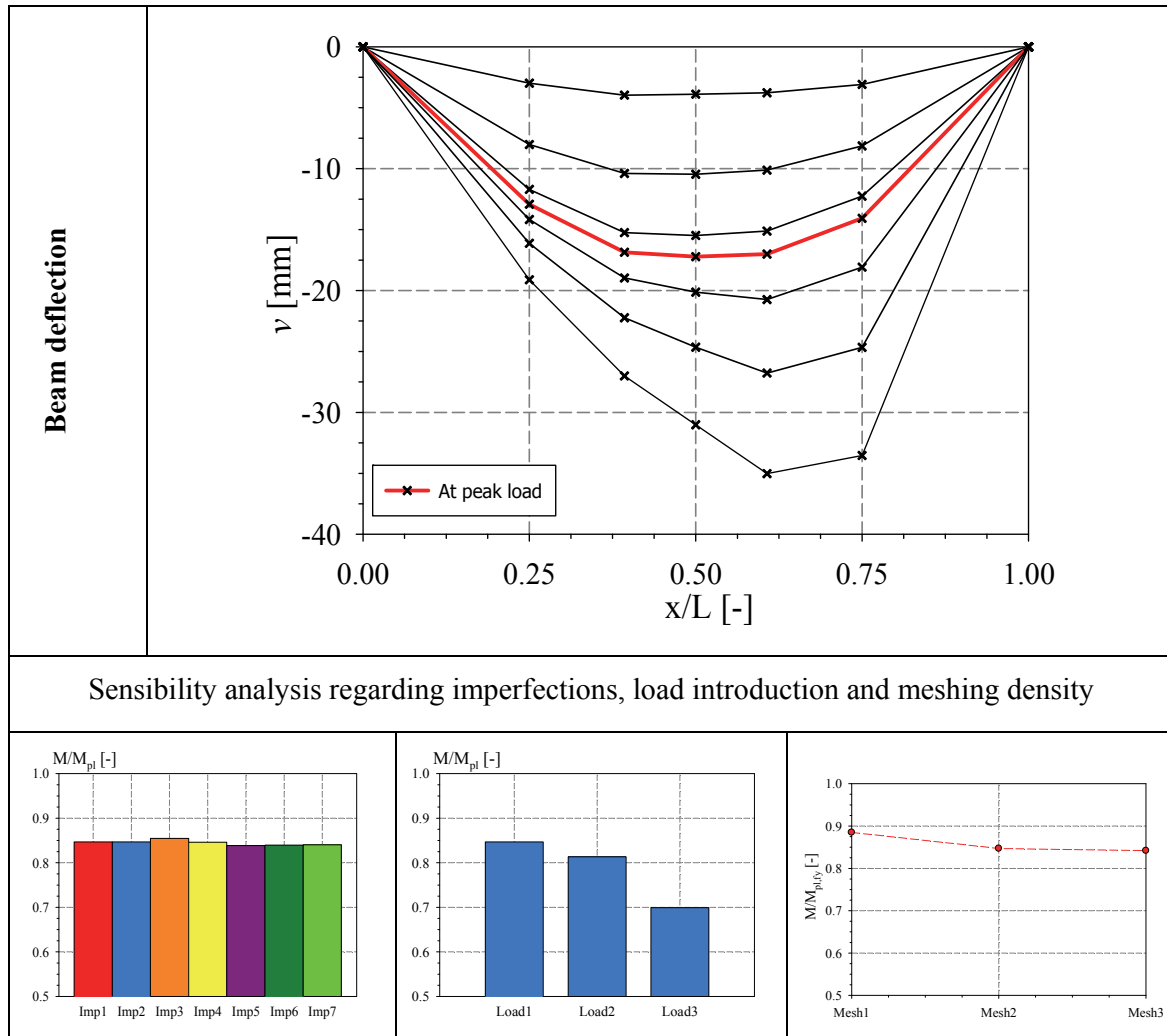
RHS_220×120×6.3_SS_4P at failure



Yield pattern of RHS_220×120×6.3_SS_4P at failure**Moment-rotation**

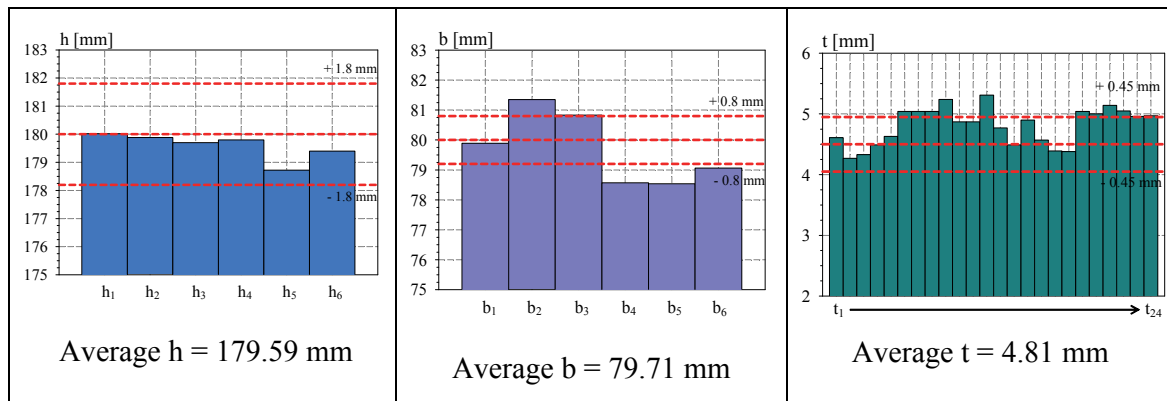






11.3.5.5 RHS_180×80×4.5_SS_4P

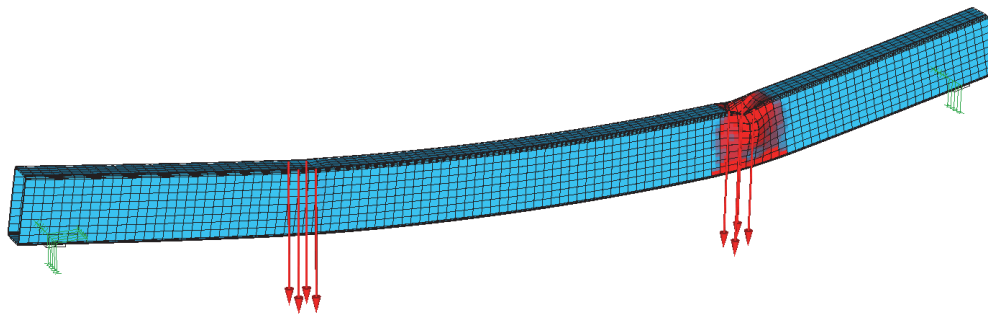
Specimen name	Nominal Details	Measured material properties (average)
RHS_180×80×4.5_SS_4P	Shape: Rectangular Hollow Section Nominal Steel grade: 355 N/mm^2 Load case: 4-point bending $h=180mm$ $b=80mm$ $t=4.5mm$ Fabrication process: Hot-rolled	$f_y = 389.2 N/mm^2$ $f_u = 539.4 N/mm^2$ $E = 198504 N/mm^2$ $\varepsilon_y = 0.20 \%$ $\varepsilon_{y2} = 1.76 \%$ $\varepsilon_u = 16.98 \%$

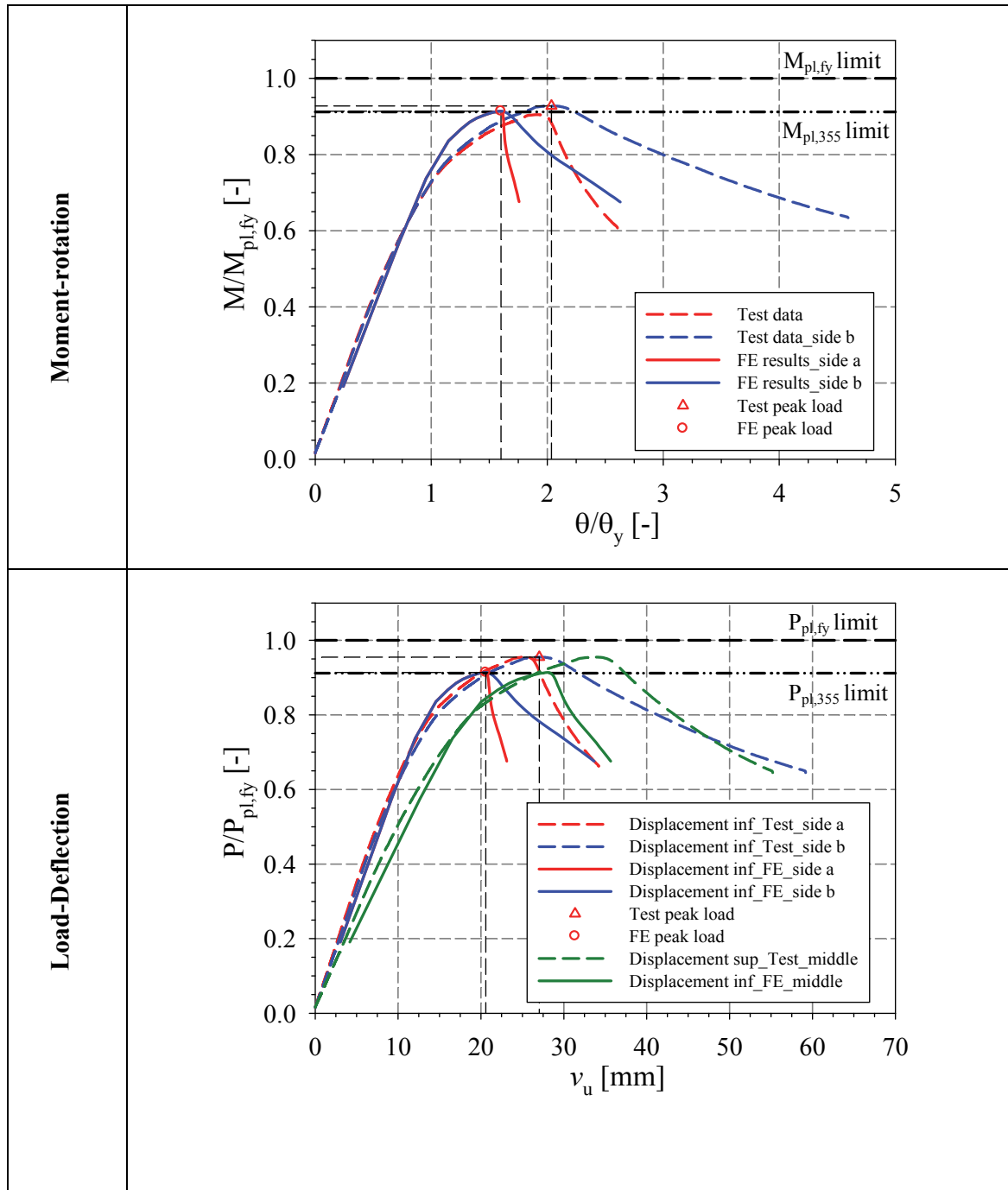


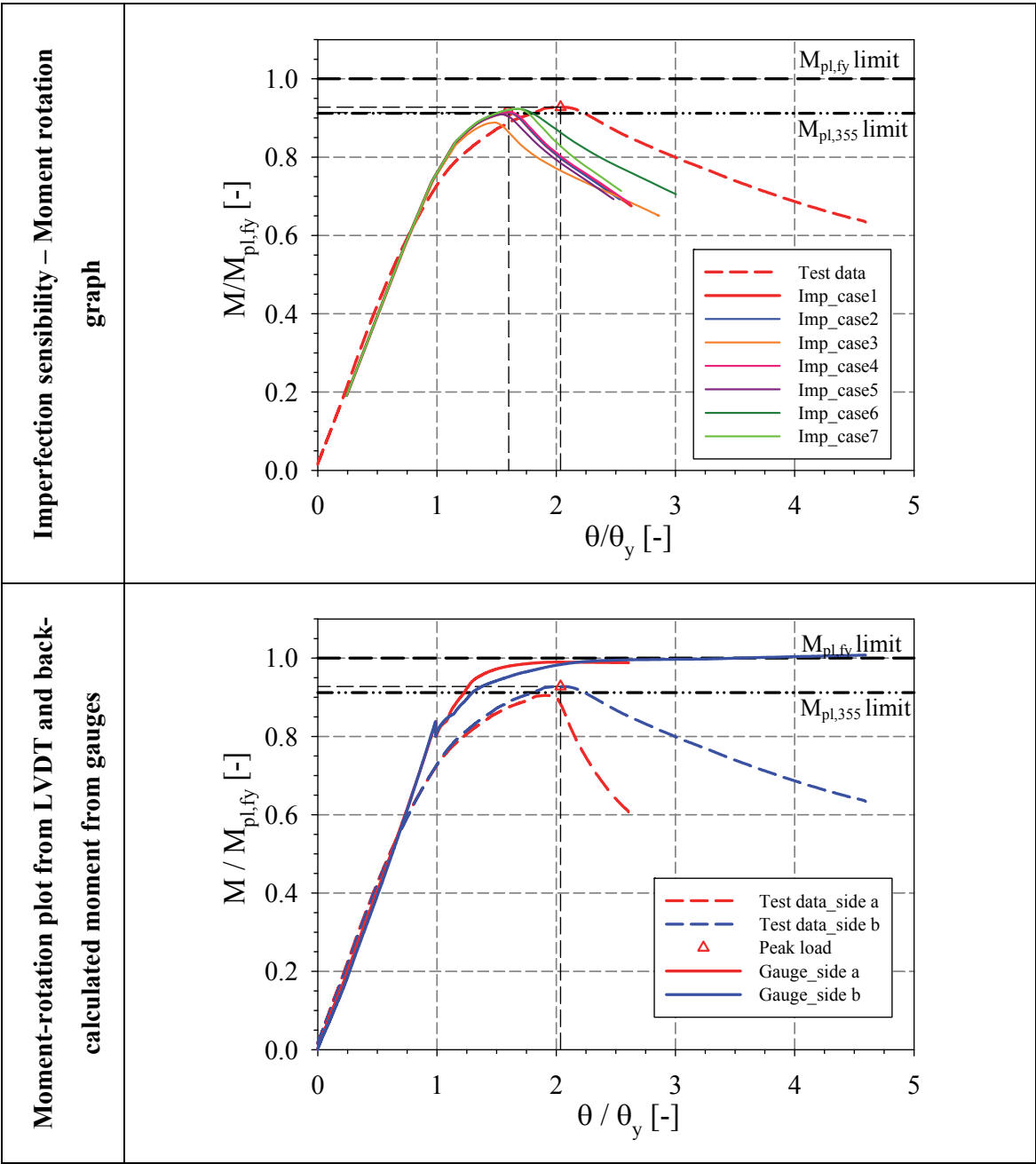
RHS_180×80×4.5_SS_4P at failure

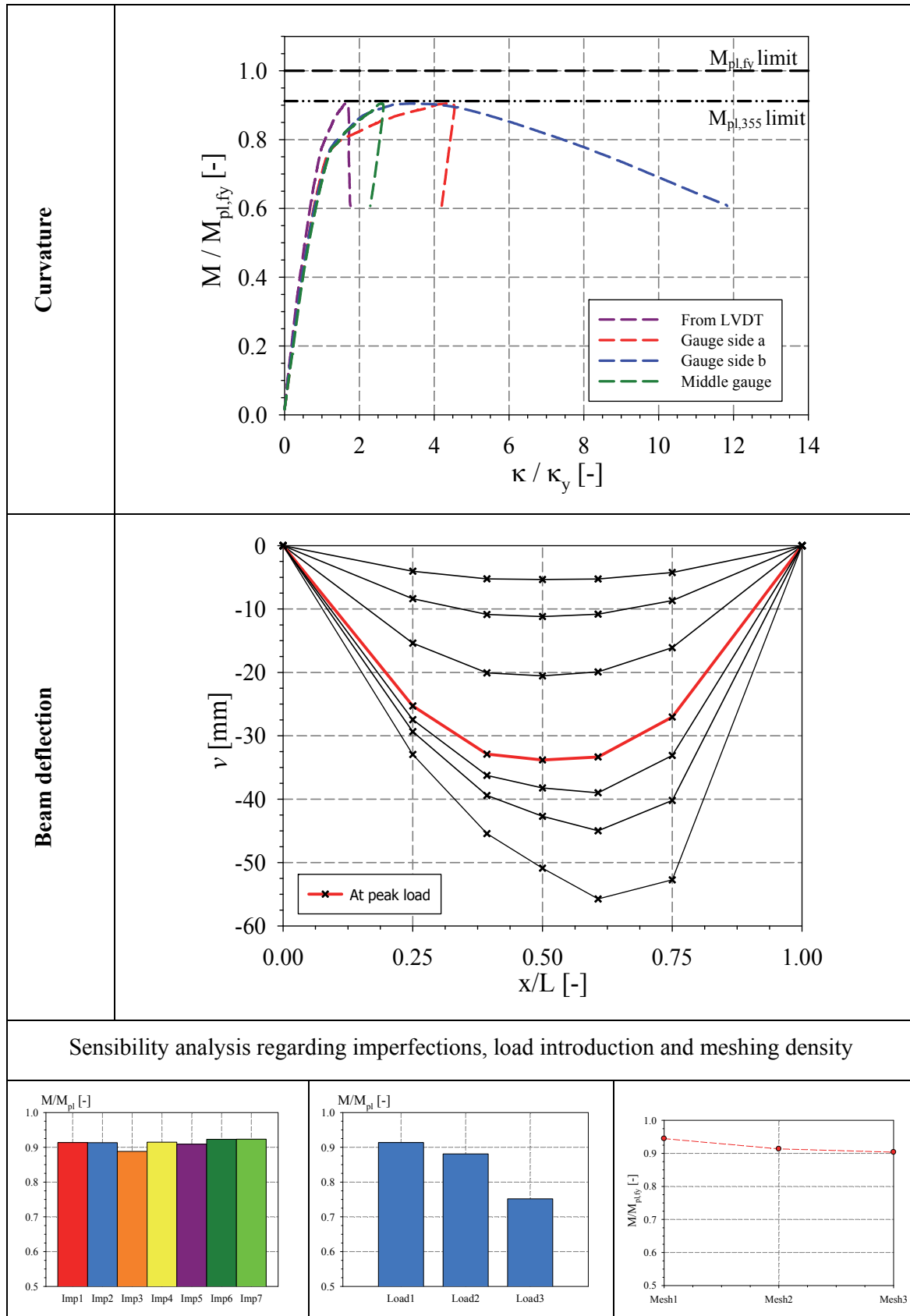


Yield pattern of RHS_180×80×4.5_SS_4P at failure

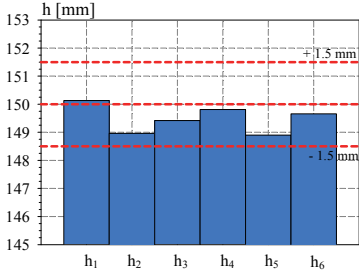
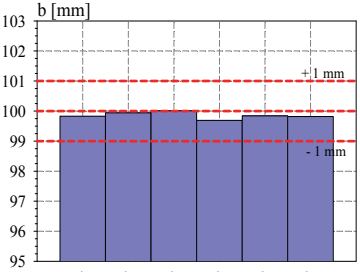
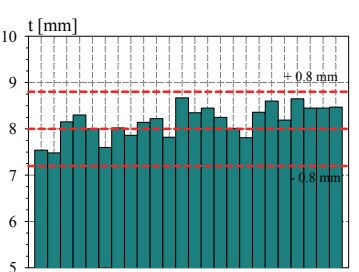



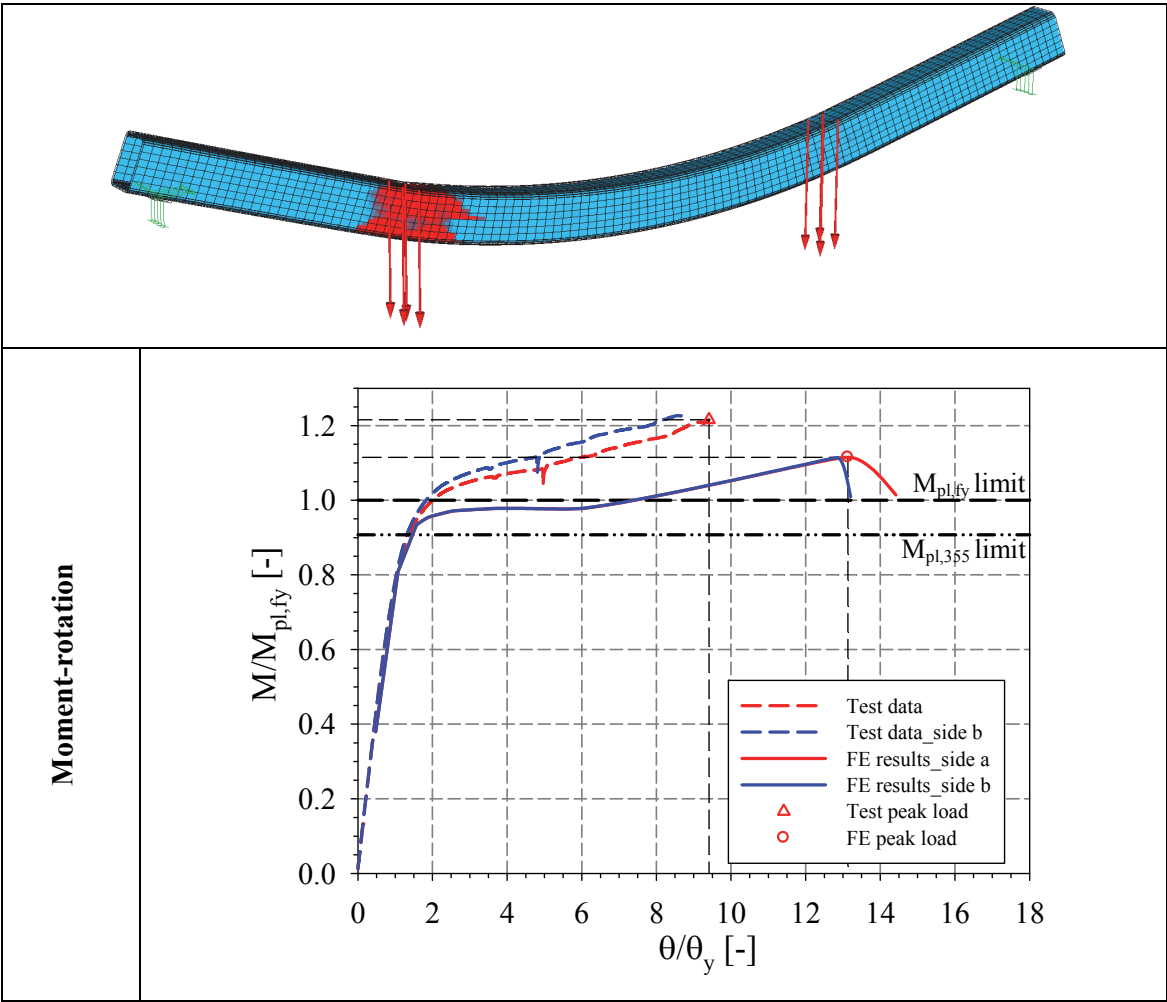


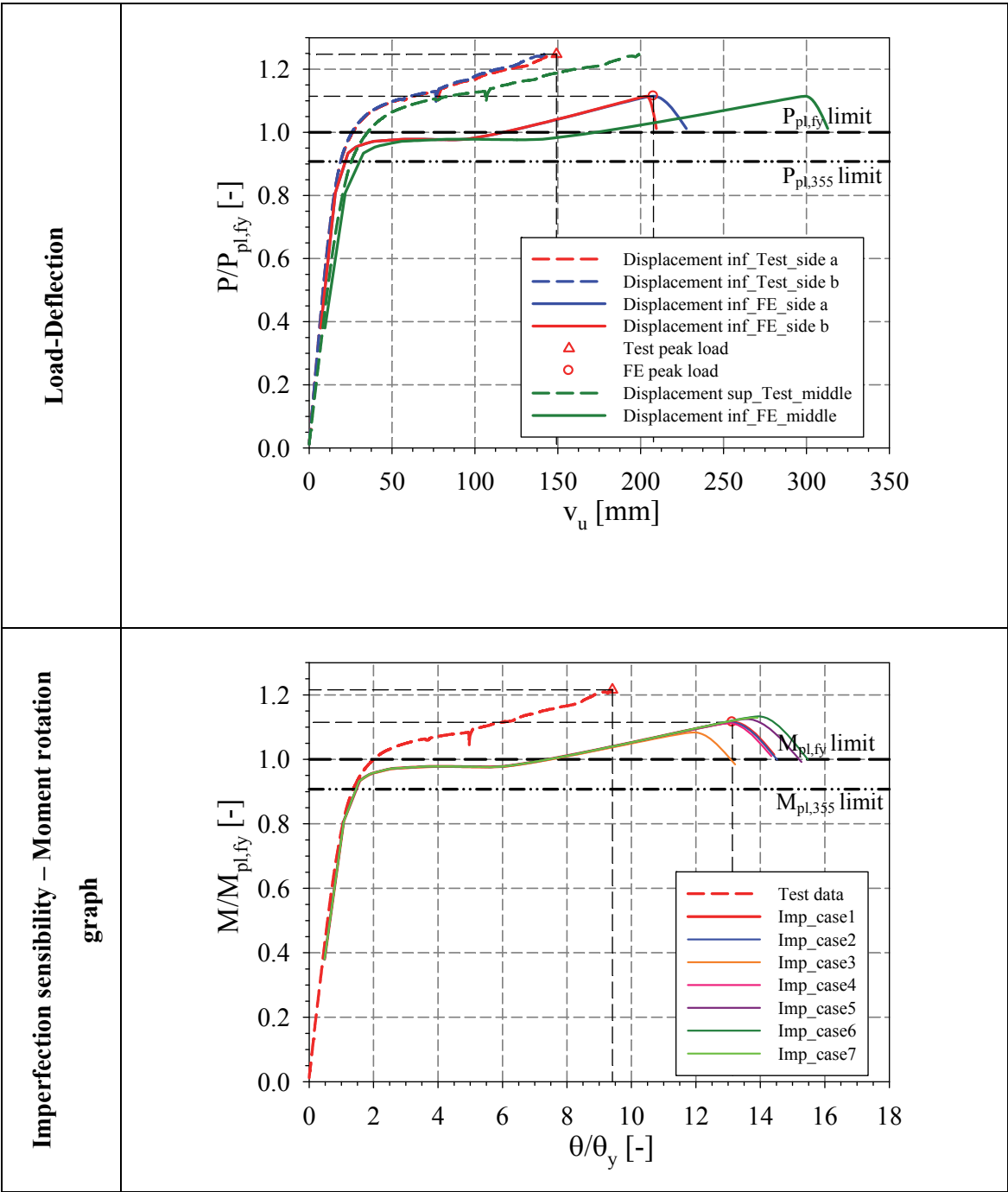


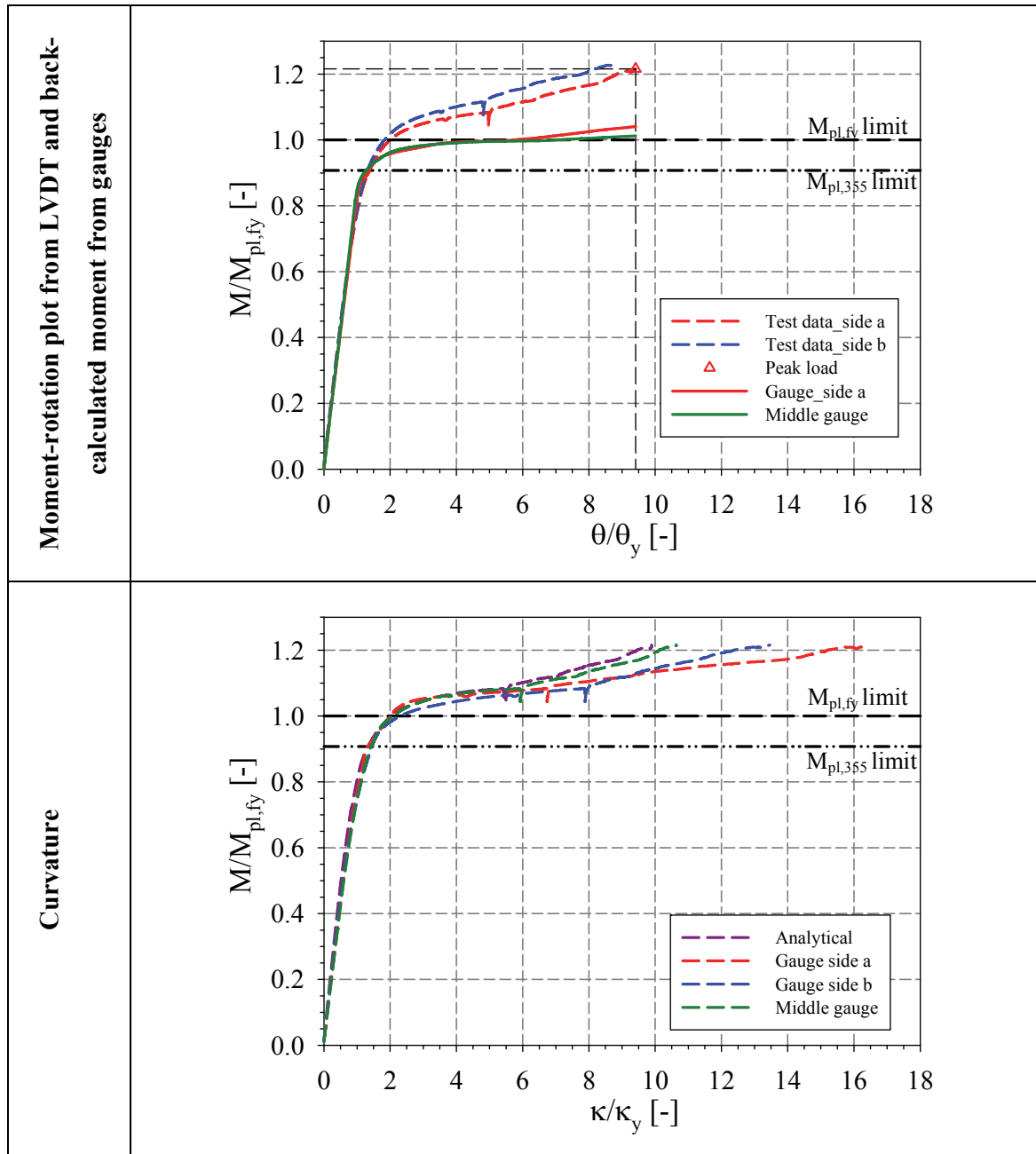


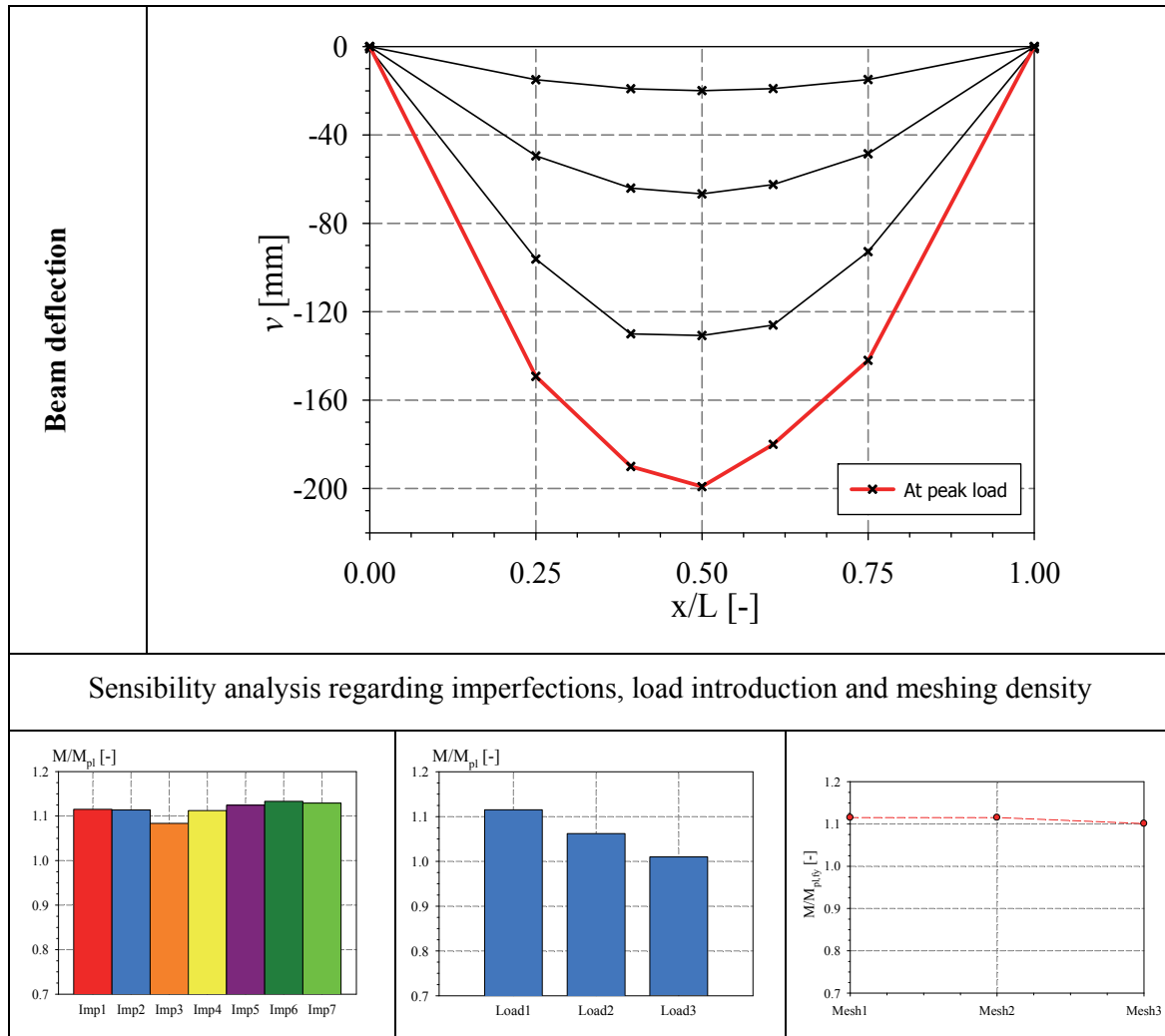
11.3.5.6 RHS_150×100×8_SS_4P

Specimen name	Nominal Details	Measured material properties (average)
RHS_150×100×8_SS_4P	Shape: Rectangular Hollow Section Nominal Steel grade: 355 N/mm ² Load case: 4-point bending h=150mm b=100mm t=8mm Fabrication process: Hot-rolled	$f_y = 391.2 \text{ N/mm}^2$ $f_u = 554.0 \text{ N/mm}^2$ $E = 205737 \text{ N/mm}^2$ $\varepsilon_y = 0.19 \%$ $\varepsilon_{y2} = 1.49 \%$ $\varepsilon_u = 12.93 \%$
 <p>Average h = 149.48 mm</p>	 <p>Average b = 99.86 mm</p>	 <p>Average t = 8.16 mm</p>
<p align="center">RHS_150×100×8_SS_4P at failure</p> 		
<p align="center">Yield pattern of RHS_150×100×8_SS_4P at failure</p>		



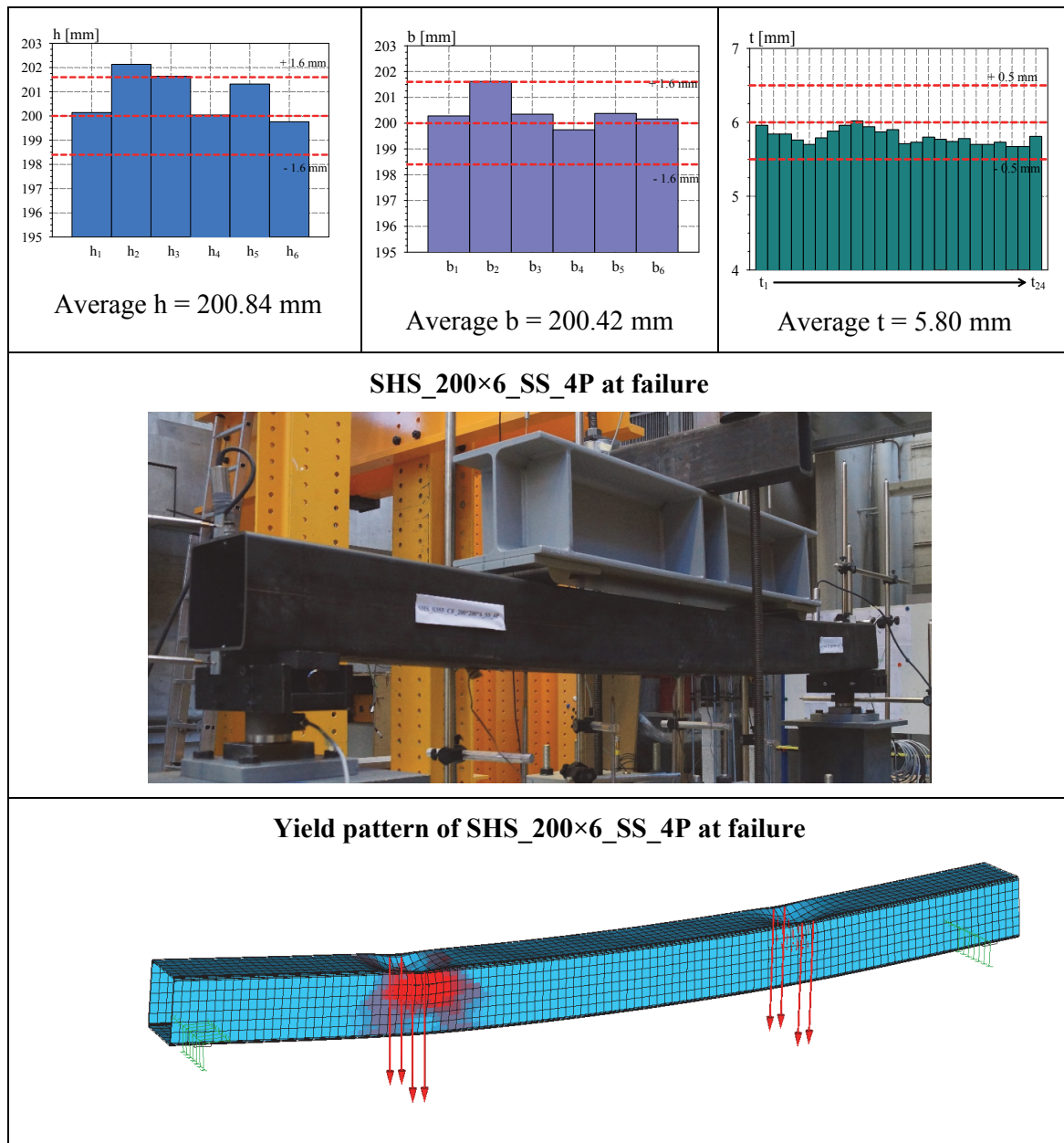


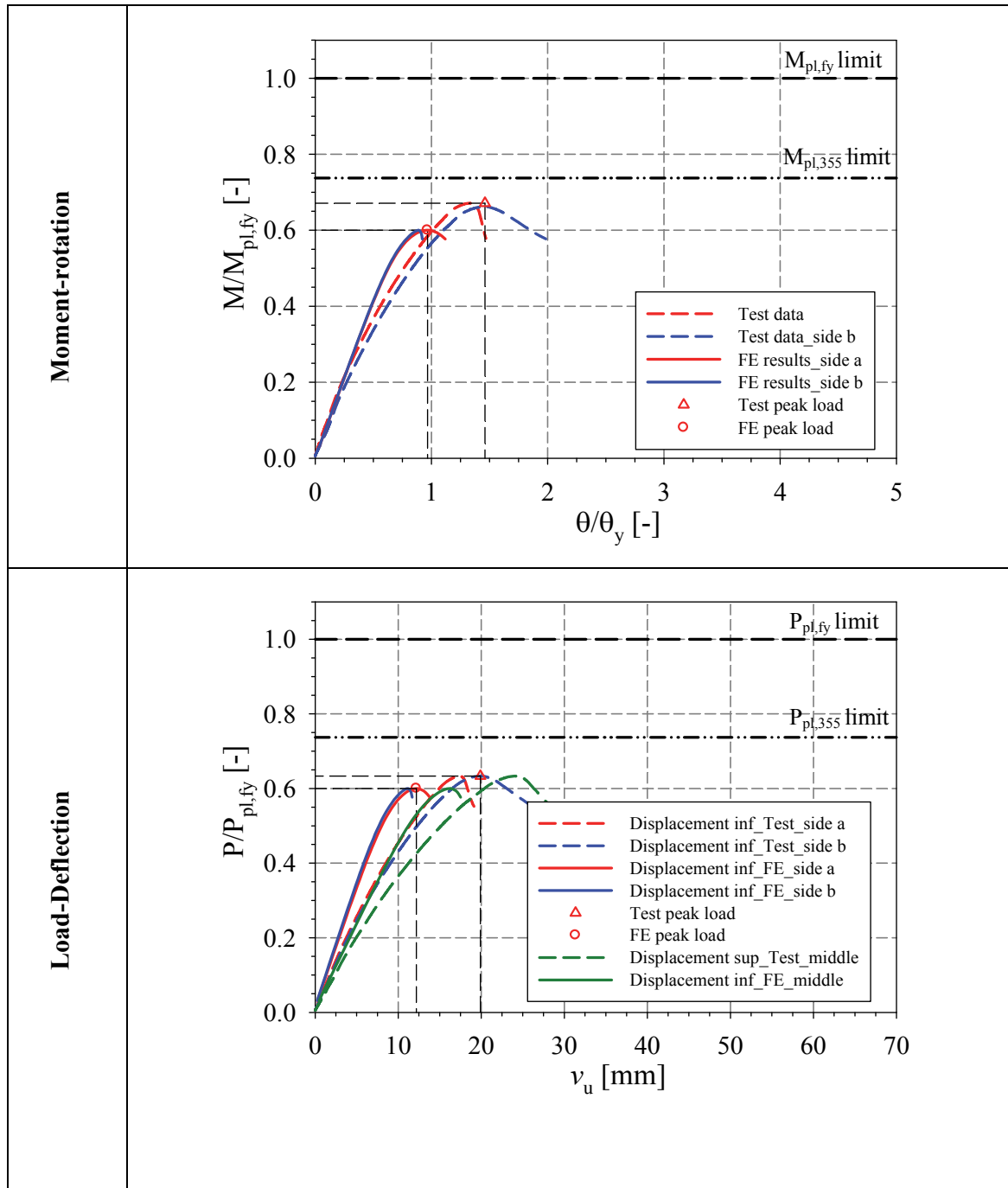


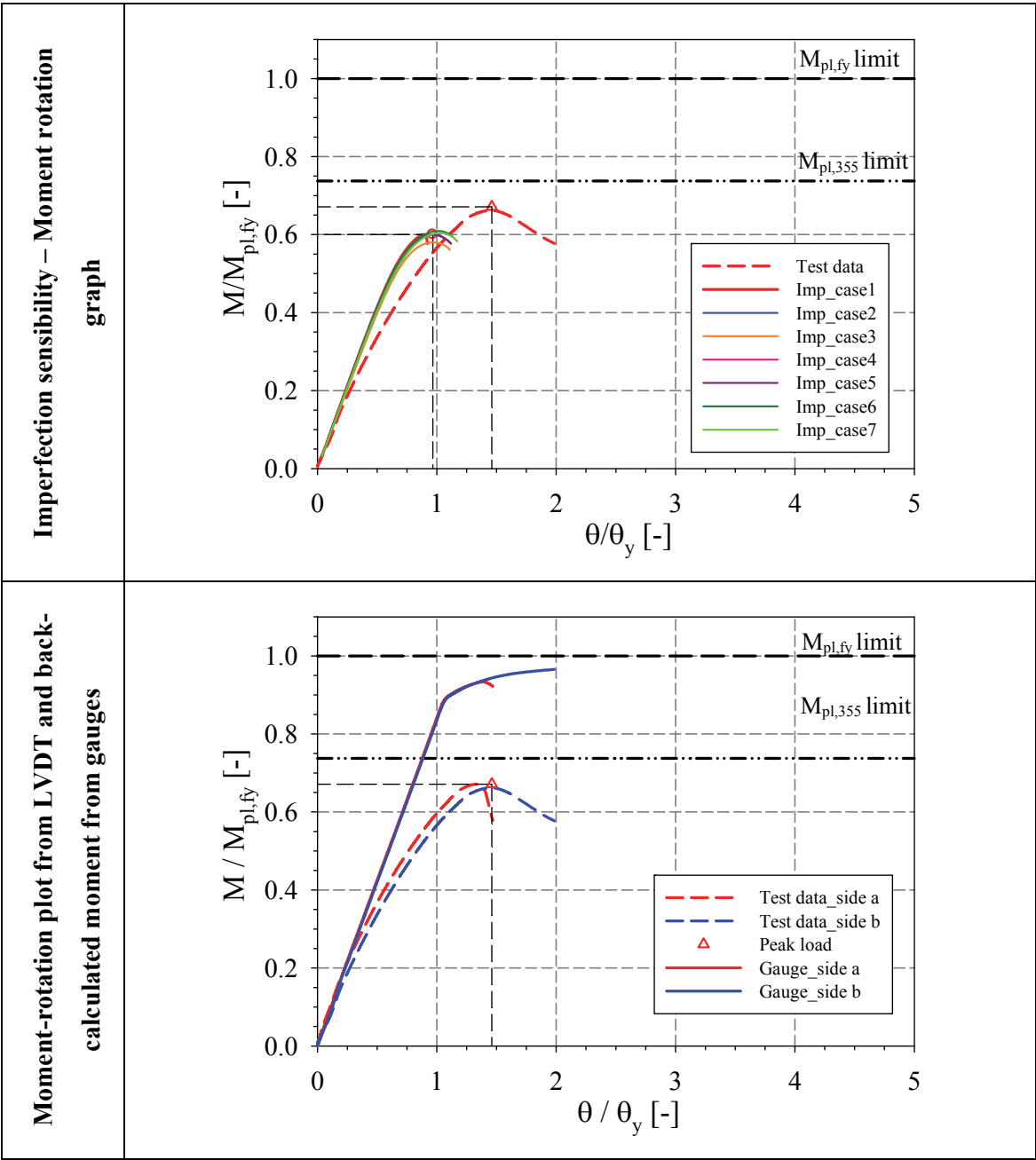


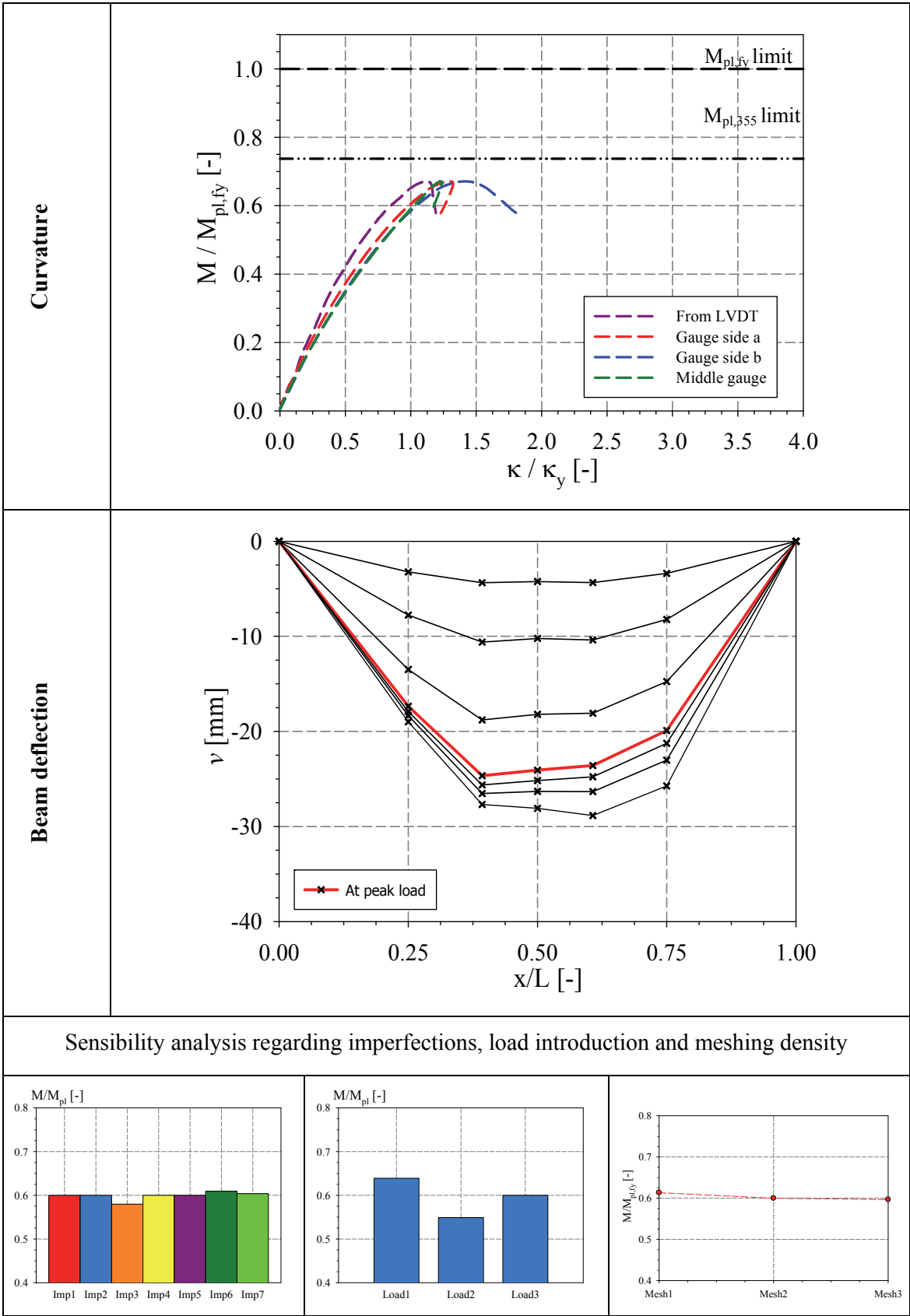
11.3.5.7 SHS_200x6_SS_4P

Specimen name	Nominal Details	Measured material properties (average)
SHS_200×6_SS_4P	Shape: Square Hollow Section Nominal Steel grade: 355 N/mm^2 Load case: 4-point bending $h=200mm$ $b=200mm$ $t=6mm$ Fabrication process: Cold formed	$f_y = 481.5 \text{ N/mm}^2$ $f_u = 569.6 \text{ N/mm}^2$ $E = 210239 \text{ N/mm}^2$ $\varepsilon_y = 0.25 \%$ $\varepsilon_u = 19.00 \%$









For the case of the cold formed section SHS_200x6_SS_4P, this beam has been tested without the presence of a 50mm thick plate to avoid load concentration, thus loading was modeled using type 2 Loading configuration and was thus applied uniformly on the corners end over a distance of 3 *cm*. For this particular case the rigidity of the system could not be fully represented as shown in the figure below and is mainly due to loading application since during testing and due load concentration the beam failed due to the yielding at one corner side and displayed unsymmetrical loading introduction.

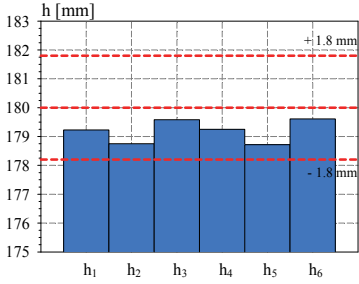
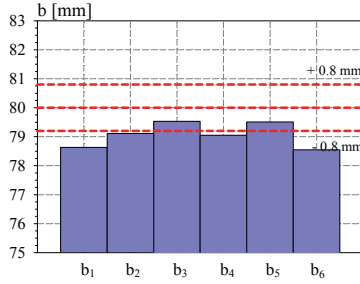
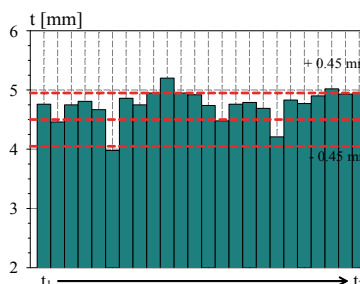

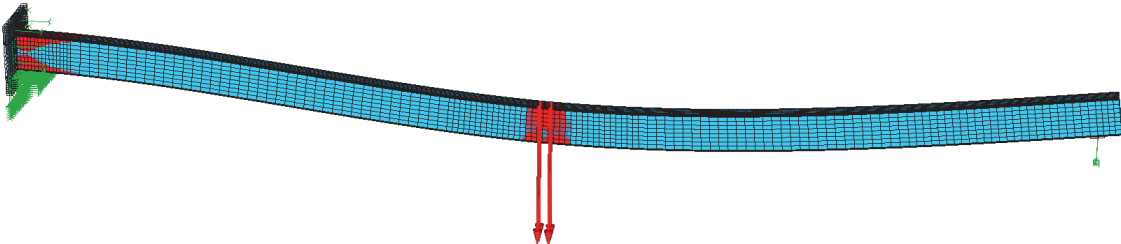


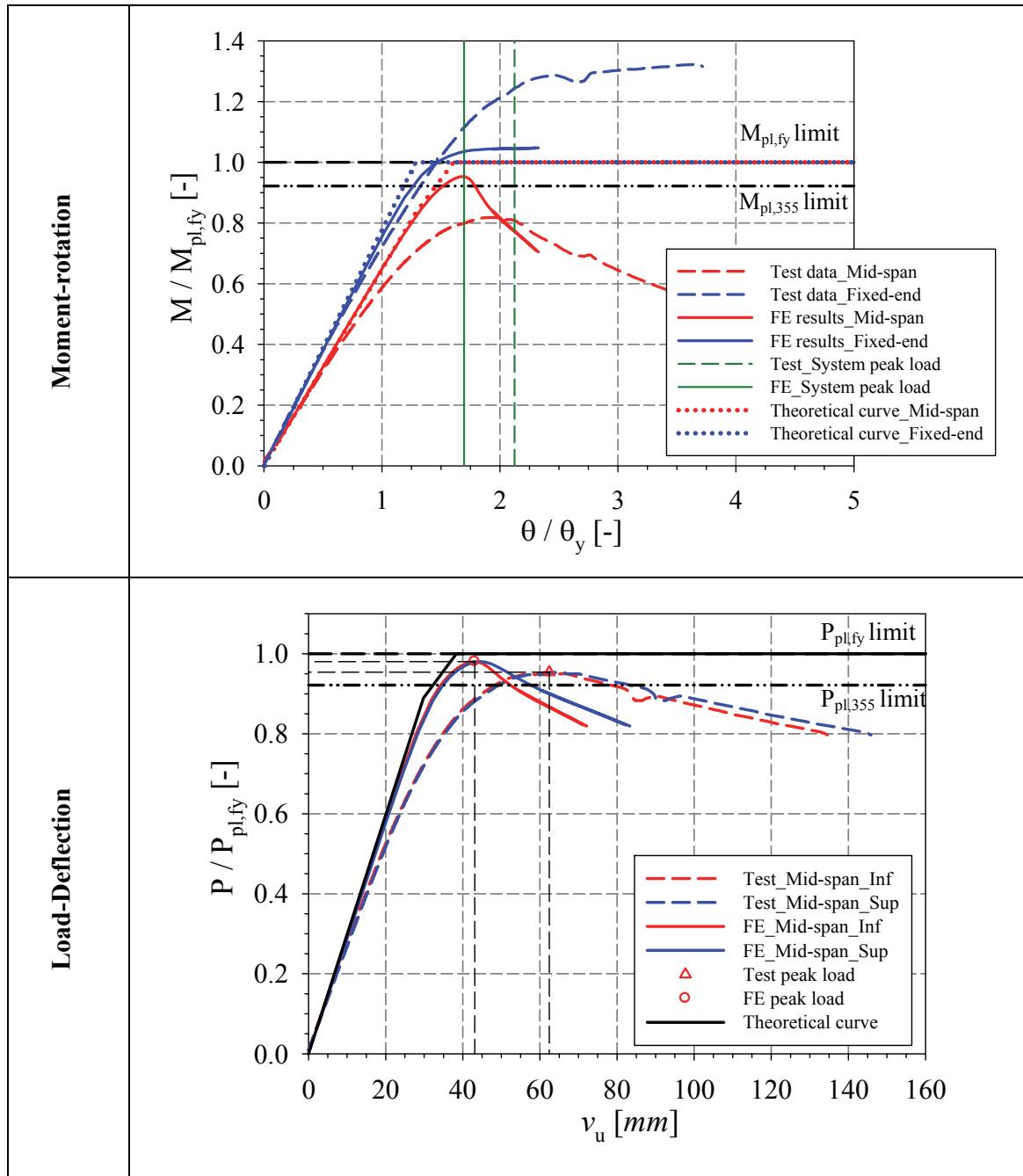
Unsymmetrical
loading

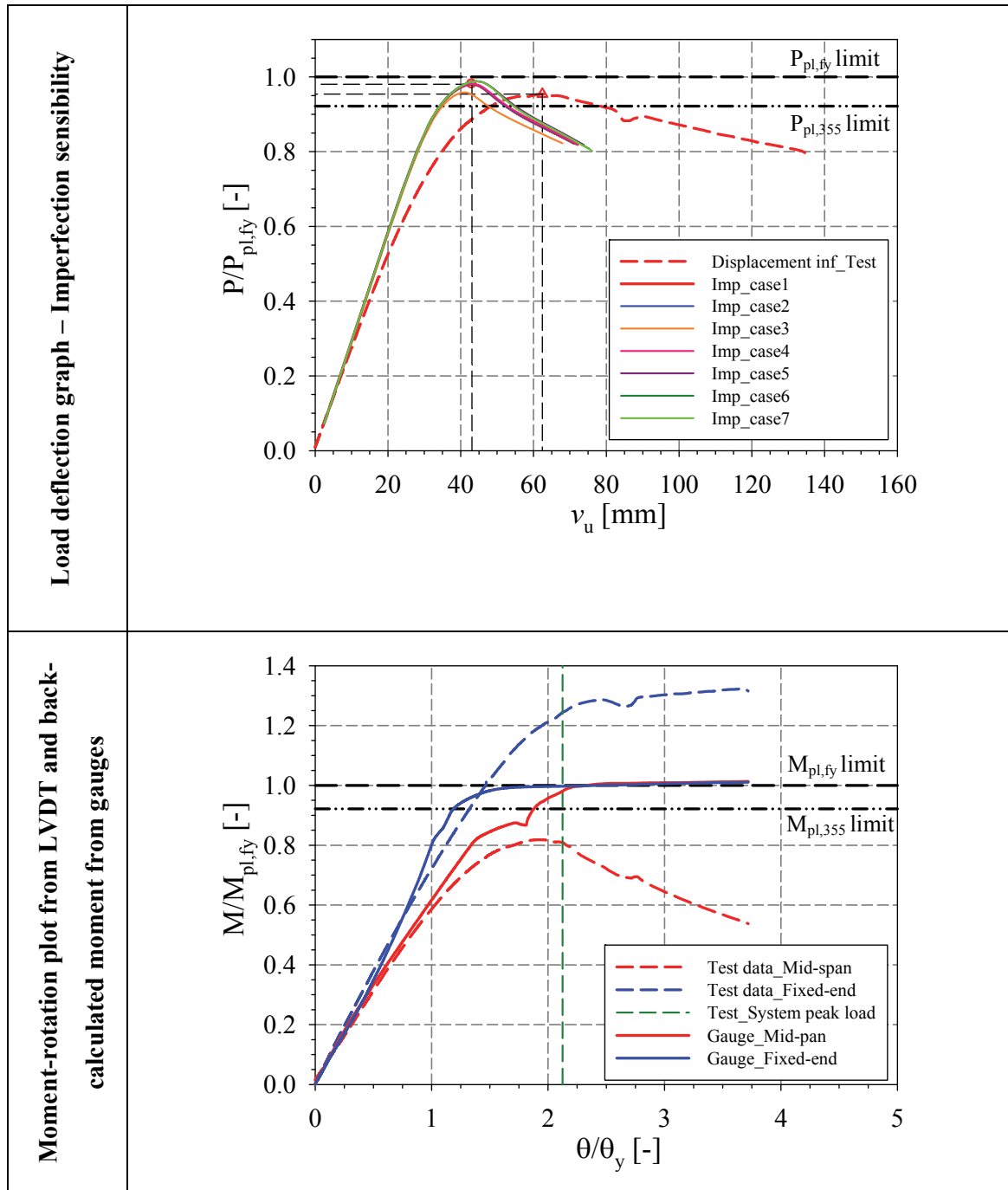
RHS_200×6.3_SS_4P at failure

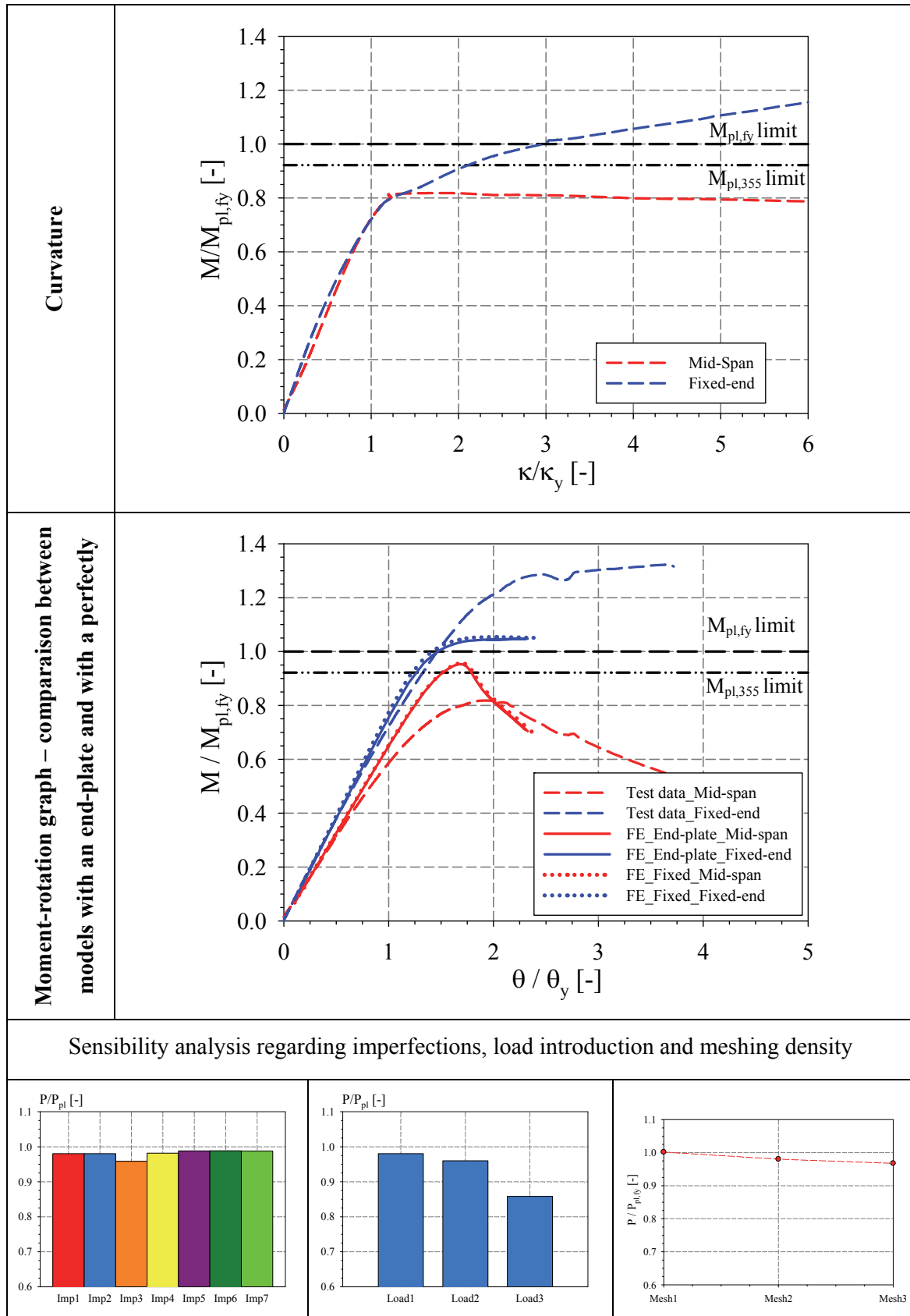
11.3.6 Summary of propped cantilever centrally loaded results

11.3.6.1 RHS_180×80×4.5_PR_C

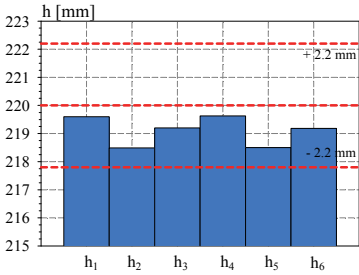
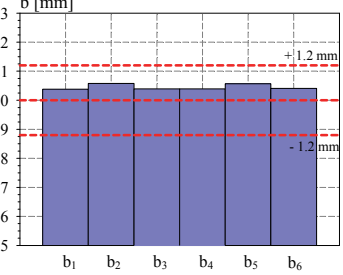
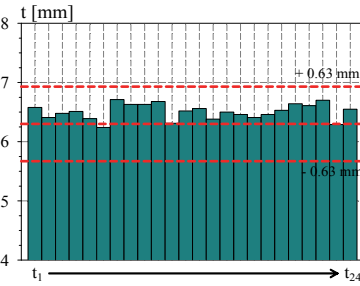
Specimen name	Nominal Details	Measured material properties (average)
RHS_180×80×4.5_PR_C	Shape: Rectangular Hollow Section Nominal Steel grade: 355 N/mm ² Load case: Propped cantilever centrally loaded h=180mm b=80mm t=4.5mm Fabrication process: Hot-rolled	$f_y = 403.9 \text{ N/mm}^2$ $f_u = 547.3 \text{ N/mm}^2$ $E = 213062 \text{ N/mm}^2$ $\epsilon_y = 0.19 \%$ $\epsilon_{y2} = 1.93 \%$ $\epsilon_u = 16.68 \%$
 <p>Average h = 179.19 qmm</p>	 <p>Average b = 79.06 mm</p>	 <p>Average t = 4.76 mm</p>
<p align="center">RHS_180×80×4.5_PR_C at failure</p> 		
<p align="center">Yield pattern of RHS_180×80×4.5_PR_C at failure</p> 		







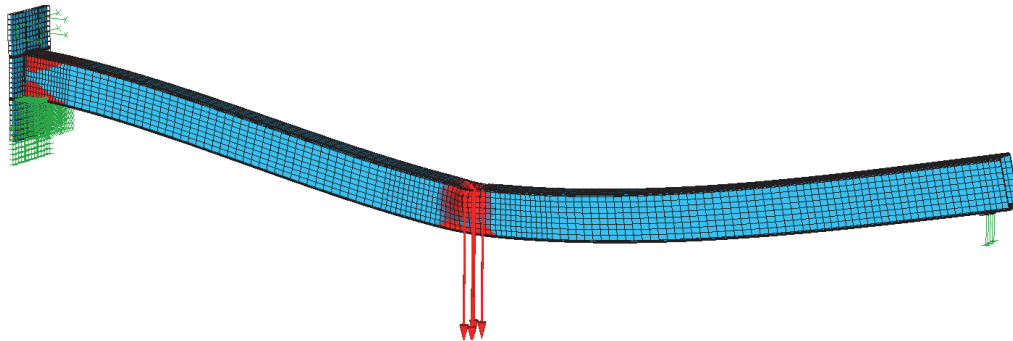
11.3.6.2 RHS_220×120×6.3_PR_C

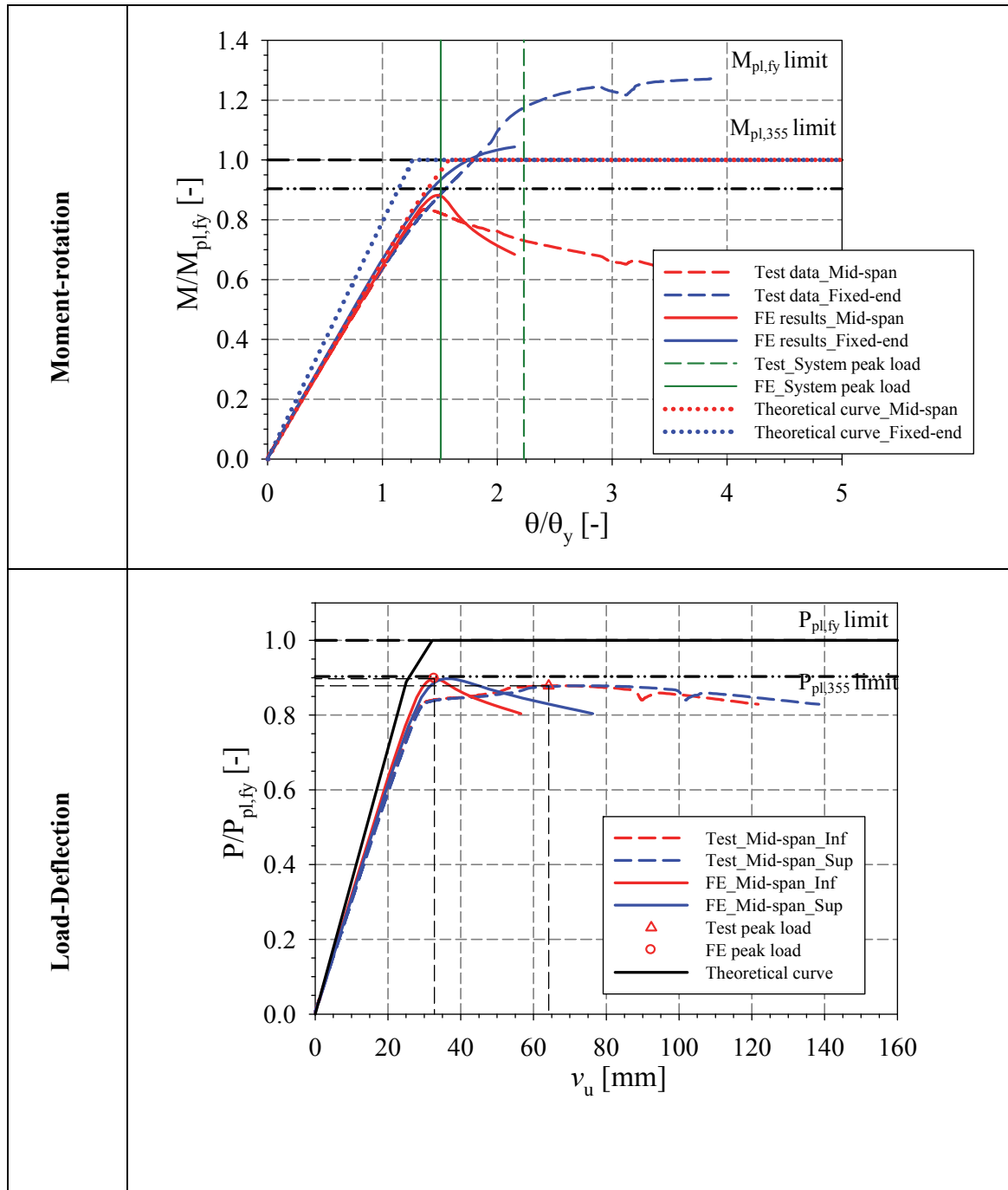
Specimen name	Nominal Details	Measured material properties (average)
RHS_220×120×6.3_PR_C	Shape: Rectangular Hollow Section Nominal Steel grade: 355 N/mm^2 Load case: Propped cantilever centrally loaded $h=220mm$ $b=120mm$ $t=6.3mm$ Fabrication process: Hot-rolled	$f_y = 393.0 N/mm^2$ $f_u = 531.8 N/mm^2$ $E = 202440 N/mm^2$ $\varepsilon_y = 0.19 \%$ $\varepsilon_{y2} = 1.83 \%$ $\varepsilon_u = 17.16 \%$
 <p>Average $h = 219.10 mm$</p>	 <p>Average $b = 120.45 mm$</p>	 <p>Average $t = 6.51 mm$</p>

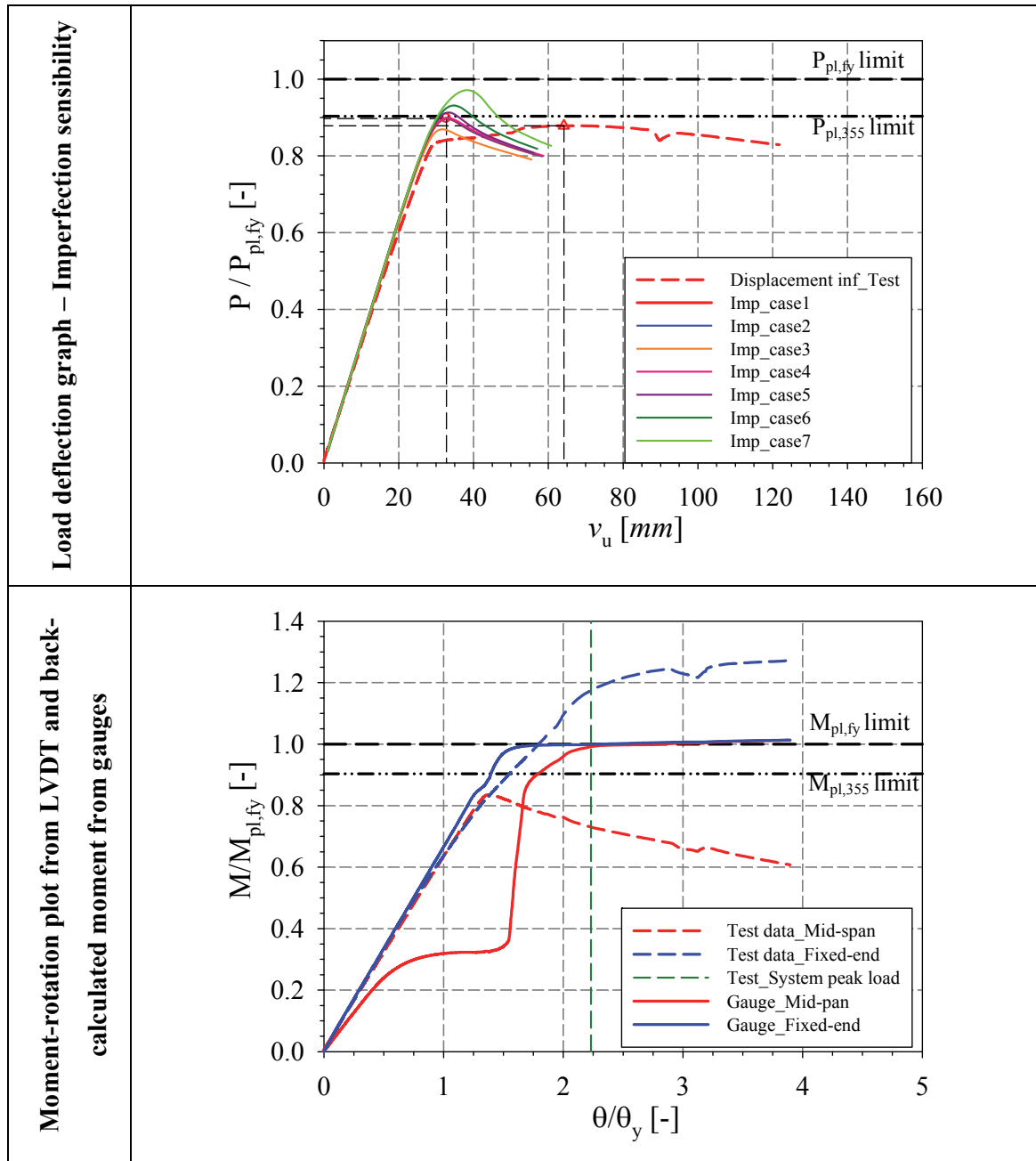
RHS_220×120×6.3_PR_C at failure

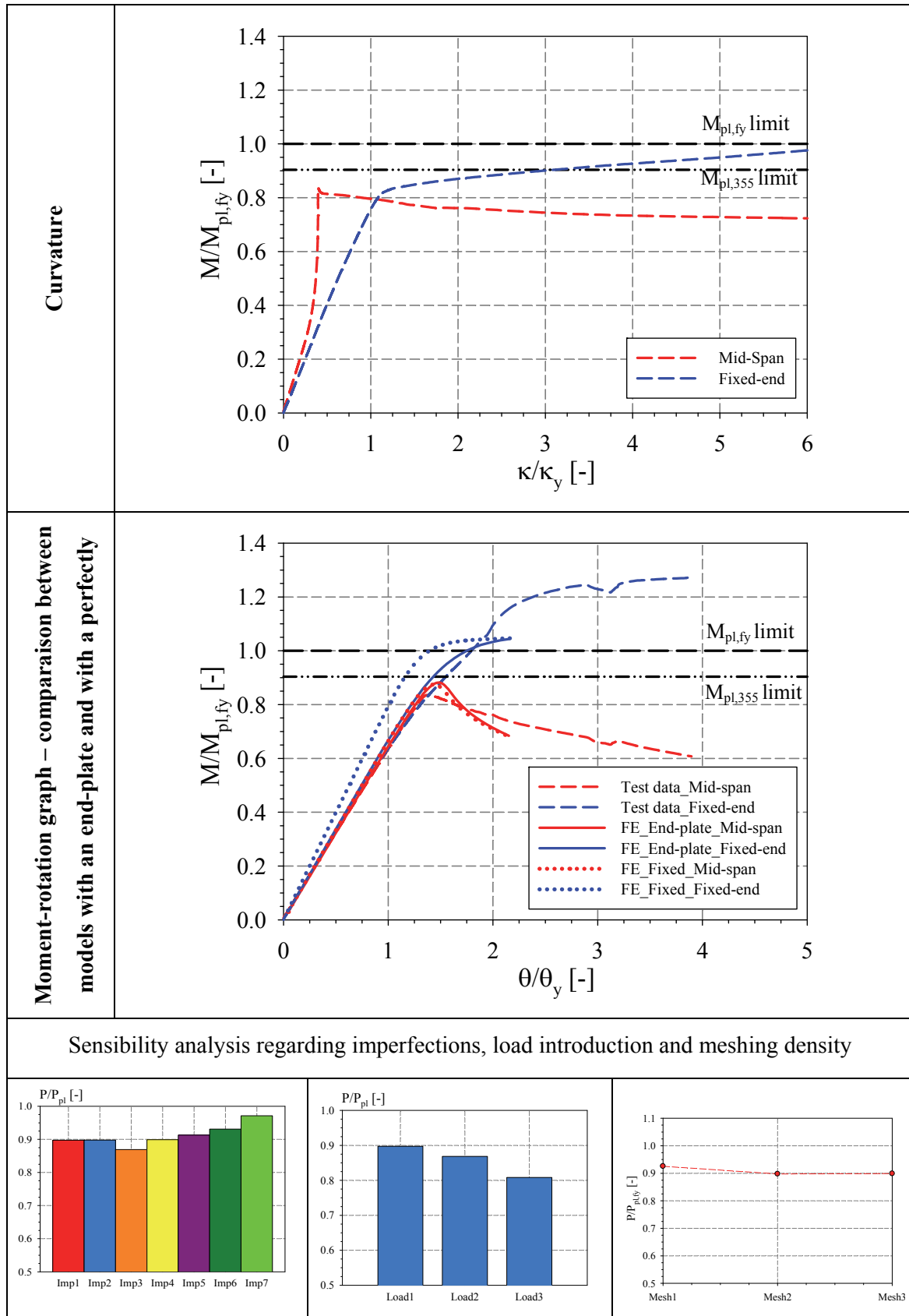


Yield pattern of RHS_220×120×6.3_PR_C at failure

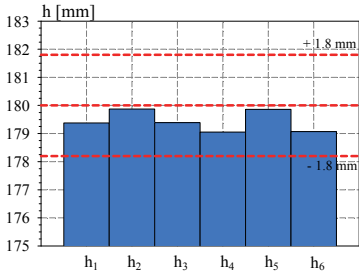
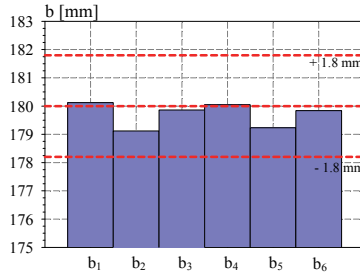
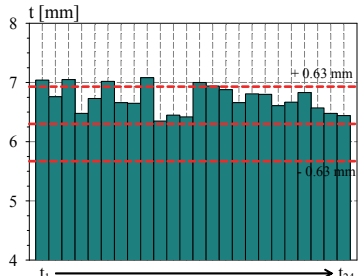

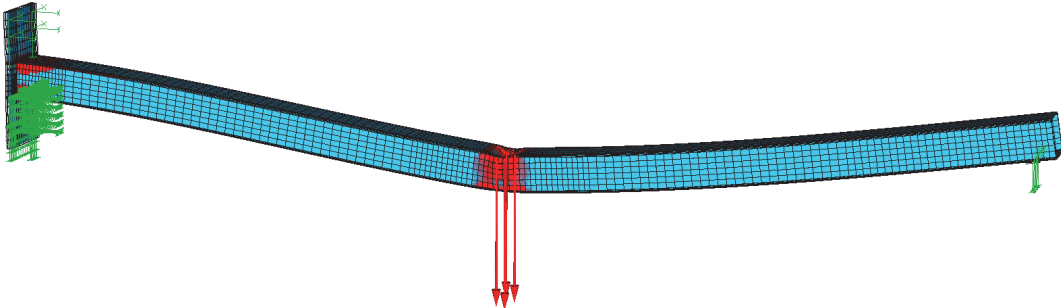


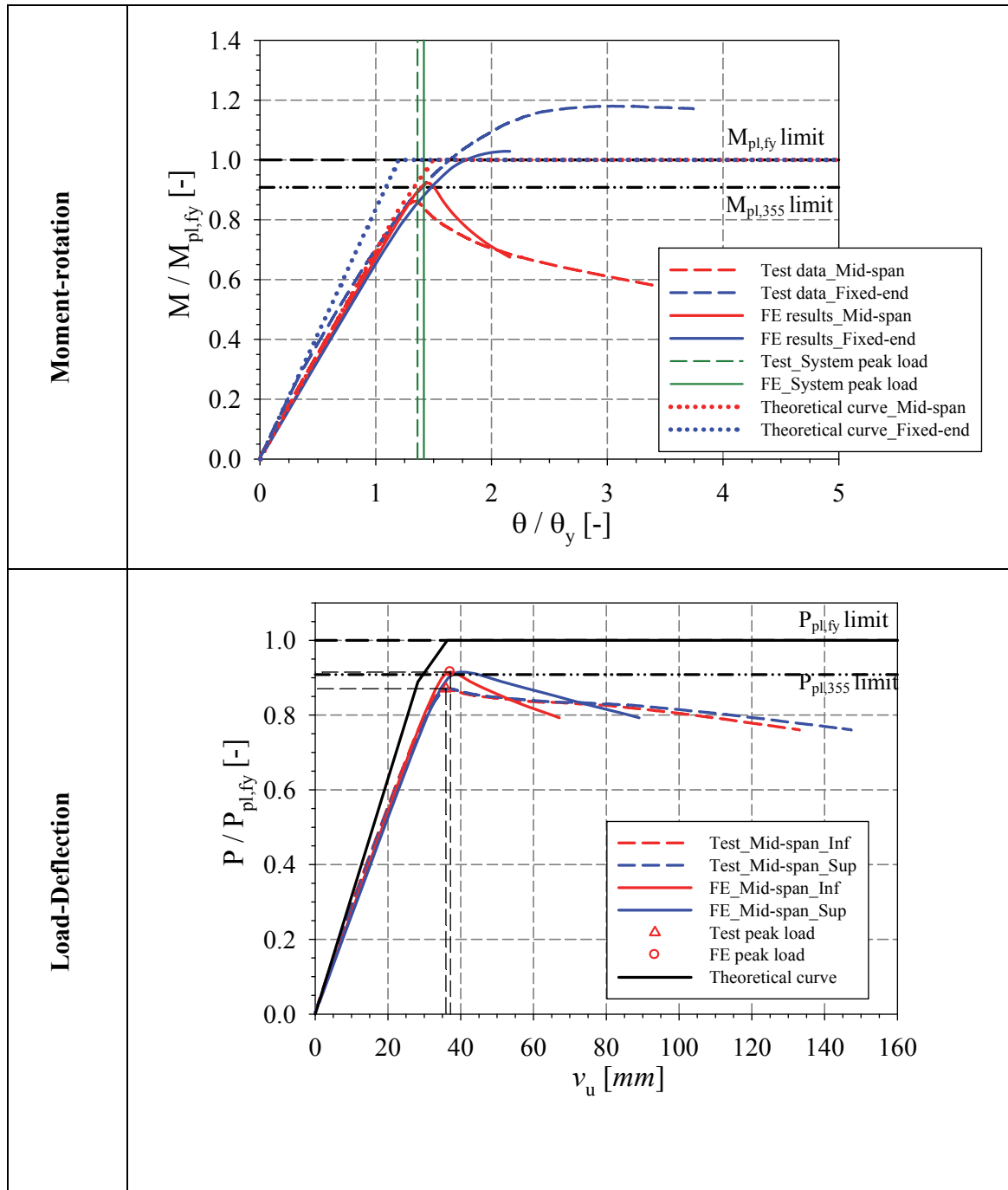


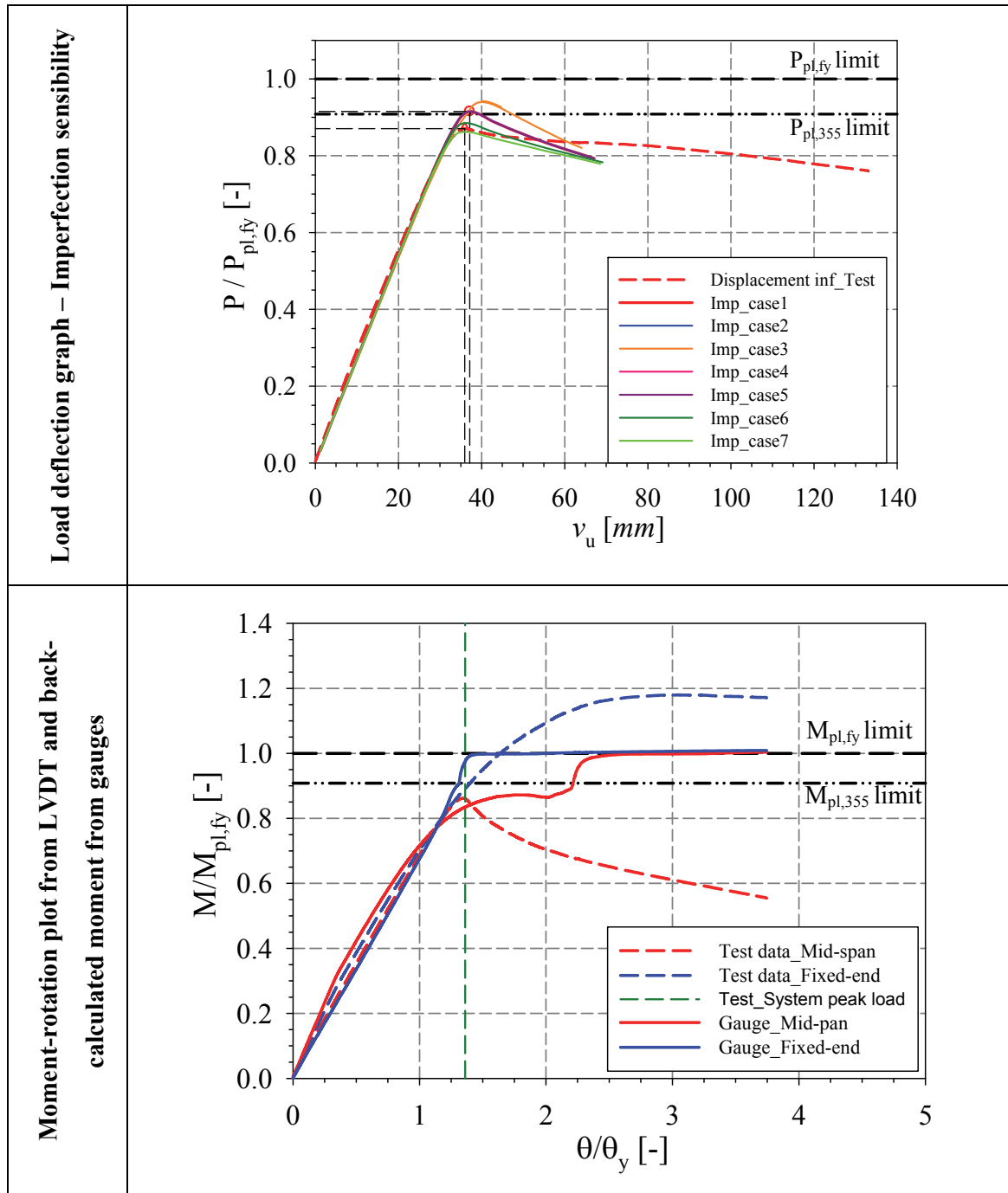


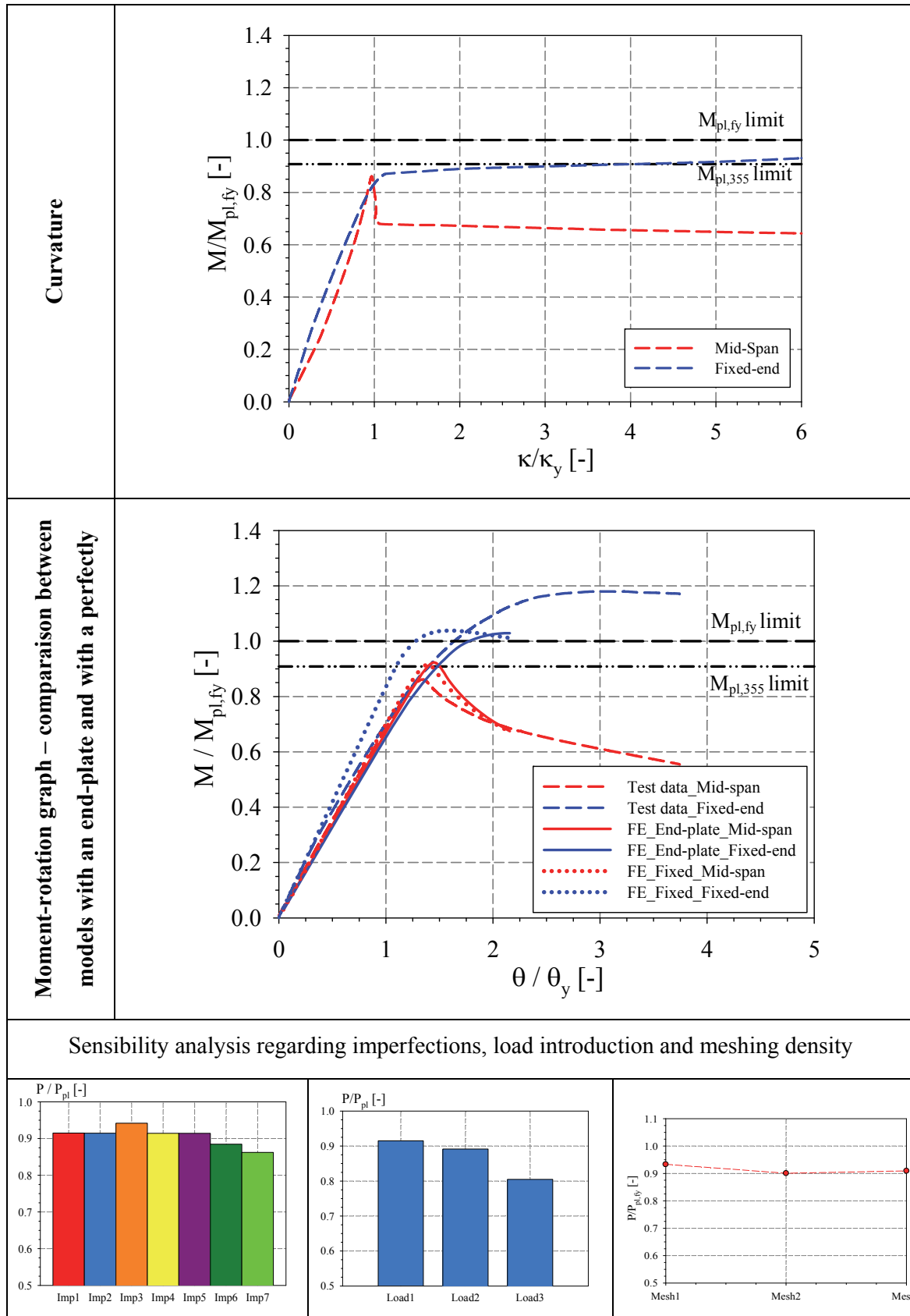


11.3.6.3 SHS_180x6.3_PR_C

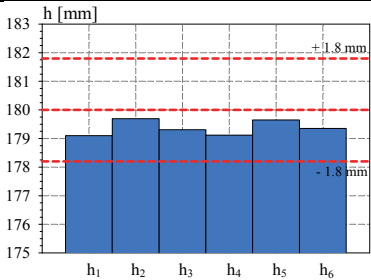
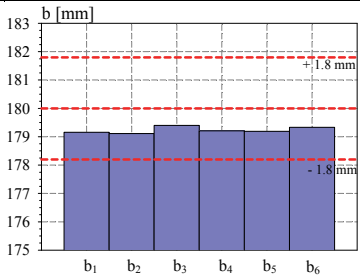
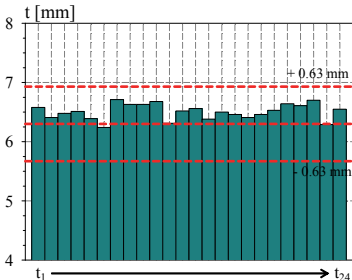
Specimen name	Nominal Details	Measured material properties (average)
SHS_180x6.3_PR_C	Shape: Square Hollow Section Nominal Steel grade: 355 N/mm ² Load case: Propped cantilever centrally loaded h=180mm b=180mm t=6.3mm Fabrication process: Hot-rolled	$f_y = 390.9 \text{ N/mm}^2$ $f_u = 532.2 \text{ N/mm}^2$ $E = 206819 \text{ N/mm}^2$ $\varepsilon_y = 0.19 \%$ $\varepsilon_{y2} = 1.79 \%$ $\varepsilon_u = 17.62 \%$
 Average h = 179.44 mm	 Average b = 179.70 mm	 Average t = 6.72 mm
<h4>SHS_180x6.3_PR_C at failure</h4> 		
<h4>Yield pattern of SHS_180x6.3_PR_C at failure</h4> 		







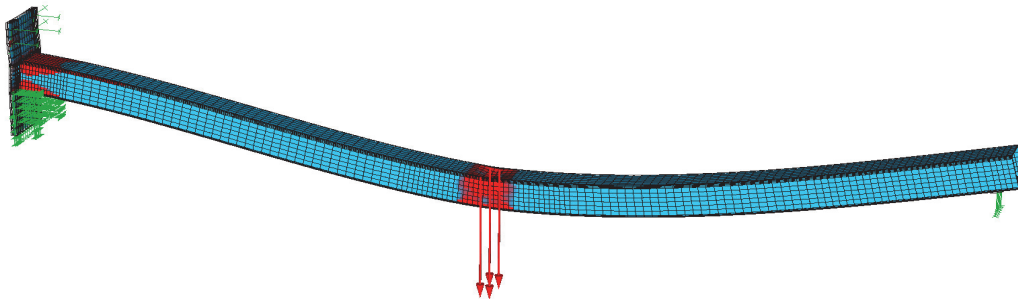
11.3.6.4 SHS_180x8_PR_C

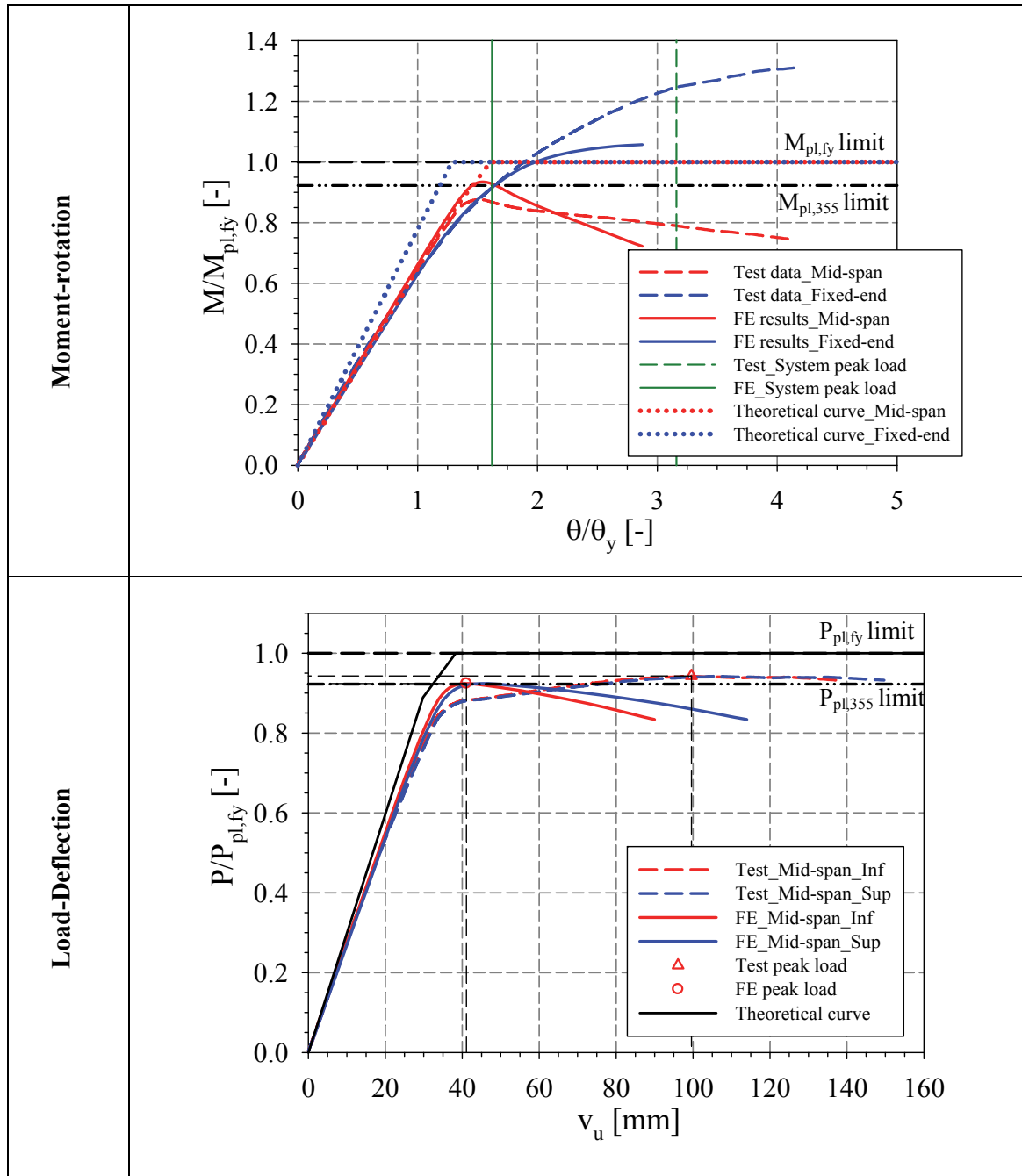
Specimen name	Nominal Details	Measured material properties (average)
SHS_180x8_PR_C	Shape: Square Hollow Section Nominal Steel grade: 355 N/mm ² Load case: Propped cantilever centrally loaded h=180mm b=180mm t=8mm Fabrication process: Hot-rolled	$f_y = 384.8 \text{ N/mm}^2$ $f_u = 529.5 \text{ N/mm}^2$ $E = 213367 \text{ N/mm}^2$ $\varepsilon_y = 0.18 \%$ $\varepsilon_{y2} = 1.70 \%$ $\varepsilon_u = 15.9 \%$
<div style="display: flex; justify-content: space-around;"> <div style="text-align: center;">  <p>Average h = 179.37 mm</p> </div> <div style="text-align: center;">  <p>Average b = 179.23 mm</p> </div> <div style="text-align: center;">  <p>Average t = 7.94 mm</p> </div> </div>		

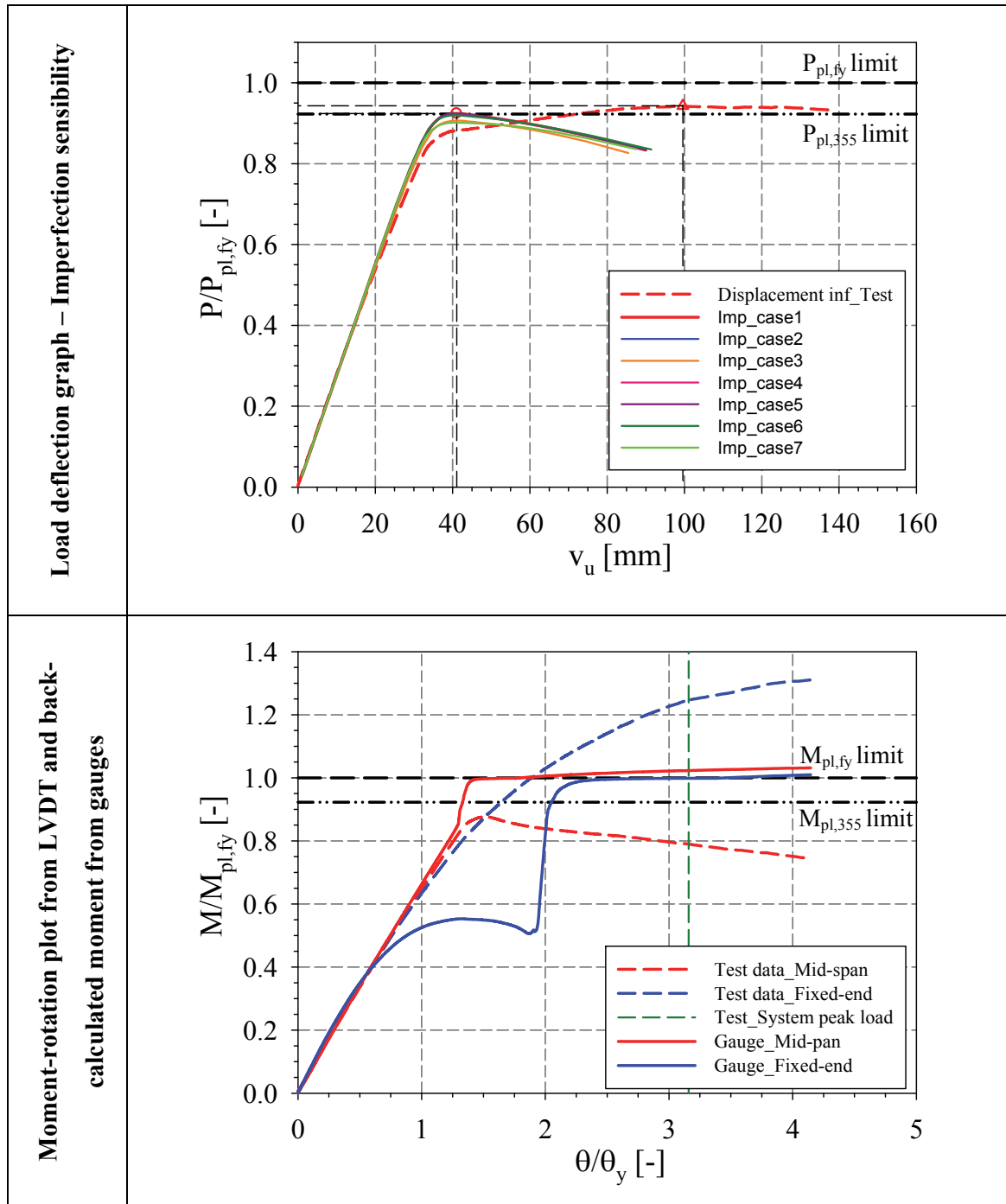
SHS_180x8_PR_C at failure

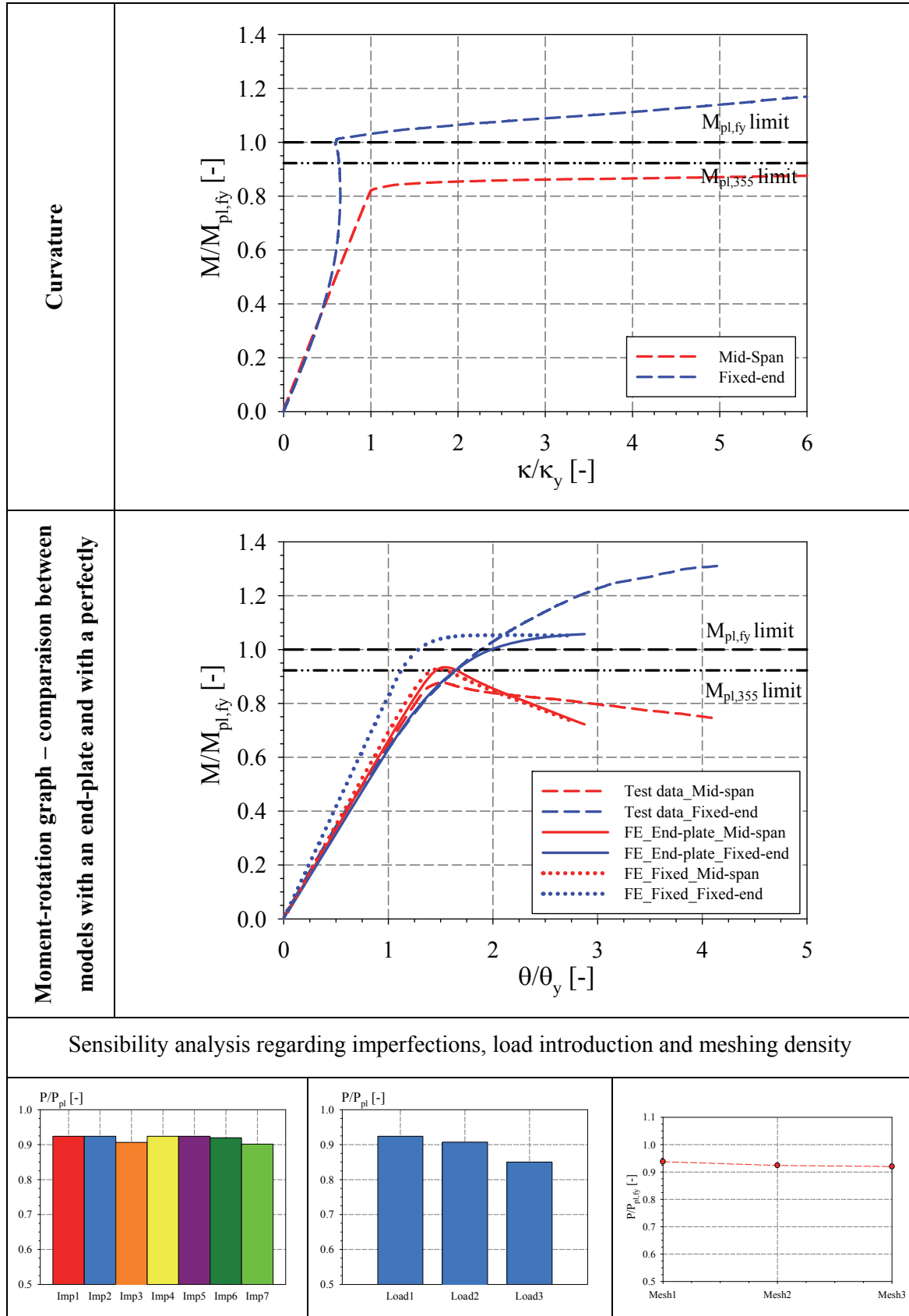


Yield pattern of SHS_180x8_PR_C at failure

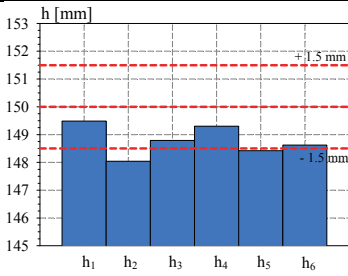
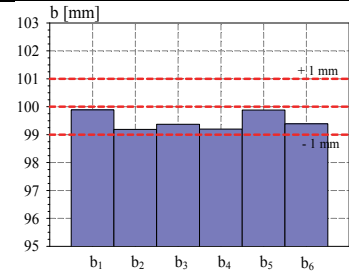
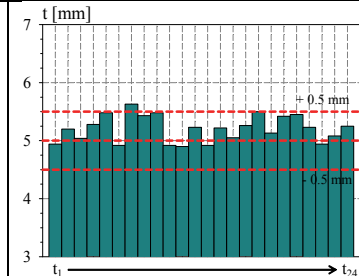

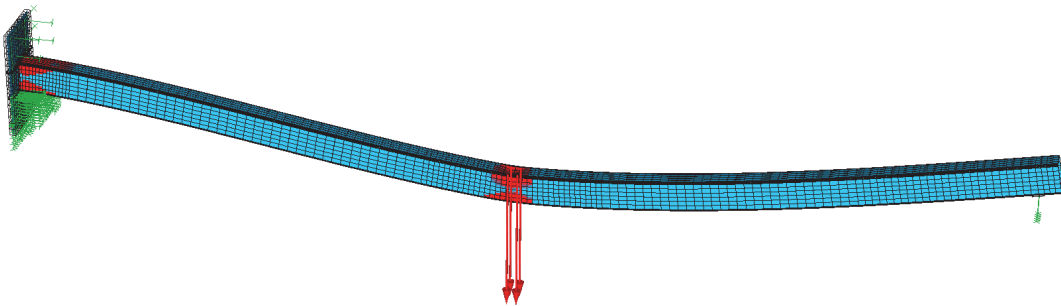


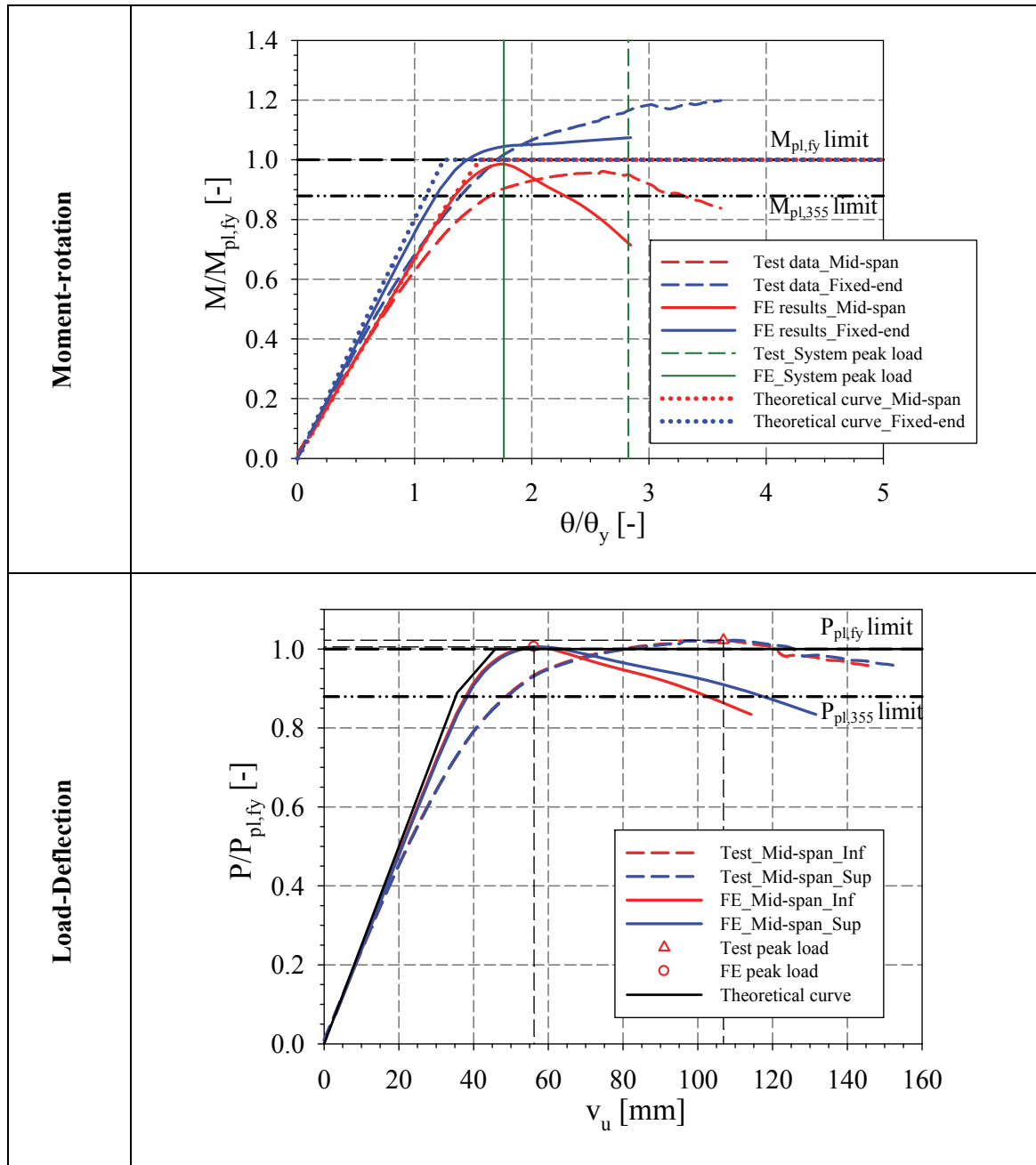


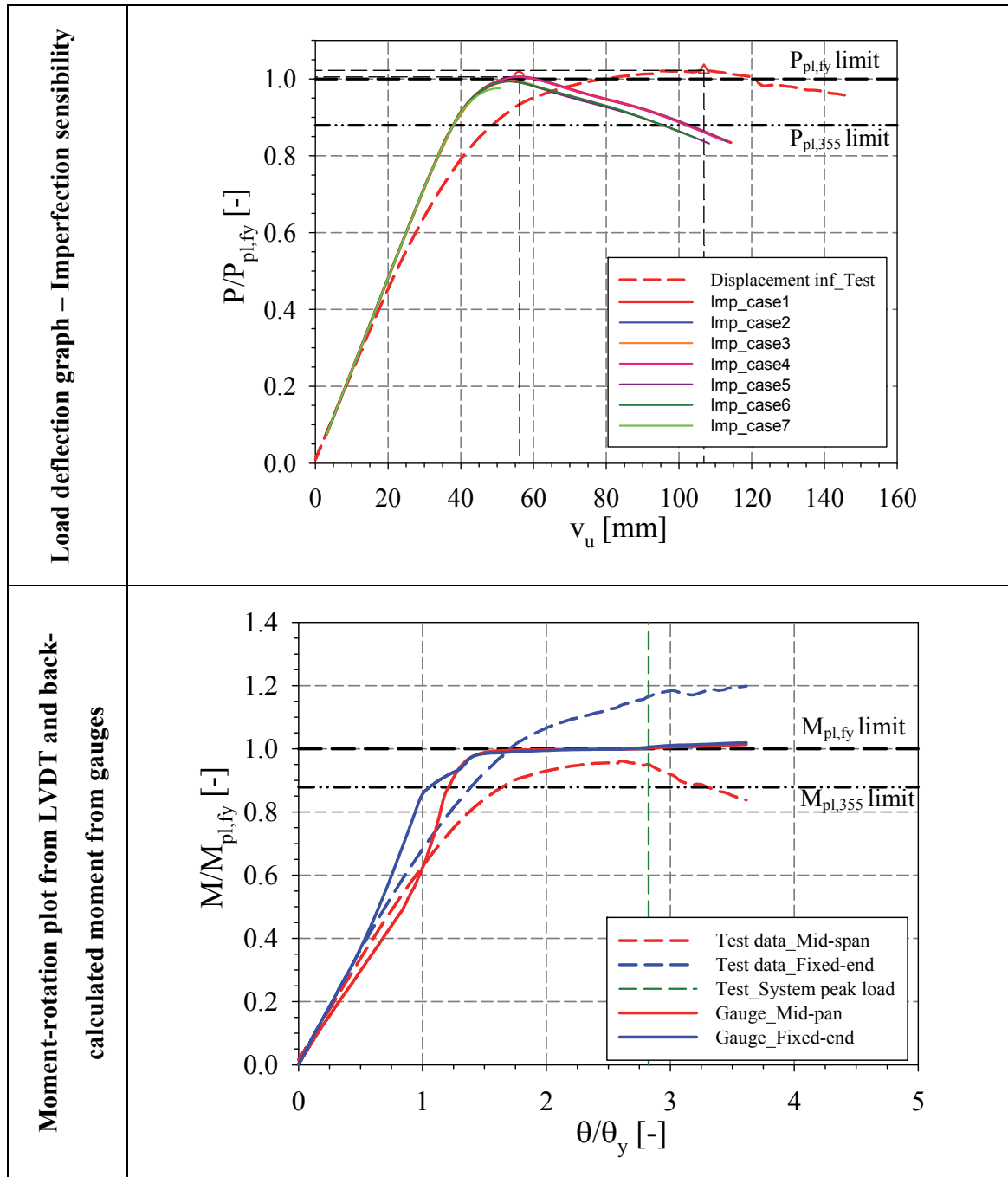


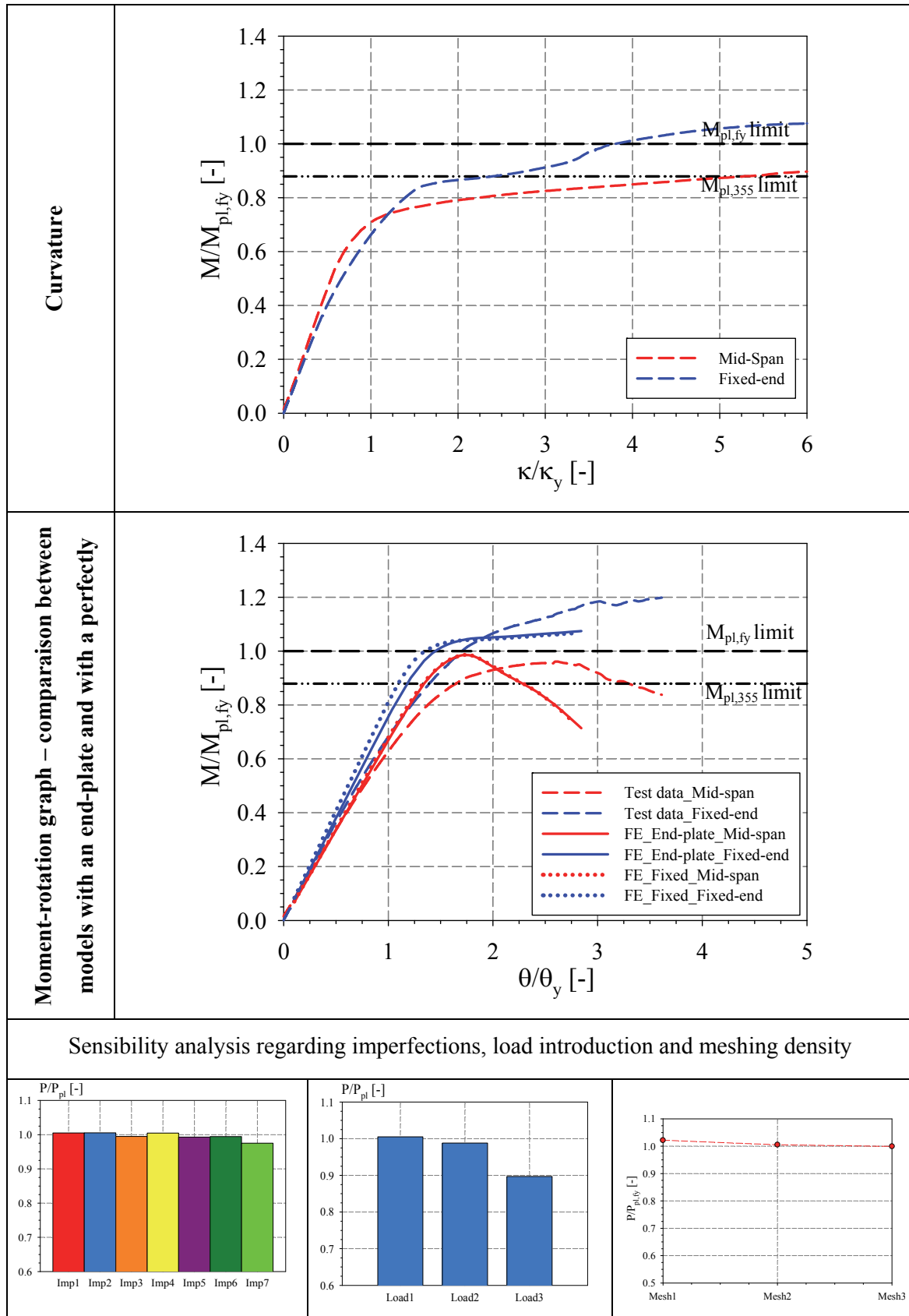


11.3.6.5 RHS_150x100x5_PR_C

Specimen name	Nominal Details	Measured material properties (average)
RHS_150×100×5_PR_C	Shape: Rectangular Hollow Section Nominal Steel grade: 355 N/mm ² Load case: Propped cantilever centrally loaded h=150mm b=100mm t=5mm Fabrication process: Hot-rolled	$f_y = 396.5 \text{ N/mm}^2$ $f_u = 552.7 \text{ N/mm}^2$ $E = 203267 \text{ N/mm}^2$ $\varepsilon_y = 0.20 \%$ $\varepsilon_{y2} = 1.72 \%$ $\varepsilon_u = 12.61 \%$
 <p>Average h = 148.78 mm</p>	 <p>Average b = 99.49 mm</p>	 <p>Average t = 5.20 mm</p>
RHS_150×100×5_PR_C at failure 		
Yield pattern of RHS_150×100×5_PR_C at failure 		

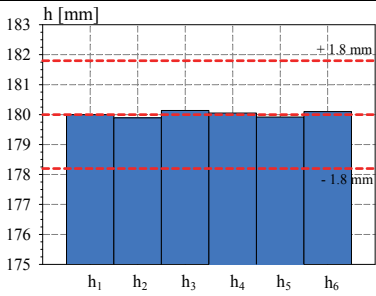
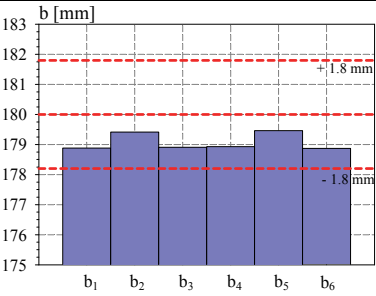
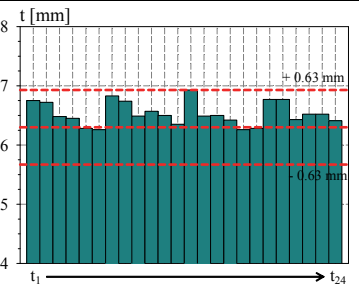

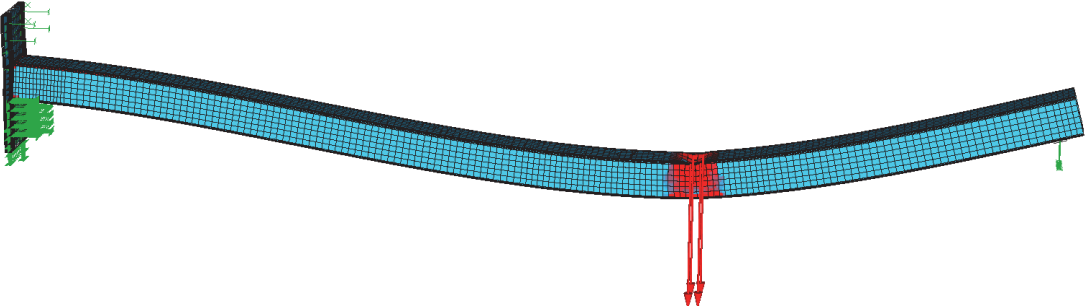


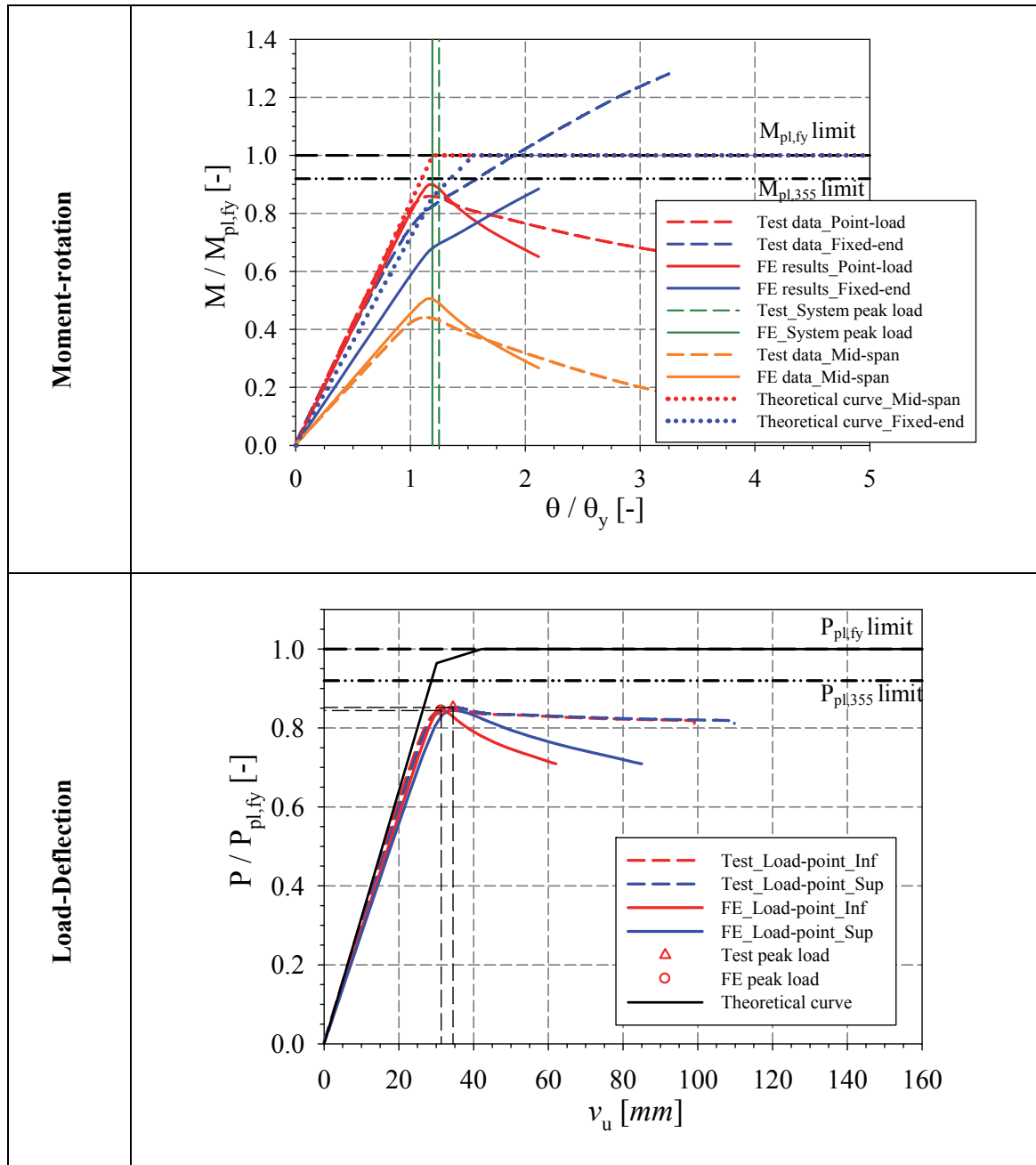


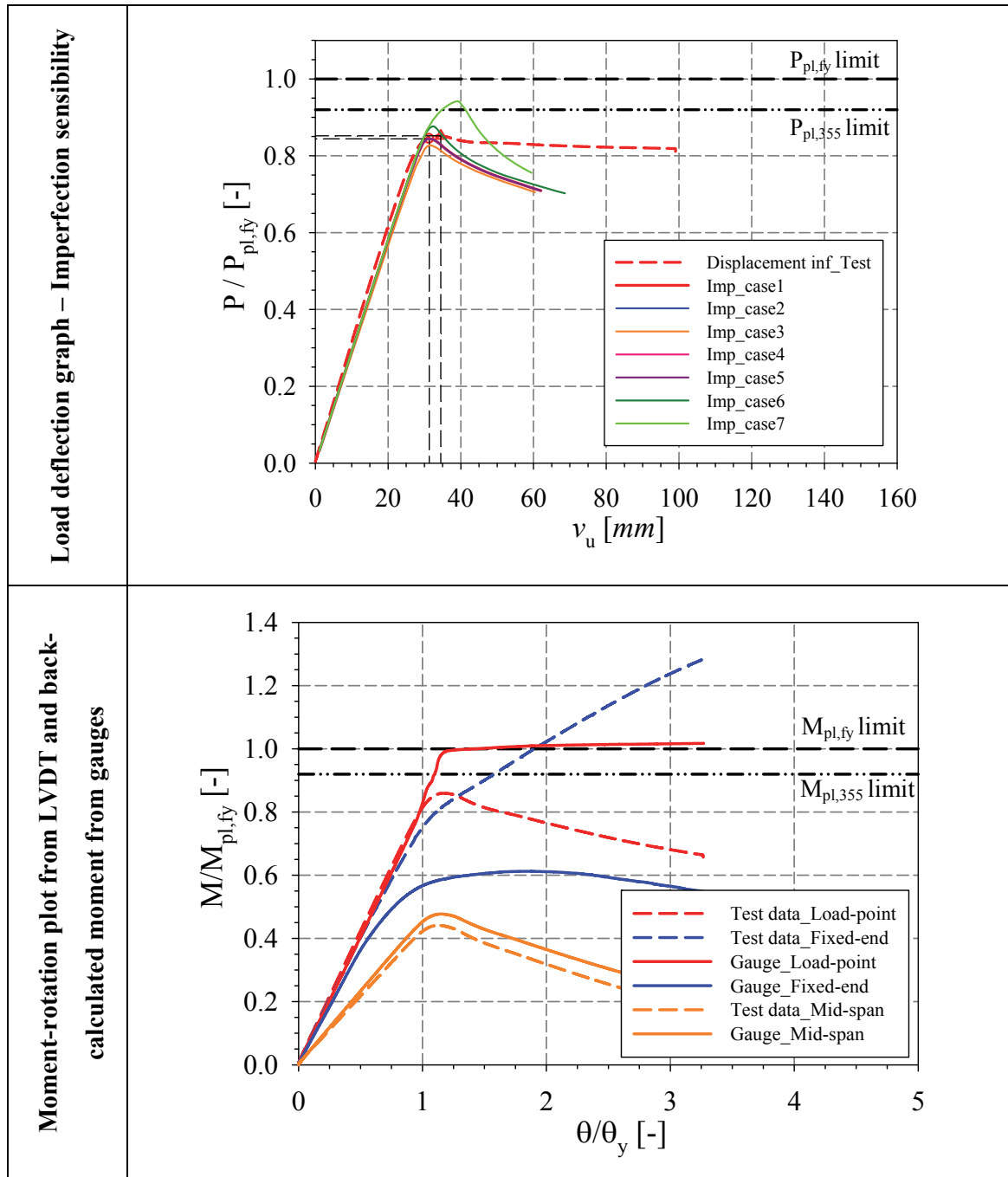


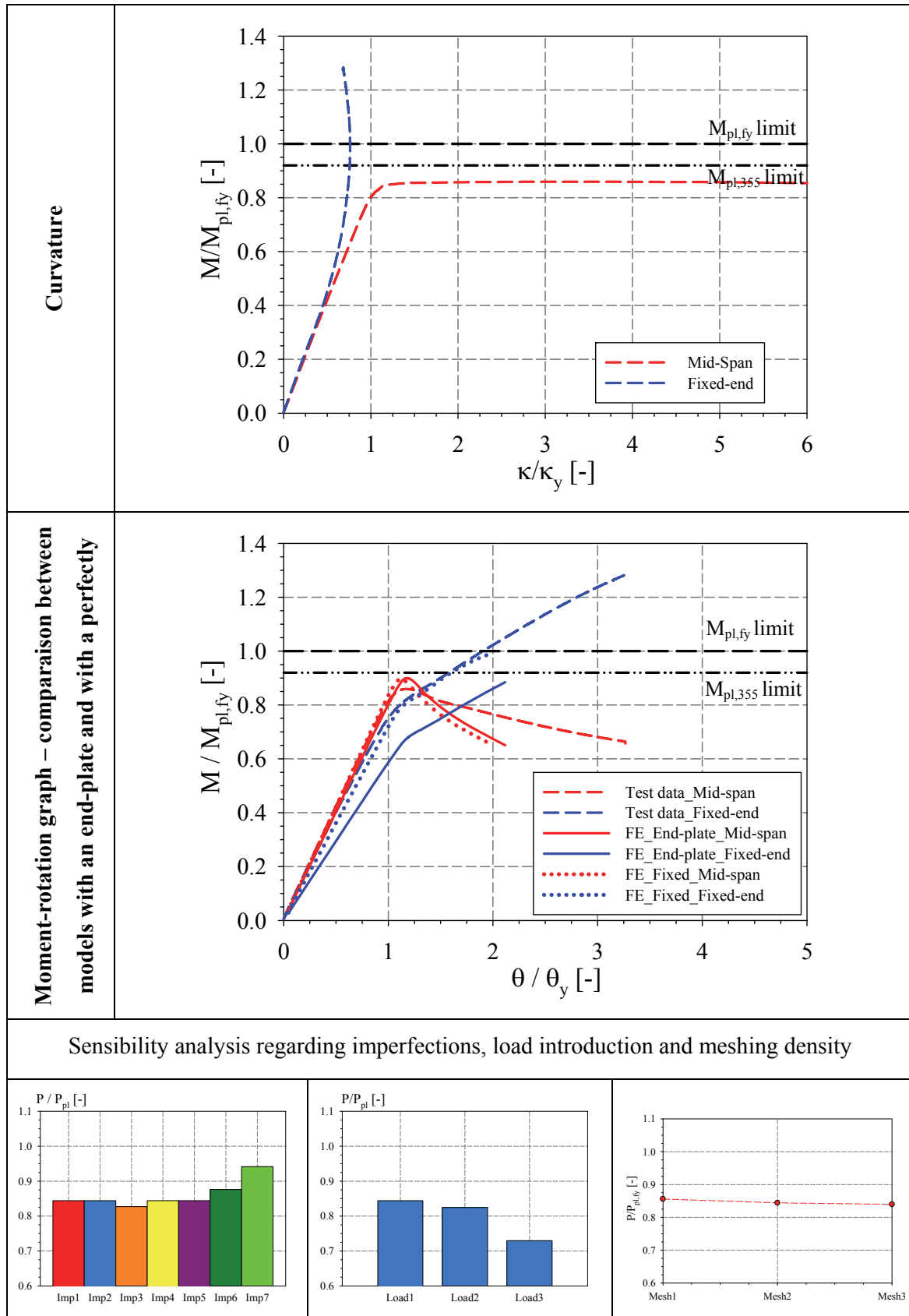
11.3.7 Summary of propped cantilever off-centrally loaded results

11.3.7.1 SHS_180x6.3_PR_O

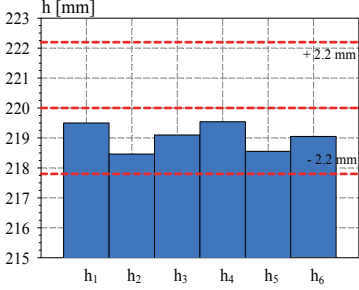
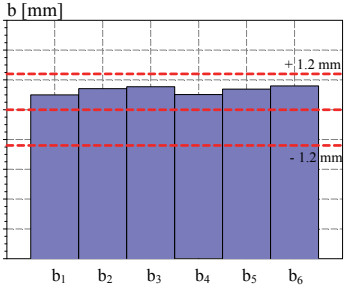
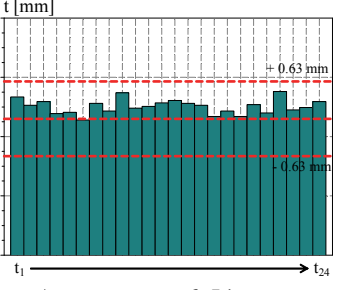

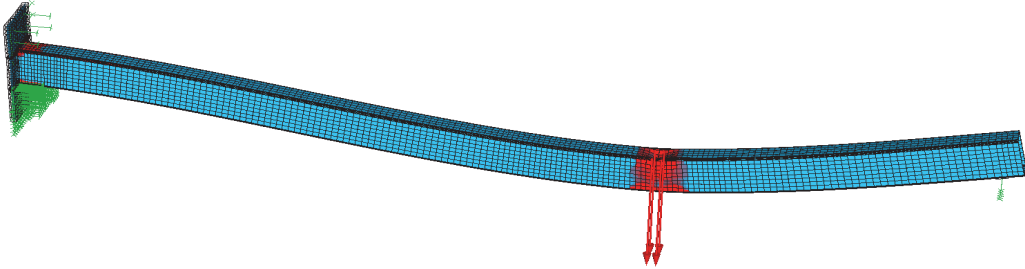
Specimen name	Nominal Details	Measured material properties (average)
SHS_180x6.3_PR_O	Shape: Square Hollow Section Nominal Steel grade: 355 N/mm ² Load case: Propped cantilever centrally loaded $h=180\text{mm}$ $b=180\text{mm}$ $t=6.3\text{mm}$ Fabrication process: Hot-rolled	$f_y = 385.8 \text{ N/mm}^2$ $f_u = 529.0 \text{ N/mm}^2$ $E = 207744 \text{ N/mm}^2$ $\epsilon_y = 0.19 \%$ $\epsilon_{y2} = 1.77 \%$ $\epsilon_u = 17.08 \%$
 Average $h = 180.02 \text{ mm}$	 Average $b = 179.08 \text{ mm}$	 Average $t = 6.53 \text{ mm}$
SHS_180x6.3_PR_O at failure 		
Yield pattern of SHS_180x6.3_PR_O at failure 		

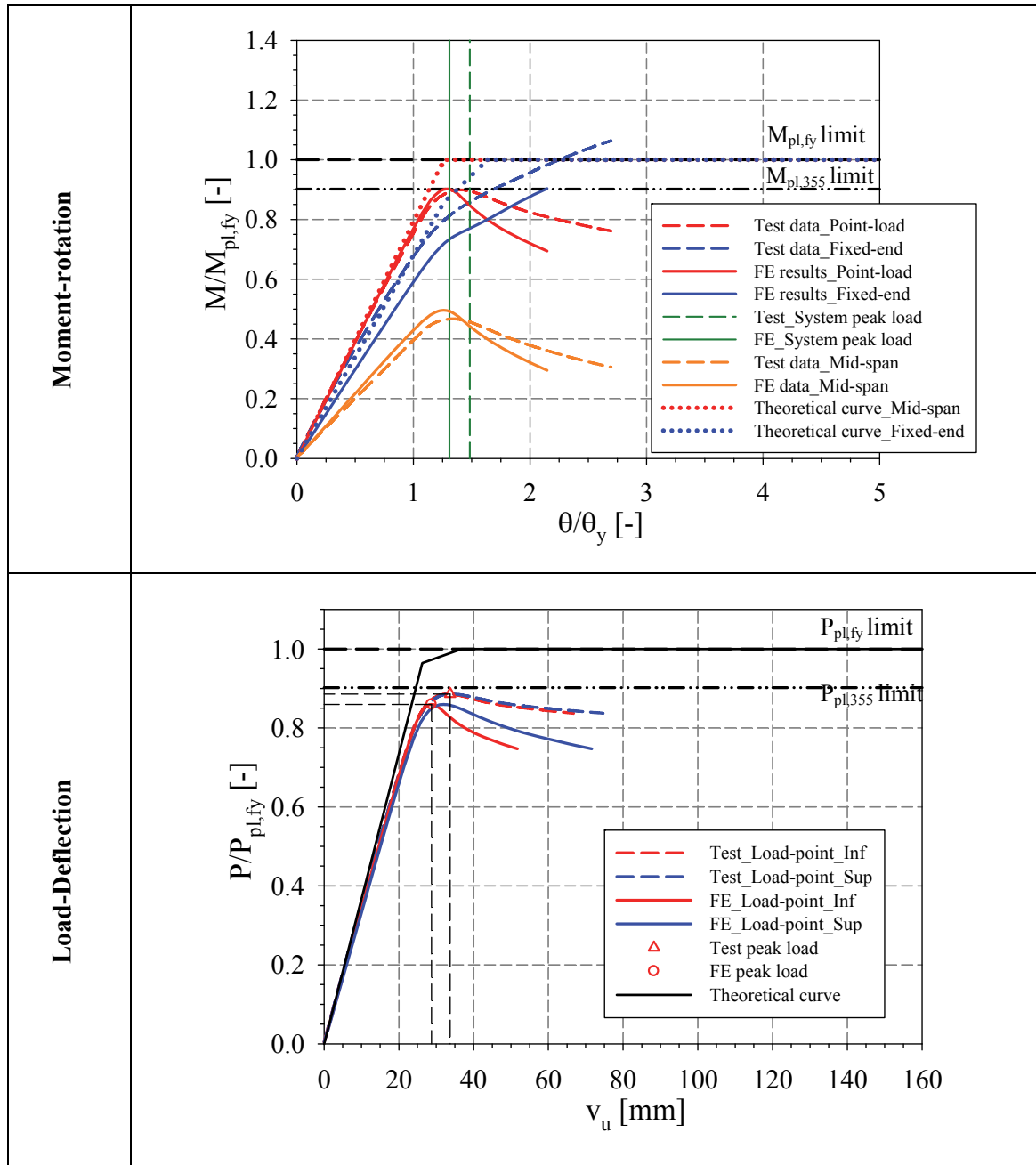


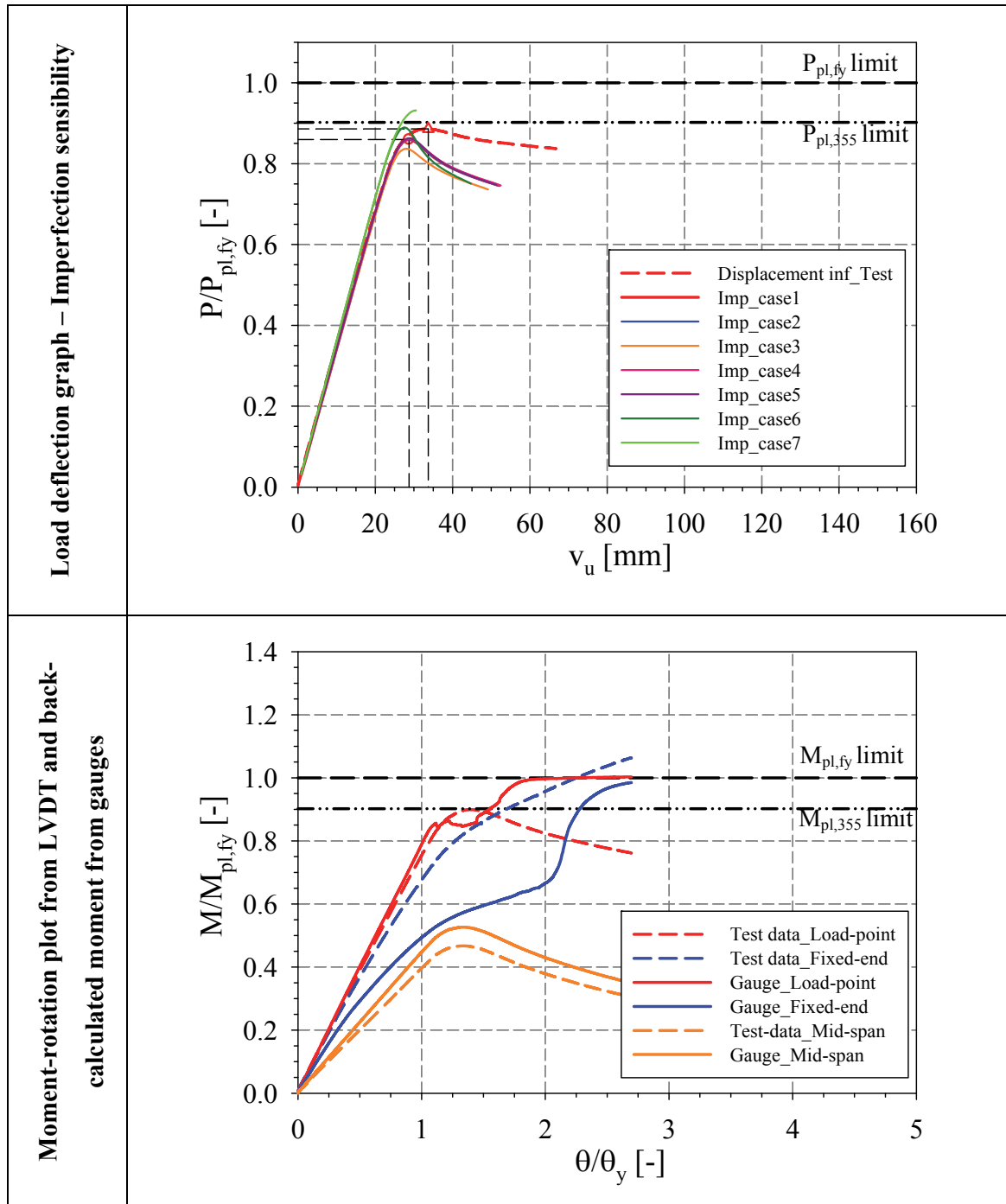


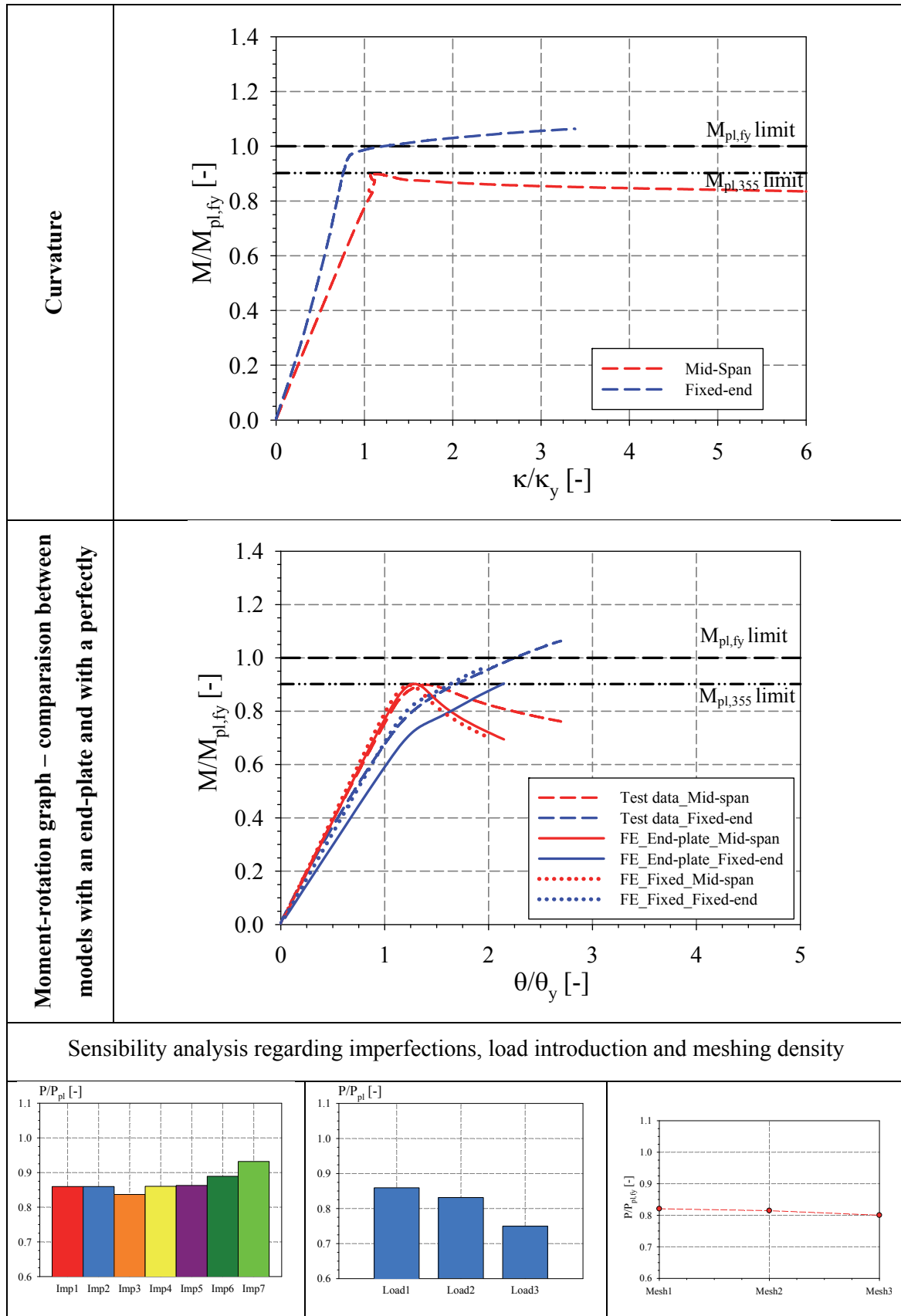


11.3.7.2 RHS_220×120×6.3_PR_O

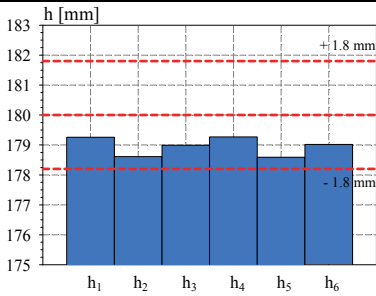
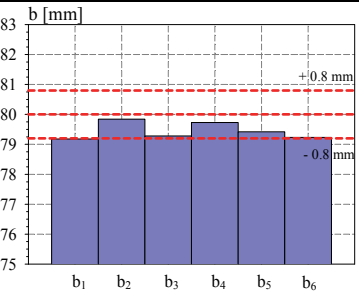
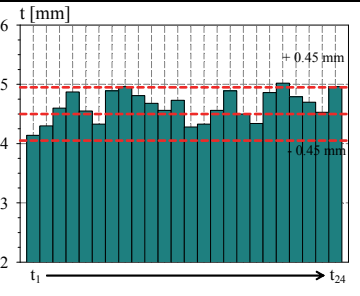
Specimen name	Nominal Details	Measured material properties (average)
RHS_220×120×6.3_PR_O	Shape: Rectangular Hollow Section Nominal Steel grade: 355 N/mm ² Load case: Propped cantilever centrally loaded h=220mm b=120mm t=6.3mm Fabrication process: Hot-rolled	$f_y = 393.6 \text{ N/mm}^2$ $f_u = 533.2 \text{ N/mm}^2$ $E = 210347 \text{ N/mm}^2$ $\varepsilon_y = 0.19 \%$ $\varepsilon_{y2} = 1.84 \%$ $\varepsilon_u = 18.58 \%$
 <p>Average h = 219.03 mm</p>	 <p>Average b = 120.66 mm</p>	 <p>Average t = 6.51 mm</p>
RHS_220×120×6.3_PR_O at failure 		
Yield pattern of RHS_220×120×6.3_PR_O at failure 		







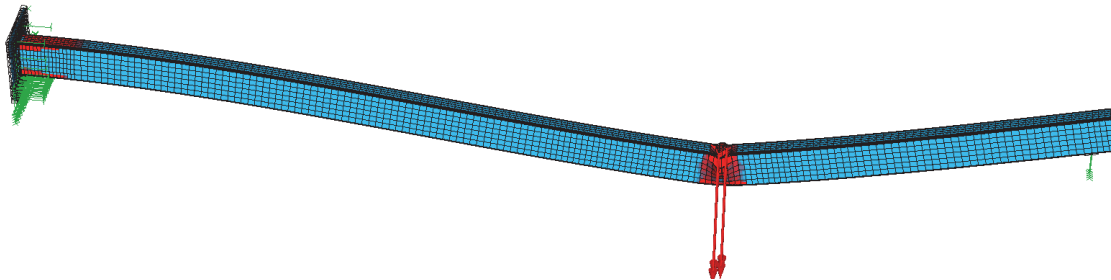
11.3.7.3 RHS_180×80×4.5_PR_O

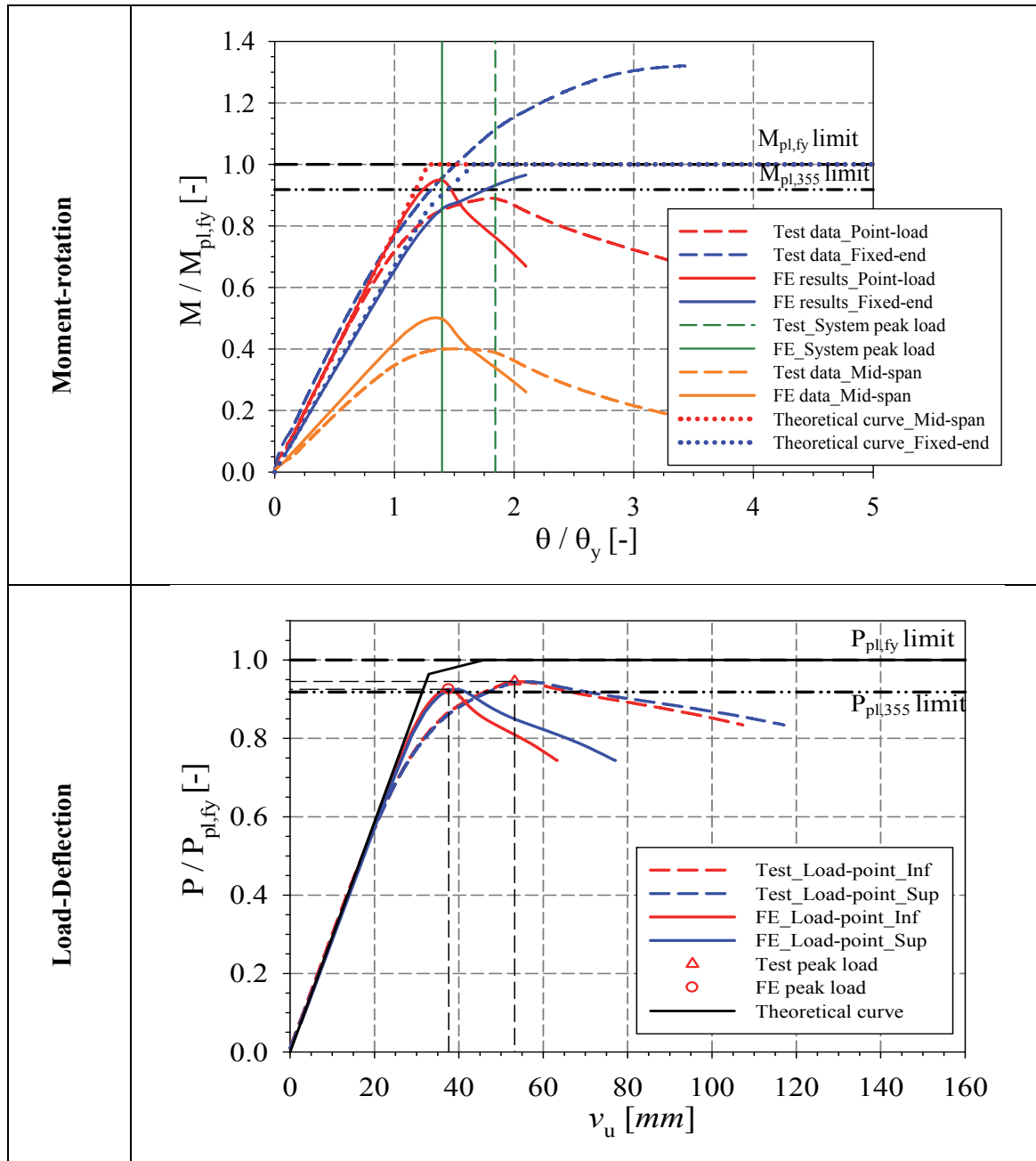
Specimen name	Nominal Details	Measured material properties (average)
RHS_180×80×4.5_PR_O	Shape: Rectangular Hollow Section Nominal Steel grade: 355 N/mm ² Load case: Propped cantilever centrally loaded $h=180\text{mm}$ $b=80\text{mm}$ $t=4.5\text{mm}$ Fabrication process: Hot-rolled	$f_y = 386.6 \text{ N/mm}^2$ $f_u = 537.1 \text{ N/mm}^2$ $E = 205414 \text{ N/mm}^2$ $\varepsilon_y = 0.19 \%$ $\varepsilon_{y2} = 1.85 \%$ $\varepsilon_u = 18.47 \%$
 <p>Average $h = 178.96 \text{ mm}$</p>	 <p>Average $b = 79.45 \text{ mm}$</p>	 <p>Average $t = 4.63 \text{ mm}$</p>

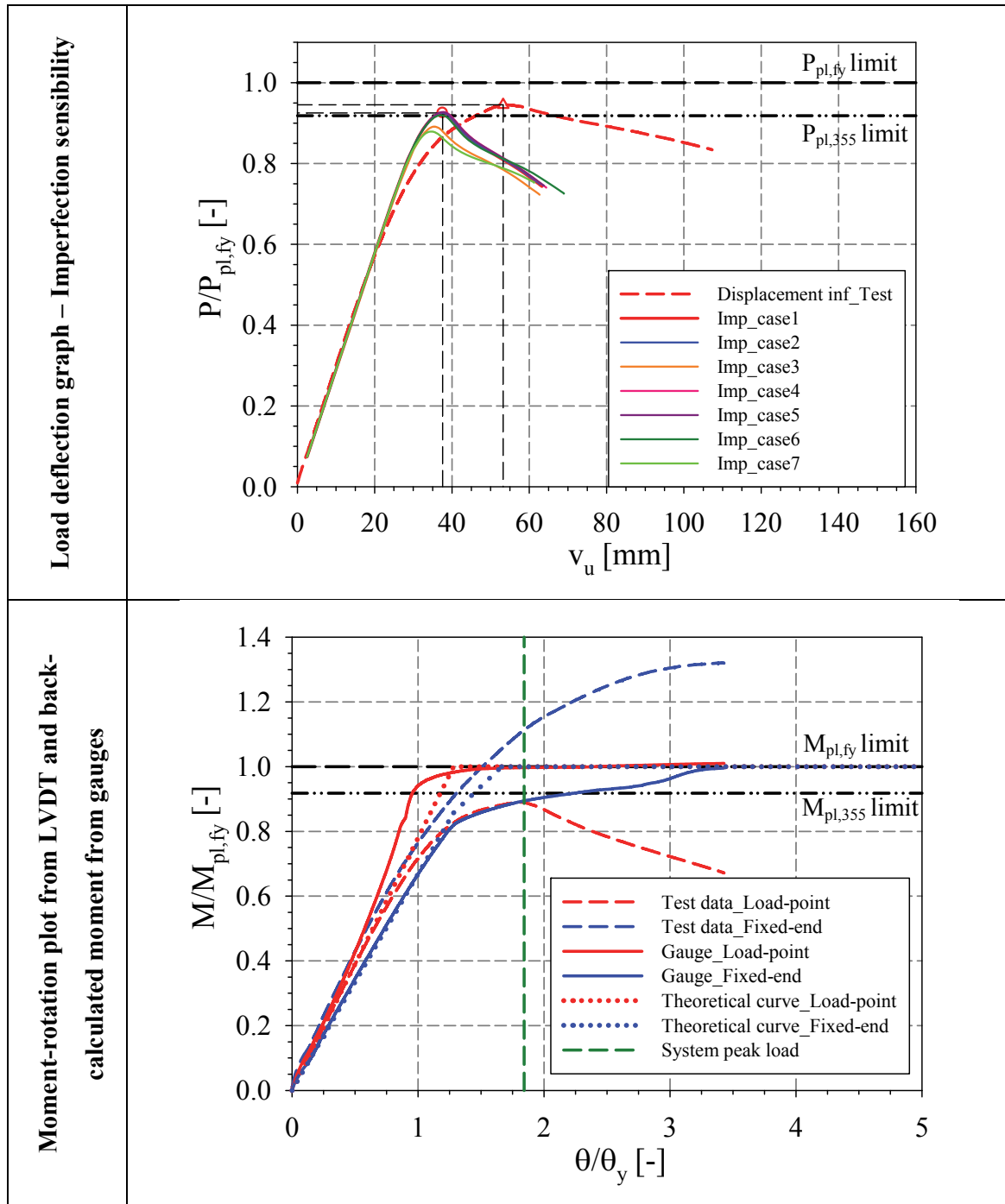
RHS_180×80×4.5_PR_O at failure

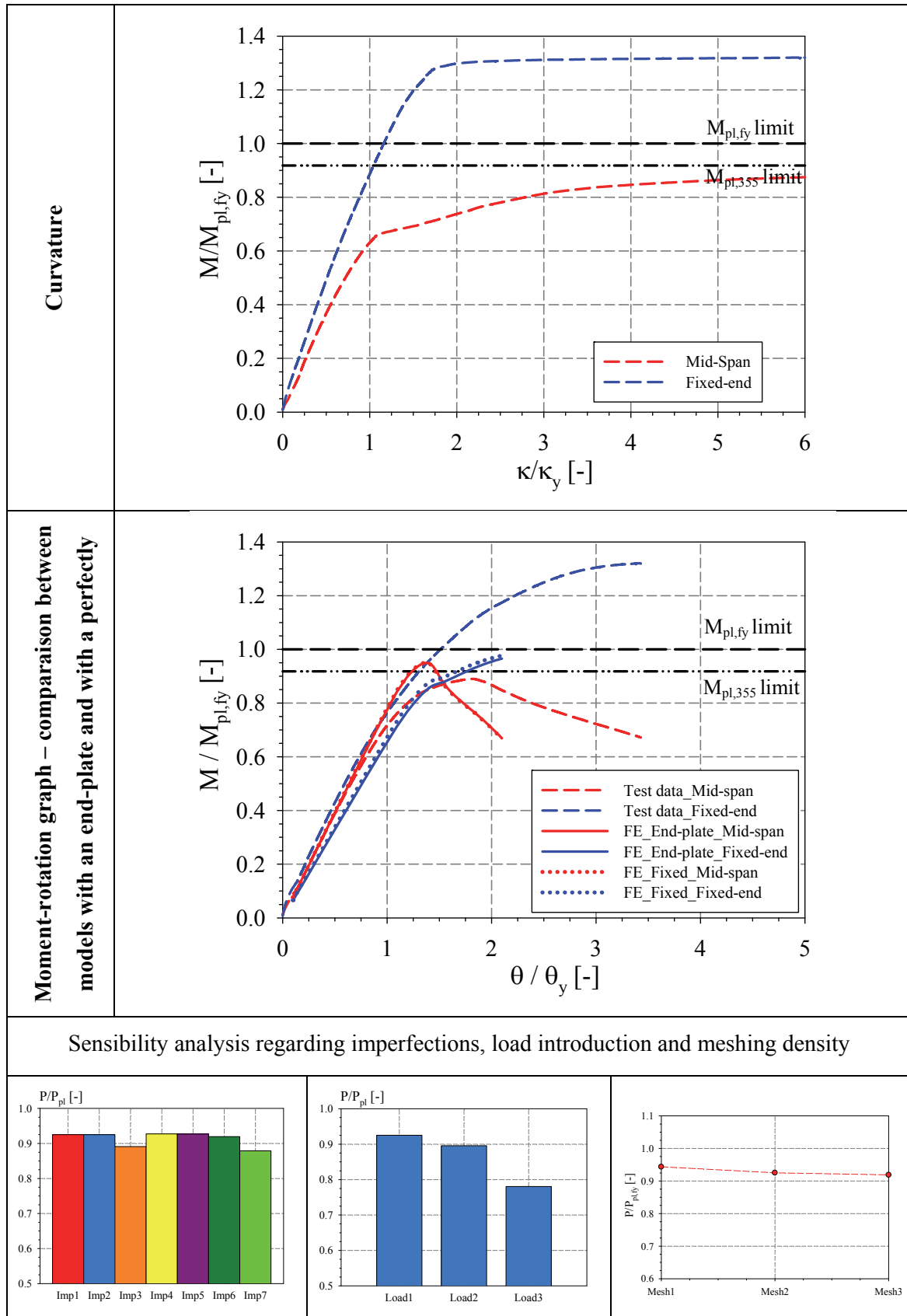


Yield pattern of RHS_180×80×4.5_PR_O at failure









11.3.8 Summary of stub columns results

11.3.8.1 Numerical model

Concerning the stub column tests, and in order to represent accurately the experimental behaviour of the specimens, a suitable corresponding F.E. model, developed by Nseir, 2015, was used for the validation of the 8 hot-finished stub columns tests. The cross section was represented using 4 linear shell elements per corner. Rigid plates of 80 mm thickness were modelled on the specimens' ends with shell elements that remain elastic during loading, in order to prevent their yielding. Trusses were connected to the rigid end plates nodes and to a specified centrally positioned node where the load was applied (see Figure 11.10). The plate thickness allowed it to be stiff enough to allow an even distribution of the applied load at the sections ends and prevent their deformation.

Measured geometrical dimensions and material properties were introduced along the section. Only local geometrical imperfections were introduced through an appropriate modification of node coordinates with adequate sine waves equations in both direction of the considered plate (square half wave pattern). The sine-wave period was taken for both web and flanges as the average of their widths. The amplitude of the “half-wave” patterns was $a / 200$ for each plate element individually with a reduction of 30% as prescribed in EC3 since auto-equilibrated residual stress patterns were introduced. Moreover a fine meshing was used that provided satisfactory accuracy.

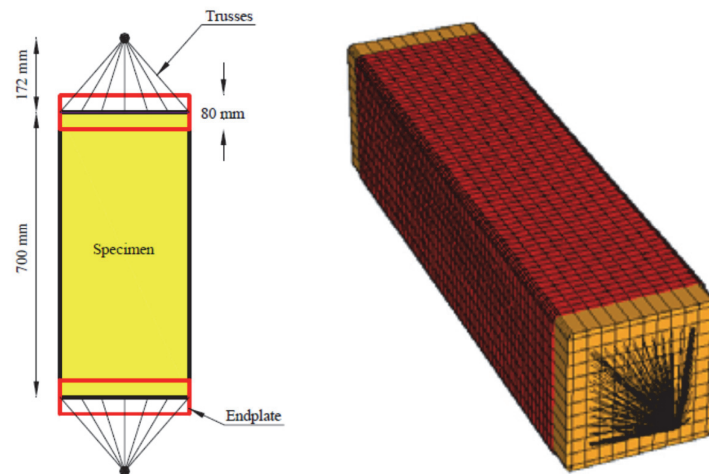


Figure 11.10 – Finite element model assumptions (Nseir, 2015)

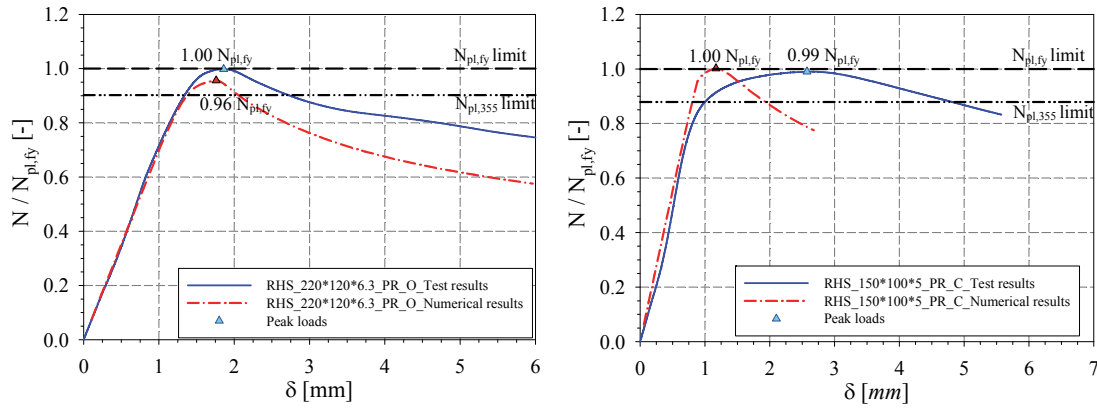


Figure 11.11 – Stub columns numerical vs. test results for normalized load-end displacement curves

The results for all specimens showed that all the load-displacement curves coincide in the elastic range indicating that the F.E. model simulates well the stiffness of the tested specimen (see Figure 11.11), the inaccuracies noticed are attributed to the measured young's modulus, representation of the test setup, loading introduction, residual stresses... Moreover, good agreement was reached in terms of ultimate load with a maximum deviation of 4%, except for the case of the RHS_150×100×8, where strain hardening was not reached in the numerical model. Concerning the displacement value at ultimate loading, a good concordance was shown between F.E. and test result except for the case of the RHS_150×100×5 displayed in Figure 11.11b. This divergence is explained by the effect of local geometrical imperfections that have a major influence in the case of hollow section in the plastic and post-peak range. Maximum reached values for all specimens are summarized in Table 11.3 below and a graphical comparison of the ultimate loads and displacement of the FE simulations and of the experiments are shown in Figure 11.12 and Figure 11.13 , the red dashed line indicates a deviation of +/- 10%.

Table 11.3 – Comparison of numerical and experimental ultimate loads and displacements

Test specimen	$N_{pl,fy}$	$F_{ult,exp}$	$F_{ult,num}$	$F_{ult,exp} / F_{ult,exp}$	$\delta_{ult,exp}$	$\delta_{ult,num}$	$\delta_{ult,exp} / \delta_{ult,num}$
	[kN]	[kN]	[kN]	[-]	[mm]	[mm]	[-]
RHS_150×100×8_Stub_(PR_C)	1440.56	1807.2	1449.2	1.25	14.78	7.65	1.93
RHS_180×80×4.5_Stub_(PR_C)	861.62	822.6	797.5	1.03	1.53	1.19	1.29
RHS_180×80×4.5_Stub_(PR_O)*	856.49	805.6	794.6	1.01	1.31	1.19	1.11
RHS_150×100×5_Stub_(PR_C)	952.58	943.4	954.4	0.99	2.57	1.17	2.20
SHS_220×120×6.3_Stub_(PR_C)*	1577.5	1577.5	1543.4	1.02	1.65	1.78	0.93
SHS_220×120×6.3_Stub_(PR_O)	1604.50	1613.7	1546.4	1.04	1.86	1.76	1.06
SHS_180×6.3_Stub_(PR_C)*	1604.5	1749.8	1726.7	1.01	1.70	1.48	1.15

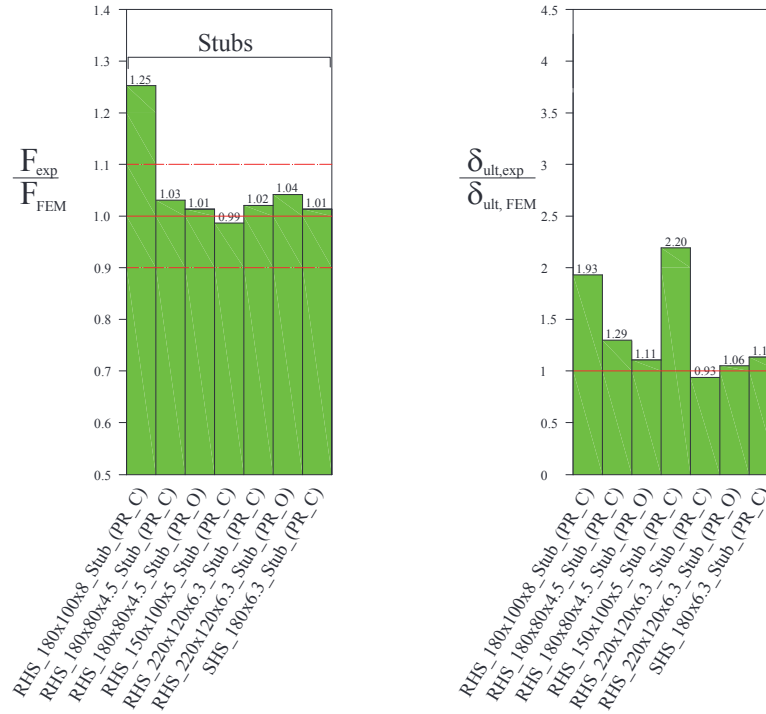


Figure 11.12 – Comparison of numerical vs. test results for Stub columns

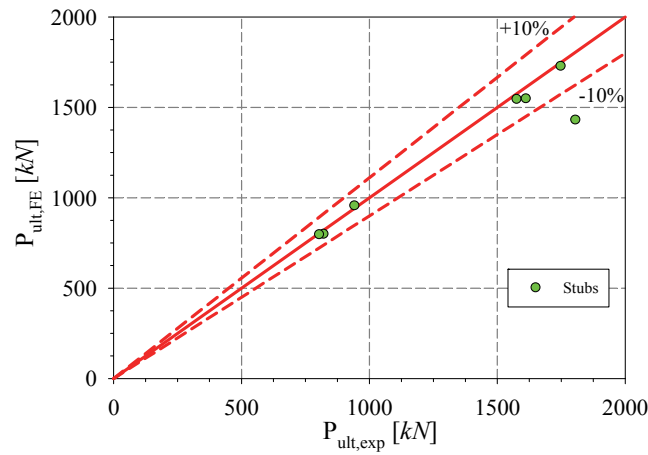
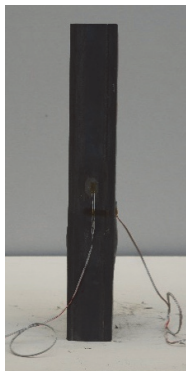
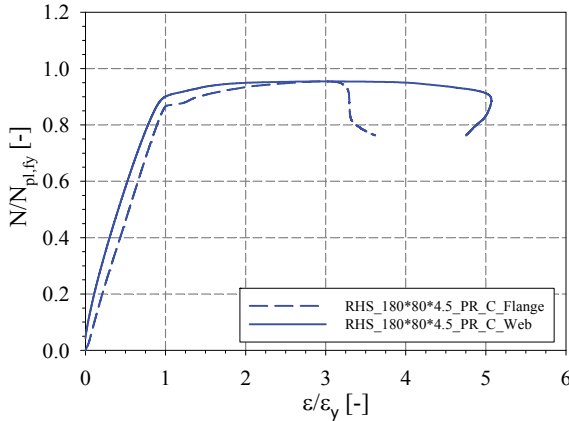
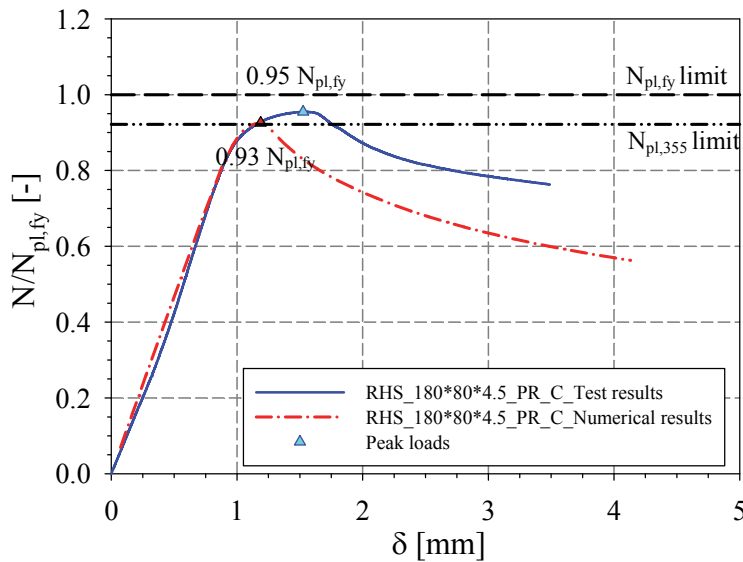
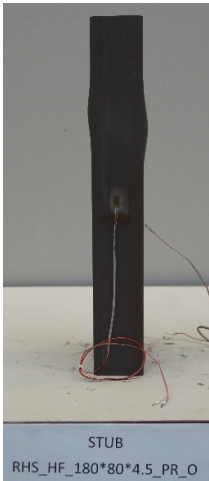
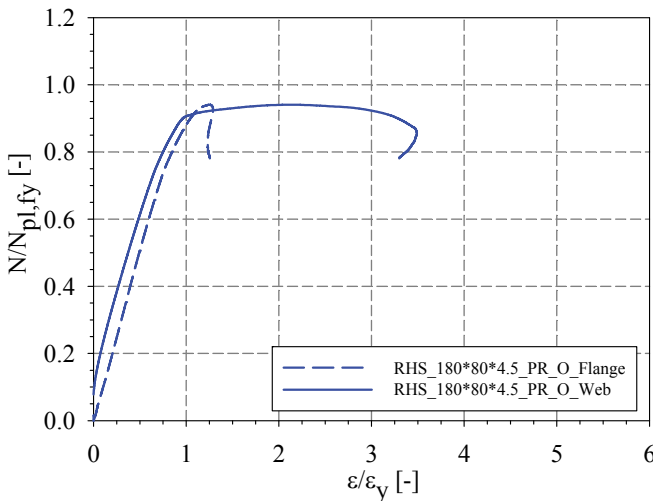
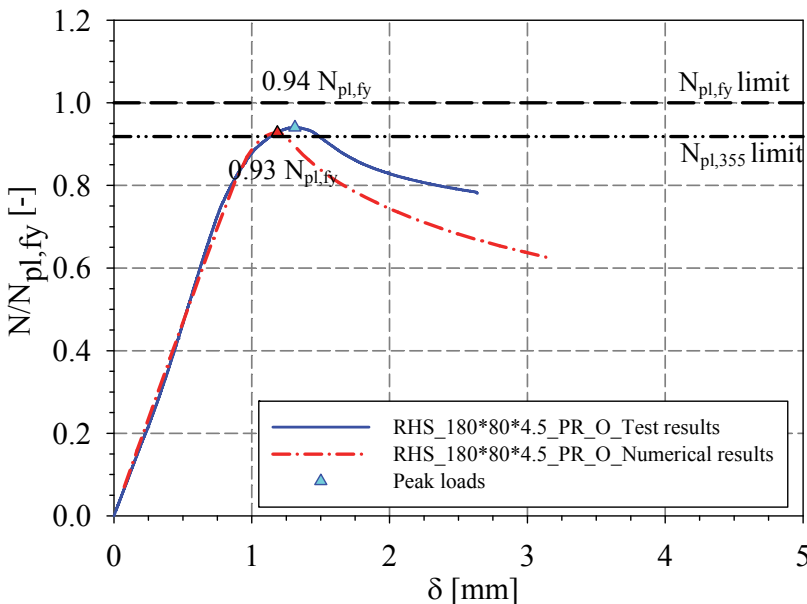


Figure 11.13 – F.E. ultimate loads vs. experimental ultimate loads for stubs

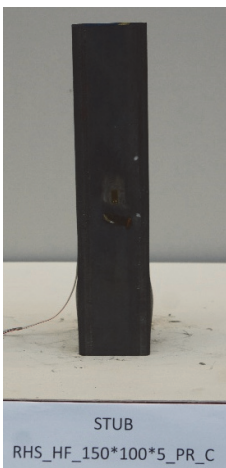
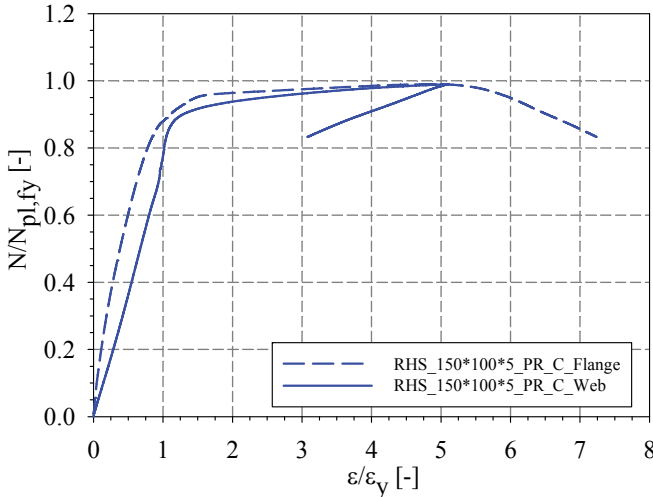
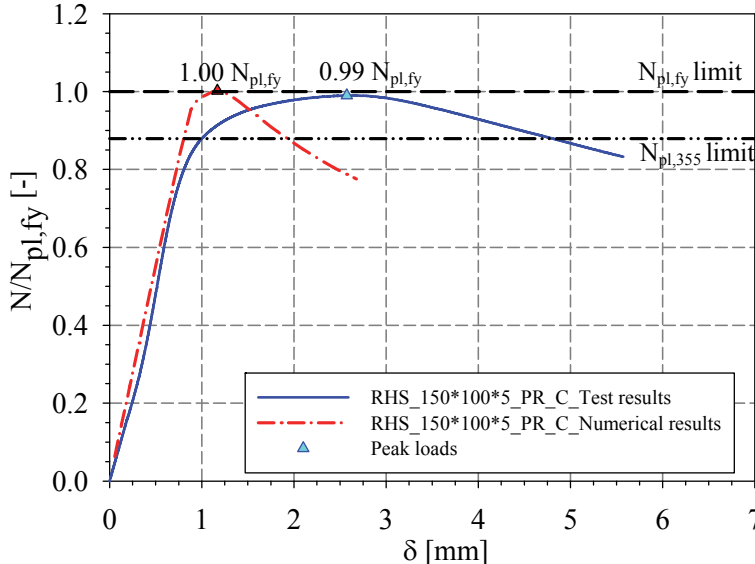
11.3.8.2 STUB_RHS_180×80×4.5_PR_C

Specimen name	Details	Measured material properties (average)
STUB_RHS_180×80×4.5_PR_C Fabrication process: Hot-rolled	Steel grade: 355 N/mm ² Load case: Stub column $h_{mes} = 179.19$ mm $b_{mes} = 79.06$ mm $t_{mes} = 4.76$ mm	$f_y = 403.9$ N/mm ² $f_u = 547.3$ N/mm ² $E = 213062$ N/mm ² $\varepsilon_y = 0.19$ % $\varepsilon_{y2} = 1.93$ % $\varepsilon_u = 16.68$ %
STUB_RHS_180×80×4.5_PR_C at failure  <div>STUB RHS_HF_180*80*4.5_PR_C</div>	Normalised Load versus Strain recorded by gauges 	
Normalised Load - Deflection graph 		

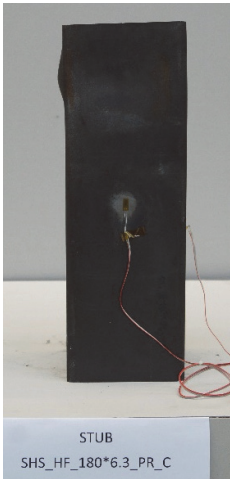
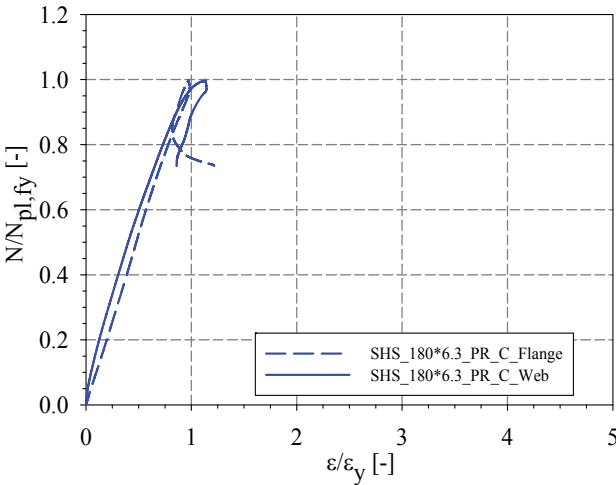
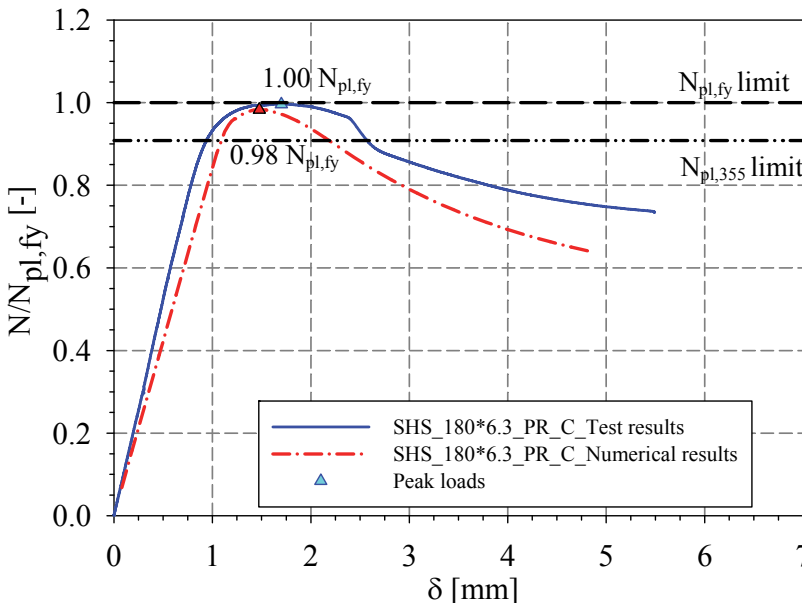
11.3.8.3 STUB_RHS_180×80×4.5_PR_O

Specimen name	Details	Measured material properties (average)
STUB_RHS_180×80×4.5_PR_O Fabrication process: Hot-rolled	Steel grade: 355 N/mm ² Load case: Stub column h_{mes} = 178.96 mm b_{mes} = 79.45 mm t_{mes} = 4.63 mm	f_y = 386.6 N/mm ² f_u = 537.1 N/mm ² E = 205414 N/mm ² ε_y = 0.19 % ε_{y2} = 1.85 % ε_u = 18.47 %
STUB_RHS_180×80×4.5_PR_O at failure 	Normalised Load versus Strain recorded by gauges 	
Normalised Load - Deflection graph 		

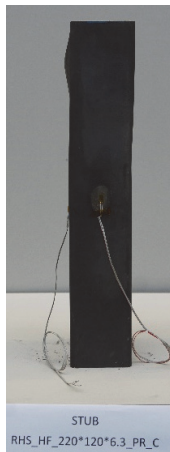
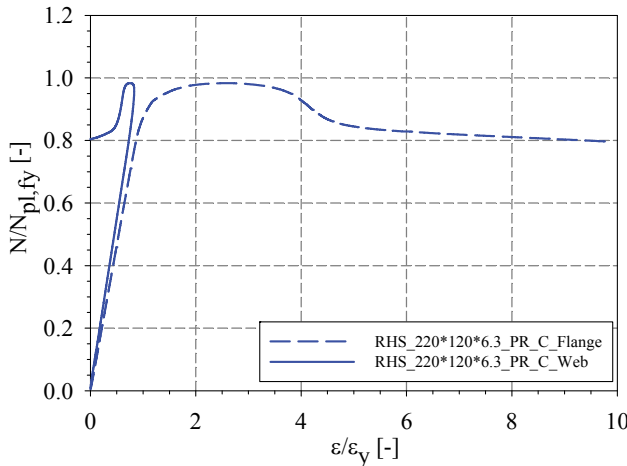
11.3.8.4 STUB_RHS_150x100x5_PR_C

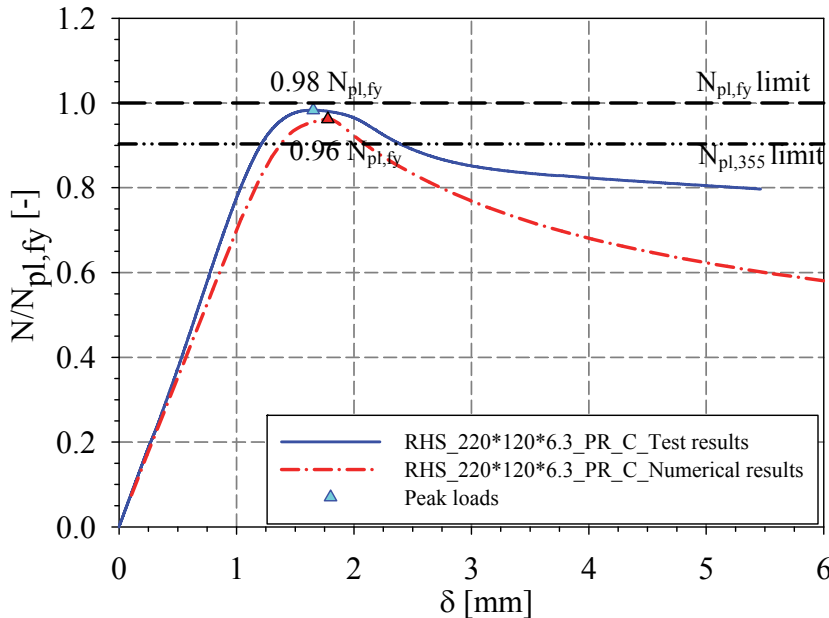
Specimen name	Details	Measured material properties (average)
STUB_RHS_150×100×5_PR_C Fabrication process: Hot-rolled	Steel grade: 355 N/mm ² Load case: Stub column h_{mes} = 148.78 mm b_{mes} = 99.49 mm t_{mes} = 5.20 mm	f_y = 396.5 N/mm ² f_u = 552.7 N/mm ² E = 203267 N/mm ² ε_y = 0.20 % ε_{y2} = 1.72 % ε_u = 12.61 %
STUB_RHS_150×100×5_PR_C at failure 	Normalised Load versus Strain recorded by gauges 	
Normalised Load - Deflection graph 		

11.3.8.5 STUB_SHS_180x6.3_PR_C

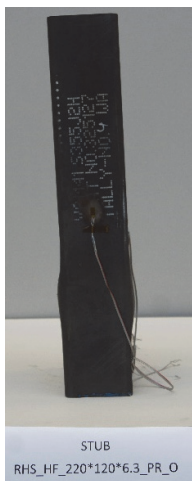
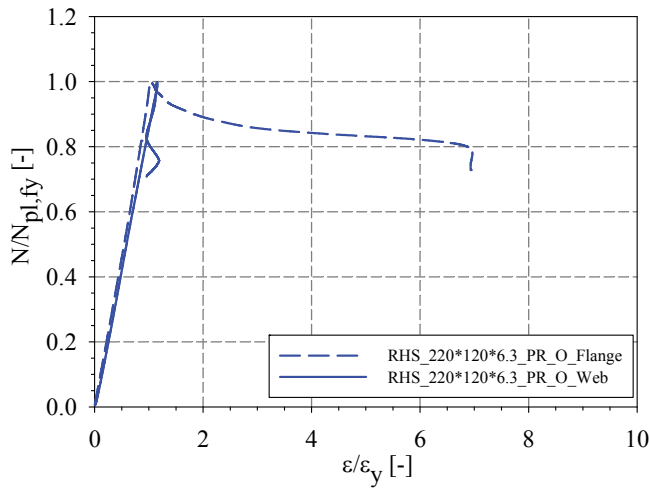
Specimen name	Details	Measured material properties (average)
STUB_SHS_180×6.3_PR_C Fabrication process: Hot-rolled	Steel grade: 355 N/mm ² Load case: Stub column h_{mes} = 179.44 mm b_{mes} = 179.70 mm t_{mes} = 6.72 mm	f_y = 390.9 N/mm ² f_u = 532.2 N/mm ² E = 206819 N/mm ² ε_y = 0.19 % ε_{y2} = 1.79 % ε_u = 17.62 %
STUB_SHS_180×6.3_PR_C at failure 	Normalised Load versus Strain recorded by gauges 	
Normalised Load - Deflection graph 		

11.3.8.6 STUB_RHS_220×120×6.3_PR_C

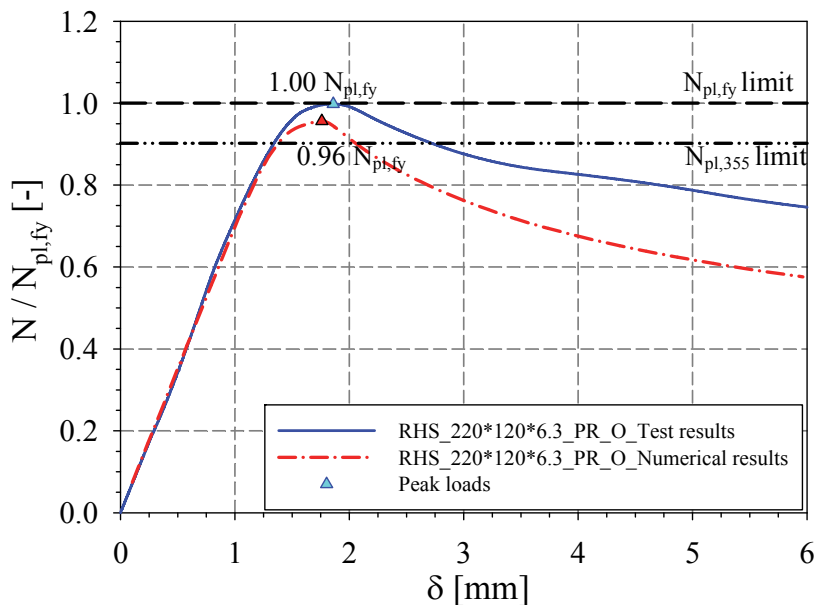
Specimen name	Details	Measured material properties (average)
STUB_RHS_220×120×6.3_PR_C Fabrication process: Hot-rolled	Steel grade: 355 N/mm ² Load case: Stub column $h_{mes} = h = 219.10$ mm $b_{mes} = 120.45$ mm $t_{mes} = 6.51$ mm	$f_y = 393.0$ N/mm ² $f_u = 531.8$ N/mm ² $E = 202440$ N/mm ² $\varepsilon_y = 0.19$ % $\varepsilon_{y2} = 1.83$ % $\varepsilon_u = 17.16$ %
STUB_RHS_220×120×6.3_PR_C at failure 	Normalised Load versus Strain recorded by gauges 	

Normalised Load - Deflection graph	
	

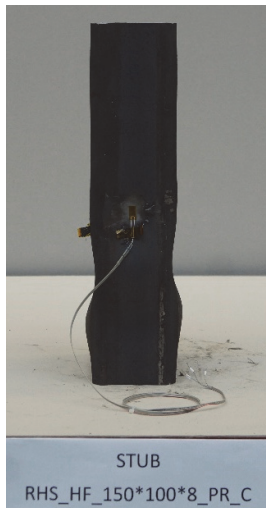
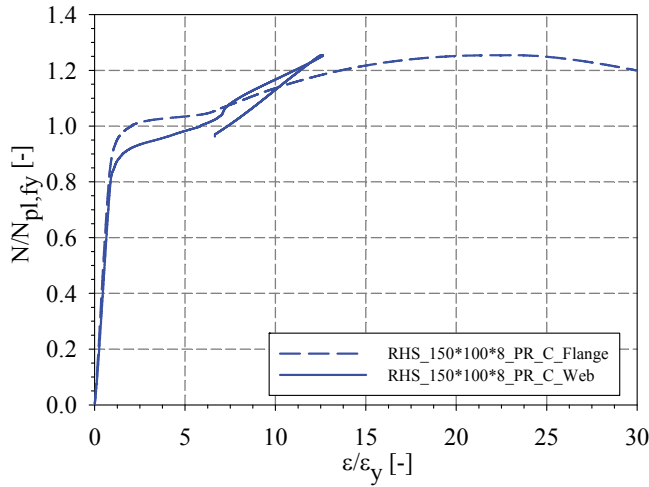
11.3.8.7 STUB_RHS_220×120×6.3_PR_O

Specimen name	Details	Measured material properties (average)
STUB_RHS_220×120×6.3_PR_O Fabrication process: Hot-rolled	Steel grade: 355 N/mm ² Load case: Stub column h_{mes} = 219.03 mm b_{mes} = 120.66 mm t_{mes} = 6.51 mm	f_y = 393.6 N/mm ² f_u = 533.2 N/mm ² E = 210347 N/mm ² ε_y = 0.19 % ε_{y2} = 1.84 % ε_u = 18.58 %
STUB_RHS_220×120×6.3_PR_O at failure 	Normalised Load versus Strain recorded by gauges 	

Normalised Load - Deflection graph



11.3.8.8 STUB_RHS_150×100×8_PR_C

Specimen name	Details	Measured material properties (average)
STUB_RHS_150×100×8_PR_C Fabrication process: Hot-rolled	Steel grade: 355 N/mm ² Load case: Stub column <i>h_{mes}</i> = 149.48 mm <i>b_{mes}</i> = 99.86 mm <i>t_{mes}</i> = 8.16 mm	<i>f_y</i> = 385.2 N/mm ² <i>f_u</i> = 527.3 N/mm ² <i>E</i> = 207854 N/mm ² <i>ε_y</i> = 0.19 % <i>ε_{y2}</i> = 1.78 % <i>ε_u</i> = 19.66 %
STUB_RHS_150×100×8_PR_C at failure 	Normalised Load versus Strain recorded by gauges 	

Normalised Load - Deflection graph

